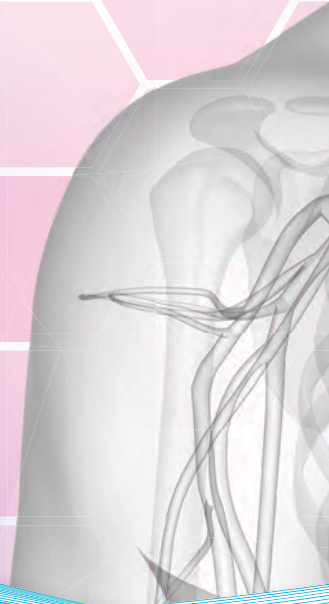


MicroVention®
TERUMO

*Leading the Way
in Neuroendovascular Therapy*

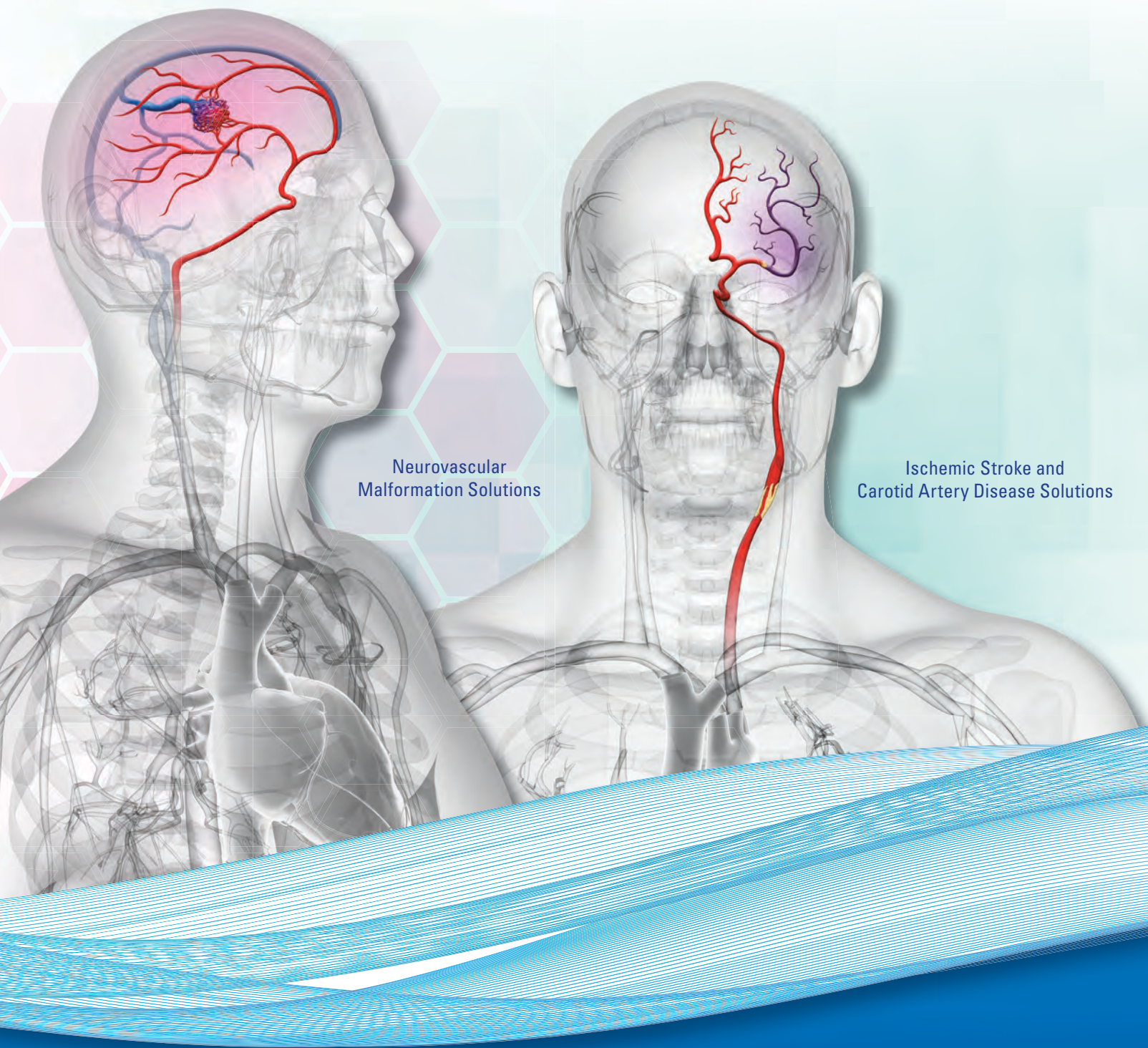
Aneurysm
Therapy Solutions



A 360-Degree Approach to

microvention.com

MICROVENTION is a registered trademark of MicroVention, Inc. Refer to Instructions for Use for additional information.
© 2016 MicroVention, Inc. 08/16



Neurovascular
Malformation Solutions

Ischemic Stroke and
Carotid Artery Disease Solutions

Performance Based Solutions

For more information or a product demonstration,
contact your local MicroVention representative:



MicroVention, Inc.
Worldwide Headquarters
1311 Valencia Avenue
Tustin, CA 92780 USA
MicroVention UK Limited
MicroVention Europe, S.A.R.L.
MicroVention Deutschland GmbH

PH +1.714.247.8000

PH +44 (0) 191 258 6777

PH +33 (1) 39 21 77 46

PH +49 211 210 798-0



ENGINEERING STROKE SOLUTIONS

Broad variety of optimal treatment options –
all from one source

ACUTE STROKE CARE

APERIO® Thrombectomy Device

For fast flow restoration

NeuroSlider® Microcatheter

For smooth and reliable device delivery

NeuroBridge® Intermediate Catheter

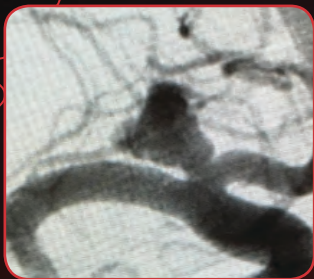
For support and aspiration

Not for sale within the territory of the United States

BARRICADE™ COIL SYSTEM

COILS THAT PERFORM

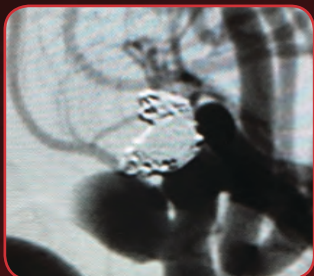
Treatment and 10 Month Follow-up of Right ICA Terminus Aneurysm and Left Pcom Aneurysm



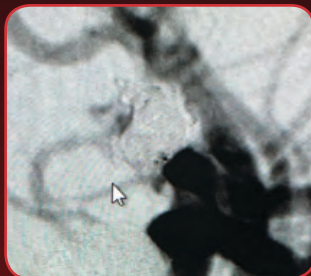
PRE-TREATMENT RIGHT ICA



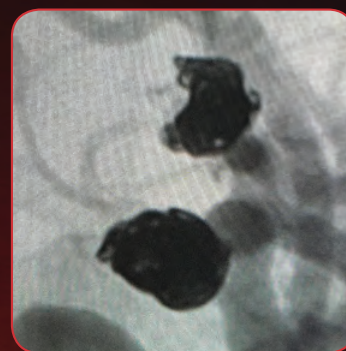
POST-TREATMENT RIGHT ICA



PRE-TREATMENT LEFT PCOM



POST-TREATMENT LEFT PCOM



10 MONTH FOLLOW-UP

“The Barricade Coil System provided great versatility in treating these two aneurysms with diverse morphologies. I am impressed with the stable and complete occlusion of both aneurysms at follow-up.”

-Timothy Malisch, M.D.

COILS THAT SAVE \$

BARRICADE
COILS
**SAVED
\$6,710***

Images courtesy of Timothy Malisch, M.D.

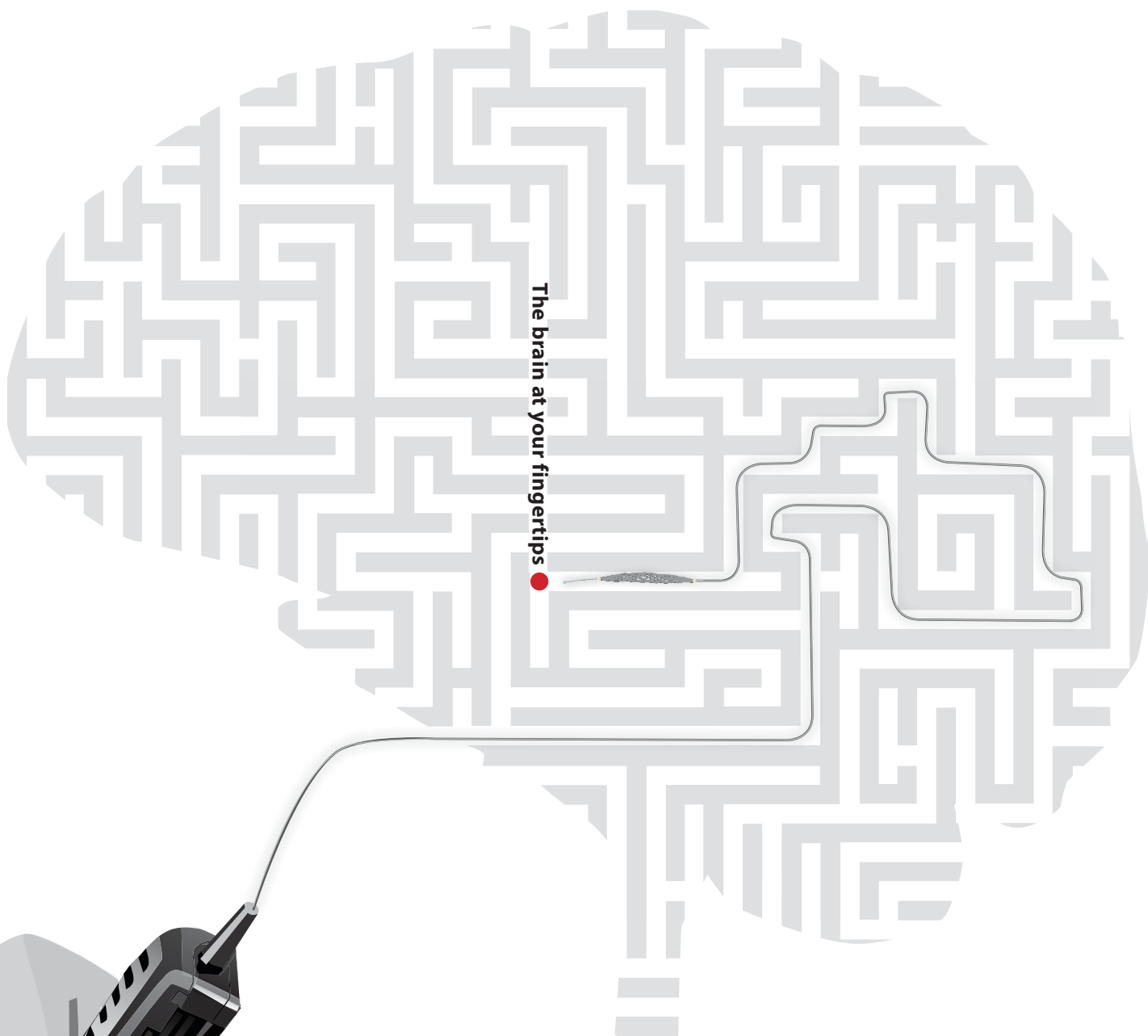
* Estimated savings in this case, data on file.

The Barricade Coil System is intended for the endovascular embolization of intracranial aneurysms and other neurovascular abnormalities such as arteriovenous malformations and arteriovenous fistulae. The System is also intended for vascular occlusion of blood vessels within the neurovascular system to permanently obstruct blood flow to an aneurysm or other vascular malformation and for arterial and venous embolizations in the peripheral vasculature. Refer to the instructions for use for complete product information.

18 TECHNOLOGY DRIVE #169, IRVINE CA 92618 | p: 949.788.1443 | f: 949.788.1444
WWW.BLOCKADEMEDICAL.COM

MKTG-060 Rev. A





 **Rapid Medical**

www.rapid-medical.com > tigertriever

Smooth and stable.

Target Detachable Coils deliver consistently smooth deployment and exceptional microcatheter stability. Designed to work seamlessly together for framing, filling and finishing. Target Coils deliver the high performance you demand.

For more information, please visit www.strykerneurovascular.com/Target or contact your local Stryker Neurovascular sales representative.



Target[®]
DETACHABLE COILS



Simplify the MOC Process



Manage your CME Credits Online

CMEgateway.org

Available to Members of Participating Societies

American Board of Radiology (ABR)
American College of Radiology (ACR)
American Roentgen Ray Society (ARRS)
American Society of Neuroradiology (ASNR)
Commission on Accreditation of Medical
Physics Educational Programs, Inc. (CAMPEP)
Radiological Society of North America (RSNA)
Society of Interventional Radiology (SIR)
SNM
The Society for Pediatric Radiology (SPR)

It's Easy and Free!

Log on to CME Gateway to:

- View or print reports of your CME credits from multiple societies from a single access point.
- Print an aggregated report or certificate from each participating organization.
- Link to SAMs and other tools to help with maintenance of certification.

American Board of Radiology (ABR) participation!

By activating ABR in your organizational profile, your MOC-fulfilling CME and SAM credits can be transferred to your own personalized database on the ABR Web site.

Sign Up Today!

go to CMEgateway.org

The Foundation of the ASNR Symposium 2017: *Discovery and Didactics* April 22-23, 2017

ASNR 55th Annual Meeting: *Diagnosis and Delivery* April 24-27, 2017



Long Beach Convention & Entertainment Center
© Long Beach Convention & Visitors Bureau

Jacqueline A. Bello, MD, FACR
ASNR 2017 Program Chair/President-Elect

*Programming developed in cooperation with and
appreciation of the...*

American Society of Functional Neuroradiology (ASFNR)

Kirk M. Welker, MD

American Society of Head and Neck Radiology (ASHNR)

Rebecca S. Cornelius, MD, FACR

American Society of Pediatric Neuroradiology (ASPNR)

Susan Palasis, MD

American Society of Spine Radiology (ASSR)

Joshua A. Hirsch, MD, FACR, FSIR

Society of NeuroInterventional Surgery (SNIS)

Blaise W. Baxter, MD

American Society of Neuroradiology (ASNR)

Health Policy Committee

Robert M. Barr, MD, FACR

Computer Sciences & Informatics (CSI) Committee

John L. Go, MD, FACR

Research Scientist Committee

Dikoma C. Shungu, PhD and Timothy, P.L. Roberts, PhD

**The International Hydrocephalus Imaging Working Group
(IHIWG)/CSF Flow Group**

William G. Bradley, Jr., MD, PhD, Harold L. Rekate, MD
and Bryn A. Martin, PhD

Abstract Deadline: Friday, December 9, 2016
Please visit www.asnr.org/2017 for more information



ASNR 55th Annual Meeting

c/o American Society of Neuroradiology
800 Enterprise Drive, Suite 205 • Oak Brook, Illinois 60523-4216
Phone: 630-574-0220 • Fax: 630 574-0661 • www.asnr.org/2017



ASFNR ASHNR ASPNR ASSR SNIS

THE FOUNDATION OF THE ASNR 

Come to the beach! Please join us in Long Beach, California, April 22-27, 2017, for the 55th Annual Meeting of the ASNR. Known for its 5.5 miles of Pacific Ocean waterfront, this southern California beach resort boasts a blend of city sophistication and seaside serenity. ASNR is delighted to provide a “4D” focus for this meeting, as depicted by our meeting logo: **Discovery and Didactics** for The Foundation of the ASNR Symposium 2017: **Diagnosis and Delivery** for the ensuing Annual Meeting Program.

Centered on Discovery and Didactics, the symposium will feature sessions on “What’s New?” in the role neuroimaging plays defining CNS disease mechanisms and how to best prepare for “What’s Next?” for our subspecialty in terms of training, teaching, and leading the process of lifelong learning. The annual meeting programming will address best practices in Diagnosis and Delivery, as we strive to provide value, promote quality in better health and care and consider cost. Our discussions will consider how to navigate the changing landscape of healthcare reform and reimbursement as subspecialists in a field that is changing at an equally “fast forward” pace!



Hyatt Regency Long Beach
© Hyatt Regency Long Beach



Westin Long Beach
© The Westin Long Beach

Go Green!

AJNR urges American Society of Neuroradiology members to reduce their environmental footprint by voluntarily suspending their print subscription.

The savings in paper, printing, transportation, and postage not only help members cut down on clutter, but go to fund new electronic enhancements and expanded content.

The digital edition of *AJNR* presents the print version in its entirety, along with extra features including:

- Publication Preview
- Case of the Week
- Podcasts
- Special Collections
- The *AJNR* Blog
- Weekly Poll

It also **reaches subscribers much faster than print**. An **electronic table of contents** will be sent directly to your mailbox to notify you as soon as it publishes.

Readers can **search, reference, and bookmark** current and archived content 24 hours a day on www.ajnr.org, rather than thumb through stacks of accumulated paper issues for articles and images they need.



<http://www.ajnr.org/cgi/feedback>

ASNR members who wish to opt out of print can do so by using the Feedback form on the *AJNR* Website (<http://www.ajnr.org/cgi/feedback>). Just type "Go Green" in the subject line to stop print and spare our ecosystem.

All the clinical evidence you need.

DynaMed Plus® is a member benefit for AMA individual members and
JAMA Network individual registered users



The American Medical Association and *DynaMed Plus* are joining forces. Now, AMA individual members and JAMA Network individual registered users get complimentary access to the most current clinical evidence available with *DynaMed Plus*, the next-generation clinical information resource.

Sign up today at
DynaMedPlusAMAOffer.com



The **JAMA** Network®

DynaMed Plus®
EBSCO Health

AXS Catalyst™ Distal Access Catheter

See package insert for complete indications, complications, warnings, and instructions for use.

INTENDED USE/INDICATIONS FOR USE

The AXS Catalyst Distal Access Catheter is indicated for use in facilitating the insertion and guidance of appropriately sized interventional devices into a selected blood vessel in the peripheral and neurovascular systems. The AXS Catalyst Distal Access Catheter is also indicated for use as a conduit for retrieval devices.

CONTRAINDICATIONS

None known.

ADVERSE EVENTS

Potential adverse events associated with the use of catheters or with the endovascular procedures include, but are not limited to: access site complications, allergic reaction, aneurysm perforation, aneurysm rupture, death, embolism (air, foreign body, plaque, thrombus), hematoma, hemorrhage, infection, ischemia, neurological deficits, pseudoaneurysm, stroke, transient ischemic attack, vasospasm, vessel dissection, vessel occlusion, vessel perforation, vessel rupture, and vessel thrombosis.

WARNING

Contents supplied sterile using an ethylene oxide (EO) process. Do not use if sterile barrier is damaged. If damage is found, call your Stryker Neurovascular representative. For single use only. Do not reuse, reprocess or resterilize. Reuse, reprocessing or resterilization may compromise the structural integrity of the device and/or lead to device failure which, in turn, may result in patient injury, illness or death. Reuse, reprocessing or resterilization may also create a risk of contamination of the device and/or cause patient infection or cross-infection, including, but not limited to, the transmission of infectious disease(s) from one patient to another.

Contamination of the device may lead to injury, illness or death of the patient. After use, dispose of product and packaging in accordance with hospital, administrative and/or local government policy.

- Limited testing has been performed with solutions such as contrast media, and saline. The use of these catheters for delivery of solutions other than the types that have been tested for compatibility is not recommended.
- Not intended for use with power injectors.
- If flow through catheter becomes restricted, do not attempt to clear catheter lumen by infusion. Doing so may cause catheter damage or patient injury. Remove and replace catheter.

- Never advance or withdraw an intravascular device against resistance until the cause of the resistance is determined by fluoroscopy. Movement of the device against resistance could dislodge a clot, perforate a vessel wall, or damage the device.

PRECAUTIONS

- Carefully inspect all devices prior to use. Verify size, length, and condition are suitable for the specific procedure. Do not use a device that has been damaged in any way. Damaged device may cause complications.
- To control the proper introduction, movement, positioning and removal of the catheter within the vascular system, users should employ standard clinical angiographic and fluoroscopic practices and techniques throughout the interventional procedure.
- Use the product prior to the "Use By" date printed on the label.
- To prevent thrombus formation and contrast media crystal formation, maintain a constant infusion of appropriate flush solution through catheter lumen.
- Torquing the catheter may cause damage which could result in kinking or separation of the catheter shaft.

Trevo® XP ProVue Retrievers

See package insert for complete indications, complications, warnings, and instructions for use.

INDICATIONS FOR USE

The Trevo Retriever is intended to restore blood flow in the neurovasculature by removing thrombus in patients experiencing ischemic stroke within 8 hours of symptom onset. Patients who are ineligible for intravenous tissue plasminogen activator (IV t-PA) or who fail IV t-PA therapy are candidates for treatment.

COMPLICATIONS

Procedures requiring percutaneous catheter introduction should not be attempted by physicians unfamiliar with possible complications which may occur during or after the procedure. Possible complications include, but are not limited to, the following: air embolism; hematoma or hemorrhage at puncture site; infection; distal embolization; pain/headache; vessel spasm, thrombosis, dissection, or perforation; emboli; acute occlusion; ischemia; intracranial hemorrhage; false aneurysm formation; neurological deficits including stroke; and death.

COMPATIBILITY

3x20mm retrievers are compatible with Trevo® Pro 14 Microcatheters (REF 90231) and Trevo® Pro 18 Microcatheters (REF 90238). 4x20mm retrievers are compatible with Trevo® Pro 18

Microcatheters (REF 90238). 4x30mm retrievers are compatible with Excelsior® XT-27® Microcatheters (150cm x 6cm straight REF 275081) and Trevo® Pro 18 Microcatheters (REF 90238). 6x25mm Retrievers are compatible with Excelsior® XT-27® Microcatheters (150cm x 6cm straight REF 275081). Compatibility of the Retriever with other microcatheters has not been established. Performance of the Retriever device may be impacted if a different microcatheter is used. Balloon Guide Catheters (such as Merci® Balloon Guide Catheter and FlowGate® Balloon Guide Catheter) are recommended for use during thrombus removal procedures. Retrievers are compatible with the Abbott Vascular DOC® Guide Wire Extension (REF Z2260). Retrievers are compatible with Boston Scientific RHV (Ref 421242).

WARNINGS

- Contents supplied STERILE, using an ethylene oxide (EO) process. Nonpyrogenic.
- To reduce risk of vessel damage, adhere to the following recommendations:
 - Take care to appropriately size Retriever to vessel diameter at intended site of deployment.
 - Do not perform more than six (6) retrieval attempts in same vessel using Retriever devices.
 - Maintain Retriever position in vessel when removing or exchanging Microcatheter.
- To reduce risk of kinking/fracture, adhere to the following recommendations:
 - Immediately after unsheathing Retriever, position Microcatheter tip marker just proximal to shaped section. Maintain Microcatheter tip marker just proximal to shaped section of Retriever during manipulation and withdrawal.
 - Do not rotate or torque Retriever.
 - Use caution when passing Retriever through stented arteries.
- Do not resterilize and reuse. Structural integrity and/or function may be impaired by reuse or cleaning.
- The Retriever is a delicate instrument and should be handled carefully. Before use and when possible during procedure, inspect device carefully for damage. Do not use a device that shows signs of damage. Damage may prevent device from functioning and may cause complications.
- Do not advance or withdraw Retriever against resistance or significant vasospasm. Moving or torquing device against resistance or significant vasospasm may result in damage to vessel or device. Assess cause of resistance

using fluoroscopy and if needed resheath the device to withdraw.

- If Retriever is difficult to withdraw from the vessel, do not torque Retriever. Advance Microcatheter distally, gently pull Retriever back into Microcatheter, and remove Retriever and Microcatheter as a unit. If undue resistance is met when withdrawing the Retriever into the Microcatheter, consider extending the Retriever using the Abbott Vascular DOC guidewire extension (REF Z2260) so that the Microcatheter can be exchanged for a larger diameter catheter such as a DAC® catheter. Gently withdraw the Retriever into the larger diameter catheter.
- Administer anti-coagulation and anti-platelet medications per standard institutional guidelines.

PRECAUTIONS

- Prescription only – device restricted to use by or on order of a physician.
- Store in cool, dry, dark place.
- Do not use open or damaged packages.
- Use by "Use By" date.
- Exposure to temperatures above 54°C (130°F) may damage device and accessories. Do not autoclave.
- Do not expose Retriever to solvents.
- Use Retriever in conjunction with fluoroscopic visualization and proper anti-coagulation agents.
- To prevent thrombus formation and contrast media crystal formation, maintain a constant infusion of appropriate flush solution between guide catheter and Microcatheter and between Microcatheter and Retriever or guidewire.
- Do not attach a torque device to the shaped proximal end of DOC® Compatible Retriever. Damage may occur, preventing ability to attach DOC® Guide Wire Extension.



Stryker Neurovascular
47900 Bayside Parkway
Fremont, CA 94538

strykerneurovascular.com

Date of Release: MAY/2016

EX_EN_US

Copyright © 2016 Stryker
NV00020190.AA

Target® Detachable Coil

See package insert for complete indications, contraindications, warnings and instructions for use.

INTENDED USE / INDICATIONS FOR USE

Target Detachable Coils are intended to endovascularly obstruct or occlude blood flow in vascular abnormalities of the neurovascular and peripheral vessels.

Target Detachable Coils are indicated for endovascular embolization of:

- Intracranial aneurysms
- Other neurovascular abnormalities such as arteriovenous malformations and arteriovenous fistulae
- Arterial and venous embolizations in the peripheral vasculature

CONTRAINDICATIONS

None known.

POTENTIAL ADVERSE EVENTS

Potential complications include, but are not limited to: allergic reaction, aneurysm perforation and rupture, arrhythmia, death, edema, embolus, headache, hemorrhage, infection, ischemia, neurological/intracranial sequelae, post-embolization syndrome (fever, increased white blood cell count, discomfort), TIA/stroke, vasospasm, vessel occlusion or closure, vessel perforation, dissection, trauma or damage, vessel rupture, vessel thrombosis. Other procedural complications including but not limited to: anesthetic and contrast media risks, hypotension, hypertension, access site complications.

WARNINGS

- Contents supplied STERILE using an ethylene oxide (EO) process. Do not use if sterile barrier is damaged. If damage is found, call your Stryker Neurovascular representative.
- For single use only. Do not reuse, reprocess or resterilize. Reuse, reprocessing or resterilization may compromise the structural integrity of the device and/or lead to device failure which, in turn, may result in patient injury, illness or death. Reuse, reprocessing or resterilization may also create a risk of contamination of the device and/or cause patient infection or cross-infection, including, but not limited to, the transmission of infectious disease(s) from one patient to another. Contamination of the device may lead to injury, illness or death of the patient.

- After use, dispose of product and packaging in accordance with hospital, administrative and/or local government policy.
- **This device should only be used by physicians who have received appropriate training in interventional neuroradiology or interventional radiology and preclinical training on the use of this device as established by Stryker Neurovascular.**
- Patients with hypersensitivity to 316LVM stainless steel may suffer an allergic reaction to this implant.
- MR temperature testing was not conducted in peripheral vasculature, arteriovenous malformations or fistulae models.
- The safety and performance characteristics of the Target Detachable Coil System (Target Detachable Coils, InZone Detachment Systems, delivery systems and accessories) have not been demonstrated with other manufacturer's devices (whether coils, coil delivery devices, coil detachment systems, catheters, guidewires, and/or other accessories). Due to the potential incompatibility of non Stryker Neurovascular devices with the Target Detachable Coil System, the use of other manufacturer's device(s) with the Target Detachable Coil System is not recommended.

- To reduce risk of coil migration, the diameter of the first and second coil should never be less than the width of the ostium.
- In order to achieve optimal performance of the Target Detachable Coil System and to reduce the risk of thromboembolic complications, it is critical that a continuous infusion of appropriate flush solution be maintained between a) the femoral sheath and guiding catheter, b) the 2-tip microcatheter and guiding catheters, and c) the 2-tip microcatheter and Stryker Neurovascular guidewire and delivery wire. Continuous flush also reduces the potential for thrombus formation on, and crystallization of infusate around, the detachment zone of the Target Detachable Coil.
- Do not use the product after the "Use By" date specified on the package.
- Reuse of the flush port/dispenser coil or use with any coil other than the original coil may result in contamination of, or damage to, the coil.
- Utilization of damaged coils may affect coil delivery to, and stability inside, the vessel or aneurysm, possibly resulting in coil migration and/or stretching.
- The fluoro-saver marker is designed for use with a Rotating Hemostatic Valve (RHV). If used without an RHV, the distal end of the coil may be beyond the alignment

marker when the fluoro-saver marker reaches the microcatheter hub.

- If the fluoro-saver marker is not visible, do not advance the coil without fluoroscopy.
- Do not rotate delivery wire during or after delivery of the coil. Rotating the Target Detachable Coil delivery wire may result in a stretched coil or premature detachment of the coil from the delivery wire, which could result in coil migration.
- Verify there is no coil loop protrusion into the parent vessel after coil placement and prior to coil detachment. Coil loop protrusion after coil placement may result in thromboembolic events if the coil is detached.
- Verify there is no movement of the coil after coil placement and prior to coil detachment. Movement of the coil after coil placement may indicate that the coil could migrate once it is detached.
- Failure to properly close the RHV compression fitting over the delivery wire before attaching the InZone® Detachment System could result in coil movement, aneurysm rupture or vessel perforation.
- Verify repeatedly that the distal shaft of the catheter is not under stress before detaching the Target Detachable Coil. Axial compression or tension forces could be stored in the 2-tip microcatheter causing the tip to move during coil delivery. Microcatheter tip movement could cause the aneurysm or vessel to rupture.
- Advancing the delivery wire beyond the microcatheter tip once the coil has been detached involves risk of aneurysm or vessel perforation.
- The long term effect of this product on extravascular tissues has not been established so care should be taken to retain this device in the intravascular space.

Damaged delivery wires may cause detachment failures, vessel injury or unpredictable distal tip response during coil deployment. If a delivery wire is damaged at any point during the procedure, do not attempt to straighten or otherwise repair it. Do not proceed with deployment or detachment. Remove the entire coil and replace with undamaged product.

- After use, dispose of product and packaging in accordance with hospital, administrative and/or local government policy.

CAUTIONS / PRECAUTIONS

- Federal Law (USA) restricts this device to sale by or on the order of a physician.
- Besides the number of InZone Detachment System units needed to complete the case, there must be an extra

InZone Detachment System unit as back up.

- Removing the delivery wire without grasping the introducer sheath and delivery wire together may result in the detachable coil sliding out of the introducer sheath.
- Failure to remove the introducer sheath after inserting the delivery wire into the RHV of the microcatheter will interrupt normal infusion of flush solution and allow back flow of blood into the microcatheter.
- Some low level overhead light near or adjacent to the patient is required to visualize the fluoro-saver marker; monitor light alone will not allow sufficient visualization of the fluoro-saver marker.
- Advance and retract the Target Detachable Coil carefully and smoothly without excessive force. If unusual friction is noticed, slowly withdraw the Target Detachable Coil and examine for damage. If damage is present, remove and use a new Target Detachable Coil. If friction or resistance is still noted, carefully remove the Target Detachable Coil and microcatheter and examine the microcatheter for damage.
- If it is necessary to reposition the Target Detachable Coil, verify under fluoroscopy that the coil moves with a one-to-one motion. If the coil does not move with a one-to-one motion or movement is difficult, the coil may have stretched and could possibly migrate or break. Gently remove both the coil and microcatheter and replace with new devices.
- Increased detachment times may occur when:
 - Other embolic agents are present.
 - Delivery wire and microcatheter markers are not properly aligned.
 - Thrombus is present on the coil detachment zone.
- Do not use detachment systems other than the InZone Detachment System.
- Increased detachment times may occur when delivery wire and microcatheter markers are not properly aligned.
- Do not use detachment systems other than the InZone Detachment System.



Stryker Neurovascular
47900 Bayside Parkway
Fremont, CA 94538

strykerneurovascular.com

Date of Release: MAR/2016

EX_EN_US

Copyright © 2016 Stryker
NV00018669.AA

Take on tortuosity.

The **AXS Catalyst™ Distal Access Catheter** family is designed for easy navigation in challenging cases.



AXS Catalyst 6

DISTAL ACCESS CATHETER

for rapid revascularization with
Trepo[®] XP ProVue Retriever


AXS Catalyst 5

DISTAL ACCESS CATHETER

for flow diversion support



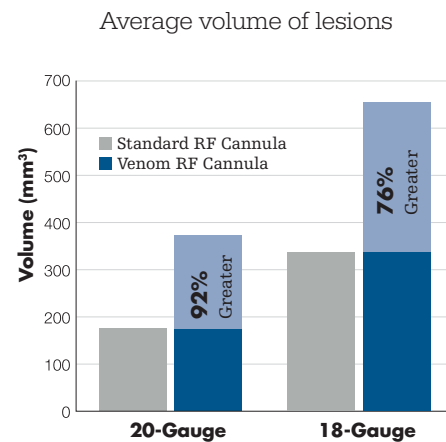
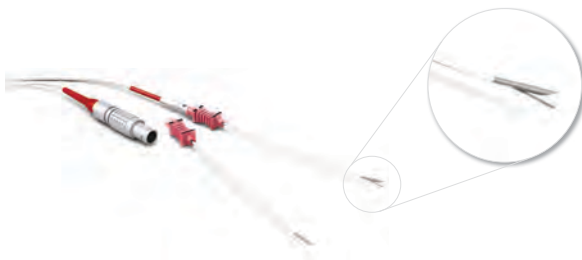
stryker



With the acquisition of the CareFusion vertebral compression fracture (VCF) portfolio from BD (Becton, Dickinson and Company), **Stryker has the most comprehensive and least invasive portfolio** of VCF treatment options

Celebrating two years of **excellence**

An elegant, cost effective approach to large lesions. The **Venom Cannula and Electrode combination** celebrates **two years of excellence** in helping you achieve larger RF lesions¹ to treat your patients suffering from chronic pain.



Stryker Corporation or its divisions or other corporate affiliated entities own, use or have applied for the following trademark: Venom. All other trademarks are trademarks of their respective owners or holders.

The information presented in this overview is intended to demonstrate the breadth of Stryker product offerings. Always refer to the package insert, product label and/or user instructions before using any Stryker product. Products may not be available in all markets. Product availability is subject to the regulatory or medical practices that govern individual markets. Please contact your Stryker representative if you have questions about the availability of Stryker products in your area.

¹ Effect of the Stryker Venom Cannula and Venom Electrode combination on Lesion Size and Anesthesia Delivery During Radiofrequency Ablation Stryker Instruments, 4100 East Milham Avenue, Kalamazoo, Michigan 49001.

strykerIVS.com

1000-025-340 Rev C

AJNR

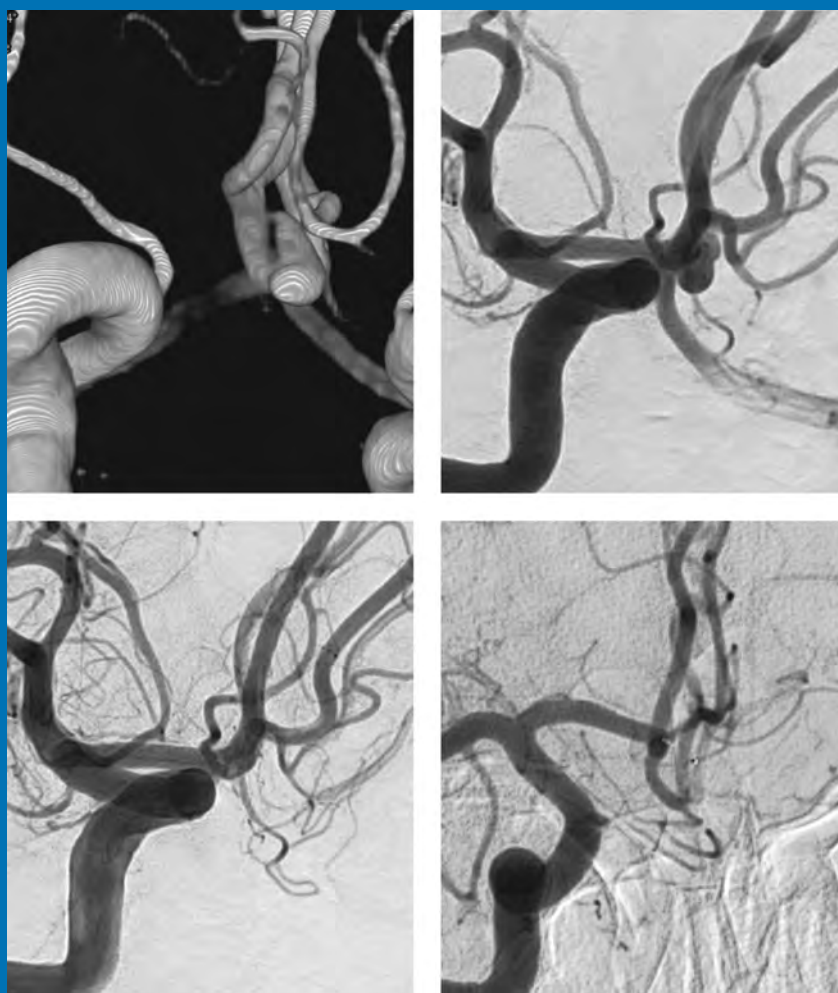
AMERICAN JOURNAL OF NEURORADIOLOGY

SEPTEMBER 2016
VOLUME 37
NUMBER 9
WWW.AJNR.ORG

THE JOURNAL OF DIAGNOSTIC AND
INTERVENTIONAL NEURORADIOLOGY

Treatment of vocal fold paralysis
WEB treatment of intracranial aneurysms
MR findings in uremic encephalopathy

Official Journal ASNR • ASFNR • ASHNR • ASPNR • ASSR



AJNR

AMERICAN JOURNAL OF NEURORADIOLOGY

SEPTEMBER 2016
VOLUME 37
NUMBER 9
WWW.AJNR.ORG



Publication Preview at www.ajnr.org features articles released in advance of print. Visit www.ajnrblog.org to comment on AJNR content and chat with colleagues and AJNR's News Digest at <http://ajnrndigest.org> to read the stories behind the latest research in neuroimaging.

1573 **PERSPECTIVES** M.I. Vargas and M.L. Vargas

REVIEW ARTICLE

-  1574 **"Finding a Voice": Imaging Features after Phonosurgical Procedures for Vocal Fold Paralysis** B.A. Vachha, et al. **HEAD & NECK**

METHODOLOGIC PERSPECTIVES

-   1581 **Response Assessment in Pediatric Neuro-Oncology: Implementation and Expansion of the RANO Criteria in a Randomized Phase II Trial of Pediatric Patients with Newly Diagnosed High-Grade Gliomas** T. Jaspan, et al. **PEDIATRICS**

GENERAL CONTENTS


-  1588 **Association of Automatically Quantified Total Blood Volume after Aneurysmal Subarachnoid Hemorrhage with Delayed Cerebral Ischemia** I.A. Zijlstra, et al. **ADULT BRAIN**
-   1594 **Centripetal Propagation of Vasoconstriction at the Time of Headache Resolution in Patients with Reversible Cerebral Vasoconstriction Syndrome** M. Shimoda, et al. **ADULT BRAIN**
-  1599 **Application of Blood-Brain Barrier Permeability Imaging in Global Cerebral Edema** J. Ivanidze, et al. **ADULT BRAIN FUNCTIONAL**
-  1604 **Uremic Encephalopathy: MR Imaging Findings and Clinical Correlation** D.M. Kim, et al. **ADULT BRAIN**
- 1610 **Probabilistic Fiber-Tracking Reveals Degeneration of the Contralateral Auditory Pathway in Patients with Vestibular Schwannoma** S.M. Rueckriegel, et al. **ADULT BRAIN**
- 1617 **Tractography at 3T MRI of Corpus Callosum Tracts Crossing White Matter Hyperintensities** W. Reginold, et al. **ADULT BRAIN**
-   1623 **Manual Segmentation of MS Cortical Lesions Using MRI: A Comparison of 3 MRI Reading Protocols** J. Maranzano, et al. **ADULT BRAIN**
-   1629 **Quantitative Susceptibility Mapping and R2* Measured Changes during White Matter Lesion Development in Multiple Sclerosis: Myelin Breakdown, Myelin Debris Degradation and Removal, and Iron Accumulation** Y. Zhang, et al. **ADULT BRAIN**

AJNR (Am J Neuroradiol ISSN 0195-6108) is a journal published monthly, owned and published by the American Society of Neuroradiology (ASNR), 800 Enterprise Drive, Suite 205, Oak Brook, IL 60523. Annual dues for the ASNR include \$170.00 for journal subscription. The journal is printed by Cadmus Journal Services, 5457 Twin Knolls Road, Suite 200, Columbia, MD 21045; Periodicals postage paid at Oak Brook, IL and additional mailing offices. Printed in the U.S.A. POSTMASTER: Please send address changes to American Journal of Neuroradiology, P.O. Box 3000, Denville, NJ 07834, U.S.A. Subscription rates: nonmember \$380 (\$450 foreign) print and online, \$305 online only; institutions \$440 (\$510 foreign) print and basic online, \$875 (\$940 foreign) print and extended online, \$365 online only (basic), extended online \$790; single copies are \$35 each (\$40 foreign). Indexed by PubMed/Medline, BIOSIS Previews, Current Contents (Clinical Medicine and Life Sciences), EMBASE, Google Scholar, HighWire Press, Q-Sensei, RefSeek, Science Citation Index, and SCI Expanded. Copyright © American Society of Neuroradiology.

		1636 Relationship between APOE Genotype and Structural MRI Measures throughout Adulthood in the Study of Health in Pomerania Population-Based Cohort <i>M. Habes, et al.</i>	ADULT BRAIN	
		1643 Differentiation of Low- and High-Grade Gliomas Using High b-Value Diffusion Imaging with a Non-Gaussian Diffusion Model <i>Y. Sui, et al.</i>	ADULT BRAIN	
			1650 Antiangiogenic Effect of Bevacizumab: Application of Arterial Spin-Labeling Perfusion MR Imaging in a Rat Glioblastoma Model <i>T.J. Yun, et al.</i>	ADULT BRAIN FUNCTIONAL
			1657 Nonaneurysmal Perimesencephalic Hemorrhage Is Associated with Deep Cerebral Venous Drainage Anomalies: A Systematic Literature Review and Meta-Analysis <i>A. Rouchaud, et al.</i>	ADULT BRAIN
		1664 Prevalence of Intracranial Aneurysms in Patients with Aortic Aneurysms <i>A. Rouchaud, et al.</i>	ADULT BRAIN	
		1669 Ventricular Microaneurysms in Moyamoya Angiopathy Visualized with 7T MR Angiography <i>T. Matsushige, et al.</i>	ADULT BRAIN	
		1673 Risk Factors for Ischemic Complications following Pipeline Embolization Device Treatment of Intracranial Aneurysms: Results from the IntrePED Study <i>W. Brinjikji, et al.</i>	INTERVENTIONAL	
			1679 WEB Treatment of Ruptured Intracranial Aneurysms <i>W.J. van Rooij, et al.</i>	INTERVENTIONAL
		1684 Contrast-Enhanced and Time-of-Flight MRA at 3T Compared with DSA for the Follow-Up of Intracranial Aneurysms Treated with the WEB Device <i>C. Timsit, et al.</i>	INTERVENTIONAL	
		1690 Incidence and Clinical Significance of Acute Reocclusion after Emergent Angioplasty or Stenting for Underlying Intracranial Stenosis in Patients with Acute Stroke <i>G.E. Kim, et al.</i>	INTERVENTIONAL	
		1696 Suspected Metallic Embolism following Endovascular Treatment of Intracranial Aneurysms <i>R. Yasuda, et al.</i>	INTERVENTIONAL	
		1700 Endovascular Coiling of Wide-Neck and Wide-Neck Bifurcation Aneurysms: A Systematic Review and Meta-Analysis <i>B. Zhao, et al.</i>	INTERVENTIONAL	
		1706 Diffusion-Weighted Imaging of Nasopharyngeal Carcinoma: Can Pretreatment DWI Predict Local Failure Based on Long-Term Outcome? <i>B.K.H. Law, et al.</i>	HEAD & NECK	
		1713 Childhood Cerebral Adrenoleukodystrophy: MR Perfusion Measurements and Their Use in Predicting Clinical Outcome after Hematopoietic Stem Cell Transplantation <i>A.M. McKinney, et al.</i>	PEDIATRICS	
		1721 Widespread Focal Cortical Alterations in Autism Spectrum Disorder with Intellectual Disability Detected by Threshold-Free Cluster Enhancement <i>V.E. Contarino, et al.</i>	PEDIATRICS	
		1727 In Vivo T1 of Blood Measurements in Children with Sickle Cell Disease Improve Cerebral Blood Flow Quantification from Arterial Spin-Labeling MRI <i>L. Václavů, et al.</i>	PEDIATRICS FUNCTIONAL	
		1733 Normal Developmental Globe Morphology on Fetal MR Imaging <i>M.T. Whitehead, et al.</i>	PEDIATRICS	
		1738 Gray Matter Growth Is Accompanied by Increasing Blood Flow and Decreasing Apparent Diffusion Coefficient during Childhood <i>N.D. Forkert, et al.</i>	PEDIATRICS	
		1745 Correlation of MRI Brain Injury Findings with Neonatal Clinical Factors in Infants with Congenital Diaphragmatic Hernia <i>R. Radhakrishnan, et al.</i>	PEDIATRICS	
		1752 Limitations of T2*-Gradient Recalled-Echo and Susceptibility-Weighted Imaging in Characterizing Chronic Subdural Hemorrhage in Infant Survivors of Abusive Head Trauma <i>J.A. Cramer, et al.</i>	PEDIATRICS	
		1757 Demonstration of Normal and Abnormal Fetal Brains Using 3D Printing from In Utero MR Imaging Data <i>D. Jarvis, et al.</i>	PEDIATRICS	
		1762 35 YEARS AGO IN AJNR		

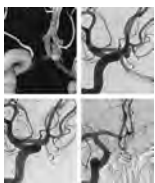
ONLINE FEATURES

LETTERS

-  **E55** **The Clinical Outcome of Posterior Reversible Encephalopathy Syndrome** *B. Gao, et al.*
- E57** **Reply** *S. Khanipour Roshan, et al.*
- E58** **Utility and Significance of Gadolinium-Based Contrast Enhancement in Posterior Reversible Encephalopathy Syndrome** *V. Bhatia, et al.*
- E59** **Reply** *S.J. Karia, et al.*
- E60** **Measures of Neuroradiologic Activities in the “Air du Temps”**
M.I. Vargas, et al.
- E61** **Is There a Need for Contrast and Local Anesthetic in Cervical Epidural Steroid Injections?** *M.P. Bolger, et al.*
- E62** **Reply** *G.M. Lagemann, et al.*

BOOK REVIEWS *R.M. Quencer, Section Editor*

Please visit www.ajnrblog.org to read and comment on Book Reviews.



WEB device treatment of intracranial ruptured aneurysm is shown with the pretreatment 3D angiogram at top left, pretreatment angiogram top right, posttreatment angiogram bottom left, and 3-month follow-up at bottom right. There is complete aneurysm occlusion by the device.



Indicates Editor's Choices selection



Indicates Fellows' Journal Club selection



Indicates open access to non-subscribers at www.ajnr.org



Indicates article with supplemental on-line table



Indicates article with supplemental on-line photo



Indicates article with supplemental on-line video



Evidence-Based Medicine Level 1



Evidence-Based Medicine Level 2



AMERICAN JOURNAL OF NEURORADIOLOGY

Publication Preview at www.ajnr.org features articles released in advance of print. Visit www.ajnrblog.org to comment on AJNR content and chat with colleagues and AJNR's News Digest at <http://ajnrndigest.org> to read the stories behind the latest research in neuroimaging.

SEPTEMBER 2016 • VOLUME 37 • NUMBER 9 • WWW.AJNR.ORG

Official Journal:

American Society of Neuroradiology
American Society of Functional Neuroradiology
American Society of Head and Neck Radiology
American Society of Pediatric Neuroradiology
American Society of Spine Radiology

EDITOR-IN-CHIEF

Jeffrey S. Ross, MD

*Professor of Radiology, Department of Radiology,
Mayo Clinic College of Medicine, Phoenix, AZ*

SENIOR EDITORS

Harry J. Cloft, MD, PhD

*Professor of Radiology and Neurosurgery,
Department of Radiology, Mayo Clinic College of
Medicine, Rochester, MN*

Thierry A.G.M. Huisman, MD

*Professor of Radiology, Pediatrics, Neurology, and
Neurosurgery, Chairman, Department of Imaging
and Imaging Science, Johns Hopkins Bayview,
Director, Pediatric Radiology and Pediatric
Neuroradiology, Johns Hopkins Hospital,
Baltimore, MD*

C.D. Phillips, MD, FACR

*Professor of Radiology, Weill Cornell Medical
College, Director of Head and Neck Imaging,
New York-Presbyterian Hospital, New York, NY*

Pamela W. Schaefer, MD

*Clinical Director of MRI and Associate Director of
Neuroradiology, Massachusetts General Hospital,
Boston, Massachusetts, Associate Professor,
Radiology, Harvard Medical School, Cambridge, MA*

Charles M. Strother, MD

*Professor of Radiology, Emeritus, University of
Wisconsin, Madison, WI*

Jody Tanabe, MD

*Professor of Radiology and Psychiatry,
Chief of Neuroradiology,
University of Colorado, Denver, CO*

STATISTICAL SENIOR EDITOR

Bryan A. Comstock, MS

*Senior Biostatistician,
Department of Biostatistics,
University of Washington, Seattle, WA*

EDITORIAL BOARD

Ashley H. Aiken, *Atlanta, GA*
Lea M. Alhilali, *Phoenix, AZ*
John D. Barr, *Dallas, TX*
Ari Blitz, *Baltimore, MD*
Barton F. Branstetter IV, *Pittsburgh, PA*
Jonathan L. Brisman, *Lake Success, NY*
Julie Bykowski, *San Diego, CA*
Keith Cauley, *Danville, PA*
Asim F. Choudhri, *Memphis, TN*
Alessandro Cianfoni, *Lugano, Switzerland*
J. Matthew Debnam, *Houston, TX*
Seena Dehkharghani, *New York, NY*
Colin Derdeyn, *Iowa City, IA*
Rahul S. Desikan, *San Francisco, CA*
Yonghong Ding, *Rochester, MN*
Clifford J. Eskey, *Hanover, NH*
Saeed Fakhran, *Phoenix, AZ*
Massimo Filippi, *Milan, Italy*
Allan J. Fox, *Toronto, Ontario, Canada*
Wende N. Gibbs, *Los Angeles, CA*
Christine M. Glastonbury, *San Francisco, CA*
John L. Go, *Los Angeles, CA*
Allison Grayev, *Madison, WI*
Brent Griffith, *Detroit, MI*
Wan-Yuo Guo, *Taipei, Taiwan*
Ajay Gupta, *New York, NY*
Rakesh K. Gupta, *Lucknow, India*
Lotfi Hacein-Bey, *Sacramento, CA*
Christopher P. Hess, *San Francisco, CA*
Andrei Holodny, *New York, NY*
Benjamin Huang, *Chapel Hill, NC*
George J. Hunter, *Boston, MA*
Mahesh V. Jayaraman, *Providence, RI*
Valerie Jewells, *Chapel Hill, NC*
Christof Karmonik, *Houston, TX*
Timothy J. Kaufmann, *Rochester, MN*
Hillary R. Kelly, *Boston, MA*
Toshibumi Kinoshita, *Akita, Japan*
Kennith F. Layton, *Dallas, TX*
Michael M. Lell, *Nürnberg, Germany*
Michael Lev, *Boston, MA*
Karl-Olof Lovblad, *Geneva, Switzerland*
Franklin A. Marden, *Chicago, IL*
M. Gisele Matheus, *Charleston, SC*
Joseph C. McGowan, *Merion Station, PA*
Stephan Meckel, *Freiburg, Germany*
Christopher J. Moran, *St. Louis, MO*
Takahisa Mori, *Kamakura City, Japan*
Suresh Mukherji, *Ann Arbor, MI*
Amanda Murphy, *Toronto, Ontario, Canada*
Alexander J. Nemeth, *Chicago, IL*
Sasan Partovi, *Cleveland, OH*
Laurent Pierot, *Reims, France*
Jay J. Pillai, *Baltimore, MD*
Whitney B. Pope, *Los Angeles, CA*

Andrea Poretti, *Baltimore, MD*
M. Judith Donovan Post, *Miami, FL*
Tina Young Poussaint, *Boston, MA*
Joana Ramalho, *Lisbon, Portugal*
Otto Rapalino, *Boston, MA*
Álex Rovira-Cañellas, *Barcelona, Spain*
Paul M. Ruggieri, *Cleveland, OH*
Zoran Rumboldt, *Rijeka, Croatia*
Amit M. Saindane, *Atlanta, GA*
Erin Simon Schwartz, *Philadelphia, PA*
Lubdh M. Shah, *Salt Lake City, UT*
Aseem Sharma, *St. Louis, MO*
J. Keith Smith, *Chapel Hill, NC*
Maria Vittoria Spampinato, *Charleston, SC*
Gordon K. Sze, *New Haven, CT*
Krishnamoorthy Thamburaj, *Hershey, PA*
Cheng Hong Toh, *Taipei, Taiwan*
Thomas A. Tomsick, *Cincinnati, OH*
Aquila S. Turk, *Charleston, SC*
Willem Jan van Rooij, *Tilburg, Netherlands*
Arastoo Vossough, *Philadelphia, PA*
Elysa Widjaja, *Toronto, Ontario, Canada*
Max Wintermark, *Stanford, CA*
Ronald L. Wolf, *Philadelphia, PA*
Kei Yamada, *Kyoto, Japan*
Carlos Zamora, *Chapel Hill, NC*

EDITORIAL FELLOW

Daniel S. Chow, *San Francisco, CA*

SPECIAL CONSULTANTS TO THE EDITOR

AJNR Blog Editor

Neil Lall, *Denver, CO*

Case of the Month Editor

Nicholas Stence, *Aurora, CO*

Case of the Week Editors

Juan Pablo Cruz, *Santiago, Chile*

Sapna Rawal, *Toronto, Ontario, Canada*

Classic Case Editor

Sandy Cheng-Yu Chen, *Taipei, Taiwan*

Facebook Editor

Peter Yi Shen, *Sacramento, CA*

Health Care and Socioeconomics Editor

Pina C. Sanelli, *New York, NY*

Physics Editor

Greg Zaharchuk, *Stanford, CA*

Podcast Editor

Yvonne Lui, *New York, NY*

Twitter Editor

Ryan Fitzgerald, *Little Rock, AR*

YOUNG PROFESSIONALS

ADVISORY COMMITTEE

Asim K. Bag, *Birmingham, AL*
Anna E. Nidecker, *Sacramento, CA*
Peter Yi Shen, *Sacramento, CA*

Founding Editor
Juan M. Taveras

Editors Emeriti

Mauricio Castillo, Robert I. Grossman,
Michael S. Huckman, Robert M. Quencer

Managing Editor
Karen Halm

Assistant Managing Editor

Laura Wilhelm

Executive Director, ASNR

James B. Gantenberg

Director of Communications, ASNR

Angelo Artemakis



Title: Esmeraldas Coast, Ecuador. The Esmeraldas Coast of the Pacific Ocean is situated at the northwestern region of Ecuador and is characterized by its sandy beaches lined with coconut palms.

Maria Isabel Vargas, MD, Geneva University Hospitals, Division of Neuroradiology, Geneva, Switzerland and Maria Leonor Vargas, Manta, Ecuador

“Finding a Voice”: Imaging Features after Phonosurgical Procedures for Vocal Fold Paralysis

 B.A. Vachha,  D.T. Ginat,  P. Mallur,  M. Cunnane, and  G. Moonis



ABSTRACT

SUMMARY: Altered communication (hoarseness, dysphonia, and breathy voice) that can result from vocal fold paralysis, secondary to numerous etiologies, may be amenable to surgical restoration. In this article, both traditional and cutting-edge phonosurgical procedures targeting the symptoms resulting from vocal fold paralysis are reviewed, with emphasis on the characteristic imaging appearances of various injectable materials, implants, and augmentation procedures used in the treatment of vocal fold paralysis. In addition, complications of injection laryngoplasty and medialization laryngoplasty are illustrated. Familiarity with the expected imaging changes following treatment of vocal fold paralysis may prevent the misinterpretation of posttreatment changes as pathology. Identifying common complications related to injection laryngoplasty and localization of displaced implants is crucial in determining specific management in patients who have undergone phonosurgical procedures for the management of vocal fold paralysis.

ABBREVIATIONS: PTFE = polytetrafluoroethylene; VFP = vocal fold paralysis

Vocal fold paralysis (VFP) is the immobilization of the true vocal fold by neural injury (ipsilateral vagus or recurrent laryngeal nerve).^{1,2} Although many cases of VFP remain asymptomatic, altered communication (hoarseness, dysphonia, and breathy voice) and decreased airway protection resulting in aspiration are often seen due to glottic incompetency. Altered sensation, pharyngeal weakness, and swallowing incoordination, among other factors, may contribute to the propensity for aspiration. Conversely, bilateral VFP manifests primarily with dyspnea and biphasic stridor, with dysphonia and dysphagia occurring less frequently.

The main goal of intervention in a patient with unilateral VFP is to eliminate the risk of aspiration pneumonia and restore voice quality.³ Intervention involves both noninvasive voice therapy and surgical procedures. Voice therapy by a speech language pathologist is invaluable in the management of VFP both in the


preoperative setting when surgical decisions are being made and for optimal postsurgical phonation training; this however is beyond the scope of the present article.³ Surgical procedures for unilateral VFP aim to restore glottic competence by restoring vocal fold tone, augmenting vocal fold size, or altering static vocal fold position; to date, no surgical procedures in clinical use are able to restore purposeful vocal fold motion.

The term “phonosurgery” was originally introduced to describe surgical procedures targeting the voice.⁴ Surgical options differ on the basis of whether the patient has unilateral or bilateral VFP. Radiologic imaging has limited utility with respect to primary preoperative planning because glottic competence cannot be evaluated through existing radiologic modalities. While laryngoscopy with stroboscopy is the principal driver of treatment selection in vocal fold paralysis, preoperative imaging should be an adjunct when certain pathologic states are anticipated. For example, altered anatomy after neck surgery or radiation may change the surgical approach, suspicion of chondronecrosis may preclude framework surgery, and paralysis in the setting of laryngeal cartilage fracture may require attention to fracture fixation before phonosurgery, especially if mucosal violation is suggested by imaging.

Here we focus on the main types of procedures performed for the treatment of unilateral VFP, including injection laryngoplasty, medialization laryngoplasty, and arytenoid adduction.^{5,6} The indications, techniques, and corresponding imaging features are summarized in Table 1, schematized in Fig 1, and elaborated in the following sections.

From the Department of Radiology (B.A.V.), Memorial Sloan Kettering Cancer Center, New York, New York; Department of Radiology (B.A.V.), Massachusetts General Hospital, Harvard Medical School, Boston, Massachusetts; Department of Radiology (D.T.G.), University of Chicago, Chicago, Illinois; Department of Otology and Laryngology (P.M.), Beth Israel Deaconess Medical Center, Harvard Medical School, Boston, Massachusetts; Department of Radiology (M.C.), Massachusetts Eye and Ear Infirmary, Harvard Medical School, Boston, Massachusetts; and Department of Radiology (G.M.), Columbia University Medical Center, New York, New York.

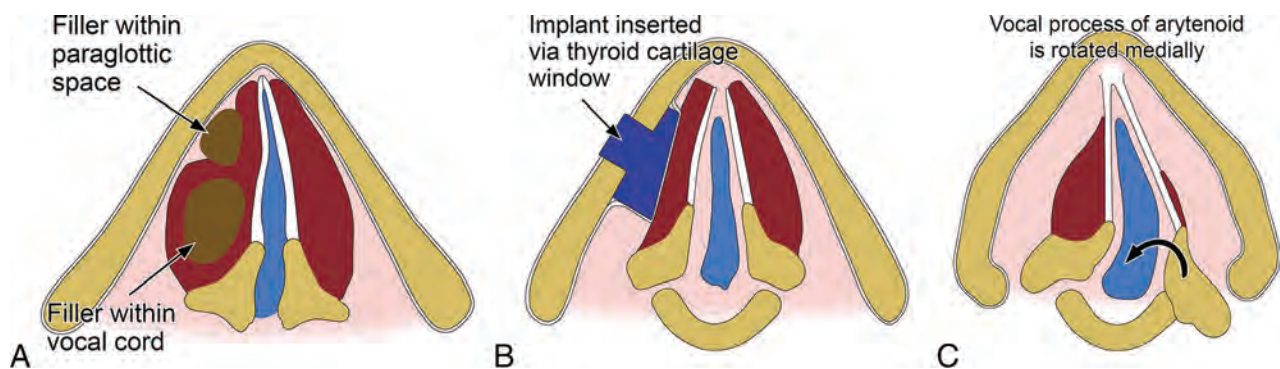
Please address correspondence to Behroze Vachha, MD, PhD, Department of Radiology, Memorial Sloan Kettering Cancer Center, 1275 York Ave, New York, NY 10065; e-mail: vachhab@msskcc.org

 Indicates open access to non-subscribers at www.ajnr.org

<http://dx.doi.org/10.3174/ajnr.A4781>

Table 1: Overview of vocal cord procedures

Procedures	Indications	Techniques	Imaging Findings
Injection laryngoplasty	Temporary correction of glottic incompetence due to unilateral vocal fold paralysis and long-term correction of mild-moderate glottic insufficiency	Percutaneous, transnasal, or peroral injection of filler material into the vocal cord or paraglottic space	Varies depending on agent injected; also refer to the text and Table 2
Medialization laryngoplasty	Permanent correction; should be reserved for cases of vocal fold paralysis in which recovery of motion is definitively not expected (time >6 months from onset, surgical recurrent nerve sacrifice, or malignant invasion)	Insertion of an implant into the vocal fold through a window in the thyroid, which results in displacement of the paralyzed vocal fold to a more medial position	The implants typically used appear as hyperattenuating on CT and low signal on T1- and T2-weighted sequences, with a triangular shape on axial images; a defect in the adjacent thyroid cartilage may be visible
Arytenoid adduction (adduction arytenopexy)	To enhance posterior glottal closure in patients with paralytic dysphonia by reproducing lateral cricoarytenoid muscle function; can be performed in conjunction with medialization laryngoplasty	The inner perichondrium of the thyroid cartilage is opened and the muscular process of the arytenoid is identified and sutured to the thyroid or cricoid cartilage	Medially rotated (adducted) arytenoid cartilage and narrowing of the posterior glottic gap

**FIG 1.** Schematic of the main categories of procedures for treating vocal cord paralysis: injection laryngoplasty (A), medialization laryngoplasty (B), and arytenoid adduction (C).**Table 2: Description of selected agents used for injection laryngoplasty**

Agents	Longevity	Imaging Findings
Hyaluronic acid gels (Restylane, Hylaform)	Temporary	Nearly fluid attenuation on CT; T1 hypointense and T2 hyperintense, similar to fluid on MRI; may display peripheral enhancement initially
Micronized cadaveric dermis (Cymetra)	Temporary	T1 and T2 hyperintense within the first year of injection
Bovine collagen preparations (Zyplast)	Temporary	Generally fluid attenuation on CT; T1 hypointense and T2 hyperintense, similar to fluid on MRI; may display peripheral enhancement initially
Calcium hydroxylapatite (Radiesse Voice)	Long-lasting	High attenuation on CT (280–700 HU); hypermetabolic on ¹⁸ F-DG-PET
Autologous fat	Long-lasting	Attenuation and signal characteristics of adipose tissue
Teflon	Permanent	Globular high attenuation on CT (200–400 HU range)

Injection Laryngoplasty

Injection laryngoplasty or vocal fold augmentation involves injection of various materials into the lateral aspect of the thyroarytenoid/lateral cricoarytenoid muscle complex of the paralyzed vocal fold.⁷ Alternatively, materials can be injected lateral to the thyroarytenoid in the paraglottic space. The result of either is a medially displaced free edge of the affected vocal fold, improving its apposition with the contralateral vocal fold.

The main indications for vocal fold injection include temporary correction of glottic incompetence due to unilateral VFP and long-term correction of mild-moderate glottic insufficiency (ie, glottic gap of <1–3 mm).^{7–9}

Injection laryngoplasty is a minimally invasive procedure that

can be performed with the patient under general anesthesia by using microscopic suspension laryngoscopy or it can be performed as an in-office procedure with the patient under local anesthesia.^{8–12} Three endoscopic approaches may be used in the office with a flexible laryngoscope: percutaneous (transcricothyroid membrane, transthyroid cartilage, and transthyrohyoid membrane), transnasal, and peroral.⁷

Injection Materials

The first attempt of vocal fold augmentation involved the use of paraffin injected through a 19-ga needle.¹⁰ Since then, different materials have been used for vocal fold augmentation. Currently, materials used for vocal fold injection/augmentation are divided

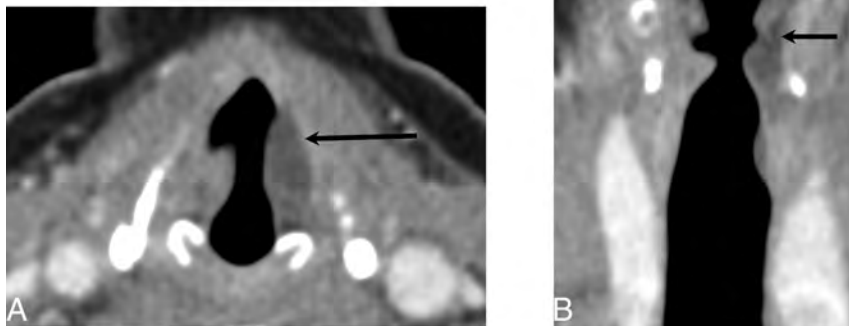


FIG 2. Hyaluronic acid gel. Axial (A) and coronal (B) contrast-enhanced CT at the level of the vocal folds demonstrates fluid attenuation material within the left vocal fold (black arrow).

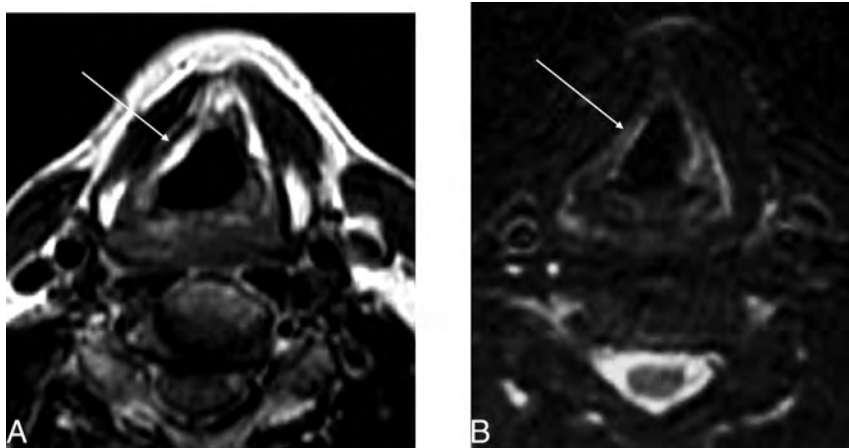


FIG 3. Micronized collagen (Cymetra) approximately 11 months after injection. A, Unenhanced T1-weighted image at the level of the true vocal folds demonstrates T1 hyperintensity within the right vocal fold (arrow; due to volume averaging, portions of the false cord are also partially seen). B, T2-weighted image demonstrates a hyperintense region in the true vocal fold on the right corresponding to the site of injection (arrow).

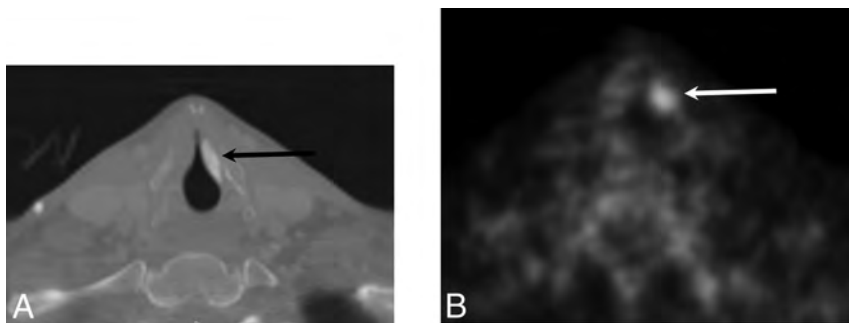


FIG 4. Calcium hydroxylapatite. A, Axial contrast-enhanced CT with a bone algorithm demonstrates hyperattenuating material in the region of the left vocal fold (black arrow). B, Axial positron-emission tomography demonstrates hypermetabolism at the site of the injected material, which can be a false-positive finding for malignant disease (white arrow).

into temporary and long-lasting. Temporary materials include carboxymethylcellulose (Radiess Voice Gel; BioForm Medical, Franksville, Wisconsin), hyaluronic acid gel (Restylane; Q-Med Scandinavia, Princeton, Virginia; Hylaform; Q-Med, Uppsala,

Sweden), micronized collagen (Cymetra; LifeCell Corporation, Bridgewater, New Jersey), bovine collagen (Zyplast; Advanced Dermatology PC, New York, New York), and bovine gelatin (Gelfoam; Pfizer, New York, New York; Surgifoam; Ethicon, Centerville, Virginia).⁷ Long-lasting materials include calcium hydroxylapatite (Radiess Voice; BioForm Medical), autologous fat, and, of historic importance, polytetrafluoroethylene (Teflon; DuPont, Wilmington, Delaware).⁷ The imaging features following injection laryngoplasty vary depending on the particular agent used, as described in the subsequent sections and Table 2.

Temporary Materials. Hyaluronic acid gels (eg, Restylane and Hylaform) are composed of water in a glycosaminoglycan matrix with a reported duration of clinical effects lasting from 4 to 6 months, though it may be detectable even 12 months after injection.¹¹⁻¹³ On CT, hyaluronic acid demonstrates nearly fluid attenuation (Fig 2). On MR imaging, the material is T1 hypointense and T2 hyperintense with an imaging appearance similar to that of water. On postcontrast T1-weighted sequences, this material may show minimal peripheral enhancement.¹⁴ Clinical studies have supported the safety and efficacy of hyaluronic acid gels in deep vocal fold augmentation in patients with VFP.

Micronized cadaveric dermis (Cymetra) is donor skin (Alloderm; LifeCell Corporation) that has been processed into a nonimmunogenic acellular matrix of human collagen and elastin.¹⁵ This material has demonstrated positive results in the treatment of VFP, with several advantages over other injection materials: Because the material is acellular, it does not incite a foreign body or hypersensitivity reaction (compare it with bovine collagen materials); no harvesting of tissue is required, thereby reducing operative time and alleviating donor site morbidity (compare with autologous fat); and injection of this material does not inhibit vibratory function (compare with hyaluronic acid gels).¹⁵⁻¹⁷ The main disadvantage of this material is the need

for overinjection to overcome unwanted absorption of the material.¹⁵ Because the material is prepared from human cadaveric dermis, there is the theoretic risk of infectious transmission, though this has not been reported clinically, to our knowledge.

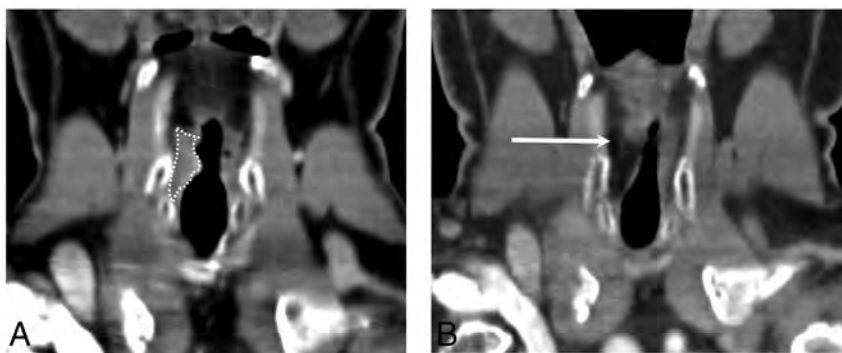


FIG 5. Autologous fat. A, Coronal CT at the level of the vocal folds demonstrates transglottic carcinoma on the right (white dotted line). B, Coronal CT posttreatment shows low-attenuation material within the right vocal fold status post fat augmentation (arrow).

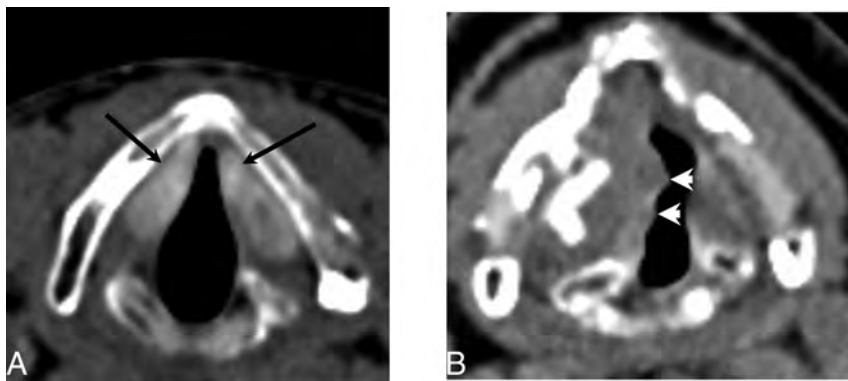


FIG 6. Teflon. A, Axial CT demonstrates hyperattenuating material in the bilateral vocal folds (arrows) consistent with Teflon injection. B, Axial CT in a different patient status post Teflon injection into the right vocal fold demonstrates a slightly nodular contour (arrowheads) consistent with granuloma formation, a common complication of Teflon.

The time course of Cymetra resorption follows a pattern that could be observed by MR imaging: Until about 11 months, the material appears T1 and T2 hyperintense (Fig 3); by 15 months, there is minimal T2 hyperintensity; and by 21 months postinjection, there is no signal alteration within the vocal folds, suggesting complete resorption of the injected material into the recipient tissue.¹⁶

Bovine collagen materials such as Zyplast may result in hypersensitivity reactions prompting skin hypersensitivity testing before using this material.^{7,9} Bovine gelatin material has been shown to be safe with predictable results as a temporary augmentation material, but the need for large-gauge needles (18- or 19-ga) and the short duration of effect (4–6 weeks) have resulted in it being less popular than its newer, longer-lasting counterparts.^{7,9}

Long-Lasting and Permanent Materials. Calcium hydroxylapatite (Radiesse Voice) consists of microspheres of calcium hydroxylapatite in a carboxymethylcellulose carrier and has been shown to provide clinical effectiveness for an average duration of approximately 18 months postinjection.^{18,19} Calcium hydroxylapatite appears as high-attenuation material on CT, with attenuation values ranging between 280 and 700 HU (Fig 4A).¹⁴ Calcium hydroxylapatite can appear hypermetabolic on ¹⁸F-FDG-positron-emission tomography and should not be misinterpreted as a neoplasm (Fig 4B).

Autologous fat is usually harvested from the patient by a lipo-

suction technique. At least initially, this filler preserves the expected imaging features of adipose tissue (Fig 5). Variability in resorption limits the predictability of the long-term voice outcomes; furthermore, the patient may require substantial overinjection and repeat lipoinjection to achieve adequate results.⁷

Teflon appears as hyperattenuating on CT (Fig 6). The use of this material is now avoided due to serious complications related to granuloma formation, which can appear as a soft-tissue mass surrounding the hyperattenuating Teflon.⁷ Furthermore, the Teflon-induced granulomas can potentially produce false-positive findings on ¹⁸F-FDG-positron-emission tomography, but the true nature of this phenomenon can be resolved by the otherwise suggestive CT appearance.²⁰

Laryngeal Framework Surgery

Although long-acting injection materials have become increasingly popular, laryngeal framework surgery remains the criterion standard long-term treatment of unilateral VFP. “Laryngeal framework surgery” is a nonspecific label referring to open surgical approaches to the cartilaginous framework. Surgical goals vary by type, and as expected, not all framework surgery is appropriate for unilateral VFP.

Broadly speaking, the 4 main categories are the following: 1) approximation laryngoplasty, which includes medialization thyroplasty/laryngoplasty and arytenoid adduction; 2) expansion laryngoplasty, which includes lateralization thyroplasty and vocal fold abduction; 3) relaxation laryngoplasty, which includes shortening thyroplasty; and 4) tensioning laryngoplasty, which includes cricothyroid approximation and elongation thyroplasty.²¹ Neither expansion nor relaxation laryngoplasty are appropriate for unilateral VFP because they are intended to improve glottic competence. Tensioning laryngoplasty may be used to restore tension often absent in unilateral VFP; however, it is usually not used, and the nuances of this procedure are beyond the scope of this article. For this review, we discuss medialization laryngoplasty and arytenoid adduction, which are the most commonly performed framework operations for unilateral VFP.

Medialization Laryngoplasty

Medialization laryngoplasty involves introducing an implant through an externally created window in the thyroid lamina at the level of the vocal fold, which results in displacement of the paralyzed vocal fold from its lateral position to a more medial position.^{5,22–25} Medialization laryngoplasty is a permanent correction and should be reserved for cases of vocal fold paralysis in which recovery of motion is definitively not expected (time >6 months from onset, surgical recurrent nerve sacrifice, or malignant inva-

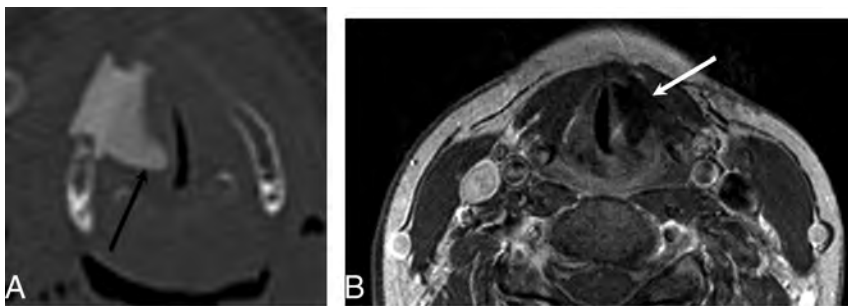


FIG 7. Montgomery Implant. A, Axial CT demonstrates a Montgomery Implant (*black arrow*) and appropriate medialization of the right vocal cord. Note the triangular configuration of the Montgomery Implant. B, Axial contrast-enhanced T1-weighted MR imaging in a different patient demonstrates triangular hypointensity adjacent to the left vocal fold, representing the Montgomery Implant (*white arrow*), with appropriate medialization of left vocal fold.

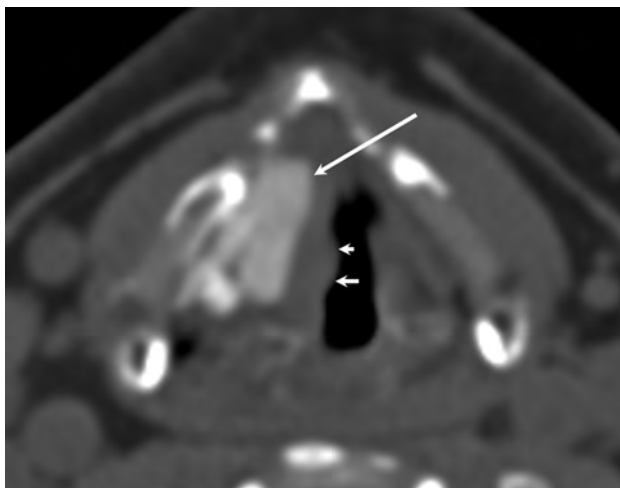


FIG 8. PTFE. Axial CT demonstrates hyperattenuating PTFE in the region of the right vocal fold with appropriate medialization of the right vocal fold. Note the slight nodular contour of the medial margin of the vocal fold (*smaller arrows*) indicating mild granuloma formation in this patient.



FIG 9. Malpositioned Montgomery Implant. Axial CT demonstrates an externally rotated Montgomery Implant, which is not flush against the thyroid window (*arrow*).

sion). Medialization laryngoplasty offers several advantages, such as preservation of the mucosal wave, no risk of reabsorption of the implant, and implants generally being more easily removed than injected material. However, disadvantages of medialization laryngoplasty include the risk of submucosal hemorrhage and implant extrusion and the effects of suboptimal shaping of the implant. Several materials are used for medialization, including silicone, polytetrafluoroethylene (PTFE; Gore-Tex; W.L. Gore & Associates, Newark, Delaware), hydroxylapatite (VoCom system; Gyrus ENT, Bartlett,

Tennessee), Silastic (preformed or carved; Dow Corning, Midland, Michigan), and titanium implants.⁵

The Montgomery Thyroplasty Implant System (Boston Medical Products, Westborough, Massachusetts) is constructed of implant-grade silicone and is inserted surgically through the thyroid lamina at the level of the vocal fold to medialize the paralyzed vocal fold.²⁶⁻²⁸ On CT, Montgomery Implants are hyperattenuated and have a characteristic triangular configuration (Fig 7).

Polytetrafluoroethylene is an expanded form of Teflon. Unlike other implants, this is inserted through a window in the thyroid lamina in the form of 0.4-mm-thick strips and layered in an accordion-like fashion in the paraglottic space. On CT, PTFE appears hyperattenuating with lobulated medial margins (Fig 8); this appearance helps distinguish it from a Montgomery Implant, which is triangular.²⁶ Although the instances of inflammatory response due to PTFE are less common than those seen with Teflon, they can nevertheless occur. Other materials used for medialization include ceramic wedges made of hydroxylapatite and titanium implants.

Complications related to implant malpositions or displacement (Figs 9 and 10), extrusion, and excess implant material are occasionally seen and may require operative correction.

Arytenoid Adduction

In certain cases of VFP, the anatomic position of the paralyzed vocal fold precludes restoration of glottic competence with medialization alone and requires vocal fold repositioning through arytenoid adduction. This situation can occur with a lateralized vocal fold with a glottic gap of ≥ 4 mm, which is typically too large to be overcome by simple medialization. Additionally, a paralyzed vocal fold will often be lower in vertical height because muscle flaccidity allows the arytenoid to slide anteriorly and twist in the caudal direction, dropping the vocal process; the resultant height mismatch prevents contact of the membranous vocal folds, contributing to glottic incompetence. Arytenoid adduction is an open approach to repositioning of the arytenoid cartilage. By placing a suture through the muscular process of the arytenoid and fixing this with anterior tension (typically through the cricothyroid membrane and above the anterior vocal fold commissure), the resultant vocal fold is medial and cranially displaced with increased longitudinal tension (Fig 11).⁵ This procedure addresses the posterior glottic gap by rotating the arytenoid vocal process,

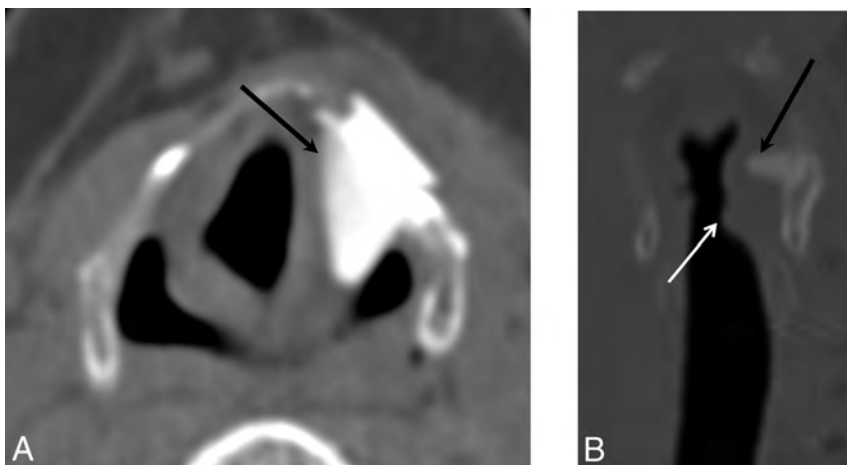


FIG 10. Malpositioned Montgomery Implant. Axial (A) and coronal (B) images demonstrate a Montgomery Implant that is displaced superiorly into the aryepiglottic fold and false cord (black arrow). White arrow indicates the appropriate level of the implant.

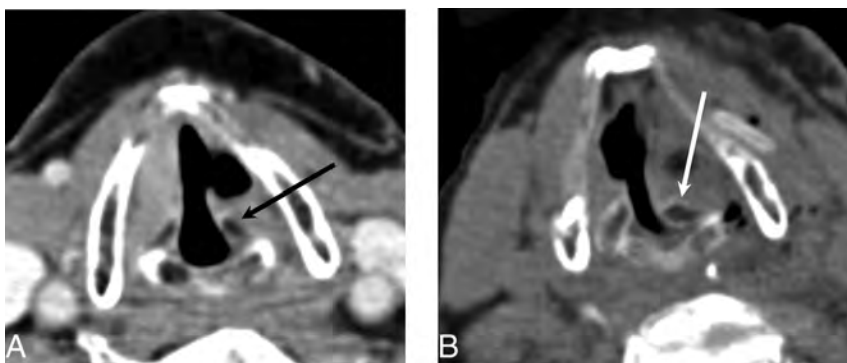


FIG 11. Arytenoid adduction. Preoperative axial CT image (A) and postoperative axial CT image (B) demonstrate the medially rotated (adducted) left arytenoid cartilage (white arrow) compared with the preoperative position (black arrow). Note that adduction turns the arytenoid in toward the vocal cord to ensure that no air leaks through the posterior glottic gap. This result helps patients achieve a more robust voice quality after the operation.

positioning the vocal fold into an adducted position. This procedure is indicated when the interarytenoid gap is >5 mm, when there is height mismatch of the paralyzed and contralateral vocal fold, or when there is loss of vocal fold tension. This is usually performed in conjunction with medialization thyroplasty.⁵

CONCLUSIONS

Familiarity with the expected imaging changes following treatment of VFP may prevent the misinterpretation of posttreatment changes as pathology. Identifying common complications related to injection laryngoplasty and localization of displaced implants is crucial in determining specific management in patients who have undergone phonosurgical procedures for the management of VFP.

Disclosures: Gul Moonis—UNRELATED: Other: blind reader for RadMD.

REFERENCES

1. Benninger MS, Gillen JB, Altman JS. **Changing etiology of vocal fold immobility.** *Laryngoscope* 1998;108:1346–50 CrossRef Medline
2. Curtin H. **The larynx.** In: Som PM, Curtin HD, eds. *Head and Neck Imaging*. 4th ed. St. Louis: Mosby; 2003:1146–67
3. Rubin AD, Sataloff RT. **Vocal fold paresis and paralysis.** *Otolaryngol Clin North Am* 2007;40:1109–31, viii–ix Medline
4. Leden H. **The history of phonosurgery.** In: Gould WJ, Sataloff RT,

Spiegel JR, eds. *Voice Surgery*. Chicago: Mosby Year Book; 1993:65–96

5. Nawka T, Hosemann W. **Surgical procedures for voice restoration.** *GMS Curr Top Otorhinolaryngol Head Neck Surg* 2005;4:Doc14 Medline
6. Zeitels SM, Healy GB. **Laryngology and phonosurgery.** *N Engl J Med* 2003;349:882–92 CrossRef Medline
7. Mallur PS, Rosen CA. **Vocal fold injection: review of indications, techniques, and materials for augmentation.** *Clin Exp Otorhinolaryngol* 2010;3:177–82 CrossRef Medline
8. Rosen CA, Statham MM. **Vocal fold injection as a treatment for glottic insufficiency: pro.** *Arch Otolaryngol Head Neck Surg* 2010;136:825–27 CrossRef Medline
9. Sulica L, Rosen CA, Postma GN, et al. **Current practice in injection augmentation of the vocal folds: indications, treatment principles, techniques, and complications.** *Laryngoscope* 2010;120:319–25 CrossRef Medline
10. Bruening W. **Über eine neue behandlungsmethode der rekurrenslähmung.** *Verh Dtsch Laryng* 1911;18:23
11. Hertegård S, Hallén L, Laurent C, et al. **Cross-linked hyaluronan versus collagen for injection treatment of glottal insufficiency: 2-year follow-up.** *Acta Otolaryngol* 2004;124:1208–14 CrossRef Medline
12. Hertegård S, Hallén L, Laurent C, et al. **Cross-linked hyaluronan used as augmentation substance for treatment of glottal insufficiency: safety aspects and vocal fold function.** *Laryngoscope* 2002;112:2211–19 CrossRef Medline
13. Molteni G, Bergamini G, Ricci-Maccarini A, et al. **Auto-crosslinked hyaluronan gel injections in phonosurgery.** *Otolaryngol Head Neck Surg* 2010;142:547–53 CrossRef Medline
14. Ginat DT, Schatz CJ. **Imaging features of midface injectable fillers and associated complications.** *AJNR Am J Neuroradiol* 2013;34:1488–95 CrossRef Medline
15. Tan M, Woo P. **Injection laryngoplasty with micronized dermis: a 10-year experience with 381 injections in 344 patients.** *Laryngoscope* 2010;120:2460–66 CrossRef Medline
16. Moonis G, Dyce O, Loevner LA, et al. **Magnetic resonance imaging of micronized dermal graft in the larynx.** *Ann Otol Rhinol Laryngol* 2005;114:593–98 CrossRef Medline
17. Lundy DS, Casiano RR, McClinton ME, et al. **Early results of transcutaneous injection laryngoplasty with micronized acellular dermis versus type-I thyroplasty for glottic incompetence dysphonia due to unilateral vocal fold paralysis.** *J Voice* 2003;17:589–95 CrossRef Medline
18. Rosen CA, Gartner-Schmidt J, Casiano R, et al. **Vocal fold augmentation with calcium hydroxylapatite: twelve-month report.** *Laryngoscope* 2009;119:1033–41 CrossRef Medline
19. Carroll VL, Rosen CA. **Long-term results of calcium hydroxylapatite for vocal fold augmentation.** *Laryngoscope* 2011;121:313–19 CrossRef Medline
20. Yeretsian RA, Blodgett TM, Branstetter BF, et al. **Teflon-induced**

- granuloma: a false-positive finding with PET resolved with combined PET and CT.** *AJNR Am J Neuroradiol* 2003;24:1164–66 Medline
21. Friedrich G, de Jong FI, Mahieu HF, et al. **Laryngeal framework surgery: a proposal for classification and nomenclature by the Phonosurgery Committee of the European Laryngological Society.** *Eur Arch Otorhinolaryngol* 2001;258:389–96 CrossRef Medline
 22. Selber J, Sataloff R, Spiegel J, et al. **Gore-Tex medialization thyroplasty: objective and subjective evaluation.** *J Voice* 2003;17:88–95 CrossRef Medline
 23. Shen T, Damrose EJ, Morzaria S. **A meta-analysis of voice outcome comparing calcium hydroxylapatite injection laryngoplasty to silicone thyroplasty.** *Otolaryngol Head Neck Surg* 2013;148:197–208 CrossRef Medline
 24. Ford CN. **Advances and refinements in phonosurgery.** *Laryngoscope* 1999;109:1891–900 CrossRef Medline
 25. Isshiki N, Morita H, Okamura H, et al. **Thyroplasty as a new phonosurgical technique.** *Acta Otolaryngol* 1974;78:451–57 CrossRef Medline
 26. Laccourreye O, El Sharkawy L, Holsinger FC, et al. **Thyroplasty type I with Montgomery implant among native French language speakers with unilateral laryngeal nerve paralysis.** *Laryngoscope* 2005;115:1411–17 CrossRef Medline
 27. McLean-Muse A, Montgomery WW, Hillman RE, et al. **Montgomery thyroplasty implant for vocal fold immobility: phonatory outcomes.** *Ann Otol Rhinol Laryngol* 2000;109:393–400 CrossRef Medline
 28. Montgomery WW, Montgomery SK. **Montgomery thyroplasty implant system.** *Ann Otol Rhinol Laryngol Suppl* 1997;170:1–16 Medline

Response Assessment in Pediatric Neuro-Oncology: Implementation and Expansion of the RANO Criteria in a Randomized Phase II Trial of Pediatric Patients with Newly Diagnosed High-Grade Gliomas

T. Jaspan, P.S. Morgan, M. Warmuth-Metz, E. Sanchez Aliaga, D. Warren, R. Calmon, J. Grill, D. Hargrave, J. Garcia, and G. Zahlmann



ABSTRACT

SUMMARY: Determination of tumor response to treatment in neuro-oncology is challenging, particularly when antiangiogenic agents are considered. Nontumoral factors (eg, blood-brain barrier disruption, edema, and necrosis) can alter contrast enhancement independent of true tumor response/progression. Furthermore, gliomas are often infiltrative, with nonenhancing components. In adults, the Response Assessment in Neuro-Oncology (RANO) criteria attempted to address these issues. No such guidelines exist yet for children. The ongoing randomized phase II trial, A Study of Avastin (bevacizumab) in Combination With Temolozomide (TMZ) and Radiotherapy in Paediatric and Adolescent Patients With High-Grade Glioma (HERBY), will establish the efficacy and safety of the antiangiogenic agent bevacizumab for the first-line treatment of newly diagnosed high-grade glioma in children ($n = 121$ patients, enrollment complete). The primary end point is event-free survival (tumor progression/recurrence by central review, second primary malignancy, or death). Determination of progression or response is based on predefined clinical and radiographic criteria, modeled on the RANO criteria and supported by expert pseudoprogression review and the use of standardized imaging protocols. The HERBY trial will also compare conventional MR imaging (T1-weighted and T2/fluid-attenuated inversion recovery sequences) with conventional MR imaging plus diffusion/perfusion imaging for response assessment. It is anticipated that HERBY will provide new insights into antiangiogenic-treated pediatric brain tumors. HERBY will also investigate the practicality of obtaining adequate quality diffusion/perfusion scans in a trial setting, and the feasibility of implementing standard imaging protocols across multiple sites. To date, 61/73 (83.6%) patients with available data have completed diffusion-weighted imaging (uptake of other nonconventional techniques has been limited). Harmonization of imaging protocols and techniques may improve the robustness of pediatric neuro-oncology studies and aid future trial comparability.

ABBREVIATIONS: HERBY = A Study of Avastin (bevacizumab) in Combination With Temolozomide (TMZ) and Radiotherapy in Paediatric and Adolescent Patients With High-Grade Glioma; HGG = high-grade glioma; RANO = Response Assessment in Neuro-Oncology; RAPNO = Response Assessment in Pediatric Neuro-Oncology

High-grade gliomas (HGGs) are primary malignant tumors of the brain and CNS, which originate from glial cells. HGGs are fast-growing, poorly differentiated, and aggressive. Their location in the brain, their ill-defined borders, and infiltrative nature makes imaging and assessment of response to therapy particularly challenging.

Currently, the predominant method for assessment of CNS tumor progression and response is contrast-enhancing conventional T1-weighted MR imaging.¹ Although widely used, contrast-enhancing conventional T1-weighted MR imaging has limitations in neuro-oncology. The degree of tumor enhancement can be influenced by a variety of neuro-oncology-related factors, including corticosteroid use, imaging technique (1.5T versus 3T, or dose and timing), surgical injury, inflammation, ischemia, edema, infection, seizures, and radiation injury. Increases in contrast enhancement, triggered by nontumoral events, can incorrectly be interpreted as progression (ie, pseudoprogression). Decreases in contrast enhancement, for example by modification of the blood-brain barrier permeability, can be incorrectly inter-

Received November 13, 2015; accepted after revision February 14, 2016.

From Nottingham University Hospitals National Health Service Trust (T.J., P.S.M.), Nottingham, UK; Würzburg University (M.W.-M.), Würzburg, Germany; VU University Medical Center (E.S.A.), Amsterdam, the Netherlands; Leeds Teaching Hospital National Health Service Trust (D.W.), Leeds, West Yorkshire, UK; Assistance Publique-Hôpitaux de Paris (R.C.), Paris, France; Gustave Roussy and Paris-Sud University (J.Grill), Villejuif, France; Great Ormond Street Hospital (D.H.), London, UK; and F. Hoffmann-La Roche (J.Garcia, G.Z.), Basel, Switzerland.

This work was sponsored by F. Hoffmann-La Roche. Support for third-party writing assistance for this manuscript was provided by F. Hoffmann-La Roche.

Previously presented in part or whole at: Annual Meeting of the American Society of Clinical Oncology, June 1–5, 2012; Chicago, Illinois; and Annual Meeting of the Society of Neuro-Oncology, November 21–24, 2013; San Francisco, California. American Society of Clinical Oncology trials in progress abstract: <http://meetinglibrary.asco.org/content/94634-114>.

Please address correspondence to Tim Jaspan, MD, Imaging Centre, B Floor, Nottingham University Hospitals National Health Service Trust, Nottingham, NG7 2UH, UK; e-mail: tjaspan@doctors.org.uk

Indicates article with supplemental on-line tables.

Indicates article with supplemental on-line photos.

<http://dx.doi.org/10.3174/ajnr.A4782>

interpreted as response (ie, pseudoreponse). In adults with newly diagnosed glioblastomas treated with radiation therapy and temozolomide (the current standard of care), rates of pseudoprogression of 21%–31% have been reported.^{2,3} The increasing interest in antiangiogenic therapies for highly vascularized brain tumors further compounds these concerns; antiangiogenic treatment can improve blood-brain barrier function, decrease enhancement (pseudoreponse), cause transient normalization of tumor vasculature, and may mask tumor changes. Finally, some tumor growth can be non-contrast-enhancing and not detected by conventional MR imaging.

Guidelines for tumor assessment in neuro-oncology were updated in 2010 by the Response Assessment in Neuro-Oncology (RANO) working group (On-line Table 1).^{4,5} These guidelines, based on evaluations of adult HGGs, replaced the previously used Macdonald criteria and aimed to provide more specific and standardized imaging protocols. The RANO working group recommended the use of T2 and FLAIR sequences to assess nonenhancing tumor growth. The potential for pseudoprogression was partially addressed but fell short of definitively distinguishing pseudoprogression from true progression; within the first 12 weeks of completion of radiation therapy, progression can only be determined if most of the new enhancement is outside of the radiation field (as per RANO criteria, an example would be enhancement beyond the high-dose region or 80% isodose line) or if there is histologic confirmation following further resection. The phase III, placebo-controlled AVAglio trial (A Study of Avastin [Bevacizumab] in Combination With Temozolomide and Radiotherapy in Patients With Newly Diagnosed Glioblastoma) for adults with newly diagnosed glioblastoma, which investigated the addition of bevacizumab to radiation therapy plus temozolomide, incorporated aspects of the RANO criteria (though it was initiated before these criteria were published).⁶ The AVAglio protocol prespecified methods to identify pseudoprogression in a consistent manner and used T2/FLAIR sequences to assess nonenhancing lesions.⁷ Progression-free survival benefits were reported with the addition of bevacizumab to standard-of-care treatment in newly diagnosed glioblastoma. To date, there have been no such studies in pediatric patient populations, and extrapolation of results from adults to children is not appropriate. Furthermore, it is not known whether the RANO criteria could be directly implemented into pediatric populations without modification.

Response Assessment in Pediatric Neuro-Oncology

The assessment of response and progression in pediatric brain tumors brings further challenges, such as the brain still being under development in childhood. Pediatric brain tumors tend to be heterogeneous with varying histology. Glial tumors, in particular, have diverse morphology and variable blood-brain barrier integrity and may be poorly circumscribed.⁷ Due to the variation in tumors within the pediatric population and the relative rarity of each individual tumor type, it can be difficult for individual study centers to gain experience in imaging each type.

To date, most neuro-oncology research and development has focused on adult trials, and randomized clinical trials in pediatric

patients are few. Accordingly, no clear relationship between tumor response and improved survival has been established in pediatric patients. Where clinical studies have been conducted, the populations tend to include a wide age range. Due to the limited information available there are, as yet, no agreed standards to define response and progression in children. Thus, the adult RANO criteria may not be directly applicable to pediatric brain tumors. A working group is examining this issue (Response Assessment in Pediatric Neuro-Oncology [RAPNO]).⁷ Given the challenges associated with pediatric brain tumors, several diagnostic uncertainties remain, including the following: the accuracy of metrics for assessing tumor response, the best way to measure enhancing tumors, whether all enhancement can be attributed to tumor tissue, whether loss of enhancement is a surrogate for response, the best way to assess nonenhancing tumors, and understanding how imaging changes correlate with clinical and neurologic status.

The HERBY Trial

A clinical trial was set up to establish the efficacy and safety of the antiangiogenic agent bevacizumab for the first-line treatment of newly diagnosed HGG in children (A Study of Avastin [bevacizumab] in Combination With Temozolomide [TMZ] and Radiotherapy in Paediatric and Adolescent Patients With High-Grade Glioma [HERBY], NCT01390948). The study has been uniquely designed to optimize the assessment of response to treatment to ensure confidence in the data by randomizing the new treatment allocation on top of the standard of care and to inform future work in this patient population with an imaging and biologic repository. In HERBY, the determination of progression or recurrence was mandated on the basis of meeting predefined clinical and radiographic criteria. In addition to investigating bevacizumab treatment, the HERBY study was required to compare the utility of “structural imaging” versus “structural plus multimodal imaging” (Fig 1).

Structural and Multimodal Imaging

Structural imaging includes standard (conventional) MR imaging (as per the RANO criteria; ie, for assessing T1-enhancing lesions [On-line Fig 1A] and using FLAIR and T2 sequences for nonenhancing lesions). However, conventional MR imaging provides limited information on physiologic tumor characteristics and the status of the perilesional tissue. Multimodal imaging uses a variety of techniques to generate physiologic and biochemical information to complement structural imaging.⁸ For example, DWI or DTI with ADC mapping can be used to evaluate cellular density and tissue injury (On-line Figs 1B and 2C). Dynamic susceptibility contrast (perfusion) MR imaging can provide an indication of tumor vascularity and capillary permeability (On-line Figs 1D and 2E). ¹H-MR spectroscopy is used to detect metabolites reflecting tissue integrity, disruption, and necrosis (eg, aromatic amino acids, choline, lipids). These advanced imaging techniques are effective in the evaluation of tumor behavior and have been used as surrogate markers of response to tumor-modulating therapy.^{9–17} Furthermore, diffusion and perfusion techniques have been used to identify radiation necrosis⁹ and pseudoprogression.¹⁰

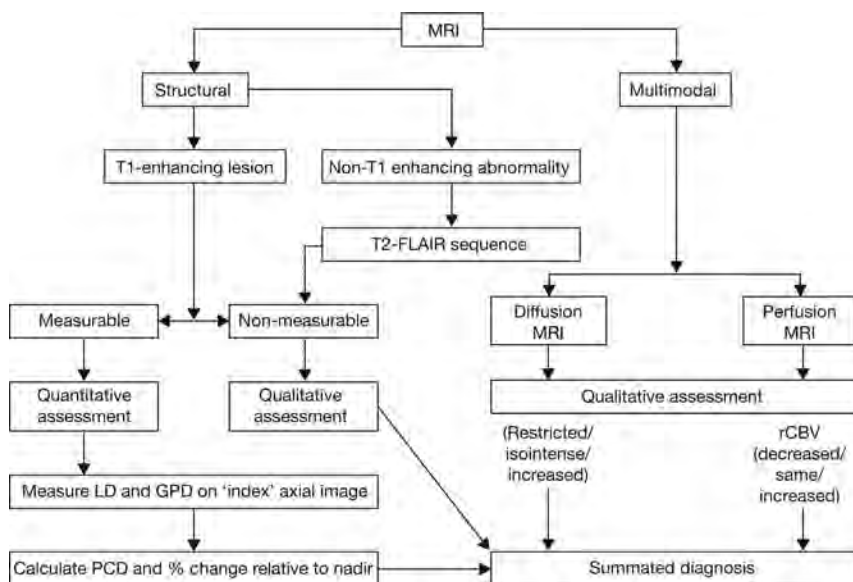


FIG 1. Structural and multimodal imaging used in the HERBY study. LD indicates longest diameter; GPD, greatest perpendicular diameter; PCD, product of cross-sectional enhancing diameters.

Compared with structural MR imaging alone, a combination of structural MR imaging and multimodal imaging represents a greater biologic approach to imaging and provides more of the “big picture” of tumor response. When used in isolation, the additional techniques described are of limited utility, but in combination with structural imaging and clinical assessment, multimodal imaging should provide an enhanced ability to assess tumor grade, viability, and response to therapy.

Implementation of multimodal imaging tools into a clinical trial requires careful consideration. To date, the techniques have been largely experimental and not all technologies are available at all clinics. Standard protocols have not yet been established. ¹H-MR spectroscopy, in particular, is still very exploratory and difficult to standardize. Diffusion and perfusion imaging are the most accessible and available techniques, but there are specific difficulties in undertaking perfusion imaging in the pediatric population due to the size of the patient (eg, obtaining adequate venous access). Regardless of imaging techniques, variability also poses a challenge for the assessment of tumor progression and response; there is intrinsic interobserver variability in the assessment of MR imaging scans, and response to therapy within a tumor itself may be variable. It is also not possible to separate treatment effects from disease effects. As part of the HERBY trial, our aims were the following: 1) to evaluate the implementation of the RANO criteria in a phase II trial of pediatric patients with HGG, 2) to assess the practicality of obtaining multimodal imaging of adequate quality, and 3) to assess the feasibility of including diffusion and perfusion into the response criteria.

MATERIALS AND METHODS

Study Design and Patients

The overall objectives of the HERBY trial are to evaluate the efficacy, safety, tolerability, and pharmacokinetics of bevacizumab when added to postoperative radiation therapy with concomitant and adjuvant temozolomide and to determine whether the addition of bevacizumab to the management of newly diagnosed HGG

in children confers a clinical benefit. It was planned to recruit 120 patients during 36 months. Enrollment is complete (121 patients have been enrolled), and the trial is ongoing as of June 2015.

As with the adult AVAglio trial, the pediatric HERBY trial is investigating the addition of bevacizumab to radiation therapy plus temozolomide in a randomized study design, but there are important differences; for example, unlike AVAglio, HERBY allowed inclusion of grade III and grade IV gliomas, was not placebo-controlled, and had no bevacizumab monotherapy component.

Patients (between 3 and 18 years of age) with histologically confirmed, localized supratentorial/infratentorial cerebellar or peduncular (non-brain stem) HGG, adequate organ function, and available preoperative MR imaging were enrolled. Written, informed con-

sent was obtained from the patient, parent, or legal representative, after institutional review board/ethics committee approval was obtained in each recruiting country. After the operation, patients underwent a postoperative MR imaging and were randomized to receive 1 of the following 2 regimens: standard arm, radiation therapy (1.8 Gy/day) and temozolomide (75 mg/m²/day) for 6 weeks, followed by a 4-week treatment break, then up to 12 four-week cycles of temozolomide (150–200 mg/m²/day); or experimental arm, bevacizumab (10 mg/kg every 2 weeks) plus radiation therapy (1.8 Gy/day) and temozolomide (75 mg/m²/day) for 6 weeks, followed by bevacizumab during a 4-week temozolomide break, and then bevacizumab (10 mg/kg every 2 weeks) concomitantly with up to 12 four-week cycles of adjuvant temozolomide (150–200 mg/m²/day) (On-line Fig 2). Patients will be randomized centrally by an interactive voice response system.

The primary end point is event-free survival, defined as the earliest occurrence of tumor progression/tumor recurrence (determined by a Central Radiology Review Committee), second primary non-HGG malignancy, or death. Secondary end points include the following: investigator-assessed event-free survival; overall survival and 1-year overall survival rate; 6-month and 1-year event-free survival rate; overall response rate determined by the Central Radiology Review Committee using RANO criteria; tumor functional changes on diffusion/perfusion MR imaging for correlative analysis in addition to structural imaging and efficacy outcome measurements; health status; neuropsychologic function; safety; feasibility; and tolerability.

HERBY has an Independent Data Monitoring Committee. This committee shares the responsibility for regularly monitoring the overall safety of patients in the trial with the sponsor and the Trial Steering Group. By carefully reviewing overall death rates, serious adverse events, and other specified safety events by treatment arms, the Independent Data Monitoring Committee provides the sponsor and the Trial Steering Group

their independent recommendations and helps to minimize patient exposure to unnecessary risk. The Independent Data Monitoring Committee will also evaluate benefits and risks by reviewing the efficacy, safety, and tolerability data during the scheduled futility analysis.

Radiographic and Clinical Response Assessment

Response evaluations will be performed by using RANO criteria by blinded site-independent central review; radiologic and clinical evaluations will be combined to provide an integrated disease assessment (Fig 2). Efficacy assessments will be performed after the chemoradiotherapy phase and treatment break but before the start of adjuvant temozolomide treatment, and thereafter every 3 months.

For radiographic response, both enhancing (T1-weighted) and nonenhancing lesions (T2-FLAIR sequences) will be considered (Fig 2) according to prespecified criteria for progression (Table). A detailed standardized imaging protocol has been provided to site investigators (On-line Table 2). Both measurable and nonmeasurable disease will be considered. Measurable disease has been defined as contrast-enhancing lesions with clearly defined

margins on T1-weighted MR imaging with 2 perpendicular diameters of ≥ 10 mm. Nonmeasurable enhancing tumors have been defined as unidimensional measurable lesions, lesions with margins not clearly defined, or lesions with at least 1 diameter of < 10 mm.

The definition of clinical deterioration has been left to the discretion of the treating physician, but it was recommended that substantial decreases in the Karnofsky Performance or Lansky Play Scales be considered deterioration. Increases in corticosteroid doses will also contribute to the evaluation of clinical deterioration.

Pseudoprogression

The risk of pseudoprogression is highest within 12 weeks of chemoradiotherapy completion; during this period in the HERBY trial, clinical decline alone will be considered insufficient to determine disease progression. Progression will be determined only if there is new enhancing disease that extends outside the radiation field or if there is unequivocal evidence of viable tumor on histology (On-line Fig 3). Experienced pediatric neuroradiologists will be available during the trial to assist local radiologists in the evaluation of progression during the early postchemoradiation period. The expert reviewer will provide an opinion to distinguish pseudoprogression from true progression, but the site investigator will make the final decision. Imaging evaluations will be performed again at the next visit (beyond the 12-week period), and if there is a continued increase in enhancing lesions, then the first scan will be considered to have represented true progression. If the lesion is decreased or stable compared with the first posttreatment scan, the increase at the preceding time point will be considered pseudoprogression.

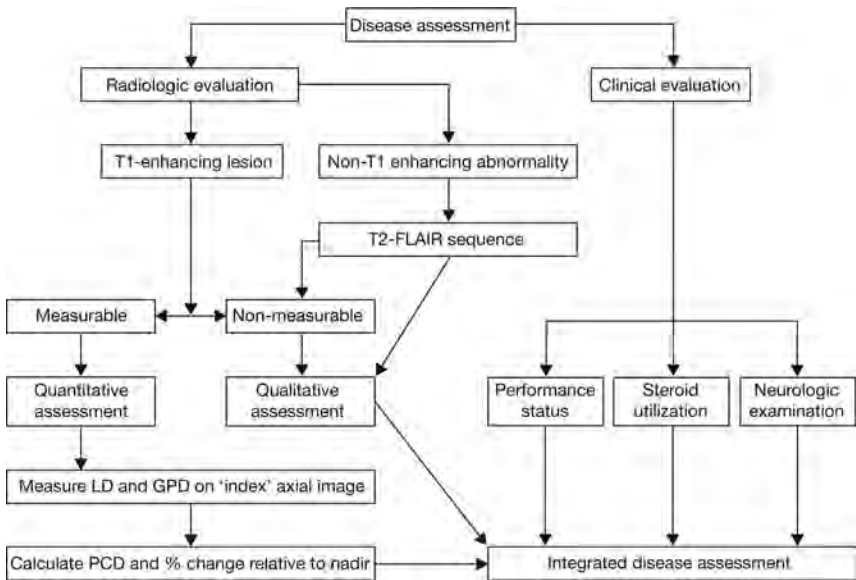


FIG 2. Response evaluation assessment algorithm. LD indicates longest diameter; GPD, greatest perpendicular diameter; PCD, product of cross-sectional enhancing diameters.

Criteria for tumor progression in HERBY (adapted from the RANO criteria)

Parameter	Criterion
T1-weighted post-Gd measurable disease	$\geq 25\%$ increase in the sum of the products of perpendicular diameters of the contrast-enhancing lesions compared with the smallest tumor measurement obtained either at baseline (if no decrease was observed) or best response with the patient on stable or increasing doses of corticosteroids
T1-weighted post-Gd nonmeasurable disease	Clear progression of nonmeasurable lesions
T2/FLAIR	Substantial increase in the T2/FLAIR nonenhancing lesion compared with the baseline scan or best response after the initiation of therapy with the patient on a stable or increasing dose of corticosteroids The increase in the T2/FLAIR signal must have occurred and not be the result of comorbid events (eg, radiation therapy, demyelination, ischemic injury, seizures, postoperative changes, or other treatment effects)
New lesions	Any new lesions
Clinical	Clear clinical deterioration due to tumor and not attributable to other causes (eg, seizures, medication adverse effects, complications of therapy, cerebrovascular events, infection, and so forth)
Failure to return	Failure to return for evaluation as a result of death or deteriorating condition

Note:—Gd indicates gadolinium.

dynamic susceptibility contrast imaging (On-line Table 3). A correlative analysis of functional changes in tumor on MR diffusion/perfusion imaging and efficacy outcome measures is to be performed at the time of the primary analysis. Correlative studies of ¹H-MR spectroscopy were planned for HERBY, but only a small number of ¹H-MR spectroscopy scans have been acquired to date, which will likely prove to be insufficient for analysis. Decision rules for assigning response status are presented in On-line Table 4. For example, if structural MR imaging indicated “complete response,” but diffusion status was decreased and perfusion status was “normal/decreased,” the combined status will be revised to “stable disease.”

Statistical Analysis Plan

For event-free survival and overall survival, Kaplan-Meier curves will be generated and 95% confidence intervals will be estimated by using the Rothman method. An estimate of the treatment effect will be expressed as the hazard ratio with corresponding 95% CI (estimated in a Cox regression analysis). Analyses comparing treatment arms will include the 2-sided log-rank test at the 5% α level. Event-free survival and overall survival rates will be estimated by using the Kaplan-Meier method with 95% CIs calculated by using the Greenwood formula. The difference in overall response rate between the treatment arms will be tested in an exploratory manner, by using a χ^2 test with Schouten correction, with 95% Pearson-Clopper CIs. We will calculate 95% Hauck-Anderson CIs for the difference in response rates between the treatment arms. Other analyses will be descriptive.

Current Status of HERBY

At the time of manuscript preparation, recruitment into the HERBY trial has been completed ($n = 121$) and the study is ongoing. To date, the RANO criteria have been successfully applied (by using the central radiologic read) for the first 73 patients.

DISCUSSION

The HERBY study aims, primarily, to establish whether bevacizumab, when added to radiation therapy and temozolomide, can improve clinical outcomes for pediatric patients with HGG. However, an additional aim of HERBY is to assess the value of the structural imaging (based on the RANO criteria) alone and when combined with multimodal imaging for pediatric neuro-oncology trials, with the potential of guiding future recommendations (RAPNO). Accordingly, the RANO criteria have been implemented into the HERBY trial, with some modifications. For example, the use of an expert reviewer for identification of pseudoprogression was incorporated into the study design. In addition, to reduce bias and variability, site-independent central review will be used to determine response to treatment.

Tumor diffusion and perfusion imaging have also been incorporated to complement the RANO criteria, to investigate whether these tools can enhance the understanding of tumor response to bevacizumab in pediatric patients with HGG. To date, the use of these tools has been variable in HERBY. Although most sites claimed that they were able to do full multimodal imaging before the trial started, the uptake has been poor for some techniques. DWI was the most prevalent technique used; its

value in the context of the RANO criteria is still to be evaluated, but currently it seems that DWI is the most likely to be pragmatically incorporated into the revised RANO criteria for pediatric patients.

A key aspect of HERBY is the provision of detailed protocols for the imaging procedures, which aim to help standardize assessment across sites and countries. Standardized imaging protocols are the subject of recent draft FDA guidance, which recommends that trials augment existing standards to create trial-specific imaging standards, particularly in cases in which images can be interpreted quantitatively.¹⁸ The guidance also recommends that when imaging modalities are vulnerable to image-quality problems, central imaging interpretation should be considered.

Standardization is important for both conventional MR imaging and the diffusion/perfusion techniques being used in HERBY, these latter being, to date, largely experimental. Future trials will require a consensus on protocols with consistent implementation to maximize their value. To this end, following a workshop held in January 2014, a recent consensus publication has outlined a standardized brain tumor anatomic imaging protocol, involving the following: patient advocates; device and pharmaceutical industry leaders; the FDA; the National Cancer Institute; and academic experts in neuro-oncology, neuroradiology, and imaging physics.¹⁹ The recommended protocol reflects recent imaging developments, particularly the use of 3D isotropic T1-weighted imaging pre- and post-gadolinium administration to enable high-quality T1-subtraction image acquisition, a technique that potentially offers improved tumor visualization and quantification of enhancing tumoral tissue.²⁰ The proposed protocol (On-line Table 5) builds on and refines that proposed within the RANO publications and reflects the dynamic and changing status of neuro-oncology imaging. While T1-subtraction images will be evaluated in HERBY, for the most part, this evaluation will depend on 2D T1-weighted image acquisitions; the protocol for the study was derived in 2010 before the current recommendations for T1 volume imaging.

The HERBY study design has several potential strengths, which are anticipated to reinforce the results. For example, the use of central review and decision rules should bring consistency to response assessment and reduce variability. HERBY also includes algorithms for early progression (potential pseudoprogression), which have proved valuable in adult trials⁶; and it incorporates detailed imaging protocols, which could potentially be used as a standard in future pediatric HGG imaging. HERBY has a relatively large patient number in comparison with other pediatric trials; however, there may be variability within the 121 patients that precludes clear conclusions on all aspects under investigation.

We hope that HERBY will meet its aims of establishing the efficacy and safety of a new regimen for the first-line treatment of newly diagnosed high-grade glioma, a condition for which new, effective treatments are very much needed. However, regardless of outcomes, it is anticipated that HERBY will provide valuable new insights into pediatric brain tumors treated with antiangiogenic therapy, which can be applied to future work. HERBY is the first study to compare standard structural imaging with structural im-

aging plus diffusion/perfusion imaging and will give an indication of whether the latter influences the perception of tumor response or progression. This randomized trial will provide valuable information on the true clinical value of these additional imaging tools. The availability of DWI and structural imaging should allow some conclusions to be drawn on the value of this technique for pediatric HGG response assessment in clinical practice. Furthermore, HERBY will allow assessment of the feasibility and practicality of using standardized imaging protocols in clinical trials.

CONCLUSIONS

RANO criteria can be implemented into pediatric trial protocols, but this requires careful consideration; we implemented a review of potential pseudoprogression by expert readers and validation of radiographic progression in the case of stable clinical parameters. The HERBY trial will assess, for the first time, whether functional imaging techniques such as diffusion and perfusion MR imaging, can strengthen the assessment of response when combined with conventional imaging tools. HERBY has also introduced standardized imaging protocols and augmented the RANO criteria with central review and expert advisors. Harmonization of imaging protocols and techniques may improve the robustness of pediatric neuro-oncology studies and aid future trial comparability.

ACKNOWLEDGMENTS

We thank the patients and parents who are participating in the HERBY study and the staff at the study sites; Louis Viviers (Institut Gustave Roussy) for initial generation of tables and figures; and Dawn Saunders, Lee Coleman, and Lisbeth Reneman for their contributions. We thank Dr Gilles Vassal for his review of the manuscript. The HERBY central review radiology reviewers are Tim Jaspan, Monika Warmuth-Metz, Esther Sanchez Aliaga, Daniel Warren, and Raphael Calmon. The HERBY Trial Steering Group includes Tim Jaspan, Paul S. Morgan, Jacques Grill, and Darren Hargrave. The HERBY Radiology Committee comprises Tim Jaspan, Paul S. Morgan, Monika Warmuth-Metz, Esther Sanchez Aliaga, Daniel Warren, Raphael Calmon, and Gudrun Zahlmann.

Disclosures: Timothy Jaspan—RELATED: Grant: Institut Gustav Roussy, which, in turn, received funding from Roche,* Comments: grant to undertake primary and secondary endpoint radiologic imaging analysis; Support for Travel to Meetings for the Study or Other Purposes: Institut Gustav Roussy, which, in turn, received funding from Roche,* Comments: attendance at European Society of Paediatric Oncology and International Symposium on Pediatric Neuro-Oncology meetings in 2014 and 2015; Fees for Participation in Review Activities such as Data Monitoring Boards, Statistical Analysis, Endpoint Committees, and the Like: Institut Gustav Roussy, which, in turn, received funding from Roche,* Comments: attendance at Trial Steering Group meetings. Paul S. Morgan—RELATED: Grant: Roche,* Comments: support for assistance for MR imaging aspects of the HERBY study; Support for Travel to Meetings for the Study or Other Purposes: Roche,* Comments: support for travel to meetings related to the HERBY study; Fees for Participation in Review Activities such as Data Monitoring Boards, Statistical Analysis, Endpoint Committees, and the Like: Roche,* Comments: for attendance at the Trial Steering Group of the HERBY study. Monika Warmuth-Metz—RELATED: Consulting Fee or Honorarium: Roche, Comments: payment for blinding evaluation of images; Support for Travel to Meetings for the Study or Other Purposes: Roche, Comments: payment of travel expenses for the imaging review training; UNRELATED: Grants/Grants Pending: German Children's Cancer Foundation,* Comments: money for the evaluation of imaging of all patients in the German brain tumor study. The German Children's Cancer Foundation is a parents' association, and the money we receive is provided by donations. Esther Sanchez Aliaga—RELATED: Consulting Fee or Honorarium: F. Hoffmann-La

Roche; Support for Travel to Meetings for the Study or Other Purposes: F. Hoffmann-La Roche. Daniel Warren—RELATED: Support for Travel to Meetings for the Study or Other Purposes: F. Hoffmann-La Roche; Fees for Participation in Review Activities such as Data Monitoring Boards, Statistical Analysis, Endpoint Committees, and the Like: F. Hoffmann-La Roche; UNRELATED: Consultancy: F. Hoffmann-La Roche. Raphael Calmon—RELATED: Support for Travel to Meetings for the Study or Other Purposes: F. Hoffmann-La Roche; Fees for Participation in Review Activities such as Data Monitoring Boards, Statistical Analysis, Endpoint Committees, and the Like: F. Hoffmann-La Roche. Jacques Grill—UNRELATED: Grants/Grants Pending: Novartis,* Roche,* Bristol-Myers Squibb.* Darren Hargrave—RELATED: Support for Travel to Meetings for the Study or Other Purposes: Roche, Comments: expenses paid for Trial Steering Group meeting; UNRELATED: Consultancy: I have provided consultancy for Roche for bevacizumab plus other portfolio products. Josep Garcia—OTHER RELATIONSHIPS: I am a clinical scientist working at Roche, which is disclosed already as part of my institution. Gudrun Zahlmann—UNRELATED: Employment: F. Hoffmann-La Roche; Stock/Stock Options: employee program of the company.* Money paid to the institution.

REFERENCES

1. Dhermain FG, Hau P, Lanfermann H, et al. **Advanced MRI and PET imaging for assessment of treatment response in patients with gliomas.** *Lancet Neurol* 2010;9:906–20 CrossRef Medline
2. Brandes AA, Franceschi E, Tosoni A, et al. **MGMT promoter methylation status can predict the incidence and outcome of pseudoprogression after concomitant radiochemotherapy in newly diagnosed glioblastoma patients.** *J Clin Oncol* 2008;26:2192–97 CrossRef Medline
3. Taal W, Brandsma D, de Bruin HG, et al. **Incidence of early pseudoprogression in a cohort of malignant glioma patients treated with chemoradiation with temozolomide.** *Cancer* 2008;113:405–10 CrossRef Medline
4. Wen PY, Macdonald DR, Reardon DA, et al. **Updated response assessment criteria for high-grade gliomas: response assessment in neuro-oncology working group.** *J Clin Oncol* 2010;28:1963–72 CrossRef Medline
5. Chinot OL, Macdonald DR, Abrey LE, et al. **Response assessment criteria for glioblastoma: practical adaptation and implementation in clinical trials of antiangiogenic therapy.** *Curr Neurol Neurosci Rep* 2013;13:347 CrossRef Medline
6. Chinot OL, Wick W, Mason W, et al. **Bevacizumab plus radiotherapy-temozolomide for newly diagnosed glioblastoma.** *N Engl J Med* 2014;370:709–22 CrossRef Medline
7. Warren KE, Poussaint TY, Vezina G, et al. **Challenges with defining response to antitumor agents in pediatric neuro-oncology: a report from the response assessment in pediatric neuro-oncology (RAPNO) working group.** *Pediatr Blood Cancer* 2013;60:1397–401 CrossRef Medline
8. Kang TW, Kim ST, Byun HS, et al. **Morphological and functional MRI, MRS, perfusion and diffusion changes after radiosurgery of brain metastasis.** *Eur J Radiol* 2009;72:370–80 CrossRef Medline
9. Cha J, Kim ST, Kim HJ, et al. **Analysis of the layering pattern of the apparent diffusion coefficient (ADC) for differentiation of radiation necrosis from tumour progression.** *Eur Radiol* 2013;23:879–86 CrossRef Medline
10. Lee WJ, Choi SH, Park CK, et al. **Diffusion-weighted MR imaging for the differentiation of true progression from pseudoprogression following concomitant radiotherapy with temozolomide in patients with newly diagnosed high-grade gliomas.** *Acad Radiol* 2012;19:1353–61 CrossRef Medline
11. Chang YW, Yoon HK, Shin HJ, et al. **MR imaging of glioblastoma in children: usefulness of diffusion/perfusion-weighted MRI and MR spectroscopy.** *Pediatr Radiol* 2003;33:836–42 CrossRef Medline
12. Batchelor TT, Gerstner ER, Emblem KE, et al. **Improved tumor oxygenation and survival in glioblastoma patients who show increased blood perfusion after cediranib and chemoradiation.** *Proc Natl Acad Sci U S A* 2013;110:19059–64 CrossRef Medline
13. Nasser M, Gahramanov S, Netto JP, et al. **Evaluation of pseudoprogression in patients with glioblastoma multiforme using dynamic magnetic resonance imaging with ferumoxytol calls**

- RANO criteria into question.** *Neuro Oncol* 2014;16:1146–54 CrossRef Medline
14. Bag AK, Cezayirli PC, Davenport JJ, et al. **Survival analysis in patients with newly diagnosed primary glioblastoma multiforme using pre- and post-treatment peritumoral perfusion imaging parameters.** *J Neurooncol* 2014;120:361–70 CrossRef Medline
 15. Ratai EM, Zhang Z, Snyder BS, et al. **Magnetic resonance spectroscopy as an early indicator of response to anti-angiogenic therapy in patients with recurrent glioblastoma: RTOG 0625/ACRIN 6677.** *Neuro Oncol* 2013;15:936–44 CrossRef Medline
 16. Orphanidou-Vlachou E, Auer D, Brundler MA, et al. **(1)H magnetic resonance spectroscopy in the diagnosis of paediatric low grade brain tumours.** *Eur J Radiol* 2013;82:e295–301 CrossRef Medline
 17. Quon H, Brunet B, Alexander A, et al. **Changes in serial magnetic resonance spectroscopy predict outcome in high-grade glioma during and after postoperative radiotherapy.** *Anticancer Res* 2011;31:3559–65 Medline
 18. Clinical Trial Imaging Endpoint Process Standards Guidance for Industry (Draft Guidance March 2015). <http://www.fda.gov/ucm/groups/fdagov-public/@fdagov-drugs-gen/documents/document/ucm268555.pdf>. Accessed October 19, 2015
 19. Ellingson BM, Bendszus M, Boxerman J, et al; Jumpstarting Brain Tumor Drug Development Coalition Imaging Standardization Steering Committee. **Consensus recommendations for a standardized brain tumor imaging protocol in clinical trials.** *Neuro Oncol* 2015;17:1188–98 CrossRef Medline
 20. Ellingson BM, Kim HJ, Woodworth DC, et al. **Recurrent glioblastoma treated with bevacizumab: contrast-enhanced T1-weighted subtraction maps improve tumor delineation and aid prediction of survival in a multicenter clinical trial.** *Radiology* 2014;271:200–10 CrossRef Medline

Association of Automatically Quantified Total Blood Volume after Aneurysmal Subarachnoid Hemorrhage with Delayed Cerebral Ischemia

I.A. Zijlstra, C.S. Gathier, A.M. Boers, H.A. Marquering, A.J. Slooter, B.K. Velthuis, B.A. Coert, D. Verbaan, R. van den Berg, G.J. Rinkel, and C.B. Majoie



ABSTRACT

BACKGROUND AND PURPOSE: The total amount of extravasated blood after aneurysmal subarachnoid hemorrhage, assessed with semiquantitative methods such as the modified Fisher and Hijdra scales, is known to be a predictor of delayed cerebral ischemia. However, prediction rates of delayed cerebral ischemia are moderate, which may be caused by the rough and observer-dependent blood volume estimation used in the prediction models. We therefore assessed the association between automatically quantified total blood volume on NCCT and delayed cerebral ischemia.

MATERIALS AND METHODS: We retrospectively studied clinical and radiologic data of consecutive patients with aneurysmal SAH admitted to 2 academic hospitals between January 2009 and December 2011. Adjusted ORs with associated 95% confidence intervals were calculated for the association between automatically quantified total blood volume on NCCT and delayed cerebral ischemia (clinical, radiologic, and both). The calculations were also performed for the presence of an intraparenchymal hematoma and/or an intraventricular hematoma and clinical delayed cerebral ischemia.

RESULTS: We included 333 patients. The adjusted OR of total blood volume for delayed cerebral ischemia (clinical, radiologic, and both) was 1.02 (95% CI, 1.01–1.03) per milliliter of blood. The adjusted OR for the presence of an intraparenchymal hematoma for clinical delayed cerebral ischemia was 0.47 (95% CI, 0.24–0.95) and of the presence of an intraventricular hematoma, 2.66 (95% CI, 1.37–5.17).

CONCLUSIONS: A higher total blood volume measured with our automated quantification method is significantly associated with delayed cerebral ischemia. The results of this study encourage the use of rater-independent quantification methods in future multicenter studies on delayed cerebral ischemia prevention and prediction.

ABBREVIATIONS: aOR = adjusted odds ratio; aSAH = aneurysmal subarachnoid hemorrhage; DCI = delayed cerebral ischemia; IPH = intraparenchymal hematoma; IVH = intraventricular hematoma; TBV = total blood volume; WFNS scale = World Federation of Neurosurgical Societies scale

Delayed cerebral ischemia (DCI) occurs in 20%–30% of patients with aneurysmal subarachnoid hemorrhage (aSAH) and is associated with poor outcome.^{1–3} Patients who develop DCI need costly intensive care. The cause of DCI is multifactorial,

including larger and smaller vessel vasospasm, cortical spreading ischemia, microvascular dysfunction, and thrombosis.³ Blood-breakdown products in the subarachnoid and CSF spaces may cause vasospasm.² Several studies have reported the positive relationship between the total amount of extravasated blood after SAH and the development of vasospasm (at that time considered the main cause of DCI) by using CT grading scales such as the modified/revisited Fisher grading scale and the Hijdra scale.^{4–7} These grading scales only provide a rough estimation of the aneurysmal total blood volume (TBV) and are observer-dependent, factors that may add to the moderate prediction rates of DCI.⁸ More reliable quantification of TBV might result in better prediction of DCI, which can help clinicians more accurately identify patients at risk and more effectively use scarce resources.⁹ To assess the association of TBV with DCI, a reliable and valid method for measuring subarachnoid blood volume is needed, with correction for possible confounding influences. We recently validated a fully automatic method for TBV quantification on NCCT.

Received October 27, 2015; accepted after revision February 7, 2016.

From the Departments of Radiology (I.A.Z., A.M.B., H.A.M., R.v.d.B., C.B.M.), Neurosurgery (B.A.C., D.V.), and Biomedical Engineering and Physics (A.M.B., H.A.M.), Academic Medical Center, Amsterdam, the Netherlands; Departments of Radiology (B.-K.V.), Intensive Care (A.J.S.), and Neurology (C.S.G., G.J.R.), University Medical Center Utrecht, Utrecht, the Netherlands; and Department of Robotics and Mechatronics (A.M.B.), University of Twente, Enschede, the Netherlands.

H.A.M. received a research grant from Fonds NutsOhra (I403–023) to study the prognostic value of quantified blood in patients with aneurysmal subarachnoid hemorrhage.

Paper previously presented at: Annual Meeting of the European Congress of Radiology, March 2–6, 2016; Vienna, Austria.

Please address correspondence to IJsbrand A. Zijlstra, MD, Department of Radiology, Academic Medical Center, Meibergdreef 9, 1105 AZ, Amsterdam, the Netherlands; e-mail ij.a.zijlstra@amc.uva.nl

<http://dx.doi.org/10.3174/ajnr.A4771>

This method is based on a relative density increase of blood after aSAH in relation to different brain structures.¹⁰ In the current study, we aimed to assess the association of automatically quantified TBV with DCI.

MATERIALS AND METHODS

Patient Population

We included consecutive patients with aSAH who were admitted between January 2009 and December 2011 to 2 large university hospitals (Academic Medical Center Amsterdam and University Medical Center Utrecht) in the Netherlands.

“Aneurysmal SAH” was defined as an aneurysmal bleeding pattern with an associated aneurysm. Patients without aneurysms proved on CTA/MRA/DSA were excluded. We further excluded patients with a baseline CT obtained >24 hours after ictus because of the risk of blood clearance and patients in whom the CT scans could not be used for the automatic quantification method because of movement artifacts or metal artifacts caused by previous treatment. Patients with technically inadequate scans (scans in 2 parts or incomplete scans) were also excluded. Patients with an external ventricular drain on the first CT were excluded because of artifacts and possible blood clearance. TBV was defined as the sum of subarachnoid (cisternal and sulcal), intraparenchymal, intraventricular, and subdural blood.

Clinical and Imaging Data Collection

All baseline characteristics of the included patients were collected through retrospective review of the clinical charts by a single observer (C.S.G.). These included age, medical history of hypertension, date of the aSAH ictus, hospital admission date, clinical condition on admission according to the World Federation of Neurological Societies scale (WFNS),¹¹ NCCT date, the occurrence of rebleeding (clinical, not CT-confirmed, or radiologic), aneurysm location (anterior or posterior circulation), aneurysm treatment (coiling, clipping, or no aneurysm treatment), and date of death. The WFNS score on admission was dichotomized into favorable (1–3) and unfavorable (4–5). This observer also assessed the presence of clinical DCI, which was defined as clinical deterioration that could not be explained by any cause other than DCI, and radiologic DCI, which was defined as the presence of cerebral infarction on CT or MR images within 6 weeks after SAH or on the latest CT scan or MR image obtained before death, which could not be attributed to other causes such as surgical clipping or endovascular treatment, according to previously published criteria.¹² The patients were followed as long as they were hospitalized.

For the volume analysis, generally the first CT scan (all 5-mm sections) after the aSAH ictus was used. Only in case of a rebleeding within 24 hours and before treatment was the CT scan after rebleeding used because of the larger blood volume. All CT scans were anonymized before assessment (H.A.M. and I.A.Z.) and were thereafter assessed for the appropriateness for automated quantification (I.A.Z.). The TBV (in milliliters) was automatically quantified (Fig 1), and the quality of the automatic segmentation was evaluated by using ITK-SNAP, Version 2.4.0 (www.itksnap.org) (I.A.Z.).¹³

All CT scans were inspected for the presence of intraparenchy-

mal hematoma (IPH) and/or intraventricular hematoma (IVH) (I.A.Z.). The presence or absence of IPH and IVH was scored dichotomously because it was not possible to measure blood volume in separate locations with our automated quantification method. The differentiation between a blood clot in the Sylvian fissure and an IPH was made on the initial CTA (I.A.Z.).¹⁴ All estimates of blood volume and blood location were performed blinded to the presence or absence of DCI.

Statistical Analysis

Descriptive Statistics. Dichotomous variables were presented as percentages. Continuous variables were tested with the Shapiro-Wilk test for normal distribution ($W > 0.9$ is considered a normally distributed variable). Normally distributed variables were expressed as means with SDs, and not normally distributed variables were expressed as medians with interquartile ranges (25%–75%). Normally distributed variables were tested with the Student *t* test, and not normally distributed variables were tested with the Mann-Whitney *U* test. Categorical variables were tested by using the Fisher exact test.

Modeling. Logistic regression analysis was used to calculate odds ratios with associated 95% confidence intervals. Bivariable analyses were performed with previously chosen covariables known to be associated with DCI on the basis of the literature to identify important confounders (defined as variables that changed the crude OR from the univariable analysis by >10%).¹⁵ In the multivariable analysis, confounders were added to the univariable model to calculate adjusted odds ratios (aORs) with associated 95% CIs.

As our primary analysis, we assessed the association between TBV and clinical DCI (with or without radiologic DCI), radiologic DCI (with or without clinical DCI), and clinical and radiologic DCI (patients with both clinical and radiologic DCI) combined. Evaluated confounders were age, sex, neurologic status on admission (dichotomized WFNS grade), treatment of the aneurysm (clipping/coiling/no treatment), rebleeding, hypertension, IPH, and IVH.

As a secondary analysis, we assessed the association between blood location (IPH and IVH) and clinical DCI (with or without radiologic DCI). We used clinical DCI as the only outcome variable because we found similar aORs for all 3 outcome variables (clinical DCI, radiologic DCI, and both) in the primary analysis. Evaluated confounders were age, sex, neurologic status on admission (dichotomized WFNS grade), treatment of the aneurysm (clipping/coiling/no treatment), rebleeding, hypertension, blood volume, IPH (in the model with IVH as the central determinant), and IVH (in the model with IPH as the central determinant).

Because patients who die within 3 days after the aSAH ictus have a much lower risk of developing DCI, we performed sensitivity analyses in the subset of patients who survived >3 days after aSAH.

RESULTS

Patient Characteristics

We initially evaluated 458 potentially eligible patients with aSAH. Of these, 333 patients were included in the analyses (Fig 2). The

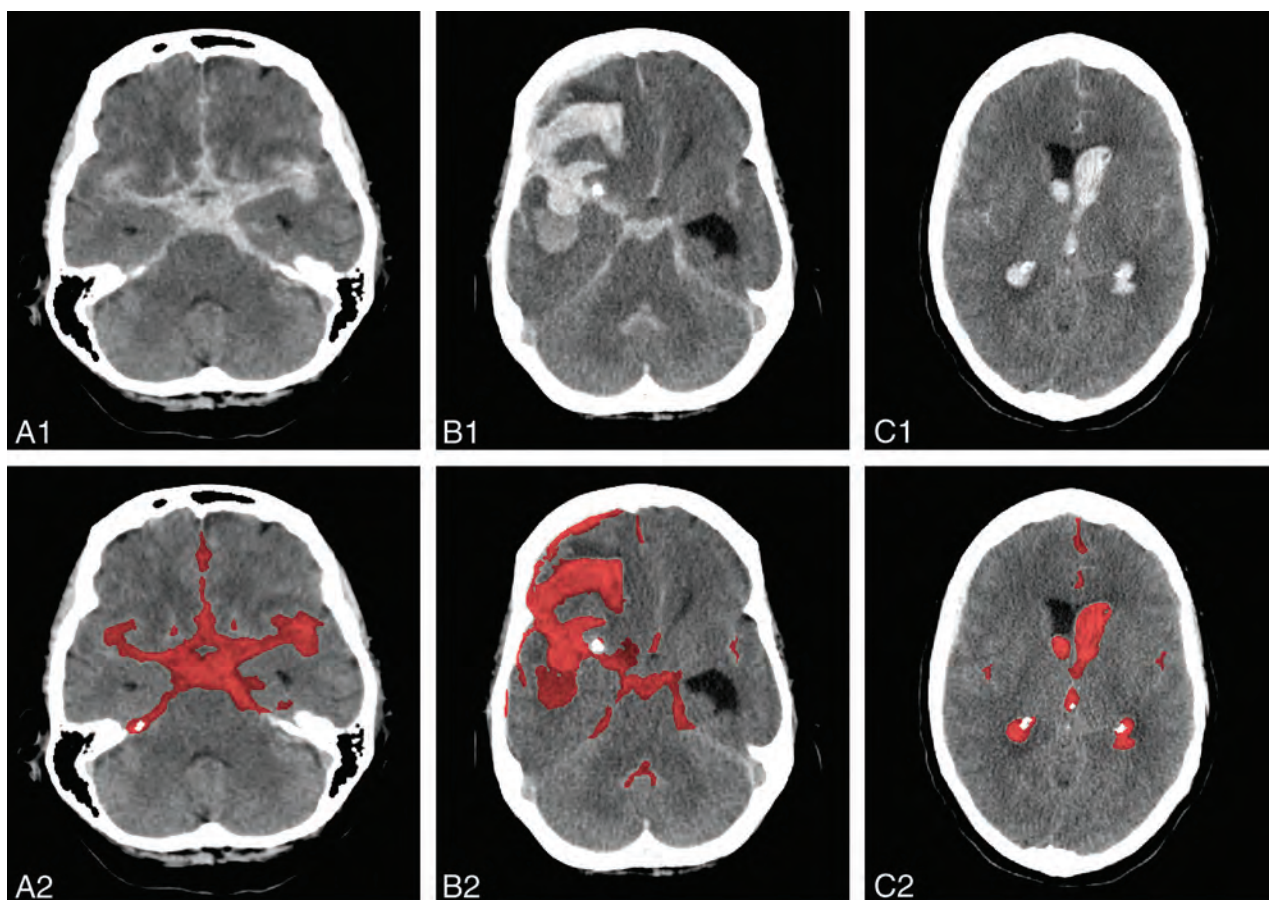


FIG 1. Examples of SAH bleeding patterns on CT (upper), with corresponding segmentations in red as provided by the automatic quantification method (lower).¹⁰ A, SAH with blood in both Sylvian fissures. B, SAH with the presence of IPH. C, SAH with the presence of IVH.

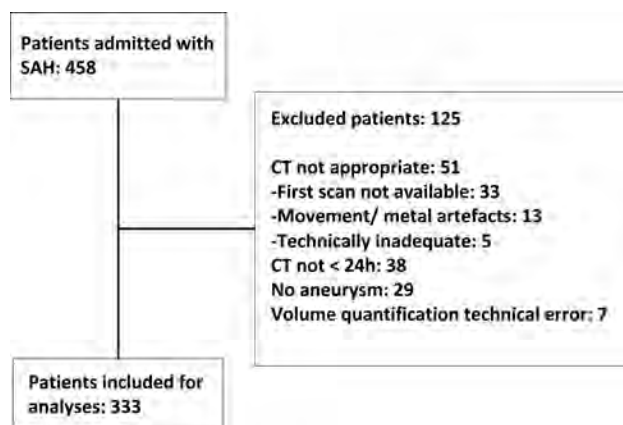


FIG 2. Flow chart of patient inclusion.

mean TBV was 46.1 ± 29.4 mL. Characteristics of the included patients are shown in Table 1.

Sixty-eight (20%) patients had clinical and/or radiologic DCI, 62 (19%) had clinical DCI (with or without radiologic DCI), 40 (12%) had radiologic DCI (with or without clinical DCI), and 34 (10%) had both clinical and radiologic DCI. Twenty-eight (8%) patients had only clinical DCI, and 6 (2%) had only radiologic DCI (Table 2). One (2.1%) patient developed clinical signs of DCI 2 days after the aSAH ictus. There were 102 patients (31%) with IPH, 203 patients (61%) with IVH, and 63 patients (19%) with

IPH and IVH combined. Forty-seven (14%) patients died within 3 days of the aSAH ictus. The mean TBV in these patients was 63.0 ± 34.1 mL.

Association between Blood Volume and Blood Location and DCI in the Total Group

The aOR (95% CI) of TBV and DCI (clinical, radiologic, both) was 1.02 (1.01–1.03) per milliliter of blood (Table 3). The aOR (95% CI) of IPH and clinical DCI was 0.47 (0.24–0.95) and of IVH and clinical DCI, 2.66 (1.37–5.17).

Sensitivity Analysis

In the 286 patients included in the sensitivity analyses, the mean TBV was 43.3 ± 27.6 mL. In the subgroup of patients without clinical DCI, the mean TBV was 40.8 ± 27.2 mL, and in the subgroup of patients with clinical DCI, 52.3 ± 27.5 mL ($P = .004$). IPH occurred in 85 (30%) patients; IVH, in 172 (60%) patients. The association results in the sensitivity analysis (Table 4) are similar to the results in the total group (Table 3).

DISCUSSION

In this study, a higher TBV, quantified with a fully automated method, was significantly associated with the development of DCI. The presence of an intraventricular hematoma was also positively associated with the development of DCI, whereas the pres-

Table 1: Patient characteristics

	Total Patient Group (%)	Patients with Clinical and/or Radiologic DCI	Patients without DCI (%)	P Value
No.	333	68 (20)	265 (80)	—
Female sex	238 (71)	47 (69)	191 (72)	.653
Age (yr) (mean) (SD)	55.7 (11.9)	56.0 (12.7)	55.7 (11.7)	.828
Hypertension in medical history	88 (26)	24 (35)	64 (24)	.090
WFNS favorable on admission (I–III)	163 (49)	34 (50)	129 (49)	.892
Mean TBV (mL) (SD) ^a	46.1 (29.4)	51.6 (27.3)	44.6 (29.8)	.080
IPH	102 (31)	16 (24)	86 (32)	.185
IVH	203 (61)	51 (75)	152 (57)	.008
IPH and IVH	63 (19)	12 (18)	51 (19)	.863
Rebleed	52 (16)	9 (13)	43 (16)	.708
Anterior circulation	245 (74)	50 (74)	195 (74)	1.000
Posterior circulation	88 (26)	18 (26)	70 (26)	
Neurosurgical treatment ^b	141 (42)	30 (44)	111 (42)	.325
Endovascular treatment ^c	135 (41)	36 (53)	99 (37)	
Death within 3 days	47 (14)	1 (1)	46 (17)	<.001

^a Automatically quantified total blood volume on noncontrast CT.

^b Two patients treated with bypass surgery.

^c One patient treated with stent, and 1 with parent vessel occlusion.

Table 2: Patient characteristics in groups with respect to DCI

	Patients with Clinical and/or Radiologic DCI	Patients with Clinical DCI (%) ^a	Patients with Radiologic DCI (%) ^b	Patients with Clinical and Radiologic DCI (%)
No.	68 (20)	62 (19)	40 (12)	34 (10)
Female sex	47 (69)	43 (69)	28 (70)	24 (71)
Age (yr) (mean) (SD)	56.0 (12.7)	55.4 (12.9)	57.9 (12.4)	57.1 (12.8)
Hypertension in medical history	24 (35)	21 (34)	18 (45)	15 (44)
WFNS favorable on admission (I–III)	34 (50)	30 (48)	18 (45)	14 (41)
Mean TBV (mL) (SD) ^c	51.6 (27.3)	52.1 (27.4)	53.2 (28.1)	54.3 (28.3)
IPH	16 (24)	14 (23)	7 (18)	5 (15)
IVH	51 (75)	47 (76)	31 (78)	27 (79)
IPH and IVH	12 (18)	10 (16)	5 (13)	3 (9)
Rebleed	9 (13)	9 (15)	6 (15)	6 (18)
Anterior circulation	50 (74)	45 (73)	28 (70)	23 (68)
Posterior circulation	18 (26)	17 (27)	12 (30)	11 (32)
Neurosurgical treatment ^d	30 (44)	28 (45)	19 (48)	17 (50)
Endovascular treatment ^e	36 (53)	33 (53)	19 (48)	16 (47)
Death within 3 days	1 (1)	1 (2)	1 (3)	1 (3)

^a Clinical DCI with or without radiologic DCI.

^b Radiologic DCI with or without clinical DCI.

^c Automatically quantified total blood volume on noncontrast CT.

^d Two patients treated with bypass surgery.

^e One patient treated with stent, and 1 with parent vessel occlusion.

ence of an intraparenchymal hematoma was negatively associated with DCI.

The association between TBV and DCI may appear small with an aOR of 1.02 per milliliter of blood. However, considering that the aOR is per milliliter of blood and that in our population, the mean TBV was 46.1 mL and the SD was almost 30 mL, this effect is substantial: A difference of 1 SD of TBV (30 mL) corresponds to an aOR of 1.81.

In both analyses assessing the association between TBV and DCI, we found similar aORs for all 3 outcome variables (clinical DCI, radiologic DCI, and both). This finding could justify using 1 outcome variable in future studies. Clinical DCI would be the most appropriate to use because almost all patients with radiologic DCI have clinical DCI. Moreover, the importance of radiologic DCI in the absence of clinical DCI is questionable. CT or MR

imaging might be performed for other reasons, showing areas of ischemia that are clinically unnoticed.

In the first publication on the relation between the amount and distribution of subarachnoid blood detected on NCCT and cerebral vasospasm (detected on angiography), it was concluded that blood localized in the subarachnoid space in sufficient amounts at specific sites is the only important etiologic factor in vasospasm.⁴ Because in our study we found an association of TBV, IPH, and IVH with clinical and radiologic DCI and not vasospasm, these studies are difficult to compare. One large difference is that in their study, not 1 patient with IVH developed clinical symptoms of DCI.

Only 1 more recent study investigated a semiautomatic blood quantification to assess the association between cisternal blood volume on NCCT and vasospasm after aSAH.¹⁶ In this study, a positive association was found. However, the method used was laborious because all blood was outlined manually. Moreover, no correction for potential confounders was performed.

Our study results are in line with results from other studies showing that patients without intraventricular blood and with a small amount of cisternal blood after aSAH are less likely to develop DCI, though the results are somewhat different because these studies used vasospasm as an end point instead of DCI.^{6,7} Nevertheless, these studies used the modified Fisher score instead of quantified blood volume to assess the amount of intracranial blood.⁴

The positive association between IVH and DCI is not yet understood. Blood can

migrate toward the ventricles in 2 ways: first, straight from the aneurysm into the ventricles through a connecting hematoma or, second, by expansion of the subarachnoid blood toward one of the cisternal-ventricular foramina (Luschka, Magendie). The latter implies an initially higher volume of subarachnoid blood, with secondary ventricular redistribution. This might explain the association of IVH and DCI in this specific population. Additionally, patients who present with a nonaneurysmal IVH have a very low risk of developing DCI according to a study describing a series of patients with ruptured arteriovenous malformations, of whom 50 had an intraventricular component. Only 1 patient who also had an SAH component developed vasospasm, without signs of DCI.¹⁷ According to these and our results, it seems that the combination of IVH and aSAH is worse than IVH or aSAH alone.

When one tries to explain the negative association of the pres-

Table 3: Associations between blood volume and blood location and DCI in the total group (N = 333)

Dependent Variable	Central Determinant	OR (95% CI)	aOR (95% CI)
Clinical DCI (with or without radiologic DCI)	TBV ^a	1.01 (1.0–1.02) ^b	1.02 (1.01–1.03) ^b
	IPH ^c	0.61 (0.32–1.16)	0.47 (0.24–0.95)
	IVH ^d	2.31 (1.23–4.33)	2.66 (1.37–5.17)
Radiologic DCI (with or without clinical DCI)	TBV ^e	1.01 (1.0–1.02) ^b	1.02 (1.01–1.03) ^b
Clinical and radiologic DCI	TBV ^f	1.01 (1.0–1.02) ^b	1.02 (1.01–1.03) ^b

^a Confounders: age, WFNS, treatment, IPH, and IVH.^b Per milliliter of blood.^c Confounder: treatment.^d Confounders: WFNS and blood volume.^e Confounders: age, treatment, IPH, and IVH.^f Confounder: treatment, IPH, and IVH.**Table 4: Associations between blood volume and blood location and DCI in patients who survived 3 days or more (n = 286)**

Dependent Variable	Central Determinant	OR (95% CI)	aOR (95% CI)
Clinical DCI (with or without radiologic DCI)	TBV ^a	1.01 (1.00–1.03) ^b	1.02 (1.01–1.03) ^b
	IPH ^c	0.65 (0.33–1.25)	0.43 (0.21–0.89)
	IVH ^d	2.41 (1.27–4.57)	2.03 (1.05–3.92)
Radiologic DCI (with or without clinical DCI)	TBV ^a	1.01 (1.00–1.03) ^b	1.02 (1.01–1.03) ^b
Clinical and radiologic DCI	TBV ^a	1.02 (1.00–1.03) ^b	1.02 (1.01–1.03) ^b

^a Confounders: IPH and IVH.^b Per milliliter of blood.^c Confounders: WFNS, blood volume, and IVH.^d Confounder: blood volume.

ence of an IPH with clinical DCI, it could very well be that in these patients, clinical DCI was less often detected because they already had a neurologic deficit due to the IPH. To our knowledge, there is no literature confirming this theory. Further studies are needed to confirm this and to determine the association between IVH and IPH and DCI. In such a study, blood volume values for each separate compartment can be determined and subsequently associated with the clinical course.

The strengths of our study are fast and objective estimation of the TBV by using a validated automatic quantification method, adjustment for confounders to make the estimation of the association more reliable, and performance of a sensitivity analysis to evaluate the robustness of the model. In addition, we used DCI as an outcome variable instead of vasospasm because DCI is a more clinically relevant outcome measure and because vasospasm and DCI can occur independently.^{2,12} In future studies, it might be possible to use the automated quantification method to study other subtypes of SAH (eg, due to intracranial dissection, AVM, benign perimesencephalic hemorrhage, and trauma).

Our study has some limitations. This was a retrospective study in which we could only study the data that were available in the clinical charts and on the available NCCTs. Because patients were followed up only during hospitalization, we may have potentially missed patients with DCI after discharge. In patients with clinical rebleeding within 24 hours after aSAH ictus, we might have underestimated the blood volume because this rebleeding was not CT-confirmed. Death during admission may be a competing risk for the development of DCI. Unfortunately, due to the composition of our data, we were unable to perform a reliable competing risk analysis.

Limitations of the automated quantification method are that imaging artifacts can make the results unreliable. Although we do

not expect differences in the detection rate of TBV and aSAH between the anterior and posterior circulations, we have not yet investigated this possibility. Very small blood volumes with low density are not well-detected with automated detection.¹⁰ The volume assessments were performed on relatively thick sections of 5 mm. Thinner sections could potentially increase accuracy. However, with thinner sections, the noise level increases as well, which may actually reduce the accuracy. The method was validated by using 5-mm sections, and 5 mm is the standard section thickness used in our hospital and the referring centers. The volume of the IPH and IVH and the blood volume in separate territories could not be separately delineated.

CONCLUSIONS

We show that a higher TBV, measured with our automated quantification method, is significantly associated with DCI. The results of this study encourage the use of rater-independent quantifica-

tion methods in future multicenter studies on DCI prevention and prediction.

Disclosures: Henk A. Marquering—RELATED: Grant: NutsOhra,* Comments: The evaluation of the prognostic value of the quantitative hemorrhage volume detection is being sponsored by a grant from NutsOhra; UNRELATED: Grants/Grants Pending: NutsOhra,* Rene van den Berg—UNRELATED: Consultancy: DePuy Codman, Comments: coil development. Charles B. Majoe—UNRELATED: Grants/Grants Pending: Dutch Heart Foundation,* Toegepast Wetenschappelijk Instituut voor Neuromodulatie Foundation*; Payment for Lectures (including service on Speakers Bureaus): Stryker.* *Money paid to the institution.

REFERENCES

1. Budohoski KP, Guilfoyle M, Helmy A, et al. **The pathophysiology and treatment of delayed cerebral ischaemia following subarachnoid haemorrhage.** *J Neurol Neurosurg Psychiatry* 2014;85:1343–53 CrossRef Medline
2. Cossu G, Messerer M, Oddo M, et al. **To look beyond vasospasm in aneurysmal subarachnoid haemorrhage.** *Biomed Res Int* 2014;2014: 628597 CrossRef Medline
3. Macdonald RL. **Delayed neurological deterioration after subarachnoid haemorrhage.** *Nat Rev Neurol* 2014;10:44–58 CrossRef Medline
4. Fisher CM, Kistler JP, Davis JM. **Relation of cerebral vasospasm to subarachnoid hemorrhage visualized by computerized tomographic scanning.** *Neurosurgery* 1980;6:1–9 CrossRef Medline
5. Frontera JA, Claassen J, Schmidt JM, et al. **Prediction of symptomatic vasospasm after subarachnoid hemorrhage: the modified Fisher scale.** *Neurosurgery* 2006;59:21–27, discussion 21–27 Medline
6. Claassen J, Bernardini GL, Kreiter K, et al. **Effect of cisternal and ventricular blood on risk of delayed cerebral ischemia after subarachnoid hemorrhage: the Fisher scale revisited.** *Stroke* 2001;32: 2012–20 CrossRef Medline
7. de Rooij NK, Greving JP, Rinkel GJ, et al. **Early prediction of delayed cerebral ischemia after subarachnoid hemorrhage: development and validation of a practical risk chart.** *Stroke* 2013;44:1288–94 CrossRef Medline

8. de Rooij NK, Rinkel GJ, Dankbaar JW, et al. **Delayed cerebral ischemia after subarachnoid hemorrhage: a systematic review of clinical, laboratory, and radiological predictors.** *Stroke* 2013;44:43–54 CrossRef Medline
9. Crobeddu E, Mittal MK, Dupont S, et al. **Predicting the lack of development of delayed cerebral ischemia after aneurysmal subarachnoid hemorrhage.** *Stroke* 2012;43:697–701 CrossRef Medline
10. Boers AM, Zijlstra IA, Gathier CS, et al. **Automatic quantification of subarachnoid hemorrhage on noncontrast CT.** *AJNR Am J Neuroradiol* 2014;35:2279–86 CrossRef Medline
11. **Report of World Federation of Neurological Surgeons Committee on a Universal Subarachnoid Hemorrhage Grading Scale.** *J Neurosurg* 1988;68:985–86 Medline
12. Vergouwen MD. **Vasospasm versus delayed cerebral ischemia as an outcome event in clinical trials and observational studies.** *Neurocrit Care* 2011;15:308–11 CrossRef Medline
13. Yushkevich PA, Piven J, Hazlett HC, et al. **User-guided 3D active contour segmentation of anatomical structures: significantly improved efficiency and reliability.** *Neuroimage* 2006;31:1116–28 CrossRef Medline
14. van der Zande JJ, Hendrikse J, Rinkel GJ. **CT angiography for differentiation between intracerebral and intra-Sylvian hematoma in patients with ruptured middle cerebral artery aneurysms.** *AJNR Am J Neuroradiol* 2011;32:271–75 CrossRef Medline
15. Twisk JW. *Inleiding in de toegepaste biostatistiek.* Vol 3. Maarssen: Elsevier Gezondheidszorg; 2014:242
16. Friedman JA, Goerss SJ, Meyer FB, et al. **Volumetric quantification of Fisher grade 3 aneurysmal subarachnoid hemorrhage: a novel method to predict symptomatic vasospasm on admission computerized tomography scans.** *J Neurosurg* 2002;97:401–07 CrossRef Medline
17. Gross BA, Du R. **Vasospasm after arteriovenous malformation rupture.** *World Neurosurg* 2012;78:300–05 CrossRef Medline

Centripetal Propagation of Vasoconstriction at the Time of Headache Resolution in Patients with Reversible Cerebral Vasoconstriction Syndrome

M. Shimoda, S. Oda, A. Hirayama, M. Imai, F. Komatsu, K. Hoshikawa, H. Shigematsu, J. Nishiyama, and T. Osada



ABSTRACT

BACKGROUND AND PURPOSE: Reversible cerebral vasoconstriction syndrome is characterized by thunderclap headache and diffuse segmental vasoconstriction that resolves spontaneously within 3 months. Previous reports have proposed that vasoconstriction first involves small distal arteries and then progresses toward major vessels at the time of thunderclap headache remission. The purpose of this study was to confirm centripetal propagation of vasoconstriction on MRA at the time of thunderclap headache remission compared with MRA at the time of reversible cerebral vasoconstriction syndrome onset.

MATERIALS AND METHODS: Of the 39 patients diagnosed with reversible cerebral vasoconstriction syndrome at our hospital during the study period, participants comprised the 16 patients who underwent MR imaging, including MRA, within 72 hours of reversible cerebral vasoconstriction syndrome onset (initial MRA) and within 48 hours of thunderclap headache remission.

RESULTS: In 14 of the 16 patients (87.5%), centripetal propagation of vasoconstriction occurred from the initial MRA to remission of thunderclap headache, with typical segmental vasoconstriction of major vessels. These mainly involved the M1 portion of the MCA (10 cases), P1 portion of the posterior cerebral artery (10 cases), and A1 portion of the anterior cerebral artery (5 cases).

CONCLUSIONS: This study found evidence of centripetal propagation of vasoconstriction on MRA obtained at the time of thunderclap headache remission, compared with MRA obtained at the time of reversible cerebral vasoconstriction syndrome onset. If clinicians remain unsure of the diagnosis during early-stage reversible cerebral vasoconstriction syndrome, this time point represents the best opportunity to diagnose reversible cerebral vasoconstriction syndrome with confidence.

ABBREVIATIONS: RCVS = reversible cerebral vasoconstriction syndrome; TCH = thunderclap headache

Reversible cerebral vasoconstriction syndrome (RCVS) is characterized by thunderclap headache (TCH) and diffuse segmental constriction of cerebral arteries that resolves spontaneously within 3 months.^{1,2} RCVS can be spontaneous or evoked by various factors such as postpartum status, vasoactive drugs, catecholamine-secreting tumors, immunosuppressants, or blood products.^{3,4} RCVS is poorly understood and has recently been estimated to be more common than previously thought.² Unpredictable and transient failure of the regulation of cerebral arterial

tone through sympathetic overactivity is thought to play a role in the development of RCVS.^{1,5}

TCH is usually the first symptom of RCVS, and typically recurs for 1–2 weeks after onset.^{3–5} The final TCH occurs at a mean of 7–8 days after onset, and all noteworthy headaches are generally gone within 3 weeks after onset.^{4,6,7} Conventional DSA was crucial to the diagnosis of RCVS in early case reports and typically showed diffuse segmental vasoconstrictions involving major vessels, like a “string of beads” or “string of sausages.”⁴ More recently, MRA has been widely used as a noninferior tool to evaluate vasoconstriction in patients with RCVS.^{3,4,6} Findings of typical segmental vasoconstriction of major vessels are not obtained in about one-third of patients with RCVS if the initial MRA is performed within 10 days of headache onset.^{4,6,8} Ducros et al^{4,9} postulated that the arterial abnormalities first involve small distal arteries and then progress toward major vessels.

This study retrospectively investigated whether centripetal propagation of vasoconstriction on MRA at the time of TCH re-

Received September 30, 2015; accepted after revision February 5, 2016.

From the Department of Neurosurgery (M.S., S.O., A.H., M.I., F.K., K.H.), Tokai University Hachioji Hospital, Tokyo, Japan; and Department of Neurosurgery (H.S., J.N., T.O.), Tokai University School of Medicine, Kanagawa, Japan.

Please address correspondence to Masami Shimoda, MD, Department of Neurosurgery, Tokai University Hachioji Hospital, 1838 Ishikawa-machi, Hachioji, Tokyo 192-0032, Japan; e-mail: mashimoda-nsu@umin.ac.jp



Indicates article with supplemental on-line table.

<http://dx.doi.org/10.3174/ajnr.A4768>

mission was evident compared with MRA at the time of RCVS onset.

MATERIALS AND METHODS

Patient Population

Patients diagnosed with RCVS in Tokai University Hachioji Hospital according to the following 5 criteria for RCVS were included in our data base: 1) acute and severe headache (often TCH) with or without focal deficits or seizures; 2) a uniphasic course without any new symptoms >1 month after clinical onset; 3) segmental, multifocal vasoconstriction of cerebral arteries as shown by DSA or indirect angiography (eg, MRA or 3D CTA); 4) no evidence of aneurysmal SAH; and 5) complete or substantial normalization of arteries on follow-up DSA or indirect angiography performed within 12 weeks after clinical onset.^{2,4} CSF analysis was not routinely performed on patients in this study.

Subjects were selected from among the 39 patients entered into the RCVS data base at Tokai University Hachioji Hospital between October 2010 and April 2015. Ten of these patients who did not undergo initial MRA/MR imaging within 72 hours of RCVS onset were excluded because they were admitted in the subacute phase (≥ 3 days after onset). In addition, 13 patients with RCVS who did not undergo MRA/MR imaging within 48 hours of TCH remission were excluded because they did not visit an outpatient clinic at the time of TCH remission (subacute phase) due to their comfortable medical condition. The remaining 16 patients with RCVS who underwent MR imaging within 72 hours of RCVS onset, within 48 hours of remission of TCH, and 3 months after RCVS onset were included in this retrospective study.

Clinical and imaging records were evaluated retrospectively. Study approval was obtained from the Institutional Review Board for Clinical Research at Tokai University School of Medicine.

Imaging Protocol

We differentiated primary angiitis of the central nervous system from RCVS on the basis of an insidious onset, low incidence of TCH, mostly irreversible angiographic irregularities, and inflammatory reactions evident in the CSF.^{2,10} At all time points, serial MR imaging included axial conventional T1WI, FLAIR images, DWI, and MRA, all performed by using a 1.5T superconducting magnet (Signa Excite or HDX; GE Healthcare, Milwaukee, Wisconsin) with a quadrature head coil. Pulse sequences were as follows: FLAIR (TR/TE, 8000/120 ms; TI, 2000 ms; section thickness/section gap, 7.0/1.0 mm; FOV, 24 × 24 cm; NEX, 1; matrix, 256 × 224), T1WI (TR/TE, 2000/24 ms; TI, 750 ms; section thickness/section gap, 7.0/1.0 mm; FOV, 24 × 24 cm; NEX, 2; matrix, 256 × 192), and 3D TOF MRA (TR/TE, 27/6.8 ms; flip angle, 16°; bandwidth, 14.7 Hz; FOV, 18 × 18 cm; slab thickness, 70 mm; section thickness, 1.2 mm; matrix, 256 × 192; NEX, 1). MR imaging was completed within 13–15 minutes.

Definition of Variables

“TCH” was defined as a severe pain peaking within seconds. The presence of TCH was diagnosed by a thorough interview of the patient. “TCH remission” was defined as the time at which the last TCH improved. “Hypertensive emergency” was defined as sys-

tolic blood pressure of >180 mm Hg or diastolic blood pressure of >120 mm Hg.

“Cortical SAH” was defined as a nontraumatic, nonaneurysmal SAH characterized by clots distributed over the cerebral convexity, sparing the basal cistern.¹¹ In patients with cortical SAH, conventional DSA or 3D CTA or both were routinely performed to rule out other causes of SAH, such as aneurysm or vessel malformation. “Posterior reversible encephalopathy syndrome” was defined as a characteristic MR imaging pattern of vasogenic edema with hemispheric boundary zones of hyperintensities on FLAIR, with increased ADC values affecting the cortex and subcortical and deep white matter to varying degrees.^{2,12}

Localization of vasoconstriction of the cerebral arteries was evaluated on MRA. “Centripetal propagation of vasoconstriction” was defined as a vasoconstriction that progressed from the distal arteries at the time of TCH (ie, on MRA performed within 72 hours of RCVS onset) to the major cerebral arteries of the circle of Willis (defined as the ICA, the A1 portion of the anterior cerebral artery, and/or the P1 portion of the posterior cerebral artery) and the M1 portion of the MCA, basilar artery, and vertebral artery on MRA performed within 48 hours of TCH remission. A “hyperintense vessel sign” was defined as a focal or tubular hyperintensity in the subarachnoid space on FLAIR¹³ that normalized within 12 weeks of clinical onset.

MR imaging findings were interpreted by at least 2 senior stroke neurosurgeons (M.S. and S.O., with 32 and 27 years of experience, respectively). In the case of disagreement between raters, diagnosis was obtained by consensus decision. Outcomes were assessed at 3 months by using the mRS.

Treatment Protocol

Vasoactive medications were stopped in all patients. Symptomatic analgesic treatment was used in all patients without a standard protocol. Oral administration of lomerizine hydrochloride was recommended for prevention of cerebral vasoconstriction. Steroids were avoided. For patients with severe TCH, a low dose of propofol was infused intravenously at 30–50 mg/h. For patients who experienced a hypertensive emergency, nicardipine was used with intravenous infusion of the dose adapted to normalize blood pressure levels.

RESULTS

Clinical Features and Associated Lesions

The On-line Table summarizes the clinical characteristics of the 16 patients with RCVS who underwent MR imaging within 72 hours of RCVS onset and within 48 hours of the remission of TCH. Ten of these 16 patients had a history of migraine before the onset of RCVS, and 3 of these 10 patients experienced an aura. All 10 patients who had a history of migraine stated that their headaches were completely different and more severe than their usual attacks. The 16 patients with RCVS included 2 postpartum women. Six of the 16 patients were using a vasoactive substance such as a selective serotonin reuptake inhibitor or triptans. Overuse of triptan was identified in only 1 case. Two of the 16 patients experienced bathing-related RCVS. Four showed a “blood pressure surge” defined as a hypertensive emergency during the peak of the TCH, and no patients displayed permanently elevated

Location of vasoconstricted vessels on initial MRA and MRA performed at TCH remission

Case	Initial MRA		Duration of TCH (Days)	MRA at TCH Remission	
	Days after Onset	Location of Vasoconstriction		Days after Onset	Location of Vasoconstriction
1	0	L-M2/3, R-P3	10	10	B-M1/2/3, B-P1/2/3, B-VA
2	0	B-M2/3, B-P2/3	8	10	R-A1, B-P1
3	2	B-M2/3, B-P2/3, B-A2/3	9	9	B-A1, B-M1, B-P1, BA
4	0	L-M3, B-P2/3	5	7	L-M1, L-P1/2
5	1	R-P3, L-M2/3	7	7	R-M1, R-P2
6	1	R-M3, B-P2/3	12	12	R-M1, B-A1, B-P1/2, BA
7	0	B-M3, B-P3	4	4	B-M1/2, B-P1/2
8	2	B-M2/3, B-P2/3	20	20	B-P2/3, B-A1/2, B-IC, L-P1, BA
9	0	B-M2/3, B-P2/3	10	10	B-M1, B-P1
10	2	B-P2/3	7	10	L-P1
11	0	B-M3, B-P2/3	5	5	B-M3, B-P1/2
12	0	B-M2/3, B-P2/3	9	9	L-P2
13	1	L-M2/3, B-P2/3	6	7	Improvement
14	0	B-M3	4	4	B-M2, L-M1
15	2	L-M2/3	8	8	L-M1, L-IC
16	0	B-M2/3, B-P2/3	4	4	L-P1

Note:—B indicates bilateral; L, left; R, right; VA, vertebral artery; BA, basilar artery; IC, internal cerebral artery.

blood pressure. The 4 patients with a hypertensive emergency showed vasoconstriction of the distal MCA and posterior cerebral artery on initial MRA.

All patients reported multiple episodes of TCH. Because the clinical records were insufficient, we were unable to investigate the exact number of events of TCH retrospectively. TCH was the only symptom of RCVS in 13 patients (81.2%).

A mean delay of 0.69 days (range, 0–2 days) was seen between RCVS onset and initial MR imaging. In 9 of the 16 patients (56.2%), initial MR imaging was performed on day 0 (ie, within 24 hours of onset). In the remaining 7 patients, initial MR imaging was performed 1–2 days after onset.

Stroke as a complication of RCVS occurred in 6 of the 16 patients (37.5%). Evidence of cortical SAH was found on MR imaging performed on days 0–2 in 5 patients. Conventional angiography, 3D CTA, MR imaging, and MRA revealed no other causes of SAH. No patients had intracerebral hemorrhage or microbleeds on T2*-weighted imaging. One patient developed MCA/posterior cerebral artery watershed infarction on day 0. Evidence of posterior reversible encephalopathy syndrome was found on MR imaging performed on day 2 in 1 patient. Findings of brain lesions on follow-up MR imaging are summarized in the On-line Table.

Hyperintense vessel signs on FLAIR imaging with the initial MR imaging were found in 5 patients. Of these 5 patients, 4 displayed evidence of some kind of stroke lesion on initial MR imaging as a complication of RCVS (On-line Table). Among these 5 patients who showed findings of vessel hyperintensity on initial MR imaging, the findings remained on MR imaging at the time of TCH remission in 2 patients.

Centripetal Propagation of Vasoconstriction

The Table presents the changes in the location of vasoconstricted vessels from the initial MRA to the time of TCH remission. On initial MRA, bilateral vasoconstriction was found in 15 of the 16

patients (93.8%); vasoconstriction of the M2 or M3 portion of the MCA, in 15 patients (93.8%); vasoconstriction of the P2 or P3 portions of the posterior cerebral artery, in 14 patients (87.5%); and vasoconstriction of the A2 or A3 portions of the anterior cerebral artery, in 1 patient. The duration of TCH ranged from 4 to 20 days (mean, 8.0 days) after onset. MRA at the time of TCH remission was performed from 4 to 20 days (mean, 8.5 days) after onset.

On MRA at the time of TCH remission, centripetal propagation of vasoconstriction had occurred in 14 of the 16 cases (87.5%, all except cases 12 and 13), as indicated by the typical segmental vasoconstriction of major vessels. Bilateral centripetal propagation of vasoconstriction occurred in 10 of the 16 patients (62.5%). Centripetal propagation occurred in the M1 portion of the MCA (10 of 16 patients, 62.5%), the P1 portion of the posterior cerebral artery (10 of 16 patients, 62.5%), the A1 portion of the anterior cerebral artery (5 of 16 patients, 31.3%), the basilar artery (2 of 16 patients, 12.5%), and the ICA (2 of 16 patients, 12.5%). Vasoconstriction outlasted headache remission in all except 1 patient (case 13). Figures 1 and 2 present typical MRA findings for the centripetal propagation of vasoconstriction.

Among the 14 patients who showed findings of centripetal propagation of vasoconstriction, vasoconstriction of the distal arteries was consistently improved, but some findings remained in 2 patients (cases 1 and 8) on MRA at the time of TCH remission. Furthermore, these 2 patients displayed persistent hyperintense vessel signs on FLAIR imaging at the time of TCH remission. No patients showed aggravation of the vasoconstriction of the distal arteries on MRA at the time of TCH remission.

Clinical Features of the Chronic Stage

By definition, all 16 patients with RCVS displayed confirmed multifocal vasoconstriction that resolved within 12 weeks, as assessed by MRA. At the 3-month follow-up, the mRS scores of all 16 patients with RCVS were zero, and all patients were able to return to their prior professional activities.

DISCUSSION

Clinical Course and Mechanisms of TCH of RCVS

In patients with RCVS, TCH is the presenting symptom and usually recurs during ~1 week. In general, TCH occurs before any detectable vasoconstriction and vasoconstriction outlasts TCH.⁴ Whereas TCH, cortical SAH, intracerebral hemorrhage, and posterior reversible encephalopathy syndrome represent early manifestations that lead to a suspicion of RCVS, ischemic stroke can occur as late as 1–2 weeks after clinical onset, sometimes when the headache has resolved or after the patient has been discharged.^{3,4,6,7,9}

Dysregulation of cerebral vascular tone is known to result

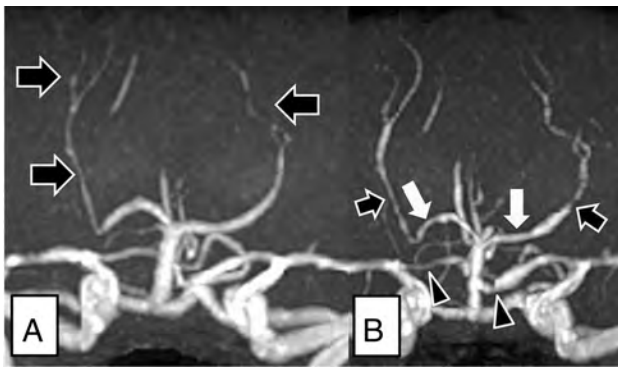


FIG 1. Images from a 28-year-old woman (case 6) with puerperium-related reversible cerebral vasoconstriction syndrome. The patient was admitted to the hospital 1 day after onset. *A*, The initial MRA obtained 1 day after the onset of thunderclap headache shows vasoconstrictions in the bilateral P2–3 portions of the posterior cerebral arteries (black arrows). *B*, MRA obtained at the time of TCH remission (12 days after onset) shows centripetal propagation of vasoconstriction in the bilateral P2 (black arrows) and P1 (white arrows) portions of the posterior cerebral arteries and bilateral A1 portions of the anterior cerebral arteries (black arrowheads).

from sympathetic overactivity, and endothelial dysfunction might be a central element in the pathogenesis of RCVS.^{2,14} Based on the characteristic clinical features of RCVS, Ducros et al⁴ postulated that the differing temporal courses of TCH, vasoconstriction, and stroke suggest that the underlying disturbance in the control of cerebral artery tone first involves small distal arteries responsible for hemorrhages and posterior reversible encephalopathy syndrome and then progresses toward the medium-sized and large arteries responsible for ischemic events. They speculated that at the initial stage of RCVS, sudden alterations in central vascular tone may lead to segmental vasoconstriction and vasodilation in small distal vessels and trigger TCH by abruptly stretching vessel walls, especially in the small distal arteries of the leptomeninges, resulting in stimulation of the trigeminal afferent nerve as a collection of perivascular pain-sensitive fibers.^{2,4,9,14}

Mechanism of Centripetal Propagation of Vasoconstriction in RCVS

Ducros² suggested that vasoconstriction of the second and first segments of large cerebral arteries might represent a reaction to distal blood-flow abnormalities, increasing during the ensuing 1 or 2 weeks. However, the precise mechanisms underlying centripetal propagation of vasoconstriction in RCVS remain unclear.

Centripetal progression of vasoconstriction from the manifestation of recurrent TCH to the remission of headaches has not been precisely delineated by using neuroradiologic imaging modalities such as MRA. Chen et al⁶ showed that vasoconstriction is maximal at TCH remission. However, they did not mention the centripetal propagation of vasoconstriction at TCH remission. Their initial MRA was performed at a mean of 10.4 ± 7.0 days (median, 9 days; range, 1–30 days) after TCH onset. We consider that the lower ratio of patients who underwent initial MRA/MR imaging within 72 hours of RCVS onset would have largely prevented identification of the centripetal propagation of vasoconstriction at TCH remission. Another review by Chen et al¹⁴ described that only a small number of their patients showed cen-

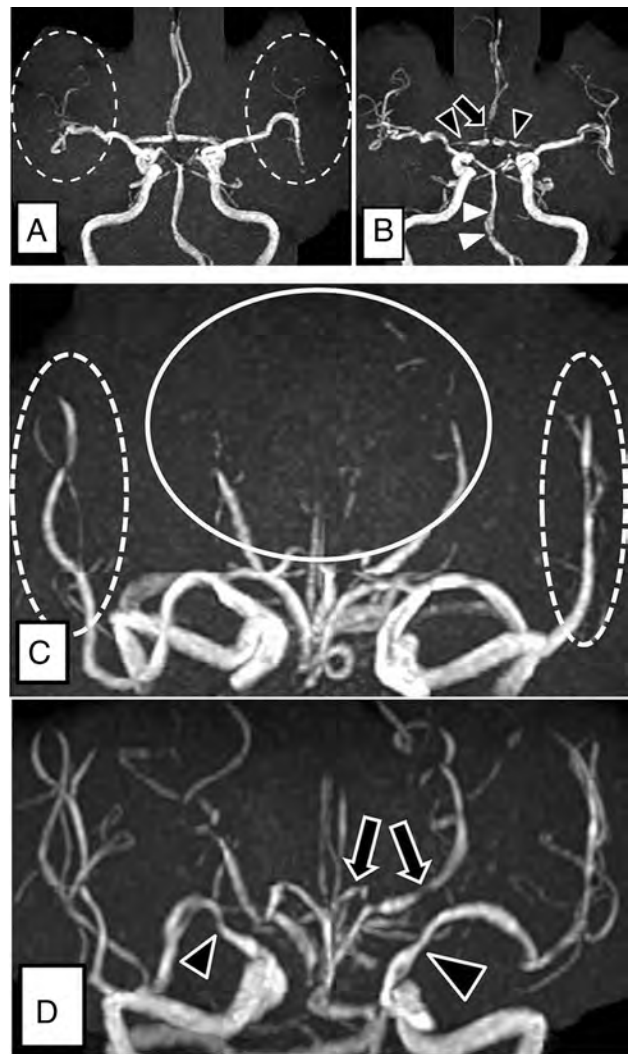


FIG 2. Images from a 60-year-old woman (case 8) with bath-related reversible cerebral vasoconstriction syndrome. The patient was admitted to the hospital 2 days after onset. *A* and *C*, Initial MRA obtained 2 days after onset of thunderclap headache shows vasoconstrictions in the bilateral distal MCAs (dotted circles) and bilateral P2–3 portions of the posterior cerebral arteries (*C*, circle). *B* and *D*, MRA obtained at the time of TCH remission (20 days after onset of TCH) shows centripetal propagation of vasoconstriction in the bilateral A1 portions (*B*, black arrowheads) and A2 portions (*B*, black arrow) of the anterior cerebral artery, bilateral internal cerebral arteries (*D*, black arrowheads), the left P1 portion of the posterior cerebral artery (*D*, black arrows), and the basilar artery (*B*, white arrowheads). Vasoconstriction of the bilateral P2–3 portions was improved, but some findings remained on MRA at the time of TCH remission.

tripetal propagation of vasoconstriction, citing their initial article.⁶

On the other hand, the purpose of this study was to prove centripetal propagation of vasoconstriction on MRA at the time of TCH remission, compared with MRA at the time of RCVS onset. The present investigation showed centripetal propagation of vasoconstriction from RCVS onset to the remission of TCH on MRA in 14 of the 16 patients with RCVS. Although the pathophysiologic mechanisms behind the centripetal propagation of vasoconstriction are unknown, this phenomenon is an important neuroradiologic finding for diagnosis.

Neuroradiologic Diagnosis of RCVS

RCVS should be considered for patients in the acute phase of cortical SAH or cryptogenic stroke with recurrent TCH.⁴ However, in the acute phase of RCVS, clinicians are likely to overlook a diagnosis of RCVS in patients who have no neuroradiologic findings of parenchymal lesions such as posterior reversible encephalopathy syndrome, intracerebral hemorrhage, or SAH on MR imaging because clinicians should diagnose RCVS only from a finding of vasoconstriction on MRA. The diagnosis of RCVS is reportedly missed in one-third of patients who undergo initial MRA within 10 days of headache onset.⁸ The diagnosis of RCVS in the acute phase by using MR imaging remains difficult because the vasoconstricted vessels are located peripherally at this time.

Patients with RCVS are predominantly women 50 years of age or younger. MRA of healthy young individuals usually depicts the MCA, posterior cerebral artery, and anterior cerebral artery branches distal to the circle of Willis and the first branch points of major vessels relatively well. A diagnosis of RCVS should thus be considered in young women reporting TCH if the depiction of peripheral vessels on MRA is poor. Furthermore, at the time of TCH remission, if a clinician confirms centripetal propagation of vasoconstriction with typical segmental vasoconstriction of the circle of Willis vessels, RCVS can be diagnosed with confidence.

Recently, a hyperintense vessel sign on FLAIR images has been reported as one of the neuroradiologic findings of vasoconstriction of a distal artery in the acute phase of RCVS.^{8,15} The hyperintense vessel sign could simply represent slow flow in collateral vessels distal to a proximal narrowing. Chen and Wang⁸ reported the presence of a hyperintense vessel sign on FLAIR images in 22% of patients with RCVS, and this sign in patients with RCVS was associated with more severe vasoconstriction that may progress to ischemic stroke or posterior reversible encephalopathy syndrome. In our study, the incidence of a hyperintense vessel sign on initial MR imaging was also low (5 of 16 patients, 31%). This sign tended to be more frequent in patients with RCVS who experienced stroke. We considered that a hyperintense vessel sign might be an indicator of the severity of RCVS, rather than a diagnostic tool.

Limitations

TOF-MRA is a widely available, noninvasive technique that requires no radiation exposure and no administration of contrast material. However, the limitations of TOF-MRA include a lower spatial resolution than DSA and CTA¹⁶ and the presence of flow-induced artifacts. These limitations may diminish the ability to depict vasoconstriction in small vessels.

Chen et al⁶ reported that vasoconstriction of M1 and P2 is important for the development of posterior reversible encephalopathy syndrome and ischemic stroke in patients with RCVS. Although the present study included only 1 patient with posterior reversible encephalopathy syndrome and 1 patient with cerebral infarction, a high proportion of patients displayed vasoconstriction of M1 or P2. This study thus found no relationship between the location of vasoconstricted vessels and the type of stroke. We believe that a more detailed examination of the relationships between the locations of constricted vessels and the type of stroke is necessary in patients with RCVS.

This was a retrospective study of a small group of patients, and prospective studies with a greater number of cases are necessary.

CONCLUSIONS

Compared with MRA at the time of RCVS onset, this study found evidence of centripetal propagation of vasoconstriction on MRA performed at the time of remission of TCH. This time point therefore may represent a useful opportunity to diagnose RCVS with greater confidence if the clinician remains unsure of the diagnosis during the early stages of RCVS.

REFERENCES

1. Calabrese LH, Dodick DW, Schwedt TJ, et al. **Narrative review: reversible cerebral vasoconstriction syndromes.** *Ann Intern Med* 2007;146:34–44 CrossRef Medline
2. Ducros A. **Reversible cerebral vasoconstriction syndrome.** *Lancet Neurol* 2012;11:906–17 CrossRef Medline
3. Chen SP, Fuh JL, Lirng JF, et al. **Recurrent primary thunderclap headache and benign CNS angiopathy: spectra of the same disorder?** *Neurology* 2006;67:2164–69 CrossRef Medline
4. Ducros A, Boukobza M, Porcher R, et al. **The clinical and radiological spectrum of reversible cerebral vasoconstriction syndrome: a prospective series of 67 patients.** *Brain* 2007;130:3091–101 CrossRef Medline
5. Dodick DW, Brown RD Jr, Britton JW, et al. **Nonaneurysmal thunderclap headache with diffuse, multifocal, segmental, and reversible vasospasm.** *Cephalalgia* 1999;19:118–23 CrossRef Medline
6. Chen SP, Fuh JL, Wang SJ, et al. **Magnetic resonance angiography in reversible cerebral vasoconstriction syndromes.** *Ann Neurol* 2010;67:648–56 CrossRef Medline
7. Chen SP, Fuh JL, Chang FC, et al. **Transcranial color Doppler study for reversible cerebral vasoconstriction syndromes.** *Ann Neurol* 2008;63:751–57 CrossRef Medline
8. Chen SP, Wang SJ. **Hyperintense vessels: an early MRI marker of reversible cerebral vasoconstriction syndrome?** *Cephalalgia* 2014;34:1038–39 CrossRef Medline
9. Ducros A, Fiedler U, Porcher R, et al. **Hemorrhagic manifestations of reversible cerebral vasoconstriction syndrome: frequency, features, and risk factors.** *Stroke* 2010;41:2505–11 CrossRef Medline
10. Chen SP, Fuh JL, Wang SJ. **Reversible cerebral vasoconstriction syndrome: an under-recognized clinical emergency.** *Ther Adv Neurol Disord* 2010;3:161–71 CrossRef Medline
11. Cuvinciu V, Viguier A, Calviere L, et al. **Isolated acute nontraumatic cortical subarachnoid hemorrhage.** *AJNR Am J Neuroradiol* 2010;31:1355–62 CrossRef Medline
12. Covarrubias DJ, Luetmer PH, Campeau NG. **Posterior reversible encephalopathy syndrome: prognostic utility of quantitative diffusion-weighted MR images.** *AJNR Am J Neuroradiol* 2002;23:1038–48 Medline
13. Iancu-Gontard D, Oppenheim C, Touzé E, et al. **Evaluation of hyperintense vessels on FLAIR MRI for the diagnosis of multiple intracerebral arterial stenoses.** *Stroke* 2003;34:1886–91 CrossRef Medline
14. Chen SP, Fuh JL, Wang SJ. **Reversible cerebral vasoconstriction syndrome: current and future perspectives.** *Expert Rev Neurother* 2011;11:1265–76 CrossRef Medline
15. Kameda T, Namekawa M, Shimazaki H, et al. **Unique combination of hyperintense vessel sign on initial FLAIR and delayed vasoconstriction on MRA in reversible cerebral vasoconstriction syndrome: a case report.** *Cephalalgia* 2014;34:1093–96 CrossRef Medline
16. Bash S, Villablanca JP, Jahan R, et al. **Intracranial vascular stenosis and occlusive disease: evaluation with CT angiography, MR angiography, and digital subtraction angiography.** *AJNR Am J Neuroradiol* 2005;26:1012–21 Medline

Application of Blood-Brain Barrier Permeability Imaging in Global Cerebral Edema

J. Ivanidze, O.N. Kallas, A. Gupta, E. Weidman, H. Baradaran, D. Mir, A. Giambrone, A.Z. Segal, J. Claassen, and P.C. Sanelli



ABSTRACT

BACKGROUND AND PURPOSE: Blood-brain barrier permeability is not routinely evaluated in the clinical setting. Global cerebral edema occurs after SAH and is associated with BBB disruption. Detection of global cerebral edema using current imaging techniques is challenging. Our purpose was to apply blood-brain barrier permeability imaging in patients with global cerebral edema by using extended CT perfusion.

MATERIALS AND METHODS: Patients with SAH underwent CTP in the early phase after aneurysmal rupture (days 0–3) and were classified as having global cerebral edema or nonglobal cerebral edema using established noncontrast CT criteria. CTP data were postprocessed into blood-brain barrier permeability quantitative maps of PS (permeability surface-area product), K^{trans} (volume transfer constant from blood plasma to extravascular extracellular space), K_{ep} (washout rate constant of the contrast agent from extravascular extracellular space to intravascular space), VE (extravascular extracellular space volume per unit of tissue volume), VP (plasmatic volume per unit of tissue volume), and F (plasma flow) by using Olea Sphere software. Mean values were compared using *t* tests.

RESULTS: Twenty-two patients were included in the analysis. K_{ep} (1.32 versus 1.52, $P < .0001$), K^{trans} (0.15 versus 0.19, $P < .0001$), VP (0.51 versus 0.57, $P = .0007$), and F (1176 versus 1329, $P = .0001$) were decreased in global cerebral edema compared with nonglobal cerebral edema while VE (0.81 versus 0.39, $P < .0001$) was increased.

CONCLUSIONS: Extended CTP was used to evaluate blood-brain barrier permeability in patients with SAH with and without global cerebral edema. K_{ep} is an important indicator of altered blood-brain barrier permeability in patients with decreased blood flow, as K_{ep} is flow-independent. Further study of blood-brain barrier permeability is needed to improve diagnosis and monitoring of global cerebral edema.

ABBREVIATIONS: BBBP = blood-brain barrier permeability; EES = extravascular extracellular space; F = plasma flow; GCE = global cerebral edema; IVS = intravascular space; K_{ep} = washout rate constant of the contrast agent from EES to IVS; K^{trans} = volume transfer constant from blood plasma to EES; PS = permeability surface-area product; VE = extravascular extracellular space volume per unit of tissue volume; VP = plasmatic volume per unit of tissue volume

The blood-brain barrier plays an important role in many CNS diseases relating to microvascular dysfunction and neuroinflammation, which are known to increase blood-brain barrier permeability (BBBP) in animal models.¹ Obtaining quantitative

BBBP information in the clinical setting would constitute a novel diagnostic and therapeutic strategy with widespread application. Global cerebral edema (GCE) represents a major complication in patients with SAH, is an independent predictor of SAH morbidity and mortality,^{2,3} and is thought to be related to disruption of the BBB. Moreover, delayed cerebral ischemia represents an independent major complication and poor prognostic factor in patients with SAH.⁴ Initial studies have shown that earlier diagnosis of delayed cerebral ischemia before manifestation of clinical symptoms, altered CBF, and NCCT findings is possible with BBBP imaging by using CTP.⁵ BBBP evaluation with CTP is a promising

Received June 22, 2015; accepted after revision February 22, 2016.

From the Departments of Radiology (J.I., O.N.K., A.G., E.W., H.B., D.M., P.C.S.), Healthcare Policy and Research (A.G.), and Neurology (A.Z.S.), Weill Cornell Medical College, New York-Presbyterian Hospital, New York, New York; and Department of Neurology (J.C.), New York-Presbyterian Hospital, Columbia University Medical Center, New York, New York.

This work was supported by the Radiological Society of North America Research and Education Foundation Resident Research Grant (awarded to J.I.), the Brain Aneurysm Foundation Grant (awarded to P.C.S.), and grant 5K23NS058387 from the National Institute of Neurological Disorders and Stroke (NINDS), a component of the National Institutes of Health (NIH). Its contents are solely the responsibility of the authors and do not necessarily represent the official view of NINDS or NIH.

Paper previously presented at: Annual Meeting of the American Society of Neuro-radiology, April 25–30, 2015; Chicago, Illinois.

Please address correspondence to Jana Ivanidze, MD, PhD, Department of Radiology, New York-Presbyterian Hospital, Weill Cornell Medical Center, New York, NY 10065; e-mail: jai9018@nyp.org; @jana_ivanidze

Indicates open access to non-subscribers at www.ajnr.org

<http://dx.doi.org/10.3174/ajnr.A4784>

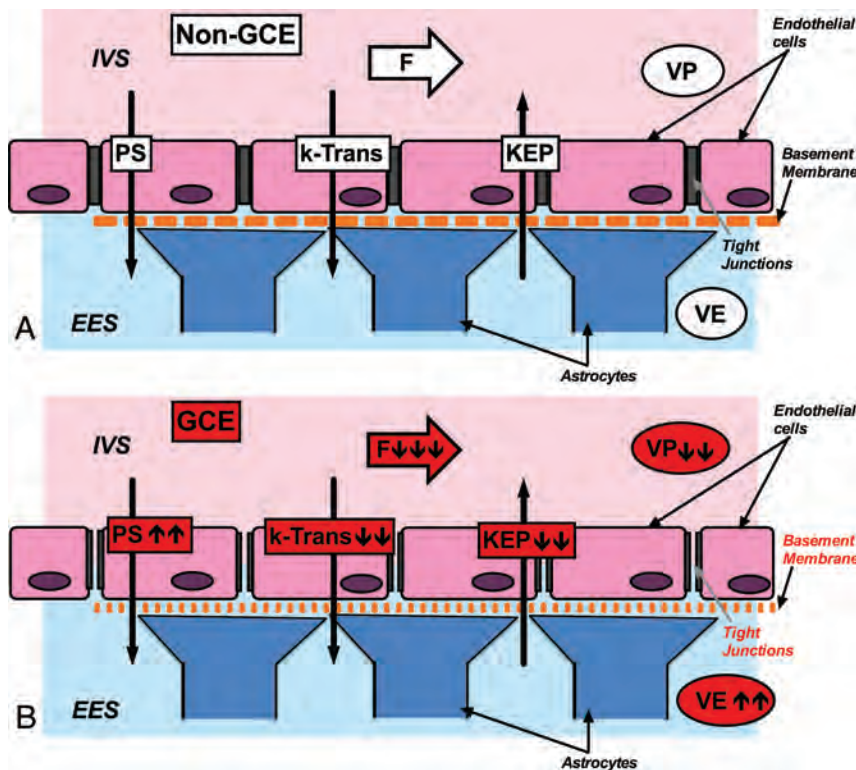


FIG 1. Cytoarchitecture of the BBB and schematic representation of BBB parameters derived from extended CTP. **A**, Non-GCE. At baseline, the BBB is composed of endothelial cells connected by tight junctions (as opposed to fenestrated endothelium outside of the CNS), the basement membrane, and the astrocyte processes. **B**, In the setting of GCE, there is an increase in EES as reflected by increased VE and decreased K_{ep} , indicating increased BBB (indicated in the drawing by a more porous basement membrane and tight junctions). PS is also elevated, indicating increased BBB. Importantly, K_{ep} is independent of F. In GCE, K_{ep} is the most reliable parameter to evaluate BBB in the setting of flow impairment.

technique, especially in patients with SAH, given that these patients are critically ill, require intensive monitoring, and often have contraindications to evaluation with MR imaging.⁵ Currently, imaging diagnosis of GCE relies on NCCT demonstrating diffuse effacement of the hemispheric sulci and diffuse obscuration of the hemispheric gray-white matter junction at the level of the centrum semiovale.³ These findings are challenging to identify in the setting of diffuse SAH and increased intracranial pressure effacing the sulci and cisterns. Moreover, NCCT fails to provide a direct assessment of the hemodynamic and microvascular dysfunction thought to be central to the underlying pathophysiology of GCE. Quantitative imaging of microvascular parameters, such as measures of BBBP, may provide for more accurate detection and monitoring of GCE compared with NCCT and could potentially improve the clinical management and outcomes of patients after SAH.

Extended CTP allows measurement of BBBP parameters not currently used in clinical practice. K_{ep} represents the washout rate constant of the contrast agent from the extravascular extracellular space (EES) to the intravascular space (IVS). K_{ep} therefore reflects the flow across the blood vessel wall from the EES to the IVS, and is independent of blood plasma flow. Based on transport equations proposed by Gowland et al⁶:

$$T = 1/K_{ep},$$

where T is the time constant for transfer across the BBB. Therefore, K_{ep} is thought to be related inversely to BBBP. K^{trans} represents the volume transfer constant from the blood plasma to the EES. PS is the permeability surface-area product and represents the flow across the blood vessel wall from the IVS to the EES. VE represents the volume in the EES per unit of tissue volume, and VP represents the plasmatic volume per unit of tissue volume. F represents the plasmatic flow. In summary, K_{ep} , PS, and K^{trans} can be viewed as the primary BBBP parameters because they reflect flow across the BBB.^{6,7} On the other hand, VE, VP, and F are descriptive of hemodynamic conditions on either side of the BBB (the IVS or the EES, respectively). Fig 1 summarizes the relationships of BBBP parameters under normal conditions and in the setting of GCE. CTP has numerous practical advantages that make it highly suitable for critically ill patients: it is widely available, can be performed with most scanners, has few contraindications, and has rapid acquisition and processing times. Assessment of these parameters offers a promising technique to evaluate BBBP in the clinical setting. However, it has not been widely adopted in clinical practice, with few published investigations studying measures of BBBP.^{5,8,9}

The purpose of our study was to apply BBBP imaging by using extended CTP in the setting of GCE and to quantitatively assess its parameters. We hypothesize that application of extended CTP is able to detect a significant difference in the BBBP parameters in patients with GCE compared with patients without GCE in the early phase after SAH.

MATERIALS AND METHODS

Population

This study was an institutional review board–approved retrospective analysis performed on consecutive patients with SAH enrolled in a prospective diagnostic accuracy trial at our institution. SAH was determined by a combination of NCCT, CTA, DSA, and/or CSF analysis. In this prospective study design, CTP was performed on days 0–3 after aneurysmal rupture to assess baseline cerebral perfusion and to compare with later examinations for interval change. All patients underwent either endovascular coiling or surgical clipping before CTP. Demographic and clinical data were collected (Table 1).

All patients with SAH with CTP performed on days 0–3 were included in our study. Exclusion criteria were CTP examinations with severe motion degradation limiting postprocessing methods and unavailable CTP data from archives for postprocessing.

Patients were classified into 3 outcome groups: GCE ($n = 11$),

Table 1: Clinical characteristics of the study population

	GCE (n = 11)	Non-GCE (n = 11)	P Value
Mean age (years)	51	49	.67
Sex			.92
Female	82% (9/11)	64% (7/11)	
Male	18% (2/11)	36% (4/11)	
Focal deficit at presentation	46% (5/11)	36% (4/11)	.66
Loss of consciousness	18% (2/11)	27% (3/11)	.61
Mean Hunt and Hess score	3.0	2.5	.15
Ventriculostomy catheter	82% (9/11)	82% (9/11)	1.00
Aneurysm location			.66
Anterior	64% (7/11)	54% (6/11)	
Posterior	36% (4/11)	46% (5/11)	
Treatment			.19
Coiled	27% (3/11)	54% (6/11)	
Clipped	73% (8/11)	46% (5/11)	

non-GCE ($n = 11$), and indeterminate ($n = 2$) based on admission NCCT. GCE was defined using the following established criteria³: complete or near-complete effacement of the hemispheric sulci and basal cisterns and bilateral and extensive disruption of the hemispheric gray-white matter junction (including basal ganglia) at the level of the centrum semiovale.³ Absence of both features resulted in classification as non-GCE. If only 1 feature was present, patients were classified as indeterminate. Classification was performed independently by 2 board-certified neuroradiologists (15 years and 3 years of experience) blinded to all other clinical and imaging data. Consensus reading was provided for adjudication. Interobserver agreement was analyzed using the κ coefficient.

Image Acquisition, Postprocessing, and Quantitative Analysis

CTP was performed in the early phase (days 0–3) after SAH, along with NCCT and CTA, as part of our study trial protocol. NCCT was performed from the foramen magnum to the vertex by using the following parameters: 120 kVp, 250 mAs, 1.0 rotation time, and 5.0-mm collimation.

Extended CTP scanning was performed on a 64-section scanner (LightSpeed Discovery HD-750; GE Healthcare, Milwaukee, Wisconsin) with an axial shuttle mode protocol for simultaneous acquisition of CTA and CTP data using the following parameters: 80 kVp, 400 mAs, 0.4 rotation time, 5.0-mm collimation with 17 cine cycles, and 2.8-second interscan delay for the first pass. Second pass technique included 10 cine cycles with a 10-second interscan delay. A total of 90 mL of nonionic contrast was intravenously administered at 4.0 mL/s followed by a 30 mL saline-bolus chaser. Average CT dose index volume was 300 mGy and average dose-length product was 2500 mGy-cm for the entire examination, including NCCT, CTA, and extended CTP.

For this study, CTP data were postprocessed off-line into maps of the BBBP parameters (K_{ep} , K^{trans} , PS, F, E [extraction fraction of contrast agent], VE, and VP), CBF, CBV, and MTT by using commercially available software (Olea Sphere V.2.0; Olea Medical, La Ciotat, France), based on previously published recommendations and guidelines.^{8,10} Quantitative analysis of CTP data was performed using standardized sampling of the cerebral cortex according to established methods^{4,11} with round, continuous ROIs

placed along the cerebral cortex. Up to 24 ROIs were included in each CTP section, distributed in the following territories: approximately 4 in the anterior cerebral artery, 12 in the middle cerebral artery, and 4 in the posterior cerebral artery territories. ROIs overlying large cortical vessels with CBF greater than 100 mL/100 g/min were excluded from the statistical analysis.¹² Mean values and 95% CIs were calculated using the remaining ROIs in all CTP sections for each patient. Unpaired t tests were performed to compare K_{ep} , K^{trans} , PS, F, extraction fraction of contrast agent, VE and VP, as well as CBF, CBV, and MTT in the GCE and non-GCE groups.

Permeability Modeling

Permeability parameters were calculated using the Delayed Lawrence and Lee Model.¹³ According to the Delayed Lawrence and Lee Model, K_{ep} represents the washout rate constant of the contrast agent from the EES to the IVS. The formula for K_{ep} is:

$$K_{ep} = K^{trans}/VE.$$

K_{ep} appears to have an inverse relationship with BBBP, and therefore decreases with increased permeability. Importantly, K_{ep} is independent of flow.⁶

K^{trans} equals the blood plasma flow per unit volume of tissue, derived through the formula:

$$K^{trans} = E \times F,$$

where E represents the extraction fraction of contrast agent that leaves the IVS in the first pass of the bolus through the vascular bed. E has no units assigned and has a value between 0 and 1. F represents the plasma flow per unit tissue volume and its units are $\text{mL} \times \text{mL}^{-1} \times \text{min}^{-1}$. K^{trans} is dependent on the blood flow.

PS represents the flow across the blood vessel wall from the IVS to the EES. The formula for PS is:

$$PS = -F \times (1 - Hct) \times \log(1 - E),$$

where Hct is the hematocrit. According to recommendations contained in the Olea Manual, a default hematocrit level is set to 0.45 for the calculation of all derived perfusion and permeability parameters for which a hematocrit level is required. PS increases with increased permeability; however, PS is also flow-dependent.⁶

In summary, K_{ep} , PS, and K^{trans} have previously been used to assess BBBP in patients^{9,14} and animal models.^{15,16} However, according to the Lawrence and Lee Model derivations above, decreasing K_{ep} most accurately reflects increasing disruption and permeability of BBB, especially in the setting of impaired CBF, such as occurs in GCE.¹²

RESULTS

Study Population

Twenty-two patients were included in the study after excluding indeterminate patients ($n = 2$) from the statistical analysis. In the 22 patients, 50% (11/22) were classified as having GCE and 50% (11/22) as non-GCE. There was statistically significant high interobserver reproducibility, with κ interobserver agreement coefficient of 0.86 ($P < .0001$) for sulcal effacement and 0.73 ($P < .0001$) for gray-white matter differentiation between the 2 blinded

Table 2: Quantitative BBBP and CTP results^a

	GCE	Non-GCE	P Value
K_{ep} (min^{-1})	1.28 (1.23–1.33)	1.52 (1.45–1.59)	<.0001
K^{trans} (min^{-1})	0.15 (0.14–0.16)	0.19 (0.18–0.20)	<.0001
PS ($\text{mL} \times \text{mL}^{-1} \times \text{min}^{-1}$)	227.4 (213.4–241.5)	208.4 (189.7–227.2)	.1095
VE	0.70 (0.61–0.78)	0.39 (0.36–0.42)	<.0001
VP	0.51 (0.48–0.53)	0.57 (0.54–0.60)	.0019
F ($\text{mL} \times \text{mL}^{-1} \times \text{min}^{-1}$)	1175 (1125–1226)	1329 (1259–1398)	.0005
CBF ($\text{mL} \times 100 \text{ g}^{-1} \times \text{min}^{-1}$)	32.57 (28.20–36.93)	42.02 (35.44–48.60)	.0148
CBV ($\text{mL} \times 100 \text{ g}^{-1}$)	5.86 (4.76–6.96)	5.86 (4.16–7.56)	.9950
MTT (s)	2.28 (1.44–3.12)	2.20 (1.99–2.40)	.8376

^a Data presented as mean (95% CI).

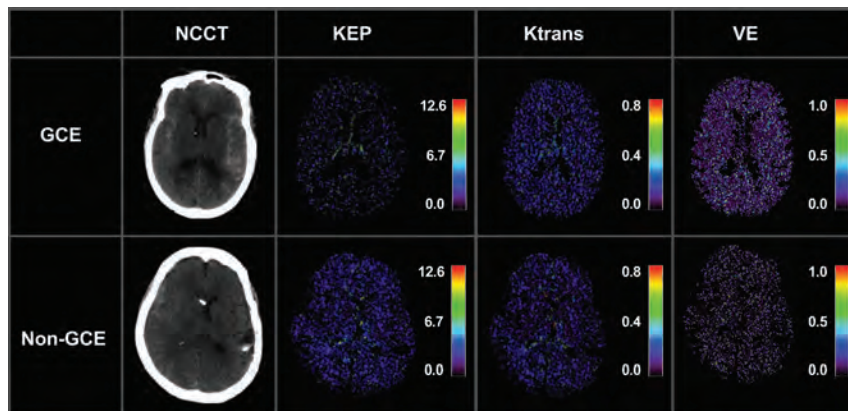


FIG 2. BBBP quantitative maps of K_{ep} , K^{trans} , and VE in a representative patient from the GCE group (top panel) and a representative patient from the non-GCE group (bottom panel). NCCT images demonstrate loss of gray-white matter differentiation and presence of sulcal effacement in the patient with GCE. Corresponding BBBP maps reveal decreased K_{ep} , slightly decreased K^{trans} , and increased VE in the same patient compared with the patient without GCE.

neuroradiologists. Clinical characteristics of the study population are summarized in Table 1.

Global BBBP Analysis

Quantitative BBBP results along with CTP results are summarized in Table 2. K_{ep} , K^{trans} , VP, and F were significantly decreased, while VE was significantly increased, in the GCE group compared with the non-GCE group. Differences in PS and extraction fraction of contrast agent did not reach statistical significance. However, there was a trend for increased PS in GCE. CBF was significantly decreased in the GCE group compared with the non-GCE group, while differences in CBV and MTT did not reach statistical significance.

Fig 2 demonstrates quantitative BBBP maps in a representative patient from the GCE group and a representative patient from the non-GCE group, respectively.

DISCUSSION

Assessment of BBBP with CTP is a novel technique that has not been adopted in clinical practice despite its numerous practical advantages, including widespread availability and relatively low cost. Quantitative BBBP evaluation in the clinical setting promises new insights into the underlying pathophysiology of many neurologic diseases. The relationship between BBBP and microvascular dysfunction and neuroinflammation plays an important role in numerous conditions, such as GCE.

GCE remains a major complication after SAH. Presently, assessment of GCE relies primarily on NCCT findings that are often

difficult to identify in the setting of diffuse SAH and increased intracranial pressure. Given the influence of GCE on SAH morbidity and mortality, earlier detection of GCE may improve outcomes in SAH.³

At present, there are no clinically established methods to assess the pathophysiologic mechanisms underlying GCE, such as microvascular dysfunction, inflammatory effects, and neurotoxic effects of blood.³ Given that these factors also play a role in BBB dysfunction, we have evaluated the utility of BBBP parameters in the assessment of GCE after SAH. However, these findings may be applicable to a wide spectrum of conditions where cerebral edema is known to occur, such as acute stroke, traumatic and anoxic brain injury, and CNS infections.

Our findings suggest that K_{ep} decreases with increased BBBP^{14,15} and may represent the most useful parameter in GCE because it is independent of low blood flow conditions. This inverse relationship between K_{ep} and BBBP could be attributed to the underlying pathophysiologic mechanisms, including time kinetics. Kinetic analysis of

BBBP changes during focused sonography-induced BBB opening demonstrated initial decrease in K_{ep} with subsequent recovery over time.¹⁶ Therefore, time kinetics are a crucial component in the assessment of the different BBBP parameters. In our study, we measured BBBP at a very early (initial) stage in patients with SAH who develop GCE demonstrating decreased K_{ep} . However, future work will show if K_{ep} recovers on follow-up examinations in these patients. The exact timing of BBBP imaging during the course of the disease is an important factor in understanding K_{ep} in these patients, as it relates to the timing of the BBB breakdown.

In contrast, K^{trans} is dependent on blood flow and also decreased with increased BBBP in our study, representing a less reliable parameter for assessment of BBBP in GCE. Furthermore, our findings demonstrate significant differences in VE and VP in patients with GCE. The mathematical derivation of VE and VP is based on the fractions of volume of the EES and IVS, respectively. Fig 1 summarizes the relationships of these BBBP parameters under normal conditions and in the setting of GCE. In the setting of interstitial edema such as GCE, fluid from the IVS (represented by VP) transgresses the BBB into the EES (represented by VE). In GCE, there is an increase in EES as reflected by increased VE and decreased K_{ep} , indicating increased BBBP. Furthermore, our findings also demonstrated significantly decreased K^{trans} and F in patients with GCE. In the literature, CBF impairment recently has been reported in patients with GCE.¹² Our data demonstrated decreased CBF in patients with GCE compared with patients without GCE and is thus concordant with previously published

studies.¹² Because the derivation of K^{trans} is dependent on F, it is a less reliable parameter in flow-restricted conditions, such as seen in GCE.¹⁷ Given that K_{ep} is independent of F, it may represent a more useful parameter to assess BBBP in the context of GCE, particularly when flow impairment occurs.¹² These findings further contribute to the development of an imaging biomarker of BBBP in flow-restricted conditions such as cerebral edema.

In this initial exploratory study, our sample was limited to patients with SAH who had an extended CTP technique performed. Future studies evaluating BBBP parameters in other patient populations such as stroke, hypoxic-ischemic injury, traumatic brain injury, neoplasm, and inflammation will be important to improving our understanding of BBBP in different clinical settings as well as to evaluate BBBP parameters as potential outcome measures in specific disease states.

Although there was a trend for increased PS in patients with GCE compared with patients without GCE, statistical significance was not achieved. However, these findings support further prospective work to elucidate the pathophysiologic processes leading to GCE after SAH.

CONCLUSIONS

Further study of BBBP is needed to improve diagnosis and monitoring of GCE. Validating a potential quantitative imaging biomarker may improve detection and management of GCE and may provide a quantitative end point for future clinical trials aimed at improving SAH outcomes.

Disclosures: Jana Ivanidze—RELATED: Grant: Radiological Society of North America Research and Education Foundation,* Comments: Resident Research Grant 2014–2015. Ajay Gupta—RELATED: Grant: CTSC Pilot Award (NIH/NCATS Grant # UL1TR000457)*; UNRELATED: Grants/Grants Pending: Foundation of the American Society of Neuroradiology Scholar Award.* Jan Claassen—UNRELATED: Consultancy: Actelion, Sage, Comments: Advisory board for study planning. Pina C. Sanelli—RELATED: Grant: Brain Aneurysm Foundation Grant 2014–2015. *Money paid to the institution.

REFERENCES

1. Germanò A, d'Avella D, Imperatore C, et al. **Time-course of blood-brain barrier permeability changes after experimental subarachnoid haemorrhage.** *Acta Neurochir (Wien)* 2000;142:575–80; discussion 580–81 CrossRef Medline
2. Kreiter KT, Copeland D, Bernardini GL, et al. **Predictors of cognitive dysfunction after subarachnoid hemorrhage.** *Stroke* 2002;33:200–08 CrossRef Medline
3. Claassen J, Carhuapoma JR, Kreiter KT, et al. **Global cerebral edema**

- after subarachnoid hemorrhage: frequency, predictors, and impact on outcome. *Stroke* 2002;33:1225–32 CrossRef Medline
4. Sanelli PC, Anumula N, Johnson CE, et al. **Evaluating CT perfusion using outcome measures of delayed cerebral ischemia in aneurysmal subarachnoid hemorrhage.** *AJNR Am J Neuroradiol* 2013;34:292–98 CrossRef Medline
5. Ivanidze J, Kesavabhotla K, Kallas ON, et al. **Evaluating blood-brain barrier permeability in delayed cerebral infarction after aneurysmal subarachnoid hemorrhage.** *AJNR Am J Neuroradiol* 2015;36:850–54 CrossRef Medline
6. Gowland P, Mansfield P, Bullock P, et al. **Dynamic studies of gadolinium uptake in brain tumors using inversion-recovery echo-planar imaging.** *Magn Reson Med* 1992;26:241–58 CrossRef Medline
7. Tofts PS, Brix G, Buckley DL, et al. **Estimating kinetic parameters from dynamic contrast-enhanced T(1)-weighted MRI of a diffusible tracer: standardized quantities and symbols.** *J Magn Reson Imaging* 1999;10:223–32 Medline
8. Dankbaar JW, Hom J, Schneider T, et al. **Dynamic perfusion CT assessment of the blood-brain barrier permeability: first pass versus delayed acquisition.** *AJNR Am J Neuroradiol* 2008;29:1671–76 CrossRef Medline
9. Ozkul-Wermester O, Guegan-Massardier E, Triquenot A, et al. **Increased blood-brain barrier permeability on perfusion computed tomography predicts hemorrhagic transformation in acute ischemic stroke.** *Eur Neurol* 2014;72:45–53 CrossRef Medline
10. Hom J, Dankbaar JW, Schneider T, et al. **Optimal duration of acquisition for dynamic perfusion CT assessment of blood-brain barrier permeability using the Patlak model.** *AJNR Am J Neuroradiol* 2009;30:1366–70 CrossRef Medline
11. Sanelli PC, Ugorec I, Johnson CE, et al. **Using quantitative CT perfusion for evaluation of delayed cerebral ischemia following aneurysmal subarachnoid hemorrhage.** *AJNR Am J Neuroradiol* 2011;32:2047–53 CrossRef Medline
12. Baradaran H, Fodera V, Mir D, et al. **Evaluating CT perfusion deficits in global cerebral edema after aneurysmal subarachnoid hemorrhage.** *AJNR Am J Neuroradiol* 2015;36:1431–35 CrossRef Medline
13. St Lawrence KS, Lee TY. **An adiabatic approximation to the tissue homogeneity model for water exchange in the brain: I. Theoretical derivation.** *J Cereb Blood Flow Metab* 1998;18:1365–77 Medline
14. Bennink E, Riordan AJ, Horsch AD, et al. **A fast nonlinear regression method for estimating permeability in CT perfusion imaging.** *J Cereb Blood Flow Metab* 2013;33:1743–51 CrossRef Medline
15. Nance E, Timbie K, Miller GW, et al. **Non-invasive delivery of stealth, brain-penetrating nanoparticles across the blood-brain barrier using MRI-guided focused ultrasound.** *J Control Release* 2014;189:123–32 CrossRef Medline
16. Chai WY, Chu PC, Tsai MY, et al. **Magnetic-resonance imaging for kinetic analysis of permeability changes during focused ultrasound-induced blood-brain barrier opening and brain drug delivery.** *J Control Release* 2014;192:1–9 CrossRef Medline
17. Kety SS. **The theory and applications of the exchange of inert gas at the lungs and tissues.** *Pharmacol Rev* 1951;3:1–41 Medline

Uremic Encephalopathy: MR Imaging Findings and Clinical Correlation

D.M. Kim, I.H. Lee, and C.J. Song



ABSTRACT

BACKGROUND AND PURPOSE: Uremic encephalopathy is a metabolic disorder in patients with renal failure. The purpose of this study was to describe the MR imaging findings of uremic encephalopathy.

MATERIALS AND METHODS: This study retrospectively reviewed MR imaging findings in 10 patients with clinically proved uremic encephalopathy between May 2005 and December 2014. Parameters evaluated were lesion location and appearance; MR signal intensity of the lesions on T1WI, T2WI, and T2 fluid-attenuated inversion recovery images; the presence or absence of restricted diffusion on diffusion-weighted images and apparent diffusion coefficient maps; and the reversibility of documented signal-intensity abnormalities on follow-up MR imaging.

RESULTS: MR imaging abnormalities accompanying marked elevation of serum creatinine (range, 4.3–11.7 mg/dL) were evident in the 10 patients. Nine patients had a history of chronic renal failure with expansile bilateral basal ganglia lesions, and 1 patient with acute renal failure had reversible largely cortical lesions. Two of 6 patients with available arterial blood gas results had metabolic acidosis. All basal ganglia lesions showed expansile high signal intensity (lentiform fork sign) on T2WI. Varied levels of restricted diffusion and a range of signal intensities on DWI were evident and were not correlated with serum Cr levels. All cortical lesions demonstrated high signal intensity on T2WI. Four patients with follow-up MR imaging after hemodialysis showed complete resolution of all lesions.

CONCLUSIONS: The lentiform fork sign is reliable in the early diagnosis of uremic encephalopathy, regardless of the presence of metabolic acidosis. Cytotoxic edema and/or vasogenic edema on DWI/ADC maps may be associated with uremic encephalopathy.

ABBREVIATIONS: ARF = acute renal failure; DM = diabetes mellitus; LFS = lentiform fork sign; SI = signal intensity; UE = uremic encephalopathy

Uremic encephalopathy is a metabolic disorder that occurs in patients with acute or chronic renal failure. This toxic-metabolic encephalopathy is a complication resulting from endogenous uremic toxins in patients with severe renal failure. The pathogenesis is complex and unclear.

Knowledge concerning a uremic encephalopathy (UE)-specific imaging feature, the so-called lentiform fork sign (LFS), is limited to case reports. The LFS may also be present in metabolic acidosis from any cause, including end-stage renal disease, methanol intoxication, and the dialysis disequilibrium syndrome.^{1–6} This study was undertaken to describe the MR imaging features in

the brains of 10 patients with UE, with the aim of identifying common imaging features and potentially clarifying the possible pathophysiology of UE.

MATERIALS AND METHODS

This retrospective study was reviewed and approved by our institutional review board. The study included 10 patients (9 men and 1 woman; mean age, 58 years; age range, 17–76 years) with clinically proved UE who had abnormalities on brain imaging when examined between May 2005 and December 2014. Eleven potential patients were identified by a search of the imaging archive at our institution for patients who had the LFS on MR imaging. Imaging findings and medical records of these 11 patients were reviewed. Two of the patients were excluded because of other toxic/metabolic diseases, such as extrapontine myelinolysis. One additional patient who underwent MR imaging after a clinical diagnosis of UE was subsequently identified and included. UE diagnoses in patients were clinical and supported by laboratory findings showing deterioration of renal function and typical neurologic complications. Other possible causative

Received August 3, 2015; accepted after revision February 12, 2016.

From the Department of Radiology, Chungnam National University Hospital, Chungnam National University School of Medicine, Daejeon, Korea.

Please address correspondence to In Ho Lee, MD, Department of Radiology, Chungnam National University Hospital, Chungnam National University School of Medicine, 282 Munhwa-ro, Jung-gu, Daejeon 301–721, Korea; e-mail: leehoi1974@hanmail.net

Indicates article with supplemental on-line table.

<http://dx.doi.org/10.3174/ajnr.A4776>

conditions, such as cerebral stroke, drug-induced movement disorder, neurodegenerative disease, or other metabolic disorders^{7,8} were excluded by chart review.

The medical records of the 10 patients were reviewed for the history and duration of diabetes mellitus (DM); hypertension; the cause of renal failure and categorization into acute renal failure (ARF) or chronic renal failure; presenting symptoms; laboratory findings (serum blood urea, nitrogen, and creatinine levels; metabolic acidosis on arterial blood gas); treatment; and recurrence. Metabolic acidosis was diagnosed on arterial blood gas if the pH was low (<7.35) and the bicarbonate levels were decreased (<24 mmol/L; normal range, 19–24 mmol/L). All patients underwent MR imaging within a few hours of the onset of symptoms. The MR imaging was performed by using a 3T scanner (Intera Achieva; Philips Healthcare, Best, the Netherlands) and a 1.5T scanner (Signa Excite; GE Healthcare, Milwaukee, Wisconsin). The protocol on the 3T scanner included T2-weighted imaging (TR/TE, 3000/80 ms; section thickness, 5 mm; section gap, 1.5 mm; FOV, 220×220 mm; matrix, 400×300 ; number of signals acquired, 1), FLAIR (TR/TE, 11,000/125 ms; section thickness, 5 mm; section gap, 1.5 mm; FOV, 220×220 mm; matrix, 316×242 ; number of signals acquired, 1), T1-weighted imaging (TR/TE, 2000/10 ms; section thickness, 5 mm; section gap, 1.5 mm; FOV, 220×220 mm; matrix, 260×166 ; number of signals acquired, 1), and axial 2D gradient recalled-echo imaging (TR/TE, 453/14 ms; flip angle, 20° ; section thickness, 5 mm; section gap, 1.5 mm; FOV, 220×220 mm; matrix, 275×275). The protocol on the 1.5T scanner included T2-weighted imaging (TR/TE, 3600/120 ms; section thickness, 5 mm; section gap, 1.5 mm; FOV, 220×220 mm; matrix, 256×256 ; number of signals acquired, 2), and T1-weighted imaging (TR/TE, 450/10 ms; section thickness, 5 mm; section gap, 1.5 mm; FOV, 220×220 mm; matrix, 320×190 ; number of signals acquired, 2).

DWI with b-values of 0 and 1000 was performed in the axial plane, by using 3 orthogonal directions of diffusion-sensitizing gradients, combined into isotropic images. Other parameters included TR/TE, 4300/46 ms; section thickness, 3 mm; section gap, 1 mm; FOV, 240×240 mm; matrix, 128×126 ; number of signals acquired, 1.

All MR imaging data were retrospectively evaluated by 2 experienced radiologists for lesion location; appearance; MR signal intensity on T1WI, T2WI, and FLAIR images; DWI and ADC maps; the presence or absence of hemorrhage; and the reversibility of signal intensity (SI) on follow-up MR imaging. The LFS was defined as bilateral, expansile, and symmetric hyperintensity in the basal ganglia surrounded by a more hyperintense rim delineating the lentiform nucleus on T2WI.

RESULTS

Clinical and imaging findings of UE in 10 patients are presented in the On-line Table. Nine of 10 patients had a history of underlying chronic renal failure, ranging from 3 months to 14 years. The remaining patient had ARF. Seven of 9 patients had underlying diabetic chronic renal disease (long-term DM; range, 5–30 years), and 2 of 9 patients had underlying hypertensive chronic renal disease without DM. All 9 patients with chronic renal failure regularly received hemodialysis. Seven patients had hypertension

(systolic pressure range, 140–178 mm Hg), and 2 patients were normotensive on emergency department visits. The blood pressure of 1 patient was not evaluated in the outpatient clinic. All patients had acute neurologic symptoms as follows: movement disorder ($n = 7$), dysarthria ($n = 4$), and altered mental status ($n = 1$). All patients had uremia; blood chemistry analyses showed marked elevation of blood urea nitrogen (range, 31.7–69 mg/dL; healthy average after dialysis, 8–20 mg/dL) and Cr (range, 4.3–11.7 mg/dL; healthy average after dialysis, 0.8–1.2 mg/dL). Other serum electrolyte and glucose levels were not significantly abnormal, excluding other causes of encephalopathy. Of 5 patients with available arterial blood gas and bilateral basal ganglia lesions, 1 (patient 2) had a mild metabolic acidosis (pH, 7.31; bicarbonate, 21.7), and 4 patients had a normal pH level. One patient (patient 7) with ARF and cortical lesions on MR imaging also had mild metabolic acidosis (pH, 7.3; bicarbonate, 19.0).

In 9 of 10 patients with chronic renal failure, MR imaging showed bilateral, expansile, symmetric basal ganglia lesions with increased SI on T2WI, FLAIR, and/or ADC maps, compatible with vasogenic edema (LFS, Fig 1A). Four of 9 patients showed diffuse mildly increased SI on DWI without restricted diffusion in the bilateral basal ganglia lesions, and 2 showed focal restricted diffusion, corresponding to cytotoxic edema, in the globus pallidi (Fig 2A, -B). The remaining 5 patients showed normal SI on DWI in the bilateral basal ganglia. One patient had restricted diffusion in the bilateral globus pallidus and left putamen (Fig 3A, -B). There was no significant difference among any of the patients regarding clinical findings, including serum Cr level (5.63–11.7 mg/dL in the group of 4 patients versus 4.3–10.8 mg/dL in the group of 5 patients).

Decreased SI on T1WI was noted in the lesions of 5 patients. There were no hemorrhages in the deep gray matter on T2WI or gradient recalled-echo images and no significant white matter abnormality in any patient.

Two of the 10 patients (patients 4 and 7) showed cortical involvement on T2WI and FLAIR. Two patients had markedly high systolic blood pressure (systolic blood pressure, 178 mm Hg; diastolic blood pressure, 86 and 58 mm Hg, respectively) on emergency department visits. One patient (patient 4) who had hypertensive chronic renal disease showed multifocal relatively symmetric, gyriform high SI on T2WI/FLAIR images and low SI on T1WI in the bilateral frontal and parieto-occipital lobes (Fig 1C) and the bilateral basal ganglia (LFS; Fig 1A) without restricted diffusion on ADC maps. Another patient (patient 7) who had ARF demonstrated multifocal gyriform high T2 SI lesions in the bilateral frontal, parieto-occipital, and right temporal lobes and subtle nodular high T2 SI in the right putamen without restricted diffusion on ADC maps. All patients showed improvement of various neurologic symptoms, normalization of serum Cr levels, and decreased serum blood urea nitrogen levels by $>60\%$ after intensive hemodialysis. In 4 patients, follow-up MR imaging, ranging from 40 days to 3 years later, showed complete resolution of imaging abnormalities (Fig 4A, -B).

DISCUSSION

UE is a neurologic complication associated with ARF or chronic renal failure. It is likely caused by the effects of neurotoxic com-

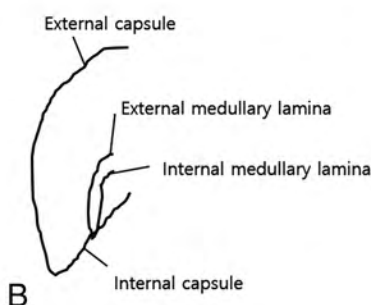
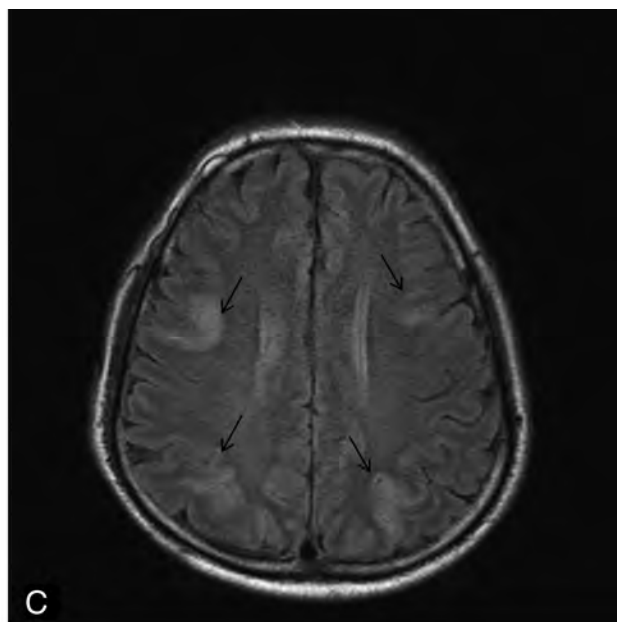
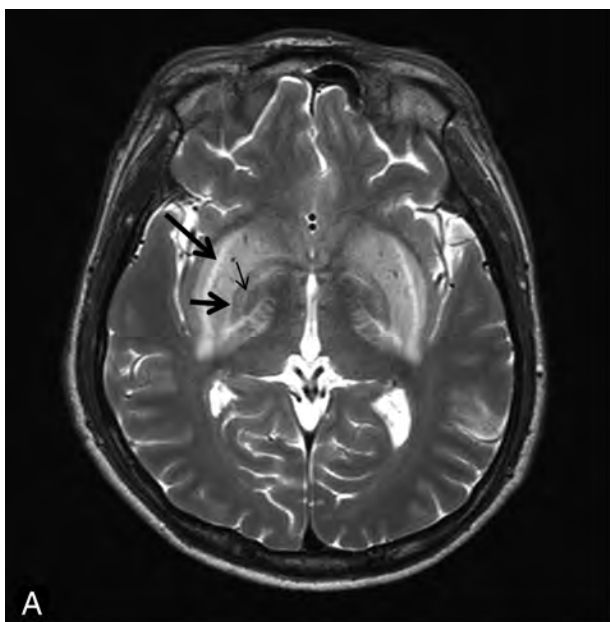


FIG 1. A 52-year-old man (patient 4) presented with seizure-like activity. A T2-weighted image (A) and diagrammatic illustration (B) show the lentiform fork sign. A bright hyperintense rim delineates the lateral (external capsule, *long arrow*) and medial boundaries (external medullary lamina [*short arrow*] and internal medullary laminae [*thin arrow*]) of both putamina. The globus pallidus is divided into 2 parts by the medial medullary laminae, which can be seen in pathologic conditions on MR images. A FLAIR image (C) shows multifocal relatively symmetric, gyriform high SI (*arrows*) in the cortex of bilateral frontal, parieto-occipital lobes and bilateral basal ganglia.

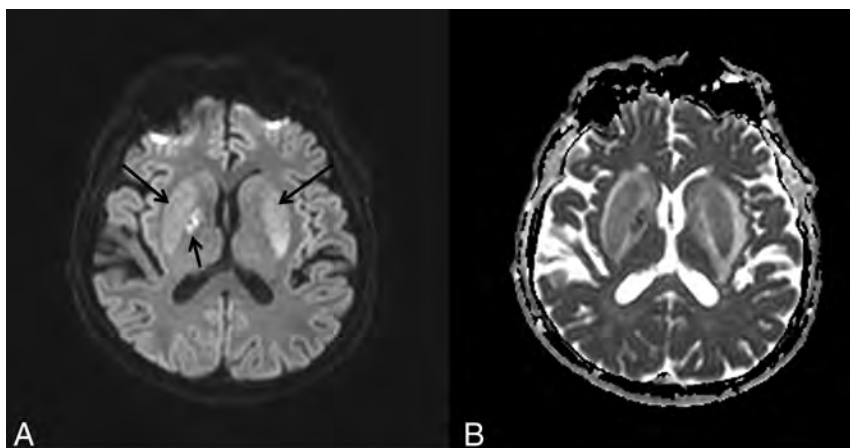


FIG 2. A 67-year-old man (patient 5) presented with unsteadiness. DWI (A) and an ADC map (B) show diffuse mildly increased SI (*long arrows*) in the whole bilateral basal ganglia lesion on DWI with focal restricted diffusion (*short arrow*), corresponding to cytotoxic edema in the right globus pallidus.

pounds. Accumulation of uremic toxins such as guanidine compounds (eg, creatinine and guanidine) might stimulate the neurotoxic effect of excitatory *N*-methyl-D-aspartate receptors, and concomitant inhibition of inhibitory γ -aminobutyric acid receptors may play an important role in the etiology of UE.⁹ It may be an interruption of polysynaptic pathways and alterations in excitatory-inhibitory amino acid balance. The manifestations of this brain disorder include various neurologic symptoms such as

movement disorders (tremor, asterixis, myoclonus), cognitive disorders, and alteration in mental status.^{10,11}

UE presents 3 patterns of imaging findings: basal ganglia involvement,¹²⁻¹⁴ cortical or subcortical involvement,^{15,16} and white matter involvement.^{17,18} Basal ganglia involvement is more common in Asian patients with DM. The LFS in patients with UE often affects Asians (from Taiwan,^{12,13} Korea,^{13,14,18} Japan¹⁹). DM may make the basal ganglia more vulnerable to uremic toxins because of endothelial dysfunction in cerebral vessels (vascular autoregulatory dysfunction²⁰), and uremic toxin inhibits mitochondrial function with destruction of the pallidum and putamen.²¹

Cortical involvement is a category of posterior reversible leukoencephalopathy syndrome,²² and DM does not have a great effect on the involvement.¹⁸ Reversible intracerebral disease entities mediated by vascular autoregulatory dysfunction can be classified into 2 distinct groups: hypertensive encephalopathy and UE.²² However, posterior reversible encephalopathy syndrome is also seen in the uremic conditions in which endothelial toxins are thought to play a role.¹⁶ Posterior reversible encephalopathy syndrome is a clinical-radiologic syndrome

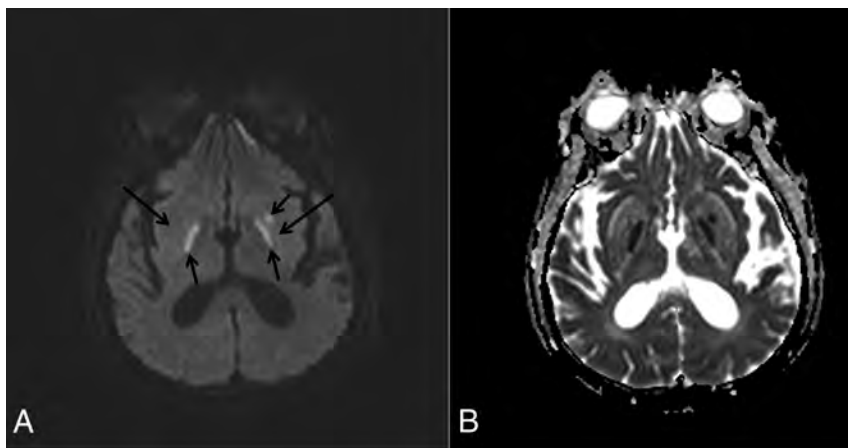


FIG 3. A 70-year-old man (patient 6) presented with involuntary movement. DWI (A) and an ADC map (B) show normal SI (*long arrows*) in the bilateral basal ganglia on DWI with restricted diffusion (*short arrows*) in the bilateral globus pallidus and left putamen, compatible with areas of cytotoxic edema in the lesions.

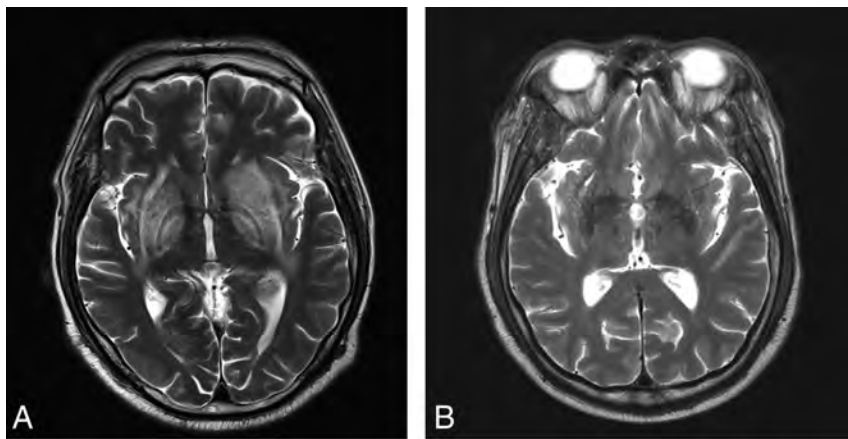


FIG 4. A 56-year-old man (patient 3) presented with dysarthria. Initial T2WI (A) shows the lenticular fork sign in the bilateral basal ganglia. Six months later, follow-up T2WI (B) shows complete resolution of the lesions.

characterized by headache, confusion, seizures, and visual disturbance and is thought to be secondary to hypertension. It classically occurs in the cortical or subcortical regions of the dominant parieto-occipital lobes, holo-hemispheric watershed zones, superior frontal sulcal area, and, rarely, the brain stem or basal ganglia.^{16,23,24} MR imaging typically demonstrates vasogenic edema in the subcortical white matter and cortex. Cytotoxic edema has been described in a relatively lower percentage of patients with posterior reversible encephalopathy syndrome.²⁵

Central-variant posterior reversible encephalopathy syndrome had been described as brain stem or basal ganglia involvement that spares the cerebral cortex and subcortical white matter.²⁶ Imaging findings of central variant posterior reversible encephalopathy syndrome include symmetric or asymmetric vasogenic edema (the pons and basal ganglia [caudate nucleus, globus pallidus, and not resulting in the LFS]; and, rarely, the thalamus, posterior limb of the internal capsule, cerebellum, periventricular white matter) without any foci of reduced diffusivity and multiple microhemorrhages in the affected regions on susceptibility-weighted images.²⁶ These imaging findings are substantially different from the imaging findings of UE. White matter

involvement is the rarest form and occurs in the supratentorial white matter regions. This form might be considered a urea cycle disorder rather than UE.

The LFS has been described on T2WI/FLAIR images as a hyperintense rim delineating the lateral (external capsule) and medial (internal capsule, internal and external medullary laminae) boundaries of both putamina, resembling a fork (Fig 1B).¹ A literature review¹ reported that the LFS was found in only 1 of 21 patients with UE admitted during a 10-year period in a retrospective single-institution study, without note of the absence or presence of DM. However, data from the same literature review showed that 10 of 11 patients with UE who had the LFS had diabetes, and 1 patient with diabetic ketoacidosis had the LFS, implicating diabetes in the production of these characteristic lenticular lesions. In this study, 7 of 9 patients with UE who had the LFS during a 10-year period had long-term DM. The results may indicate a higher prevalence of the LFS in Asian patients with DM and UE.

Metabolic acidosis associated with disruption of the blood-brain barrier is an essential element in the generation of the LFS,^{1,2} and this sign may be attributable to differences in metabolic vulnerability between neurons of the basal ganglia and the astrocytes of surrounding white matter. Although UE is associated with metabolic acidosis, in this study, 1 of 5 patients with the LFS had mild metabolic acidosis, and the other 4 patients had normal pH levels on arterial blood gas. These

findings are different from the results of a literature review that showed that metabolic acidosis is the basis of the LFS, and the absence of LFS might be reflective of a normal pH.¹ We propose that the LFS can be seen in UE regardless of the presence of metabolic acidosis, though coexistent metabolic acidosis may exacerbate the damage of neurons in the basal ganglia.

In this study, T2WI/FLAIR images showed uniform imaging findings. Diffuse vasogenic edema in the bilateral basal ganglia and/or cortical lesions represents increased interstitial fluid from a disruption of autoregulation. These results correspond well with those of the earlier studies.^{13,14} There was no significant difference between groups with diffuse mildly increased SI on DWI without restricted diffusion and others with normal SI on DWI in basal ganglia lesions.

Three of 9 patients who underwent DWI showed cytotoxic edema within the vasogenic edema of the basal ganglia, and all 3 lesions had cytotoxic edema in the unilateral or bilateral globus pallidus. Thus, the globus pallidus may be more vulnerable to cytotoxic damage than the putamen in UE. The globus pallidus is thought to be a vulnerable area of toxic/metabolic injury because of its high energy requirements and resultant sensitivity to mitochondrial and nuclear dysfunction.^{21,27} Toxic/metabolic enceph-

alopathy, including carbon monoxide, cyanide, cocaine, opiate, and manganese intoxication, and Wilson disease involve selective vulnerability of pallidal neurons.^{28–31} However, the vulnerability of the globus pallidus in UE has not been established, though cytotoxic edema in the globus pallidus has been described in UE.^{13,14} Several pathologic studies reported cytotoxic edema in posterior reversible encephalopathy syndrome associated with fibrinoid necrosis and microinfarction³² and suggested a causal relationship between cytotoxic edema and larger areas of vasogenic edema.³³ However, in this study, there was no significant difference in the extent of vasogenic edema between groups with cytotoxic edema and other groups with vasogenic edema in basal ganglia lesions.

Cortical or subcortical lesions of UE are predominantly found in the parieto-occipital lobes.¹⁶ Cortical lesion in patients with UE may share pathophysiologic and imaging features with posterior reversible encephalopathy syndrome. Combined clinical features (the presence of neurologic impairment, renal dysfunction, renal failure, DM, metabolic acidosis, systemic hypertension, eclampsia, pre-eclampsia, vascular disease, autoimmune disease, or cancer chemotherapy) and imaging features (the presence of bilateral basal ganglia involvement with LFS, vasogenic/cytotoxic edema in affected regions, or micro-hemorrhage) should be considered in the differential diagnosis of UE and posterior reversible encephalopathy syndrome.

UE in renal failure is reversibly associated with hemodialysis or peritoneal dialysis, which removes neurotoxic compounds.³⁴ In this study, all patients showed improvement of their neurologic symptoms, normalization of serum Cr levels, decreased serum blood urea nitrogen levels by more than 60%, and complete resolution of imaging abnormalities on available follow-up MR imaging after intensified hemodialysis.

There are some limitations to this study. First, the sample size was small. Follow-up MR imaging was not performed in the patients who had restricted diffusion (cytotoxic edema) in their basal ganglia lesions. We cannot comment on the reversibility of these lesions. The sensitivity/specificity of the LFS for UE was not determined because of selection bias in this study. Finally, this study has not reliably demonstrated that the more severe the UE, the more likely it is to demonstrate the LFS on MR imaging, also due to selection bias.

CONCLUSIONS

The LFS on T2WI/FLAIR imaging is important in the early diagnosis of UE, regardless of the presence of metabolic acidosis. Cytotoxic edema and/or vasogenic edema on DWI and ADC mapping may be helpful findings associated with UE.

REFERENCES

- Kumar G, Goyal MK. **Lentiform fork sign: a unique MRI picture— is metabolic acidosis responsible?** *Clin Neurol Neurosurg* 2010;112: 805–12 CrossRef Medline
- Grasso D, Borreggine C, Perfetto, F, et al. **Lentiform fork sign: a magnetic resonance finding in a case of acute metabolic acidosis.** *Neuroradiol J* 2014;27:288–92 CrossRef Medline
- Fabiani G, Teive HA, Munhoz RP. **Lentiform fork sign and fluctuating, reversible parkinsonism in a patient with uremic encephalopathy.** *Mov Disord* 2013;28:1053 CrossRef Medline
- Blanco M, Casado R, Vazquez F, et al. **CT and MR imaging findings in methanol intoxication.** *AJNR Am J Neuroradiol* 2006;27:452–54 Medline
- Arora V, Nijjar IB, Multani AS, et al. **MRI findings in methanol intoxication: a report of two cases.** *Br J Radiol* 2007;80:e243–46 CrossRef Medline
- da Rocha AJ, Maia AC Jr, da Silva CJ, et al. **Lentiform fork sign in a child with dialysis disequilibrium syndrome: a transient MRI pattern which emphasizes neurologic consequence of metabolic acidosis.** *Clin Neurol Neurosurg* 2013;115:790–92 CrossRef Medline
- Roos KL. *Emergency Neurology*. New York: Springer-Verlag; 2012: xii
- Barton B, Zauber SE, Goetz CG. **Movement disorders caused by medical disease.** *Semin Neurol* 2009;29:97–110 CrossRef Medline
- Vanholder R, De Smet R, Glorieux G; European Uremic Toxin Work Group. **Review on uremic toxins: classification, concentration, and interindividual variability.** *Kidney Int* 2003;63:1934–43 CrossRef Medline
- Seifter JL, Samuels MA. **Uremic encephalopathy and other brain disorders associated with renal failure.** *Semin Neurol* 2011;31: 139–43 CrossRef Medline
- Etgen T. **Kidney disease as a determinant of cognitive decline and dementia.** *Alzheimers Res Ther* 2015;7:29 CrossRef Medline
- Wang HC, Cheng SJ. **The syndrome of acute bilateral basal ganglia lesions in diabetic uremic patients.** *J Neurol* 2003;250:948–55 CrossRef Medline
- Lee EJ, Park JH, Ihn Y, et al. **Acute bilateral basal ganglia lesions in diabetic uraemia: diffusion-weighted MRI.** *Neuroradiology* 2007;49: 1009–13 CrossRef Medline
- Yoon CH, Seok JI, Lee DK, et al. **Bilateral basal ganglia and unilateral cortical involvement in a diabetic uremic patient.** *Clin Neurol Neurosurg* 2009;111:477–79 CrossRef Medline
- Schmidt M, Sitter T, Lederer SR, et al. **Reversible MRI changes in a patient with uremic encephalopathy.** *J Nephrol* 2001;14: 424–27 11730279
- Tatsumoto N, Fujisaki K, Nagae H, et al. **Reversible posterior leuko-encephalopathy syndrome in a patient with severe uremic encephalopathy.** *Clin Nephrol* 2010;74:154–58 CrossRef Medline
- Prüss H, Siebert E, Masuhr, F. **Reversible cytotoxic brain edema and facial weakness in uremic encephalopathy.** *J Neurol* 2009;256: 1372–73 CrossRef Medline
- Kang E, Jeon SJ, Choi SS. **Uremic encephalopathy with atypical magnetic resonance features on diffusion-weighted images.** *Korean J Radiol* 2012;13:808–11 CrossRef Medline
- Okada J, Yoshikawa K, Matsuo H, et al. **Reversible MRI and CT findings in uremic encephalopathy.** *Neuroradiology* 1991;33:524–26 CrossRef Medline
- Kwok RP, Juorio AV. **Concentration of striatal tyramine and dopamine metabolism in diabetic rats and effect of insulin administration.** *Neuroendocrinology* 1986;43:590–96 Medline
- Albin RL. **Basal ganglia neurotoxins.** *Neurol Clin* 2000;18:665–80 CrossRef Medline
- Port JD, Beauchamp NJ Jr. **Reversible intracerebral pathologic entities mediated by vascular autoregulatory dysfunction.** *Radiographics* 1998;18:353–67 CrossRef Medline
- Bartynski WS, Boardman JF. **Distinct imaging patterns and lesion distribution in posterior reversible encephalopathy syndrome.** *AJNR Am J Neuroradiol* 2007;28:1320–27 CrossRef Medline
- Kastrup O, Schlamann M, Moenninghoff C, et al. **Posterior reversible encephalopathy syndrome: the spectrum of MR imaging patterns.** *Clin Neuroradiol* 2015;25:161–71 CrossRef Medline
- Gao B, Yu BX, Li RS, et al. **Cytotoxic edema in posterior reversible encephalopathy syndrome: correlation of MRI features with serum albumin levels.** *AJNR Am J Neuroradiol* 2015;36:1884–89 CrossRef Medline
- McKinney AM, Jagadeesan BD, Truwit CL. **Central-variant posterior reversible encephalopathy syndrome: brainstem or basal ganglia involvement lacking cortical or subcortical cerebral edema.** *AJR Am J Roentgenol* 2013;201:631–38 CrossRef Medline
- Sharrief AZ, Raffel J, Zee DS. **Vitamin B(12) deficiency with bilateral globus pallidus abnormalities.** *Arch Neurol* 2012;69:769–772 CrossRef Medline
- Spadoni F, Stefani A, Morello, M, et al. **Selective vulnerability of pallidal neurons in the early phases of manganese intoxication.** *Exp Brain Res* 2000;135:544–51 CrossRef Medline

29. Sharma P, Eesa M, Scott JN. **Toxic and acquired metabolic encephalopathies: MRI appearance.** *AJR Am J Roentgenol* 2009;193: 879–86 CrossRef Medline
30. Valk J, van der Knaap MS. **Toxic encephalopathy.** *AJNR Am J Neuroradiol* 1992;13:747–60 Medline
31. Alquist CR, McGoe R, Bastian F, et al. **Bilateral globus pallidus lesions.** *J La State Med Soc* 2012;164:145–46 Medline
32. Jacquot C, Glastonbury CM, Tihan T. **Is posterior reversible encephalopathy syndrome really reversible? Autopsy findings 4.5 years after radiographic resolution.** *Clin Neuropathol* 2015;34:26–33 CrossRef Medline
33. Li Y, Gor D, Walicki D, et al. **Spectrum and potential pathogenesis of reversible posterior leukoencephalopathy syndrome.** *J Stroke Cerebrovasc Dis* 2012;21:873–82 CrossRef Medline
34. Burn DJ, Bates D. **Neurology and the kidney.** *J Neurol Neurosurg Psychiatry* 1998;65:810–21 CrossRef Medline

Probabilistic Fiber-Tracking Reveals Degeneration of the Contralateral Auditory Pathway in Patients with Vestibular Schwannoma

S.M. Rueckriegel, G.A. Homola, M. Hummel, N. Willner, R.-I. Ernestus, and C. Matthies

ABSTRACT

BACKGROUND AND PURPOSE: Vestibular schwannomas cause progressive hearing loss by direct damage to the vestibulocochlear nerve. The cerebral mechanisms of degeneration or plasticity are not well-understood. Therefore, the goal of our study was to show the feasibility of probabilistic fiber-tracking of the auditory pathway in patients with vestibular schwannomas and to compare the ipsi- and contralateral volume and integrity, to test differences between the hemispheres.

MATERIALS AND METHODS: Fifteen patients with vestibular schwannomas were investigated before surgery. Diffusion-weighted imaging (25 directions) was performed on a 3T MR imaging system. Probabilistic tractography was performed for 3 partial sections of the auditory pathway. Volume and fractional anisotropy were determined and compared ipsilaterally and contralaterally. The laterality ratio was correlated with the level of hearing loss.

RESULTS: Anatomically reasonable tracts were depicted in all patients for the acoustic radiation. Volume was significantly decreased on the hemisphere contralateral to the tumor side for the acoustic radiation and diencephalic section, while fractional anisotropy did not differ significantly. Tracking did not yield meaningful tracts in 3 patients for the thalamocortical section and in 5 patients for the diencephalic section. No statistically significant correlations between the laterality quotient and classification of hearing loss were found.

CONCLUSIONS: For the first time, this study showed that different sections of the auditory pathway between the inferior colliculus and the auditory cortex can be visualized by using probabilistic tractography. A significant volume decrease of the auditory pathway on the contralateral hemisphere was observed and may be explained by transsynaptic degeneration of the crossing auditory pathway.

ABBREVIATIONS: FA = fractional anisotropy; IC = inferior colliculus; MGN = medial geniculate nucleus

Vestibular schwannoma, also known as acoustic neurinoma, is a common intrameatal and intracranial tumor evolving from the eighth cranial nerve with an incidence of 10–15 per million per year.¹ The tumor usually arises from Schwann cells within the vestibular part of the eighth cranial nerve. The benign tumor is characterized by a slow growth pattern for years.^{2,3} The slow-but-steady increase in size causes progressive damage to the neurons of the eighth cranial nerve, leading to hearing impairment, tinni-

tus, and vertigo.⁴⁻⁶ Typically the vertigo symptoms are transient, while hearing impairment can progressively deteriorate toward unilateral deafness ipsilateral to the lesion side. To estimate the extent of hearing loss, examination of tone audiometry and speech discrimination is crucial.⁶⁻⁹ Large tumors involving neighboring structures such as the fifth or seventh cranial nerve or even the brain stem and cerebellum may cause facial paresis and numbness, cerebellar ataxia, or corticospinal tract–related sensorimotor deficits. There are various classification systems, but tumor extension is usually classified on the basis of the size from T1 (intrameatal localization) to T4 (compression of the brain stem).¹⁰ Treatment options include surgical removal of the tumor and radiation therapy. During the past decades, the surgical goal has shifted from gross total resection toward optimal functional outcome.^{8,11}

Despite surgical tumor removal, improvement of hearing is unusual, even if anatomic preservation of the eighth cranial nerve has been achieved and resection has led to decompression of the nerve. Apparently, the cochlear nerve itself and possibly cortical

Received October 2, 2015; accepted after revision March 6, 2016.

From the Departments of Neurosurgery (S.M.R., M.H., N.W., R.-I.E., C.M.) and Neuroradiology (G.A.H.), Würzburg University Hospital, Würzburg, Germany.

A research grant as part of the “program of first grant application” was provided by the Interdisciplinary Center of Clinical Research, University Hospital Würzburg, to Stefan Rueckriegel.

Paper previously presented in part at: Annual Meeting of the German Society of Neurosurgery, June 7–10, 2015; Karlsruhe, Germany.

Please address correspondence to Stefan Rueckriegel, MD, Department of Neurosurgery, Würzburg University Hospital, Josef-Schneider-Str II, 97080 Würzburg, Germany; e-mail: rueckriege_s@ukw.de

<http://dx.doi.org/10.3174/ajnr.A4833>

and subcortical auditory structures have a low potential for regeneration after nerve damage. In contrast, the function of the damaged vestibular nerve is compensated by the integrating circuitry of the equilibrium: The latter involves the vestibular, visual, and somatosensory systems¹² and therefore provides a more robust reserve for compensation. Although functional outcome has been the treatment focus, the interest was limited to the individual nerve structures, while the cerebral mechanisms of degeneration or plasticity of the associated white matter tracts and cortex areas are rarely investigated and understood.

The first studies by DTI, in unselected hearing disorders, succeeded, in some cases, in illustrating abnormality of white matter integrity of the auditory pathway. Wu et al¹³ found decreased fractional anisotropy (FA) at the contralateral inferior colliculus and lateral lemniscus in 19 patients with non-tumor-related sensorineural hearing loss. Chang et al¹⁴ reported abnormalities of fractional anisotropy in several parts of the auditory pathway when comparing 10 patients with sensorineural hearing loss with healthy subjects. Both investigations indicated a transsynaptic degeneration of the auditory pathway. An association between DTI-derived measures and abnormalities in brain stem auditory-evoked potentials was illustrated in preterm infants.¹⁵ These previous investigations measured DTI-derived parameters like FA or radial diffusivity by using ROI analyses. While the feasibility of fiber-tracking has been shown previously in auditory pathway investigation,¹⁶⁻¹⁸ this method has not been hitherto applied to the auditory pathway in patients with vestibular schwannoma. A detailed analysis of the white matter microstructure of the auditory pathway and of possible abnormalities in patients with vestibular schwannoma does not exist, to our knowledge. Therefore, the primary goal of our study was to show the feasibility of probabilistic fiber-tracking of partial sections of the auditory pathway in patients with vestibular schwannomas and to quantify the volume and integrity of these sections ipsi- and contralateral to the tumor side to test for differences between the hemispheres. The secondary goal was to identify associations of the integrity of the auditory pathway with audiometric measurements, including speech discrimination and the electrophysiologic brain stem-evoked potentials.

MATERIALS AND METHODS

Fifteen patients (7 women, 8 men; mean age, 50.5 ± 13.7 years; demographic details in Table 1) with a unilateral vestibular schwannoma and a given indication to undergo tumor resection with a retrosigmoid approach were included in this pilot study. None of the patients were previously diagnosed with another disease of the central nervous system such as Alzheimer disease or multiple sclerosis. Patients underwent routine preoperative MR imaging, including contrast-enhanced T1-weighted imaging and CISS sequences. DTI and high-resolution 3D T1-weighted MPRAGE images were added to the preoperative routine imaging performed on a 3T scanner (Magnetom Trio; Siemens, Erlangen, Germany) with a 12-channel head coil. Two DTI datasets were obtained by using 25 directions (section thickness, 3.6 mm; in-plane resolution, 1.8×1.8 mm²). Diffusion data were converted from DICOM to NIfTI format and further processed by using the

Table 1: Patient characteristics^a

Patient No.	Age (yr)	Sex	T. Side	T. Size	AC	EC
1	64	M	L	T3a	H1	A4
2	47	M	R	T4b	H2	A2
3	44	M	R	T3b	H3	A3
4	54	F	L	T2a	H2	A2
5	50	M	L	T3b	H2	A2
6	60	F	L	T4a	H5	A5
7	57	F	L	T3b	H6	A4
8	46	F	L	T3a	H2	A2
9	58	F	L	T3b	H4	A3
10	73	F	R	T2a	H3	A4
11	43	M	R	T2b	H4	A3
12	23	M	R	T4b	H2	A3
13	42	M	R	T4a	H2	A2
14	68	M	L	T3a	H6	A5
15	29	F	R	T4b	H6	A5

Note:—T. indicates tumor; AC, audiometric classification; EC, electrophysiologic classification based on auditory brain stem responses; L, left; R, right.

^a Fifteen patients with vestibular schwannoma were included in the study. Tumor size was between T2a and T4b.

FMRIB Software Library (FSL, Version 5.0; <http://www.fmrib.ox.ac.uk/fsl>).¹⁹ After applying eddy current correction, brain extraction, and fitting the tensor models averaging the 2 datasets (DTIFit; <http://fsl.fmrib.ox.ac.uk/fsl/fslwiki/FDT/UserGuide#BEDPOSTX>), we further processed data by using bedpostX (<http://fsl.fmrib.ox.ac.uk/fsl/fslwiki/FDT/UserGuide#BEDPOSTX>).

The high-resolution T1-weighted image was coregistered to the diffusion space to define the seed masks for fiber-tracking in diffusion space. We accepted the lower resolution of diffusion space so that seed volumes would not have to be coregistered subsequently to a different space, introducing spatial uncertainty for the tracking procedure. An overlay of the coregistered T1-weighted and FA images was used to define the seed masks for the fiber-tracking process. Three partial sections of the auditory pathway were tracked by using 2 seed masks per section at the start and ending points of the tracts: Seed masks of the lateral section (Fig 1) were defined at the auditory cortex and Sylvian fissure. Seed masks of the long lateral section (Fig 2) were defined at the auditory cortex and the medial geniculate nucleus (MGN). Seed masks of the diencephalic section (Fig 3) were defined at the inferior colliculus and MGN. Each seed mask was assigned to a specific volume in all patients. Seed masks were defined on both hemispheres.

Probabilistic fiber-tracking experiments were performed for these 3 partial sections of the auditory pathway, with 6 fiber-tracking runs per patient by using probtrackx, part of FSL (<http://fsl.fmrib.ox.ac.uk/fsl/fslwiki/FDT/UserGuide>).²⁰⁻²² The “multiple masks” option of probtrackx was applied. A termination mask of fractional anisotropy < 0.1 was used to avoid tracking throughout the cortex and fissures. The number of samples of probabilistic tracking was set at 5000, the curvature threshold was 0.2, and a loop check was performed. The maximum number of steps was 2000, and the step length was 0.5 mm. The threshold of probability values was adjusted individually in the resulting volumes to exclude anatomically unreasonable voxels with low probability. The volume and FA of the results were determined. We did not determine further diffusivity indices because a higher number of tests would be statistically disadvantageous in the rather small sample size. FA and volume were compared intraindi-

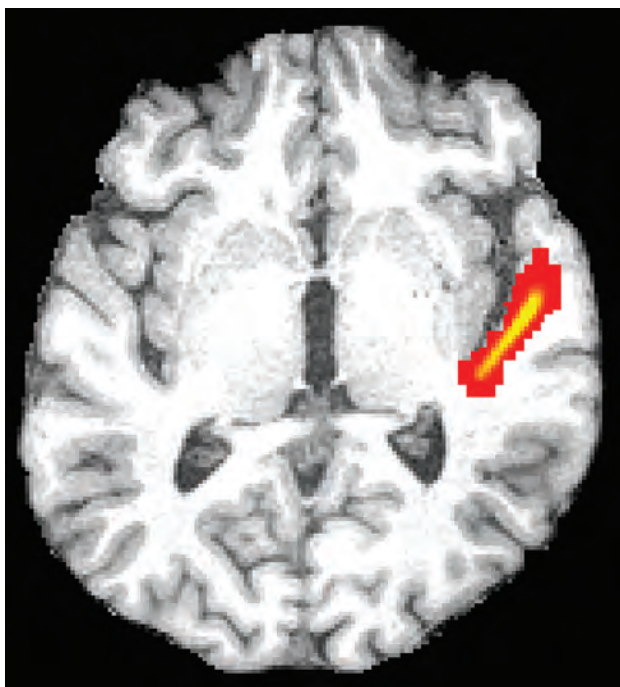


FIG 1. Illustration of the probabilistic fiber-tracking results of patient 3 of the left lateral section of the auditory pathway from the postero-medial Sylvian fissure to the primary auditory cortex on a representative axial section (red indicates low probability values; yellow, high probability values). Volume and mean fractional anisotropy of the 3D-depicted fiber tracts were determined ipsi- and contralateral to the tumor.

vidually between the ipsi- and contralateral hemisphere by using the Wilcoxon test. A laterality ratio was built by dividing the ipsilateral by the contralateral parameters. The laterality ratio was correlated with classifications of the audiometric and electrophysiologic (brain stem–evoked potentials) levels of hearing loss.

Speech discrimination and hearing function on both sides were tested preoperatively, and an audiometric classification was carried out according to the Hannover classification,⁷ which consists of 6 classes and is divided into 20-dB steps. Class 1 is the best one and includes hearing loss up to 20 dB as an average in the 1- to 3-kHz zone and patients with a speech discrimination score of at least 95%. The speech discrimination score is the percentage of words that were identified by the patient in the speech audiometry. Class 2 includes a 21- to 40-dB hearing loss and a minimum of a 70% speech discrimination score. Class 3 includes a 41- to 60-dB hearing loss and at least a 40% speech discrimination score. Class 4 includes 61- to 80-dB hearing loss and at least a 10% speech discrimination score. Class 5 is >80-dB hearing loss and a 0%–9% speech discrimination score. Class 6 is the worst class and includes >100 dB hearing loss and a 0% speech discrimination score.

Auditory Brainstem Response was recorded by needle electrodes, and as a stimulus, we used a click that was applied by air-conducted earphones. Auditory Brainstem Response measurements were performed during the entire operation. To build an electrophysiologic classification, the Auditory Brainstem Response quality at the beginning of surgery was categorized according to the Hannover classification and used for correlation.⁶ The

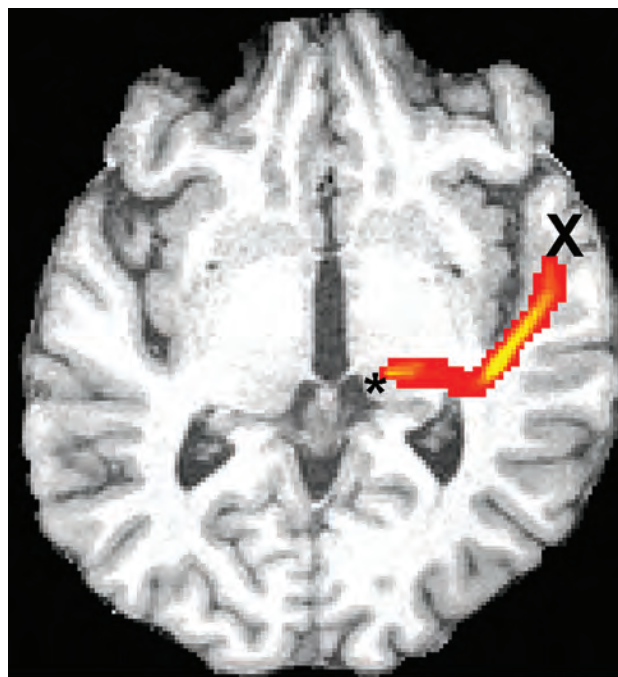


FIG 2. Illustration of the probabilistic fiber-tracking results of patient 3 of the left long lateral section of the auditory pathway from the medial geniculate nucleus (*asterisk*) to the primary auditory cortex (X) on a representative axial section. The tract crosses the external capsule and bends posteriorly along the Sylvian fissure, then anteriorly toward the primary auditory cortex.

Auditory Brainstem Response quality was categorized according to the presence of waves I, III, and V according to the Hannover classification. Class 1, the best one, shows an Auditory Brainstem Response with waves I, III, and V at normal latency such as in healthy individuals; class 2 shows the same waves with pathologic latencies; in class 3, wave III is lost; in class 4, only wave I or wave V is reproducible; and in class 5, no reproducible waves exist.

The examiners who postprocessed the diffusion data were blinded to the clinical data of the patients.

The University Hospital Ethics Committee approved the study, and all patients gave informed consent.

Statistical Analysis

A paired group comparison between the ipsilateral and the contralateral parameters (volume and FA) of each section of the auditory pathway was performed by using the Wilcoxon signed rank test.

To perform a correlation analysis with functional parameters, we built the laterality quotient between ipsilateral and contralateral parameters (volume and FA) for each section of the auditory pathway. We used a Spearman correlation coefficient to assess the association between audiometric and electrophysiologic measurements and the laterality quotients of the auditory pathway volumes and FA. Furthermore, we used a Spearman correlation coefficient to assess the association between the size of the tumor according to the tumor-size classification (T2a–T3b, ordinal scale) and the laterality quotients of the auditory pathway volumes and FA.

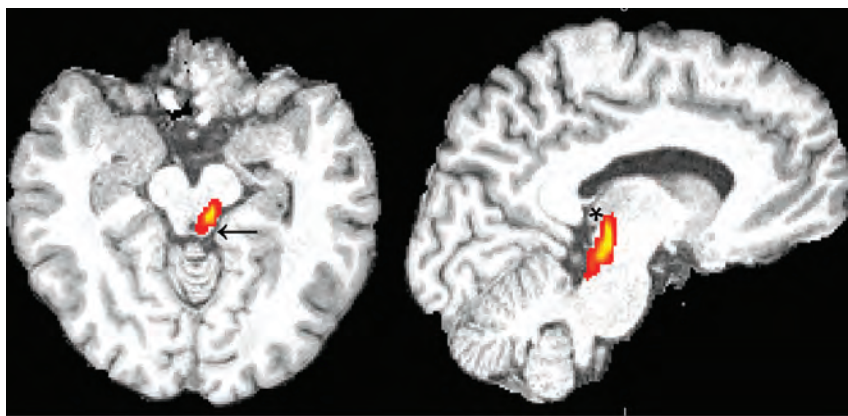


FIG 3. Illustration of the probabilistic fiber-tracking result of patient 4 of the left diencephalic section from the inferior colliculus (arrow) to the medial geniculate nucleus (asterisk) on sagittal and axial sections.

Table 2: Volume and FA of the ipsilateral and contralateral sections of the auditory pathway

Section	Volume IL	Volume CL	P	FA IL	FA CL	P
Lateral	1957 ± 668	1480 ± 516	.017 ^a	0.38 ± 0.04	0.36 ± 0.04	.72
Long lateral	1753 ± 756	1930 ± 532	.314	0.44 ± 0.04	0.45 ± 0.06	.72
Diencephalic	571.9 ± 249	410.7 ± 390	.009 ^a	0.31 ± 0.08	0.32 ± 0.07	1.00

Note:—IL indicates ipsilateral; CL, contralateral.

^a $P < .05$.

Table 3: Correlations between laterality quotients of tracking parameters and audiometric or electrophysiologic classifications^a

Laterality Quotient	AC	EC	Tumor Size
Volume of lateral section	$r = -0.08, P = .78$	$r = -0.08, P = .78$	$r = 0.19, P = .49$
FA of lateral section	$r = 0.14, P = .62$	$r = 0.14, P = .62$	$r = -0.45, P = .09$
Volume of long lateral section	$r = -0.12, P = .74$	$r = -0.12, P = .74$	$r = 0.28, P = .42$
FA of long lateral section	$r = 0.46, P = .18$	$r = 0.46, P = .18$	$r = 0.03, P = .95$
Volume of diencephalic section	$r = 0.56, P = 0.09$	$r = 0.56, P = .09$	$r = -0.94, P = .80$
FA of diencephalic section	$r = -0.40, P = .26$	$r = 0.40, P = .26$	$r = 0.20, P = .59$

Note:—AC indicates audiometric classification; EC, electrophysiologic classification based on auditory brain stem responses.

^a No significant correlations were found between tracking parameters and audiometric measurements, electrophysiologic measurements, or tumor size (ordinal scale according to tumor classification T2a–T4b).

RESULTS

Anatomically reasonable tracts were depicted in all patients on both sides for the lateral section of the auditory pathway (Fig 1). Because this part of the auditory pathway was short and broad, high probability values were reached. The volume of the lateral section was significantly decreased on the hemisphere contralateral to the tumor side (mean volume ipsilateral, 1.957 ± 0.668 ; mean volume contralateral, 1.480 ± 0.516 ; $P = .017$; Table 2), while fractional anisotropy did not differ significantly.

It was possible to depict the long lateral section between the MGN and auditory cortex in most patients; the tracking result was a long, thin volume passing through the posterior limb of the internal capsule, the external capsule, and the corona radiata (Fig 2). Tracking did not yield any meaningful tracts in 3 patients for the long lateral section on both hemispheres and in 2 patients on 1 hemisphere. Therefore, the intraindividual comparison was possible with only 10 patients. No significant differences in volume or FA were found in the long lateral section (mean volume ipsilateral, 1.75 ± 0.76 ; mean volume contralateral, 1.225 ± 0.53 ; $P = .31$).

The diencephalic section of the auditory pathway was identi-

fied between the inferior colliculus (IC) and the ipsilateral MGN (Fig 3). It was not possible to track this section in 3 patients on both sides and again in 2 patients on 1 side. Hence, intraindividual comparison was again possible with only 10 patients. Nevertheless, the volume of the contralateral diencephalic section was significantly decreased (mean volume ipsilateral, 0.572 ± 0.249 ; mean volume contralateral, 0.411 ± 0.390 ; $P = .009$), while fractional anisotropy did not differ.

No significant correlations between the laterality quotient and the audiometric and electrophysiologic classifications of hearing loss and tumor size were found (Table 3). Nevertheless, a trend toward associations between the laterality quotient of the diencephalic section volume of the auditory pathway and the electrophysiologic and audiometric quality classification by using the Hannover classification was detected (Table 3). A high laterality quotient was associated with impaired audiometric and electrophysiologic hearing function.

DISCUSSION

Tractography of the Auditory Pathway

This study shows, for the first time, that visualization of different sections of the auditory pathway between the IC and auditory cortex is feasible by using probabilistic tractography in an anatomically reasonable manner in patients with ves-

tibular schwannomas. There are several advantages of a tractography-based analysis of white matter tracts compared with ROI-based approaches. The anatomic course of the acoustic radiation is 3D and complex in shape, so the definition of the ROIs on axial 2D tensor maps would not be precise. Furthermore, ROI-based analyses do not comprise crossing fibers and their effect on fractional anisotropy, which is crucial given the anatomic course of the acoustic radiation crossing perpendicular fiber tracts such as the external capsule. In contrast, the fiber-tracking technology we used is capable of modeling crossing fibers and thereby minimizing their effects on the target parameters. Only a few previous publications have described tractography experiments of the auditory pathway itself. Keifer et al¹⁶ used the same methodology (probtrackx, FSL) and showed, in 13 healthy subjects, the connectivity of the MGN with the auditory cortex passing through the internal capsule, particularly the posterior limb, and crossing over the external capsule. This finding is the precondition to tracking the auditory pathway shown in our study. Profant et al¹⁷ also succeeded in tracking the auditory pathway by using probabilistic fiber-tracking in an investigation on aging in 54 subjects; how-

ever, only the index of longitudinal diffusivity trended toward positive correlation with increasing age. A direct tracking of the IC to the auditory cortex was performed, though passing through the MGN with low FA; therefore, a high uncertainty has to be assumed. Javad et al¹⁸ combined fMRI with hearing paradigms for sound, pitch, and melody and probabilistic fiber-tracking in 13 healthy subjects. The spatial tracking results from the activation areas to the IC were anatomically similar to our resulting volumes of the long lateral section.

Degeneration of the Auditory Pathway

We identified a significant decrease in volume of the lateral and diencephalic sections on the contralateral hemisphere. This decrease indicates a degeneration of the auditory pathway that is pronounced at the hemisphere contralateral to the lesion. Anatomic studies previously revealed the predominant projection of fiber tracts from the cochlear nucleus to the contralateral IC and MGN, while ipsilateral projections also exist.^{23,24}

However, the comparison of the ipsi- and contralateral sides of the lesion might not fully represent the extent of degeneration because of bilaterally projecting fibers. Degeneration of bilateral fibers might result in decreased volumes of the auditory pathway on both hemispheres. The comparison of FA of the investigated sections of the auditory pathway did not reveal significant differences; this may also be attributed to degenerative effects of bilateral projecting fibers causing only nonsignificant side differences. Furthermore, previous anatomic and MR image studies indicated a structural difference between the dominant and the nondominant hemisphere per se, which is also true for the white matter of the superior temporal lobe.^{25,26}

This structural difference between the dominant and non-dominant hemispheres might further mask potential differences of FA not identified in our analysis. Kurtcan et al²⁷ previously demonstrated a decrease of FA at the level of the IC by using an ROI analysis when comparing patients with vestibular schwannoma and healthy controls. This decrease was bilateral but stronger on the contralateral side; this finding supports the hypothesis that a bilateral degeneration with a stronger impact on the contralateral side occurred. However, a decrease of FA was not found at the levels of the MGN and auditory cortex in the analysis of Kurtcan et al. The ROI approach with a small transverse section of 4 pixels did not allow determination of a tract volume. Thus, it cannot be directly compared to our results. Furthermore, the determination of FA within the gray matter of the relay stations and cortex (IC, MGN, and auditory cortex) produces results with higher uncertainty because the baseline FA of the cortex and nuclear regions is low.

In the literature, there is no previous description of fiber tract integrity of the auditory pathway in patients with vestibular schwannomas, to our knowledge. However, some studies used DTI in patients with different disorders associated with hearing impairment. Especially patients with tinnitus were investigated by using DTI.^{28,29} Most interesting, probabilistic fiber-tracking in comparison with a healthy control group showed decreased FA of the connectivity between the auditory cortex and amygdala in patients with tinnitus.³⁰ On the other hand, Husain et al³¹ found a stronger decrease of gray matter volume and FA in cerebral

regions associated with hearing in patients with hearing loss without tinnitus than in those with tinnitus. Furthermore, previous studies by using ROI analyses of DTI indices found significant alterations of the auditory pathway in patients with congenital and traumatic sensorineural hearing loss.^{13,14,32,33} Another pilot study with a small number of patients focused on changes of the auditory nerve in patients with sensorineural hearing loss.³⁴ This study showed significant changes of DTI metrics of the auditory nerve itself compared with healthy control subjects, suggesting a degeneration of the neuronal projections of the auditory nerve.

Our finding of decreased volume of contralateral sections of the auditory pathway might correspond to a transsynaptic degeneration of the crossing auditory pathway secondary to the damage of the ipsilateral cochlear nerve. A previous structural analysis of gray matter volume in 15 patients with vestibular schwannoma found a correlation between volume increase of the contralesional auditory cortex and stronger hearing impairment,³⁵ which might be attributed to a compensatory allocation of the cortical field. Despite this volume increase of the cortical field, we found evidence of volume decrease of the auditory pathway conveying the auditory information to the contralesional cortex. Therefore, compensatory mechanisms seem to take place at the level of the cortical primary, projection, and association areas. Whether this compensatory mechanism is actually useful for the hearing function is a matter for future investigation. Most interesting, volume increase was also found bilaterally in the primary somatosensory cortices and the motion-sensitive cortex of the medial temporal gyrus. This may be linked to a multisensory compensation of the lesion and the vestibular system. However, the degeneration of the contralateral auditory tract that we showed in the current analysis might be a further reason, besides the lesion of the cochlear nerve itself, for the limited capacity of regaining hearing function after surgery in patients with vestibular schwannomas.

Although the audiometric and electrophysiologic classifications are also based on a functional deterioration by degeneration of the auditory pathway, we were not able to detect significant associations. Nevertheless, the laterality quotient of the tract volume of the diencephalic section of the auditory pathway tended to correlate with the audiometric and electrophysiologic classifications of hearing function. Most interesting, the electrophysiologic measurement included the fifth wave, which corresponds to a response of the inferior colliculus. The inferior colliculus was part of the diencephalic section of the auditory pathway that trended toward correlation. However, the missing detection of a significant association among morphologic tract integrity, hearing function, and tumor size might be due to the rather low patient number. One previous study reported a significant association between DTI-derived measures and abnormalities in the Auditory Brainstem Response in 56 preterm infants.¹⁵ Moreover, a variety of electrophysiologic measures were fed into the correlation analysis with DTI parameters.

Limitations and Perspectives

At present, the interpretation of our study results is restricted due to some limitations. The sample size of 15 patients is rather low; therefore, the statistical power of the tests performed is limited.

Because the diffusion tensor imaging was integrated into the

standard preoperative MR imaging, the scanning time for the sequences was limited. Therefore, rather thick sections of 3.6 mm were chosen. Thirty-two directions are sufficient for the application of probabilistic fiber-tracking, yet a higher number of directions would have enhanced the quality of the data.

The distribution of tumor size is not representative because it did not contain any T1 tumors, and it did contain a high proportion, 80%, of rather large tumors (T3a–T4b). Furthermore, the intraindividual comparison of fiber tracts cannot identify bilateral degeneration, but merely lateralized alterations. Patients with left- and right-sided tumors were included; thus, a possible effect of hemisphere dominance might confound the results. Hence, larger cross-sectional and longitudinal studies should be performed comparing changes of fiber tracts in patients with vestibular schwannoma versus healthy controls. Nonetheless, the identification of volume decrease contralateral to the tumor side provides an important finding for clinical discussion and decision-making: It explains, at least in part, why recovery of auditory function is rare and why auditory rehabilitation by hearing implants after tumor surgery is currently limited.³⁶ Whether early tumor resection can prevent the described neurodegeneration will be a subject for future investigations.

CONCLUSIONS

This study shows, for the first time, that different sections of the auditory pathway between the inferior colliculus and the auditory cortex can be visualized by using probabilistic tractography. A significant volume decrease of the lateral and diencephalic sections on the contralateral hemisphere was observed and may be explained by transsynaptic degeneration of the crossing auditory pathway evolving from damage to the ipsilateral cochlear nerve. This might be a reason for the limited potential of hearing rehabilitation in these patients. Further longitudinal studies investigating changes of the auditory pathway and associated tracts with time are warranted for a better understanding of disease- and therapy-related degeneration and plasticity.

Disclosures: Stefan M. Rueckriegel, Maria Hummel, Ralf-Ingo Ernestus—RELATED: Grant: A grant of the Interdisziplinäres Zentrum für Klinische Forschung, University Hospital Würzburg, provided cofunding for a technician position.* Money paid to Institution.

REFERENCES

- Howitz MF, Johansen C, Tos M, et al. **Incidence of vestibular schwannoma in Denmark, 1977–1995.** *Am J Otol* 2000;21:690–94 Medline
- Bakkouri WE, Kania RE, Guichard JP, et al. **Conservative management of 386 cases of unilateral vestibular schwannoma: tumor growth and consequences for treatment.** *J Neurosurg* 2009;110:662–69 CrossRef Medline
- Hajioff D, Raut VV, Walsh RM, et al. **Conservative management of vestibular schwannomas: third review of a 10-year prospective study.** *Clin Otolaryngol* 2008;33:255–59 Medline
- Axelsson A, Ringdahl A. **Tinnitus: a study of its prevalence and characteristics.** *Br J Audiol* 1989;23:53–62 Medline
- Sughrue ME, Yang I, Aranda D, et al. **The natural history of untreated sporadic vestibular schwannomas: a comprehensive review of hearing outcomes.** *J Neurosurg* 2010;112:163–67 CrossRef Medline
- Matthies C, Samii M. **Management of vestibular schwannomas (acoustic neuromas): the value of neurophysiology for evaluation and prediction of auditory function in 420 cases.** *Neurosurgery* 1997;40:919–29; discussion 929–30 Medline
- Samii M, Matthies C. **Management of 1000 vestibular schwannomas (acoustic neuromas): hearing function in 1000 tumor resections.** *Neurosurgery* 1997;40:248–60; discussion 260–62 Medline
- Gardner G, Robertson JH. **Hearing preservation in unilateral acoustic neuroma surgery.** *Ann Otol Rhinol Laryngol* 1988;97:55–66 Medline
- Samii M, Gerganov V, Samii A. **Improved preservation of hearing and facial nerve function in vestibular schwannoma surgery via the retrosigmoid approach in a series of 200 patients.** *J Neurosurg* 2006;105:527–35 Medline
- Sekiya T, Hatayama T, Shimamura N, et al. **A comprehensive classification system of vestibular schwannomas.** *J Clin Neurosci* 2000;7:129–33 Medline
- Akard W, Tubbs RS, Seymour ZA, et al. **Evolution of techniques for the resection of vestibular schwannomas: from saving life to saving function.** *J Neurosurg* 2009;110:642–47 CrossRef Medline
- Bronstein AM. **Vision and vertigo: some visual aspects of vestibular disorders.** *J Neurol* 2004;251:381–87 Medline
- Wu CM, Ng SH, Wang JJ, et al. **Diffusion tensor imaging of the subcortical auditory tract in subjects with congenital cochlear nerve deficiency.** *AJNR Am J Neuroradiol* 2009;30:1773–77 CrossRef Medline
- Chang Y, Lee SH, Lee YJ, et al. **Auditory neural pathway evaluation on sensorineural hearing loss using diffusion tensor imaging.** *Neuroreport* 2004;15:1699–703 Medline
- Reiman M, Parkkola R, Johansson R, et al. **Diffusion tensor imaging of the inferior colliculus and brainstem auditory-evoked potentials in preterm infants.** *Pediatr Radiol* 2009;39:804–09 CrossRef Medline
- Keifer OP, Jr., Gutman DA, Hecht EE, et al. **A comparative analysis of mouse and human medial geniculate nucleus connectivity: a DTI and anterograde tracing study.** *Neuroimage* 2015;105:53–66 CrossRef Medline
- Profant O, Škoch A, Balogová Z, et al. **Diffusion tensor imaging and MR morphometry of the central auditory pathway and auditory cortex in aging.** *Neuroscience* 2014;260:87–97 CrossRef Medline
- Javad F, Warren JD, Micallef C, et al. **Auditory tracts identified with combined fMRI and diffusion tractography.** *Neuroimage* 2014;84:562–74 CrossRef Medline
- Smith SM, Jenkinson M, Woolrich MW, et al. **Advances in functional and structural MR image analysis and implementation as FSL.** *Neuroimage* 2004;23(suppl 1):S208–19 Medline
- Behrens TE, Berg HJ, Jbabdi S, et al. **Probabilistic diffusion tractography with multiple fibre orientations: what can we gain?** *Neuroimage* 2007;34:144–55 Medline
- Behrens TE, Woolrich MW, Jenkinson M, et al. **Characterization and propagation of uncertainty in diffusion-weighted MR imaging.** *Magn Reson Med* 2003;50:1077–88 Medline
- Jbabdi S, Sotiropoulos SN, Savio AM, et al. **Model-based analysis of multishell diffusion MR data for tractography: how to get over fitting problems.** *Magn Reson Med* 2012;68:1846–55 CrossRef Medline
- Anderson LA, Malmierca MS, Wallace MN, et al. **Evidence for a direct, short latency projection from the dorsal cochlear nucleus to the auditory thalamus in the guinea pig.** *Eur J Neurosci* 2006;24:491–98 Medline
- Schofield BR, Motts SD, Mellott JG, et al. **Projections from the dorsal and ventral cochlear nuclei to the medial geniculate body.** *Front Neuroanat* 2014;8:10 CrossRef Medline
- Vandermosten M, Poelmans H, Snaert S, et al. **White matter lateralization and interhemispheric coherence to auditory modulations in normal reading and dyslexic adults.** *Neuropsychologia* 2013;51:2087–99 CrossRef Medline
- Anderson B, Southern BD, Powers RE. **Anatomic asymmetries of the posterior superior temporal lobes: a postmortem study.** *Neuropsychiatry Neuropsychol Behav Neurol* 1999;12:247–54 Medline
- Kurtcan S, Alkan A, Kilicarslan R, et al. **Auditory pathway features**

- determined by DTI in subjects with unilateral acoustic neuroma. *Clin Neuroradiol* 2015 Mar 27. [Epub ahead of print] Medline
28. Lee YJ, Bae SJ, Lee SH, et al. **Evaluation of white matter structures in patients with tinnitus using diffusion tensor imaging.** *J Clin Neurosci* 2007;14:515–19 Medline
 29. Aldhafeeri FM, Mackenzie I, Kay T, et al. **Neuroanatomical correlates of tinnitus revealed by cortical thickness analysis and diffusion tensor imaging.** *Neuroradiology* 2012;54:883–92 CrossRef Medline
 30. Crippa A, Lanting CP, van Dijk P, et al. **A diffusion tensor imaging study on the auditory system and tinnitus.** *Open Neuroimag J* 2010; 4:16–25 CrossRef Medline
 31. Husain FT, Medina RE, Davis CW, et al. **Neuroanatomical changes due to hearing loss and chronic tinnitus: a combined VBM and DTI study.** *Brain Res* 2011;1369:74–88 CrossRef Medline
 32. Manners DN, Rizzo G, La Morgia C, et al. **Diffusion tensor imaging mapping of brain white matter pathology in mitochondrial optic neuropathies.** *AJNR Am J Neuroradiol* 2015;36:1259–65 CrossRef Medline
 33. Lin Y, Wang J, Wu C, et al. **Diffusion tensor imaging of the auditory pathway in sensorineural hearing loss: changes in radial diffusivity and diffusion anisotropy.** *J Magn Reson Imaging* 2008;28:598–603 Medline
 34. Vos SB, Haakma W, Versnel H, et al. **Diffusion tensor imaging of the auditory nerve in patients with long-term single-sided deafness.** *Hear Res* 2015;323:1–8 CrossRef Medline
 35. Helmchen C, Klinkenstein JC, Krüger A, et al. **Structural brain changes following peripheral vestibulo-cochlear lesion may indicate multisensory compensation.** *J Neurol Neurosurg Psychiatry* 2011;82:309–16 CrossRef Medline
 36. Merkus P, Di Lella F, Di Trapani G, et al. **Indications and contraindications of auditory brainstem implants: systematic review and illustrative cases.** *Eur Arch Otorhinolaryngol* 2014;271:3–13 CrossRef Medline

Tractography at 3T MRI of Corpus Callosum Tracts Crossing White Matter Hyperintensities

W. Reginold, J. Itorralba, A.C. Luedke, J. Fernandez-Ruiz, J. Reginold, O. Islam, and A. Garcia

ABSTRACT

BACKGROUND AND PURPOSE: The impact of white matter hyperintensities on the diffusion characteristics of crossing tracts is unclear. This study used quantitative tractography at 3T MR imaging to compare, in the same individuals, the diffusion characteristics of corpus callosum tracts that crossed white matter hyperintensities with the diffusion characteristics of corpus callosum tracts that did not pass through white matter hyperintensities.

MATERIALS AND METHODS: Brain T2 fluid-attenuated inversion recovery–weighted and diffusion tensor 3T MR imaging scans were acquired in 24 individuals with white matter hyperintensities. Tractography data were generated by the Fiber Assignment by Continuous Tracking method. White matter hyperintensities and corpus callosum tracts were manually segmented. In the corpus callosum, the fractional anisotropy, radial diffusivity, and mean diffusivity of tracts crossing white matter hyperintensities were compared with the fractional anisotropy, radial diffusivity, and mean diffusivity of tracts that did not cross white matter hyperintensities. The cingulum, long association fibers, corticospinal/bulbar tracts, and thalamic projection fibers were included for comparison.

RESULTS: Within the corpus callosum, tracts that crossed white matter hyperintensities had decreased fractional anisotropy compared with tracts that did not pass through white matter hyperintensities ($P = .002$). Within the cingulum, tracts that crossed white matter hyperintensities had increased radial diffusivity compared with tracts that did not pass through white matter hyperintensities ($P = .001$).

CONCLUSIONS: In the corpus callosum and cingulum, tracts had worse diffusion characteristics when they crossed white matter hyperintensities. These results support a role for white matter hyperintensities in the disruption of crossing tracts.

ABBREVIATIONS: CC = corpus callosum; CC-WMH tracts = corpus callosum tracts crossing white matter hyperintensities; FA = fractional anisotropy; MD = mean diffusivity; RD = radial diffusivity; WMH = white matter hyperintensities; WMH tracts = tracts crossing white matter hyperintensities

The corpus callosum (CC) is the largest commissural tract with >200 million axons connecting the cerebral hemispheres.¹ Atrophy of the CC is a marker of neurodegeneration and has been reported in cerebrovascular disease.^{2–8} White matter hyperintensities (WMH) are high-signal lesions on T2-weighted MR imaging that represent cerebral small vessel disease and have been associated with CC atrophy.^{7,9–14} The reason for changes in the corpus callosum with WMH is unclear. Earlier studies have sug-

gested that WMH may be an incidental finding and that CC atrophy results from a coexisting disease process.^{7,10–17} For example, WMH are seen with Alzheimer disease, in which CC atrophy can occur by cortical atrophy and subsequent Wallerian degeneration of corpus callosum fibers originating from pyramidal neurons.^{7,10,13,15,16} These studies also suggest that WMH may directly cause CC atrophy by disrupting fibers of the corpus callosum as they are passing through the ischemic lesions in the deep white matter.^{7,10–17}

Diffusion tensor imaging can detect early changes in white matter microstructure before atrophy occurs and could clarify the relationship between WMH and the CC.¹⁸ In DTI, pathologic processes that alter the structural integrity of tracts lead to changes in water diffusion and mean diffusivity (MD) and radial diffusivity (RD) as well as changes in the directionality of diffusion and fractional anisotropy (FA).^{18,19} In patients with WMH, decreased FA and increased MD were found in the CC.¹³ Another study demonstrated correlations among CC atrophy, the FA/MD of deep white matter, and the FA/MD of the CC.¹⁷ These results

Received December 24, 2015; accepted after revision February 16, 2016.

From the Departments of Medical Imaging (W.R.) and Life Sciences (J.R.), University of Toronto, Toronto, Ontario, Canada; Memory Clinics (W.R., A.G.), Division of Geriatric Medicine, Department of Medicine, and Centre for Neuroscience Studies (J.I., A.G., A.C.L.), Queen's University, Kingston, Ontario, Canada; Facultad de Medicina, (J.F.-R.), Universidad Nacional Autónoma de México, Coyoacán, México; and Department of Diagnostic Radiology (O.I.), Kingston General Hospital, Queen's University, Kingston, Ontario, Canada.

Please address correspondence to William Reginold, MD, Department of Medical Imaging, University of Toronto, 4th floor, 263 McCaul St, Toronto, ON M5T 1W7, Canada; e-mail: wreginold@qmed.ca

<http://dx.doi.org/10.3174/ajnr.A4788>

Table 1: Demographic and clinical data for participants^a

	Total
No.	24
Age (yr)	70.4 ± 9.2
Sex (M/F count)	8/16
WMH volume (voxels)	1190 ± 3030
MoCA	27.7 ± 1.7

Note:—MoCA indicates Montreal Cognitive Assessment.

^a Values are means and SDs unless otherwise noted.

confirm an association between WMH and the entire CC but do not distinguish between the effects of WMH on callosum tracts that cross WMH (CC-WMH) and those that do not cross WMH. If CC-WMH tracts had worse diffusion characteristics than CC tracts not crossing WMH, this feature would support an increased role for WMH in changes in the corpus callosum.

Tractography is an application of DTI that allows the reconstruction of white matter tracts.¹⁸ In quantitative tractography, the diffusion characteristics (MD, RD, and FA) along the full trajectory of select fiber tracts can be assessed.¹⁸ This study used quantitative tractography to compare the diffusion characteristics of CC-WMH tracts with those of CC tracts not crossing WMH. For comparison, this study also performed a similar analysis in tracts that crossed WMH (WMH tracts) compared with those that did not cross WMH (lesion-free tracts) in the cingulum, long association fibers, corticospinal/bulbar tracts, and thalamic projection fibers. We hypothesized that CC-WMH tracts would have worse diffusion characteristics (increased MD and RD and decreased FA) compared with CC tracts not crossing WMH.

MATERIALS AND METHODS

Participants

The study was approved by the research ethics board of Queen's University. All participants provided written informed consent before entering the study. All participants underwent a 3T MR imaging brain scan within 2 weeks of cognitive testing, which included the Montreal Cognitive Assessment,²⁰ the Wechsler Memory Scale-III longest span backward,²¹ the Wechsler Memory Scale-III longest span forward,²¹ the Stroop Test,²² and Letter-Number Sequencing.²¹ Exclusion criteria included a diagnosis of mild cognitive impairment or dementia or the presence of metallic objects, devices, or conditions unsafe for MR imaging. The inclusion criterion was the presence of white matter hyperintensities on T2 FLAIR imaging. Ninety-one participants had MR imaging scans, of which 24 subjects met the inclusion criteria for the study. The demographic characteristics of the participants are shown in Table 1.

MR Imaging

All brain imaging was acquired in 1 session on a 3T Magnetom Trio MR imaging system (Siemens, Erlangen, Germany) with a 12-channel head coil. A high-resolution anatomic scan was acquired with a sagittal T1-weighted 3D magnetization-prepared rapid acquisition of gradient echo sequence (FOV, 256 mm; spatial resolution, 1 × 1 × 1 mm³; TR, 1760 ms; TE, 2.2 ms; flip angle, 9°; number of sections, 176). An axial T2-weighted 2D fluid-attenuated inversion recovery sequence interleaved scan was acquired for detecting white matter hyperintensities (FOV, 250 mm; voxel size, 1 × 1 × 3 mm³; TR, 9000 ms; TE, 79 ms; flip angle,

180°; number of sections, 40). Diffusion tensor imaging data were acquired in 30 directions by using a single-shot echo-planar imaging sequence with 31 volumes of 60 axial sections (b-value 1 = 0 s/mm² and b-value 2 = 1000 s/mm²; section thickness, 2 mm; TR/TE, 7800/95 ms; FOV, 256 × 256 mm²; acquisition matrix, 128 × 128, resulting in a resolution of 2 × 2 × 2 mm³).

Image Analysis

Analysis was performed with a method described in earlier studies.^{23,24} Briefly, diffusion-weighted images were corrected for eddy current distortions by using the Diffusion Toolbox in the FMRIB Software Library (FSL; www.fmrib.ox.ac.uk/fsl/fslwiki/FDT²⁵). DTI reconstruction of the preprocessed data from FSL was completed with the Diffusion Toolkit 0.5 (TrackVis; www.trackvis.org/dtk). The output included diffusion tensor data, parametric diffusion-weighted imaging, and FA and MD maps. Tracts were created in the Diffusion Toolkit by the Fiber Assignment by Continuous Tracking method.²⁶ The subject's T2 FLAIR MR imaging was registered to the diffusion-weighted image map by using 3DSlicer 4.1 (www.slicer.org). Tractography data and registered T2 FLAIR were analyzed with TrackVis. All WMH on axial T2 FLAIR were segmented manually. The borders of individual WMH were identified with windowing of the axial T2 FLAIR sections. Individual WMH were outlined section-by-section on all 40 axial T2 FLAIR sections for each patient by using a mouse-controlled interface on TrackVis. Although there is high intrarater and interrater variability, expert manual segmentation of WMH is the criterion standard for segmenting WMH.²⁷ The software generated a single ROI that encompassed all voxels within outlined areas. WMH lesion volume was measured as the total number of voxels that were within the WMH. The locations of WMH were manually classified by using axial, sagittal, and coronal T2 FLAIR reconstructions as periventricular (contiguous with the ventricular system), deep frontal, deep temporal, deep parietal, and deep occipital.²⁸⁻³¹

For the analysis of the specific white matter tracts, ROIs were manually placed within tracts of interest by using axial and sagittal color FA maps and T2 FLAIR. Tracts of interest were segmented by choosing tracts with any part through the ROIs. Segmented tracts included the corpus callosum, cingulum, long association fibers, corticospinal/bulbar tracts, and thalamic projection fibers (example in Fig 1). For the analysis of WMH tracts, ROIs were combined to select tracts. For example, to segment CC-WMH tracts, tracts with any part through the WMH ROI and any part through the ROI for segmenting the corpus callosum were selected (Fig 1A). The number, mean FA, mean MD, and RD (average of the second and third eigenvalues¹⁹) of WMH tracts were measured. For the analysis of tracts not crossing WMH, ROIs were again combined. For example, to segment tracts within the corpus callosum that did not cross WMH, tracts with no part through the WMH ROI and any part through the ROI for segmenting the corpus callosum were selected (Fig 1A). The number, mean FA, mean MD, and RD of these lesion-free tracts were measured. The percentage of WMH tracts was calculated as the ratio of the number of WMH tracts to the combined number of WMH tracts and lesion-free tracts.

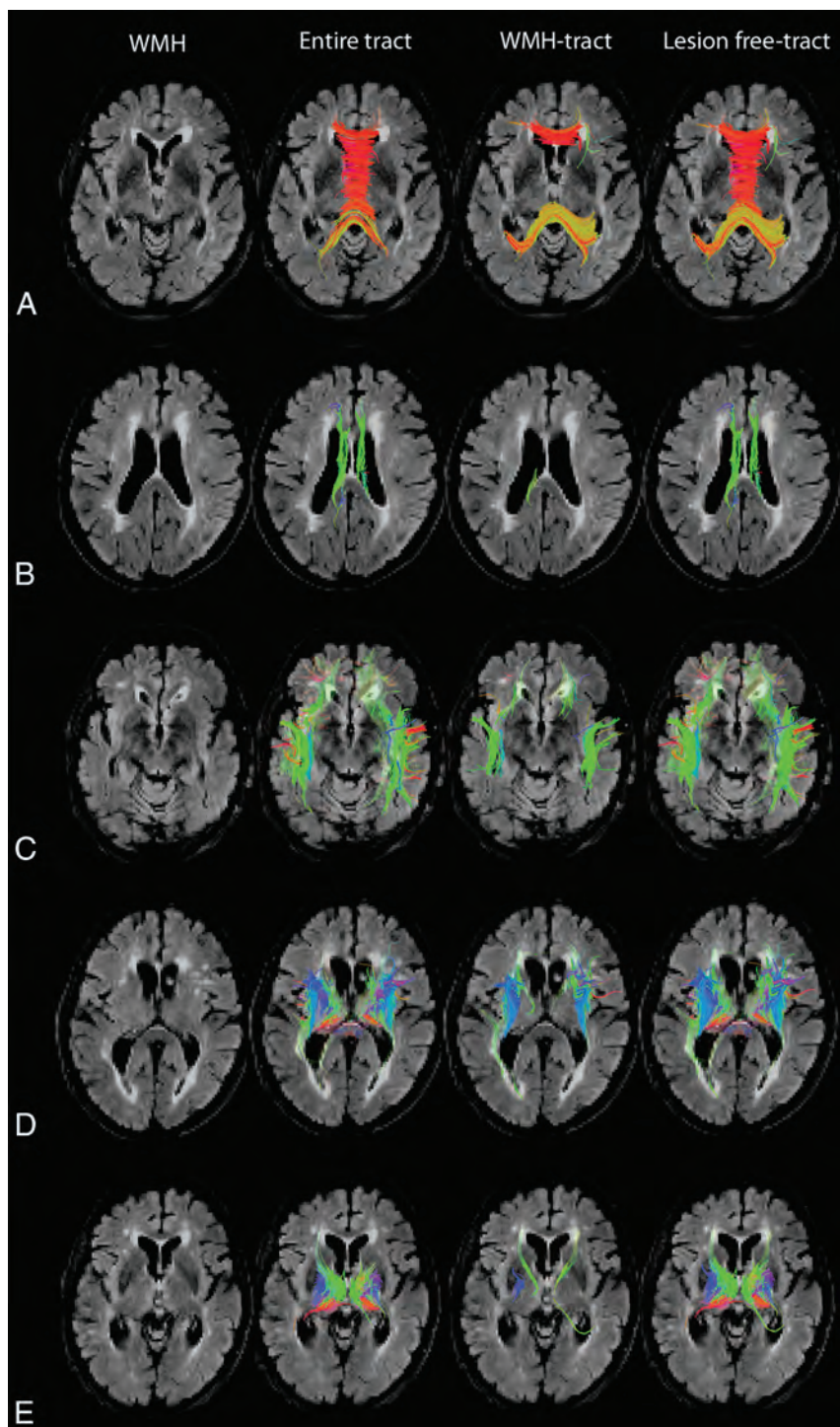


FIG 1. Tract segmentation, WMH tracts, and lesion-free tracts. Axial T2 FLAIR demonstrates white matter hyperintensities, tractography representation of the entire tracts, WMH tracts, and lesion-free tracts in the corpus callosum (A), cingulum (B), association fibers (C), corticospinal/bulbar tract (D), and thalamic tracts (E).

Statistical Analysis

StatPlus for Windows (AnalystSoft, Walnut, California) was used for statistical analysis. The nonparametric sign test was used to compare the FA, MD, and RD of tracts crossing WMH with tracts not crossing WMH within subjects. Subjects were included in the analysis when they had tracts crossing WMH. Due to multiple testing, a Bonferroni correction was used to

adjust *P* values. *P* values < .01 were considered statistically significant.

RESULTS

The demographic characteristics of the participants are described in Table 1. The age of participants ranged from 56 to 89 years. All participants had periventricular WMH, 18 (75%) had deep frontal WMH, 11 (46%) had deep parietal WMH, 3 (13%) had deep occipital WMH, and no participants had deep temporal WMH. WMH were located in the CC in all 24 participants, in the cingulum of 17 (71%) participants, in the association tracts of 21 (88%) participants, in the corticospinal/bulbar tract of 20 (83%) participants, and in the thalamic tracts of 16 (67%) participants. Within these tracts, the mean percentage of fibers crossing WMH was $14\% \pm 14\%$ of the CC, $3\% \pm 5\%$ of the cingulum, $4\% \pm 4\%$ of association fibers, $4\% \pm 6\%$ of the corticospinal/bulbar tract, and $1\% \pm 2\%$ of thalamic tracts. The CC-WMH tracts and cingulum WMH tracts crossed only periventricular WMH.

CC-WMH tracts had decreased FA compared with CC lesion-free tracts (Table 2). The percentage decrease in FA of WMH tracts compared with lesion-free tracts was $9\% \pm 9\%$ in the CC, $1\% \pm 13\%$ in the cingulum, $3\% \pm 11\%$ in the association fibers, $6\% \pm 12\%$ in the corticospinal/bulbar tracts, and $-2\% \pm 14\%$ in the thalamic tracts. There was no significant difference in the MD or RD between CC-WMH tracts and CC lesion-free tracts (Table 2). There was increased RD in cingulum-WMH tracts compared with cingulum lesion-free tracts (Table 2). The percentage increase in the RD of WMH tracts compared with lesion-free tracts was $-2\% \pm 15\%$ in the CC, $21\% \pm 23\%$ in the cingulum, $1\% \pm 7\%$ in the association fibers, $6\% \pm 15\%$ in the corticospinal/bulbar tracts, and $5\% \pm 25\%$ in the thalamic tracts. For the other major white matter tracts, there were no significant differences in the FA, MD, or RD between tracts crossing WMH and those not crossing WMH (Table 2).

DISCUSSION

This is the first tractography study to compare tracts on the basis of whether they crossed WMH. Decreased FA was found in CC-WMH tracts compared with CC tracts not crossing WMH and is

Table 2: Comparison in major white matter tracts of the fractional anisotropy, mean diffusivity, and radial diffusivity of tracts crossing and not crossing WMH^a

	No. of Subjects with Tracts			
	Crossing WMH	Crossing WMH	Not Crossing WMH	P Value
Fractional anisotropy				
Corpus callosum	24	0.539 ± 0.057	0.591 ± 0.046	.002 ^b
Cingulum	17	0.442 ± 0.076	0.448 ± 0.047	.152
Association fibers	21	0.410 ± 0.054	0.424 ± 0.034	.093
Corticospinal tract	20	0.446 ± 0.061	0.477 ± 0.032	.027
Thalamus	16	0.452 ± 0.073	0.441 ± 0.032	.130
Mean diffusivity				
Corpus callosum	24	0.00085 ± 0.0001	0.000932 ± 0.0001	.053
Cingulum	17	0.0009 ± 0.0002	0.0008 ± 0.0001	.013
Association fibers	21	0.00079 ± 0.0001	0.00078 ± 0.0001	.122
Corticospinal tract	20	0.0008 ± 0.0001	0.0007 ± 0.0001	.047
Thalamus	16	0.00078 ± 0.0002	0.0008 ± 0.0001	.145
Radial diffusivity				
Corpus callosum	24	0.0006 ± 0.0001	0.0006 ± 0.0001	.140
Cingulum	17	0.0007 ± 0.0002	0.0006 ± 0.0001	.001 ^b
Association fibers	21	0.0006 ± 0.0001	0.0006 ± 0.0001	.143
Corticospinal tract	20	0.0006 ± 0.0001	0.0005 ± 0.0001	.070
Thalamus	16	0.0007 ± 0.0002	0.0006 ± 0.0001	.126

^a Values are means and SDs unless otherwise noted.

^b Statistically significant.

indicative of greater white matter abnormalities in CC tracts crossing through WMH. WMH were associated with modest white matter abnormalities in the CC (8% reduction in FA in 14% of all CC tracts). The association between decreased FA in the CC and WMH is consistent with that in earlier studies.^{13,17} Increased RD was found in the cingulum WMH tracts compared with cingulum lesion-free tracts and is suggestive of greater abnormalities in the myelination of cingulum tracts crossing through WMH. WMH were also associated with modest white matter abnormalities in the cingulum (a 21% increase in RD in 3% of all cingulum tracts). Earlier studies have reported involvement of the cingulum by WMH; however, this is the first study to detect increased RD.³²⁻³⁴ This tractography study demonstrates that WMH are associated with modest altered diffusion characteristics in crossing tracts.

Earlier studies have suggested that WMH may be incidental markers of a disease process that is disrupting white matter tracts.^{7,10-17} If WMH are markers of a disease process, our results suggest that WMH are preferentially located on tracts with greater disruption by that disease process. WMH are known to preferentially develop in normal-appearing white matter areas with lower FA than in areas that remain lesion-free.³⁵ Earlier studies have also suggested that WMH may disrupt passing tracts.^{7,10-17} Our results support this theory because the structural integrity of the CC and cingulum tracts was worse when they passed through WMH. WMH consist of mild-to-marked demyelination, axonal loss, and astrogliosis and have reduced FA, increased MD, and increased RD within the lesions.³⁵⁻³⁷ The FA of CC-WMH tracts or the RD of cingulum WMH tracts reflects a combination of the diffusion characteristics within the WMH and the portions of the tracts extending beyond the lesions. If the altered diffusion characteristics within WMH accounted for the differences between CC-WMH tracts and CC tracts not crossing WMH or cingulum WMH tracts and cingulum lesion-free tracts, we would have expected to see similar differences in FA and RD between WMH tracts and lesion-free tracts in the long association fibers, corticospinal/bulbar tracts, and thalamic projection fibers. We were

unable to detect any difference between WMH tracts and lesion-free tracts in any of the other major white matter tracts, suggesting that WMH may have additional effects on segments of CC-WMH tracts and cingulum WMH tracts outside the lesions. WMH have been previously associated with diffusion abnormalities in normal-appearing white matter closer to WMH.^{35,36} Wallerian degeneration is a mechanism by which a lesion can produce disruption elsewhere along the length of the tract.^{7,10,13,15,16} Decreased FA and increased RD, which we have detected in this study, have been previously associated with Wallerian degeneration.^{19,38,39}

Consistent with earlier studies, the periventricular area was the most common location of WMH.²⁸⁻³¹ In this study, CC-WMH tracts and cingulum WMH tracts crossed only periventricular WMH. In this study, the CC was the tract most likely, in participants, to cross

through WMH and had the greatest proportion of fibers crossing through WMH. The greater involvement by WMH and altered FA may explain why atrophy of the CC has been noted earlier with WMH.^{7,10,11-14} In this study, the cingulum, long association fibers, corticospinal/bulbar tract, and thalamic fibers were all shown to cross WMH. The cingulum was the only other tract to demonstrate abnormal diffusion in WMH tracts.

It is unclear why CC-WMH tracts were not associated with increased MD and RD and why cingulum WMH tracts were not associated with decreased FA or increased MD. This lack of information may relate to the small sample size of this study. The altered diffusion characteristics detected were modest in size, and the study may have been underpowered to detect other smaller diffusion changes. The decreased tract involvement by WMH of long association fibers and corticospinal/bulbar tract and thalamic fibers compared with the CC may account for no diffusion abnormalities being detected in these tracts. Another limitation of this study is the accuracy of WMH tract reconstruction. The tractography methodology used in this study relies on FA for fiber tracking and reconstruction.²⁶ Some tracts crossing WMH may not have been propagated through the WMH due to the decreased FA within the lesions. This omission may have resulted in some WMH tracts being incorrectly classified as lesion-free tracts. The T2 FLAIR and diffusion tensor images had different resolutions and required registration. Due to errors in alignment, some tracts may have been incorrectly classified as WMH tracts or lesion-free tracts. Another limitation of this study is that diffusion characteristics are an indirect measure of axonal integrity.¹⁸ While poor diffusion measures are suggestive of structural disruption, they do not necessarily represent functional disconnection.

Despite these limitations, this study suggests the role WMH have in the disruption of CC and cingulum favors tracts crossing through WMH lesions. WMH may be marking injury or causing disruption of crossing tracts. Future studies with larger cohorts should assess longitudinal changes in WMH and the diffusion

characteristics of the CC and cingulum, as the temporal sequence of changes may improve our understanding of WMH as a cause or marker of tract disruption.

CONCLUSIONS

Tractography at 3T MR imaging of the corpus callosum demonstrated that tracts that crossed white matter hyperintensities had decreased fractional anisotropy compared with tracts that did not pass through white matter hyperintensities ($P = .002$). In the cingulum, tracts that crossed white matter hyperintensities had increased radial diffusivity compared with tracts that did not cross white matter hyperintensities ($P = .001$). These differences in fractional anisotropy and radial diffusivity between tracts crossing and not crossing white matter hyperintensities were not detected in the long association fibers, corticospinal/bulbar tracts, and thalamic projection fibers. Overall, these results support a role for white matter hyperintensities in the disruption of crossing corpus callosum and cingulum tracts.

REFERENCES

1. Tomasch J. **Size, distribution, and number of fibers in the human corpus callosum.** *Anat Rec* 1954;119:119–35 CrossRef Medline
2. Jokinen H, Ryberg C, Kalska H, et al; LADIS group. **Corpus callosum atrophy is associated with mental slowing and executive deficits in subjects with age-related white matter hyperintensities: the LADIS Study.** *J Neurol Neurosurg Psychiatry* 2007;78:491–96 Medline
3. Di Paola M, Spalletta G, Caltagirone C. **In vivo structural neuroanatomy of corpus callosum in Alzheimer's disease and mild cognitive impairment using different MRI techniques: a review.** *J Alzheimers Dis* 2010;20:67–95 CrossRef Medline
4. Granberg T, Bergendal G, Shams S, et al. **MRI-defined corpus callosal atrophy in multiple sclerosis: a comparison of volumetric measurements, corpus callosum area and index.** *J Neuroimaging* 2015;25:996–1001 CrossRef Medline
5. Crawford HE, Hobbs NZ, Keogh R, et al; TRACK-HD Investigators. **Corpus callosal atrophy in premanifest and early Huntington's disease.** *J Huntingtons Dis* 2013;2:517–26 CrossRef Medline
6. Wu TC, Wilde EA, Bigler ED, et al. **Longitudinal changes in the corpus callosum following pediatric traumatic brain injury.** *Dev Neurosci* 2010;32:361–73 CrossRef Medline
7. Meguro K, Constans JM, Courtheoux P, et al. **Atrophy of the corpus callosum correlates with white matter lesions in patients with cerebral ischaemia.** *Neuroradiology* 2000;42:413–19 CrossRef Medline
8. Tomimoto H, Lin JX, Matsuo A, et al. **Different mechanisms of corpus callosum atrophy in Alzheimer's disease and vascular dementia.** *J Neurol* 2004;251:398–406 CrossRef Medline
9. Dettie S, Markus HS. **The clinical importance of white matter hyperintensities on brain magnetic resonance imaging: systematic review and meta-analysis.** *BMJ* 2010;26:341:c3666 CrossRef Medline
10. Vermersch P, Roche J, Hamon M, et al. **White matter magnetic resonance imaging hyperintensity in Alzheimer's disease: correlations with corpus callosum atrophy.** *J Neurol* 1996;243:231–34 CrossRef Medline
11. Ryberg C, Rostrup E, Sjöstrand K, et al; LADIS study group. **White matter changes contribute to corpus callosum atrophy in the elderly: the LADIS study.** *AJNR Am J Neuroradiol* 2008;29:1498–504 CrossRef Medline
12. Ryberg C, Rostrup E, Paulson OB, et al; LADIS study group. **Corpus callosum atrophy as a predictor of age-related cognitive and motor impairment: a 3-year follow-up of the LADIS study cohort.** *J Neurol Sci* 2011;307:100–05 CrossRef Medline
13. Wu XP, Gao YJ, Yang JL, et al. **Quantitative measurement to evaluate morphological changes of the corpus callosum in patients with subcortical ischemic vascular dementia.** *Acta Radiol* 2015;56:214–18 CrossRef Medline
14. Yamauchi H, Fukuyama H, Shio H. **Corpus callosum atrophy in patients with leukoaraiosis may indicate global cognitive impairment.** *Stroke* 2000;31:1515–20 CrossRef Medline
15. Teipel SJ, Hampel H, Alexander GE, et al. **Dissociation between corpus callosum atrophy and white matter pathology in Alzheimer's disease.** *Neurology* 1998;51:1381–85 CrossRef Medline
16. Teipel SJ, Bayer W, Alexander GE, et al. **Progression of corpus callosum atrophy in Alzheimer disease.** *Arch Neurol* 2002;59:243–48 CrossRef Medline
17. Otsuka Y, Yamauchi H, Sawamoto N, et al. **Diffuse tract damage in the hemispheric deep white matter may correlate with global cognitive impairment and callosal atrophy in patients with extensive leukoaraiosis.** *AJNR Am J Neuroradiol* 2012;33:726–32 CrossRef Medline
18. Behrens TE, Jbabdi S. **MR diffusion tractography.** In: Johansen-Berg H, Behrens TE, eds. *Diffusion MRI: from Quantitative Measurement to in vivo Neuroanatomy.* New York: Elsevier; 2009:333–51
19. Song SK, Sun SW, Ramsbottom MJ, et al. **Dysmyelination revealed through MRI as increased radial (but unchanged axial) diffusion of water.** *Neuroimage* 2002;17:1429–36 CrossRef Medline
20. Nasreddine ZS, Phillips NA, Bédirian V, et al. **The Montreal Cognitive Assessment, MoCA: a brief screening tool for mild cognitive impairment.** *J Am Geriatr Soc* 2005;53:695–99 CrossRef Medline
21. Wechsler D. *Wechsler Memory Scale.* 3rd ed. San Antonio: Psychological Corporation; 1987
22. Stroop JR. **Studies of interference in serial verbal reactions.** *Journal of Experimental Psychology* 1935;18:643–62 CrossRef
23. Reginold W, Luedke AC, Tam A, et al. **Cognitive function and 3-Tesla magnetic resonance imaging tractography of white matter hyperintensities in elderly persons.** *Dement Geriatr Cogn Dis Extra* 2015;5:387–94 CrossRef Medline
24. Reginold W, Itorralba J, Tam A, et al. **Correlating quantitative tractography at 3T MRI and cognitive tests in healthy older adults.** *Brain Imaging Behav* 2015 Dec 9. [Epub ahead of print] Medline
25. Smith SM, Jenkinson M, Woolrich MW, et al. **Advances in functional and structural MR image analysis and implementation as FSL.** *Neuroimage* 2004;23:S208–19 Medline
26. Wiegell MR, Larsson HB, Wedeen VJ. **Fiber crossing in human brain depicted with diffusion tensor MR imaging.** *Radiology* 2000;217:897–903 CrossRef Medline
27. Simões R, Mönninghoff C, Dlugaj M, et al. **Automatic segmentation of cerebral white matter hyperintensities using only 3D FLAIR images.** *Magn Reson Imaging* 2013;31:1182–89 CrossRef Medline
28. Fazekas F, Kapeller P, Schmidt R, et al. **The relation of cerebral magnetic resonance signal hyperintensities to Alzheimer's disease.** *J Neurol Sci* 1996;142:121–25 CrossRef Medline
29. DeCarli C, Fletcher E, Ramey V, et al. **Anatomical mapping of white matter hyperintensities (WMH): exploring the relationships between periventricular WMH, deep WMH, and total WMH burden.** *Stroke* 2005;36:50–55 CrossRef Medline
30. Yoshita M, Fletcher E, Harvey D, et al. **Extent and distribution of white matter hyperintensities in normal aging, MCI, and AD.** *Neurology* 2006;67:2192–98 CrossRef Medline
31. Wen W, Sachdev P. **The topography of white matter hyperintensities on brain MRI in healthy 60- to 64-year-old individuals.** *Neuroimage* 2004;22:144–54 CrossRef Medline
32. Glodzik L, Kuceyeski A, Rusinek H, et al. **Reduced glucose uptake and Aβ in brain regions with hyperintensities in connected white matter.** *Neuroimage* 2014;100:684–91 CrossRef Medline
33. Tuladhar AM, van Norden AG, de Laat KF, et al. **White matter integrity in small vessel disease is related to cognition.** *Neuroimage Clin* 2015;7:518–24 CrossRef Medline
34. Taylor WD, Kudra K, Zhao Z, et al. **Cingulum bundle white matter lesions influence antidepressant response in late-life depression: a pilot study.** *J Affect Disord* 2014;162:8–11 CrossRef Medline

35. de Groot M, Verhaaren BF, de Boer R, et al. **Changes in normal-appearing white matter precede development of white matter lesions.** *Stroke* 2013;44:1037–42 CrossRef Medline
36. Gouw AA, Seewann A, van der Flier WM, et al. **Heterogeneity of small vessel disease: a systematic review of MRI and histopathology correlations.** *J Neurol Neurosurg Psychiatry* 2011;82:126–35 CrossRef Medline
37. Bastin ME, Clayden JD, Pattie A, et al. **Diffusion tensor and magnetization transfer MRI measurements of periventricular white matter hyperintensities in old age.** *Neurobiol Aging* 2009;30:125–36 CrossRef Medline
38. Sun SW, Liang HF, Cross AH, et al. **Evolving Wallerian degeneration after transient retinal ischemia in mice characterized by diffusion tensor imaging.** *Neuroimage* 2008;40:1–10 CrossRef Medline
39. Thomalla G, Glauche V, Weiller C, et al. **Time course of Wallerian degeneration after ischaemic stroke revealed by diffusion tensor imaging.** *J Neurol Neurosurg Psychiatry* 2005;76:266–68 CrossRef Medline

Manual Segmentation of MS Cortical Lesions Using MRI: A Comparison of 3 MRI Reading Protocols

J. Maranzano, D.A. Rudko, D.L. Arnold, and S. Narayanan



ABSTRACT

BACKGROUND AND PURPOSE: Double inversion recovery has been suggested as the MR imaging contrast of choice for segmenting cortical lesions in patients with multiple sclerosis. In this study, we sought to determine the utility of double inversion recovery for cortical lesion identification by comparing 3 MR imaging reading protocols that combine different MR imaging contrasts.

MATERIALS AND METHODS: Twenty-five patients with relapsing-remitting MS and 3 with secondary-progressive MS were imaged with 3T MR imaging by using double inversion recovery, dual fast spin-echo proton-density/T2-weighted, 3D FLAIR, and 3D T1-weighted imaging sequences. Lesions affecting the cortex were manually segmented by using the following 3 MR imaging reading protocols: Protocol 1 (P1) used all available MR imaging contrasts; protocol 2 (P2) used all the available contrasts except for double inversion recovery; and protocol 3 (P3) used only double inversion recovery.

RESULTS: Six hundred forty-three cortical lesions were identified with P1 (mean = 22.96); 633, with P2 (mean = 22.6); and 280, with P3 (mean = 10). The counts obtained by using P1 and P2 were not significantly different ($P = .93$). The counts obtained by using P3 were significantly smaller than those obtained by using either P1 ($P < .001$) or P2 ($P < .001$). The intraclass correlation coefficients were P1 versus P2 = 0.989, P1 versus P3 = 0.615, and P2 versus P3 = 0.588.

CONCLUSIONS: MR imaging cortical lesion segmentation can be performed by using 3D T1-weighted and 3D FLAIR images acquired with a 1-mm isotropic voxel size, supported by conventional T2-weighted and proton-density images with 3-mm-thick sections. Inclusion of double inversion recovery in this multimodal reading protocol did not significantly improve the cortical lesion identification rate. A multimodal approach is superior to using double inversion recovery alone.

ABBREVIATIONS: DIR = double inversion recovery; CL = cortical lesion; ICC = intraclass correlation coefficient; PD = proton-density; P1 = protocol 1; P2 = protocol 2; P3 = protocol 3

Multiple sclerosis is an inflammatory and neurodegenerative disease that affects both the white matter and gray matter of the central nervous system. Postmortem immunohistochemical characterization of cortical lesions (CLs) has allowed the identification of a substantial burden of cortical GM lesions in patients with long-standing MS.¹⁻⁵ However, the prevalence of cortical lesions at earlier stages of MS is underexplored.⁶ As a result, an efficient, standardized MR imaging protocol for segmentation of CLs in early-stage MS has become an important research goal.

Double inversion recovery (DIR) MR imaging has generally been selected because it enhances the conspicuity of GM by suppressing unwanted signal from both WM and CSF. However, DIR images have a low signal-to-noise ratio due to the application of 2 inversion pulses. They are also prone to hyperintense vascular artifacts, which can confound CL identification.⁷⁻¹⁴

In 2011, an international panel of experts formulated consensus recommendations for scoring CLs at 1.5T and 3T by using DIR.¹¹ As part of the recommendations, they noted that in the future, the additional use of other MR imaging contrasts (T1-weighted, T2-weighted, or fluid-attenuated inversion recovery images) in combination with DIR could improve the detection of cortical lesions by reducing the number of false-positives and false-negatives. Several groups have since reported on such multicontrast approaches for segmenting CLs. Examples include the following: 1) CL segmentation performed by using a single MR imaging contrast followed by subsequent verification of lesion labels on other contrasts¹³; 2) CL segmentation performed inde-

Received September 23, 2015; accepted after revision March 4, 2016.

From the Department of Neurology and Neurosurgery, Montreal Neurological Hospital and Institute, McGill University, Montreal, Quebec, Canada.

Please address correspondence to Sridar Narayanan, PhD, Department of Neurology and Neurosurgery, Montreal Neurological Institute, McGill University, 3801 Rue University, Montreal, Quebec, Canada, H3A 2B4; e-mail: sridar.narayanan@mcgill.ca

Indicates open access to non-subscribers at www.ajnr.org

Indicates article with supplemental on-line table.

<http://dx.doi.org/10.3174/ajnr.A4799>

MRI acquisition parameters^a

	TIWI	PD/T2WI	FLAIR	DIR
Sequence	3D FLASH	Dual-echo TSE	3D SPACE (tse_vfl)	3D SPACE (tse_vfl)
Orientation	Axial	Axial	Sagittal	Sagittal
TR (ms)	22	2200	6000	7500
TE (ms)	5	12, 83	355	323
TI (ms)	NA	NA	2200	3000
Sections	192	60	176	120
Voxel size (mm × mm × mm)	1 × 1 × 1	1 × 1 × 3	1 × 1 × 1	1.5 × 1.5 × 1.5
Scan time (min:sec)	9:38	7:02	8:5	6:53

Note:—SPACE indicates sampling perfection with application-optimized contrasts by using different flip angle evolutions (Siemens, Erlangen, Germany); tse_vfl, turbo spin echo-variable flip angle; NA, not applicable.

^a Pertinent MRI sequence acquisition parameters for the 5 MRI contrasts used in our manual cortical lesion-segmentation methods.

pendently by using 2 different MR imaging contrasts, where a tight correlation between the counts is considered evidence that each MR imaging contrast yields counts proportional to the real lesion load¹⁵; 3) CL segmentation performed by using a single MR imaging contrast with the results subsequently reviewed by a second (more experienced) rater who uses other contrasts to resolve ambiguities/potential false-positives¹⁶; and 4) CL segmentation performed independently for each independent contrast, and then each count compared with the counts obtained from the other MR imaging contrasts to determine which one detects the highest number of lesions.¹⁷ The variability among these methods has led to difficulty in developing a standardized CL segmentation protocol.¹¹ Consequently, a major goal of this work was to identify a robust, multicontrast CL segmentation protocol that could be used with more generally available MR imaging pulse sequences at clinically accessible magnetic field strengths.

According to the consensus recommendations, only type I leukocortical and type II intracortical lesions should be considered for radiologic scoring¹¹ in MS. However, type I lesions affecting both the cortex and the juxtacortical white matter are often difficult to differentiate from purely juxtacortical lesions. Consequently, these lesions can be misclassified. Type II lesions are the smallest and affect the cortex without reaching either the pial or white matter boundaries. These lesions are also challenging to detect visually by using 1.5T or 3T MR imaging. Subpial lesions (type III and IV), extending from the pial boundary down to the white matter surface, are not considered within the consensus guidelines for MR imaging at 1.5 and 3T due to their low detectability at these clinical field strengths. Even with these simplifying assumptions in place, CL identification has been highly variable.^{10,13,18,19} The prevalence of MR imaging-identified intracortical lesions ranges from 8.2% to 46% across different published reports.^{10,12,13,18,19} This variability may partially reflect the variable sensitivity of current MR imaging protocols but also may indicate the inherent variability of cortical lesion involvement across MS disease stages and individual patients. Support for this hypothesis is provided by histology studies in which the percentage of intracortical lesions (type II) also shows a wide range: 7%–31% and 17%–71% when we consider types I and type II combined.^{1–6,19,20,21}

A significant aim of our study was to simplify and improve the process of manual cortical lesion segmentation when using multiple MR imaging contrasts derived from 3T MR imaging. We specifically strived to identify a lesion-segmentation method with

reduced variability and reduced false-positive identifications. To do this, we avoided classification of cortical lesions into subtypes.

MATERIALS AND METHODS**Participants**

A cohort of 20 patients with MS (15 female, 5 male; 17 with relapsing-remitting MS, 3 with secondary-progressive MS; between 26 and 63 years of age) was recruited from the MS Clinic of the Montreal Neurological Hospital in a prospective study designed to assess cor-

tical GM pathology. Twenty-eight scans were used for testing 3 MR imaging-based, multicontrast CL segmentation protocols. Eight subjects had a second MR imaging 24 months after the first one (these scans were included in the 28 scans). None of the patients underwent treatment with corticosteroids in the month before the MR imaging. Fourteen patients were receiving immunomodulating treatment. The median Expanded Disability Status Scale score was 2 (range, 0–8).

MR Imaging Acquisition

All patients were imaged on a Tim Trio 3T (Siemens, Erlangen, Germany) whole-body MR imaging scanner with a volume-transmit coil and a 12-channel receive coil. For each patient, we acquired the following images: T1-weighted images collected with a 3D gradient recalled-echo sequence, proton density-weighted (PD-weighted) and T2-weighted images obtained from a dual-echo turbo spin-echo sequence, and 3D FLAIR and 3D DIR images. Scan parameters for each sequence are listed in the Table.

MR Imaging Analysis

All MR images were scored by 1 rater (J.M. with >10 years of experience in quantification procedures on MR imaging research scans of patients with MS). After bias field correction (Sled et al²²) of all images, 3D FLAIR, PD-weighted, T2-weighted, and DIR images were linearly registered and resampled to the image space of the T1-weighted image (1-mm³ isotropic voxels). Subsequently, CLs were manually segmented by using the interactive software package Display, part of the minc-toolkit (<https://github.com/BIC-MNI>) developed at the McConnell Brain Imaging Center of the Montreal Neurological Institute. This program allows simultaneous viewing and segmentation in the coronal, sagittal, and axial planes and cycling between each image volume. The image volumes are coregistered so that when assessing a given voxel or region and switching from one contrast (eg, DIR) to another (eg, FLAIR), the rater is assessing the intensity signal of the same region of the brain on each contrast. Each window allows zooming in and out, and a painting tool allows marking voxels with a given color (label number). All CLs identified in one plane are simultaneously shown in the other 2 orientations. Marked voxels are saved in a separate label file that can be loaded on its own or superimposed on the brain images.

For lesion segmentation, the rater scrolled through contiguous sections in the axial plane while inspecting the images in the following order for each axial section: T1WI, FLAIR, DIR, PD-

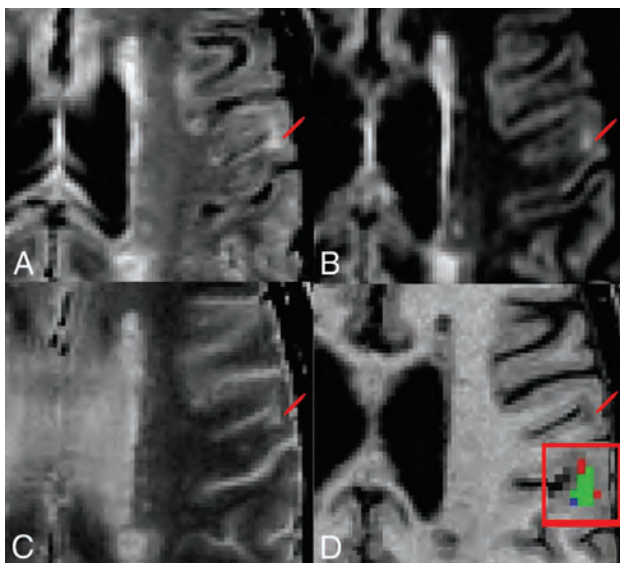


FIG 1. Representative multicontrast cortical lesion segmentation examples. Image contrasts shown include FLAIR, DIR, T2WI, and T1WI (A–D). Lesion location is demarcated by a red pointer. D, Enlarged view of the lesion showing the overlap of labels produced by using protocols P1 and P2. The green voxels represent the overlap between masks generated with P1 and P2, the red voxels identify voxels segmented only with P1, and the blue voxels represent voxels segmented only with P2.

weighted, and T2WI and cycling back and forth between each contrast, as needed. The preferred image orientation used for CL segmentation was the axial plane. However, results were verified by examining the image volume in the sagittal and coronal planes, and the operator could examine sections above and below to resolve any ambiguities and assess the shape of the candidate lesion in 3D.

To be considered a CL, an image region had to include at least 3 contiguous voxels; be hyperintense on T2-weighted images, FLAIR, and DIR; and be hypointense on T1-weighted images in relation to normal-appearing adjacent cortex. These criteria were adopted in an attempt to reduce the number of false-positive identifications. We found the high gray matter/white matter contrast and resolution of the 3T T1-weighted sequence particularly useful in assessing whether a CL crossed the cortical boundary or was simply adjacent to the boundary (juxtacortical lesions).

The 3 multicontrast rating protocols used in this study were defined as follows:

- Protocol 1 (P1): CLs were segmented by using T1WI, FLAIR, DIR, PD-weighted, and T2WI. All images were bias field corrected, resampled to 1-mm isotropic resolution, and linearly registered to the image space of the T1-weighted image.
- Protocol 2 (P2): CLs were segmented by using T1WI, FLAIR, PD-weighted, and T2WI. All images were bias field corrected, resampled to 1-mm isotropic resolution, and linearly registered to the image space of the T1-weighted image.
- Protocol 3 (P3): CLs were segmented by using DIR alone. The DIR image was bias field corrected, and segmentation was performed by using the DIR at the native resolution of $1.5 \times 1.5 \times 1.5 \text{ mm}^3$.

There was an interval of at least 8 days between each protocol read (8 days between the end of the read using P1 and the beginning of the read with P2 and 10 days between P2 and P3). During this time, the rater performed manual cortical lesion segmenta-

tion of scans from a completely different cohort of subjects to minimize recall of lesion locations and morphology before commencing the next rating protocol.

All scans were read in random order to minimize any recall effect. CL subtype classification (intracortical, leukocortical, and so forth) was not performed to avoid ambiguity. Only CLs that affected the neocortical gray matter were considered. No segmentation of lesions in the cerebellum or subcortical gray matter was performed.

Once all the CL segmentations were completed, the intersection of the labels generated by using P1 and P2 was computed to calculate the percentage of lesions that were detected by both P1 and P2. The same operation was performed by using the labels from P1 and P3, and then from P2 and P3. These comparisons were performed to determine the percentage of lesions detected in common across the 3 rating protocols.

Statistical Analysis

We quantitatively compared the results from each protocol by using 3 approaches:

1) Intraclass correlation coefficients (ICCs) were calculated between reading protocols (ie, P1 versus P2, P1 versus P3, and P2 versus P3). We used the ICC because it provides a general measurement of agreement between ≥ 2 raters or evaluation methods. In our case, we were comparing 3 evaluation methods: our 3 MR imaging reading protocols. Additionally, the ICC describes how strongly units in the same group resemble each other and operates on data structured as groups. Our 3 groups are the lesion count results of each reading protocol, and the units of the group are the counts obtained in each of 20 cases. We only used the 20 baseline scans for ICC and did not include the 8 repeat scans acquired at month 24. The value 1 represents perfect agreement; and zero, no agreement at all.

2) A nonparametric, Wilcoxon signed rank test for correlated samples was applied to test significant differences in lesion counts obtained between different segmentation protocols.

3) The pair-wise percentage agreement in lesion location between reading protocols was assessed on the basis of the spatial correspondence of the segmented labels for each lesion. To be considered the same lesion, the segmented regions had to have a minimum of 3 overlapping voxels. Note that here we were not assessing the degree of overlap of the lesion labels at the voxel level but the agreement in capturing the same lesions across the different protocols, independent of the extent or borders of each lesion.

RESULTS

Six hundred forty-three CLs were segmented by using protocol P1; 633, using P2; and 279 using P3 (On-line Table). The counts obtained by using P1 and P2 were not significantly different ($P = .93$). The counts obtained by using P3 were significantly smaller than those obtained by using either P1 ($P < .001$) or P2 ($P < .001$). The intraclass correlation coefficient of P1 versus P2 was 0.989, the ICC of P1 versus P3 was 0.615, and the ICC of P2 versus P3 was 0.588.

The percentage agreement among the labels (Fig 1) generated by using each reading protocol demonstrates that CLs segmented by using P1 (75%) are largely the same as those segmented by

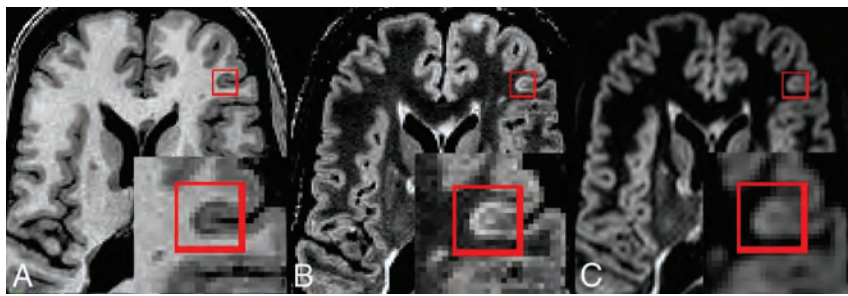


FIG 2. Cortical lesions not apparent on DIR: T1-weighted (A), FLAIR (B), and DIR (C). CLs affecting the cortex are marked with a red square and zoomed. Note the clear hypointense signal on the T1-weighted image and the clear hyperintense signal on FLAIR images. The lesion is less evident on DIR because it is only slightly hyperintense compared with surrounding cortex, possibly due to greater partial volume effects than in FLAIR.

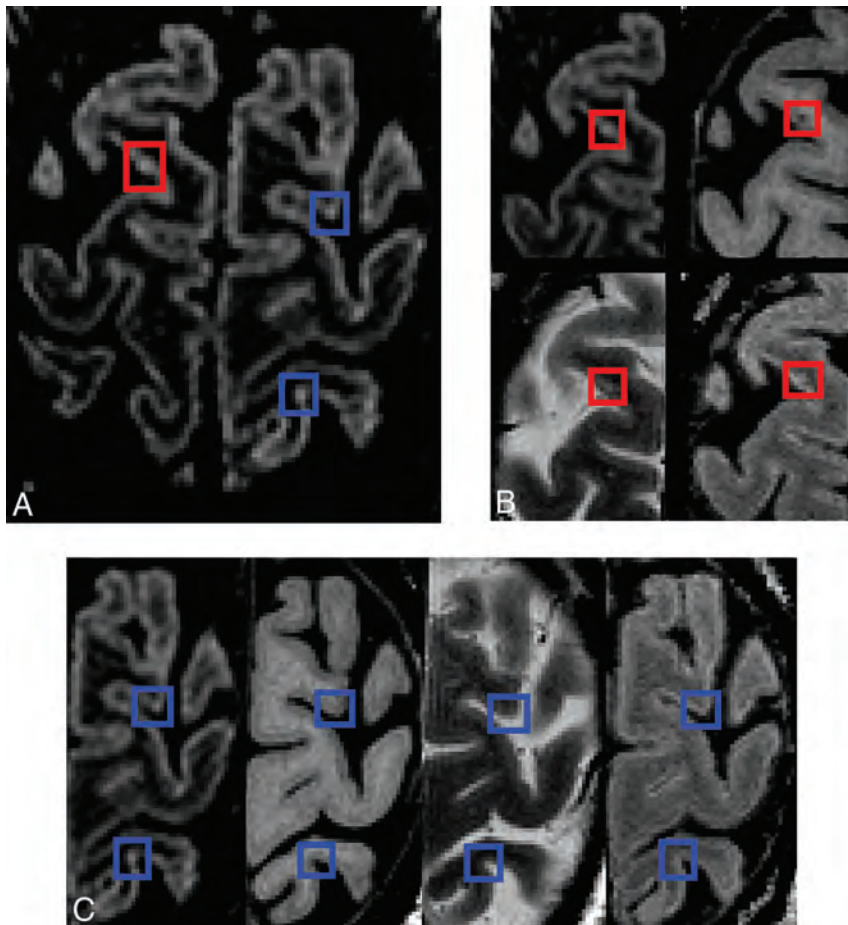


FIG 3. Cortical lesions visible in all sequences with demonstration of confounding artifacts (high-signal noise or potential vascular artifacts). A, DIR. B, Magnified view of DIR, T1-weighted, T2-weighted, and FLAIR: The true cortical lesion visible on all contrasts is in red boxes. C, Magnified view of DIR, T1-weighted, T2-weighted, and FLAIR: Blue boxes show hyperintense voxels visible on DIR only. Because there are no corresponding intensity changes on the other contrasts, these artifacts are clearly identifiable.

using P2 (76%). Most lesions segmented with P3 (76.4%) were also segmented in the first 2 reading protocols. This feature suggests that the lower total lesion counts obtained by using P3 may be due to a higher number of false-negatives obtained when reading DIR images alone.

When assessing the discrepancies in lesion segmentation across protocols, we can make several general observations:

- Discrepancies in the lesions segmented as true-positives by using P1 and P2 arose in cases in which the involvement of the cortex was unclear. Specific examples are as follows: 1) lesions considered leukocortical on one contrast and juxtacortical on a different one; 2) areas that appeared hypointense on T1WI but very slightly hyperintense in either FLAIR, DIR, and/or T2WI (Fig 2); and 3) areas that had the expected intensity characteristics of a CL but were found in regions in which there were clear, colocalized, CSF flow artifacts.
- Lesions detected by using P3, but not in P1 or P2, were most frequently a result of: 1) labeling purely juxtacortical lesions with no cortical involvement as cortical lesions and 2) voxels with high signal only on DIR without evidence of lesions in all the other modalities (Fig 3), which could be explained by intrinsic noise of the technique or vascular artifacts.
- Lesions not identified by using P3 were related to the following: 1) considering a hyperintense area as vascular artifacts when, in fact, the area was a lesion (Fig 3)^{11,13,18}; 2) leukocortical lesions that were incorrectly identified as being juxtacortical; 3) CLs in areas where the cortex appears to have higher signal on DIR (eg, the cingulate cortex, insular cortex), resulting in the CLs being more difficult to identify with confidence; 4) CLs that appeared almost isointense with adjacent normal-appearing cortex on DIR images but that appeared hyperintense on inspection of FLAIR and hypointense on T1-weighted images (Fig 2).

DISCUSSION

Using 3 MR imaging reading protocols, this work has demonstrated the advantage of a multicontrast approach to segmenting CLs. Careful side-by-side comparison of CLs on different MR imaging contrasts demonstrates how some areas

of the cortex may have lesions that are easily missed by using DIR alone. In particular, most of the areas of discrepancy were observed when CLs had partial involvement of both the cortex and the adjacent cerebral white matter. This problem has also been identified by other groups^{10,13,18,23,24} that demonstrated that different kinds of high-resolution T1-weighted images (MPRAGE, phase-sensitive inversion recovery) can aid in classifying a CL as

leukocortical (hence true-positive) or purely juxtacortical (hence false-positive).

Some CLs not identified by using P3 were related to a lack of clear hyperintense signal in CL voxels on DIR. The use of other contrasts to segment these cases is beneficial. For example in Fig 3, a more clearly visible CL, hyperintense on FLAIR and hypointense on T1, was identified, though DIR showed an ambiguous hyperintensity in relation to the surrounding cortex. Additionally, some areas not identified as CL by using P3 might be related to a tendency to be conservative when one uses DIR alone, treating focal small hyperintensities as possible vascular artifacts or cortical signal heterogeneity, hence not being segmented and counted as CLs.

In cortical lesion segmentation methods to date, most groups have used a single imaging contrast.^{10,11,16,17,19,25} A systematic comparison of the spatial correspondence of lesions obtained from different MR imaging contrasts has not been performed, to our knowledge. We have addressed this issue in 2 ways: 1) by using software that overlaps the masks created by using different segmentation protocols, and 2) by careful side-by-side comparison of the different image contrasts registered to the T1-weighted image space. These methods allowed us to assess areas that were consistently rated as CLs in all 3 protocols. They also provided more information about which areas were marked as lesions in one protocol but not in another.

Our results (On-line Table) suggest that DIR alone detects a lower number of lesions compared with protocols P1 and P2. However, if we considered the areas common to all 3 protocols, the rater consistently scored the same 75%–76% of lesions. When spatially overlapping the lesions labeled on P1 and P2, we see that 75% of lesions counted in P1 were also labeled as lesions in P2 and that 76% of the total lesions labeled in P2 were labeled as lesions in P1. Additionally, 76.4% of all lesions labeled by P3 colocalized with lesions obtained by both P1 and P2. This colocalization of 76.4% shows that P3 (DIR alone) does detect what is considered CL by using additional MR imaging contrasts, which implies good specificity, but with a lower frequency, which implies a lower sensitivity than the multiprotocol approaches. This is likely due to lower rater confidence in equivocal lesion candidates when observed on DIR alone.

In the absence of a formal mathematic calculation of sensitivity and specificity (due to the lack of histologic or 7T gold standard counts for these data), the overlapping of the areas assessed could be considered indirect evidence of the lower sensitivity of DIR when used independent of other contrasts. This consideration is important when deciding on sample sizes in any given study.

We acknowledge that our *in vivo* study does not have a true gold standard due to the absence of either brain tissue biopsy samples or concomitant ultra-high-field MR images. Our main aim was to compare the CL segmentation performed with DIR with 2 multimodal techniques. The segmentation performed by using all available MR imaging contrasts, including DIR, was taken as the reference. Our motivation to do this study was that the consensus recommendations for MS cortical lesion scoring suggest that the use of DIR alone is sufficient, while the addition of other MR imaging contrasts is merely helpful.¹¹ Our results showed that the multimodal protocols were significantly more

sensitive than the use of DIR by itself. The visual characteristics (intensity, shape, and location) of the additional lesions detected with the multimodal reading protocols were comparable with those of the lesions detected by using DIR alone. The main difference was that these additional lesions were nearly isointense with surrounding cortical gray matter and were therefore difficult to ascertain as lesions with confidence (due to cortical signal heterogeneity typical of DIR¹¹) without supporting information from other sequences.

The similarity of our results by using P1 and P2 suggests that within a multimodal MS protocol with sufficient resolution, 3D FLAIR appears to be as useful as DIR in the visual assessment of cortical lesions. Although a prior postmortem study showed the superior sensitivity of 3D DIR to 3D FLAIR at 3T when used alone, that study used a matched resolution for 3D DIR and 3D FLAIR.¹⁹ Scan times were not reported, but to achieve the same resolution with adequate SNR, the 3D DIR likely had a much longer scan time than the 3D FLAIR, which would limit the feasibility for an *in vivo* multicontrast protocol. In another study from the same group, but at 7T,¹⁷ the sensitivity of 3D FLAIR to cortical lesions was shown to be superior to that of 3D DIR. In addition to the effect of field strength, the authors concluded that the higher resolution of the 3D FLAIR contributed to its superior sensitivity. Because DIR is not available as a product sequence on many platforms, but only as a “works-in-progress” sequence available to academic sites with research agreements, the use of high-resolution (1-mm isotropic or better) 3D FLAIR and MPRAGE within a multimodal protocol could allow more centers to score cortical lesions routinely.

Our observation of an increased yield of cortical lesions by using a multicontrast reading protocol has clear relevance to MR imaging research studies looking at the relationship of cortical lesions to, for example, cognition or disease progression. In addition, the ability to detect cortical lesions on clinical scans may become increasingly important because future diagnostic criteria for MS are likely to include the presence of cortical lesions as a radiologic feature supportive of a diagnosis of MS.²⁶ As such, clinicians may want to consider including these isotropic acquisitions as part of their standard MS protocols. An accelerated 1-mm isotropic T1-weighted MPRAGE sequence could be acquired in about 5 minutes, while 3D FLAIR, though on the order of 7–8 minutes, can be reformatted in multiple planes at any desired thickness and thus could replace the standard set of sagittal and axial FLAIR images typically used to assess white matter lesions.

Future work should assess the prevalence of false-negative and false-positive counts obtained with combinations of different contrasts, with reference to either 7T MR imaging or histology. However, histologic examination of MS tissue samples is usually performed with cases of late-stage disease,^{2,4,5,20,27} which do not necessarily represent the *in vivo* characteristics of cortical MS tissue. An alternative approach would be to focus on the simultaneous use of 7T MR imaging and 3T multicontrast MR imaging for validation of proposed 3T MR imaging CL segmentation protocols.

CONCLUSIONS

A multicontrast approach to CL segmentation has been presented. The first 2 multicontrast reading protocols (P1 and P2)

detected a higher number of lesions compared with DIR alone (P3), providing preliminary evidence that the incorporation of multiple contrasts for CL segmentation facilitates CL detection at the clinically accessible field strength of 3T. Most important, P1 and P2 use MR imaging contrasts that are generally available on most scanners at clinical field strengths of 1.5T and 3T. Consequently, these reading protocols are amenable to use in large-scale clinical trials of MS disease-modifying therapies, where the availability of DIR may be limited.

Disclosures: Josefina Maranzano—*RELATED: Grant:* Canadian Institutes of Health Research (CIHR, MOP 84367)*; *UNRELATED: Employment:* I worked at NeuroRx Research between January 2005 and June 2014. David A. Rudko—*RELATED: Grant:* Canadian Institutes of Health Research*; *UNRELATED: Grants/Grants Pending:* Canadian Institutes of Health Research*; *UNRELATED: Consultancy:* Acorda, Biogen, Hoffman-La Roche, MedImmune, Mitsubishi, Novartis, Receptos, Sanofi-Aventis; *Grants/Grants Pending:* Biogen, Novartis; *Other:* equity interest in NeuroRx Research. Sridar Narayanan—*RELATED: Grant:* Canadian Institutes of Health Research; *Comments:* I was a coapplicant on the grant application by the Principal Investigator Douglas L. Arnold, who is also a coauthor of this article; *UNRELATED: Consultancy:* NeuroRx Research; *Payment for Lectures (including service on Speakers Bureaus):* Novartis Canada, *Comments:* educational lecture unrelated to any Novartis product. *Money paid to the institution.

REFERENCES

- Gray E, Thomas TL, Betmouni S, et al. **Elevated activity and microglial expression of myeloperoxidase in demyelinated cerebral cortex in multiple sclerosis.** *Brain Pathol* 2008;18:86–95 CrossRef Medline
- Wegner C, Esiri MM, Chance SA, et al. **Neocortical neuronal, synaptic, and glial loss in multiple sclerosis.** *Neurology* 2006;67:960–67 CrossRef Medline
- Bø L, Vedeler CA, Nyland H, et al. **Intracortical multiple sclerosis lesions are not associated with increased lymphocyte infiltration.** *Mult Scler* 2003;9:323–31 CrossRef Medline
- Peterson JW, Bö L, Mörk S, et al. **Transected neurites, apoptotic neurons, and reduced inflammation in cortical multiple sclerosis lesions.** *Ann Neurol* 2001;50:389–400 CrossRef Medline
- Kidd D, Barkhof F, McConnell R, et al. **Cortical lesions in multiple sclerosis.** *Brain* 1999;122(pt 1):17–26 CrossRef Medline
- Lucchinetti CF, Popescu BF, Bunyan RF, et al. **Inflammatory cortical demyelination in early multiple sclerosis.** *N Engl J Med* 2011;365:2188–97 CrossRef Medline
- Chard D. **Cortical lesion counts by double inversion recovery should be part of the MRI monitoring process for all MS patients: no.** *Mult Scler* 2014;20:539–40 CrossRef Medline
- Rovira A, Auger C. **Cortical lesion counts by double inversion recovery should be part of the MRI monitoring process for all MS patients: commentary.** *Mult Scler* 2014;20:541–42 CrossRef Medline
- Calabrese M, De Stefano N. **Cortical lesion counts by double inversion recovery should be part of the MRI monitoring process for all MS patients: yes.** *Mult Scler* 2014;20:537–38 CrossRef Medline
- Sethi V, Muhlert N, Ron M, et al. **MS cortical lesions on DIR: not quite what they seem?** *PLoS One* 2013;8:e78879 CrossRef Medline
- Geurts JJ, Roosendaal SD, Calabrese M, et al; MAGNIMS Study Group. **Consensus recommendations for MS cortical lesion scoring using double inversion recovery MRI.** *Neurology* 2011;76:418–24 CrossRef Medline
- Simon B, Schmidt S, Lukas C, et al. **Improved in vivo detection of cortical lesions in multiple sclerosis using double inversion recovery MR imaging at 3 Tesla.** *Eur Radiol* 2010;20:1675–83 CrossRef Medline
- Tallantyre EC, Morgan PS, Dixon JE, et al. **3 Tesla and 7 Tesla MRI of multiple sclerosis cortical lesions.** *J Magn Reson Imaging* 2010;32:971–77 CrossRef Medline
- Geurts JJ, Pouwels PJ, Uitdehaag BM, et al. **Intracortical lesions in multiple sclerosis: improved detection with 3D double inversion-recovery MR imaging.** *Radiology* 2005;236:254–60 CrossRef Medline
- Mistry N, Abdel-Fahim R, Mouglin O, et al. **Cortical lesion load correlates with diffuse injury of multiple sclerosis normal appearing white matter.** *Mult Scler* 2014;20:227–33 CrossRef Medline
- Papadopoulou A, Muller-Lenke N, Naegelin Y, et al. **Contribution of cortical and white matter lesions to cognitive impairment in multiple sclerosis.** *Mult Scler* 2013;19:1290–96 CrossRef Medline
- Kilsdonk ID, de Graaf WL, Soriano AL, et al. **Multicontrast MR imaging at 7T in multiple sclerosis: highest lesion detection in cortical gray matter with 3D-FLAIR.** *AJNR Am J Neuroradiol* 2013;34:791–96 CrossRef Medline
- Nielsen AS, Kinkel RP, Tinelli E, et al. **Focal cortical lesion detection in multiple sclerosis: 3 Tesla DIR versus 7 Tesla FLASH-T2.** *J Magn Reson Imaging* 2012;35:537–42 CrossRef Medline
- Seewann A, Kooi EJ, Roosendaal SD, et al. **Postmortem verification of MS cortical lesion detection with 3D DIR.** *Neurology* 2012;78:302–08 CrossRef Medline
- Geurts JJ, Bö L, Pouwels PJ, et al. **Cortical lesions in multiple sclerosis: combined postmortem MR imaging and histopathology.** *AJNR Am J Neuroradiol* 2005;26:572–77 Medline
- Bø L, Vedeler CA, Nyland HI, et al. **Subpial demyelination in the cerebral cortex of multiple sclerosis patients.** *J Neuropathol Exp Neurol* 2003;62:723–32 CrossRef Medline
- Sled JG, Zijdenbos AP, Evans AC. **A nonparametric method for automatic correction of intensity nonuniformity in MRI data.** *IEEE Trans Med Imaging* 1998;17:87–97 CrossRef Medline
- Moraal B, Roosendaal SD, Pouwels PJ, et al. **Multi-contrast, isotropic, single-slab 3D MR imaging in multiple sclerosis.** *Eur Radiol* 2008;18:2311–20 CrossRef Medline
- Nelson F, Poonawalla A, Hou P, et al. **3D MPRAGE improves classification of cortical lesions in multiple sclerosis.** *Mult Scler* 2008;14:1214–19 CrossRef Medline
- Calabrese M, Rocca MA, Atzori M, et al. **A 3-year magnetic resonance imaging study of cortical lesions in relapse-onset multiple sclerosis.** *Ann Neurol* 2010;67:376–83 CrossRef Medline
- Filippi M, Rocca MA, Calabrese M, et al. **Intracortical lesions: relevance for new MRI diagnostic criteria for multiple sclerosis.** *Neurology* 2010;75:1988–94 CrossRef Medline
- Gray E, Thomas TL, Betmouni S, et al. **Elevated myeloperoxidase activity in white matter in multiple sclerosis.** *Neurosci Lett* 2008;444:195–98 CrossRef Medline

Quantitative Susceptibility Mapping and R2* Measured Changes during White Matter Lesion Development in Multiple Sclerosis: Myelin Breakdown, Myelin Debris Degradation and Removal, and Iron Accumulation

Y. Zhang, S.A. Gauthier, A. Gupta, W. Chen, J. Comunale, G.C.-Y. Chiang, D. Zhou, G. Askin, W. Zhu, D. Pitt, and Y. Wang



ABSTRACT

BACKGROUND AND PURPOSE: Quantitative susceptibility mapping and R2* are sensitive to myelin and iron changes in multiple sclerosis lesions. This study was designed to characterize lesion changes on quantitative susceptibility mapping and R2* at various gadolinium-enhancement stages.

MATERIALS AND METHODS: This study included 64 patients with MS with different enhancing patterns in white matter lesions: nodular, shell-like, nonenhancing < 1 year old, and nonenhancing 1–3 years old. These represent acute, late acute, early chronic, and late chronic lesions, respectively. Susceptibility values measured on quantitative susceptibility mapping and R2* values were compared among the 4 lesion types. Their differences were assessed with a generalized estimating equation, controlling for Expanded Disability Status Scale score, age, and disease duration.

RESULTS: We analyzed 203 lesions: 80 were nodular-enhancing, of which 77 (96.2%) were isointense on quantitative susceptibility mapping; 33 were shell-enhancing, of which 30 (90.9%) were hyperintense on quantitative susceptibility mapping; and 49 were nonenhancing lesions < 1 year old and 41 were nonenhancing lesions 1–3 years old, all of which were hyperintense on quantitative susceptibility mapping. Their relative susceptibility/R2* values were 0.5 ± 4.4 parts per billion/ -5.6 ± 2.9 Hz, 10.2 ± 5.4 parts per billion/ -8.0 ± 2.6 Hz, 20.2 ± 7.8 parts per billion/ -3.1 ± 2.3 Hz, and 33.2 ± 8.2 parts per billion/ -2.0 ± 2.6 Hz, respectively, and were significantly different ($P < .005$).

CONCLUSIONS: Early active MS lesions with nodular enhancement show R2* decrease but no quantitative susceptibility mapping change, reflecting myelin breakdown; late active lesions with peripheral enhancement show R2* decrease and quantitative susceptibility mapping increase in the lesion center, reflecting further degradation and removal of myelin debris; and early or late chronic nonenhancing lesions show both quantitative susceptibility mapping and R2* increase, reflecting iron accumulation.

ABBREVIATIONS: Gd = gadolinium; GRE = gradient-echo; QSM = quantitative susceptibility mapping

The pathologic changes in active white matter MS lesions include inflammatory infiltration with immune cells, myelin breakdown and removal by microglia/macrophages, and iron accumulation in immune cells within the lesion and the lesion periphery.^{1,2}

MR imaging staging of white-matter MS lesions uses gadolinium (Gd) enhancement to differentiate between active (enhancing) and nonactive (nonenhancing) lesions. However, enhancement provides only a short window into inflammatory activity

Received October 5, 2015; accepted after revision February 18, 2016.

From the Department of Radiology (Y.Z., W.C., W.Z.), Tongji Hospital, Tongji Medical College, Huazhong University of Science and Technology, Wuhan, China; Departments of Radiology (Y.Z., A.G., J.C., G.C.-Y.C., D.Z., Y.W.), Neurology (S.A.G.), and Healthcare Policy and Research (G.A.), Weill Cornell Medical College, New York, New York; Department of Neurology (D.P.), School of Medicine, Yale University, New Haven, Connecticut; and Department of Biomedical Engineering (Y.W.), Cornell University, Ithaca, New York.

Authors' contributions: Acquisition of data, analysis and interpretation of data, writing (Y.Z.); conception and design, acquisition of data, clinical study, manuscript revision (S.A.G.); acquisition of data, interpretation of image data, manuscript revision (A.G., W.C., J.C., G.C.-Y.C.); conception and design, manuscript revision (D.Z.); statistical analysis of data, statistical analysis writing (G.A.); conception and design, manuscript revision, study supervision (W.Z.); study conception, manuscript revision (D.P.); study conception and design, critical revision of manuscript, study supervision (Y.W.).

All authors had the "final approval of the version to be published" and "agreement to be accountable for all aspects of the work in ensuring that questions related to the accuracy or integrity of any part of the work are appropriately investigated and resolved."

This work was supported by grant NS090464 from the U.S. Department of Health and Human Services–National Institutes of Health–National Institute of Neurological Disorders and Stroke, grant EB134432 from the U.S. Department of Health and Human Services–National Institutes of Health–National Institute of Biomedical Imaging and Bioengineering, and grant 81401390 from the National Natural Science Foundation of China.

Please address correspondence to Yi Wang, PhD, Department of Radiology, Weill Cornell Medical College, 515 East 71st St, New York, NY 10021; e-mail: yiwang@med.cornell.edu

Indicates open access to non-subscribers at www.ajnr.org

<http://dx.doi.org/10.3174/ajnr.A4825>

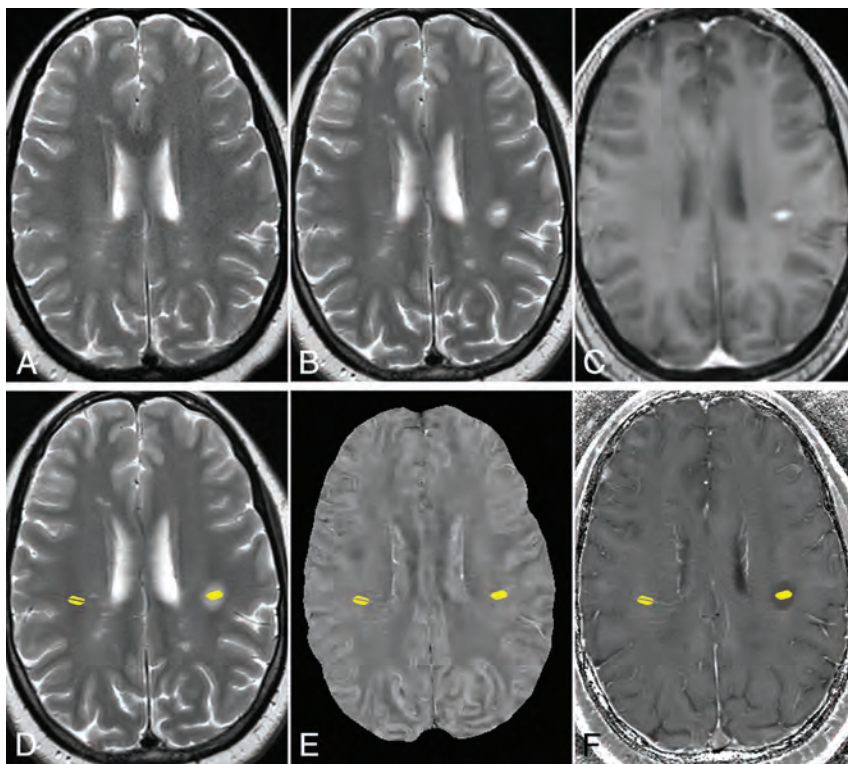


FIG 1. Example of ROIs of an MS lesion and reference at normal-appearing WM in a 44-year-old woman with MS. A, T2WI 8 months before the appearance of the enhancing lesion. B, T2WI, and C, T1WI + Gd image of 1 enhancing MS lesion. D, T2WI, E, QSM, and F, R2* images with ROIs of the enhancing lesion (*left side*) and the normal-appearing WM (*right side*). The vein inside the selected normal-appearing WM is excluded.

because it is preceded and outlasted by infiltration with immune cells. Enhancement on T1WI + Gd reflects BBB damage, whereas conventional MR imaging (T2WI and T1WI) sensitizing water mobility does not reflect specific microstructural and compositional changes in active lesions.³ In contrast, gradient-echo (GRE) imaging is sensitive to the magnetic fields induced by inhomogeneous myelin and highly paramagnetic iron, offering the potential to study microstructural and compositional changes in active MS lesions.^{4–11} GRE imaging data can be processed to generate quantitative susceptibility mapping (QSM)^{12,13} and R2* maps. QSM measures the underlying total magnetic susceptibility sources in a voxel.^{7,12} R2* reflects the sum of the T2 relaxation rate that depends on cellular content¹⁴ and the field dispersion associated with susceptibility microstructural heterogeneity multiplied by TE.^{6,12} Breakdown of intact myelin decreases R2* but does not change QSM signal, whereas degradation of diamagnetic myelin debris within macrophages and removal of degraded myelin increase susceptibility measured on QSM. Finally, iron accumulation increases both R2* and QSM.^{6,7,9,15,16} Therefore, by using both QSM and R2*, we would be able to differentiate between acute myelin breakdown, advanced myelin degradation and removal, and iron accumulation in MS lesions.

MATERIALS AND METHODS

Patients

The Weill Cornell Medical College institutional review board approved this MR imaging study of patients with MS from August 2011 to April 2015. The inclusion criteria were patients who 1)

had undergone, within 12 months, 2 successive MRIs that included T2WI, and pre- and post-Gd T1WI, with the second MR imaging including a multiecho GRE imaging; and 2) had new hyperintense white matter lesions on the second T2WI. A total of 65 patients met the inclusion criteria; 1 patient was excluded a posteriori because of motion artifacts on GRE images. The mean age of the 64 patients (13 men and 51 women) was 35.29 ± 8.12 years, with age ranging from 11–51 years. Patients were receiving the steroid Solu-Medrol intravenous injection (3 mg/day for 3 to 5 days). All their disease durations ranged from 0–17 years (6.0 ± 4.71 years) and the Expanded Disability Status Scale scores ranged from 0–6 (median, 1.5; interquartile range, 3).

Imaging Protocol and Reconstruction

MR imaging was performed on a 3T MR scanner (Signa HDxt; GE Healthcare, Milwaukee, Wisconsin) with an 8-channel head coil. The sequences for each patient were: 1) T2-weighted FSE (TR/TE = 5250/86 msec, flip angle = 90°, 3-mm-thick section at 0 intervals, 416×256 matrix, 24-cm FOV); 2) pre- and 3) post-Gd 3D inversion recovery-prepared T1-weighted fast echo-spoiled gradient-echo (TR/TE = 8.8/3.4 msec, flip angle = 15°, 256×256 matrix, 24-cm FOV, $0.45 \times 0.45 \times 1.2$ mm³ resolution); and 4) 3D T2*-weighted spoiled multiecho GRE sequence. Imaging parameters for the multiecho GRE sequence were as follows: TR = 57 msec; number of echoes = 11; first TE = 4.3 msec; TE spacing = 4.8 msec; flip angle = 20°; bandwidth = 244 kHz; FOV = 24 cm; thickness = 2 mm; acquisition matrix = 416×320 ; acquisition voxel size = $0.5 \times 0.5 \times 2$ mm³. The GRE sequence was performed before Gd injection, and the post-Gd T1WI was performed at 4 minutes after Gd injection.

QSM was reconstructed from the data acquired with the GRE sequence by using the morphology-enabled dipole inversion¹⁷ method, and R2* maps were generated by using a Gauss-Newton least-squares mono-exponential fit of the 11 echoes.¹⁸ QSM and R2* were reconstructed to a matrix of 512×512 , resulting in a voxel size of $0.47 \times 0.47 \times 2$ mm³. All images of 1 patient were registered to the QSM image by using the FMRIB Linear Image Registration Tool (FLIRT; <http://www.fmrib.ox.ac.uk/>).¹⁹

Lesion Analysis

New white matter MS lesions were identified on the second MR imaging, which was performed at 0.77 ± 0.37 year after the first MR imaging. Three neuroradiologists (J.C., A.G., and G.C.-Y.C., with 18, 9, and 8 years of experience, respectively) independently

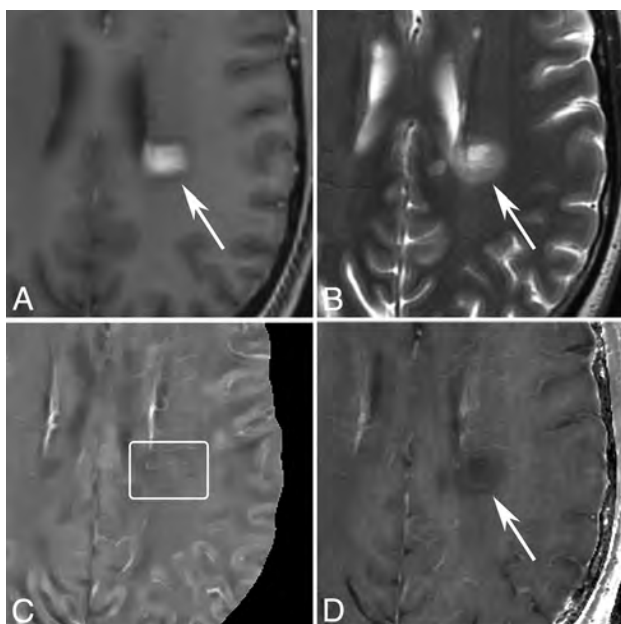


FIG 2. MR images of a nodular-enhancing lesion in a 43-year-old man with MS. A, T1WI + Gd. B, T2WI. C, QSM. D, R2*. A nodular-enhancing lesion (arrows) is found on the T1WI + Gd and appears QSM isointense (C, box).

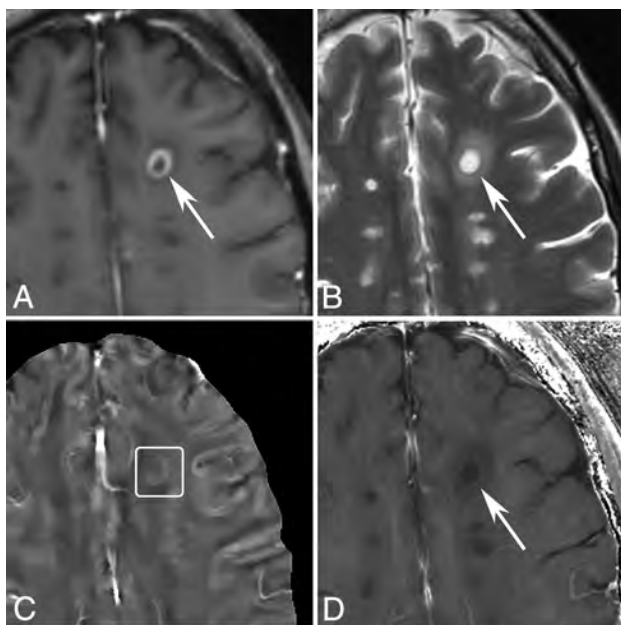


FIG 3. MR images of a shell-enhancing lesion in a 51-year-old man with MS. A, T1WI + Gd. B, T2WI. C, QSM. D, R2*. A shell-enhancing lesion (arrows) is found on the T1WI + Gd and appears slightly QSM hyperintense (C, box).

reviewed all images of the selected patients and classified new lesions into 3 groups based on enhancement on T1WI + Gd (nodular-enhancing [solid in 2D], shell-enhancing [ringlike in 2D],²⁰ and nonenhancing < 1 year old). By comparison to an MR imaging < 3 years old, lesions 1–3 years old (1.57 ± 0.46 years; error, 0.88 ± 0.34 years) from the same cohort were identified as a fourth group. The method of estimating lesion age referred to a previous study.⁷ All these lesions were independently assessed by the 3 neuroradiologists to be hyperintense or isointense on QSM

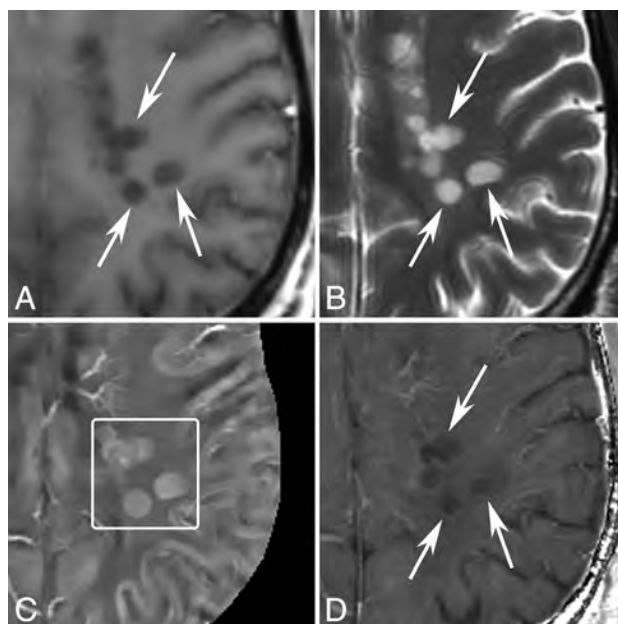


FIG 4. MR images of new T2 nonenhancing lesions (< 0.7 years old) in a 42-year-old man with MS. A, T1WI + Gd. B, T2WI. C, QSM. D, R2*. More than 3 new nonenhancing lesions (arrows) are found by comparing with the former MR imaging 0.7 years ago. All of them appear QSM hyperintense (C, box) and have hyperintense rims on R2*.

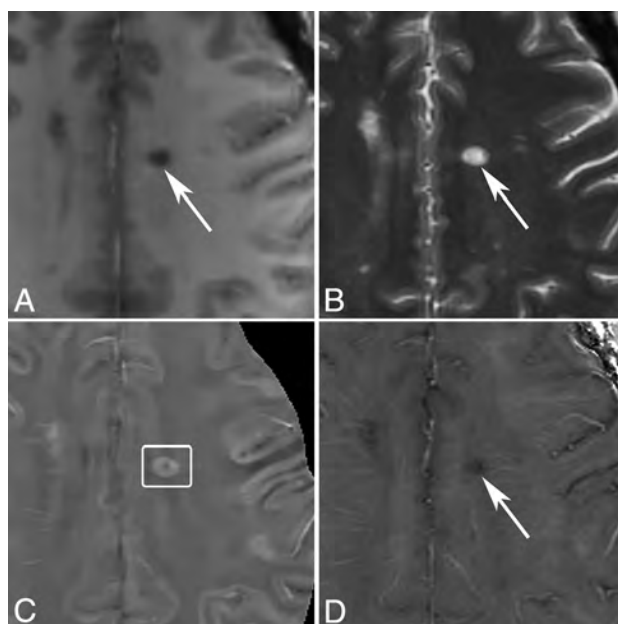


FIG 5. MR images of a nonenhancing lesion that is 1.2 years old in a 48-year-old woman with MS. A, T1WI + Gd. B, T2WI. C, QSM. D, R2*. One lesion appears hyperintense with a thick rim on QSM and hypointense on R2*.

images. These 3 readings were combined, with all differences resolved by majority votes.

ROIs of the lesions were placed on the lesion's hyperintense area on T2-weighted images, but the edema around was not included. If a lesion had a hypointense rim on T2WI, we also excluded this rim (example is shown on Fig 1). ROIs as normal-appearing white matter references were drawn on the contralateral mirror site of the lesions with similar shape and size.

One neuroradiologist (Y.Z., 4 years of experience) drew the ROIs on T2WI and then overlaid them on QSM and R2* maps by using in-house ROI semiautomatic software implemented for OsiriX (<http://www.osirix-viewer.com>). The veins and artifacts inside lesions on QSM and R2* were carefully removed by hand.

Statistical Analysis

The differences in relative susceptibilities and R2* values of lesions in the 4 groups were assessed by a generalized estimating equation. This model assumes a Gaussian distribution and an exchangeable correlation structure to account for the multiple

QSM and R2* measurements per patient. A multivariable model was used to assess the independent effect of enhancing patterns on QSM and R2*, controlling for Expanded Disability Status Scale score, age, and disease duration. Age, Expanded Disability Status Scale score, and disease duration were assessed for the presence of collinearity. All analyses were performed in SAS Version 9.4 (SAS Institute, Cary, North Carolina). $P < .05$ was considered statistically significant.

RESULTS

Lesion Pattern Characteristics

A total of 205 white matter lesions (115 enhancing and 90 nonenhancing) were examined in the 64 patients. Two enhancing lesions were excluded because they were too close to the cranium and did not appear intact on QSM. The 203 white matter lesions analyzed consisted of 80 (39.4%) new nodular-enhancing lesions, 33 (16.3%) shell-enhancing lesions, 49 (24.1%) new nonenhancing lesions < 1 year old, and 41 (20.2%) nonenhancing lesions 1–3 years old. Of the 80 new nodular-enhancing lesions, 77 (96.2%) appeared isointense on QSM and 3 (3.8%) lesions were hyperintense on QSM. Of the 33 new shell-enhancing lesions, 30 (90.9%) appeared hyperintense on QSM and 3 (9.1%) lesions were isointense on QSM. All nonenhancing lesions (49 [100%] with age < 1 year and 41 [100%] with age 1–3 years old) were hyperintense on QSM. Example images are shown in Figs 2–5.

Lesion Susceptibility and R2* Value Analyses

The reference areas on the contralateral site of 5 new lesions (3 nodular-enhancing, 1 shell-enhancing, and 1 nonenhancing) were covered by MS lesions, which prevented us from assessing reference values for susceptibilities and R2*. The relative susceptibilities and R2* values were measured and calculated in 198 lesions (77 nodular-enhancing, 32 shell-enhancing, 48 nonenhancing with age < 1 year, and 41 nonenhancing with age 1–3 years).

Quantitative susceptibilities and R2* values are plotted in Fig 6 and are summarized in Table 1. Nodular-enhancing lesions had relative susceptibilities near zero (0.5 ± 4.4 parts per billion), shell-enhancing lesions had increased relative susceptibilities (10.2 ± 5.4 parts per billion), nonenhancing lesions < 1 year old had higher relative susceptibilities (20.2 ± 7.8 parts per billion), and nonenhancing lesions 1–3 years old had the highest relative susceptibility (33.2 ± 8.2 parts per billion). In the generalized estimating equation model, after controlling for Expanded Disability Status Scale score, age, and disease duration, there were significant differences between each 2 types of lesions ($P < .0001$).

The nodular-enhancing, shell-enhancing, and new nonenhancing lesion types (< 1 year) had lower relative susceptibilities compared with the more stable lesions (1–3 years). These relationships were significant at all levels ($P < .0001$). R2* values relative to normal-appearing WM were -5.6 ± 2.9 Hz, -8.0 ± 2.6 Hz, -3.1 ± 2.3 Hz, and -2.0 ± 2.6 Hz of nodular-enhancing, shell-enhancing, nonenhancing < 1 year old, and nonenhancing 1–3 years old lesions, respectively. These relation-

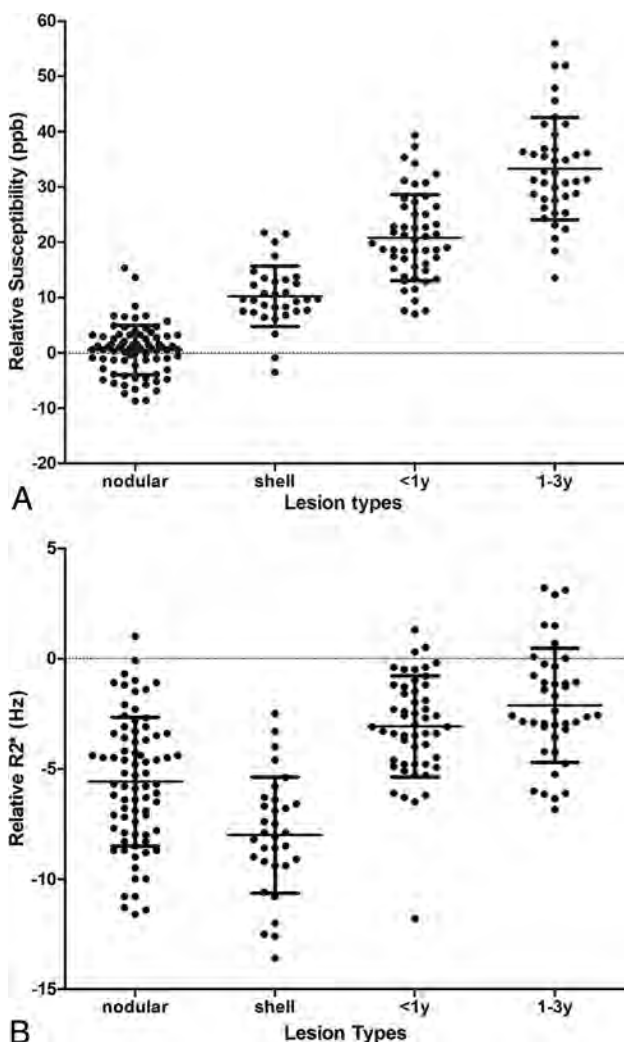


FIG 6. Scatterplot of susceptibility relative to normal-appearing WM measured on A, QSM and B, R2*. ppb indicates parts per billion.

Table 1: Quantitative susceptibility and R2* values for nodular-enhancing, shell-enhancing, nonenhancing < 1 year, and nonenhancing 1–3 years old lesions

	Nodular	Shell	Nonenhancing < 1 Year	Nonenhancing 1–3 Years
No. of lesions	77	32	48	41
No. of patients	32	21	27	20
Susceptibility relative to NAWM, ppb	0.5 ± 4.4	10.2 ± 5.4	20.2 ± 7.8	33.2 ± 8.2
R2* values relative to NAWM, Hz	-5.6 ± 2.9	-8.0 ± 2.6	-3.1 ± 2.3	-2.0 ± 2.6

Note:—NAWM indicates normal-appearing white matter; ppb, parts per billion.

Table 2: Statistical comparison of relative susceptibility from 4 groups of lesions^a

Comparison	Nodular	Shell	<1 year
Shell	−9.8621, (−11.7759, −7.9484), <i>P</i> < .0001	—	—
<1 year	−20.3123, (−23.0288, −17.5959), <i>P</i> < .0001	−10.4502, (−13.6101, −7.2903), <i>P</i> < .0001	—
1–3 years	−32.6287, (−35.9416, −29.3159), <i>P</i> < .0001	−22.7666, (−26.2751, −19.2581), <i>P</i> < .0001	−12.3164, (−16.3345, −8.2983), <i>P</i> < .0001

^a Data given as relative parameter estimates (β), (95% confidence limits), *P* value. Parameter estimates, 95% CI, and SE from multivariable generalized estimating equation, controlling for age, Expanded Disability Status Scale score, and disease duration. β estimates were obtained by setting the reference category to different lesion group.

Table 3: Statistical comparison of relative R2* from 4 groups of lesions^a

Comparison	Nodular	Shell	<1 year
Shell	2.3409, (1.4980, 3.1837), <i>P</i> < .0001	—	—
<1 year	−2.4309, (−3.1174, −1.7443), <i>P</i> < .0001	−4.7717, (−5.7643, −3.7792), <i>P</i> < .0001	—
1–3 years	−3.6385, (−4.6191, −2.6578), <i>P</i> < .0001	−5.9793, (−7.0956, −4.863), <i>P</i> < .0001	−1.2076, (−2.0439, −0.3712), <i>P</i> = .0047

^a Data given as relative parameter estimates (β), (95% confidence limits), *P* value. Parameter estimates, 95% CI, and SE from multivariable generalized estimating equation, controlling for age, Expanded Disability Status Scale, and disease duration. β estimates were obtained by setting the reference category to different lesion group.

ships were maintained in the generalized estimating equation model after controlling for the relevant clinical characteristics of age, Expanded Disability Status Scale score, and disease duration. Lesion types of nodular-enhancing, shell-enhancing, and new nonenhancing lesions < 1 year old were associated with lower R2* values compared with stable lesions (1–3 years), with shell-enhancing lesions having the largest relative decrease. All associations were significant at the *P* < .01 level. The results of statistical analysis are shown in Tables 2 and 3.

DISCUSSION

Our results demonstrate the following QSM and R2* patterns for MS lesions: nodular-enhancing lesions on T1WI + Gd that are isointense on QSM and hypointense on R2*; susceptibility increases and R2* decreases as lesions develop from nodular- to ring-enhancing; and increase in susceptibility and R2* in lesions that become nonenhancing. According to the imaging physics¹² and the known pathophysiology of MS white matter lesions,² these observed QSM and R2* patterns can be interpreted as sequential pathologic changes in myelin and iron content² that occur during the early stages of lesion development. Our results suggest that GRE data provide valuable information about MS lesion pathology beyond conventional MR imaging sequences.

We used T1WI + Gd to characterize the temporal sequence of MS lesions, which is important for pathologic interpretation of QSM and R2* patterns. A new MS lesion initially presents as nodular-enhancing on T1WI + Gd. This early stage of active lesion development is characterized by breakdown of the BBB,²¹ manifesting as enhancement throughout the lesion on T1WI + Gd,²⁰ and myelin damage and uptake by macrophages. The myelin breaking down into debris leads to reduced microstructural heterogeneity, manifesting as R2* hypointensity. At this point, iron does not accumulate in microglia and macrophages, making lesions isointense on QSM. Edema that is present in acute lesions as detected on T2WI may dilute susceptibility contents, decreasing both R2* and QSM. However, our data of QSM isointensity suggest that edema only marginally affects QSM.

As the BBB is reconstituted starting in the center of the lesion, within a timeframe of 1 week to several months (average 3 weeks),^{22,23} the enhancement pattern changes from nodular- to shell-enhancing on T1WI + Gd.^{20,23,24} Myelin debris in the lesion's center is also being further degraded within macrophages, some of which are moving out of the lesion into the peripheral circulation^{2,25,26} (see myelin content difference between the 2 le-

sions in Fig 1 in Mehta et al²⁷). This further reduces microstructural heterogeneity and manifests as reduction in R2*. Moreover, loss of diamagnetic lipids increases susceptibility as measured on QSM. Therefore, R2* decrease and QSM increase reflect degradation and removal of myelin debris.

As MS lesions mature into chronic lesions with a closed BBB, iron accumulates predominantly in microglia at the lesion rim, which has been suggested to promote proinflammatory polarization in these cells.^{27,28} In contrast to demyelination that causes QSM increase and R2* decrease, iron accumulation increases both QSM and R2*. Therefore, simultaneous increase in both QSM and R2* when lesions change from enhancing to nonenhancing may be interpreted as iron accumulation in lesions. There may be slow removal of residual lip degradation products at the same time, but that would only marginally increase QSM and decrease R2*.

It should be noted that BBB recovers at different rates,^{21,29} which may explain the few outliers that we observed. The QSM hyperintensity in 3 nodular-enhancing lesions may be caused by delayed repair of the BBB or accelerated degradation of myelin. Likewise, the 3 shell-enhancing lesions that are QSM isointense may exhibit fast repair of BBB leakage that leaves no time for susceptibility contents (ie, myelin lipids) to change. Compared with nodular-enhancing lesions, shell-enhancing lesions were captured less frequently in this study and may have more complex structures caused by dynamic pathology.³⁰

MS lesion appearances on QSM and R2* captured at one time point have been reported as heterogeneous or diverse.³¹ This diversity in susceptibility and R2* values may be caused by the capture of lesions in different stages of development. The dynamic susceptibility change in MS lesion, suggested first by phase imaging⁸ and cross-section QSM,⁷ has recently been confirmed in a longitudinal QSM study.³² Our study provides further evidence of dynamic changes in lesion susceptibility and R2*. Here, we attempt to explore the relationship between lesion susceptibility and R2* signal with the underlying pathophysiologic changes that occur over time in MS lesions.² This provides a biophysically meaningful way to understand lesion diversity, which may be translated into improved patient management.

For example, the data in Fig 6 suggest that 1) T2WI lesions with relative susceptibility value near zero may be nodular-enhancing, opening another venue for the current exploration of identifying enhancing lesions without Gd injection^{33–35} and 2) simultaneous QSM and R2* increases indicate iron accumulation

in MS lesions, offering an in vivo tool to study iron-related inflammation behind a sealed BBB that cannot be demonstrated with conventional imaging.

There were several limitations in our study. First, this study was not based on longitudinal evaluation of MS lesions but on cross-sectional data. Second, the number of shell-enhancing lesions was low compared with the other types of lesions. Thus, our cross-sectional results warrant future longitudinal studies that may address both limitations.

CONCLUSIONS

Early lesions that are nodular-enhancing on T1WI + Gd show decrease in R2* but no change in QSM, reflecting early breakdown of myelin. As lesions evolve toward shell-enhancing, susceptibility increases and R2* further decreases with progressive degradation and removal of myelin debris. Finally, as lesions become chronic, iron accumulation is demonstrated as both QSM and R2* increase. Thus, combining QSM and R2* can help identify changes in myelin and iron contents as white matter MS lesions develop.

Disclosures: Susan Gauthier—UNRELATED: Consultancy: Genzyme, Biogen, Comments: Participated in advisory board meeting; Grants/Grants Pending: Genzyme, Biogen, Novartis, Questcor, EMD Serono. Weiwei Chen—RELATED: Grant: National Natural Science Foundation of China (81401390). * Yi Wang—RELATED: Grant: National Institutes of Health (R01EB013443, R01NS090464)*; UNRELATED: Grants/Grants Pending: National Institutes of Health*; Patents (planned, pending or issued): Cornell University.* Comments: One of the inventors named on QSM patent; OTHER RELATIONSHIPS: Ownership in Medimagetric LLC, which is working with Cornell University on QSM commercialization. David Pitt—UNRELATED: Consultancy: Biogen Idec; Grants/Grants Pending: Biogen Idec, Novartis; Payment for Lectures (including service on speakers bureaus): Biogen Idec. *Money paid to the institution.

REFERENCES

1. Lassmann H. **Review: the architecture of inflammatory demyelinating lesions: implications for studies on pathogenesis.** *Neuropathol Appl Neurobiol* 2011;37:698–710 CrossRef Medline
2. Kutzelnigg A, Lassmann H. **Pathology of multiple sclerosis and related inflammatory demyelinating diseases.** *Handb Clin Neurol* 2014;122:15–58 CrossRef Medline
3. Filippi M, Rocca MA, Barkhof F, et al. **Association between pathological and MRI findings in multiple sclerosis.** *Lancet Neurol* 2012;11:349–60 CrossRef Medline
4. Haacke EM, Makki M, Ge Y, et al. **Characterizing iron deposition in multiple sclerosis lesions using susceptibility weighted imaging.** *J Magn Reson Imaging* 2009;29:537–44 CrossRef Medline
5. Hagemeier J, Heininen-Brown M, Poloni GU, et al. **Iron deposition in multiple sclerosis lesions measured by susceptibility-weighted imaging filtered phase: a case control study.** *J Magn Reson Imaging* 2012;36:73–83 CrossRef Medline
6. Paling D, Tozer D, Wheeler-Kingshott C, et al. **Reduced R2' in multiple sclerosis normal appearing white matter and lesions may reflect decreased myelin and iron content.** *J Neurol Neurosurg Psychiatry* 2012;83:785–92 CrossRef Medline
7. Chen W, Gauthier SA, Gupta A, et al. **Quantitative susceptibility mapping of multiple sclerosis lesions at various ages.** *Radiology* 2014;271:183–92 CrossRef Medline
8. Wiggermann V, Hernández Torres E, Vavasour IM, et al. **Magnetic resonance frequency shifts during acute MS lesion formation.** *Neurology* 2013;81:211–18 CrossRef Medline
9. Bagnato F, Hametner S, Yao B, et al. **Tracking iron in multiple sclerosis: a combined imaging and histopathological study at 7 Tesla.** *Brain* 2011;134:3602–15 CrossRef Medline
10. Hammond KE, Metcalf M, Carvajal L, et al. **Quantitative in vivo**

- magnetic resonance imaging of multiple sclerosis at 7 Tesla with sensitivity to iron.** *Ann Neurol* 2008;64:707–13 CrossRef Medline
11. Ropele S, de Graaf W, Khalil M, et al. **MRI assessment of iron deposition in multiple sclerosis.** *J Magn Reson Imaging* 2011;34:13–21 CrossRef Medline
12. Wang Y, Liu T. **Quantitative susceptibility mapping (QSM): decoding MRI data for a tissue magnetic biomarker.** *Magn Reson Med* 2015;73:82–101 CrossRef Medline
13. de Rochefort L, Liu T, Kressler B, et al. **Quantitative susceptibility map reconstruction from MR phase data using Bayesian regularization: validation and application to brain imaging.** *Magn Reson Med* 2010;63:194–206 CrossRef Medline
14. Wang Y. *Principles of Magnetic Resonance Imaging: Physics Concepts, Pulse Sequences & Biomedical Applications.* CreatSpace Independent Publishing Platform; 2012
15. Yablonskiy DA, Luo J, Sukstanskii AL, et al. **Biophysical mechanisms of MRI signal frequency contrast in multiple sclerosis.** *Proceedings of the National Academy of Sciences of the United States of America* 2012;109:14212–17 CrossRef Medline
16. Schweser F, Deistung A, Lehr BW, et al. **Quantitative imaging of intrinsic magnetic tissue properties using MRI signal phase: an approach to in vivo brain iron metabolism?** *Neuroimage* 2011;54:2789–807 CrossRef Medline
17. Liu J, Liu T, de Rochefort L, et al. **Morphology enabled dipole inversion for quantitative susceptibility mapping using structural consistency between the magnitude image and the susceptibility map.** *Neuroimage* 2012;59:2560–68 CrossRef Medline
18. Baudrexel S, Volz S, Preibisch C, et al. **Rapid single-scan T2*-mapping using exponential excitation pulses and image-based correction for linear background gradients.** *Magn Reson Med* 2009;62:263–68 CrossRef Medline
19. Jenkinson M, Bannister P, Brady M, et al. **Improved optimization for the robust and accurate linear registration and motion correction of brain images.** *Neuroimage* 2002;17:825–41 CrossRef Medline
20. Gaitan MI, Shea CD, Evangelou IE, et al. **Evolution of the blood-brain barrier in newly forming multiple sclerosis lesions.** *Ann Neurol* 2011;70:22–29 CrossRef Medline
21. Schoderboeck L, Adzemovic M, Nicolussi EM, et al. **The “window of susceptibility” for inflammation in the immature central nervous system is characterized by a leaky blood-brain barrier and the local expression of inflammatory chemokines.** *Neurobiol Dis* 2009;35:368–75 CrossRef Medline
22. He J, Grossman RI, Ge Y, et al. **Enhancing patterns in multiple sclerosis: evolution and persistence.** *AJNR Am J Neuroradiol* 2001;22:664–69 Medline
23. Cotton F, Weiner HL, Jolesz FA, et al. **MRI contrast uptake in new lesions in relapsing-remitting MS followed at weekly intervals.** *Neurology* 2003;60:640–46 CrossRef Medline
24. Guttmann CR, Ahn SS, Hsu L, et al. **The evolution of multiple sclerosis lesions on serial MR.** *AJNR Am J Neuroradiol* 1995;16:1481–91 Medline
25. Lee SC, Moore GR, Golenwsky G, et al. **Multiple sclerosis: a role for astroglia in active demyelination suggested by class II MHC expression and ultrastructural study.** *J Neuropathol Exp Neurol* 1990;49:122–36 CrossRef Medline
26. Bruck W, Porada P, Poser S, et al. **Monocyte/macrophage differentiation in early multiple sclerosis lesions.** *Ann Neurol* 1995;38:788–96 CrossRef Medline
27. Mehta V, Pei W, Yang G, et al. **Iron is a sensitive biomarker for inflammation in multiple sclerosis lesions.** *PLoS One* 2013;8:e57573 CrossRef Medline
28. Hametner S, Wimmer I, Haider L, et al. **Iron and neurodegeneration in the multiple sclerosis brain.** *Ann Neurol* 2013;74:848–61 CrossRef Medline
29. Lassmann H. **A dynamic view of the blood-brain barrier in active multiple sclerosis lesions.** *Ann Neurol* 2011;70:1–2 CrossRef Medline
30. Henderson AP, Barnett MH, Parratt JD, et al. **Multiple sclerosis:**

- distribution of inflammatory cells in newly forming lesions. *Ann Neurol* 2009;66:739–53 CrossRef Medline
31. Li X, Harrison DM, Liu H, et al. **Magnetic susceptibility contrast variations in multiple sclerosis lesions.** *J Magn Reson Imaging* 2016; 43:463–73 CrossRef Medline
 32. Zhang Y, Gauthier SA, Gupta A, et al. **Longitudinal change in magnetic susceptibility of new enhanced multiple sclerosis (MS) lesions measured on serial quantitative susceptibility mapping (QSM).** *J Magn Reson Imaging* 2016 Jan 22. [Epub ahead of print] CrossRef Medline
 33. Shinohara RT, Goldsmith J, Mateen FJ, et al. **Predicting breakdown of the blood-brain barrier in multiple sclerosis without contrast agents.** *AJNR Am J Neuroradiol* 2012;33:1586–90 CrossRef Medline
 34. Treabă CA, Bălașa R, Podeanu DM, et al. **Cerebral lesions of multiple sclerosis: is gadolinium always irreplaceable in assessing lesion activity?** *Diagn Interv Radiol* 2014;20:178–84 CrossRef Medline
 35. Blystad I, Håkansson I, Tisell A, et al. **Quantitative MRI for analysis of active multiple sclerosis lesions without gadolinium-based contrast agent.** *AJNR Am J Neuroradiol* 2016;37:94–100 CrossRef Medline

Relationship between *APOE* Genotype and Structural MRI Measures throughout Adulthood in the Study of Health in Pomerania Population-Based Cohort

M. Habes, J.B. Toledo, S.M. Resnick, J. Doshi, S. Van der Auwera, G. Erus, D. Janowitz, K. Hegenscheid, G. Homuth, H. Völzke, W. Hoffmann, H.J. Grabe, and C. Davatzikos



ABSTRACT

BACKGROUND AND PURPOSE: The presence of the *apolipoprotein E* $\epsilon 4$ allele is the strongest sporadic Alzheimer disease genetic risk factor. We hypothesized that *apolipoprotein E* $\epsilon 4$ carriers and noncarriers may already differ in imaging patterns in midlife. We therefore sought to identify the effect of *apolipoprotein E* genotype on brain atrophy across almost the entire adult age span by using advanced MR imaging–based pattern analysis.

MATERIALS AND METHODS: We analyzed MR imaging scans of 1472 participants from the Study of Health in Pomerania (22–90 years of age). We studied the association among age, *apolipoprotein E* $\epsilon 4$ carrier status, and brain atrophy, which was quantified by using 2 MR imaging–based indices: Spatial Pattern of Atrophy for Recognition of Brain Aging (summarizing age-related brain atrophy) and Spatial Pattern of Abnormality for Recognition of Early Alzheimer Disease (summarizing Alzheimer disease–like brain atrophy patterns), as well as the gray matter volumes in several Alzheimer disease– and *apolipoprotein E*–related ROIs (lateral frontal, lateral temporal, medial frontal, and hippocampus).

RESULTS: No significant association was found between *apolipoprotein E* $\epsilon 4$ carrier status and the studied ROIs or the MR imaging–based indices in linear regression models adjusted for age, sex, and education, including an interaction term between *apolipoprotein E* and age.

CONCLUSIONS: Our study indicates that measurable *apolipoprotein E*–related brain atrophy does not occur in early adulthood and midlife and suggests that such atrophy may only occur more proximal to the onset of clinical symptoms of dementia.

ABBREVIATIONS: AD = Alzheimer disease; *APOE* = *apolipoprotein E*; MCI = mild cognitive impairment; SHIP = Study of Health in Pomerania; SNP = single nucleotide polymorphism; SPARE-AD = Spatial Pattern of Abnormality for Recognition of Early Alzheimer Disease; SPARE-BA = Spatial Pattern of Atrophy for Recognition of Brain Aging

The presence of the *apolipoprotein E* gene (*APOE*) $\epsilon 4$ allele is the strongest genetic sporadic Alzheimer disease (AD) risk factor.^{1,2} The *APOE* gene has 2 additional codominant alleles (*APOE* $\epsilon 2$ and $\epsilon 3$). These alleles code for the 3 corresponding

apolipoprotein isoforms (ApoE $\epsilon 2$, $\epsilon 3$, and $\epsilon 4$). Compared with individuals with the $\epsilon 3$ allele,² which is the most common in the general population, those with the *APOE* $\epsilon 4$ allele have a higher risk of AD, whereas the *APOE* $\epsilon 2$ allele is associated with a lower risk of AD. The *APOE* genotype modifies the age at which cognitively healthy subjects present biomarker changes that define AD preclinical stages.^{3,4} There are several mechanisms that have been

Received October 6, 2015; accepted after revision March 4, 2016.

From the Institute for Community Medicine (M.H., H.V., W.H.), Department of Psychiatry (M.H., S.V.d.A., D.J., H.J.G.), Department of Radiology (K.H.), and Institute for Genetics and Functional Genomics (G.H.), University of Greifswald, Greifswald, Germany; Center for Biomedical Image Computing and Analytics (M.H., J.D., G.E., C.D.), University of Pennsylvania, Philadelphia, Pennsylvania; Department of Pathology and Laboratory Medicine (J.B.T.), Institute on Aging, Center for Neurodegenerative Disease Research, University of Pennsylvania Perelman School of Medicine, Philadelphia, Pennsylvania; Laboratory of Behavioral Neuroscience (S.M.R.), National Institute on Aging, Bethesda, Maryland; and German Center for Neurodegenerative Diseases (W.H., H.J.G.), Rostock/Greifswald, Germany.

M. Habes and J.B. Toledo contributed equally to this work. C. Davatzikos and H.J. Grabe contributed equally to this work.

The corresponding authors (M.H. and J.B.T.) confirm that each author has contributed to all of the following: drafting the article or revising it critically for important intellectual content, final approval of the version to be published, and agreement to be accountable for all aspects of the work in ensuring that questions related to the accuracy or integrity of any part of the work are appropriately investigated and resolved. In addition, each author's contribution was the following: M.H., J.B.T.: conception and design, acquisition of data, analysis and interpretation

of data; S.M.R.: analysis and interpretation of data; J.D.: analysis and interpretation of data; S.V.d.A.: acquisition of data; G.E.: analysis and interpretation of data; D.J.: acquisition of data; K.H.: acquisition of data; G.H.: acquisition of data; H.V.: acquisition of data, analysis and interpretation of data; W.H.: acquisition of data, analysis and interpretation of data; and H.J.G. and C.D.: conception and design, acquisition of data, and analysis and interpretation of data.

Please address correspondence to Mohamad Habes, PhD, Center for Biomedical Image Computing and Analytics, University of Pennsylvania, 3700 Hamilton Walk, Philadelphia, PA 19104; e-mail: habesm@uphs.upenn.edu; Jon B. Toledo, MD, Department of Pathology and Laboratory Medicine, Institute on Aging, Center for Neurodegenerative Disease Research, University of Pennsylvania Perelman School of Medicine, Philadelphia, Third Floor Maloney Building, 3600 Spruce St, Philadelphia, PA 19104; e-mail: jtoledo@mail.med.upenn.edu

Indicates article with supplemental on-line appendix and tables.

Indicates article with supplemental on-line photos.

<http://dx.doi.org/10.3174/ajnr.A4805>

Table 1: Description of the SHIP sample included in this study (n = 1472)

Characteristic	SHIP-2	SHIP-TREND	SHIP-2 and SHIP-TREND (Analysis Sample)
Age (median) (SD) (yr)	56.3 (12.2)	51.1 (13.4) ^a	53.3 (13.0)
Education (No.) (%)			
<8 yr	137 (18.4)	77 (10.6) ^a	214 (14.5)
8–10 yr	430 (57.8)	415 (57.0) ^a	845 (57.4)
>10 yr	177 (23.8)	236 (32.4) ^a	413 (28.1)
APOE genotype: at least 1 $\epsilon 4$ allele (No.) (%) positive	145 (19.5)	177 (24.3) ^a	322 (21.9)
Female sex (No.) (%)	399 (53.6)	421 (57.8)	820 (55.7)
Verbal Learning and Memory Test (mean) (SD)	8.6 (3.0)		
Nuremberg Age Inventory (mean) (SD)		11.2 (2.5)	

^aSignificant difference at $P < .05$.

associated with the influence of *APOE* $\epsilon 4$ on AD risk: decreased clearance of amyloid from the brain, impaired synaptic plasticity, altered blood-brain barrier permeability, and immune response and impaired membrane repair following neuronal injury.^{5–7} In line with these results, neuropathologic studies have shown that plaques and tangles mediate *APOE*-related clinical changes.⁸ ApoE is present in plasma and CSF, but there is a weak correlation between ApoE concentrations within these 2 compartments.^{9,10} In *APOE* genotype-adjusted models, CSF, but not plasma, ApoE levels are associated with cognitive changes and brain atrophy.⁹ Nevertheless, a large longitudinal study reported associations with plasma ApoE levels that dropped to borderline significance when adjusted for the *APOE* genotype.¹¹

Most *APOE*-related findings regarding brain structure have been reported in elderly subjects. However, due to the long AD preclinical stage, it could be expected that subtle neuroimaging changes may appear at younger ages and become more pronounced with advancing age. In line with this hypothesis, there is limited information regarding associations related to brain structural changes and *APOE* genotypes in younger subjects. Previous studies have reported lower hippocampal, orbitofrontal, and entorhinal volumes in subjects with *APOE* $\epsilon 4$ in the first decades of life.^{12,13} Other studies have shown brain hypometabolism in AD-related areas¹⁴ and increased activation of the default mode network¹⁵ in young *APOE* $\epsilon 4$ carriers but no differences in gray matter volume. The aforementioned changes reported in these studies would be taking place during the 3 decades before the ages that show at least 1% AD prevalence. These findings suggest that AD could have a neurodevelopmental component. However, the relation between regional brain atrophy and the *APOE* genotype needs to be evaluated across the adult life span.

We hypothesized that *APOE* $\epsilon 4$ carriers and noncarriers could present different imaging patterns that start differing in midlife, much earlier than clinical diagnosis. To investigate this hypothesis, we sought to model structural MR imaging brain changes associated with the *APOE* genotype in a large population-based study spanning the third-to-ninth decades of life by using sensitive pattern-based aging and AD summary indices.

MATERIALS AND METHODS

Participants from the Study of Health in Pomerania

The Study of Health in Pomerania (SHIP) is a prospective cohort whose subjects are recruited from the general population of the

German State of Mecklenburg–Western Pomerania. It is led by the Institute for Community Medicine at the Medical Faculty of the University of Greifswald.¹⁶ SHIP started at baseline with SHIP-0 between 1997 and 2001. After about 5 years, all participants were re-invited for a follow-up visit (ie, SHIP-1). From 2008 to 2012, the second follow-up examination, SHIP-2, was performed. Concurrent with SHIP-2, a new population sample from the same area was drawn, and similar examinations were undertaken between 2008 and 2012 (SHIP-TREND). SHIP-2 and

SHIP-TREND included whole-body MR imaging scans,¹⁷ which were not present in SHIP-0 and SHIP-1. Trained certified radiologists, each with >5 years of MR imaging interpretation experience, visually inspected head MR imaging scans for artifacts and clinical findings. In our study, we included 1472 subjects of the total 3256 subjects with T1-weighted brain scans available in SHIP-2 and SHIP-TREND, 22–90 years of age at enrollment. We excluded 1784 subjects from this analysis on the basis of the following: 1) the presence of stroke, multiple sclerosis, epilepsy, cerebral tumor, intracranial cyst, or hydrocephalus ($n = 150$); 2) a high level of motion artifacts ($n = 98$); 3) failed quality control of the automatically skull-stripped data ($n = 121$); 4) lack of genomewide association study data ($n = 1008$); 5) an unidentifiable *APOE* genotyping ($n = 35$); and 6) lack of clinical data (cognitive scores, $n = 190$, or covariates, $n = 182$).

Clinical data, including sociodemographic factors and medical history, were collected in a standardized computer-assisted face-to-face interview. Years of education were recorded and grouped into 3 categories: <8 years, 8–10 years, and >10 years. In SHIP, two cognitive tests were obtained: the Verbal Learning and Memory Test (the German version of the California Verbal Learning and Memory Test¹⁸) for SHIP-2 and the Nuremberg Age Inventory for SHIP-TREND. The Nuremberg Age Inventory is a German test developed to measure the cognitive abilities during brain aging.¹⁹ It consists of subtests including, but not limited to, speed (eg, numbers) and memory (eg, words, numbers, and images). A description of the final SHIP sample included in our analysis ($n = 1472$) is shown in Table 1. The Ethics Committee of the Medical Faculty of the University of Greifswald approved SHIP.

Image Acquisition

In SHIP-2 and SHIP-TREND, a comprehensive whole-body MR imaging protocol was used. A full description of the image-acquisition parameters for SHIP can be found in Hegenscheid et al.¹⁷ The neurocranium unit of SHIP included, among others, T1-weighted and fluid-attenuated inversion recovery sequences. Briefly, all images were obtained by using a 1.5T MR imaging scanner (Magnetom Avanto; Siemens, Erlangen, Germany). In this study, we used only the T1-weighted axial MPRAGE images for measuring regional patterns of AD-related brain atrophy. The T1-weighted image was acquired with the following parameters:

1 × 1 mm in-plane spatial resolution, section thickness = 1.0 mm, flip angle = 15°, TE = 3.4 ms, TR = 1900 ms.

Image Processing

An automated multias segmentation method was applied on the T1-weighted image of each subject to calculate a brain mask, by removing extracranial material on the T1-weighted image.²⁰ Total intracranial volume was estimated by calculating the volume of a subject's brain mask, which included the volumes of gray matter, white matter, ventricles, and the CSF that were contained within the outer brain boundary. Each brain mask was visually inspected for quality, by M.H., and all low-quality brain masks (including either under- or oversegmented brain) were excluded.

A multias label fusion–based segmentation method²¹ was applied for segmentation of the brain into a set of anatomic ROIs. The volumes of ROIs were calculated and were normalized by total intracranial volume. In this analysis, we selected a set of gray matter ROIs on the basis of areas that were associated with AD-related atrophy and previously reported *APOE*-related findings. Further details are given in the On-line Appendix (On-line Method 1).

MR Imaging Pattern Classification

A pattern-classification method was previously proposed to derive Spatial Pattern of Abnormality for Recognition of Early AD (SPARE-AD),²² an index summarizing the high-dimensional imaging data with a single value that quantifies the atrophy patterns in AD-related regions. SPARE-AD has been shown to discriminate between normal cognition and mild cognitive impairment (MCI)²³ and conversion from MCI to AD.²⁴ We calculated, in this study, the SPARE-AD index for the SHIP population by using a model based on a linear support vector machine,²⁵ which was trained on the external training dataset described in Da et al²⁴ and had been validated earlier.²² More positive SPARE-AD implies a more Alzheimer disease–like brain structure, while more negative values reflect more normal brain structure.

Similar to the calculation of the SPARE-AD index, a linear support vector machine–based model was designed to predict an individual's age from the MR image and was used for quantifying Brain Aging (BA), summarized by the SPARE-BA index. The classification model was trained for optimally discriminating young and old subject groups and has been recently described.^{26,27} The SPARE-BA index for an individual implied fewer brain aging patterns for higher (positive) values and the presence of more aging-related atrophy patterns for lower (negative) values. While the SPARE-AD index captured more localized atrophy patterns in AD-related regions, such as in the hippocampus and temporal lobe, the SPARE-BA index captured more global aging patterns, distributed in the cortex, but particularly in the frontal lobe. Further details are given in the On-line Appendix (On-line Method 2).

APOE Determination in SHIP

The *APOE* genotypes were determined on the basis of rs429358(C;C) and rs7412(T;T) from the resulting imputation of the SHIP genotyping. More details can be found in the On-line Appendix (On-line Method 3).

Statistical Analysis

We studied the association between age, the *APOE* $\epsilon 4$ genotype, and AD-related gray matter volume (lateral frontal, lateral temporal, medial frontal, and hippocampus), as well as SPARE-AD and SPARE-BA, for the 1472 SHIP participants included in this study. In this study, subjects with at least 1 $\epsilon 4$ allele were considered to have the *APOE* $\epsilon 4$ genotype.

We applied linear regression models, which included total intracranial volume normalized ROI volumes as outcomes, and age square (if significant), age, *APOE* $\epsilon 4$ carrier status, and sex as predictors adjusting for education level and study cohort. We also investigated the significance of interaction terms between the *APOE* $\epsilon 4$ status and the variables: age², age, education, and sex, after adding those interaction terms one at a time to the regression models as predictors. Results were considered statistically significant if the 2-sided *P* value was <.05. No multiple comparison adjustment was applied because analyses were performed on a small number of predictors that were selected on the basis of previously published findings rather than determined on the basis of the data derived therein. To identify potentially cognitively impaired subjects on the basis of the residuals of linear regressions between age and the available cognitive scores, we labeled those subjects with a *z*-score of less than −1.5 SDs as possibly cognitively impaired (*n* = 98) (On-line Fig 1). Spearman rank correlation coefficients were used to assess correlations between variables. The Student *t* test was used to compare continuous variables, and the Pearson χ^2 test, to compare categorical variables. Analyses were performed by using the R statistical and computing software, Version 3.1 (<http://www.r-project.org/>).²⁸

RESULTS

Subjects Included in the Study

A total of 1472 participants, from which 744 belonged to SHIP-2 and 728 belonged to SHIP-TREND, with ages ranging from 22 to 90 years (median, 53.3 years), were included in the analyses. Cohorts did not differ in sex, but significant differences were present with respect to education level (*P* < .001), age (*P* < .0001), and the number of *APOE* $\epsilon 4$ carriers (*P* = .03). No differences were seen between subjects included in the study and those who were excluded based on the inclusion criteria described in the “Materials and Methods” section, except for sex (On-line Table 1).

Association between the MR Imaging–Based Indices and Age

The Spearman rank correlation coefficient was *r* = 0.36 between age and SPARE-AD, and *r* = −0.77 between age and SPARE-BA (*P* < .001). The Spearman rank correlation coefficient between SPARE-AD and SPARE-BA was *r* = −0.44 (*P* < .001).

Association between *APOE* and MR Imaging Findings

Figure 1 shows the relationship between the AD-related gray matter regions and age in *APOE* $\epsilon 4$ carrier and noncarrier individuals. Similarly, Fig 2 shows the relationship between the MR imaging–based indices and age. In the age- and sex-adjusted models that included the interaction term between *APOE* and age, no significant association was found between *APOE* $\epsilon 4$ carrier status and the studied MR imaging measurements in the regression models that in-

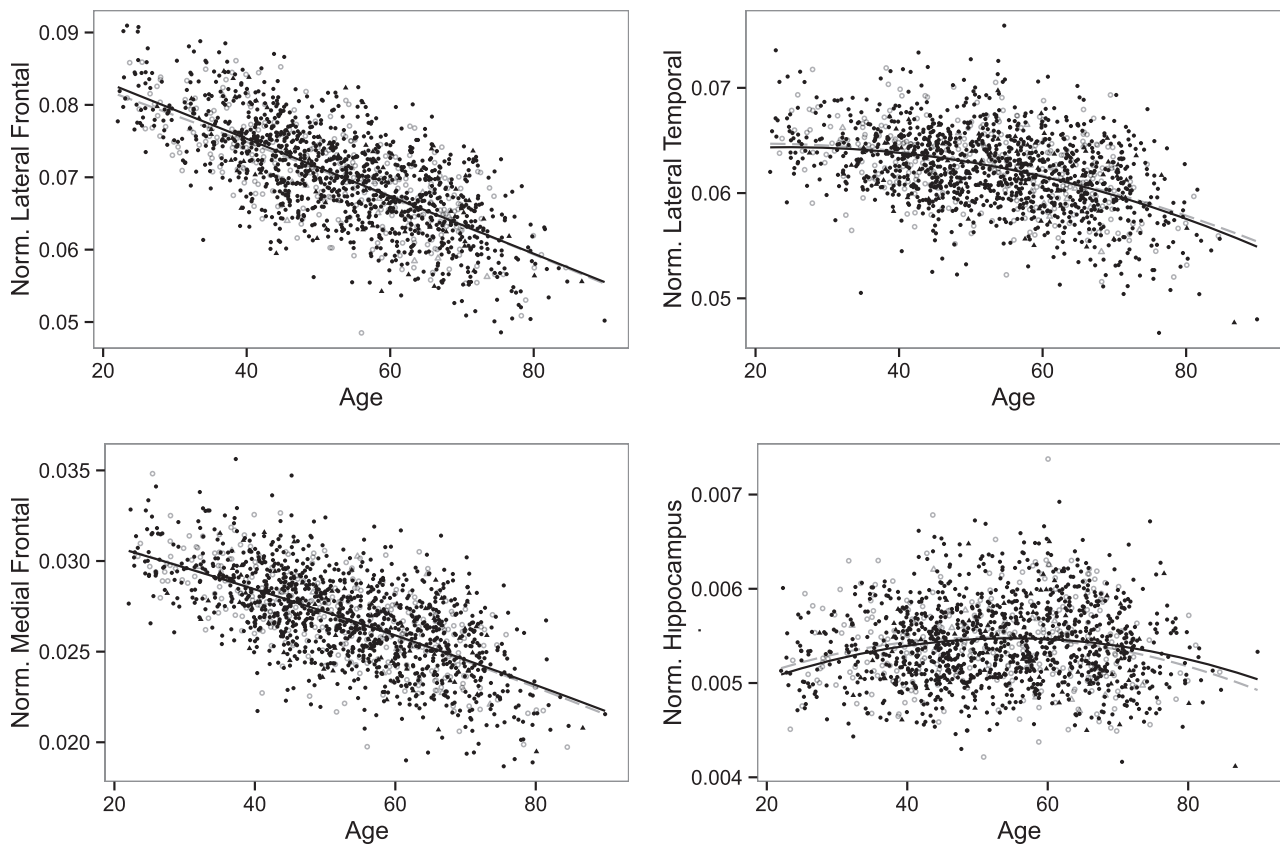


FIG 1. Relationship between AD-related gray matter regions (lateral frontal, lateral temporal, medial frontal, and hippocampus; all regions were normalized by total intracranial volume) and age within *APOE* $\epsilon 4$ carrier (open objects, gray) and noncarrier (filled objects, black) SHIP individuals. Circles indicate cognitively healthy individuals, and triangles indicate cognitively impaired ones.

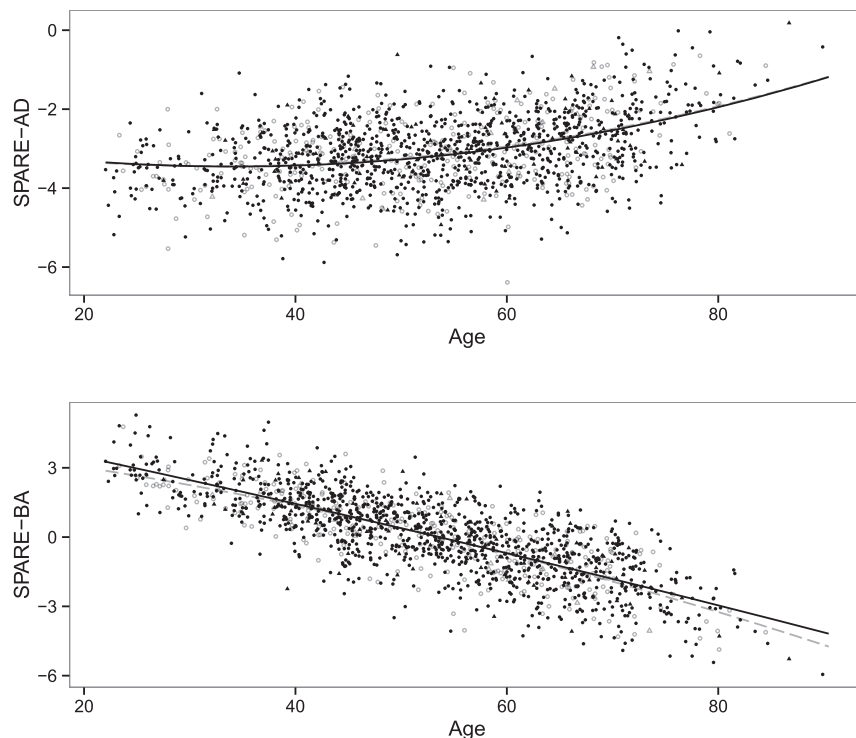


FIG 2. Relationship between age and SPARE-AD and between age and SPARE-BA in *APOE* $\epsilon 4$ carrier (open objects, gray) and noncarrier (filled objects, black) individuals. Circles indicate cognitively healthy individuals, and triangles indicate cognitively impaired ones.

cluded the ROI volumes or the SPARE indices as outcomes (Table 2). Similarly, there was no significant interaction between *APOE* $\epsilon 4$ carrier status and age ($P > .1$). In all models, older age was associated with greater brain atrophy, and a nonlinear square age term was significant for the models that included the lateral temporal regions, hippocampus, or SPARE-AD scores as outcomes (Table 2). Besides age, male participants showed smaller regional volumes, higher SPARE-AD, and lower SPARE-BA values over the studied life span. In additional analyses limiting the sample to younger (22–40 years) or older (60–90 years) participants, we did not find any *APOE* genotype-related differences (On-line Tables 2 and 3).

Association between *APOE* and Cognitive Scores

No significant association was detected among the Verbal Learning and Memory Test, Nuremberg Age Inventory, and *APOE* $\epsilon 4$ carrier status in a linear regression model after adjusting for age, sex, and education (On-line Tables 4 and 5).

Table 2: Linear regression models between age and ROI volumes (normalized by total intracranial volume) and SPARE-AD and SPARE-BA^a

Outcome	Age	Age ²	Female	APOE $\epsilon 4$ Carriers
Lateral frontal volume	−0.0003900 (<.001) ^b	—	0.0021720 (<.001) ^b	−0.0002459 (.433)
Lateral temporal volume	0.0001020 (.040) ^b	−0.0000021 (<.001) ^b	0.0003695 (.040) ^b	0.0001112 (.605)
Medial frontal volume	−0.0001291 (<.001) ^b	—	0.0010690 (<.001) ^b	−0.0000055 (.964)
Hippocampal volume	0.0000415 (<.001) ^b	−0.0000005 (<.001) ^b	0.0001919 (<.001) ^b	0.0000118 (.649)
SPARE-AD	−0.0438960 (<.001) ^b	0.0006549 (<.001) ^b	−0.1775256 (<.001) ^b	0.0293579 (.582)
SPARE-BA	−0.1062550 (<.001) ^b	—	0.6416590 (<.001) ^b	−0.0514570 (.452)

^a If age² was not significant in a model, the coefficients were recalculated after excluding. Data are coefficient (*P* value).

^b Significant at *P* < .05. Models are adjusted for education and study cohort effects. Including interaction terms between APOE status and age², age, sex, and education one at a time to those regression models showed no significant interaction (*P* > .1).

DISCUSSION

Although the APOE $\epsilon 4$ allele is the strongest genetic sporadic AD risk factor accounting for most of AD genetic-related risk and is associated with an earlier clinical onset of dementia and preclinical biomarker changes, we did not find brain volume differences between APOE $\epsilon 4$ carriers and noncarriers.

Here we studied the association between the APOE genotype and brain structure in a large cohort of subjects with a wide age range recruited from the general population whose MR imaging scans were obtained by using a standardized sequence in all subjects. We quantified structural brain changes by using 2 approaches: 1) an ROI approach, guided by previous findings; and 2) a pattern-based analysis by using 2 machine-learning-based summary indices. The imaging indices, the SPARE-AD and the SPARE-BA, were developed to quantify AD- and age-related brain changes, respectively. SPARE-AD has been shown to predict early AD-related changes²³ and MCI stages.²⁴ The SPARE-AD index outperformed ROI-defined volumes in detecting the earliest changes associated with initial cognitive symptoms and showed that 1 single brain volume measure alone is unlikely to adequately reflect the complexity of neurodegeneration in AD, as previously demonstrated in Fan et al.²⁹ Therefore, it is unlikely that a lack of sensitivity of our approaches can explain the absence of associations between APOE and the structural MR imaging measures.

The difference in SPARE-AD scores of APOE $\epsilon 4$ carriers and noncarriers was statistically insignificant. Our results indicate that APOE-related MR imaging atrophy is not prominent at younger ages and suggest that atrophy may only be observable more proximal to the onset of clinical symptoms. Whereas older subjects with more severe degrees of cognitive impairment might be underrepresented in our population-based sample and thus lead to an underrepresentation of APOE $\epsilon 4$ carriers in the elderly (21.9% APOE $\epsilon 4$ carriers among the individuals older than 60 years of age), this underrepresentation would have not been the case for the younger subjects (27.0% APOE $\epsilon 4$ carriers among the individuals younger than 40 years of age). Therefore, we would not expect any recruitment bias to explain the lack of observed associations in the younger individuals included in our study.

Our findings agree with studies following cognitively healthy subjects with autosomal dominant mutations with an expected age at onset of disease, which report structural MR imaging changes taking place within ≤ 1 decade from the diagnosis of dementia.^{30,31} In addition, recent CSF and postmortem biomarker studies have shown that amyloid deposition starts in the fifth decade,^{3,32} usually without the individual having scans positive for

amyloid. On the basis of the current AD biomarker³³ model that predicts occurrence of amyloid β deposition before brain atrophy, a finding of brain atrophy in the third decade of life would be unlikely.

Previous studies have reported lower hippocampal, orbitofrontal, and entorhinal volumes in subjects with APOE $\epsilon 4$ in the early decades of life.^{12,13} The possible reasons for conflicting results could be differences in selection of the sample, the sample size, or processing pipelines of the MR imaging scans. Another potential explanation is that negative results are less likely to be reported than positive ones. Our study included a similar, or even larger, sample size than that in previous studies and applied sensitive methods to detect even subtle MR imaging changes associated with early AD-related changes and aging. However, it is possible that differences in functional changes associated with the APOE genotype at a younger age, as reported previously, precede structural changes^{14,15} and potentially even widespread amyloid β deposition, though this hypothesis still requires larger samples to validate initial reports based on small-sized cohorts.

In recent work, AD pathology from preclinical-to-clinical stages was associated with a decrease in the metabolism of the posterior cingulate cortex, even before any sign of AD.³⁴ The appearance of hypometabolism before clinical change could vary depending on cognitive reserve. The results on cognitive reserve and APOE are controversial in the literature. However, APOE does not seem to modulate the effect of cognitive reserve on cognitive function.³⁵ Due to the lack of functional imaging measures in our cohort, we could not evaluate the presence of these changes in the framework of SHIP.

While we did not find associations between APOE and brain volume measures, several studies reported the effects of the APOE genotype on white matter microstructure, which we did not assess in the current study. APOE was associated with white matter microstructure in 2 of 14 tracts in elderly persons free of dementia and preclinical dementia.³⁶ Furthermore, APOE $\epsilon 4$ was associated with a decline in fractional anisotropy, a marker of white matter integrity, compared with noncarriers.³⁷ On the other hand, APOE $\epsilon 2$ carriers had more robust white matter integrity.³⁸ The mechanisms underlying the white matter microstructural changes are still not well-understood,³⁹ but it is possible that detection of more subtle associations between APOE and brain structure in preclinical dementia requires microstructural assessment.

Limitations of our study include the use of imputed genotype data from single nucleotide polymorphism (SNP) arrays and not a specific assay for APOE⁴⁰ to determine the APOE genotype, the

limited clinical testing data available for the subjects, and the lack of longitudinal MR imaging scans.

CONCLUSIONS

Our study indicates that measurable APOE-related brain atrophy does not occur during early adulthood and midlife and suggests that APOE-related MR imaging atrophy may only be present later in life, more proximal to clinical disease onset.

ACKNOWLEDGMENTS

SHIP is part of the Community Medicine Research net of the University of Greifswald, Germany, which is funded by the Federal Ministry of Education and Research (grants no. 01ZZ9603, 01ZZ0103, and 01ZZ0403), the Ministry of Cultural Affairs, and the Social Ministry of the Federal State of Mecklenburg–West Pomerania. Genomewide data in SHIP and MR imaging scans in SHIP and SHIP-TREND have been supported by a joint grant from Siemens, Erlangen, Germany, and the Federal State of Mecklenburg–West Pomerania. Genomewide genotyping in SHIP-TREND-0 was supported by the Federal Ministry of Education and Research (grant No. 03ZIK012). M.H. was supported by the Alfried Krupp von Bohlen und Halbach Foundation. J.B.T. is supported by P01 AG032953, P01 AG017586, P30 AG010124, and P50 NS053488. S.M.R. is supported by the Intramural Research Program, National Institute on Aging, National Institutes of Health.

Disclosures: Mohamad Habes—RELATED: Other: Supported by the Alfried Krupp von Bohlen und Halbach Foundation.* Jon B. Toledo—UNRELATED: Grants/Grants Pending: National Institute of Health grants.* Sandra Van der Auwera—RELATED: Grant: German Federal Ministry of Education and Research (grant No. 01ZX1314E).* Hans J. Grabe—UNRELATED: Grants/Grants Pending: German Research Foundation.* Grants from the German Ministry of Education and Research.* *Money paid to the institution.

REFERENCES

- Corder E, Saunders A, Strittmatter W, et al. **Gene dose of apolipoprotein E type 4 allele and the risk of Alzheimer's disease in late onset families.** *Science* 1993;261:921–23 CrossRef Medline
- Strittmatter WJ, Saunders AM, Schmechel D, et al. **Apolipoprotein E: high-avidity binding to beta-amyloid and increased frequency of type 4 allele in late-onset familial Alzheimer disease.** *Proc Natl Acad Sci U S A* 1993;90:1977–81 CrossRef Medline
- Toledo JB, Zetterberg H, van Harten AC, et al; Alzheimer's Disease Neuroimaging Initiative. **Alzheimer's disease cerebrospinal fluid biomarker in cognitively normal subjects.** *Brain J Neurol* 2015;138:2701–15 CrossRef Medline
- Jack CR, Wiste HJ, Weigand SD, et al. **Age-specific population frequencies of cerebral β -amyloidosis and neurodegeneration among people with normal cognitive function aged 50–89 years: a cross-sectional study.** *Lancet Neurol* 2014;13:997–1005 CrossRef Medline
- Keene CD, Cudaback E, Li X, et al. **Apolipoprotein E isoforms and regulation of the innate immune response in brain of patients with Alzheimer's disease.** *Neurobiol Dis* 2011;21:920–28 CrossRef Medline
- Zlokovic BV. **Cerebrovascular effects of apolipoprotein E: implications for Alzheimer disease.** *JAMA Neurol* 2013;70:440–44 CrossRef Medline
- Verghese PB, Castellano JM, Holtzman DM. **Apolipoprotein E in Alzheimer's disease and other neurological disorders.** *Lancet Neurol* 2011;10:241–52 CrossRef Medline
- Mungas D, Tractenberg R, Schneider JA, et al. **A 2-process model for neuropathology of Alzheimer's disease.** *Neurobiol Aging* 2014;35:301–08 CrossRef Medline
- Toledo J, Da X, Weiner M, et al; Alzheimer's Disease Neuroimaging Initiative. **CSF Apo-E levels associate with cognitive decline and MRI changes.** *Acta Neuropathol (Berl)* 2014;127:621–32 CrossRef Medline
- Martínez-Morillo E, Hansson O, Atagi Y, et al. **Total apolipoprotein E levels and specific isoform composition in cerebrospinal fluid and plasma from Alzheimer's disease patients and controls.** *Acta Neuropathol (Berl)* 2014;127:633–43 CrossRef Medline
- Rasmussen KL, Tybjaerg-Hansen A, Nordestgaard BG, et al. **Plasma levels of apolipoprotein E and risk of dementia in the general population.** *Ann Neurol* 2015;77:301–11 CrossRef Medline
- Shaw P, Lerch JP, Pruessner JC, et al. **Cortical morphology in children and adolescents with different apolipoprotein E gene polymorphisms: an observational study.** *Lancet Neurol* 2007;6:494–500 CrossRef Medline
- O'Dwyer L, Lamberton F, Matura S, et al. **Reduced hippocampal volume in healthy young ApoE4 carriers: an MRI study.** *PLoS One* 2012;7:e48895 CrossRef Medline
- Reiman EM, Chen K, Alexander GE, et al. **Functional brain abnormalities in young adults at genetic risk for late-onset Alzheimer's dementia.** *Proc Natl Acad Sci U S A* 2004;101:284–89 CrossRef Medline
- Filippini N, MacIntosh BJ, Hough MG, et al. **Distinct patterns of brain activity in young carriers of the APOE-epsilon4 allele.** *Proc Natl Acad Sci U S A* 2009;106:7209–14 CrossRef Medline
- Völzke H, Alte D, Schmidt CO, et al. **Cohort profile: the Study of Health in Pomerania.** *Int J Epidemiol* 2011;40:294–307 CrossRef Medline
- Hegenscheid K, Kühn JP, Völzke H, et al. **Whole-body magnetic resonance imaging of healthy volunteers: pilot study results from the population-based SHIP study.** *Rofo* 2009;181:748–59 CrossRef Medline
- Woods SP, Delis DC, Scott JC, et al. **The California Verbal Learning Test—second edition: test-retest reliability, practice effects, and reliable change indices for the standard and alternate forms.** *Arch Clin Neuropsychol* 2006;21:413–20 CrossRef Medline
- Fleischmann UM, Oswald WD. *Nürnberger-Alters-Inventar (NAI); NAI-Testmanual und -Textband.* Göttingen: Hogrefe, Verlag für Psychologie; 1999
- Doshi J, Erus G, Ou Y, et al. **Multi-atlas skull-stripping.** *Acad Radiol* 2013;20:1566–76 CrossRef Medline
- Doshi J, Erus G, Ou Y, et al; Alzheimer's Neuroimaging Initiative. **MUSE: multi-atlas region segmentation utilizing ensembles of registration algorithms and parameters, and locally optimal atlas selection.** *Neuroimage* 2016;127:186–95 CrossRef Medline
- Fan Y, Shen D, Gur RC, et al. **COMPARE: Classification of Morphological Patterns Using Adaptive Regional Elements.** *Med Imaging IEEE Trans* 2007;26:93–105 CrossRef Medline
- Toledo J, Weiner M, Wolk D, et al; Alzheimer's Disease Neuroimaging Initiative. **Neuronal injury biomarkers and prognosis in ADNI subjects with normal cognition.** *Acta Neuropathol Commun* 2014;2:26 CrossRef Medline
- Da X, Toledo JB, Zee J, et al; Alzheimer's Neuroimaging Initiative. **Integration and relative value of biomarkers for prediction of MCI to AD progression: spatial patterns of brain atrophy, cognitive scores, APOE genotype and CSF biomarkers.** *Neuroimage Clin* 2014;4:164–73 CrossRef Medline
- Vapnik VN. *The Nature of Statistical Learning Theory.* New York: Springer-Verlag; 2000
- Habes M, Erus G, Toledo JB, et al. **White matter hyperintensities and imaging patterns of brain ageing in the general population.** *Brain* 2016;139(pt 4):1164–79 CrossRef Medline
- Habes M, Janowitz D, Erus G, et al. **Advanced brain aging: relationship with epidemiologic and genetic risk factors, and overlap with Alzheimer disease atrophy patterns.** *Transl Psychiatry* 2016;6:e775 CrossRef Medline

28. R Core Team R: *A Language and Environment for Statistical Computing*. Vienna: R Foundation for Statistical Computing; 2014
29. Fan Y, Batmanghelich N, Clark CM, et al; Alzheimer's Disease Neuroimaging Initiative. **Spatial patterns of brain atrophy in MCI patients, identified via high-dimensional pattern classification, predict subsequent cognitive decline.** *Neuroimage* 2007;39:1731–43 Medline
30. Bateman RJ, Xiong C, Benzinger TLS, et al.; Dominantly Inherited Alzheimer Network. **Clinical and biomarker changes in dominantly inherited Alzheimer's disease.** *N Engl J Med* 2012;367:795–804 CrossRef Medline
31. Villemagne VL, Burnham S, Bourgeat P, et al; Australian Imaging Biomarkers and Lifestyle (AIBL) Research Group. **Amyloid β deposition, neurodegeneration, and cognitive decline in sporadic Alzheimer's disease: a prospective cohort study.** *Lancet Neurol* 2013;12:357–67 CrossRef Medline
32. Pletnikova O, Rudow GL, Hyde TM, et al. **Alzheimer lesions in the autopsied brains of people 30 to 50 years of age.** *Cogn Behav Neurol* 2015;28:144–52 CrossRef Medline
33. Jack CR Jr, Knopman DS, Jagust WJ, et al. **Tracking pathophysiological processes in Alzheimer's disease: an updated hypothetical model of dynamic biomarkers.** *Lancet Neurol* 2013;12:207–16 CrossRef Medline
34. Teipel S, Grothe MJ; Alzheimer's Disease Neuroimaging Initiative. **Does posterior cingulate hypometabolism result from disconnection or local pathology across preclinical and clinical stages of Alzheimer's disease?** *Eur J Nucl Med Mol Imaging* 2016;43:526–36 CrossRef Medline
35. Ward DD, Summers MJ, Saunders NL, et al. **The BDNF Val66Met polymorphism moderates the relationship between cognitive reserve and executive function.** *Transl Psychiatry* 2015;5:e590 CrossRef Medline
36. Laukka EJ, Lövdén M, Kalpouzos G, et al. **Microstructural white matter properties mediate the association between APOE and perceptual speed in very old persons without dementia.** *PLoS One* 2015;10:e0134766 CrossRef Medline
37. Persson J, Lind J, Larsson A, et al. **Altered brain white matter integrity in healthy carriers of the APOE epsilon4 allele: a risk for AD?** *Neurology* 2006;66:1029–33 CrossRef Medline
38. Chiang GC, Zhan W, Schuff N, et al. **White matter alterations in cognitively normal apoE ϵ 2 carriers: insight into Alzheimer resistance?** *AJNR Am J Neuroradiol* 2012;33:1392–7 CrossRef Medline
39. Gold BT, Johnson NF, Powell DK, et al. **White matter integrity and vulnerability to Alzheimer's disease: preliminary findings and future directions.** *Biochim Biophys Acta* 2012;1822:416–22 CrossRef Medline
40. Saykin AJ, Shen L, Foroud TM, et al; Alzheimer's Disease Neuroimaging Initiative. **Alzheimer's Disease Neuroimaging Initiative biomarkers as quantitative phenotypes: genetics core aims, progress, and plans.** *Alzheimers Dement* 2010;6:265–73 CrossRef Medline

Differentiation of Low- and High-Grade Gliomas Using High b-Value Diffusion Imaging with a Non-Gaussian Diffusion Model

Y. Sui, Y. Xiong, J. Jiang, M.M. Karaman, K.L. Xie, W. Zhu, and X.J. Zhou



ABSTRACT

BACKGROUND AND PURPOSE: Imaging-based tumor grading is highly desirable but faces challenges in sensitivity, specificity, and diagnostic accuracy. A recently proposed diffusion imaging method by using a fractional order calculus model offers a set of new parameters to probe not only the diffusion process itself but also intravoxel tissue structures, providing new opportunities for noninvasive tumor grading. This study aimed to demonstrate the feasibility of using the fractional order calculus model to differentiate low- from high-grade gliomas in adult patients and illustrate its improved performance over a conventional diffusion imaging method using ADC (or D).

MATERIALS AND METHODS: Fifty-four adult patients (18–70 years of age) with histology-proved gliomas were enrolled and divided into low-grade ($n = 24$) and high-grade ($n = 30$) groups. Multi-b-value diffusion MR imaging was performed with 17 b-values ($0–4000 \text{ s/mm}^2$) and was analyzed by using a fractional order calculus model. Mean values and SDs of 3 fractional order calculus parameters (D , β , and μ) were calculated from the normal contralateral thalamus (as a control) and the tumors, respectively. On the basis of these values, the low- and high-grade glioma groups were compared by using a Mann-Whitney U test. Receiver operating characteristic analysis was performed to assess the performance of individual parameters and the combination of multiple parameters for low- versus high-grade differentiation.

RESULTS: Each of the 3 fractional order calculus parameters exhibited a statistically higher value ($P \leq .011$) in the low-grade than in the high-grade gliomas, whereas there was no difference in the normal contralateral thalamus ($P \geq .706$). The receiver operating characteristic analysis showed that β (area under the curve = 0.853) produced a higher area under the curve than D (0.781) or μ (0.703) and offered a sensitivity of 87.5%, specificity of 76.7%, and diagnostic accuracy of 82.1%.

CONCLUSIONS: The study demonstrated the feasibility of using a non-Gaussian fractional order calculus diffusion model to differentiate low- and high-grade gliomas. While all 3 fractional order calculus parameters showed statistically significant differences between the 2 groups, β exhibited a better performance than the other 2 parameters, including ADC (or D).

ABBREVIATIONS: AUC = area under the curve; FROC = fractional order calculus; ROC = receiver operating characteristic; WHO = World Health Organization

Gliomas are the most common primary brain tumors seen in adults, accounting for approximately one-third to one-half of all cases diagnosed¹ and 82% of malignant brain tumors.² According to the latest classification by the World Health Organization

(WHO), gliomas can be divided into 4 grades, spanning a broad spectrum of biologic aggressiveness.³ Accurate grading of gliomas is essential to patient management, not only for selecting the most effective therapy for malignant tumors but also for avoiding unnecessary aggressive treatment for low-grade tumors before malignant transformation, maximizing the quality of life for patients.

MR imaging has been widely used for the initial diagnosis of brain tumors. Its role for tumor grading, however, is less estab-

Received November 25, 2015; accepted after revision February 22, 2016.

From the Center for MR Research (Y.S., Y.X., M.M.K., X.J.Z.) and Departments of Bioengineering (Y.S., X.J.Z.), Radiology (K.L.X., X.J.Z.), and Neurosurgery (X.J.Z.), University of Illinois at Chicago, Chicago, Illinois; and Department of Radiology (Y.X., J.J., W.Z.), Tongji Hospital, Tongji Medical College, Huazhong University of Science and Technology, Wuhan, Hubei, China.

Yi Sui and Ying Xiong contributed equally and share the first authorship.

This work was supported, in part, by the National Natural Science Foundation of China (grant number: 30870702), the National Program of the Ministry of Science and Technology of China during the “12th Five-year Plan” (grant No. 2011BAI08B10), and the National Institutes of Health (grant No. 1S10RR028898).

Paper previously presented in part at: Annual Meeting of the Radiological Society of North America, November 30 to December 5, 2014; Chicago, Illinois.

Please address correspondence to Xiaohong Joe Zhou, PhD, Advanced Imaging Center, Suite 103, 2242 West Harrison St, Chicago, IL 60612; e-mail: xjzhou@uic.edu or Wenzhen Zhu, MD, Department of Radiology, Tongji Hospital, 1095 Jiefang Ave, Wuhan, Hubei 430030, China; email: zhuwenzhen@hotmail.com

Indicates open access to non-subscribers at www.ajnr.org

Indicates article with supplemental on-line photos.

<http://dx.doi.org/10.3174/ajnr.A4836>

lished.⁴ Conventional MR imaging techniques, including precontrast T1-weighted, T2-weighted, T2-weighted FLAIR, and postcontrast T1-weighted imaging, have limited sensitivity (eg, 72.5%) and specificity (eg, 65.0%) for differentiating low- and high-grade gliomas.^{4,5} Perfusion imaging (eg, CBV) can improve the sensitivity to >90%,⁶ but the specificity (eg, 57.5%) remains inadequate and is subject to the choice of CBV threshold values, depending on tumor types.⁷⁻⁹ With the ability to reveal tumor metabolic changes, MR spectroscopy has also been used for tumor grading.^{6,10,11} The long data-acquisition times, poor spatial resolution, and magnetic susceptibility perturbations at specific locations (eg, near the sinus and the skull) have hindered its widespread clinical application.^{6,10,11} Because of the aforementioned challenges and limitations faced by MR imaging/MR spectroscopy, tissue biopsy remains the criterion standard for tumor classification and grading, despite its sampling errors, invasiveness, and inability to evaluate residual tumor tissue after cytoreductive surgery.⁵

During the past 2 decades, diffusion imaging based on ADC has been evaluated for tumor grading.¹²⁻¹⁴ Despite the potential, several studies indicate that ADC values overlap considerably among different tumor grades in both adult¹⁵⁻¹⁷ and pediatric patients.^{14,18-20} The ADC values of tumor tissues are obtained by characterizing the diffusion MR imaging signals with a monoexponential function, also known as a Gaussian diffusion model, which assumes that the diffusion process within a voxel is homogeneous.²¹ Unlike low-grade gliomas, high-grade gliomas have an increased degree of tissue heterogeneity,^{22,23} which is not adequately captured by ADC. To overcome this limitation, a number of non-Gaussian diffusion models²⁴⁻³² have been developed to extract tissue microstructural information, including tissue heterogeneity, beyond what ADC can provide. The fractional order calculus (FROC) model,^{26,29} for example, can produce a set of parameters, including diffusion coefficient D (in square millimeters/second), fractional order derivative in space β , and a spatial parameter μ (in micrometers). These parameters provide additional avenues to probing not only the diffusion process itself (D) but also the intravoxel tissue heterogeneity (β) that can be used to improve tumor characterization.^{26,29,33} In this study, we demonstrate the feasibility of using a new set of parameters from the FROC model to improve MR imaging-based differentiation of low- and high-grade gliomas in adult patients.

MATERIALS AND METHODS

Patients

The institutional review board of the performing hospital (Tongji Hospital, Wuhan, China) approved this prospective study, and written informed consent was obtained from all participating patients. Fifty-six adult patients (18–70 years of age) with an initial diagnosis of gliomas were recruited and underwent multi-b-value diffusion MR imaging before biopsy or surgical treatment. Two patients were excluded from the analysis due to excessive motion. Among the 54 patients included in the study, histopathology revealed 24 low-grade gliomas, including 1 pilocytic astrocytoma (WHO I), 2 oligodendrogliomas (WHO I and II), 20 astrocytomas (WHO II, predominantly diffuse tumors), 1 ganglioglioma (WHO II), and 30 high-grade gliomas, including 2 anaplastic oli-

godendrogliomas (WHO III), 10 anaplastic astrocytomas (WHO III), and 18 glioblastoma multiformes (WHO IV), according to the WHO guideline of 2007.³

Image Acquisition

All MR imaging examinations were performed on a 3T scanner (MR750; GE Healthcare, Milwaukee, Wisconsin) with a 32-channel phased-array head coil. The imaging protocol included precontrast T1-weighted FLAIR, T2-weighted FLAIR, T2-weighted PROPELLER, and multi-b-value diffusion-weighted sequences, followed by postcontrast T1-weighted imaging. Susceptibility-weighted imaging was performed on selected patients when the conventional sequences were inadequate to characterize hemorrhage within tumors. In all sequences, an FOV of 24 cm and a section thickness of 5 mm were used. The parameters specific to each anatomic imaging sequence were the following: T1-weighted FLAIR: TR/TE = 1750/32.4 ms, TI = 860 ms, flip angle = 90°, and matrix size = 320 × 320; T2-weighted PROPELLER: TR/TE = 4260/102 ms, echo-train length = 32, and matrix size = 320 × 224; T2-weighted FLAIR: TR/TE = 8400/150 ms, TI = 2100 ms, echo-train length = 26, and matrix size = 256 × 256. The DWIs were produced by using a single-shot echo-planar imaging sequence with 17 b-values (0, 20, 50, 100, 200, 400, 600, 800, 1000, 1200, 1600, 2000, 2400, 2800, 3200, 3600, and 4000 s/mm², in which the subscript denotes the number of averages). At each b-value, a Stejskal-Tanner diffusion gradient was successively applied along the x-, y-, and z-axes to obtain a trace-weighted image to minimize the influence of diffusion anisotropy. The key data acquisition parameters were TR/TE = 3025/94.5 ms, sensitivity encoding acceleration factor = 2, separation between 2 diffusion gradient lobes Δ = 38.6 ms, duration of each diffusion gradient δ = 32.2 ms, matrix size = 160 × 160 (reconstructed with a 256 × 256 matrix), and scan time = 4 minutes 30 seconds.

Image Analysis

Equation 1 was used to fit the intensity (S) of the multi-b-value diffusion images voxel-by-voxel, according to the FROC diffusion model^{26,29}:

$$1) \quad S = S_0 \exp \left[-D \mu^{2(\beta-1)} (\gamma G_d \delta)^{2\beta} \left(\Delta - \frac{2\beta-1}{2\beta+1} \delta \right) \right],$$

where S_0 is the signal intensity without diffusion weighting, G_d is the diffusion gradient amplitude, and δ and Δ are defined earlier. The β parameter (dimensionless; $0 < \beta \leq 1$) is a fractional order derivative with respect to space, and μ (in units of micrometers) is a spatial constant to preserve the nominal units of the diffusion coefficient D (in square millimeters/second). In the fitting, D (which reflects the intrinsic diffusivity) was estimated by a monoexponential model by using the data acquired at lower b-values (≤ 1000 s/mm²), in an attempt to make D equivalent to conventional ADC. After D was determined, β and μ were subsequently obtained from a voxelwise nonlinear fitting by using a Levenberg-Marquardt algorithm³⁴ with all b-values.

ROIs were first placed on the normal contralateral thalamus, which served as an internal control, followed by placing ROIs on the solid region of tumors by 2 neuroradiologists (Y.X. and K.L.X.

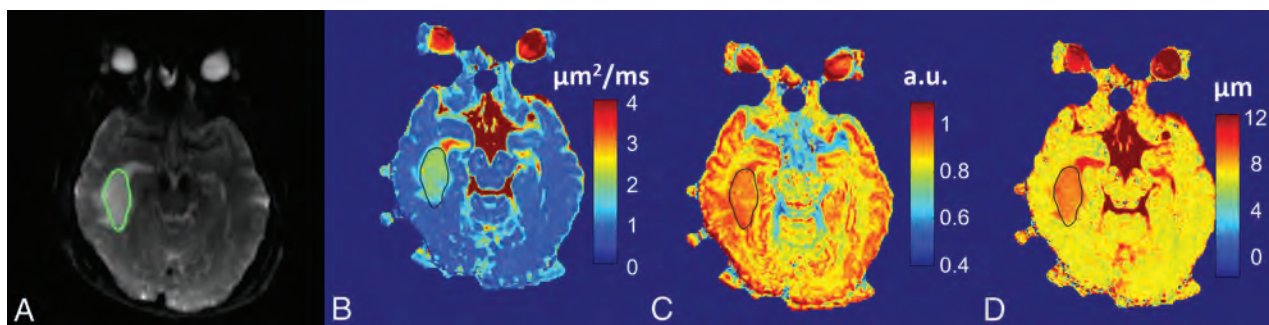


FIG 1. A 41-year-old female patient with a low-grade glioma (oligodendroglioma, WHO grade I). T2-weighted EPI at $b=0$ with the tumor ROI encircled in green (A), and FROC parameter maps of D (B), β (C), and μ (D) with the tumor ROIs indicated by the black contours (see On-line Fig 1 for a complete set of images, including axial precontrast T1-weighted FLAIR, postcontrast T1-weighted FLAIR, precontrast T2-weighted FLAIR, and precontrast T2WI PROPELLER images). Compared with the patient with glioblastoma multiforme in Fig 2, all 3 FROC parameters exhibited higher values. a.u. indicates arbitrary units. The color scale in (B) is expressed in square micrometers/millisecond.

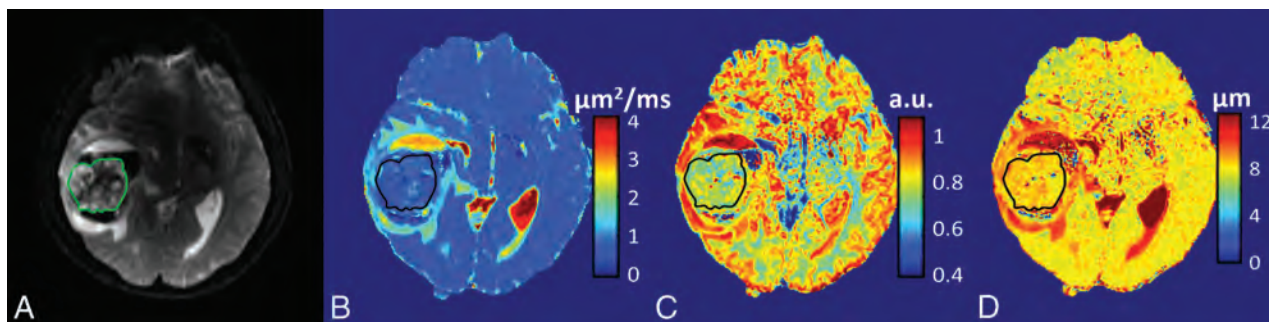


FIG 2. A 38-year-old male patient with a high-grade glioma (glioblastoma multiforme, WHO grade IV). T2-weighted EPI at $b=0$ with the tumor ROI encircled in green (A) and FROC parameter maps of D (B), β (C), and μ (D) with the tumor ROIs indicated by the black contours (see On-line Fig 2 for a complete set of images including axial precontrast T1-weighted FLAIR, postcontrast T1-weighted FLAIR, T2-weighted FLAIR, and T2-weighted PROPELLER images). Compared with the patient with an oligodendroglioma in Fig 1, all 3 FROC parameters exhibited lower values. a.u. indicates arbitrary units. The color scale in (B) is expressed in square micrometers/millisecond.

with 8 and 15 years of clinical experience, respectively) blinded to the histology grades. Guided by the high-resolution anatomic images, regions of hemorrhage, cystic change, and/or necrosis were excluded. In the solid region of tumors, the enhancing components and the nonenhancing (or not-so-obvious enhancing) components were measured and averaged. The ROI-based image analysis was performed with customized software developed in Matlab (MathWorks, Natick, Massachusetts).

Statistical Analysis

The mean and SD of D , β , and μ for each patient were calculated from the normal contralateral thalamus and the tumor ROIs, respectively. On the basis of these values, the low-grade and high-grade glioma groups were compared by using a Mann-Whitney U test with a statistical significance set at $P < .05$.

To investigate the potential value of using combinations of the FROC parameters (D , β , and μ) for differentiation of low- and high-grade gliomas, we employed a logistic regression model:

$$2) \quad P_0 = \exp(a_0 + a_1 D + a_2 \beta + a_3 \mu) / [1 + \exp(a_0 + a_1 D + a_2 \beta + a_3 \mu)],$$

where a_0 is a constant, and a_1 , a_2 , and a_3 are the regression coefficients for D , β , and μ , respectively. The regression coefficients were estimated by using a maximum-likelihood method.³⁵ Receiver operating characteristic (ROC) analysis was performed to

determine the area under the ROC curve (AUC) for assessing the performance of tumor differentiation by using each of the 3 FROC parameters individually and the combination of FROC parameters represented by P_0 . The best cutoff values in the ROC analysis were determined by using the Youden index. To determine the generalizability of the proposed method, we used a hold-out cross-validation algorithm by applying the logistic regression model, Equation 2, on a "training dataset" and a "test dataset" (randomly and equally split from the samples). The Pearson correlation coefficients were then determined between the predicted values and the "true" histopathologic results. All statistical analyses were performed by using SPSS software (IBM, Armonk, New York).

RESULTS

Comparison among Representative Patients in Each Group

Figure 1 shows a set of axial images from a representative patient (oligodendroglioma, WHO I) in the low-grade glioma group, including T2-weighted EPI (Fig 1A), and the FROC maps (color images in Fig 1B–D). The precontrast and postcontrast T1-weighted FLAIR, precontrast T2-weighted FLAIR, and T2-weighted PROPELLER images are available in On-line Fig 1. The D , β , and μ maps (Fig 1B–D, respectively) all exhibited higher values in the tumor than in the surrounding brain parenchyma. Figure 2 shows a set of axial images from a representative patient

(glioblastoma multiforme, WHO IV) in the high-grade glioma group by using a layout similar to that of Fig 1. The FROC parameters D , β , and μ (Fig 2B–D, respectively) were considerably lower compared with those in Fig 1B–D, leading to a distinct difference between the high- and low-grade tumors. Additional anatomic images are available (On-line Fig 2).

Group Comparison Based on the FROC Parameters

After calculating the mean values of the FROC parameters from each tumor ROI, we obtained the means and SDs from each patient group; they are listed in Table 1. Because D is the mathematic equivalent to the conventional ADC (see “Materials and Methods”), an agreement of >96% was observed between D from the FROC model and ADC from a monoexponential fitting by using 2 b-values ($b = 0$ and 1000 s/mm^2), as is typical in clinical studies. Thus, ADC and D are used interchangeably in this study. Comparison of the FROC parameters between the 2 tumor groups is shown in a set of boxplots (Fig 3). Consistent with the representative cases in Figs 1 and 2, the group analysis exhibited statistically higher values ($P \leq .011$) in the low-grade than the high-grade gliomas for each of the 3 FROC parameters. In comparison, the internal control by using a normal contralateral thalamus showed no significant differences ($P \geq .706$) in the FROC parameters between the 2 patient groups, as summarized in Table 1.

Table 1: FROC parameters of gliomas and normal contralateral thalamus of patients with low-grade and high-grade gliomas

	$D \text{ (}\mu\text{m}^2/\text{ms)}$	β	$\mu \text{ (}\mu\text{m)}$
Gliomas			
LG	1.54 ± 0.35	0.85 ± 0.05	8.43 ± 0.63
HG	1.19 ± 0.36	0.77 ± 0.06	8.01 ± 0.59
$P \text{ value}^a$	<.001	<.001	.011
NCTH			
LG	0.76 ± 0.06	0.78 ± 0.03	7.33 ± 0.38
HG	0.76 ± 0.04	0.78 ± 0.03	7.34 ± 0.33
$P \text{ value}^a$.876	.706	.890

Note:—NCTH indicates normal contralateral thalamus; LG, low-grade; HG, high-grade.
^aMann-Whitney U test.

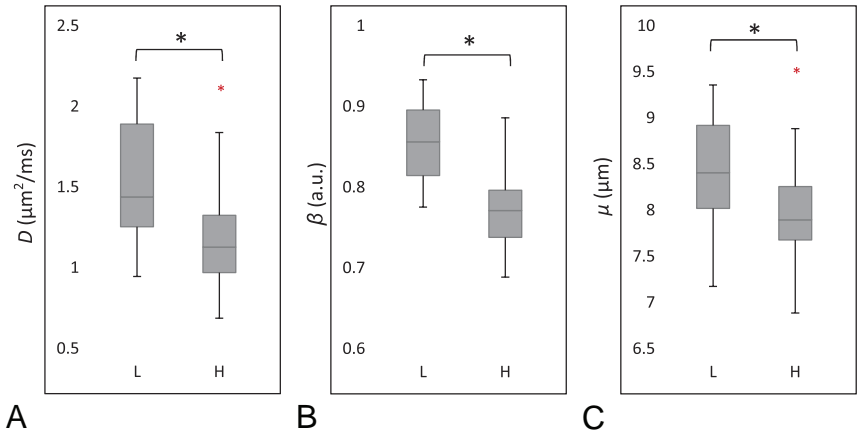


FIG 3. Boxplots of FROC parameters D (A), β (B), and μ (C) between the low- (L) and high-grade (H) gliomas. Boxes represent the 25th and 75th percentiles with the median indicated by the middle line in the box. Vertical end bars denote the range of data except for the outliers (ie, values larger than the 75th percentile or smaller than the 25th percentile) represented by a red asterisk. The black asterisk indicates a significant difference ($P < .05$) between the low- and high-grade gliomas.

ROC Analysis

Figure 4 illustrates the ROC curves using individual FROC parameters for differentiating low- (positive) from high-grade (negative) gliomas. Because D and μ were strongly correlated (see the results in Fig 5), μ was excluded from the logistic regression to avoid overweighing. The constant and regression coefficients of D and β were 19.936, -0.012 , and -24.145 , respectively (see Equation 2), and the corresponding P_0 was used in ROC analysis to represent the combination of D and β . Table 2 summarizes the cutoff values with the corresponding sensitivity, specificity, accuracy, positive and negative predictive values, and asymptotic significance (P value). Although D offered the highest sensitivity (91.7%), its specificity was the lowest (63.3%), leading to moderate accuracy (77.5%). The sensitivity was noticeably improved by β or the combination of β and D , which resulted in the best accuracy (82.1%). The AUC values of the ROC analyses together with their 95% confidence intervals and standard errors are given in Table 3. The parameter β had a higher AUC (0.853) than D (0.781) or μ (0.703), indicating a better performance for glioma differentiation. The combination of D and β did not improve the sensitivity, specificity, accuracy, or AUC compared with β .

The cross-validation analysis showed that the Pearson correlation coefficients between the predicted values and the “true” histopathologic results were 0.529 ($P < .01$) for the training set and 0.625 ($P < .01$) for the test set. The significance test for the difference between the 2 correlations (Fisher Z-test) resulted in a P value of .617, suggesting that the training and test datasets did not produce statistically different correlations.

The scatterplots in Fig 5 illustrate the possible (or lack of) correlation among the FROC parameters using all patient data. A very strong correlation between D and μ was observed (Fig 5A) with a Pearson correlation coefficient of $r = 0.930$ ($P < .001$). In contrast, a noticeably weaker correlation was seen between D and β ($r = 0.766$, $P < .001$). In Fig 5B, the best cutoff values of D and β are indicated by the vertical (red) and the horizontal (green) lines, respectively. The oblique black line in Fig 5B corresponds to the cutoff probability of $P_0 = .662$ for the combination of D and β .

The close proximity between the black and green lines is a reflection of the fact that D has a considerably smaller role than β in the equation $P_0 = \exp(19.936 - 0.012D - 24.145\beta) / [1 + \exp(19.936 - 0.012D - 24.145\beta)]$.

DISCUSSION

We have investigated the feasibility of using a set of novel FROC diffusion parameters to differentiate low- from high-grade gliomas in adults and demonstrated that D , β , and μ exhibited significant differences between the 2 tumor groups. When used individually, β outperformed the other 2 parameters. These results are important because they demonstrate that new parameters from the FROC diffusion model can contrib-

ute positively to glioma differentiation and extend the capability of diffusion imaging beyond conventional ADC.

During the past 2 decades, ADC has been applied to differentiating a number of brain tumors,^{14,16,18,36} including gliomas. Although the sensitivity of using ADC to detect neoplastic changes

has been demonstrated, considerable overlap in ADC values exists between low- and high-grade brain tumors,^{14,16,17} compromising the specificity and diagnostic accuracy. The suboptimal performance of ADC for tumor grading originates, at least in part, from the use of a Gaussian diffusion model (ie, the monoexponential model), which assumes a homogeneous diffusion process in the tumor, despite overwhelming evidence of tumor heterogeneity.³⁷⁻³⁹ In the presence of heterogeneity, non-Gaussian diffusion models can be more effective in characterizing the complex diffusion process, particularly at high b-values (eg, $b \geq 1500$ s/mm²).^{15,21-32,36,40}

Like other non-Gaussian diffusion models, the FROC diffusion model provides new parameters complementary to ADC. In the FROC model, correlation between β and intravoxel tissue heterogeneity has been suggested in several studies on phantoms and tissue specimens.^{26,29,41,42} This correlation is also supported by in vivo studies indicating that tissues with a smaller β -value exhibit a larger degree of intravoxel heterogeneity.^{22,27,33,43} Tissue heterogeneity is also a contributing factor to the WHO tumor grading system.⁴⁴ Thus, the β parameter may provide a link between an MR imaging measurement and WHO grades. The lower β values (ie, a high degree of intravoxel heterogeneity) seen in high-grade gliomas (Figs 2 and 3) are consistent with the increased degree of tissue heterogeneity due to the presence of edema, necrosis, hemorrhage, microcalcification, and so forth. This observation is also consistent with a recent study on pediatric brain tumors^{33,43} in which high-grade tumors showed significantly lower β values compared with their low-grade counterparts. Further studies on well-controlled excised tissues are needed to directly establish and validate the correlation between diffusion heterogeneity suggested by β and structural heterogeneity revealed by histopathology.

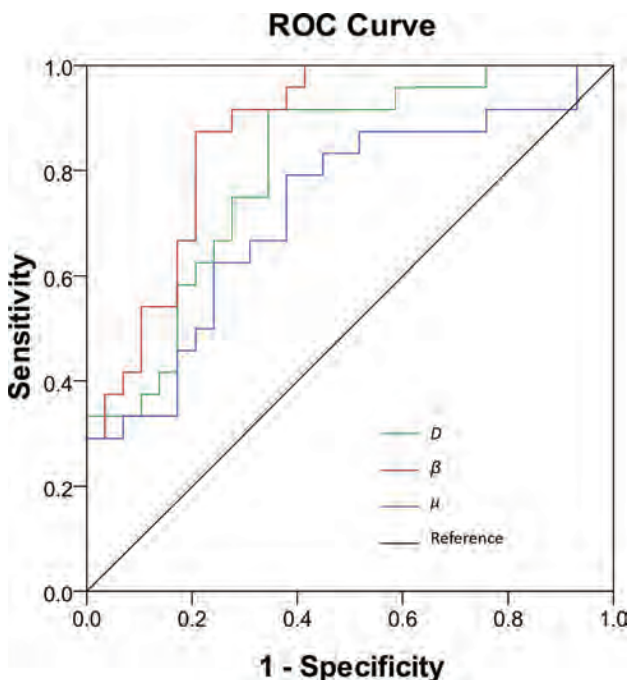


FIG 4. ROC curves for β (in red), D (in green), and μ (in blue) for differentiating low- and high-grade gliomas. The diagonal line serves as a reference.

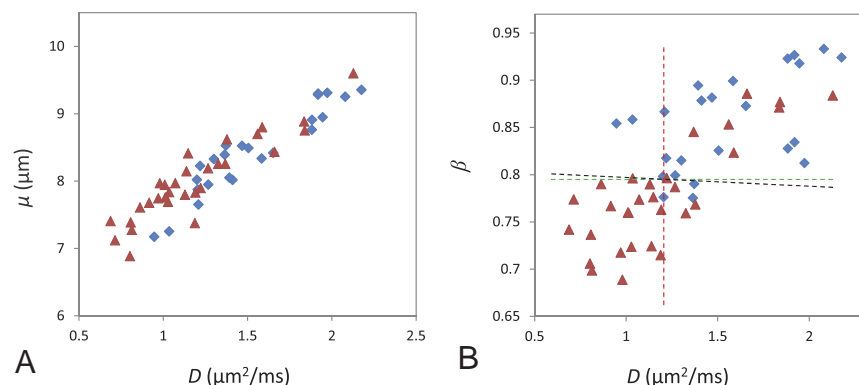


FIG 5. Scatterplots of D versus μ (A) and D versus β (B) from all patients (the blue diamonds represent low-grade and the red triangles denote high-grade gliomas). A very strong correlation between D and μ (A) (Pearson correlation coefficient $r = 0.930$; $P < .001$) and a weaker correlation between D and β (B) (Pearson correlation coefficient $r = 0.766$; $P < .001$) are illustrated. B, The dashed lines indicate the cutoff values for D (red), β (green), and the combination of D and β (black; linear equation: $\beta = 0.000497D + 0.798$).

Table 2: Cutoff, sensitivity, specificity, diagnostic accuracy, and asymptotic significance (P value) using D , β , μ , and a combination of D and β for differentiating low- (positive) from high-grade (negative) gliomas^a

	Cutoff	Sensitivity	Specificity	Accuracy	PPV	NPV	P Value
D	1.189	91.7%	63.3%	77.5%	66.7%	90.5%	<.001
β	0.797	87.5%	76.7%	82.1%	75.0%	88.5%	<.001
μ	7.969	79.2%	60.0%	69.6%	61.3%	78.3%	.0059
$D + \beta$	0.657	87.5%	76.7%	82.1%	75.0%	88.5%	<.001

Note:—PPV indicates positive predictive value; NPV, negative predictive value.

^a ROC analyses were used.

Kwee et al²⁷ recently studied high-grade gliomas by using an alternative non-Gaussian diffusion model based on a stretched-exponential formulism.²⁸ Although this model is similar to the FROC model, the stretched-exponential is developed empirically instead of using the fractionalized Fick diffusion equation. The heterogeneity index α in the stretched-exponential model resembles β in this study. The α value for high-grade gliomas was reported to be 0.58 ± 0.08 , which is lower than $\beta = 0.77 \pm 0.06$ in our study. This finding is most likely due to the different diffusion times (Δ) used in these studies.⁴⁵ Compared with the study of Kwee et al, our study produced a noticeably smaller SD in β because of the relatively large number of b-values used. Although a minimum of 4 b-values is needed to obtain the 3 FROC parameters, a larger number of b-values improves the robustness of the nonlinear fitting, particularly when the SNR is low.

Using all the patient data in this study, we observed a strong linear correlation between D and μ (Fig 5A). Be-

Table 3: AUC values of the ROC analyses with their 95% confidence intervals and standard errors using D , β , μ , and a combination of D and β for differentiating low- (positive) from high-grade (negative) gliomas

	AUC	95% CI of AUC ^a	SE ^b
D	0.781	0.647–0.882	0.0633
β	0.853	0.730–0.934	0.0511
μ	0.703	0.563–0.819	0.0736
$D + \beta$	0.853	0.730–0.934	0.0511

Note:—SE indicates standard error.

^a Binomial exact CIs.

^b SEs were computed by the method of DeLong et al⁴⁶ using MedCalc for Windows (MedCalc Software, Mariakerke, Belgium).

cause μ has been related to the dimension of free diffusion space,²⁶ the correlation in Fig 5A reflects the classic relationship between the diffusion rate and mean free length. β was less correlated with D or μ . This weaker correlation can be exploited to improve specificity and diagnostic accuracy because these 2 parameters act more independently. In this study, we have seen evidence suggesting that β is more dominant than D for differentiating low- from high-grade gliomas because the combination of β with D did not improve the performance compared with using β alone. This finding suggests the important role of tumor heterogeneity in various tumor grades.

Our study has several limitations. First, despite the improvement offered by the FROC model in glioma grading, the sensitivity, specificity, and diagnostic accuracy remain suboptimal. An extension of the FROC model to quantifying temporal heterogeneity, as demonstrated recently,^{42,43} suggests new opportunities to further improve the performance. These non-Gaussian diffusion imaging techniques may eventually help in complementing surgical biopsy in situations in which tissue biopsy is difficult or risky. Second, the number of patients enrolled in the study is moderate. As such, we did not attempt to further distinguishing glioma subtypes or individual grades. Finally, limited by the SNR, the highest b-value attempted in this study was 4000 s/mm², though an even higher b-value may further improve the reliability of extracting the FROC diffusion parameters.^{26,29,45}

CONCLUSIONS

We have demonstrated the feasibility of using high-b-value diffusion MR imaging with the FROC diffusion model to improve differentiation between low- and high-grade gliomas. In particular, the new parameter β offers a higher diagnostic accuracy than using the diffusion coefficient (D or ADC) alone and is the most useful and dominant parameter among the 3 FROC parameters for differentiating glioma grades. Although the focus of this study is on gliomas, the non-Gaussian diffusion imaging approach demonstrated herein is expected to have applications in other disease processes that involve tissue-heterogeneity changes.

ACKNOWLEDGMENTS

The authors are grateful to Drs Keith R. Thulborn, Kejia Cai, and Frederick C. Damen for helpful discussions.

Disclosures: Yi Sui—UNRELATED: Employment: GE Healthcare, Comments: joined GE Healthcare after the work was done. Xiaohong Joe Zhou—RELATED: Grant: National Institutes of Health grant No. 1S10RR028898*; UNRELATED: Consultancy: Horizon Medical Physics Services, Comments: consulting fees and ownership; Grants/Grants Pending: National Institutes of Health Grant No. 1R21EB023050–01,* AbbVie

Pharmaceuticals,* Comments: federal or industrial grant support; Royalties: Elsevier Publishing, Comments: royalty payment for a book I coauthored. *Money paid to the institution.

REFERENCES

- Ostrom QT, Gittleman H, Liao P, et al. CBTRUS statistical report: primary brain and central nervous system tumors diagnosed in the United States in 2007–2011. *Neuro Oncol* 2014;16(suppl 4):iv1–63 CrossRef Medline
- Omuro A, DeAngelis LM. Glioblastoma and other malignant gliomas: a clinical review. *JAMA* 2013;310:1842–50 CrossRef Medline
- Louis DN, Ohgaki H, Wiestler OD, et al. The 2007 WHO classification of tumours of the central nervous system. *Acta Neuropathol* 2007;114:97–109 Medline
- Upadhyay N, Waldman AD. Conventional MRI evaluation of gliomas. *Br J Radiol* 2011;84(Spec No 2):S107–11 CrossRef Medline
- Law M, Yang S, Wang H, et al. Glioma grading: sensitivity, specificity, and predictive values of perfusion MR imaging and proton MR spectroscopic imaging compared with conventional MR imaging. *AJNR Am J Neuroradiol* 2003;24:1989–98 Medline
- Poussaint TY, Rodríguez D. Advanced neuroimaging of pediatric brain tumors: MR diffusion, MR perfusion, and MR spectroscopy. *Neuroimaging Clin N Am* 2006;16:169–92, ix Medline
- Law M, Young RJ, Babb JS, et al. Gliomas: predicting time to progression or survival with cerebral blood volume measurements at dynamic susceptibility-weighted contrast-enhanced perfusion MR imaging. *Radiology* 2008;247:490–98 Medline
- Young GS, Setayesh K. Spin-echo echo-planar perfusion MR imaging in the differential diagnosis of solitary enhancing brain lesions: distinguishing solitary metastases from primary glioma. *AJNR Am J Neuroradiol* 2009;30:575–77 CrossRef Medline
- Hirai T, Murakami R, Nakamura H, et al. Prognostic value of perfusion MR imaging of high-grade astrocytomas: long-term follow-up study. *AJNR Am J Neuroradiol* 2008;29:1505–10 Medline
- Schneider JF, Confort-Gouny S, Viola A, et al. Multiparametric differentiation of posterior fossa tumors in children using diffusion-weighted imaging and short echo-time 1H-MR spectroscopy. *J Magn Reson Imaging* 2007;26:1390–98 Medline
- Ishimaru H, Morikawa M, Iwanaga S, et al. Differentiation between high-grade glioma and metastatic brain tumor using single-voxel proton MR spectroscopy. *Eur Radiol* 2001;11:1784–91 Medline
- Kang Y, Choi SH, Kim YJ, et al. Gliomas: histogram analysis of apparent diffusion coefficient maps with standard- or high-b-value diffusion-weighted MR imaging—correlation with tumor grade. *Radiology* 2011;261:882–90 CrossRef Medline
- Raab P, Hattingen E, Franz K, et al. Cerebral gliomas: diffusional kurtosis imaging analysis of microstructural differences. *Radiology* 2010;254:876–81 CrossRef Medline
- Rumboldt Z, Camacho DL, Lake D, et al. Apparent diffusion coefficients for differentiation of cerebellar tumors in children. *AJNR Am J Neuroradiol* 2006;27:1362–69 Medline
- Bian W, Khayal IS, Lupo JM, et al. Multiparametric characterization of grade 2 glioma subtypes using magnetic resonance spectroscopic, perfusion, and diffusion imaging. *Transl Oncol* 2009;2:271–80 Medline
- Maier SE, Sun Y, Mulkern RV. Diffusion imaging of brain tumors. *NMR Biomed* 2010;23:849–64 CrossRef Medline
- Yamasaki F, Kurisu K, Satoh K, et al. Apparent diffusion coefficient of human brain tumors at MR imaging. *Radiology* 2005;235:985–91 Medline
- Bull JG, Saunders DE, Clark CA. Discrimination of paediatric brain tumours using apparent diffusion coefficient histograms. *Eur Radiol* 2012;22:447–57 CrossRef Medline
- Poretti A, Meoded A, Huisman TA. Neuroimaging of pediatric posterior fossa tumors including review of the literature. *J Magn Reson Imaging* 2012;35:32–47 CrossRef Medline
- Porto L, Jurcoane A, Schwabe D, et al. Differentiation between high

- and low grade tumours in paediatric patients by using apparent diffusion coefficients. *Eur J Paediatr Neurol* 2013;17:302–07 CrossRef Medline
21. Le Bihan D. The ‘wet mind’: water and functional neuroimaging. *Phys Med Biol* 2007;52:R57–90 Medline
 22. Pfister S, Hartmann C, Korshunov A. Histology and molecular pathology of pediatric brain tumors. *J Child Neurol* 2009;24:1375–86 CrossRef Medline
 23. Gauvain KM, McKinsty RC, Mukherjee P, et al. Evaluating pediatric brain tumor cellularity with diffusion-tensor imaging. *AJR Am J Roentgenol* 2001;177:449–54 Medline
 24. Le Bihan D. Intravoxel incoherent motion perfusion MR imaging: a wake-up call. *Radiology* 2008;249:748–52 Medline
 25. Jensen JH, Helpert JA, Ramani A, et al. Diffusional kurtosis imaging: the quantification of non-Gaussian water diffusion by means of magnetic resonance imaging. *Magn Reson Med* 2005;53:1432–40 Medline
 26. Magin RL, Abdullah O, Baleanu D, et al. Anomalous diffusion expressed through fractional order differential operators in the Bloch-Torrey equation. *J Magn Reson* 2008;190:255–70 Medline
 27. Kwee TC, Galbán CJ, Tsien C, et al. Intravoxel water diffusion heterogeneity imaging of human high-grade gliomas. *NMR Biomed* 2010;23:179–87 CrossRef Medline
 28. Bennett KM, Schmainda KM, Bennett RT, et al. Characterization of continuously distributed cortical water diffusion rates with a stretched-exponential model. *Magn Reson Med* 2003;50:727–34 Medline
 29. Zhou XJ, Gao Q, Abdullah O, et al. Studies of anomalous diffusion in the human brain using fractional order calculus. *Magn Reson Med* 2010;63:562–69 CrossRef Medline
 30. Ozarslan E, Basser PJ, Shepherd TM, et al. Observation of anomalous diffusion in excised tissue by characterizing the diffusion-time dependence of the MR signal. *J Magn Reson* 2006;183:315–23 Medline
 31. Yablonskiy DA, Bretthorst GL, Ackerman JJ. Statistical model for diffusion attenuated MR signal. *Magn Reson Med* 2003;50:664–69 Medline
 32. Bar-Shir A, Cohen Y. High b-value q-space diffusion MRS of nerves: structural information and comparison with histological evidence. *NMR Biomed* 2008;21:165–74 Medline
 33. Sui Y, Wang H, Liu G, et al. Differentiation of low- and high-grade pediatric brain tumors with high b-value diffusion-weighted MR imaging and a fractional order calculus model. *Radiology* 2015;277:489–96 Medline
 34. Press WH, Teukolsky SA, Vetterling WT, et al. *Numerical Recipes 3rd Edition: The Art of Scientific Computing*. New York: Cambridge University Press; 2007:799–806
 35. Menard SW. *Applied Logistic Regression Analysis*. Thousand Oaks, California: Sage Publications; 2001:1–120
 36. Khayal IS, McKnight TR, McGue C, et al. Apparent diffusion coefficient and fractional anisotropy of newly diagnosed grade II gliomas. *NMR Biomed* 2009;22:449–55 CrossRef Medline
 37. Janiszewska M, Beca F, Polyak K. Tumor heterogeneity: the Lernaean hydra of oncology? *Oncology (Williston Park)* 2014;28:781–82, 784 Medline
 38. Burrell RA, McGranahan N, Bartek J, et al. The causes and consequences of genetic heterogeneity in cancer evolution. *Nature* 2013;501:338–45 CrossRef Medline
 39. Marusyk A, Almendro V, Polyak K. Intra-tumour heterogeneity: a looking glass for cancer? *Nat Rev Cancer* 2012;12:323–34 CrossRef Medline
 40. Grinberg F, Farrher E, Kaffanke J, et al. Non-Gaussian diffusion in human brain tissue at high b-factors as examined by a combined diffusion kurtosis and biexponential diffusion tensor analysis. *Neuroimage* 2011;57:1087–102 CrossRef Medline
 41. Magin RL, Akpa BS, Neuberger T, et al. Fractional order analysis of Sephadex gel structures: NMR measurements reflecting anomalous diffusion. *Commun Nonlinear Sci Numer Simul* 2011;16:4581–87 Medline
 42. Ingo C, Magin RL, Colon-Perez L, et al. On random walks and entropy in diffusion-weighted magnetic resonance imaging studies of neural tissue. *Magn Reson Med* 2014;71:617–27 CrossRef Medline
 43. Karaman MM, Sui Y, Wang H, et al. Differentiating low- and high-grade pediatric brain tumors using a continuous-time random-walk diffusion model at high b-values. *Magn Reson Med* 2015 Oct 31. [Epub ahead of print] CrossRef Medline
 44. Rosenblum MK. The 2007 WHO Classification of Nervous System Tumors: newly recognized members of the mixed glioneuronal group. *Brain Pathol* 2007;17:308–13 Medline
 45. Zhou XJ, Gao Q, Sirinivasan G, et al. Dependence of fractional order diffusion model parameters on diffusion time. In: *Procedures of the Annual Meeting of the International Society for Magnetic Resonance in Medicine*, Honolulu, Hawaii. April 18–24, 2009
 46. DeLong ER, DeLong DM, Clarke-Pearson DL. Comparing the areas under two or more correlated receiver operating characteristic curves: a nonparametric approach. *Biometrics* 1988;44:837–45 Medline

Antiangiogenic Effect of Bevacizumab: Application of Arterial Spin-Labeling Perfusion MR Imaging in a Rat Glioblastoma Model

T.J. Yun, H.R. Cho, S.H. Choi, H. Kim, J.-K. Won, S.-W. Park, J.-h. Kim, C.-H. Sohn, and M.H. Han



ABSTRACT

BACKGROUND AND PURPOSE: The usefulness of arterial spin-labeling for the evaluation of the effect of the antiangiogenic therapy has not been elucidated. Our aim was to evaluate the antiangiogenic effect of bevacizumab in a rat glioblastoma model based on arterial spin-labeling perfusion MR imaging.

MATERIALS AND METHODS: DSC and arterial spin-labeling perfusion MR imaging were performed by using a 9.4T MR imaging scanner in nude rats with glioblastoma. Rats were randomly assigned to the following 3 groups: control, 3-day treatment, and 10-day treatment after bevacizumab injection. One-way analysis of variance with a post hoc test was used to compare perfusion parameters (eg, normalized CBV and normalized CBF from DSC MR imaging and normalized CBF based on arterial spin-labeling) with microvessel area on histology. The Pearson correlations between perfusion parameters and microvessel area were also determined.

RESULTS: All of the normalized CBV from DSC, normalized CBF from DSC, normalized CBF from arterial spin-labeling, and microvessel area values showed significant decrease after treatment ($P < .001$, $P < .001$, $P = .005$, and $P < .001$, respectively). In addition, normalized CBV and normalized CBF from DSC and normalized CBF from arterial spin-labeling strongly correlated with microvessel area (correlation coefficient, $r = 0.911$, 0.869 , and 0.860 , respectively; $P < .001$ for all).

CONCLUSIONS: Normalized CBF based on arterial spin-labeling and normalized CBV and normalized CBF based on DSC have the potential for evaluating the effect of antiangiogenic therapy on glioblastomas treated with bevacizumab, with a strong correlation with microvessel area.

ABBREVIATIONS: ASL = arterial spin-labeling; GBM = glioblastoma; MVA = microvessel area; nCBF = normalized CBF; nCBV = normalized CBV; rCBF = relative CBF; rCBV = relative CBV

Glioblastoma (GBM) is the most common primary malignant brain tumor in adults. Surgical tumor resection followed by radiation therapy and concurrent chemotherapy with temozolomide is the current standard therapy for patients with GBM.¹ Despite multiple treatment approaches, however, the prognosis for patients with GBM is still extremely dismal.^{2,3}

GBMs are highly vascularized tumors and have been seen as attractive targets for antiangiogenic therapies.⁴ In particular, vascular endothelial growth factor has been identified as a critical

regulator of angiogenesis. Bevacizumab is a recombinant humanized monoclonal antibody that binds to human vascular endothelial growth factor and inhibits angiogenesis.^{5,6} It received accelerated FDA approval for treating recurrent GBM in the United States and many other countries and has become the standard of care for treating GBM.^{5,6}

DSC perfusion MR imaging can be used as a surrogate marker of perfusion to measure relative CBV (rCBV) and relative CBF (rCBF) of patients with GBM.⁷⁻¹⁰ DSC perfusion MR imaging has shown potential as an imaging biomarker to evaluate the antiangiogenic treatment in human patients with GBM.⁸⁻¹¹ Some re-

Received September 25, 2015; accepted after revision March 4, 2016.

From the Department of Radiology (T.J.Y., H.R.C., S.H.C., H.K., S.-W.P., J.-h.K., C.-H.S., M.H.H.), Seoul National University College of Medicine, Republic of Korea; Departments of Radiology (T.J.Y., H.R.C., S.H.C., H.K., J.-h.K., C.-H.S., M.H.H.), Pathology (J.-K.W.), and Neurosurgery (M.H.H.), Seoul National University Hospital, Seoul, Republic of Korea; and Department of Radiology (S.-W.P.), Seoul National University Boramae Medical Center, Seoul, Republic of Korea.

This study was supported by a grant from the National Research Foundation of Korea (NRF-2013RIA1A2008332), Seoul National University Hospital Research Fund (04-2012-1000), Seoul National University College of Medicine Research Fund (800-20140025), and the Institute for Basic Science (IBS-R006-D1) in Korea.

Please address correspondence to Seung Hong Choi, MD, PhD, Department of Radiology, Seoul National University College of Medicine, 28, Yongon-dong, Chongno-gu, Seoul, 110-744, Korea; e-mail: choiseunghong@gmail.com

Indicates open access to non-subscribers at www.ajnr.org

indicates article with supplemental on-line tables.

Indicates article with supplemental on-line photo.

<http://dx.doi.org/10.3174/ajnr.A4800>

searchers have investigated the change in rCBV or rCBF in animal GBM models and found significant reduction in animals treated with bevacizumab compared with controls.^{12,13} However, the correlation between perfusion parameters based on DSC perfusion MR imaging and microvascular environment in histologic specimens in subjects treated with antiangiogenic therapy has not been elucidated, to our knowledge.

Arterial spin-labeling (ASL) is a promising perfusion MR imaging technique without using exogenous gadolinium-based contrast agent for CBF quantification, in which the spin population in arterial water magnetically labeled by inversion is used as an endogenous diffusible tracer.^{14,15} Recently, it has been suggested that ASL has the potential to evaluate the response to antiangiogenic therapy in patients with recurrent GBM receiving bevacizumab.¹⁶

Therefore, the objective of this study was to evaluate the antiangiogenic effect of bevacizumab in a rat GBM model based on ASL perfusion MR imaging relative to a more established technique based on DSC perfusion MR imaging with histopathology.

MATERIALS AND METHODS

Tumor Cell Line

Human glioma cells U87 (ATCC, Rockville, Maryland) were cultured at 37°C in a humidified CO₂ incubator in RPMI 1640 Medium (Sigma Aldrich, St. Louis, Missouri), supplemented with 10% fetal bovine serum.

Animal Model

This study was approved by the Institutional Animal Care and Use Committee in Seoul National University Hospital (#12-0238-C1A0) and was performed in accordance with institutional guidelines. Nude athymic rats (200–250 g; Koatec, Gyeonggi-do, Korea) were anesthetized by intraperitoneal injection of a mixture of zolazepam and xylazine, and they were placed in a stereotaxic device. A burr-hole (2-mm-wide) was made on the right side 3 mm lateral to the midline and 2 mm proximal to the bregma by using a dental drill. Nude rats were inoculated with U87 glioma cells (3×10^6 cells per 3 μ L of serum-free RPMI Medium) in the right caudate-putamen region. Cells were injected into the brain by using a Hamilton syringe (Sigma Aldrich) fitted with a 28-gauge needle positioned with a syringe attachment fitted to the stereotaxic device. With stereotaxic guidance, 0, 1.4, and 3.0 mm were used in areas posterior, lateral, and dorsal to the bregma in the right caudate-putamen, respectively.

Tumor growth was verified by MR imaging at 2 weeks after implantation. Animals were randomly assigned to a control group ($n = 4$), 3-day treatment group ($n = 6$), and 10-day treatment group ($n = 4$). Control animals were sacrificed for brain harvest right after the first MR imaging. For the 3- and 10-day treatment groups, bevacizumab was administered intraperitoneally at 20 mg/kg in saline right after the first MR imaging.¹⁷ After 3 days, animals underwent the second MR imaging. Animals in the 3-day treatment group were sacrificed right after the second MR imaging. At 7 days after the second MR imaging, animals in the 10-day treatment group underwent the third MR imaging. They were sacrificed right after the third MR imaging. In addition, to exclude the possible effect of the tumor-volume change on the perfusion

parameters, DSC perfusion MR imaging was performed at 0, 3, and 10 days in 4 rats in whom bevacizumab was not injected (10-day-without-treatment group).

The *in vivo* experimental design of the present study is shown in Fig 1.

MR Imaging Acquisition

All MR image acquisitions were performed by 2 authors (H.K. with >10 years' experience in neuroimaging and T.J.Y. with >10 years' experience in neuroradiology) by using a 9.4T MR imaging scanner (Agilent 9.4T/160AS; Agilent Technologies, Santa Clara, California). A volume coil for radiofrequency transmission and a phased array 4-channel surface coil for signal reception (Agilent Technologies) were used for the control, 3-day treatment, and 10-day treatment groups; a single-channel surface coil was used for radiofrequency transmission; and a signal reception (loop coil) (Agilent Technologies) was used for the 10-day-without-treatment group.

Before MR imaging, animals were anesthetized with 1.5% isoflurane in room air and placed inside a magnet. Animals were physiologically monitored throughout the MR imaging experiments. To avoid potential changes in cerebral blood perfusion during data collection, we carefully maintained their respiration at ~ 40 beats per minute.

Following the acquisition of routine scout images in all 3 orthogonal directions, an automatic shimming procedure was performed. Unenhanced anatomic T2-weighted images were collected by using a fast spin-echo sequence with the following parameters: TR/TE_{eff}, 2000/45 ms; FOV, 33×35 mm²; matrix size, 256×256 ; echo-train length, 4; 15 sections without gap; section thickness, 1 mm; 1 signal average; 2 dummy scans; and receiver bandwidth, 100 kHz.

For perfusion data acquisitions by using the ASL technique, an amplitude-modulated pseudocontinuous arterial spin-labeling sequence was used with a single-shot spin-echo echo-planar imaging readout (mCASL; Agilent Technologies).¹⁸ Vascular and fat-suppression modules were also used with a labeling pulse duration of 3 seconds. Postlabeling delay and the gap between the labeling plane and the central imaging plane were 300 and 20 mm, respectively. Other sequence parameters were the following: TR/TE, 4000/28 ms; FOV, 33×35 mm²; matrix size, 64×64 ; 3 sections; section thickness, 2 mm; bandwidth, 250 kHz; 60 repetitions for labeled and control data. For quantitative analysis of cerebral blood perfusion, T1 mapping was performed by using a fat-suppressed, single-shot, inversion-recovery spin-echo echo-planar imaging sequence with TR, 8000 ms and TIs of 15, 35, 80, 200, 450, 1000, 2300, or 5400 ms. The rest of the sequence parameters were identical to those used for pseudocontinuous ASL data acquisition.¹⁸ The typical total scan time of ASL was ~ 10 minutes.

Finally, DSC images were acquired from the same imaging planes as used for the pseudocontinuous ASL experiments by using a gradient-echo pulse sequence. The sequence parameters were the following: TR/TE, 25/5 ms; flip angle, 10°; matrix size, 128×96 ; 4 signal averages; bandwidth, 100 kHz; 70 repetitions. After an initial 30-second baseline acquisition, a bolus of gadoterate meglumine (0.1 mmol per kilogram of body weight; Dotarem; Guerbet, Aulnay-sous-Bois, France) was administered to the

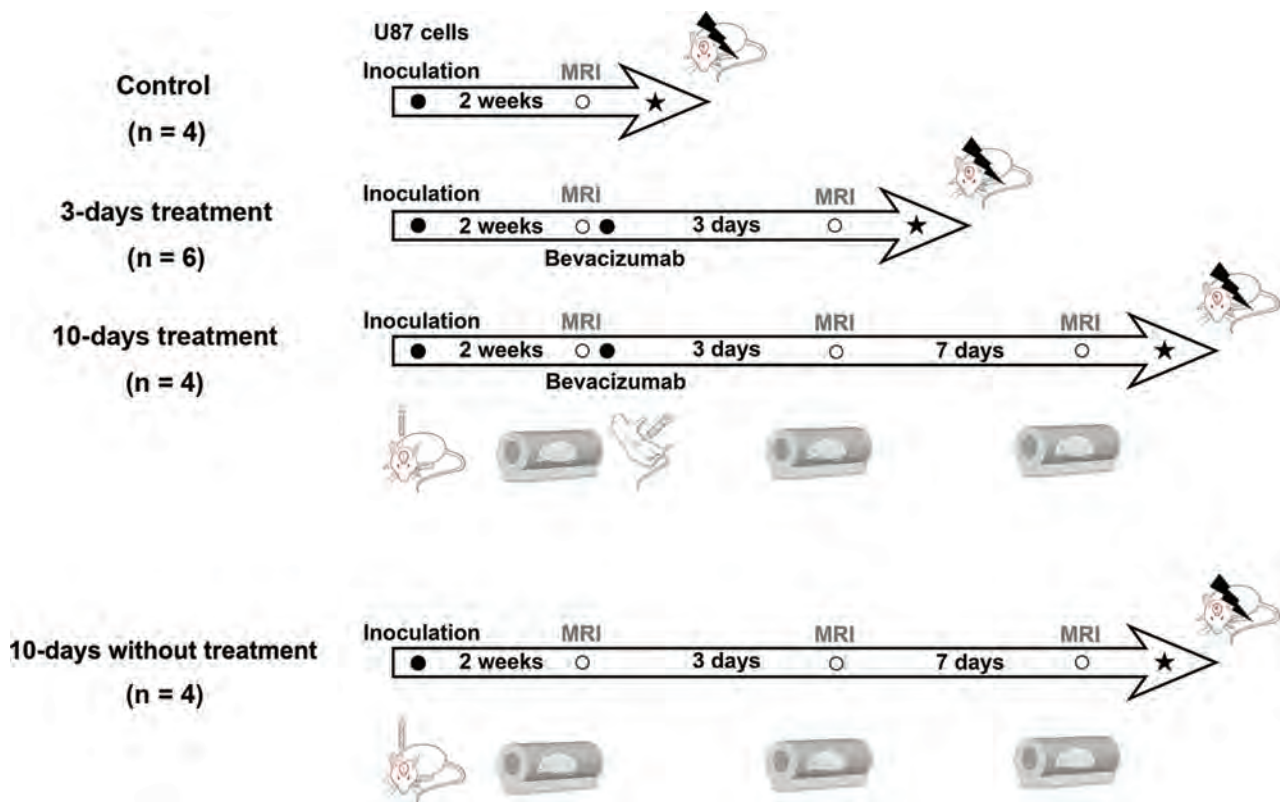


FIG 1. Experimental design showing the timeline of each group for U87 glioma cell inoculation, bevacizumab therapy, MR imaging, and sacrifice for brain harvest.

animals via a tail vein catheter by using a syringe pump (1 mL/min; Harvard Apparatus, Holliston, Massachusetts), which was immediately followed by a 1-mL saline flush. The typical total scan time of DSC was ~ 11 minutes.

MR Imaging Data Analysis

All pseudocontinuous ASL images were analyzed by using Matlab (MathWorks, Natick, Massachusetts). CBF maps were derived according to previous reports.^{18,19} A 3-parameter fit was used for estimating T1 maps. Once T1 maps and control and labeled images were obtained, tissue blood flow images were formed according to the following formula: $CBF = (\lambda / T1) \times (S_{\text{control}} - S_{\text{label}}) / (2\alpha \times S_{\text{control}})$, where $\lambda = 0.9$ was the tissue/blood partition coefficient for water,¹⁹ S_{control} was the control image signal intensity, S_{label} was the labeled image signal intensity, T1 was the T1 map, and α was 0.63 as the degree of labeling efficiency.¹⁸

For DSC perfusion MR imaging, additional preprocessing was performed by using commercial software (nordicICE; Nordic-NeuroLab, Bergen, Norway), in which T2WIs were used for structural imaging. rCBV maps were generated by using established tracer kinetic models applied to first-pass data.^{20,21} To reduce the effect of recirculation, we fitted $\Delta R2^* (1/T2^*)$ curves to the γ -variate function, which was an approximation of the first-pass response as it would appear in the absence of recirculation or leakage. The dynamic curves were mathematically corrected to reduce contrast agent leakage effects.²²

T2WI, rCBV, and rCBF maps based on DSC, and CBF maps based on ASL were analyzed by using a commercial PACS console. One investigator (T.J.Y. with >10 years' experience in neuroradi-

ology) who was blinded to the experimental data drew ROIs containing the entire tumor in the plane in which the tumor area was the largest. Tumor boundaries were defined with reference to high-signal-intensity areas thought to represent tumor tissue on the T2WI. ROIs were copied and placed on coregistered rCBV and rCBF maps based on the DSC and CBF maps from ASL. The mean rCBV and mean rCBF of each tumor were measured on rCBV and rCBF maps. The mean rCBV and mean rCBF of the contralateral hemispheres were also measured as reference values for perfusion parameters. Normalized CBV (nCBV) and normalized CBF (nCBF) were derived by using the following formulas: $nCBV = rCBV_{\text{tumor}} / rCBV_{\text{reference}}$ and $nCBF = rCBF_{\text{tumor}} / rCBF_{\text{reference}}$ (On-line Fig 1).

Histologic Analysis

All rats were euthanized in a CO₂ chamber soon after MR imaging. Coronal sections sampled across the center of the tumors were fixed in 10% buffered formaldehyde solution and paraffin-embedded. Coronal paraffin sections were used for histologic hematoxylin-eosin staining and immunohistochemical analysis. Histologic evaluation was performed by a pathologist (J.-K.W. with >10 years' experience in neuropathology) by using a standard light microscope. Microvessel area (MVA) was determined on the basis of CD34 immunostains. Briefly, areas with the highest microvascular attenuation on CD34-stained sections were identified around the center of the tumor at scanning power. After that, MVAs consisting of endothelial area and vessel lumen were quantified with a higher power ($\times 200$ field) in the selected area.

Table 1: Comparison of volume and perfusion parameters based on DSC and ASL MR imaging in all tumors^a

Variables	0 Days (n = 14)	3 Days (n = 10)	10 Days (n = 4)	Paired t Test			Unpaired t Test		
				P Value ^b	P Value ^c	P Value ^d	P Value ^b	P Value ^c	P Value ^d
Volume (mm ³)	40.0 (32.3–61.8)	91.9 (53.9–124.1)	203.7 (103.0–301.3)	.015	.200	.117	.002	.090	.086
nCBV _{DSC}	5.9 (5.7–6.3)	2.7 (2.4–2.9)	0.8 (0.6–1.4)	<.001	.004	<.001	<.001	.002	.005
nCBF _{DSC}	3.7 (3.2–4.0)	1.8 (1.4–2.2)	0.7 (0.6–1.0)	<.001	.020	<.001	<.001	.075	.004
nCBF _{ASL}	1.7 (1.2–2.0)	0.3 (0.2–0.5)	0.1 (0.1–0.1)	<.001	.041	<.001	.004	.029	.050

Note:—nCBV_{DSC} indicates nCBV based on DSC; nCBF_{DSC}, nCBF based on DSC; nCBF_{ASL}, nCBF based on ASL.

^a Values are presented as medians (interquartile range, range from the 25th to the 75th percentile).

^b Results between 0 and 3 days.

^c Results between 3 and 10 days.

^d Results between 0 and 10 days.

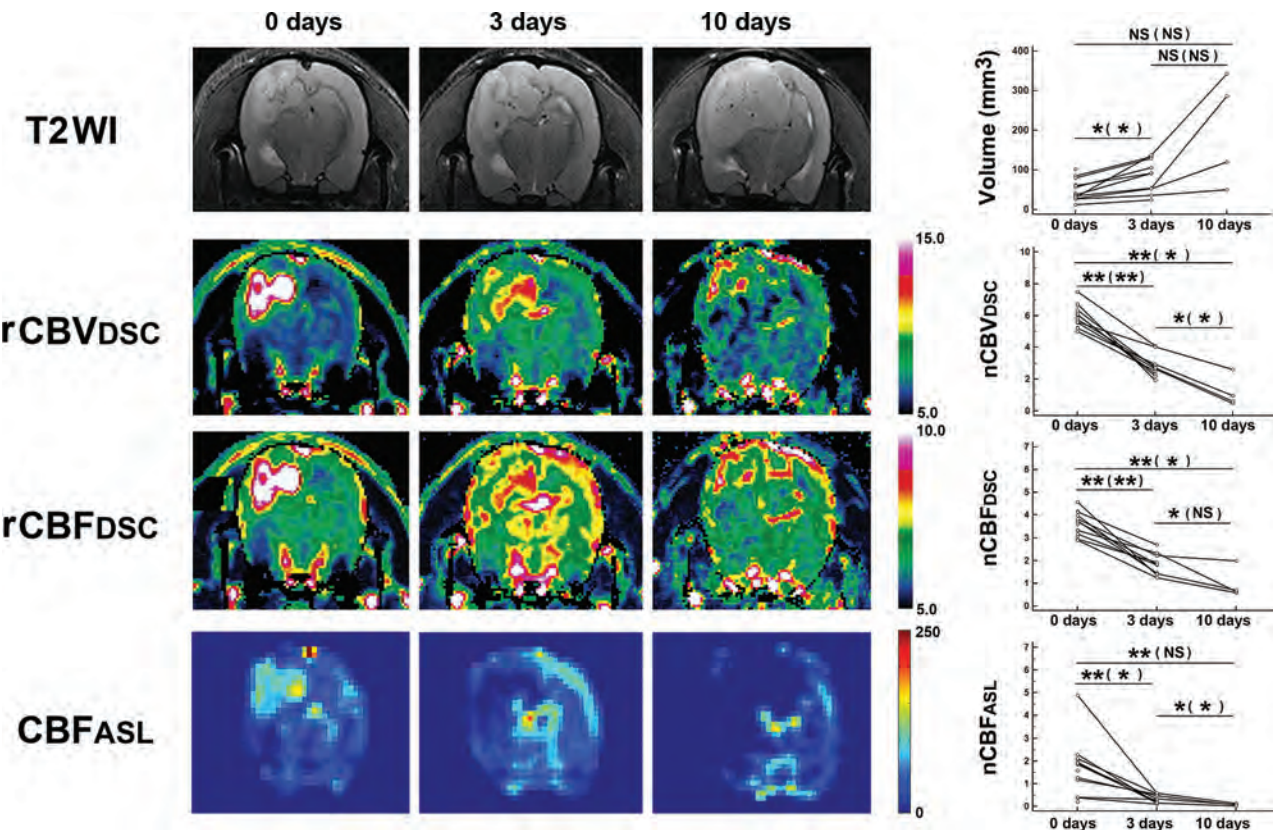


FIG 2. Quantification of tumor volume and perfusion parameters in all tumors. T2WI and perfusion maps were acquired from a rat belonging to the 10-day treatment group. Serial reductions in rCBV and rCBF based on DSC and CBF based on ASL are shown. Graphs in the right column show serial changes of tumor volume and perfusion parameters in all tumors. Scale units of rCBV_{DSC}, rCBF_{DSC}, and CBF_{ASL} are milliliters $\times 100 \text{ g}^{-1}$, milliliters $\times 100 \text{ g}^{-1} \times \text{min}^{-1}$, and milliliters $\times 100 \text{ g}^{-1} \times \text{min}^{-1}$, respectively. Data are mean results from paired *t* tests (unpaired *t* tests). One asterisk indicates $P < .05$; 2 asterisks, $P < .001$; NS, not significant; nCBV_{DSC}, nCBV based on DSC; nCBF_{DSC}, nCBF based on DSC; nCBF_{ASL}, nCBF based on ASL.

Results were expressed as the ratio of the area of microvessel to the total area of analysis within any single $\times 200$ microscopic field.

Statistical Analysis

Paired and unpaired *t* tests were used to compare parameters on perfusion MR imaging and MVA on histology within subjects and between groups. For tumors for which histology was available, 1-way analysis of variance with a Scheffe post hoc test was used to analyze differences. Pearson correlation analysis was performed to determine the correlation among perfusion parameters of perfusion MR imaging and MVA. Statistical analysis was performed with the commercially available software: SPSS (Version 12.0 for Windows; IBM, Armonk, New York) and MedCalc for Windows

(Version 9.3.0.0; MedCalc Software, Mariakerke, Belgium). Statistical significance was $P < .05$.

RESULTS

Analysis of Tumor Volume and Perfusion Parameters based on DSC or ASL Perfusion MR Imaging in All Tumors

The changes of tumor volume and perfusion parameters in all tumors before and after bevacizumab treatment are summarized in On-line Table 1 and Table 1. In addition, representative images are shown in Fig 2.

After bevacizumab treatment, a tendency of consistent increase in tumor volume was revealed on an unpaired *t* test ($P < .1$).

The nCBV of tumors based on DSC showed significant serial

Table 2: Comparison and correlation of perfusion parameters based on DSC and ASL MR imaging with MVA in tumors with available histology^a

Variables	Control (n = 4)	3-Day Treatment (n = 6)	10-Day Treatment (n = 4)	P Value ^b	Different Groups ^c
Volume (mm ³)	51.9 (40.8–72.1)	99.7 (91.8–124.1)	203.7 (103.0–301.3)	0.066	
nCBV _{DSC}	6.0 (5.7–6.3)	2.4 (2.2–2.7)	0.8 (0.6–1.4)	<.001	(Control) (3 days) (3 days) (10 days) (Control) (10 days)
nCBF _{DSC}	3.5 (3.3–3.7)	1.8 (1.5–1.9)	0.7 (0.6–1.0)	<.001	(Control) (3 days) (Control) (10 days)
nCBF _{ASL}	1.4 (1.0–1.7)	0.3 (0.2–0.5)	0.1 (0.1–0.1)	0.005	(Control) (3 days) (Control) (10 days)
MVA (×10 ⁻²)	7.5 (6.9–7.9)	2.8 (2.3–3.3)	2.4 (1.9–2.9)	<.001	(Control) (3 days) (Control) (10 days)

^a Values are presented as medians (interquartile range, range from the 25th to the 75th percentile).

^b Results from 1-way analyses of variances.

^c Results from Scheffe post hoc multiple comparisons.

decrease in values after treatment ($P < .05$). In addition, the nCBF values based on DSC also showed significant serial decreases in values ($P < .05$) after treatment, except the results from the unpaired t test between 3 and 10 days ($P = .075$).

The nCBF values based on ASL showed significant serial decreases ($P < .05$) after treatment, except the results from the unpaired t test between 0 and 10 days ($P = .050$).

Analysis of Tumor Volume and Perfusion Parameters based on DSC and ASL Perfusion MR Imaging and MVA in Tumors with Available Histology

Comparison and correlation of tumor volume and perfusion parameters from DSC and ASL perfusion MR imaging and MVA in tumors with available histology are summarized in Table 2. In addition, representative images are shown in Fig 3.

There was a tendency toward an increase in tumor volume with $P < .1$ ($P = .066$).

All the nCBV from DSC, nCBF from DSC, nCBF from ASL, and MVA values showed significant decreases after treatment ($P < .001$, $P < .001$, $P = .005$, and $P < .001$, respectively). The Scheffe post hoc multiple comparisons revealed significant ($P < .05$) differences, except between the 3- and the 10-day treatment groups for nCBF from DSC, nCBF from ASL, and MVA values.

The nCBV and nCBF based on DSC and nCBF based on ASL significantly correlated with MVA (correlation coefficient, $r = 0.911$, 0.869 , and 0.860 , respectively; $P < .001$ for all). nCBF from ASL perfusion MR imaging also had a positive and significant correlation with nCBF and nCBV based on DSC MR imaging ($r = 0.8298$ and 0.789 , respectively; $P < .001$ for both) (On-line Fig 2). However, nCBF (median [interquartile range], 0.2 [0.1 – 0.6]) measured on ASL perfusion MR imaging was significantly less than nCBF (1.9 [1.4 – 3.0]) based on DSC MR imaging ($P < .001$).

Analysis of Tumor Volume and Perfusion Parameters based on DSC in the 10-Days-without-Treatment Group

The changes of tumor volume and perfusion parameters in tumors without antiangiogenic treatment are summarized in On-line Table 2.

At 10 days after the first MR imaging, the volume of tumors increased with significant differences between any days (P values between 0 and 3 days, 3 and 10 days, and 0 and 10 days, $.041$, $.013$, and $<.001$, respectively).

The nCBV of tumors in the 10-day group was significantly higher than that in the 0-day group (P values between 0 and 3 days, 3 and 10 days, and 0 and 10 days, $.034$, $.067$, and $.040$, re-

spectively). The nCBF of tumors in the 10-day group was not significantly higher than that in the 0-day group (P values between 0 and 3 days, 3 and 10 days, and 0 and 10 days, $.156$, $.055$, and $.070$, respectively) (On-line Fig 3).

DISCUSSION

In the present study, we assessed the changes of perfusion parameters in the GBM rat model treated with the antiangiogenic agent bevacizumab based on DSC and ASL perfusion MR imaging. We found that perfusion parameters based on ASL and DSC perfusion MR imaging decreased after antiangiogenic treatment, which correlated well with histopathology results such as MVA.

Because bevacizumab has been reported to have an antiangiogenic effect in GBM and is approved as a treatment agent either alone or in combination with chemotherapy,^{5,23} the potential of perfusion MR imaging to precisely characterize the microvascular environment is clinically relevant. However, it was unclear whether perfusion MR imaging can be applied as an imaging biomarker to quantify the microvascular environment mainly due to significant intra- and intertumoral biologic heterogeneity of GBM. Although some researchers have investigated the potential of DSC perfusion MR imaging in GBMs treated with bevacizumab in animal models,^{12,24} direct correlation between perfusion parameters and histologic features was not elucidated. In terms of the ASL perfusion MR imaging technique, a previous report has suggested the potential of using ASL perfusion MR imaging to evaluate the response to antiangiogenic therapy in a patient with recurrent GBM who received bevacizumab.¹⁶ However, additional investigation in human studies or animal models has not been elucidated, to our knowledge.

According to our results, nCBV and nCBF values based on DSC showed significant serial reduction after bevacizumab treatment with a strong correlation with MVA in histology. Thus, they have the potential as imaging biomarkers to evaluate the antiangiogenic effect in GBM treated with bevacizumab. In addition, our results revealed that nCBF values based on the ASL technique have significant serial reduction after bevacizumab treatment with a strong correlation with MVA.

The measurement of hemodynamic parameters such as CBV and CBF based on DSC perfusion MR imaging can be compromised by elevated vascular permeability and leakage of contrast agent, both of which can be heavily influenced by the biologic changes in GBM under treatment.²⁵ However, the ASL perfusion MR imaging technique uses endogenous contrast agents without the need to inject contrast agent. Therefore, the ASL perfusion

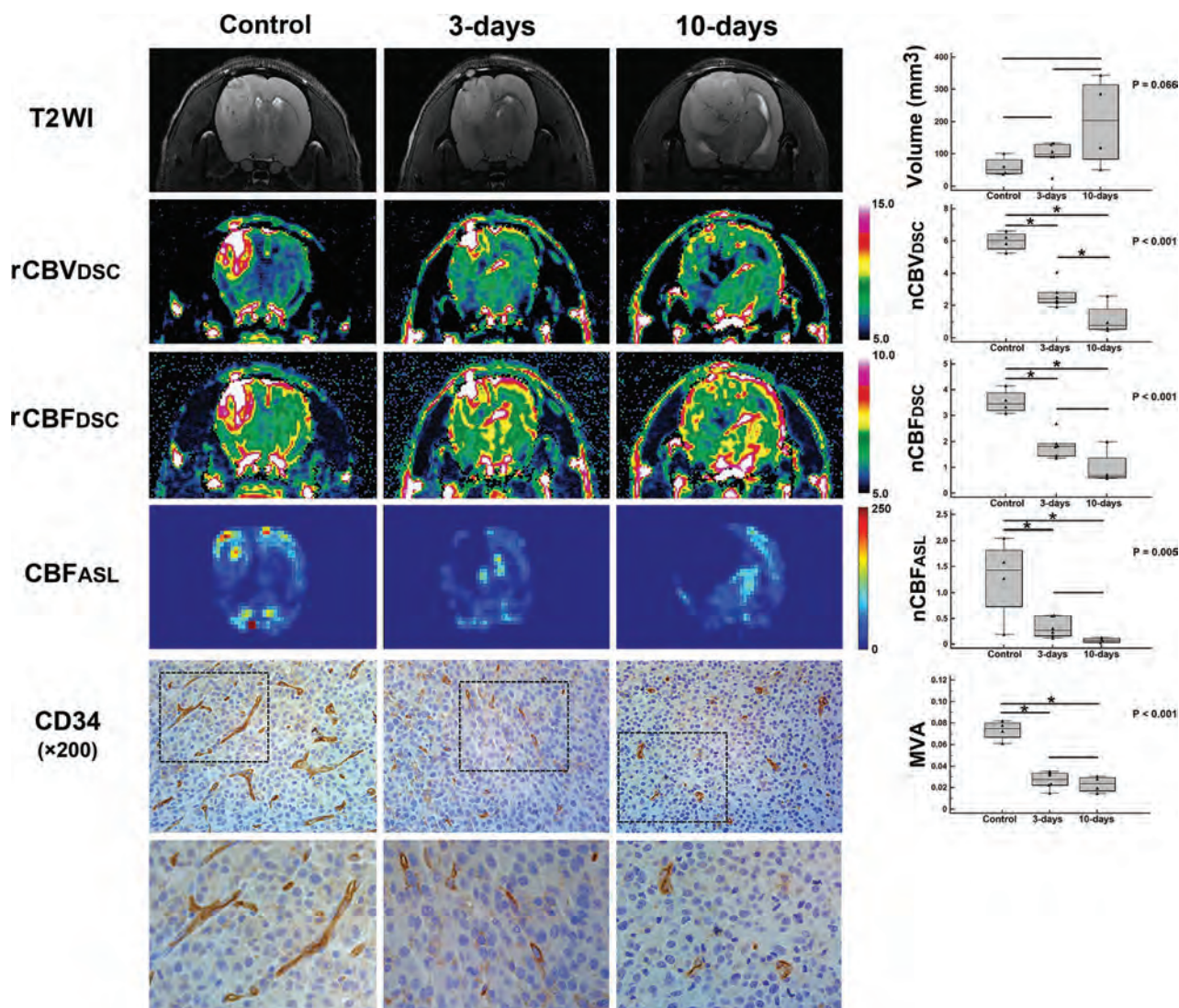


FIG 3. Quantification of tumor volume, perfusion parameters, and MVA in tumors with available histology. T2WI and perfusion maps were acquired from rats in the control group, 3-day treatment group, or 10-day treatment group. Differences in rCBV and rCBF based on DSC, CBF based on ASL, and MVA are shown. Graphs in the right column show differences in the tumor volume and hemodynamic parameters and MVA. In the lower images, the tumors stained immunohistochemically with anti-CD34 show positive brown cytoplasmic staining of the endothelial area and vessel lumen. Scale units of rCBV_{DSC}, rCBF_{DSC}, and CBF_{ASL} are milliliters $\times 100 \text{ g}^{-1}$, milliliters $\times 100 \text{ g}^{-1} \times \text{min}^{-1}$, and milliliters $\times 100 \text{ g}^{-1} \times \text{min}^{-1}$, respectively. *P* values were based on 1-way analyses of variances. One asterisk indicates a significant ($P < .05$) difference from the Scheffe post hoc multiple comparisons.

MR imaging technique might overcome the drawbacks of DSC perfusion MR imaging. In addition, ASL perfusion MR imaging techniques can make it feasible to characterize the microvascular environment and to evaluate the antiangiogenic effect against GBM in patients who have contraindications to contrast agent administration.

However, nCBF values based on ASL perfusion MR imaging had a significantly lower value compared with those based on DSC. Leakage of contrast agent on DSC and insufficient labeling efficacy due to unestablished postlabeling decay time in animal models may contribute to the difference in nCBF values based on DSC and ASL. Because the appropriate postlabeling decay time has been established for brain imaging in humans, such discrepancies may be minimized in the application of ASL perfusion MR imaging for human GBM. Even though nCBV values based on DSC perfusion MR imaging had significant differences in animals

between the 3-day and 10-day-treatment groups, no significant difference in the MVA values was found between the 2 groups. Therefore, perfusion parameters based on DSC perfusion MR imaging might have been influenced by other factors related to the antiangiogenic mechanism beyond MVA.

Most interesting, the present study revealed a tendency of consistent increase in tumor volume despite reduced nCBV and nCBF values ($P < 0.1$). Although we used 20 mg/kg of bevacizumab in this study based on a previous report that investigated its dose-dependent effect on GBM blood vessels,¹⁷ the tumor volume showed a serial increase in all tumors (even though the growth rate seems to be lower than that in the 10-day-without-treatment group). Our result is consistent with those in previous reports,^{12,17} suggesting a possible insufficient effect of antiangiogenic therapy on tumor proliferation and/or a possible evasion mechanism against the antiangiogenic drug in GBM.

CONCLUSIONS

We demonstrated that CBF values based on ASL and CBV and CBF values based on DSC have good performance for evaluating antiangiogenic therapy, with strong correlations with MVA in a rat GBM model. ASL perfusion MR imaging has the potential to be used as a noninvasive imaging biomarker to monitor the effect of antiangiogenic therapy for GBM.

Disclosures: Tae Jin Yun, Seung Hong Choi—RELATED: Grant: government fund.* Moon Hee Han—UNRELATED: Consultancy: MicroVenton. *Money paid to the institution.

REFERENCES

1. Stupp R, Mason WP, van den Bent MJ, et al; European Organisation for Research and Treatment of Cancer Brain Tumor and Radiotherapy Groups, National Cancer Institute of Canada Clinical Trials Group. **Radiotherapy plus concomitant and adjuvant temozolomide for glioblastoma.** *N Engl J Med* 2005;352:987–96 CrossRef Medline
2. Erpolat OP, Akmansu M, Goksel F, et al. **Outcome of newly diagnosed glioblastoma patients treated by radiotherapy plus concomitant and adjuvant temozolomide: a long-term analysis.** *Tumori* 2009;95:191–97 Medline
3. Jeon HJ, Kong DS, Park KB, et al. **Clinical outcome of concomitant chemoradiotherapy followed by adjuvant temozolomide therapy for glioblastomas: single-center experience.** *Clin Neurol Neurosurg* 2009;111:679–82 CrossRef Medline
4. Jain RK, di Tomaso E, Duda DG, et al. **Angiogenesis in brain tumours.** *Nat Rev Neurosci* 2007;8:610–22 CrossRef Medline
5. Friedman HS, Prados MD, Wen PY, et al. **Bevacizumab alone and in combination with irinotecan in recurrent glioblastoma.** *J Clin Oncol* 2009;27:4733–40 CrossRef Medline
6. Kreisl TN, Kim L, Moore K, et al. **Phase II trial of single-agent bevacizumab followed by bevacizumab plus irinotecan at tumor progression in recurrent glioblastoma.** *J Clin Oncol* 2009;27:740–45 CrossRef Medline
7. Artzi M, Blumenthal DT, Bokstein F, et al. **Classification of tumor area using combined DCE and DSC MRI in patients with glioblastoma.** *J Neurooncol* 2015;121:349–57 CrossRef Medline
8. Harris RJ, Cloughesy TF, Hardy AJ, et al. **MRI perfusion measurements calculated using advanced deconvolution techniques predict survival in recurrent glioblastoma treated with bevacizumab.** *J Neurooncol* 2015;122:497–505 CrossRef Medline
9. Schmainda KM, Prah M, Connelly J, et al. **Dynamic-susceptibility contrast agent MRI measures of relative cerebral blood volume predict response to bevacizumab in recurrent high-grade glioma.** *Neuro Oncol* 2014;16:880–88 CrossRef Medline
10. Stadlbauer A, Pichler P, Karl M, et al. **Quantification of serial changes in cerebral blood volume and metabolism in patients with recurrent glioblastoma undergoing antiangiogenic therapy.** *Eur J Radiol* 2015;84:1128–36 CrossRef Medline
11. Sawlani RN, Raizer J, Horowitz SW, et al. **Glioblastoma: a method for predicting response to antiangiogenic chemotherapy by using MR perfusion imaging—pilot study.** *Radiology* 2010;255:622–28 CrossRef Medline
12. Jalali S, Chung C, Foltz W, et al. **MRI biomarkers identify the differential response of glioblastoma multiforme to anti-angiogenic therapy.** *Neuro Oncol* 2014;16:868–79 CrossRef Medline
13. Keunen O, Johansson M, Oudin A, et al. **Anti-VEGF treatment reduces blood supply and increases tumor cell invasion in glioblastoma.** *Proc Natl Acad Sci U S A* 2011;108:3749–54 CrossRef Medline
14. Detre JA, Alsop DC. **Perfusion magnetic resonance imaging with continuous arterial spin labeling: methods and clinical applications in the central nervous system.** *Eur J Radiol* 1999;30:115–24 CrossRef Medline
15. Detre JA, Leigh JS, Williams DS, et al. **Perfusion imaging.** *Magn Reson Med* 1992;23:37–45 CrossRef Medline
16. Fellah S, Girard N, Chinot O, et al. **Early evaluation of tumoral response to antiangiogenic therapy by arterial spin labeling perfusion magnetic resonance imaging and susceptibility weighted imaging in a patient with recurrent glioblastoma receiving bevacizumab.** *J Clin Oncol* 2011;29:e308–11 CrossRef Medline
17. von Baumgarten L, Brucker D, Tirniceru A, et al. **Bevacizumab has differential and dose-dependent effects on glioma blood vessels and tumor cells.** *Clin Cancer Res* 2011;17:6192–205 CrossRef Medline
18. Utting JF, Thomas DL, Gadian DG, et al. **Understanding and optimizing the amplitude modulated control for multiple-slice continuous arterial spin labeling.** *Magnetic Reson Med* 2005;54:594–604 CrossRef Medline
19. Silva AC, Kim SG, Garwood M. **Imaging blood flow in brain tumors using arterial spin labeling.** *Magnetic Reson Med* 2000;44:169–73 Medline
20. Maeda M, Itoh S, Kimura H, et al. **Tumor vascularity in the brain: evaluation with dynamic susceptibility-contrast MR imaging.** *Radiology* 1993;189:233–38 CrossRef Medline
21. Rollin N, Guyotat J, Streichenberger N, et al. **Clinical relevance of diffusion and perfusion magnetic resonance imaging in assessing intra-axial brain tumors.** *Neuroradiology* 2006;48:150–59 CrossRef Medline
22. Aronen HJ, Gazit IE, Louis DN, et al. **Cerebral blood volume maps of gliomas: comparison with tumor grade and histologic findings.** *Radiology* 1994;191:41–51 CrossRef Medline
23. Vredenburgh JJ, Desjardins A, Herndon JE 2nd, et al. **Phase II trial of bevacizumab and irinotecan in recurrent malignant glioma.** *Clin Cancer Res* 2007;13:1253–59 CrossRef Medline
24. Keunen O, Taxt T, Gruner R, et al. **Multimodal imaging of gliomas in the context of evolving cellular and molecular therapies.** *Adv Drug Deliv Rev* 2014;76:98–115 CrossRef Medline
25. Essig M, Shiroishi MS, Nguyen TB, et al. **Perfusion MRI: the five most frequently asked technical questions.** *AJR Am J Roentgenol* 2013;200:24–34 CrossRef Medline

Nonaneurysmal Perimesencephalic Hemorrhage Is Associated with Deep Cerebral Venous Drainage Anomalies: A Systematic Literature Review and Meta-Analysis

 A. Rouchaud,  V.T. Lehman,  M.H. Murad,  A. Burrows,  H.J. Cloft,  E.P. Lindell,  D.F. Kallmes, and  W. Brinjikji



ABSTRACT

BACKGROUND AND PURPOSE: Mechanisms underlying bleeding in nonaneurysmal perimesencephalic SAH remain unclear. Previous investigators have suggested a relationship between nonaneurysmal perimesencephalic SAH and primitive venous drainage of the basal vein of Rosenthal. We performed a meta-analysis to evaluate the relation between primitive basal vein of Rosenthal drainage and nonaneurysmal perimesencephalic SAH.

MATERIALS AND METHODS: We performed a comprehensive literature search of all studies examining the prevalence of primitive basal vein of Rosenthal drainage in patients with aneurysmal SAH and nonaneurysmal perimesencephalic SAH. Data collected were primitive basal vein of Rosenthal drainage (direct connection of perimesencephalic veins into the dural sinuses instead of the Galenic system) in at least 1 cerebral hemisphere, normal bilateral basal vein of Rosenthal drainage systems, and the number of overall primitive venous systems in the nonaneurysmal perimesencephalic SAH and aneurysmal SAH groups. Statistical analysis was performed by using a random-effects meta-analysis.

RESULTS: Eight studies with 888 patients (334 with nonaneurysmal perimesencephalic SAH and 554 with aneurysmal SAH) and 1657 individual venous systems were included. Patients with nonaneurysmal perimesencephalic SAH were more likely to have a primitive basal vein of Rosenthal drainage in at least 1 hemisphere (47.7% versus 22.1%; OR, 3.31; 95% CI, 2.15–5.08; $P < .01$) and were less likely to have bilateral normal basal vein of Rosenthal drainage systems than patients with aneurysmal SAH (18.3% versus 37.4%; OR, 0.27; 95% CI, 0.14–0.52; $P < .01$). When we considered individual venous systems, there were higher rates of primitive venous systems in patients with nonaneurysmal perimesencephalic SAH than in patients with aneurysmal SAH (34.9% versus 15.3%; OR, 3.90; 95% CI, 2.37–6.43; $P < .01$).

CONCLUSIONS: Patients with nonaneurysmal perimesencephalic SAH have a higher prevalence of primitive basal vein of Rosenthal drainage in at least 1 hemisphere than patients with aneurysmal SAH. This finding suggests a venous origin of some nonaneurysmal perimesencephalic SAHs. A primitive basal vein of Rosenthal pattern is an imaging finding that has the potential to facilitate the diagnosis of nonaneurysmal perimesencephalic SAH.

ABBREVIATIONS: aSAH = aneurysmal subarachnoid hemorrhage; BVR = basal vein of Rosenthal; NAPH = nonaneurysmal perimesencephalic subarachnoid hemorrhage

Nonaneurysmal perimesencephalic subarachnoid hemorrhage (NAPH) represents approximately 10%–15% of all spontaneous SAH cases.^{1–5} NAPHs are characterized by the ab-

sence of an aneurysm or other source of bleeding on 4-vessel digital subtraction angiography and subarachnoid blood located predominantly in the perimesencephalic cistern (Fig 1).^{1,6–17} The prognosis for NAPH is usually much better than that of aneurysmal subarachnoid hemorrhage (aSAH), with a benign clinical course and low risk of rebleeding or vasospasm.^{13,16,18–21}


The cause and the mechanisms of bleeding have yet to be established. Many different sources of bleeding have been proposed, including microaneurysm or microangioma, rupture of pontine perforating arteries, bleeding from perimesencephalic or deep internal veins, or hemorrhage from basilar trunk dissections and intramural hematoma.^{13,22–35}


Other studies have suggested a possible link between abnormal drainage of the basal vein of Rosenthal (BVR) and NAPH.^{33,36–41}


Received October 14, 2015; accepted after revision February 9, 2016.

From the Departments of Radiology (A.R., V.T.L., H.J.C., E.P.L., D.F.K., W.B.), Preventive Medicine and Center for the Science of Healthcare Delivery (M.H.M.), and Neurosurgery (A.B.), Mayo Clinic, Rochester, Minnesota.

Please address correspondence to Aymeric Rouchaud, MD, Department of Radiology, Mayo Clinic, 200 First St SW, Rochester, MN 55905; e-mail: aymeric.rouchaud@gmail.com

 Indicates article with supplemental on-line table.

 Indicates article with supplemental on-line photo.

 Evidence-Based Medicine Level 2.

<http://dx.doi.org/10.3174/ajnr.A4806>

Because of the rarity of this pathology, most series reporting BVR drainage in patients with NAPH are small retrospective single-center case series. Thus, the exact link between abnormal BVR drainage and NAPH has yet to be established. Because of this lack of information, we performed a systematic review and meta-analysis of studies examining BVR drainage patterns in patients with NAPH compared with those with aSAH. The deep cerebral venous drainage patterns are classified as the following: Type A or “normal continuous,” in which the basal vein of Rosenthal is continuous with the deep middle cerebral vein and drains mainly into the vein of Galen; Type B or “normal discontinuous,” in which there is discontinuous dual drainage, both anterior to the uncus and posterior to the vein of Galen; and Type C or “primitive,” which drains directly into the dural sinuses instead of the

Galenic system. Types A and B are considered normal variant patterns, whereas Type C or primitive venous drainage is considered abnormal.^{33,40} Illustrations of the 3 drainage patterns are provided in Fig 2.

MATERIALS AND METHODS

Literature Search

We identified all studies published between 1980 and September 2015 that reported BVR drainage in patients with NAPH and aSAH. A comprehensive literature search of the data bases PubMed, Ovid MEDLINE, and Ovid EMBASE was designed and conducted by an experienced librarian with input from the authors. The key words “perimesencephalic,” “subarachnoid hemorrhage,” “basal vein,” “Rosenthal,” and “drainage” were used in both “AND” and “OR” combinations. Studies were selected by using the following criteria: 1) NAPH, 2) involving subjects 18 years of age or older, 3) with available data on venous drainage by using the above-defined criteria, 4) comparing venous drainage to patients with aneurysmal SAH, 5) retrospective or prospective studies with at least 3 patients, and 6) published in English.

Two authors separately searched the data base and selected potentially relevant articles based on the title and abstract and obtained the full text for detailed review. We also searched the reference lists of retrieved articles and published review articles for additional studies. We screened duplicate publications that drew on the same datasets (ie, data overlapping with those in other included studies). In duplicate publications, only those with the most complete data were included. The included stud-

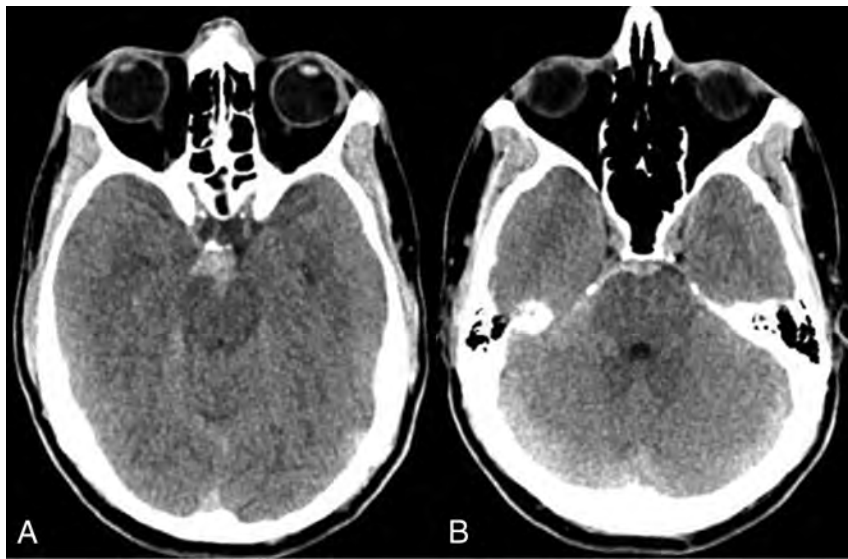


FIG 1. Pattern of nonaneurysmal perimesencephalic hemorrhage. Nonaneurysmal perimesencephalic hemorrhage in a 54-year-old man with a headache after sneezing. The CT demonstrates blood isolated to the perimesencephalic cistern with some extension into the right ambient cistern. No blood is seen in the bilateral Sylvian fissures, and there was no intraventricular hemorrhage.

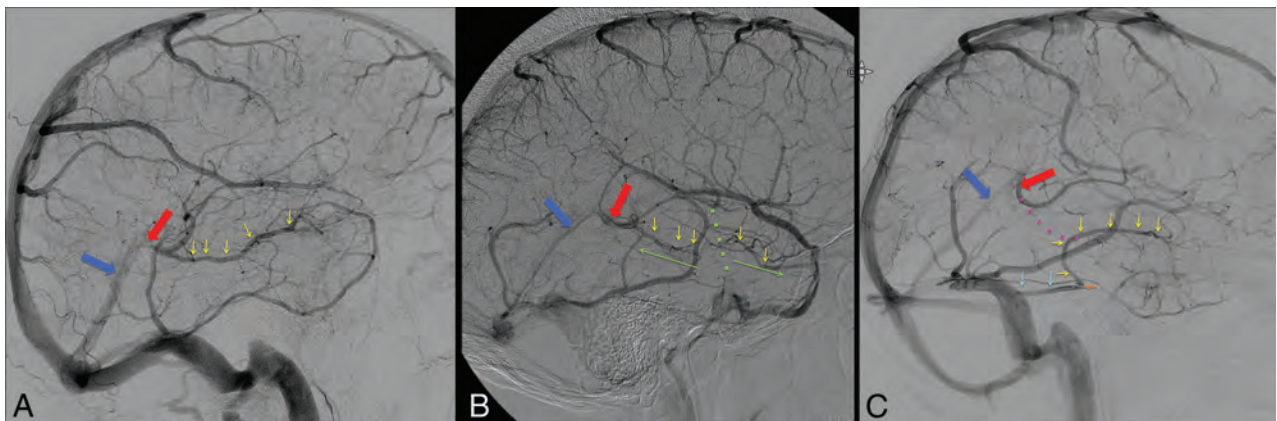


FIG 2. Lateral venous phase DSA images illustrating the different variants of the basal vein of Rosenthal: BVR (yellow arrows), vein of Galen (red arrow), and straight sinus (dark blue arrow). A, Type A (normal continuous pattern). The BVR is continuous and drains mainly posteriorly into the vein of Galen. B, Type B (normal discontinuous pattern). Discontinuous dual drainage of the BVR anterior into the cavernous sinus via the uncus and posterior to the vein of Galen. The green dotted line and the 2 green arrows illustrate anterior and posterior drainage. C, Type C (primitive pattern). BVR drains into veins (the uncus, anterior pontomesencephalic, or lateral mesencephalic veins or the tentorial sinus) other than the vein of Galen. The anterior segment of the BVR (yellow arrow) drains into the lateral mesencephalic vein to the petrosal sinus (light blue arrows), ultimately into the sigmoid sinus. The middle and posterior segments are absent (normal course is illustrated by the pink dotted line).

Meta-analysis: comparison of BVR drainage patterns in patients with NAPH versus aSAH

	Nonaneurysmal Perimesencephalic Hemorrhage	Aneurysmal Subarachnoid Hemorrhage	OR	P Value	I ²
Patients with at least 1 primitive BVR drainage pattern	47.7% (148/310)	22.1% (75/340)	3.31 (2.15–5.08)	<.01	29%
Patients with normal bilateral BVR drainage pattern	18.3% (61/334)	37.4% (207/554)	0.27 (0.14–0.52)	<.01	57%
Abnormal BVR drainage by venous system	34.9% (220/630)	15.3% (157/1027)	3.90 (2.37–6.43)	<.01	70%

ies reported the definition of NAPH with homogeneity as an accumulation of subarachnoid blood predominantly in the perimesencephalic cisterns with the center of the hemorrhage located in front of the mesencephalon without blood in the interhemispheric and lateral Sylvian fissures (except minute amounts) and no important intraventricular hemorrhage (Fig 1),¹ and absence of an aneurysm or other source of bleeding identified on arterial imaging including DSA. All the studies reported the venous drainage patterns on diagnostic cerebral angiography according to the 3 grades previously described as Type A (normal continuous), in which the BVR is continuous with the deep middle cerebral vein and drains mainly into the vein of Galen; Type B (normal discontinuous), in which there is discontinuous venous drainage anterior to the uncus vein and posterior to the vein of Galen; and Type C (primitive variant), in which there is drainage mainly to veins other than the vein of Galen. These include perimesencephalic veins draining into the superior petrosal sinus or the BVR draining directly into the transverse or straight sinus.^{33,40} Illustrations of the 3 drainage patterns are provided in Fig 2.

Data were extracted independently by 2 authors by using a standardized form, and any disagreement was resolved by consensus. We did not contact the authors of the studies to request incomplete or unpublished data. For each study, we extracted the following data: patient demographics, number patients with at least 1 primitive (Type C) BVR drainage pattern, number of patients with a Type A bilateral BVR drainage pattern, and number of venous systems with primitive (Type C) drainage. Comparisons were performed between patients with NAPH versus those with aSAH.

Statistical Analysis

All included studies were comparative. Meta-analysis results were expressed as an odds ratio for binary outcomes by using a random-effects meta-analysis.⁴² For all outcomes, we quantified between-study heterogeneity by creating forest plots and calculating the I² statistic.⁴³ We explored the impact of publication bias by constructing funnel plots and testing their symmetry with the Egger test.

Risk-of-Bias Assessment

Risk-of-bias assessment was performed by using the Newcastle-Ottawa Scale. This tool is used for assessing the risk of bias of nonrandomized studies included in systematic reviews or meta-analyses. Each study is judged on 8 items categorized into 3 groups: 1) selection of the study groups, 2) comparability of the study groups, and 3) ascertainment of the outcome of interest.⁴⁴

RESULTS**Literature Review**

The initial literature search yielded 243 articles. On initial abstract and title review, 221 were excluded because they were deemed not relevant to our study. Full texts of the remaining 22 articles were retrieved. Of these, 14 were excluded because they were either case reports, review articles, or did not provide data on the predefined study outcomes.

In total, 8 studies with 334 patients

with NAPH and 554 with aSAH were included. The definition of NAPH was similar between studies. This total represented 1657 individual venous systems. A summary of included studies is provided in the On-line Table. Of the 334 patients with NAPH, 61 (18.3%) had normal (Type A) bilateral BVR drainage and 166 (49.7%) had primitive (Type C) BVR drainage in at least 1 hemisphere. Of the 630 venous systems analyzed in patients with NAPH, 220 (34.9%) were abnormal (Type C). Of the 554 patients with aSAH, 207/554 (37.4%) had normal (Type A) bilateral BVR drainage and 75/340 (22.1%) had primitive (Type C) BVR drainage in at least 1 hemisphere. Of the 1027 venous systems analyzed in patients with aSAH, 157 (15.3%) were abnormal (Type C).

Venous Drainage Pattern in Patients with NAPH versus Those with aSAH

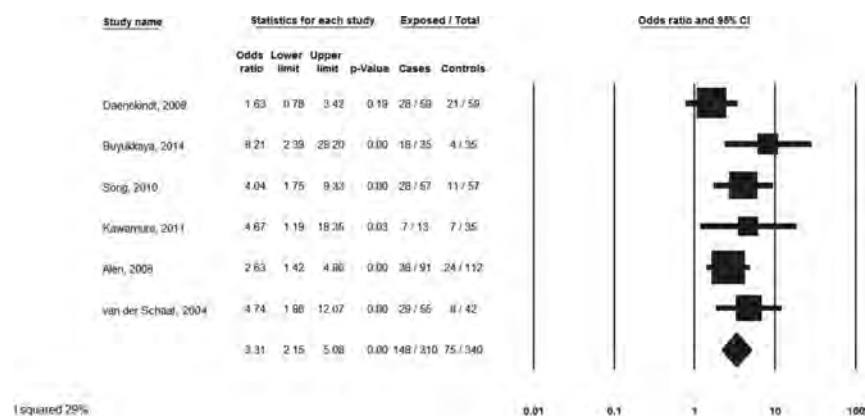
Patients with NAPH had lower rates of normal bilateral BVR drainage than those with aSAH (18.3% versus 37.4%; OR, 0.27; 95% CI, 0.14–0.52; $P < .01$) but higher rates of the primitive BVR drainage pattern in at least 1 hemisphere (47.7% versus 22.1%; OR, 3.31; 95% CI, 2.15–5.08; $P < .01$). Considered individually, there were higher rates of abnormal venous systems in patients with NAPH than in those with aSAH (34.9% versus 15.3%) with an odds ratio of 3.90 (95% CI, 2.37–6.43; $P < .01$). These data are summarized in the Table. Forest plots are provided in Fig 3A–C.

Risk of Bias

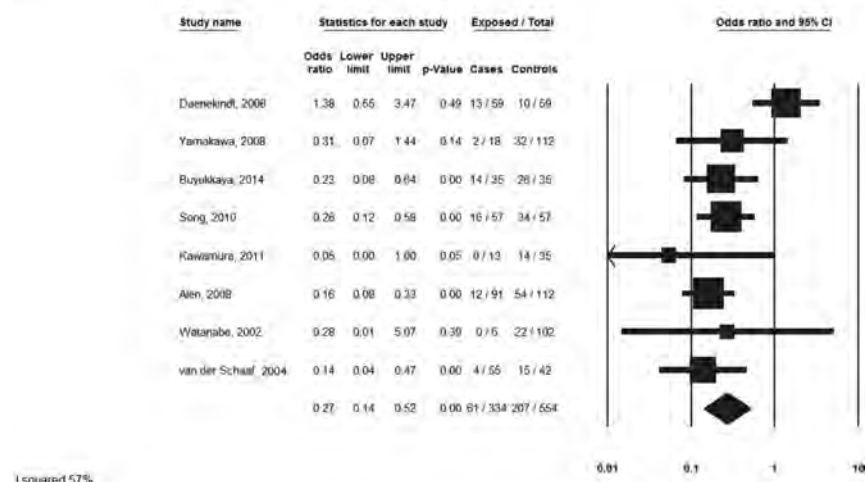
All studies had a low risk of bias. In all studies, the NAPH and aSAH groups were selected from a consecutive series of patients with angiographically confirmed presence or absence of intracranial aneurysm. Venous drainage patterns were assessed by using diagnostic cerebral angiography in all cases. Study groups were comparable, with no significant differences in baseline characteristics between groups. The ascertainment of the outcome of interest was satisfactory in all studies because readers were blinded to the nature of the patients' SAHs.

I² values for meta-analysis demonstrated fair homogeneity for the outcome "patients with at least 1 primitive BVR drainage pattern" (I² statistics = 29%) and substantial heterogeneity for the outcomes "patients with a normal bilateral BVR drainage pattern" (I² statistics = 57%) and "abnormal BVR drainage by venous system" (I² statistics = 70%).

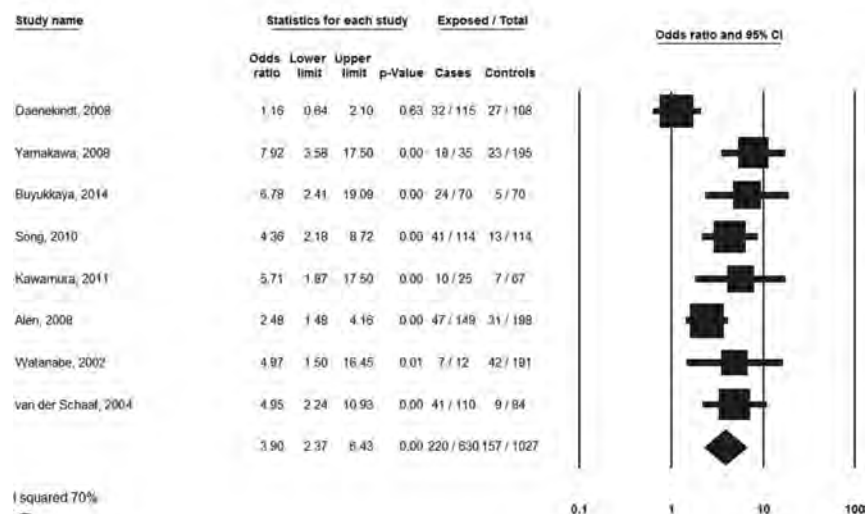
No evidence of publication bias was observed on the basis of the Egger test ($P > .05$ for all 3 outcomes). Funnel plots are provided in On-line Fig 1.



A



B



C

FIG 3. Meta-analyses. A, Comparison of the proportion of patients with at least 1 primitive BVR drainage. B, Comparison of the proportion of patients with a normal bilateral BVR drainage pattern. C, Comparison of the proportion of abnormal BVR drainage by the venous system.

DISCUSSION

Our meta-analysis demonstrated that patients with NAPH were more likely to have primitive BVR drainage in at least 1 hemisphere and were less likely to have bilateral normal BVR drainage systems. Regarding individual venous systems, there were higher

rates of abnormal venous systems in patients with NAPHs than in those with aSAH. Overall, these findings suggest that the occurrence of some NAPHs is associated with the primitive drainage pattern of the BVR. While the diagnosis of NAPH is still a diagnosis of exclusion, the radiologic identification of a primitive

drainage pattern in case of SAH could help affirm the diagnosis of NAPH in some cases.

The deep venous system of the brain is composed of the internal cerebral vein, the great vein of Galen, the BVR, and their respective tributaries.^{45,46} Anatomically, the BVR begins just anterior to the midbrain near the anterior perforated substance, runs around the brain stem, and terminates posteriorly, usually into the Galenic system via the great vein of Galen.⁴⁷ The BVR may also drain into the straight sinus or the internal cerebral veins. Embryologically, the BVR is not one of the original pial veins but is rather a secondary vessel formed by longitudinal anastomoses of 3 primitive veins during development: the telencephalic, diencephalic, and mesencephalic veins.⁴⁸ In the early embryonic stage, these primitive veins drain into the tentorial sinuses. Later, many channels draining into the tentorial sinus usually spontaneously obliterate with a secondarily posteromedial and superior drainage of the BVR into the Galenic venous system via the anastomotic channels. However, discontinuity due to maldevelopment of longitudinal anastomoses of the 3 primitive veins during the embryologic stages could lead to posterolateral and inferior drainage of the BVR into the transverse sinus via the tentorial sinus as a more primitive form.⁴⁷⁻⁵⁰

This meta-analysis confirms that compared with patients with aSAH, those with NAPH had more primitive forms of the BVR, including primitive venous drainage directly into dural sinuses (the cavernous sinus via the uncus vein, the superior petrosal sinus via the tentorial sinus, or the perimesencephalic vein) instead of into the Galenic system.^{33,36,38} These findings suggest that the primitive drainage pattern of the BVR is a risk factor for NAPH in some cases.³⁹ There are a number of reasons why a primitive venous pattern could be associated with NAPH. The direct connection of perimesencephalic veins with the dural sinuses may predispose to sudden increases in venous pressure with engorgement and rupture of the veins as a result.^{33,36,39} Intracranial venous congestion caused by straining might tear a vein fixed to a dural sinus or cause abrupt swelling of the tributaries of the BVR in patients with the primitive pattern.^{1,33,51} Any stimulus similar to the Valsalva maneuver increases intrathoracic pressure, which blocks the internal jugular venous return and results in elevated intracranial venous pressure or mechanical swelling of intracranial veins and potentially leads to venous or capillary breakdown.³⁹ In addition, some of the primitive veins circulate across the tentorial margin, exposing them to torsion or friction and making them even more prone to rupture where they cross the tentorial margin.^{1,51}

Lending further support to the idea that this anatomic variant is a potential culprit in NAPH is a study by van der Schaaff et al,³⁸ which demonstrated that in patients with unilateral primitive drainage, blood primarily extravasated on the side of the primitive drainage. The BVR caliber may also have an etiologic role in patients who experience NAPH as suggested by Buyukkaya et al,⁴¹ who identified a relationship between low-calibration BVR and NAPH in patients with normal drainage patterns. However, if aberrant drainage patterns are somehow linked to NAPH, it is surprising that the incidence of rebleeding is very low because anatomic venous drainage patterns are not likely to change after bleeding.⁵²⁻⁵⁶ However, this low rebleeding rate could be ex-

plained by spontaneous healing of the venous rupture by fibrous tissue reaction, which could reinforce the wall of the vein, as speculated by Matsumaru et al.^{33,51}

Strengths and Limitations

The strengths of this study include following a protocol established a priori, a comprehensive literature search that involved multiple databases, and the process of study selection performed by independent reviewers. The main limitation of this analysis is that most studies did not include a control group of patients without hemorrhage. Thus, we could not determine whether patients with NAPH are more likely than healthy controls to have abnormal venous drainage patterns. I^2 values for meta-analysis demonstrated fair homogeneity for the outcome “patients with at least 1 primitive BVR drainage pattern” and substantial heterogeneity for the outcomes “patients with normal bilateral BVR drainage pattern” and “abnormal BVR drainage by venous system,” which could affect the results of our meta-analysis. Publication bias is a limitation of many meta-analyses. However, we did not detect any publication bias based on funnel plots and Egger tests.

CONCLUSIONS

NAPH is associated with the presence of a primitive variant pattern of BVR drainage with direct connection of perimesencephalic veins in the dural sinuses in at least 1 hemisphere. These results support a venous origin of some NAPHs. A primitive BVR pattern could represent an imaging argument to affirm the diagnosis of NAPH in some cases.

Disclosures: David F. Kallmes—UNRELATED: Consultancy: Medtronic,* Comments: steering committee of a clinical trial; Grants/Grants Pending: MicroVention,* Sequent Medical,* Surmodics,* Codman,* Medtronic,* NeuroSigma,* Comments: pre-clinical research and clinical trials; Travel/Accommodations/Meeting Expenses Unrelated to Activities Listed: Medtronic,* Comments: presentation at FDA panel meeting. *Money paid to the institution.

REFERENCES

1. van Gijn J, van Dongen KJ, Vermeulen M, et al. **Perimesencephalic hemorrhage: a nonaneurysmal and benign form of subarachnoid hemorrhage.** *Neurology* 1985;35:493–97 CrossRef Medline
2. Farrés MT, Ferraz-Leite H, Schindler E, et al. **Spontaneous subarachnoid hemorrhage with negative angiography: CT findings.** *J Comput Assist Tomogr* 1992;16:534–37 CrossRef Medline
3. Ferbert A, Hubo I, Biniek R. **Non-traumatic subarachnoid hemorrhage with normal angiogram: long-term follow-up and CT predictors of complications.** *J Neurol Sci* 1992;107:14–18 CrossRef Medline
4. Pinto AN, Ferro JM, Canhao P, et al. **How often is a perimesencephalic subarachnoid haemorrhage CT pattern caused by ruptured aneurysms?** *Acta Neurochir (Wien)* 1993;124:79–81 CrossRef Medline
5. Boswell S, Thorell W, Gogela S, et al. **Angiogram-negative subarachnoid hemorrhage: outcomes data and review of the literature.** *J Stroke Cerebrovasc Dis* 2013;22:750–57 CrossRef Medline
6. Alén JF, Lagares A, Lobato RD, et al. **Comparison between perimesencephalic nonaneurysmal subarachnoid hemorrhage and subarachnoid hemorrhage caused by posterior circulation aneurysms.** *J Neurosurg* 2003;98:529–35 CrossRef Medline
7. Brismar J, Sundbärg G. **Subarachnoid hemorrhage of unknown origin: prognosis and prognostic factors.** *J Neurosurg* 1985;63:349–54 CrossRef Medline
8. Cioffi F, Pasqualin A, Cavazzani P, et al. **Subarachnoid haemorrhage of unknown origin: clinical and tomographical aspects.** *Acta Neurochir (Wien)* 1989;97:31–39 CrossRef Medline

9. Eskesen V, Sorensen EB, Rosenorn J, et al. **The prognosis in subarachnoid hemorrhage of unknown etiology.** *J Neurosurg* 1984;61:1029–31 CrossRef Medline
10. Gomez PA, Lobato RD, Rivas JJ, et al. **Subarachnoid haemorrhage of unknown aetiology.** *Acta Neurochir (Wien)* 1989;101:35–41 CrossRef Medline
11. Nishioka H, Torner JC, Graf CJ, et al. **Cooperative study of intracranial aneurysms and subarachnoid hemorrhage: a long-term prognostic study, III: subarachnoid hemorrhage of undetermined etiology.** *Arch Neurol* 1984;41:1147–51 CrossRef Medline
12. Ronkainen A, Hernesniemi J. **Subarachnoid haemorrhage of unknown aetiology.** *Acta Neurochir (Wien)* 1992;119:29–34 CrossRef Medline
13. Schwartz TH, Solomon RA. **Perimesencephalic nonaneurysmal subarachnoid hemorrhage: review of the literature.** *Neurosurgery* 1996;39:433–40; discussion 440 CrossRef Medline
14. Velthuis BK, Rinkel GJ, Ramos LM, et al. **Perimesencephalic hemorrhage: exclusion of vertebrobasilar aneurysms with CT angiography.** *Stroke* 1999;30:1103–09 CrossRef Medline
15. Rinkel GJ, Wijdicks EF, Vermeulen M, et al. **Nonaneurysmal perimesencephalic subarachnoid hemorrhage: CT and MR patterns that differ from aneurysmal rupture.** *AJNR Am J Neuroradiol* 1991;12:829–34 Medline
16. Van Calenbergh F, Plets C, Goffin J, et al. **Nonaneurysmal subarachnoid hemorrhage: prevalence of perimesencephalic hemorrhage in a consecutive series.** *Surg Neurol* 1993;39:320–23 CrossRef Medline
17. Brinjikji W, Kallmes DF, White JB, et al. **Inter- and intraobserver agreement in CT characterization of nonaneurysmal perimesencephalic subarachnoid hemorrhage.** *AJNR Am J Neuroradiol* 2010;31:1103–05 CrossRef Medline
18. Canhão P, Ferro JM, Pinto AN, et al. **Perimesencephalic and nonperimesencephalic subarachnoid haemorrhages with negative angiograms.** *Acta Neurochir (Wien)* 1995;132:14–19 CrossRef Medline
19. Rinkel GJ, Wijdicks EF, Hasan D, et al. **Outcome in patients with subarachnoid haemorrhage and negative angiography according to pattern of haemorrhage on computed tomography.** *Lancet* 1991;338:964–68 CrossRef Medline
20. Cruz JP, Sarma D, Noel de Tilly L. **Perimesencephalic subarachnoid hemorrhage: when to stop imaging?** *Emerg Radiol* 2011;18:197–202 CrossRef Medline
21. Jung JY, Kim YB, Lee JW, et al. **Spontaneous subarachnoid haemorrhage with negative initial angiography: a review of 143 cases.** *J Clin Neurosci* 2006;13:1011–17 CrossRef Medline
22. Boukobza M, Crassard I, Bousser MG, et al. **Radiological findings in cerebral venous thrombosis presenting as subarachnoid hemorrhage: a series of 22 cases.** *Neuroradiology* 2016;58:11–16 CrossRef Medline
23. Mathews MS, Brown D, Brant-Zawadzki M. **Perimesencephalic nonaneurysmal hemorrhage associated with vein of Galen stenosis.** *Neurology* 2008;70:2410–11 CrossRef Medline
24. Oda S, Shimoda M, Hoshikawa K, et al. **Cortical subarachnoid hemorrhage caused by cerebral venous thrombosis.** *Neurol Med Chir (Tokyo)* 2011;51:30–36 CrossRef 21273741
25. Schievink WI, Wijdicks EF. **Origin of pretruncal nonaneurysmal subarachnoid hemorrhage: ruptured vein, perforating artery, or intramural hematoma?** *Mayo Clin Proc* 2000;75:1169–73 CrossRef Medline
26. Bohmfalk GL, Story JL. **Intermittent appearance of a ruptured cerebral aneurysm on sequential angiograms: case report.** *J Neurosurg* 1980;52:263–65 CrossRef Medline
27. Crawford JV, Russell DS. **Cryptic arteriovenous and venous hamartomas of the brain.** *J Neurol Neurosurg Psychiatry* 1956;19:1–11 CrossRef Medline
28. Forster DM, Steiner L, Hakanson S, et al. **The value of repeat panangiography in cases of unexplained subarachnoid hemorrhage.** *J Neurosurg* 1978;48:712–16 CrossRef Medline
29. Ildan F, Tuna M, Erman T, et al. **Prognosis and prognostic factors in nonaneurysmal perimesencephalic hemorrhage: a follow-up study in 29 patients.** *Surg Neurol* 2002;57:160–65; discussion 165–66 CrossRef Medline
30. Ildan F, Tuna M, Erman T, et al. **Prognosis and prognostic factors for unexplained subarachnoid hemorrhage: review of 84 cases.** *Neurosurgery* 2002;50:1015–24; discussion 1024–25 CrossRef Medline
31. Matsumaru Y, Yanaka K, Muroi A, et al. **Significance of a small bulge on the basilar artery in patients with perimesencephalic nonaneurysmal subarachnoid hemorrhage: report of two cases.** *J Neurosurg* 2003;98:426–29 CrossRef Medline
32. Alexander MS, Dias PS, Uttley D. **Spontaneous subarachnoid hemorrhage and negative cerebral panangiography: review of 140 cases.** *J Neurosurg* 1986;64:537–42 CrossRef Medline
33. Watanabe A, Hirano K, Kamada M, et al. **Perimesencephalic nonaneurysmal subarachnoid haemorrhage and variations in the veins.** *Neuroradiology* 2002;44:319–25 CrossRef Medline
34. Wijdicks EF, Schievink WI. **Perimesencephalic nonaneurysmal subarachnoid hemorrhage: first hint of a cause?** *Neurology* 1997;49:634–36 CrossRef Medline
35. Tatter SB, Buonanno FS, Ogilvy CS. **Acute lacunar stroke in association with angiogram-negative subarachnoid hemorrhage: mechanistic implications of two cases.** *Stroke* 1995;26:891–95 CrossRef Medline
36. Yamakawa H, Ohe N, Yano H, et al. **Venous drainage patterns in perimesencephalic nonaneurysmal subarachnoid hemorrhage.** *Clin Neurol Neurosurg* 2008;110:587–91 CrossRef Medline
37. Kawamura Y, Narumi O, Chin M, et al. **Variant deep cerebral venous drainage in idiopathic subarachnoid hemorrhage.** *Neurol Med Chir (Tokyo)* 2011;51:97–100 CrossRef Medline
38. van der Schaaf IC, Velthuis BK, Gouw A, et al. **Venous drainage in perimesencephalic hemorrhage.** *Stroke* 2004;35:1614–18 CrossRef Medline
39. Song JH, Yeon JY, Kim KH, et al. **Angiographic analysis of venous drainage and a variant basal vein of Rosenthal in spontaneous idiopathic subarachnoid hemorrhage.** *J Clin Neurosci* 2010;17:1386–90 CrossRef Medline
40. Alén JF, Lagares A, Campollo J, et al. **Idiopathic subarachnoid hemorrhage and venous drainage: are they related?** *Neurosurgery* 2008;63:1106–11; discussion 1111–12 CrossRef Medline
41. Buyukkaya R, Yildirim N, Cebeci H, et al. **The relationship between perimesencephalic subarachnoid hemorrhage and deep venous system drainage pattern and calibrations.** *Clin Imaging* 2014;38:226–30 CrossRef Medline
42. DerSimonian R, Laird N. **Meta-analysis in clinical trials.** *Control Clin Trials* 1986;7:177–88 CrossRef Medline
43. Higgins JP, Thompson SG, Deeks JJ, et al. **Measuring inconsistency in meta-analyses.** *BMJ* 2003;327:557–60 CrossRef Medline
44. Deeks JJ, Dinnes J, D'Amico R, et al. **Evaluating non-randomised intervention studies.** *Health Technol Assess* 2003;7:iii-x, 1–173 Medline
45. Wolf BS, Huang YP, Newman CM. **The lateral anastomotic mesencephalic vein and other variations in drainage of the basal cerebral vein.** *Am J Roentgenol Radium Ther Nucl Med* 1963;89:411–22 Medline
46. Chung JI, Weon YC. **Anatomic variations of the deep cerebral veins, tributaries of basal vein of Rosenthal: embryologic aspects of the regressed embryonic tentorial sinus.** *Interv Neuroradiol* 2005;11:123–30 Medline
47. Huang YP, Wolf BS. **The basal cerebral vein and its tributaries.** In: Newton TH, Potts DG, eds. *Radiology of the Skull and Brain: Angiography*. Vol 2. St Louis: Mosby; 1974:2111–54
48. Padgett DH. **The cranial venous system in man in reference to development, adult configuration, and relation to the arteries.** *Am J Anat* 1956;98:307–55 CrossRef Medline
49. Tubbs RS, Loukas M, Louis RG Jr, et al. **Surgical anatomy and landmarks for the basal vein of Rosenthal.** *J Neurosurg* 2007;106:900–02 CrossRef Medline
50. San Millán D, Gailloud P, Rüfenacht DA, et al. **The craniocervical**

- venous system in relation to cerebral venous drainage. *AJNR Am J Neuroradiol* 2002;23:1500–08 Medline
51. Matsumaru Y, Yanaka K, Matsumura A. **Is perimesencephalic nonaneurysmal hemorrhage of venous origin?** *Stroke* 2004;35:2753–54; author reply 2754 Medline
 52. Greebe P, Rinkel GJ. **Life expectancy after perimesencephalic subarachnoid hemorrhage.** *Stroke* 2007;38:1222–24 CrossRef Medline
 53. Kalra VB, Wu X, Matouk CC, et al. **Use of follow-up imaging in isolated perimesencephalic subarachnoid hemorrhage: a meta-analysis.** *Stroke* 2015;46:401–06 CrossRef Medline
 54. Kapadia A, Schweizer TA, Spears J, et al. **Nonaneurysmal perimesencephalic subarachnoid hemorrhage: diagnosis, pathophysiology, clinical characteristics, and long-term outcome.** *World Neurosurg* 2014;82:1131–43 CrossRef Medline
 55. Naidech AM, Rosenberg NF, Maas MB, et al. **Predictors of hemorrhage volume and disability after perimesencephalic subarachnoid hemorrhage.** *Neurology* 2012;78:811–15 CrossRef Medline
 56. Kong Y, Zhang JH, Qin X. **Perimesencephalic subarachnoid hemorrhage: risk factors, clinical presentations, and outcome.** *Acta Neurochir Suppl* 2011;110(pt 1):197–201 CrossRef Medline
 57. Daenekindt T, Wilms G, Thijs V, et al. **Variants of the basal vein of Rosenthal and perimesencephalic nonaneurysmal hemorrhage.** *Surg Neurol* 2008;69:526–29; discussion 529 CrossRef Medline

Prevalence of Intracranial Aneurysms in Patients with Aortic Aneurysms

A. Rouchaud, M.D. Brandt, A.M. Rydberg, R. Kadirvel, K. Flemming, D.F. Kallmes, and W. Brinjikji

ABSTRACT

BACKGROUND AND PURPOSE: Previous studies have suggested an association between aortic aneurysms and intracranial aneurysms with a higher prevalence of intracranial aneurysms in patients with aortic aneurysms. The aims of the present study were to evaluate the incidence of intracranial aneurysms in a large cohort of patients with aortic aneurysms and to identify potential risk factors for intracranial aneurysms in this population.

MATERIALS AND METHODS: We included all patients with aortic aneurysms (either abdominal and/or thoracic) who had available cerebral arterial imaging and were seen at our institution during a 15-year period. We identified patients with intracranial aneurysms. Patient demographics, comorbidities, and aortic aneurysm and intracranial aneurysm sizes and locations were analyzed. Univariate analysis was performed with a χ^2 test for categorical variables and a Student *t* test or ANOVA for continuous variables.

RESULTS: A total of 1081 patients with aortic aneurysms were included. Of them, 440 (40.7%) had abdominal aortic aneurysms, 446 (41.3%) had thoracic aortic aneurysms, and 195 (18.0%) had both abdominal aortic and thoracic aortic aneurysms. The overall prevalence of associated intracranial aneurysms in patients with aortic aneurysms was 11.8% (128/1081), with 12.7% (56/440), 10.8% (48/446), and 12.3% (24/195), respectively, in patients with abdominal aortic aneurysms, thoracic aortic aneurysms, and both thoracic aortic aneurysms and abdominal aortic aneurysms. Female patients had a higher risk of associated intracranial aneurysms (OR = 2.08; 95% CI, 1.49–3.03; *P* = .0002). There was a slight association between abdominal aortic aneurysm size and the prevalence of intracranial aneurysms (OR = 1.02; 95% CI, 1.01–1.03; *P* = .045). There was no significant association between the locations of the aortic and intracranial aneurysms (*P* = .93).

CONCLUSIONS: The prevalence of intracranial aneurysms is high in patients with aortic aneurysms. Further studies examining the role and cost-effectiveness of intracranial aneurysm screening in patients are warranted.

ABBREVIATIONS: AA = aortic aneurysm; AAA = abdominal aortic aneurysm; ADPKD = autosomal dominant polycystic kidney disease; IA = intracranial aneurysm; TAA = thoracic aortic aneurysm

The overall prevalence of unruptured intracranial aneurysms (IAs) in the general population is estimated as 3.2%.¹ The overall prevalence of aortic aneurysms (AAs), with both thoracic (TAAs) and abdominal (AAAs) aortic aneurysms, is estimated at around 1%–2% in the general population with up to 10% prevalence in older age groups.² Previous studies have identified a link between intracranial aneurysms and aortic diseases such as coarctation of the aorta or a bicuspid aortic valve.^{3–6} A few studies have

reported an association between abdominal aortic aneurysms and thoracic aortic aneurysms and IAs, with a higher prevalence of IA in patients with aortic aneurysms.^{6–14} However, contrary to other pathologies such as autosomal dominant polycystic kidney disease (ADPKD), which is associated with IA in 12.4% of cases, no systematic screening for IA is proposed for patients with AA.¹⁵ The aims of the present study were to evaluate the prevalence of IA in a large cohort of patients with AA and to identify potential risk factors for IA in this population.

MATERIALS AND METHODS

Patient Population

Following institutional review board approval, we performed a search of our imaging and clinical data base for all patients with clinical or radiologic notes between January 2001 and June 2015 with the key words “aortic aneurysms,” “abdominal aortic aneurysm,” and “thoracic aortic aneurysm.” We selected patients who

Received November 20, 2015; accepted after revision February 22, 2016.

From the Departments of Radiology (A.R., M.D.B., A.M.R., R.K., D.F.K., W.B.) and Neurology (K.F.), Mayo Clinic, Rochester, Minnesota.

Aymeric Rouchaud received financial support from a research grant from the French Society of Radiology and the Thérèse and René Planiol Foundation.

Please address correspondence to Aymeric Rouchaud, MD, Department of Radiology, Mayo Clinic, 200 First St SW, Rochester, MN 55901; e-mail: aymeric.rouchaud@gmail.com

<http://dx.doi.org/10.3174/ajnr.A4827>

Table 1: Summary of baseline characteristics by AA type

	All Patients	AAA	TAA	AAA and TAA	P
No. (%)	1081	440 (40.7)	446 (41.3)	195 (18.0)	—
Mean age (yr) (SD)	69.3 (16.2)	77.8 (9.3)	62.2 (17.0)	70.8 (16.7)	<.0001
Mean max AAA diameter	49.3 (14.3)	49.6 (14.4)	—	48.5 (14.0)	—
Mean max TAA diameter	50.2 (11.1)	—	48.5 (9.2)	54.5 (13.8)	—
Sex					
Male	800 (74.0)	348 (79.1)	310 (69.5)	142 (72.8)	.005
Female	281 (26.0)	92 (20.9)	136 (30.5)	53 (27.2)	
Comorbidities					
Stroke/TIA	509 (47.1)	236 (53.6)	163 (36.6)	110 (56.4)	<.0001
Coronary artery disease	510 (47.3)	278 (63.3)	125 (28.1)	107 (54.9)	<.0001
Hypertension	855 (79.2)	394 (89.8)	283 (63.5)	178 (91.3)	<.0001
Diabetes	208 (19.3)	119 (27.2)	56 (12.6)	33 (16.9)	<.0001
Hyperlipidemia	743 (68.8)	369 (84.1)	228 (51.1)	146 (74.9)	<.0001
Current/former smoker	356 (33.0)	214 (48.8)	68 (15.3)	74 (38.0)	<.0001
Bicuspid aortic valve	142 (13.1)	3 (0.7)	132 (29.6)	7 (3.6)	<.0001
Imaging					
MRA	903 (83.5)	373 (84.8)	369 (82.7)	161 (82.6)	.66
CTA	249 (23.0)	94 (21.4)	104 (23.3)	51 (26.2)	.52
DSA	114 (10.5)	55 (12.5)	40 (9.0)	19 (9.7)	.34
No. (%) with intracranial aneurysms	128 (11.8)	56 (12.7)	48 (10.8)	24 (12.3)	.44
No. of aneurysms	172	70	65	37	—
No. (%) of patients with multiple aneurysms	30 (23.4)	14 (25.0)	10 (15.4)	6 (25.0)	.34
Mean size	6.0 (5.8)	5.4 (4.4)	6.3 (6.5)	7.1 (7.2)	.54
Location					
ICA	93 (54.1)	36 (51.4)	34 (52.3)	23 (62.2)	.67
ACA	16 (9.3)	7 (10.0)	7 (10.8)	2 (5.4)	
AcomA	16 (9.3)	5 (7.1)	8 (12.3)	3 (8.1)	
MCA	24 (14.0)	12 (17.1)	7 (10.8)	5 (13.5)	
Basilar artery	13 (7.6)	8 (11.4)	3 (4.6)	2 (5.4)	
PICA	5 (2.9)	1 (1.4)	2 (3.1)	2 (2.7)	
PCA	4 (2.3)	1 (1.4)	3 (4.6)	0 (0.0)	
Vertebral artery	2 (1.2)	0 (0.0)	1 (1.5)	1 (2.7)	
Location by anterior/posterior					
Anterior	148 (86.0)	60 (83.3)	56 (86.2)	32 (86.5)	.99
Posterior	24 (14.0)	10 (16.7)	9 (13.8)	5 (13.5)	

Note:—Max indicates maximum; ACA, anterior cerebral artery; AcomA, anterior communicating artery; PICA, posterior inferior cerebellar artery; PCA, posterior cerebral artery.

were 18 years of age or older who had an aortic aneurysm and cerebral arterial imaging (CTA, MRA, or DSA). Patients with known connective tissue diseases (ie, Marfan, Ehlers-Danlos, and Loeys-Dietz syndromes) were excluded.

Data Collection

The diagnosis of AA was determined according to previous reports for each patient. The definition of an abdominal aortic aneurysm was a diameter of ≥ 3.5 cm, and the diameter of a thoracic aortic aneurysm was ≥ 4.5 cm. The location of the AA (TAA, AAA, or both) and the size of the aneurysms were retrieved from available reports. In case the size was not reported, a radiologist measured the maximum aneurysm diameter on available examinations (CT or MR imaging). The primary outcome of this study was the prevalence of saccular intracranial aneurysms. Head CTA, MRA, and DSA radiology reports of patients with AA read by board-certified neuroradiologists were queried for the terms “aneurysm,” “dilatation,” or “saccular.” All reports that did not have one of these terms were considered negative for aneurysms. Among those that did have a mention of the terms in their radiology reports, imaging was further evaluated to confirm the presence, location, and size of an intracranial aneurysm. This was performed by a neuroradiologist with 4 years of training. Patients with dissecting and fusiform aneurysms were excluded because

these lesions are associated with a distinct natural history and pathophysiology compared with saccular aneurysms (20 patients). Partially thrombosed aneurysms were included in this study. Patients undergoing CTA evaluation had CT angiography on either 16-, 32-, or 64-section CT scanners. MR imaging and MRA were performed on 1.5T or 3T scanners. Each aneurysm was described according to its location and maximum diameter.

In addition to the presence of a saccular aneurysm, we collected the following baseline data: age at diagnosis of the intracranial aneurysm, sex, hypertension, coronary artery disease, diabetes mellitus, previous or current tobacco use, bicuspid aortic valve, and hyperlipidemia.

Statistical Analysis

All categorical variables were analyzed by using a χ^2 test. All continuous variables were analyzed by using a Student *t* test or ANOVA. We performed a subgroup analysis of AA location (ie, TAA, AAA, or both TAA and AAA). We also determined whether any of the above-mentioned baseline characteristics were associated with the presence of intracranial aneurysms. Odds ratios and their associated 95% confidence intervals were calculated. To determine

which variables, if any, were independently associated with the presence of an intracranial aneurysm, we performed a multivariate analysis, adjusting for aortic aneurysm type and any variables that were associated with the presence of aneurysms on univariate analysis (ie, carotid artery disease, female sex, and aortic aneurysm size). All statistical analyses were performed by using JMP 12.0 (SAS Institute, Cary, North Carolina).

RESULTS

Baseline Characteristics

A total of 1081 patients with AA were included. Of them, 440 (40.7%) had AAAs, 446 (41.3%) had TAAs, and 195 (18.0%) had both AAAs and TAAs. Baseline demographics and aneurysm characteristics according to the AA location are presented in Table 1.

The mean age of all patients was 69.3 ± 16.2 years, with 74.0% (800/1081) of patients being men. The mean maximal diameters of the AAs were 49.3 ± 14.3 mm and 50.2 ± 11.1 mm for AAAs and TAAs, respectively. There were statistically significant differences regarding the comorbidities and cardiovascular risk factors between the AAA and TAA groups, with a higher prevalence of stroke/TIA, coronary artery disease, hypertension, diabetes, hyperlipidemia, and smoking history in the AAA group than in the TAA group (all *P* values <.01), demonstrating that AAAs are

Table 2: Risk factors for intracranial aneurysms in patients with aortic aneurysms

	All		AAA Only		TAA Only		TAA and AAA	
	OR (95% CI)	P	OR (95% CI)	P	OR (95% CI)	P	OR (95% CI)	P
Age (1-yr increase)	0.99 (0.91–1.08)	.29	0.99 (0.95–1.04)	.61	1.00 (0.97–1.03)	.61	0.96 (0.92–0.98)	.01
AAA size (mm increase)	1.02 (1.01–1.03)	.045	1.01 (0.96–1.07)	.36	—	—	1.04 (1.02–1.06)	.03
TAA size (mm increase)	1.01 (0.97–1.04)	.49	—	—	1.00 (0.96–1.04)	.83	1.02 (0.98–1.06)	.14
Female sex	2.08 (1.49–3.03)	.0002	1.31 (0.68–2.51)	.42	2.32 (1.26–4.26)	.006	4.74 (1.95–11.50)	.0002
Comorbidities								
Stroke/TIA	0.83 (0.58–1.20)	.035	0.61 (0.35–1.07)	.08	1.40 (0.76–2.57)	.27	0.51 (0.21–1.21)	.12
CAD	0.68 (0.47–0.99)	.047	0.63 (0.37–1.11)	.11	0.40 (0.18–0.92)	.03	0.97 (0.41–2.28)	.94
HTN	0.93 (0.60–1.46)	.76	0.64 (0.28–1.46)	.29	0.96 (0.51–1.77)	.88	1.06 (0.23–4.94)	.94
DM	0.85 (0.52–1.39)	.52	0.70 (0.36–1.38)	.34	0.43 (0.13–1.45)	.16	2.30 (0.87–6.08)	.13
HLP	0.82 (0.55–1.20)	.31	0.41 (0.21–0.78)	.006	1.26 (0.69–2.30)	.54	0.63 (0.25–1.58)	.32
Bicuspid aortic valve	0.72 (0.40–1.32)	.33	NA	.84	0.59 (0.29–1.23)	.16	5.96 (1.25–28.50)	.01
Current/former smoker	1.25 (0.86–1.84)	.24	0.82 (0.47–1.45)	.57	0.94 (0.40–2.20)	.89	3.90 (1.58–9.64)	.002

Note:—CAD indicates carotid artery disease; HTN, hypertension; DM, diabetes mellitus; HLP, hyperlipidemia; NA, not applicable.

Table 3: Prevalence of aneurysms by comorbidity

	Aneurysm Prevalence (%)			
	All Patients	AAA	TAA	AAA and TAA
Sex				
Male	51/281 (18.2)	42/348 (12.1)	25/310 (8.1)	10/142 (7.0)
Female	77/800 (9.6)	14/92 (15.2)	23/136 (16.9)	14/53 (26.4)
Comorbidities				
Stroke/TIA	55/509 (10.8)	24/236 (10.2)	21/163 (12.9)	10/110 (9.1)
CAD	50/510 (9.8)	30/278 (10.8)	7/125 (5.6)	13/107 (12.2)
HTN	100/855 (11.7)	48/394 (12.2)	30/283 (10.6)	22/178 (12.4)
DM	22/208 (10.6)	12/119 (10.1)	3/56 (5.4)	7/33 (21.2)
HLP	83/743 (11.2)	40/369 (10.8)	27/228 (11.8)	16/146 (11.0)
Bicuspid aortic valve	13/142 (9.2)	0/3 (0.0)	10/132 (7.6)	3/7 (42.9)
Current/former smoker	48/308 (13.5)	25/214 (11.7)	7/68 (10.3)	16/74 (21.6)

Note:—CAD indicates carotid artery disease; HTN, hypertension; DM, diabetes mellitus; HLP, hyperlipidemia.

linked to cardiovascular risk factors. TAAs were strongly associated with bicuspid aortic valve ($P < .0001$). Patients with TAAs or both TAAs and AAAs were significantly younger than patients with AAAs alone ($P < .0001$).

Prevalence and Risk Factors for Aneurysm

Of the overall cohort, 128 patients (11.8%) had IAs, with a total of 172 IAs. The mean size of the IAs was 6.0 ± 5.8 mm. The IAs were located in the anterior circulation in 86.0% (148/172) of cases.

IAs were identified in 12.7% (56/440), 10.8% (48/446), and 12.3% (24/195), respectively, in patients with AAAs, TAAs, and both AAAs and TAAs. There was no statistical difference across groups for the location of associated IAs ($P = .67$), even when aneurysm locations were grouped into anterior or posterior cerebral circulation ($P = .93$). Similarly, the sizes of IAs were not different across the various groups ($P = .54$). The number of patients with multiple IAs was not different across the 3 AA groups ($P = .34$). The size of the AAAs or TAAs was not significantly associated with a higher prevalence of associated IAs in the different groups, except in the patients with both AAAs and TAAs and associated IAs who had larger AAAs than patients without associated IAs ($P = .003$).

A summary of risk factors for intracranial aneurysms in patients with aortic aneurysms is provided in Table 2. Prevalences of intracranial aneurysms by comorbidity are provided in Table 3. Among all patients, female sex was associated with higher odds of an intracranial aneurysm (OR = 2.08; 95% CI, 1.49–3.03; $P = .0002$). In addition, increased AAA size was associated with an

increased prevalence of IAs (OR = 1.02; 95% CI, 1.01–1.03; $P = .045$). Among patients with only AAAs, no variables were associated with an increased prevalence of IAs. Among patients with TAAs, only female sex (OR = 2.32; 95% CI, 1.26–4.26; $P = .006$) was associated with a higher risk of IA. No other variable, including the presence of a bicuspid valve, was associated with IAs. Among patients with both TAAs and AAAs, variables associated with IA formation were female sex (OR = 4.74; 95% CI, 1.95–11.50; $P = .0002$), the

presence of a bicuspid valve (OR = 5.96; 95% CI, 1.25–28.50; $P = .01$), and smoking history (OR = 3.90; 95% CI, 1.58–9.64; $P = .002$).

On multivariate logistic regression analysis, adjusting for aortic aneurysm type, aortic aneurysm size, sex, and the presence of carotid artery disease, female sex was the only variable independently associated with the presence of intracranial aneurysms (OR = 2.17; 95% CI, 1.25–3.70; $P = .006$).

Aneurysm Rupture

Of the 128 patients with intracranial aneurysms in this study, 8 had aneurysm rupture (6.3%). Five patients with ruptured aneurysms were men and 3 were women. Four had AAAs without TAAs, 2 had TAAs without AAAs, and 2 had both TAAs and AAAs. The mean size of the AAAs in the ruptured aneurysm population was 56 ± 12.2 mm, and the mean size of the TAAs was 41.5 ± 3.4 mm. Mean intracranial aneurysm size was 9.6 ± 10.5 mm. Six ruptured aneurysms were located in the anterior circulation, and 2 were located in the posterior circulation.

DISCUSSION

The present study demonstrates, in a large cohort of patients with AA, that the prevalence of associated IAs is high, with a global prevalence of 11.8%. This prevalence is about 4 times higher than that in the general population. Furthermore, this association is higher in women with TAAs. Female sex was the only variable independently associated with IAs in the AA population. There was no significant relation between the AA type and the pres-

ence of IAs. We also identified patients with coronary artery disease and hyperlipidemia having lower odds of IA. We did not find any significant association between the AA size and the presence of an IA or its location. These results are important because they suggest that further studies examining the role of IA screening in patients with AAA and TAA are warranted.

Our results are in accordance with a recent study published by Shin et al,¹⁴ who reported a 11.6% prevalence of IAs in a cohort of 611 patients with AAs. In a small study, Kuzmik et al¹³ observed a 9.0% prevalence of IAs in a series of 212 patients with TAAs. Unlike the study of Shin et al, we found that female sex was a significant risk factor for the presence of IAs, and we did not find any association between AA type and IA size or location. We did not find any higher risk for IAs in patients with AAs with hypertension or smoking history, contrary to the findings of Kuzmik et al.¹³

The present results suggest potential common pathophysiologic mechanisms for IA and AA. However, TAA and AAA have different origins, risk factors, and pathomechanisms.¹⁶ AAAs are related to cardiovascular risk factors,² as confirmed in our cohort, with significantly more patients with stroke/TIA, coronary artery disease, hypertension, diabetes, hyperlipidemia, and smoking history in the AAA group than in the TAA group. On the contrary, TAAs and IAs are mostly considered nonatherosclerotic arteriopathies, even though they share some common risk factors with AAAs, such as hypertension or tobacco use.^{1,11,14,16,17} TAAs usually appear in younger patients. However, the present study shows that whatever the location of the AA (either TAA or AAA), there is a high prevalence of associated IAs that appears to be independent of cardiovascular risk factors. A potential explanation is that the aorta and intracranial arteries embryologically originate from the neural crest cells, and some anomalous development of these cells (neurocristopathy) could explain the susceptibility for both AA and IA.^{18–20} However, despite the origin and susceptibility factors for AA and IA, their origin is probably a combination of genetic and environmental factors.

Furthermore, our study identified a prevalence of IAs in the AA population 4 times higher than in the general population. This is very important and should be taken into account when considering patients with AAs for a systematic screening to identify IAs. Indeed, in patients with autosomal dominant polycystic kidney disease, the prevalence of associated IA was around 10%, with a 4 times higher risk.^{15,17} According to this relative risk, some have advised a systematic screening with MRA for IA in ADPKD.^{21–26} However, to date, there is no proved benefit in morbidity, mortality, or reduction in subarachnoid hemorrhage among patients with ADPKD screened for IA,²⁷ potentially due to other factors such as a higher risk of IA treatment in patients with ADPKD, as recently suggested by Rozenfeld et al.^{28,29} In our study, the IA prevalence in patients with AAs was similar to the IA prevalence in the ADPKD population. Our results suggest that future prospective studies examining the role of IA screening in patients with AAs could be warranted, especially in female patients with TAAs.^{28,29}

Also, there is a high association of IA with AA in the perioperative care of AA. Indeed, the pressure on the cerebral arteries varies substantially due to cross-clamping and declamping of the

aorta during aortic surgery.³⁰ There is a theoretic potential risk of IA rupture with increasing cerebral perfusion pressure by occluding the aorta, albeit temporarily.³ Surgeons should be aware of the presence of an IA to avoid large pressure variations. In addition, measures such as strict postoperative blood pressure control can also be taken with a known IA, to reduce the risk of rupture.¹³ Systematic identification of an IA in patients with AAs seems beneficial to prevent IA rupture.

Limitations

Our study is limited by its retrospective nature. We could not exclude a potential selection bias because patients with previous neurologic symptoms were more likely to have cerebral arterial imaging available and to be included in the present study; this feature could create the possibility of skewing the data toward a greater prevalence of IA. It is also possible that we underestimated the prevalence of IA in this population. We did not search for the indication of arterial intracranial imaging, which could potentially introduce a selection bias if the imaging was performed to search for an intracranial aneurysm. We also did not document the time of IA detection in relation to the AA detection. There is also a limitation in the ascertainment of the smoking status because we did not differentiate patients with previous or current smoking history and did not perform any analysis regarding the pack-year consumption. Also for the TAA, we did not separate ascending and descending TAAs, which could potentially have different results regarding the incidence of associated IAs. Our study did not find any significant association between AA and IA locations, which could potentially be due to the low statistical power of multiple subgroup analyses; however, the global population of our cohort was the largest compared with previously published series.

CONCLUSIONS

This study shows that in a large AA cohort, prevalence of IAs is high in patients with AA. Women were at higher risk for concomitant IA. Further studies are needed to determine whether patients with known AAs should be screened for IAs.

Disclosures: Ramanathan Kadirvel—UNRELATED: Grants/Grants Pending: National Institutes of Health.* David F. Kallmes—UNRELATED: Board Membership: GE Healthcare.* Comments: Cost-Effectiveness Board; Consultancy: Medtronic.* Comments: planning and implementing clinical trials; Grants/Grants Pending: Medtronic.* MicroVent,.* Codman,* NeuroSigma,* Sequent Medical,* Surmodics.* *Money paid to the institution.

REFERENCES

1. Vlak MH, Algra A, Brandenburg R, et al. **Prevalence of unruptured intracranial aneurysms, with emphasis on sex, age, comorbidity, country, and time period: a systematic review and meta-analysis.** *Lancet Neurol* 2011;10:626–36 CrossRef Medline
2. Svensjo S, Björck M, Gürtelschmid M, et al. **Low prevalence of abdominal aortic aneurysm among 65-year-old Swedish men indicates a change in the epidemiology of the disease.** *Circulation* 2011;124:1118–23 CrossRef Medline
3. Curtis SL, Bradley M, Wilde P, et al. **Results of screening for intracranial aneurysms in patients with coarctation of the aorta.** *AJNR Am J Neuroradiol* 2012;33:1182–86 CrossRef Medline
4. Connolly HM, Huston J 3rd, Brown RD Jr, et al. **Intracranial aneurysms in patients with coarctation of the aorta: a prospective mag-**

- netic resonance angiographic study of 100 patients. *Mayo Clin Proc* 2003;78:1491–99 CrossRef Medline
5. Schievink WI, Raissi SS, Maya MM, et al. **Screening for intracranial aneurysms in patients with bicuspid aortic valve.** *Neurology* 2010; 74:1430–33 CrossRef Medline
 6. Shin YW, Jung KH, Kim JM, et al. **Echocardiographic evidence of innate aortopathy in the human intracranial aneurysm.** *PLoS One* 2014;9:e100569 CrossRef Medline
 7. Fields WS, Gonzalez-Angulo A. **Multiple aneurysmal dilatations of cerebral and peripheral arteries.** *Tex Med* 1965;61:899–905 Medline
 8. Kanai H, Umezu M, Koide K, et al. **Ruptured intracranial aneurysm associated with unruptured abdominal aortic aneurysm: case report.** *Neurol Med Chir (Tokyo)* 2001;41:260–63 CrossRef Medline
 9. Kubo S, Nakagawa H, Imaoka S. **Systemic multiple aneurysms of the extracranial internal carotid artery, intracranial vertebral artery, and visceral arteries: case report.** *Neurosurgery* 1992;30:600–02 CrossRef Medline
 10. Moore MT. **Multiple cerebral aneurysms in a patient with an abdominal aortic aneurysm: report of a case.** *J Neurosurg* 1965;23: 626–29 CrossRef Medline
 11. Southerland AM, Meschia JF, Worrall BB. **Shared associations of nonatherosclerotic, large-vessel, cerebrovascular arteriopathies: considering intracranial aneurysms, cervical artery dissection, Moyamoya disease and fibromuscular dysplasia.** *Curr Opin Neurol* 2013;26:13–28 CrossRef Medline
 12. Miyazawa N, Akiyama I, Yamagata Z. **Risk factors for the association of intracranial and aortic aneurysms.** *Acta Neurochir (Wien)* 2007; 149:221–29; discussion 229 CrossRef Medline
 13. Kuzmik GA, Feldman M, Tranquilli M, et al. **Concurrent intracranial and thoracic aortic aneurysms.** *Am J Cardiol* 2010;105:417–20 CrossRef Medline
 14. Shin YW, Jung KH, Moon J, et al. **Site-specific relationship between intracranial aneurysm and aortic aneurysm.** *Stroke* 2015;46: 1993–96 CrossRef Medline
 15. Xu HW, Yu SQ, Mei CL, et al. **Screening for intracranial aneurysm in 355 patients with autosomal-dominant polycystic kidney disease.** *Stroke* 2011;42:204–06 CrossRef Medline
 16. Norman PE, Powell JT. **Site specificity of aneurysmal disease.** *Circulation* 2010;121:560–68 CrossRef Medline
 17. Rinkel GJ, Djibuti M, Algra A, et al. **Prevalence and risk of rupture of intracranial aneurysms: a systematic review.** *Stroke* 1998;29:251–56 CrossRef Medline
 18. Noisa P, Raivio T. **Neural crest cells: from developmental biology to clinical interventions.** *Birth Defects Res C Embryo Today* 2014;102: 263–74 CrossRef Medline
 19. Weston JA, Thierry JP. **Pentimento: neural crest and the origin of mesectoderm.** *Dev Biol* 2015;401:37–61 CrossRef Medline
 20. Sattur M, Pines AR, Bendok B. **Thinking from the heart: neurocris-topathy, aortic abnormalities, and intracranial aneurysms.** *World Neurosurg* 2016;85:25–27 CrossRef Medline
 21. Wiebers DO, Torres VE. **Screening for unruptured intracranial aneurysms in autosomal dominant polycystic kidney disease.** *N Engl J Med* 1992;327:953–55 CrossRef Medline
 22. Huston J 3rd, Torres VE, Wiebers DO, et al. **Follow-up of intracranial aneurysms in autosomal dominant polycystic kidney disease by magnetic resonance angiography.** *J Am Soc Nephrol* 1996;7: 2135–41 Medline
 23. Chapman AB, Rubinstein D, Hughes R, et al. **Intracranial aneurysms in autosomal dominant polycystic kidney disease.** *N Engl J Med* 1992;327:916–20 CrossRef Medline
 24. Ruggieri PM, Poulos N, Masaryk TJ, et al. **Occult intracranial aneurysms in polycystic kidney disease: screening with MR angiography.** *Radiology* 1994;191:33–39 CrossRef Medline
 25. Mariani L, Bianchetti MG, Schroth G, et al. **Cerebral aneurysms in patients with autosomal dominant polycystic kidney disease: to screen, to clip, to coil?** *Nephrol Dial Transplant* 1999;14:2319–22 CrossRef Medline
 26. Huston J 3rd, Torres VE, Sullivan PP, et al. **Value of magnetic resonance angiography for the detection of intracranial aneurysms in autosomal dominant polycystic kidney disease.** *J Am Soc Nephrol* 1993;3:1871–77 Medline
 27. Chapman AB, Devuyst O, Eckardt KU, et al; Conference Participants. **Autosomal-dominant polycystic kidney disease (ADPKD): executive summary from a Kidney Disease—Improving Global Outcomes (KDIGO) Controversies Conference.** *Kidney Int* 2015;88: 17–27 CrossRef Medline
 28. Rozenfeld MN, Ansari SA, Mohan P, et al. **Autosomal dominant polycystic kidney disease and intracranial aneurysms: is there an increased risk of treatment?** *AJNR Am J Neuroradiol* 2016;37:290–93 CrossRef Medline
 29. Niemczyk M. **Treatment of unruptured intracranial aneurysms in autosomal dominant polycystic kidney disease: primum non nocere.** *AJNR Am J Neuroradiol* 2016;37:294–95 CrossRef Medline
 30. Liu G, Burcev I, Pott F, et al. **Middle cerebral artery flow velocity and cerebral oxygenation during abdominal aortic surgery.** *Anaesth Intensive Care* 1999;27:148–53 Medline

Ventricular Microaneurysms in Moyamoya Angiopathy Visualized with 7T MR Angiography

T. Matsushige, M. Kraemer, M. Schlamann, P. Berlit, M. Forsting, M.E. Ladd, U. Sure, and K.H. Wrede

ABSTRACT

SUMMARY: The pathophysiologic role of hemodynamic alteration to peripheral vessels in Moyamoya angiopathy and the formation of microaneurysms remains unclear. The purpose of this study was to investigate microaneurysms in collateral Moyamoya vessels by using 7T ultra-high-field MR imaging. Ten patients with Moyamoya disease were evaluated with TOF-MRA at 7T acquired with $0.22 \times 0.22 \times 0.41$ mm³ resolution. In 10 patients, 4 microaneurysms located in the ventricles were delineated. The mean diameters of collateral vessels and microaneurysms arising from those vessels were 0.87 mm (range, 0.79–1.07 mm) and 0.80 mm (range, 0.56–0.96 mm), respectively. In 1 case with follow-up scans 6 months after a direct extracranial-intracranial bypass operation, the microaneurysm disappeared. Ventricular microaneurysms in Moyamoya angiopathy collateral vessels, inaccessible by conventional imaging techniques, can be detected by 7T TOF-MRA.

ABBREVIATION: MMA = Moyamoya angiopathy

Moyamoya angiopathy (MMA) is a rare cerebrovascular pathology characterized by progressive occlusion of the terminal carotid arteries associated with the formation of collateral Moyamoya vessels.^{1,2} The patients could have ischemic and/or hemorrhagic stroke, though there are notable differences in clinical symptoms among the age of onset and race.^{3–6} The proposed pathophysiologic mechanism for hemorrhage in MMA is long-term hemodynamic stress to collateral vessels.^{5–8} It has been hypothesized that formation of microaneurysms might be an additional pathophysiologic explanation. Small aneurysms (2–3 mm) of these collateral vessels have been associated with intraventricular hemorrhage in several reports.^{7–11} However, the incidence and natural history of microaneurysms associated with MMA remain unclear because detection of submillimeter-range aneu-

rysms remains unfeasible with conventional imaging techniques. This study aimed to investigate underlying microaneurysms of collateral vessels by using ultra-high-field 7T TOF-MRA.

MATERIALS AND METHODS

In addition to a standard clinical work-up with 3T TOF-MRA and selective DSA, patients with MMA were prospectively recruited in a 7T TOF-MRA feasibility study between October 2011 and November 2012.¹² These data were recently re-evaluated to screen for the presence of microaneurysms in collateral Moyamoya vessels. The study was conducted according to the principles expressed in the Declaration of Helsinki and was approved by the University Duisburg-Essen institutional review board. Written informed consent was obtained before each examination. All 7T examinations were performed by using a whole-body MR imaging system (Magnetom 7T; Siemens, Erlangen, Germany) equipped with a 1-channel transmit/32-channel receive head radiofrequency coil (Nova Medical, Wilmington, Massachusetts). The system has a gradient system providing 45 mT/m maximum amplitude and a slew rate of 200 mT/m/ms. For MRA, a previously described customized 3D fast low-angle shot TOF pulse sequence was applied.^{12,13} Datasets were acquired with the following parameters: flip angle $\alpha = 18^\circ$, TE = 4.34 ms, TR = 20 ms, FOV = $200 \times 169 \times 46$ mm³, 112 sections per slab (oversampling 14%), parallel imaging (generalized autocalibrating partially parallel acquisition) with an acceleration factor R = 4 (phase direction), partial Fourier 6/8 in both section and phase directions, matrix = 896×756 (noninterpolated), voxel size = $0.22 \times$

Received December 18, 2015; accepted after revision February 5, 2016.

From the Departments of Neurosurgery (T.M., U.S., K.H.W.) and Diagnostic and Interventional Radiology and Neuroradiology (M.S., M.F.), University Hospital Essen, University Duisburg-Essen, Essen, Germany; Department of Neurosurgery (T.M.), Graduate School of Biomedical and Health Sciences, Hiroshima University, Hiroshima, Japan; Erwin L. Hahn Institute for Magnetic Resonance Imaging (T.M., M.E.L., K.H.W.), University Duisburg-Essen, Essen, Germany; Department of Neurology (M.K., P.B.), Alfried Krupp Hospital, Essen, Germany; Department of Neuroradiology (M.S.), University Hospital Giessen, Giessen, Germany; and Division of Medical Physics in Radiology (M.E.L.), German Cancer Research Center, Heidelberg, Germany.

T. Matsushige and M. Kraemer contributed equally to this work.

Karsten H. Wrede was supported by the University Duisburg-Essen (IFORES grant: Programm zur internen Forschungsförderung Essen).

Please address correspondence to Toshinori Matsushige, MD, University Hospital Essen, Department of Neurosurgery, Hufelandstr 55, 45147 Essen, Germany; e-mail: Toshinori.Matsushige@uk-essen.de, karsten.wrede@uk-essen.de

<http://dx.doi.org/10.3174/ajnr.A4786>

Patient demographics and anatomic characteristics for all microaneurysms

Pt No.	No.	Age (yr)	Sex	Bypass Surgery	Collateral Vessels	Microaneurysm	Location	Maximum Diameter (mm)	Diameter of a Ventricular Collateral Vessel (mm)
1	1	23	M	Pre	+	—			
	2	24		Post	+	—			
2	3	46	M	Post	+	—			
3	4	26		Pre	—	—			
4	5	35	F	Pre	++	+	3rd Vent.	0.76	1.07
5	6	34	F	Pre	++	+	3rd Vent.	0.56	0.82
	7	34		Post	++	Disappeared ^a	Disappeared ^a		
6	8	29	F	Pre	+	+	Lateral Vent.	0.96	0.79
7	9	58	F	Post	+	—			
8	10	42	F	Post	+	+	Subependium	0.93	0.81
9	11	38	F	Pre	—	—			
10	12	35	F	Pre	+	—			

Note:—Pt indicates patient; Pre, before; Post, after; +, moderate development of collateral vessels in the ventricles; ++, advanced development of collateral vessels in the ventricles; —, not delineated; Vent., ventricle.

^a Disappeared after bypass surgery.

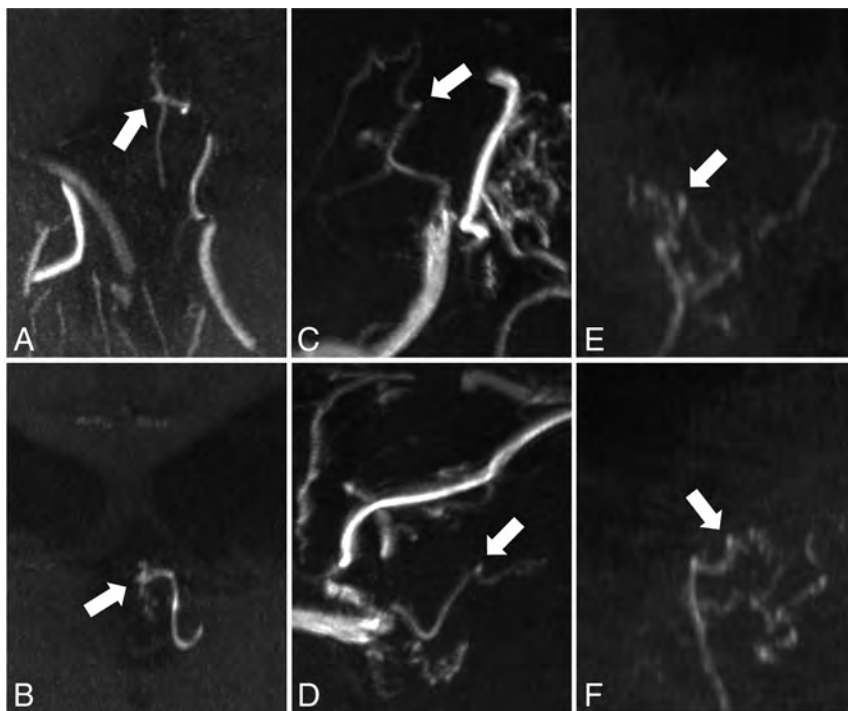


FIG 1. Two different projections of MIP from TOF-MRA at 7T in cases 4 (A and B), 6 (C and D), and 8 (E and F) demonstrate an intraventricular microaneurysm (arrow) arising from collateral vessels.

0.22 × 0.41 mm³ (noninterpolated), and total acquisition time of 6 minutes 22 seconds. Images were analyzed by 2 experienced vascular neurosurgeons (T.M. and K.H.W.) and an experienced neuroradiologist (M.S.) in a consensus reading by using an open-source medical image viewer (Horos; <http://www.horosproject.org/>) in a 3-step evaluation process. At first, every rater individually assessed the transverse source images for the presence of microaneurysms. In the second step, multiplanar 3D image reconstructions and MIPs were similarly evaluated. Finally, all 3 raters discussed their individual evaluations to establish a consensus reading.

RESULTS

Basic demographic data for all patients and major anatomic features of microaneurysms are summarized in the Table. There

were no signs of acute hemorrhage or bleeding remnants in any patient. Collateral vessels in the ventricles branching from the posterior choroidal arteries were present in 8 of 10 patients. Neither conventional MRA nor DSA detected microaneurysms in these collateral Moyamoya vessels. All raters detected 3 microaneurysms in transverse source images during the initial evaluation (cases 5, 6, and 8). Two raters detected a microaneurysm in transverse source images (case 4), which was only suspected in these images by the third rater. All 4 microaneurysms were individually detected by the raters in multiplanar 3D image reconstructions and MIPs. After individual assessments, all findings were discussed to have a consensus reading. There was no false-positive or false-negative detection of a microaneurysm by a single rater. The mean diameters of collateral vessels and microaneurysms arising from those vessels were 0.87 mm (range, 0.79–1.07 mm) and 0.80 mm (range, 0.56–0.96 mm), respectively.

Figure 1 illustrates specific features of 3 microaneurysms. One microaneurysm disappeared on the follow-up examination 6 months after the direct extracranial-intracranial bypass operation (Figs 2 and 3).

DISCUSSION

This is the first presentation of MMA with microaneurysms in collateral Moyamoya vessels. This study illustrates the possible clinical application of 7T TOF-MRA to detect submillimeter-range microaneurysms arising from peripheral collateral vessels in MMA. So far, only 1 histopathologic study has analyzed the presence of microaneurysms (200- to 550-μm diameter) in MMA.¹⁴ It revealed true microaneurysm formation or degenerative changes in the vessels predisposing to rupture of perforating

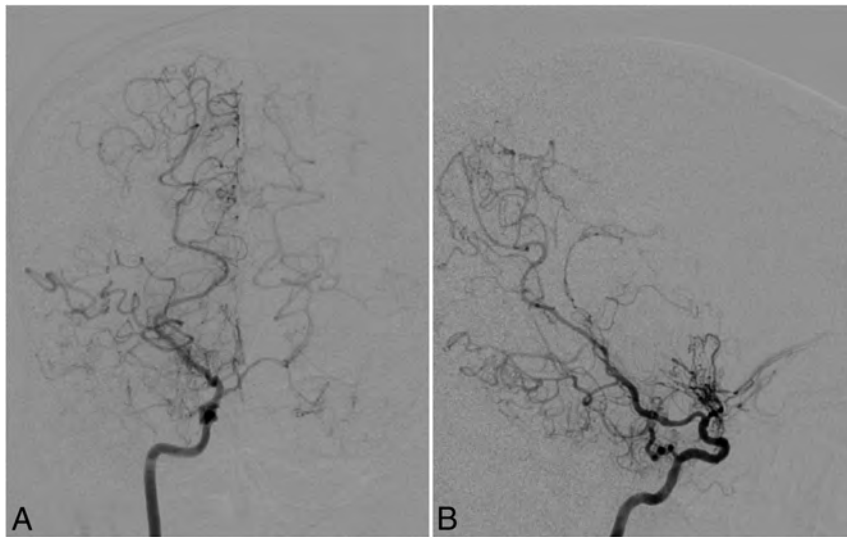


FIG 2. Cerebral angiography with anteroposterior (A) and lateral (B) views in case 5. Right internal carotid angiography reveals occlusion of the right carotid fork and tiny basal collateral vessels. The right posterior cerebral artery and right posterior choroidal artery are also prominent as collateral vessels. No intracranial aneurysms can be delineated.

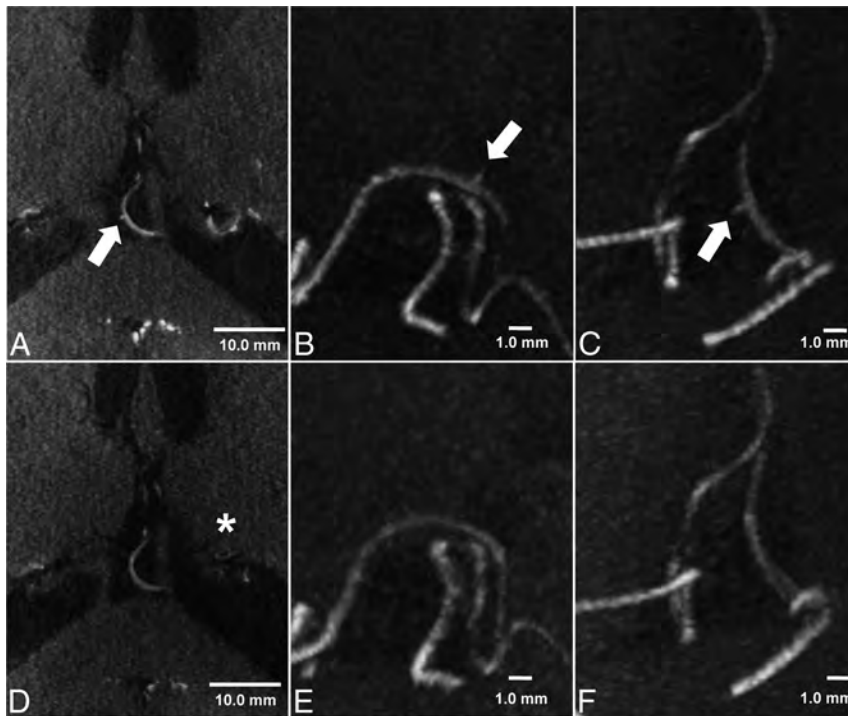


FIG 3. TOF-MRA and MIP of TOF-MRA at 7T before (A–C) and 6 months after (D–F) the bypass operation in case 5. A microaneurysm (560- μ m maximum diameter) is delineated arising from a collateral vessel of the posterior choroidal artery in the third ventricle (arrow). Six months after the bypass operation, MIP of TOF-MRA shows disappearance of the microaneurysm. The signal intensity of collateral vessels has decreased in the matched axial planes (asterisk). The scale bar indicates 10.0 mm (TOF-MRA, A and D) and 1.0 mm (MIP image, B and C; E and F), respectively.

arteries. However, the prevalence of these microaneurysms remains unclear because current imaging techniques are unable to detect them. Given the previously published histopathologic data,¹⁴ spatial resolution has to be well below the diameter of Moyamoya vessels to be capable of visualizing microaneurysms. Detecting these submillimeter-range microaneurysms in com-

plex and tiny collateral Moyamoya vessels remains unfeasible even for DSA, the current criterion standard, or high-resolution 3T MRA. The high spatial resolution used in the presented study allowed visualizing these microaneurysms in vivo for the first time. Several recent studies showed the excellent diagnostic accuracy of this imaging technique to delineate microvascular structures and vessel walls.^{15–18}

The formation of flow-related aneurysms has recently been investigated in patients with cerebral arteriovenous malformations.¹⁹ The proposed pathophysiologic mechanism involves hemodynamic alterations to peripheral vessel walls that cannot compensate for increased blood flow.¹⁹ The same pathophysiologic mechanism seems to play a key role in aneurysm formation in MMA and can explain intracranial hemorrhage in patients with Moyamoya disease.^{5–8} Nevertheless, dedicated computational flow simulations are pending to evaluate this hypothesis. Several authors suggested the relevance of hemodynamic changes for the treatment of flow-related peripheral aneurysms.^{9–11} In their recent study, Miyamoto et al²⁰ showed a significant reduction of intracranial hemorrhage after superficial temporal artery–MCA bypass surgery. They speculated that reduction of long-term hemodynamic alterations in fragile Moyamoya collateral vessels might explain their findings. The disappearance of 1 microaneurysm in the present case series (case 5) might support the hypothesis of favorable hemodynamic alterations after a bypass operation.

The prevalence of microaneurysms and their pathophysiologic relevance remains unclear. This report warrants further prospective studies to reveal the prevalence of microaneurysms associated with MMA and their fate after treatment.

Limitations

The lack of a diagnostic criterion standard for nonsurgical detection of microaneurysms is the main limitation of the present study. None of the patients underwent surgical exposure of parent vessels and microaneurysms. Thus, histopathologic validation of the microaneurysms was not available. However, the dedicated 3-step image assessment by 3 experienced raters and the high spatial resolution of the

applied 7T TOF sequence yields reliable results. The high diagnostic accuracy to delineate microvascular structures has recently been shown for the applied TOF sequence.

The small number patients was another limitation to the study. However, enlisting a substantially larger number of patients with MMA for a 7T MR imaging study remains restricted due the low incidence of MMA and the limited availability of 7T MR imaging systems.

CONCLUSIONS

Ventricular microaneurysms in MMA collateral vessels, inaccessible by conventional imaging techniques, can be detected by 7T TOF-MRA.

Disclosures: Markus Kraemer—UNRELATED: Grants/Grants Pending: Novartis grant, grant from German Neurology Society; Payment for Lectures (including service on Speakers Bureaus): Teva, Novartis, Merck Serono, Shire; Travel/Accommodations/Meeting Expenses Unrelated to Activities Listed: Teva, Biogen, Novartis. Peter Berlit—UNRELATED: Payment for Lectures (including service on Speakers Bureaus): Merck, Sharp & Dohme GmbH, Bayer HealthCare Pharmaceuticals, Novartis. Karsten H. Wrede—RELATED: Grant: IFORES (Programm zur internen Forschungsförderung Essen, University Duisburg-Essen).

REFERENCES

1. Suzuki J, Takaku A. Cerebrovascular “moyamoya” disease: disease showing abnormal net-like vessels in base of brain. *Arch Neurol* 1969;20:288–99 CrossRef Medline
2. Research Committee on the Pathology and Treatment of Spontaneous Occlusion of the Circle of Willis; Health Labour Sciences Research Grant for Research on Measures for Infractable Diseases. Guidelines for diagnosis and treatment of moyamoya disease (spontaneous occlusion of the circle of Willis). *Neurol Med Chir (Tokyo)* 2012;52:245–66 CrossRef Medline
3. Hallemeier CL, Rich KM, Grubb RL Jr, et al. Clinical features and outcome in North American adults with moyamoya phenomenon. *Stroke* 2006;37:1490–96 CrossRef Medline
4. Kraemer M, Heienbrok W, Berlit P. Moyamoya disease in Europeans. *Stroke* 2008;39:3193–200 CrossRef Medline
5. Kuroda S, Houkin K. Moyamoya disease: current concepts and future perspectives. *Lancet Neurol* 2008;7:1056–66 CrossRef Medline
6. Takahashi JC, Miyamoto S. Moyamoya disease: recent progress and outlook. *Neurol Med Chir (Tokyo)* 2010;50:824–32 CrossRef Medline
7. Kawaguchi S, Sakaki T, Morimoto T, et al. Characteristics of intracranial aneurysms associated with moyamoya disease: a review of 111 cases. *Acta Neurochir* 1996;138:1287–94 CrossRef Medline
8. Kobayashi E, Saeki N, Oishi H, et al. Long-term natural history of hemorrhagic moyamoya disease in 42 patients. *J Neurosurg* 2000;93:976–80 CrossRef Medline
9. Adams HP Jr, Kassell NF, Wisoff HS, et al. Intracranial saccular aneurysm and moyamoya disease. *Stroke* 1979;10:174–79 CrossRef Medline
10. Kuroda S, Houkin K, Kamiyama H, et al. Effects of surgical revascularization on peripheral artery aneurysms in moyamoya disease: report of three cases. *Neurosurgery* 2001;49:463–67; discussion 67–68 CrossRef Medline
11. Ni W, Xu F, Xu B, et al. Disappearance of aneurysms associated with moyamoya disease after STA-MCA anastomosis with encephaloduro myosynangiosis. *J Clin Neurosci* 2012;19:485–87 CrossRef Medline
12. Wrede KH, Johst S, Dammann P, et al. Improved cerebral time-of-flight magnetic resonance angiography at 7 Tesla: feasibility study and preliminary results using optimized venous saturation pulses. *PLoS One* 2014;9:e106697 CrossRef Medline
13. Johst S, Wrede KH, Ladd ME, et al. Time-of-flight magnetic resonance angiography at 7 T using venous saturation pulses with reduced flip angles. *Invest Radiol* 2012;47:445–50 CrossRef Medline
14. Yamashita M, Oka K, Tanaka K. Histopathology of the brain vascular network in moyamoya disease. *Stroke* 1983;14:50–58 CrossRef Medline
15. Conijn MM, Geerlings MI, Biessels GJ, et al. Cerebral microbleeds on MR imaging: comparison between 1.5 and 7T. *AJNR Am J Neuroradiol* 2011;32:1043–49 CrossRef Medline
16. van der Kolk AG, Zwanenburg JJ, Denswil NP, et al. Imaging the intracranial atherosclerotic vessel wall using 7T MRI: initial comparison with histopathology. *AJNR Am J Neuroradiol* 2015;36:694–701 CrossRef Medline
17. Matsushige T, Chen B, Ringelstein A, et al. Giant intracranial aneurysms at 7T MRI. *AJNR Am J Neuroradiol* 2015 Nov 12. [Epub ahead of print] Medline
18. Matsushige T, Chen B, Dammann P, et al. Microanatomy of the subcallosal artery: an in-vivo 7 T magnetic resonance angiography study. *Eur Radiol* 2015 Nov 24. [Epub ahead of print] Medline
19. Shakur SF, Amin-Hanjani S, Mostafa H, et al. Hemodynamic characteristics of cerebral arteriovenous malformation feeder vessels with and without aneurysms. *Stroke* 2015;46:1997–99 CrossRef Medline
20. Miyamoto S, Yoshimoto T, Hashimoto N, et al; JAM Trial Investigators. Effects of extracranial-intracranial bypass for patients with hemorrhagic moyamoya disease: results of the Japan Adult Moyamoya Trial. *Stroke* 2014;45:1415–21 CrossRef Medline

Risk Factors for Ischemic Complications following Pipeline Embolization Device Treatment of Intracranial Aneurysms: Results from the IntrePED Study

W. Brinjikji, G. Lanzino, H.J. Cloft, A.H. Siddiqui, E. Boccardi, S. Cekirge, D. Fiorella, R. Hanel, P. Jabbour, E. Levy, D. Lopes, P. Lylyk, I. Szikora, and D.F. Kallmes



ABSTRACT

BACKGROUND AND PURPOSE: Risk factors for acute ischemic stroke following flow-diverter treatment of intracranial aneurysms are poorly understood. Using the International Retrospective Study of Pipeline Embolization Device (IntrePED) registry, we studied demographic, aneurysm, and procedural characteristics associated with postoperative acute ischemic stroke following Pipeline Embolization Device (PED) treatment.

MATERIALS AND METHODS: We identified patients in the IntrePED registry with post-PED-treatment acute ischemic stroke. The rate of postoperative acute ischemic stroke was determined by demographics, comorbidities, aneurysm characteristics, and procedure characteristics (including anticoagulation use, platelet testing, number of devices used, sheaths, and so forth). Categorical variables were compared with χ^2 testing, and continuous variables were compared with the Student *t* test. Odds ratios and 95% confidence intervals were obtained by using univariate logistic regression. Multivariate logistic regression analysis was used to determine which factors were independently associated with postoperative stroke.

RESULTS: Of 793 patients with 906 aneurysms, 36 (4.5%) patients had acute ischemic stroke. Twenty-six (72.2%) strokes occurred within 30 days of treatment (median, 3.5 days; range, 0–397 days). Ten patients died, and the remaining 26 had major neurologic morbidity. Variables associated with higher odds of acute ischemic stroke on univariate analysis included male sex, hypertension, treatment of MCA aneurysms, treatment of fusiform aneurysms, treatment of giant aneurysms, and use of multiple PEDs. However, on multivariate analysis, the only one of these variables independently associated with stroke was treatment of fusiform aneurysms (OR, 2.74; 95% CI, 1.11–6.75; *P* = .03). Fusiform aneurysms that were associated with stroke were significantly larger than those not associated with stroke (mean, 24.5 ± 12.5 mm versus 13.6 ± 6.8 mm; *P* < .001).

CONCLUSIONS: Ischemic stroke following PED treatment is an uncommon-but-devastating complication. Fusiform aneurysms were the only variable independently associated with postoperative stroke.

ABBREVIATIONS: PED = Pipeline Embolization Device; IntrePED = International Retrospective Study of Pipeline Embolization Device

The Pipeline Embolization Device (PED; Covidien, Irvine, California) is increasingly used in the treatment of intracranial aneurysms.^{1–5} The bare metal construct of the PED serves as a

scaffold for neointimal proliferation, thereby excluding the aneurysm sac from the parent artery.^{6,7} A number of previous studies have demonstrated that the PED is associated with high rates of aneurysm occlusion with relatively low complication rates.^{1,3} Although uncommon, postoperative acute ischemic stroke is the most common neurologic complication to occur following treatment of aneurysms with flow diverters such as the PED, with estimated rates of 3%–6% of patients.^{3,8,9} Understanding the risk factors for post-Pipeline ischemic complications is important for risk stratification and consent of these patients. Using the International Retrospective Study of Pipeline Embolization Device

Received October 19, 2015; accepted after revision February 9, 2016.

From the Departments of Radiology (W.B., G.L., H.J.C., D.F.K.) and Neurosurgery (G.L., H.J.C., D.F.K.), Mayo Clinic, Rochester, Minnesota; Department of Neurosurgery (A.H.S., D.F., E.L.), State University of New York, Buffalo, New York; Department of Neuroradiology (E.B.), Ospedale Niguarda-Ca' Granda, Milan, Italy; Department of Radiology (S.C.), Hacettepe University Hospitals, Ankara, Turkey; Department of Neurosurgery (R.H.), Baptist Neurological Institute, Jacksonville, Florida; Department of Neurosurgery (P.J.), Thomas Jefferson University Hospital, Philadelphia, Pennsylvania; Department of Neurosurgery (D.L.), Rush University Medical Center, Chicago, Illinois; Department of Interventional Neuroradiology (P.L.), Instituto Clínico ENERI, Buenos Aires, Argentina; and Department of Neuroradiology (I.S.), National Institute of Neurosciences, Budapest, Hungary.

The lead author had access to all data. The authors were responsible for the decision to publish the manuscript.

This work was funded by Medtronic.

Please address correspondence to Waleed Brinjikji, MD, Mayo Clinic, 200 First St SW, OL1-112 SMH, Rochester, MN 55905; e-mail: brinjikji.waleed@mayo.edu; @wbrinjikji

Indicates article with supplemental on-line table.

<http://dx.doi.org/10.3174/ajnr.A4807>

registry (IntrePED), we compared the clinical and procedural characteristics of patients who had postoperative acute ischemic stroke with those who did not, to determine which clinical and procedural characteristics were associated with this condition.

MATERIALS AND METHODS

Study Design and Participants

This study is a subanalysis of the IntrePED study, which has been previously published.⁹ Details regarding ethics committee and institutional review board approval and inclusion and exclusion criteria are provided in the original article.⁹ Several additional subgroup analyses separate from this study are currently underway using data from the IntrePED registry. This study will be the only subgroup analysis performed examining variables associated with acute ischemic stroke in the IntrePED registry. We retrospectively evaluated all patients with intracranial aneurysms treated with the Pipeline Embolization Device in the IntrePED registry. Seven hundred ninety-three patients with 906 treated aneurysms were enrolled.

Procedures

Because this was a retrospective registry, procedural details and patient management varied across centers. All centers reported baseline characteristics of patients and aneurysms, procedural information, and follow-up information from clinic visits or telephone calls by using a common study protocol form. Site investigators identified patients with acute ischemic stroke by using the study protocol form. All complications, including acute ischemic stroke, were reviewed in detail by an Adverse Events Review Committee, comprising 3 members of the Steering Committee, including the overall study principal investigator. The committee determined whether the acute ischemic stroke was major or minor. A “major” adverse event was defined as an ongoing clinical deficit at 7 days following the event. All major adverse events are included in the neurologic morbidity and mortality rates. Timing of all adverse events was in relation to the time of PED placement.

Baseline Characteristics and Outcomes

For each patient, the following characteristics were collected as part of this study: age, sex, hypertension, control of hypertension, smoking status, aneurysm location, aneurysm rupture status, aneurysm type, aneurysm size, use of antiplatelet medications before the procedure, use of platelet aggregation studies, heparin administration and reversal, number of PEDs used, type of sheath used, type of guide catheter used, type of microcatheter used, type of guidewire used, balloons used, and type of closure device used. The incidence of acute ischemic stroke was calculated for each of the above-mentioned variables.

In addition, for patients with any acute ischemic stroke, we obtained the following information: whether the stroke was ipsilateral or contralateral to the device, timing after the operation, and final clinical outcome (minor morbidity, major morbidity, or death). “Minor morbidity” was defined as a clinical deficit that persisted for <7 days, and “major morbidity” was defined as a clinical deficit that persisted ≥ 7 days.

Statistical Analysis

Statistical analyses were performed by using SAS, Version 9.2 (SAS Institute, Cary, North Carolina). Descriptive statistics were used to present the data and to summarize the results. Discrete variables are presented by using frequency distributions and cross-tabulations. Continuous variables are summarized by presenting the number of observations, mean, and SD and median, minimum, and maximum values. For categorical variables, differences between the groups were tested by using appropriate contingency table analyses (exact or χ^2 approximations). For continuous variables, the differences were tested by using an unpaired Student *t* test or a nonparametric test, depending on variable distribution. Odds ratios and 95% confidence intervals were obtained by using univariate logistic regression. We also performed a multivariate logistic regression analysis to determine which factors were independently associated with postoperative stroke. Variables included in this model were those that were statistically significantly associated with postoperative stroke on the univariate analysis. Because treatment of fusiform aneurysms was the only variable significantly associated with postoperative stroke on the multivariate analysis, we performed a separate post hoc subgroup analysis comparing the features of fusiform aneurysms that were and were not associated with stroke. All statistical analyses were performed on a per-patient basis.

Role of the Funding Source

The principal investigator and steering committee were independent of the funding source (Medtronic; Dublin, Ireland). The steering committee interpreted the results, and the principal investigator wrote the report. The study sponsor was responsible for site management, data management, statistical analysis, and safety reporting. The corresponding author had full access to all study data and had final responsibility for the decision to submit for publication.

RESULTS

Patient and Aneurysm Characteristics and Acute Ischemic Stroke

A summary of the baseline characteristics of all patients included in the IntrePED registry is provided elsewhere.⁹ Thirty-six (4.5%) patients had postoperative acute ischemic stroke, while 757 patients (95.5%) did not. There was no difference in the mean age of patients with and without acute ischemic stroke (54.2 ± 15.6 years versus 57.0 ± 14.1 years, $P = .2516$); 8.1% of male patients (13/161) and 3.6% of female patients (23/632) had acute ischemic stroke ($P = .02$). Hypertension was also associated with postoperative stroke because 9.2% of patients with hypertension (23/249) and 3.8% of patients without hypertension (12/318) had stroke ($P = .009$). These data are summarized in Table 1.

There was no difference in the rate of acute ischemic stroke between anterior circulation aneurysms (30/704, 4.3%) and posterior circulation aneurysms (6/89, 6.7%) ($P = .29$). Patients with middle cerebral artery aneurysms had higher odds of stroke than those with internal carotid artery aneurysms (12.5%, 5/40 versus 3.9%, 23/590; $P = .01$). The rate of stroke (9.3%, 4/43) in patients

Table 1: Demographic and aneurysm characteristics

Variable	No. Stroke/No. Total (%)	OR (95% CI)	P Value
Age (yr)	54.2 ± 15.6/57.0 ± 14.1	0.99 (0.97–1.01)	.2516
Sex			
Male	8.1% (13/161)	2.33 (1.15–4.70)	.0187
Female	3.6% (23/632)	Ref	
Hypertension			
Yes	9.2% (23/249)	2.60 (1.26–5.33)	.0093
No	3.8% (12/318)	Ref	
Controlled hypertension			
Yes	8.7% (18/206)	3.03 (1.54–5.94)	.0013
No	0.0% (0/4)	Ref	
Current smoker			
Yes	4.3% (4/94)	0.93 (0.32–2.68)	.8878
No	4.6% (32/699)	Ref	
Aneurysm location			
Posterior circulation	6.7% (6/89)	1.62 (0.66–4.02)	.2940
Anterior circulation	4.3% (30/704)	Ref	
Aneurysm location by vessel			
Internal carotid artery	3.9% (23/590)	Ref	
Anterior cerebral artery	12.5% (1/8)	4.83 (0.72–32.44)	.1052
Basilar artery	9.3% (4/43)	2.75 (0.94–8.02)	.0636
Middle cerebral artery	12.5% (5/40)	3.74 (1.38–10.16)	.0096
PcomA	1.9% (1/53)	0.69 (0.13–3.74)	.6668
Vertebral artery	6.1% (2/33)	1.92 (0.49–7.55)	.3523
Other	0.0% (0/26)	0.46 (0.03–8.12)	.5928
Rupture status			
Ruptured	5.4% (4/74)	1.23 (0.42–3.57)	.7074
Unruptured	4.5% (32/719)	Ref	
Aneurysm type			
Saccular	3.2% (19/600)	Ref	
Fusiform	12.7% (13/102)	4.47 (2.13–9.36)	.0001
Dissecting	3.8% (2/53)	1.20 (0.27–5.29)	.8105
Other	5.3% (2/38)	1.70 (0.38–7.58)	.4873
Aneurysm size			
<10 mm	2.6% (10/387)	Ref	
10–24.9 mm	4.7% (16/338)	1.87 (0.84–4.19)	.1260
≥25 mm	14.3% (9/63)	6.28 (2.44–16.16)	.0001

Note:—Ref. indicates reference; PcomA, posterior communicating artery.

Table 2: Multivariate analysis

Variable	OR (95% CI)	P Value
Male	1.21 (0.51–2.85)	.6636
HTN	2.01 (0.99–4.08)	.0533
ACA vs ICA	4.47 (0.58–34.44)	.1502
BAS vs ICA	1.12 (0.31–4.04)	.8584
MCA vs ICA	2.79 (0.91–8.60)	.0734
Other artery vs ICA	0.53 (0.03–9.04)	.6596
PcomA vs ICA	0.84 (0.15–4.53)	.8351
Vertebral artery vs ICA	1.27 (0.27–6.09)	.7620
Dissecting vs saccular	0.83 (0.19–3.63)	.8089
Fusiform vs saccular	2.74 (1.11–6.75)	.0283
Other aneurysm type vs saccular	1.71 (0.44–6.66)	.4370
Aneurysm size	1.03 (0.99–1.07)	.1370
PED No.	1.17 (0.94–1.45)	.1610

Note:—HTN indicates hypertension; ACA, anterior cerebral artery; BAS, basilar artery; PcomA, posterior communicating artery.

with basilar artery aneurysms was higher than in those with internal carotid artery aneurysms, but the difference trended toward statistical significance ($P = .06$). There was no difference in stroke rates between ruptured (5.4%, 4/74) and unruptured (4.5%, 32/719) aneurysms ($P = .71$). Patients with fusiform aneurysms had significantly higher stroke rates (12.7%, 13/102) than those with saccular aneurysms (3.2%, 19/600; $P = .0001$). Giant aneurysms had higher

rates of stroke than small aneurysms (14.3%, 9/63 versus 2.6%, 10/387; $P = .0001$). These data are summarized in Table 1.

Treatment Characteristics and Acute Stroke

The stroke rate in patients with 1 PED was 3.0% (16/533) compared with 7.1% (13/183) in patients with 2 PEDs ($P = .02$) and 9.2% (7/76) in patients with ≥ 3 PEDs ($P = .008$). There was no difference in stroke rates based on how PEDs were used. Use of a microcatheter other than the Marksman (Covidien) was associated with a 16.7% risk of stroke (4/24), while the use of a Marksman was associated with a 5.7% risk of stroke (32/557, $P = .04$). There was no difference in stroke rates between patients with and without preprocedural antiplatelet therapy (4.6%, 31/681 versus 4.5%, 5/112; $P = .97$) or among patients with and without preprocedural platelet aggregation studies (5.1%, 29/564 versus 3.1%, 7/229, $P = .21$). These data are summarized in the On-line Table.

Multivariate Analysis

On multivariate analysis, the only variable independently associated with postoperative stroke was treatment of fusiform aneurysms (OR, 2.74; 95% CI, 1.11–6.75, $P = .03$). Higher rates of

acute stroke were observed in patients with hypertension (OR, 2.01; 95% CI, 0.99–4.08; $P = .053$) and in patients with aneurysms of the MCA (OR, 2.79; 95% CI, 0.91–8.60; $P = .07$), but the differences were not statistically significant. The use of multiple PEDs was not independently associated with postoperative infarct (OR, 1.17; 95% CI, 0.94–1.45; $P = .16$). These data are summarized in Table 2.

Timing and Clinical Outcomes of Stroke

Of the 36 patients with stroke, 21 (58.3%) had stroke within 1 week of the procedure. Five patients (13.9%) had stroke between 1 week and 1 month of the procedure, 5 patients (13.9%) had stroke between 1 and 6 months after the procedure, and 5 patients had stroke ≥ 6 months after the procedure (13.9%). The median time of onset for stroke was 3.5 days, and the mode was 0 days as 8 patients had stroke on day 0. Among patients with stroke, 10 (27.0%) died and 26 (73.0%) had major neurologic morbidity. The location of the stroke was ipsilateral to the device in 34 of 36 patients (94.4%), including 2 patients who also had contralateral infarcts. In 2 patients, the infarcted area was located contralateral to the device and there was no ipsilateral infarct. None of the strokes occurred in the intraoperative period.

Table 3: Subgroup analysis of fusiform aneurysms

Aneurysm Characteristics	With Stroke	Without Stroke	P Value
Aneurysm size (mm)			<.001
Mean (No.)	24.5 ± 12.5 (12)	13.6 ± 6.8 (88)	
Median (range)	21.0 (13.0–55.0)	11.8, (1.6–42.0)	
Aneurysm neck (mm)			.010
Mean (No.)	26.2 ± 19.5 (9)	10.2 ± 5.2 (60)	
Median (range)	22.0 (8.0–53.0)	9.0 (2.0–27.0)	
Aneurysm location			.211
Posterior circulation	38.5% (5/13)	22.5% (20/89)	
Anterior circulation	61.5% (8/13)	77.5% (69/89)	
Aneurysm location by vessel			.677
ICA	53.8% (7/13)	59.6% (53/89)	
ACA	0.0% (0/13)	1.1% (1/89)	
BA	23.1% (3/13)	10.1% (9/89)	
MCA	7.7% (1/13)	13.5% (12/89)	
PcomA	0.0% (0/13)	0.0% (0/89)	
VA	15.4% (2/13)	10.1% (9/89)	
Other	0.0% (0/13)	5.6% (5/89)	
Presented with ruptured aneurysm	0.0% (0/13)	5.6% (5/89)	.381

Note:—BA indicates basilar artery; VA, vertebral artery; PcomA, posterior communicating artery; ACA, anterior cerebral artery.

Subgroup Analysis of Fusiform Aneurysms

On the subgroup analysis of fusiform aneurysms, 13 fusiform aneurysms were included in the stroke group and 89 were included in the nonstroke group. Fusiform aneurysms associated with stroke were significantly larger than those not associated with stroke (mean, 24.5 ± 12.5 mm versus 13.6 ± 6.8 mm; $P < .001$). Aneurysm neck size was also significantly larger in the stroke subgroup than in the nonstroke subgroup (mean, 26.2 ± 19.5 mm versus 10.2 ± 5.2 mm; $P = .01$). There was no difference in aneurysm location or rupture status between groups. These data are summarized in Table 3.

DISCUSSION

Our current large, multicenter study of flow-diversion therapy demonstrated that approximately 5% of patients have postoperative acute ischemic stroke with most occurring in the early postoperative period. All patients who experienced postoperative acute ischemic stroke in our study either had major morbidity or died. In our series, treatment variables associated with stroke included male sex, hypertension, treatment of MCA aneurysms, giant aneurysms, fusiform aneurysms, and the use of multiple PEDs. However, treatment of fusiform aneurysms was the only variable independently associated with postoperative stroke. Most interesting, fusiform aneurysms made up more than one-third of all cases of postoperative stroke, while comprising slightly more than one-tenth of all patients with PED. Fusiform aneurysms associated with stroke were generally large or giant with a mean size of nearly 25 mm and a mean neck size of 26 mm. These findings are important because they provide additional information that can be used to risk-stratify patients treated with the PED by using a multi-institutional real-world data base.

The stroke rate in IntrePED is similar to that in other large studies. In one meta-analysis, Brinjikji et al³ noted an acute ischemic stroke rate of 5.0% within 30 days of flow-diverter treatment and 3.0% beyond 30 days. These findings are similar to those of our study in which we found that nearly 75% of acute ischemic stroke events occurred within 30 days of the procedure. Ischemic stroke rates in a more recently published meta-analysis on aneu-

rysm treatment with flow diverters found an ischemic stroke rate of 4.1%, similar to that seen in our study.¹⁰ In the Pipeline for Uncoiled or Failed Aneurysms (PUFS) trial, the rate of acute ischemic stroke within 180 days of treatment was 6.5%, with 2.8% of patients having stroke secondary to in-stent thrombosis or occlusion caused by in-stent stenosis.⁸ The rate of stroke after 6 months in PUFS was 0%, while in our study, the stroke rate after 6 months was just 0.6% (5/793).⁸

There are a number of potential mechanisms for postoperative cerebral infarction following PED therapy. Perioperative stroke secondary to catheter-related thromboemboli is a common mechanism of stroke in this population as many studies have now demonstrated

that well over 50% of patients treated with flow diverters have multiple foci of restricted diffusion on immediate postoperative MR imaging.¹¹ Acute and subacute in-stent thrombosis during the procedure and in the postoperative period resulting in occlusion of the parent vessel with or without distal emboli is another common mechanism of stroke, possibly related to the thrombogenic nature of the bare metal construct or lack of adequate antiplatelet therapy.^{12,13} Other mechanisms of stroke include particle emboli from devices such as catheters or sheaths.^{14–16} Intraoperatively, acute thrombus formation can be mitigated by prompt injection of glycoprotein IIb/IIIa platelet inhibitors; however, it is difficult to reduce the long-term risk of thromboembolic events associated with flow-diverter treatment.^{3,9} In general, delayed ischemic events are uncommon.¹⁷

In our series, higher stroke rates were seen following treatment of MCA and basilar artery aneurysms than in ICA aneurysms, though these results are not statistically significant. Prior studies have demonstrated that aneurysms of the posterior circulation and MCA are at higher risk of thromboembolic complications due to the risk of perforator infarction.^{3,18} Perforator infarction due to coverage of the lenticulostriates and brain stem perforators secondary to reduced flow and perforator occlusion are likely responsible for the higher stroke rates seen in these patients in some studies.^{18,19} In a study of 17 patients with flow-diverter coverage of perforator arteries, Gawlitza et al¹⁸ noted that 7 of 17 patients had infarctions in the territory of the covered perforators, of which 2 were symptomatic. In their meta-analysis of >1300 cases, Brinjikji et al³ noted a perforator infarction rate of 3.0% among all treated aneurysms with a significantly higher rate of perforator infarction in the treatment of posterior circulation aneurysms than in anterior circulation aneurysms.

A number of studies have reported poor outcomes and high rates of thrombosis in the treatment of dolichoectatic and fusiform aneurysms, particularly of the posterior circulation, with flow diverters in general.^{9,20,21} High rates of infarction

seen in these patients are likely due to a combination of poor wall apposition due to the large size of the aneurysm, early discontinuation of antiplatelet therapy, and the requirement for multiple PEDs.^{20,21} Recently, there has been increased interest in the relationship between wall apposition of the flow diverter and rates of delayed postoperative stroke.²² It is thought that poor wall apposition can result in delayed endothelialization of the stent, resulting in an increased risk of in-stent thrombosis in the delayed postoperative period.^{20,21} This is supported by the fact that the fusiform aneurysms that were associated with stroke in our series were generally large or giant, with a mean aneurysm size of nearly 25 mm and a mean neck size of 26 mm. The large aneurysm maximum diameter and neck size likely made achieving good wall apposition, thus increasing the risk of in-stent thrombosis. As a means to mitigate the risk of delayed thromboembolic events in the treatment of fusiform aneurysms secondary to delayed endothelialization, some authors have advocated the use of prolonged dual-antiplatelet therapy.²¹ However, the efficacy of such regimens needs to be studied systematically.

Limitations

Our study has limitations. First, the interpretation of outcomes in this study should be viewed with caution because the study was not randomized, did not include an active comparator group, or was not powered to demonstrate a significant association of postoperative ischemic stroke with any of the variables studied. The study protocol did not require regular postoperative CT or MR imaging, and there were variable lengths of patient follow-up. Thus, we cannot determine the rate of silent ischemia in these patients, and it is possible that patients who had strokes in the delayed postoperative period were not included due to incomplete follow-up. Patients were not censored early before ascertainment of the primary outcome. Another limitation is that for patients undergoing platelet testing, we do not have information regarding platelet responsiveness before the ischemic event or whether and how antiplatelet prescriptions changed in response to these tests. Adverse events were self-reported in this study, and there is a general tendency toward underestimation of adverse events when they are self-reported. Last, we do not have any consistent data regarding how these strokes were managed.

CONCLUSIONS

In conclusion, acute ischemic stroke following endovascular treatment of intracranial aneurysms with the PED is an uncommon-but-devastating complication, with 100% of patients having major morbidity or mortality. Several patient and procedural characteristics as well as aneurysm shape, size, and location appear to be associated with postoperative ischemic stroke after PED treatment. Fusiform aneurysms were the only variable independently associated in the multivariate analysis. Most strokes occurred within 1 month of the procedure, and delayed ischemic events were rare.

Disclosures: Giuseppe Lanzino—UNRELATED: Consultancy: Covidien/Medtronic.* Adnan H. Siddiqui—UNRELATED: Codman & Shurtliff, Covidien Neurovascular, IAC Vascular Testing, Medina Medical, Comments: advisory board membership; Consul-

tancy: Codman & Shurtliff, Covidien Vascular Therapies, GuidePoint Global consulting, Penumbra, Stryker, Pulsar Vascular, MicroVention, Lazarus Effect, Blockade Medical, Reverse Medical, and W.L. Gore and Associates, National Institutes of Health, Comments: The National Institutes of Health (co-investigator: National Institute of Neurological Disorders and Stroke 1R01NS064592-01A1, Hemodynamic Induction of Pathologic Remodeling Leading to Intracranial Aneurysms), National Institutes of Health (co-investigator: National Institute of Biomedical Imaging and Bioengineering 5R01EB002873-07, Micro-Radiographic Image for Neurovascular Interventions), National Institutes of Health (co-investigator: National Institutes of Health/National Institute of Neurological Disorders and Stroke 1R01NS091075, Virtual Intervention of Intracranial Aneurysms); Payment for Lectures (including service on Speakers Bureaus): Codman & Shurtliff; Stock/Stock Options: Hotspur, Intratech Medical, Stim-Sox, Valor Medical, Blockade Medical, Lazarus Effect, Pulsar Vascular, Medina Medical; Other: Penumbra, Covidien, MicroVention, Comments: member of steering committees for Penumbra, 3D Separator Trial, Covidien, Solitaire With the Intention For Thrombectomy as PRIMary Endovascular Treatment Trial, MicroVention, Pivotal Study of the FRED Stent System in the Treatment of Intracranial Aneurysms Trial. Edoardo Boccardi—RELATED: Consulting Fee or Honorarium: Covidien/Medtronic; UNRELATED: Consultancy: Covidien/Medtronic. Saruhan Cekiç—RELATED: Consultancy: Covidien; UNRELATED: Consultancy: MicroVention, Sequent Medical. David Fiorella—RELATED: Consulting Fee or Honorarium: Medtronic; Support for Travel to Meetings for the Study or Other Purposes: Medtronic; UNRELATED: Consultancy: Codman/Johnson & Johnson, MicroVention, Sequent Medical, Penumbra; Grants/Grants Pending: Sequent Medical,* MicroVention,* Penumbra,* Comments: National Principal Investigator for clinical trials; Travel/Accommodations/Meeting Expenses Unrelated to Activities Listed: Codman/Johnson and Johnson, MicroVention, Sequent Medical, Penumbra. Ricardo Hanel—RELATED: Consulting Fee or Honorarium: Medtronic; UNRELATED: Board Membership: Medina Medical; Consultancy: Stryker, Codman, MicroVention; Stock/Stock Options: Blockade Medical. Pascal Jabbour—UNRELATED: Consultancy: Covidien. Elad Levy—UNRELATED: Consultancy: Pulsar; Expert Testimony: renders medical/legal opinion as an expert witness; Payment for Lectures (including service on Speakers Bureaus): Covidien, Comments: honorarium for training and lectures; Payment for Development of Educational Presentations: Abbott Laboratories, Comments: carotid training sessions for physicians; Stock/Stock Options: Intratech Medical; Blockade Medical; Medina Medical, Comments: shareholder/ownership interest; Other: Covidien, Comments: National Principal Investigator for Solitaire With the Intention For Thrombectomy as PRIMary Endovascular Treatment trials. Demetrius Lopes—RELATED: Grant: Medtronic; Consulting Fee or Honorarium: Medtronic; Fees for Participation in Review Activities such as Data Monitoring Boards, Statistical Analysis, Endpoint Committees, and the Like: Medtronic; UNRELATED: Board Membership: Siemens, Stryker, Medtronic, Blockade Medical; Consultancy: Siemens, Stryker, Medtronic, Blockade Medical; Grants/Grants Pending: Siemens. Pedro Lylyk—UNRELATED: Travel/Accommodations/Meeting Expenses Unrelated to Activities Listed: Medtronic, Stryker, Cardia. Istvan Szikora—RELATED: Consulting Fee or Honorarium: Covidien Neurovascular; Fees for Participation in Review Activities such as Data Monitoring Boards, Statistical Analysis, Endpoint Committees, and the Like: Covidien Neurovascular, Comments: Steering Committee; UNRELATED: Consultancy: Covidien Neurovascular, Stryker Neurovascular, Sequent Medical; Travel/Accommodations/Meeting Expenses Unrelated to Activities Listed: Covidien Neurovascular, Sequent Medical. David F. Kallmes—RELATED: Grant: Medtronic,* Comments: funding for clinical trial; Consulting Fee or Honorarium: Medtronic,* Comments: funding for serving as Principal Investigator; Support for Travel to Meetings for the Study or Other Purposes: Medtronic,* Comments: travel reimbursement for participation in FDA panel meeting; Fees for Participation in Review Activities such as Data Monitoring Boards, Statistical Analysis, Endpoint Committees, and the Like: Medtronic,* Comments: Clinical Events Committee member; UNRELATED: Board Membership: GE Healthcare,* Comments: Cost-Effectiveness Board; Consultancy: Medtronic,* Comments: role as Principal Investigator in clinical trials; Grants/Grants Pending: MicroVention,* Medtronic,* SurModics,* Sequent,* NeuroSigma,* Codman,* Comments: preclinical research and clinical trials. *Money paid to the institution.

REFERENCES

- Arrese I, Sarabia R, Pintado R, et al. Flow-diverter devices for intracranial aneurysms: systematic review and meta-analysis. *Neurosurgery* 2013;73:193–99; discussion 199–200 CrossRef Medline
- Briganti F, Napoli M, Tortora F, et al. Italian multicenter experience with flow-diverter devices for intracranial unruptured aneurysm treatment with periprocedural complications: a retrospective data analysis. *Neuroradiology* 2012;54:1145–52 CrossRef Medline
- Brinjikji W, Murad MH, Lanzino G, et al. Endovascular treatment of intracranial aneurysms with flow diverters: a meta-analysis. *Stroke* 2013;44:442–47 CrossRef Medline

4. Yu SC, Kwok CK, Cheng PW, et al. **Intracranial aneurysms: mid-term outcome of Pipeline embolization device—a prospective study in 143 patients with 178 aneurysms.** *Radiology* 2012;265:893–901 CrossRef Medline
5. Nelson PK, Lylyk P, Szikora I, et al. **The Pipeline embolization device for the intracranial treatment of aneurysms trial.** *AJNR Am J Neuroradiol* 2011;32:34–40 CrossRef Medline
6. Kallmes DF, Ding YH, Dai D, et al. **A new endoluminal, flow-disrupting device for treatment of saccular aneurysms.** *Stroke* 2007;38:2346–52 CrossRef Medline
7. Kallmes DF, Ding YH, Dai D, et al. **A second-generation, endoluminal, flow-disrupting device for treatment of saccular aneurysms.** *AJNR Am J Neuroradiol* 2009;30:1153–58 CrossRef Medline
8. Becske T, Kallmes DF, Saatci I, et al. **Pipeline for uncoilable or failed aneurysms: results from a multicenter clinical trial.** *Radiology* 2013;267:858–68 CrossRef Medline
9. Kallmes DF, Hanel R, Lopes D, et al. **International retrospective study of the Pipeline embolization device: a multicenter aneurysm treatment study.** *AJNR Am J Neuroradiol* 2015;36:108–15 CrossRef Medline
10. Briganti F, Leone G, Marseglia M, et al. **Endovascular treatment of cerebral aneurysms using flow-diverter devices: a systematic review.** *Neuroradiol J* 2015;28:365–75 CrossRef Medline
11. Tan LA, Keigher KM, Munich SA, et al. **Thromboembolic complications with Pipeline embolization device placement: impact of procedure time, number of stents and pre-procedure P2Y12 reaction unit (PRU) value.** *J Neurointerv Surg* 2015;7:217–21 CrossRef Medline
12. Szikora I, Berentei Z, Kulcsar Z, et al. **Treatment of intracranial aneurysms by functional reconstruction of the parent artery: the Budapest experience with the Pipeline embolization device.** *AJNR Am J Neuroradiol* 2010;31:1139–47 CrossRef Medline
13. Skukalek SL, Winkler AM, Kang J, et al. **Effect of antiplatelet therapy and platelet function testing on hemorrhagic and thrombotic complications in patients with cerebral aneurysms treated with the Pipeline embolization device: a review and meta-analysis.** *J Neurointerv Surg* 2016;8:58–65 CrossRef Medline
14. Hu YC, Deshmukh VR, Albuquerque FC, et al. **Histopathological assessment of fatal ipsilateral intraparenchymal hemorrhages after the treatment of supraclinoid aneurysms with the Pipeline embolization device.** *J Neurosurg* 2014;120:365–74 CrossRef Medline
15. Shapiro M, Ollenschleger MD, Baccin C, et al. **Foreign body emboli following cerebrovascular interventions: clinical, radiographic, and histopathologic features.** *AJNR Am J Neuroradiol* 2015;36:2121–26 CrossRef Medline
16. Cruz JP, Marotta T, O’Kelly C, et al. **Enhancing brain lesions after endovascular treatment of aneurysms.** *AJNR Am J Neuroradiol* 2014;35:1954–58 CrossRef Medline
17. Morales-Valero SF, Brinjikji W, Wald JT, et al. **Low frequency of delayed ischemic events on MRI after flow diversion for intracranial aneurysms.** *J Neurosurg Sci* 2015 Jul 10. [Epub ahead of print] Medline
18. Gawlitza M, Januel AC, Tall P, et al. **Flow diversion treatment of complex bifurcation aneurysms beyond the circle of Willis: a single-center series with special emphasis on covered cortical branches and perforating arteries.** *J Neurointerv Surg* 2015 Apr 15. [Epub ahead of print] CrossRef Medline
19. Peschillo S, Caporlingua A, Cannizzaro D, et al. **Flow diverter stent treatment for ruptured basilar trunk perforator aneurysms.** *J Neurointerv Surg* 2016;8:190–96 CrossRef Medline
20. Szikora I, Turanyi E, Marosfoi M. **Evolution of flow-diverter endothelialization and thrombus organization in giant fusiform aneurysms after flow diversion: a histopathologic study.** *AJNR Am J Neuroradiol* 2015;36:1716–20 CrossRef Medline
21. Klisch J, Turk A, Turner R, et al. **Very late thrombosis of flow-diverting constructs after the treatment of large fusiform posterior circulation aneurysms.** *AJNR Am J Neuroradiol* 2011;32:627–32 CrossRef Medline
22. van der Marel K, Gounis MJ, Weaver JP, et al. **Grading of Regional Apposition after Flow-Diverter Treatment (GRAFT): a comparative evaluation of VasoCT and intravascular OCT.** *J Neurointerv Surg* 2015 Jul 28. [Epub ahead of print] CrossRef Medline

WEB Treatment of Ruptured Intracranial Aneurysms

W.J. van Rooij, J.P. Peluso, R.S. Bechan, and M. Sluzewski



ABSTRACT

BACKGROUND AND PURPOSE: The Woven EndoBridge (WEB) device was recently introduced for intrasaccular treatment of wide-neck aneurysms without the need for adjunctive support. We present our first experience in using the WEB for small ruptured aneurysms.

MATERIALS AND METHODS: During 11 months, 32 of 71 (45%) endovascularly treated acutely ruptured aneurysms were treated with the WEB. The patients were 12 men and 20 women, with a mean age of 61 years (range, 34–84 years). The mean aneurysm size was 4.9 mm, and 14 were ≤ 4 mm. Of 32 aneurysms, 24 (75%) had a wide neck.

RESULTS: All 32 aneurysms were adequately occluded after WEB placement. There were no procedural ruptures and no complications related to the WEB device. No adjunctive stents or balloons were needed. In 3 patients, thromboembolic complications occurred. One patient developed an infarction, and 2 patients were asymptomatic. The procedural complication rate was 3%. Seven patients admitted in poor clinical grade conditions died during hospital admission due to the sequelae of SAH. In 18 patients with angiographic follow-up at 3 months, 16 aneurysms remained adequately occluded. Two aneurysms showed slight compression of the WEB without reopening. Clinical follow-up in the 25 patients who survived the hospital admission period revealed mRS 1–2 in 24 and mRS 4 in 1. There were no rebleeds from the ruptured aneurysms during follow-up.

CONCLUSIONS: WEB treatment of small ruptured aneurysms was safe and effective without the need for anticoagulation, adjunctive stents, or balloons. Our preliminary experience indicates that the WEB may be a valuable alternative to coils in the treatment of acutely ruptured aneurysms.

ABBREVIATIONS: DL = Dual-Layer; SL = Single-Layer; SLS = Single-Layer Sphere; WEB = Woven EndoBridge

Endovascular treatment with coils of wide-neck intracranial aneurysms remains a technical challenge. To prevent extrusion of coils from the aneurysmal sac, a temporary protection balloon or a stent can be used. However, this makes the procedure more complicated with a higher chance of complications.^{1,2} With the use of stents, periprocedural dual-antiplatelet therapy is required and has to be prolonged for 3–6 months. With this anticoagulation, stent-assisted coiling in ruptured aneurysms has a higher inherent risk for early rebleed or hemorrhage in the postoperative period.³

Recently, an intrasaccular flow disruptor, Woven EndoBridge

(WEB; Sequent Medical, Aliso Viejo, California), has been developed. The primary use of the WEB is the treatment of bifurcation or wide-neck aneurysms without the need of adjunctive devices. There is a growing body of literature on the use of the WEB device with excellent safety and efficacy profiles. Most of the published series comprised wide-necked, unruptured aneurysms.^{4–16} When the WEB became available in our hospital, our initial results in unruptured aneurysms were encouraging, and we decided to expand the indications to both ruptured and unruptured aneurysms suitable for accommodating a WEB device, regardless of neck size. Our intention was to avoid using stents or balloons in ruptured aneurysms. In this article, we present our first results of the use of the WEB device in small ruptured aneurysms.

MATERIALS AND METHODS

General

This observational study with prospectively collected data was compliant with institutional privacy policy. The institutional review board gave exempt status for approval and informed consent.

Received January 14, 2016; accepted after revision February 28.

From the Department of Radiology, Sint Elisabeth Ziekenhuis, Tilburg, the Netherlands.

Please address correspondence to Willem Jan van Rooij, MD, PhD, Department of Radiology, Sint Elisabeth Ziekenhuis, Hilvarenbeekseweg 60, 5022GC Tilburg, the Netherlands; e-mail: radiol@eztilburg.nl



Indicates open access to non-subscribers at www.ajnr.org



Indicates article with supplemental on-line videos.

<http://dx.doi.org/10.3174/ajnr.A4811>

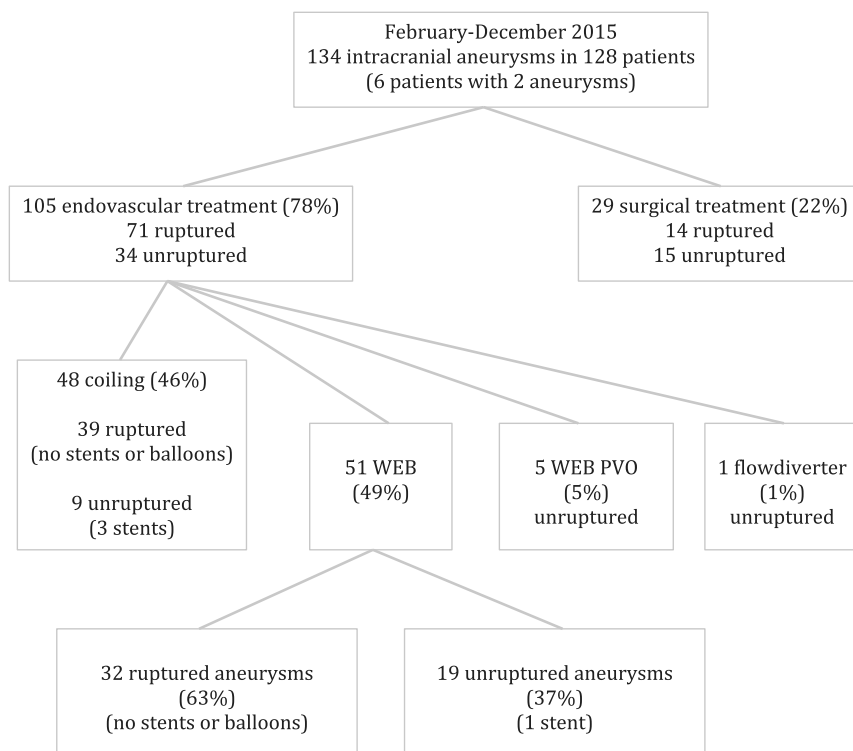


FIG 1. Flow chart of all treated patients with aneurysms between February and December 2015. PVO indicates parent vessel occlusion.

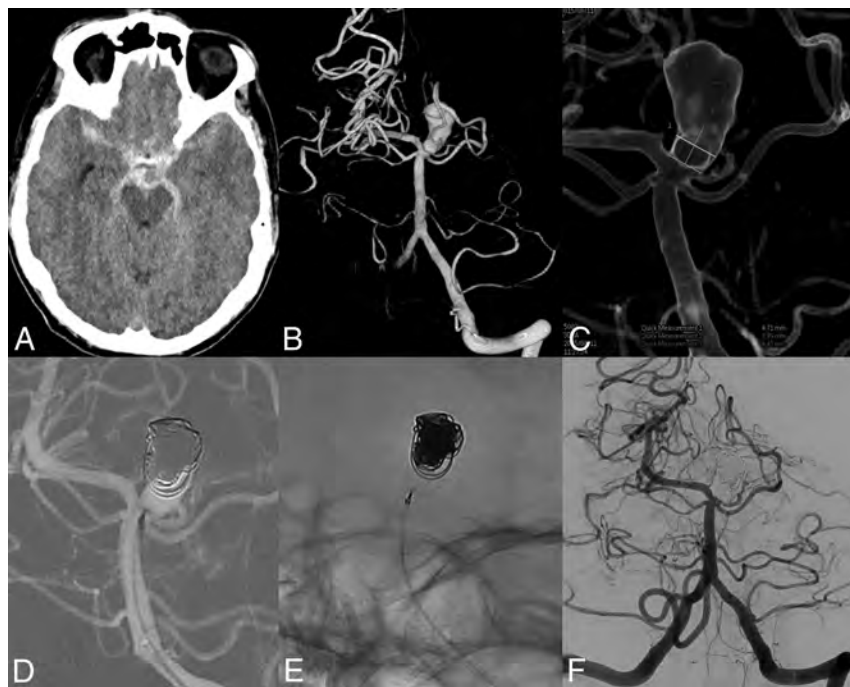


FIG 2. A 61-year-old man with a ruptured basilar tip aneurysm treated with the WEB and coils. A, CT scan with subarachnoid blood. B, 3D angiogram reveals a 13-mm basilar tip aneurysm. C, Neck measurement on a 3D angiogram. D and E, After placement of coils in the dome and a WEB-SL, 6 × 3 mm, in the neck. F, Three-month follow-up angiogram with complete occlusion.

The WEB Device

The Woven EndoBridge system is a self-expanding, pumpkin-shaped, braided mesh of platinum cored nitinol wires that can be deployed in the aneurysm sac. The design of the WEB device has progressed from a Dual-Layer configuration (WEB-DL) into a

Single-Layer version (WEB-SL) with a higher number of nitinol wires. The WEB-SL device is available in diameters ranging between 4 and 11 mm and heights ranging between 3 and 9 mm. The WEB-Single-Layer Sphere (SLS) has a spheric shape and is available in diameters ranging between 4 and 11 mm, each with a fixed height ranging between 2.6 and 9.6 mm. The WEBs with diameters of 4–7 mm can be delivered through a 0.021-inch internal-diameter microcatheter; the WEBs with diameters of 8–9 mm, through a 0.027-inch microcatheter; and the WEBs with diameters of 10–11 mm, through a 0.033-inch microcatheter. Placed in the aneurysm, the WEB modifies the blood flow at the level of the neck and induces aneurysmal thrombosis. The WEB can be fully retrieved until final detachment by an electrothermal detachment system contained in a hand-held controller. Experience of early users of the WEB indicated that slight oversizing of the device (1–2 mm oversizing depending on aneurysm size) was advisable to ensure a stable WEB position.¹⁷

General Indications in This Study

The WEB device was initially developed for the treatment of wide-neck intracranial aneurysms as an alternative to balloon- or stent-assisted treatment. After our first experiences in unruptured wide-neck aneurysms, during the study period we decided to gradually expand the indications to all aneurysms suitable for the WEB, regardless of neck size or rupture status. In general, these are aneurysms of ≤10 mm with a shape and geometry suitable for catheterization with a 0.021-inch microcatheter and with a possible fit of a pumpkin-shaped or spheric WEB device.

With the patient under general anesthesia, we advanced a microcatheter (VIA 0.021 inch or VIA 0.027 inch; Sequent Medical) into the aneurysm via a coaxial or triaxial approach. Apart from heparin in the pressure bags for flushing (1000 IU/L), no anticoagulation was used.

Patient demographics and treatment and aneurysm characteristics were collected. Clinical grading during admission was according to the Hunt and Hess scale, and clinical follow-up was classified according to the modified Rankin Scale. For surviving patients, angiographic



FIG 3. A 57-year-old woman with a ruptured anterior communicating artery aneurysm. A, 3D angiogram shows a small anterior communicating artery aneurysm. Note the spasm in the left A1. B, Measurement of the height (3.9 mm) and neck width (2.3 mm). C, Angiogram directly after placement of a 4-mm WEB-SLS. Note some opacification inside the WEB. D, Angiogram at 3 months demonstrates complete occlusion of the aneurysm.

follow-up was scheduled at 3 months, and MR imaging follow-up, at 6 months.

Patients

Between February and December 2015, 134 intracranial aneurysms in 128 patients were treated in our institution (Fig 1). Six patients had 2 treated aneurysms.

Of 134 aneurysms, 105 (78%, 71 ruptured and 34 unruptured) were treated with endovascular techniques and 29 aneurysms (22%) were treated surgically. Of 71 ruptured aneurysms treated endovascularly, 39 (55%) were treated with selective coiling and 32 (45%) were treated with the WEB.

The 32 patients with a ruptured aneurysm treated with the WEB were the subjects of this study. There were 12 men and 20 women with a mean age of 61 years (range, 34–84 years). Clinical condition at the time of treatment was Hunt and Hess 1–2 in 14, Hunt and Hess 3 in 9, and Hunt and Hess 4–5 in 14 patients. The timing of treatment after SAH was 0–1 day in 26, 2–4 days in 4, and >4 days in 2 patients. Aneurysm location was the anterior communicating artery in 11; middle cerebral artery in 8; posterior communicating artery in 7; pericallosal artery in 3; and basilar tip, superior cerebellar, and ophthalmic arteries, 1 in each. The mean aneurysm size was 4.9 mm (median, 5 mm; range, 3–12 mm), and 14 aneurysms were ≤ 4 mm (Figs 1 and 2). Of 32 aneurysms, 24 (75%) had a wide neck defined as ≥ 4 mm or a dome/neck ratio of ≤ 1.5 . Three patients had 2 aneurysms treated in the same session, 1 with WEB and 2 with coils.



FIG 4. A 42-year-old man with a ruptured anterior communicating artery aneurysm. A, 3D angiogram shows a small anterior communicating artery aneurysm with a bleb pointing upward. Angiogram before (B) and after (C) placement of a 4-mm WEB-SLS inside the aneurysm. Note complete aneurysm occlusion with slight protrusion of the WEB into the parent vessel (arrow). D, Angiogram at 3 months demonstrates persistent complete occlusion.

RESULTS

Initial Results and Complications

After WEB placement with sealing of the aneurysm neck, the position of the WEB inside the aneurysm was judged as good in 31 aneurysms without filling of aneurysm remnants. In 1 patient with a ruptured pericallosal artery aneurysm, a small aneurysm remnant was present. In 2 patients, coils were placed in the aneurysm dome through a jailed second microcatheter before detachment of the WEB (Fig 2). There were no procedural ruptures and no complications related to the WEB device. In 3 patients, thromboembolic complications occurred with occlusion of an M2 branch in 2 and a P3 branch in 1. All 3 vessels could be reopened during the procedure by mechanical thrombectomy. One patient developed a partial middle cerebral artery infarction, and 2 patients were asymptomatic. In 1 patient, catheterization caused a dissection of the internal carotid artery, which was successfully treated with a stent.

Clinical and Imaging Follow-Up

Of 32 patients, 7 died during hospital admission due to sequelae of SAH. All 7 patients were admitted with poor-grade conditions (Hunt and Hess 4–5). One of these patients had a thromboembolic complication in an M2 branch during treatment, leading to partial right frontal brain infarction (procedural mortality, 3%; 1 of 32; 95% CI, 0.01%–17%). Of the remaining 25 patients, 18 had 3-month angiographic follow-up and 6 of these 18 had 6-month MR imaging follow-up. In 7 patients, imaging follow-up is pending.

Fifteen aneurysms (83%) remained completely occluded (Figs 3 and 4). One aneurysm remained subtotally occluded. Two an-

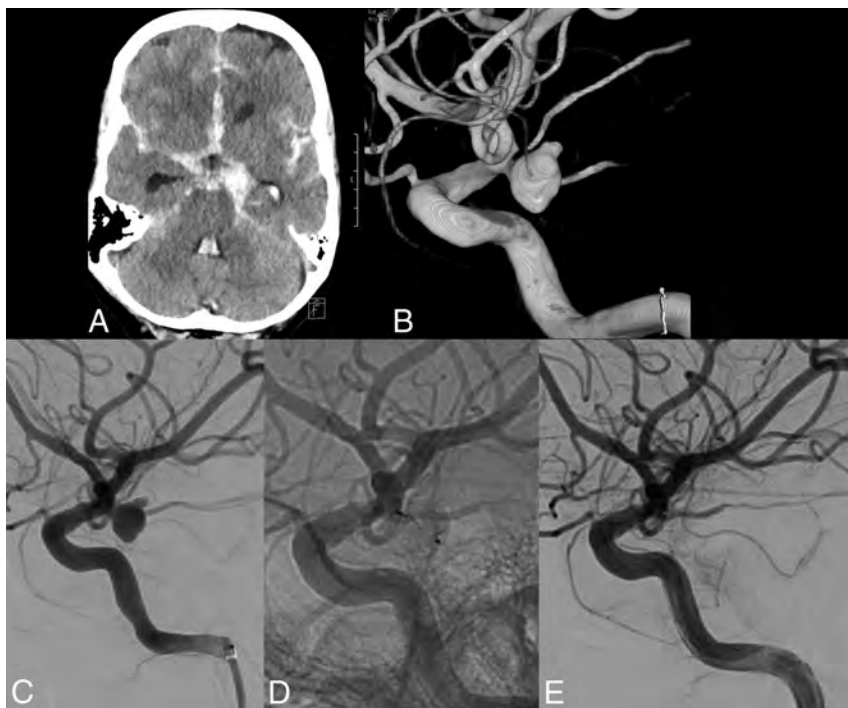


FIG 5. A 60-year-old woman with a ruptured small-neck posterior communicating artery aneurysm. A, CT scan shows subarachnoid hemorrhage. B, 3D angiogram reveals a 6-mm posterior communicating artery aneurysm with a small neck. Angiogram before (C) and after (D and E) placement of a 6-mm WEB-SLS shows complete aneurysm occlusion.

eurysms showed opacification of the central recess due to slight compression of the WEB. In all 6 patients with MR imaging follow-up, the aneurysm was stable in the 3- to 6-month period. Clinical follow-up in the 25 patients who survived the hospital admission period revealed mRS 1–2 in 24 and mRS 4 in 1. There were no rebleeds from the ruptured aneurysms during follow-up.

DISCUSSION

Our initial experience with endovascular treatment of ruptured intracranial aneurysms by using the WEB device was encouraging. With growing skill and confidence, more and more, even small, ruptured aneurysms were treated with the WEB, in addition to small aneurysms with a small neck (Fig 5). During the study, 32 of 71 endovascularly treated ruptured aneurysms (45%) were treated with the WEB. Once the microcatheter was inside the aneurysm, deployment of the WEB was technically straightforward and quick in most cases. Despite aneurysms being very small, no procedural ruptures occurred. The detachment system proved fast and reliable. In most cases, the position of the WEB after deployment in the aneurysm was easily evaluated. With complicated anatomy, a 3D angiographic run proved helpful in exactly delineating the position of the WEB inside the aneurysm lumen and in relation to the parent vessels. In wide-neck aneurysms, the WEB-SL bridges the neck without the need for a stent or balloon. (Examples of WEB treatment can be found in the On-line Videos). In fact, in none of the 71 endovascularly treated ruptured aneurysms was balloon- or stent assistance necessary (Fig 1).

In our opinion based on our own and previous experience,¹⁷ the most important aspect of the WEB treatment was the siz-

ing. Oversizing the WEB seems crucial for good immediate and long-term results. With oversizing, the WEB anchors itself against the aneurysm wall while bridging the neck completely. Oversizing the compressed WEB width results in increased height, and one has to be sure that the aneurysm can accommodate this augmented height. Oversizing protects against displacement, overturning, and compression of the WEB during follow-up. In small aneurysms, oversizing of 1 mm will usually be sufficient, while in larger aneurysms, at least 2-mm oversizing is necessary for stably securing the device in the neck.

A stable position of the microcatheter inside the aneurysm is important for WEB deployment. The WEB system is slightly more rigid than most coil systems, and negotiating slack in the microcatheter during advancement may result in unwanted forward or backward movement of the catheter tip. Therefore, advancing the WEB should be done under constant fluoroscopic control. Distal-access guiding

catheters are preferably used to enhance the stability of the microcatheter.

We used the newer 0.021-inch VIA microcatheter in the treatment of small aneurysms in WEB sizes up to 7 mm. Although this microcatheter is less rigid than the 0.027-inch one used in previous studies, the system is still stiffer than most coil systems. In fact, negotiating the curve into the A1 for anterior communicating artery aneurysms proved impossible with the VIA 0.021 in 6 cases, and all 6 aneurysms were coiled with 0.017-inch microcatheters. However, the recently introduced lower profile VIA 0.017 microcatheter will probably overcome most problems encountered with the thicker microcatheters.

Our excellent clinical and imaging results are in concordance with those in previous studies.^{4,6–8,10,15,16} Complications were low; there were no procedural ruptures, no early rebleeds, and no reopenings at short-term follow-up. However, our patient group with only ruptured small aneurysms differed from those in other series, in which mostly wide-neck unruptured aneurysms were treated.

CONCLUSIONS

In our opinion, WEB treatment of ruptured intracranial aneurysms is feasible and safe. The WEB can be a valuable alternative to coils in many aneurysms and reduces or eliminates the need for adjunctive devices such as stents and balloons. Anticoagulation in the periprocedural period is not necessary; this finding is a great advantage in view of possible surgical procedures that are needed in patients with acutely ruptured aneurysms. In our practice, WEB treatment has become the first choice in both ruptured and unruptured aneurysms.

Disclosures: Willem Jan van Rooij—UNRELATED: Payment for Lectures (including service on Speakers Bureaus); Sequent Medical; Other: proctoring WEB cases. Jo P. Peluso—UNRELATED: Payment for Lectures (including service on Speakers Bureaus); Sequent Medical; Other: proctoring WEB cases.

REFERENCES

1. Piotin M, Blanc R, Spelle L, et al. **Stent-assisted coiling of intracranial aneurysms: clinical and angiographic results in 216 consecutive aneurysms.** *Stroke* 2010;41:110–15 CrossRef Medline
2. Bartolini B, Blanc R, Pistocchi S, et al. **“Y” and “X” stent-assisted coiling of complex and wide-neck intracranial bifurcation aneurysms.** *AJNR Am J Neuroradiol* 2014;35:2153–58 CrossRef Medline
3. Bechan RS, Sprengers ME, Majoie CB, et al. **Stent-assisted coil embolization of intracranial aneurysms: complications in acutely ruptured versus unruptured aneurysms.** *AJNR Am J Neuroradiol* 2016; 37:502–07 CrossRef Medline
4. Lubicz B, Klisch J, Gauvrit JY, et al. **WEB-DL endovascular treatment of wide-neck bifurcation aneurysms: short- and midterm results in a European study.** *AJNR Am J Neuroradiol* 2014;35:432–38 CrossRef Medline
5. Colla R, Cirillo L, Princiotta C, et al. **Treatment of wide-neck basilar tip aneurysms using the WEB II device.** *Neuroradiol J* 2013;6:669–77 Medline
6. Pierot L, Moret J, Turjman F, et al. **WEB treatment of intracranial aneurysms: clinical and anatomic results in the French Observatory.** *AJNR Am J Neuroradiol* 2016;37:655–59 CrossRef Medline
7. Pierot L, Spelle L, Molyneux A, et al. **Clinical and anatomical follow-up in patients with aneurysms treated with the WEB device: 1-year follow-up report in the cumulated population of 2 prospective, multicenter series (WEBCAST and French Observatory).** *Neurosurgery* 2016;78:133–41 CrossRef Medline
8. Liebig T, Kabbasch C, Strasilla C, et al. **Intrasaccular flow disruption in acutely ruptured aneurysms: a multicenter retrospective review of the use of the WEB.** *AJNR Am J Neuroradiol* 2015;36:1721–27 CrossRef Medline
9. Bozzetto Ambrosi P, Gory B, Sivan-Hoffmann R, et al. **Endovascular treatment of bifurcation intracranial aneurysms with the WEB SL/SLS: 6-month clinical and angiographic results.** *Interv Neuroradiol* 2015;4:462–69 CrossRef Medline
10. Pierot L, Costalat V, Moret J, et al. **Safety and efficacy of aneurysm treatment with WEB: results of the WEBCAST study.** *J Neurosurg* 2015 Sep 18:1–7. [Epub ahead of print] Medline
11. Sivan-Hoffmann R, Gory B, Riva R, et al. **One-year angiographic follow-up after WEB-SL endovascular treatment of wide-neck bifurcation intracranial aneurysms.** *AJNR Am J Neuroradiol* 2015;36: 2320–24 CrossRef Medline
12. Leyon JJ, Chavda S, Lamin S, et al. **Corking the WEB and coiling through a jailed microcatheter: WEB assisted coiling, a useful technique avoiding the use of stents in treating wide-necked large intracranial aneurysms.** *J Neurointerv Surg* 2015 May 7. [Epub ahead of print] CrossRef Medline
13. Gherasim DN, Gory B, Sivan-Hoffmann R, et al. **Endovascular treatment of wide-neck anterior communicating artery aneurysms using WEB-DL and WEB-SL: short-term results in a multicenter study.** *AJNR Am J Neuroradiol* 2015;36:1150–54 CrossRef Medline
14. Cognard C, Januel AC. **Remnants and recurrences after the use of the WEB intrasaccular device in large-neck bifurcation aneurysms.** *Neurosurgery* 2015;76:522–30; discussion 530 CrossRef Medline
15. Caroff J, Mihalea C, Dargento F, et al. **Woven Endobridge (WEB) device for endovascular treatment of ruptured intracranial wide-neck aneurysms: a single-center experience.** *Neuroradiology* 2014; 56:755–61 CrossRef Medline
16. Armoiry X, Turjman F, Hartmann DJ, et al. **Endovascular treatment of intracranial aneurysms with the WEB device: a systematic review of clinical outcomes.** *AJNR Am J Neuroradiol* 2015 Nov 19. [Epub ahead of print] Medline
17. Pierot L. **Letter: WEB aneurysm treatment—occlusion stability and “compression.”** *Neurosurgery* 2015;77:E666–67 CrossRef Medline

Contrast-Enhanced and Time-of-Flight MRA at 3T Compared with DSA for the Follow-Up of Intracranial Aneurysms Treated with the WEB Device

C. Timsit, S. Soize, A. Benaissa, C. Portefaix, J.-Y. Gauvrit, and L. Pierot

ABSTRACT

BACKGROUND AND PURPOSE: Imaging follow-up at 3T of intracranial aneurysms treated with the WEB Device has not been evaluated yet. Our aim was to assess the diagnostic accuracy of 3D–time-of-flight MRA and contrast-enhanced MRA at 3T against DSA, as the criterion standard, for the follow-up of aneurysms treated with the Woven EndoBridge (WEB) system.

MATERIALS AND METHODS: From June 2011 to December 2014, patients treated with the WEB in our institution, then followed for ≥ 6 months after treatment by MRA at 3T (3D–TOF–MRA and contrast-enhanced MRA) and DSA within 48 hours were included. Aneurysm occlusion was assessed with a simplified 2-grade scale (adequate occlusion [total occlusion + neck remnant] versus aneurysm remnant). Interobserver and intermodality agreement was evaluated by calculating the linear weighted κ . MRA test characteristics and predictive values were calculated from a 2×2 contingency table, by using DSA data as the standard of reference.

RESULTS: Twenty-six patients with 26 WEB-treated aneurysms were included. The interobserver reproducibility was good with DSA ($\kappa = 0.71$) and contrast-enhanced-MRA ($\kappa = 0.65$) compared with moderate with 3D–TOF–MRA ($\kappa = 0.47$). Intermodality agreement with DSA was fair with both contrast-enhanced MRA ($\kappa = 0.36$) and 3D–TOF–MRA ($\kappa = 0.36$) for the evaluation of total occlusion. For aneurysm remnant detection, the prevalence was low (15%), on the basis of DSA, and both MRA techniques showed low sensitivity (25%), high specificity (100%), very good positive predictive value (100%), and very good negative predictive value (88%).

CONCLUSIONS: Despite acceptable interobserver reproducibility and predictive values, the low sensitivity of contrast-enhanced MRA and 3D–TOF–MRA for aneurysm remnant detection suggests that MRA is a useful screening procedure for WEB-treated aneurysms, but similar to stents and flow diverters, DSA remains the criterion standard for follow-up.

ABBREVIATIONS: CE = contrast-enhanced; DL = Dual-Layer; EV = Enhanced-Visualization; SL = Single-Layer; SLS = Single-Layer Sphere; WEB = Woven EndoBridge

Endovascular treatment is now the first-line treatment for the management of ruptured and unruptured intracranial aneurysms.^{1–4} However, the limitations of standard coiling for complex aneurysms (large, wide-neck, or developed in a bifurcation) have contributed to the development of new endovascular approaches, including balloon-assisted coiling, stent-assisted coiling, flow diversion, and flow disruption.⁵

The Woven EndoBridge (WEB) aneurysm embolization sys-

tem (Sequent Medical, Aliso Viejo, California) is an intrasaccular device designed to disrupt the intra-aneurysmal flow at the level of the neck.^{6,7} Initial experience with the WEB–Dual-Layer (DL) showed the clinical utility of this device in wide-neck bifurcation aneurysms with high technical success and low acute morbidity and mortality.^{6–16} Several WEB devices are now available, including Single-Layer (WEB–SL), Single-Layer Sphere (WEB–SLS), and WEB–DL subtypes.^{12,13} Recently, Enhanced-Visualization (EV) versions were developed to improve fluoroscopic visualization of the devices during treatment.

Because of the potential risk of aneurysm recanalization after endovascular treatment, regular imaging follow-up is recommended. Digital subtraction angiography is the criterion standard for the follow-up of intracranial aneurysms after endovascular treatment but has some disadvantages, including potential neurologic complications, iodinated contrast injection, and radiation exposure. With the goal of avoiding DSA drawbacks, several MR angiography techniques have been tested to follow intracranial

Received November 6, 2015; accepted after revision February 28, 2016.

From the Department of Neuroradiology (C.T., S.S., A.B., L.P.), Hôpital Maison Blanche, Université de Champagne-Ardenne, Reims, France; CReSTIC SIC EA3804 (C.P.), Université de Champagne-Ardenne, Reims, France; Department of Neuroradiology (J.-Y.G.), Hôpital Pontchaillou, Rennes, France; and Unité VISAGES U746 INSERM-INRIA (J.-Y.G.), IRISA UMR CNRS 6074, University of Rennes, Rennes, France.

Please address correspondence to Laurent Pierot, MD, PhD, Department of Diagnostic and Therapeutic Neuroradiology, Maison Blanche Hospital, 45 Rue Cognacq-Jay, Reims 51092, France; e-mail: lpierot@gmail.com

<http://dx.doi.org/10.3174/ajnr.A4791>

aneurysms. 3D-TOF-MRA and contrast-enhanced MRA (CE-MRA) at 3T are appropriate techniques for the follow-up of coiled aneurysms but have some limitations for the aneurysms treated with stents or flow diverters.¹⁷⁻²³ Because the WEB is a relatively new device, the value of 3D-TOF-MRA and CE-MRA for the follow-up of WEB-treated intracranial aneurysms has been evaluated in a small number of patients at 1.5T.²⁴

The aim of this single-center prospective study was to assess the diagnostic accuracy of 3D-TOF-MRA and CE-MRA at 3T against DSA, as the criterion standard, for the evaluation of aneurysm occlusion after WEB treatment.

MATERIALS AND METHODS

Study Population

Institutional review board approval was obtained, and informed consent was waived according to the design of the study. The present study complies with the Standards for Reporting of Diagnostic Accuracy.²⁵ Between June 2011 and December 2014, consecutive patients treated at the University Hospital of Reims with the WEB were prospectively included in a data base. Patients treated with the WEB and followed for ≥ 6 months after treatment with both MRA and DSA were included retrospectively. Additional inclusion criteria were the following: patients older than 18 years of age treated with the WEB; followed with both MRA techniques (3D-TOF-MRA and CE-MRA) at 3T and DSA, with MRA and DSA being performed within < 48 hours.

To avoid redundant data, in case of multiple MRA or DSA examinations, we used only the last examination.

Imaging Technique for Intra-Arterial DSA

DSA was performed with a biplane angiographic system (Axiom Artis dBA; Siemens, Erlangen, Germany). Using transfemoral catheterization, we performed selective injections of the internal carotid artery or vertebral artery according to the aneurysm location.

Anteroposterior and lateral working view standard projections were obtained with an additional 3D rotational angiography sequence. For the ICA, 8 mL of nonionic contrast agent (iodixanol, Visipaque; GE Healthcare, Piscataway, New Jersey) was injected with a velocity of 4 mL/s. For the vertebral artery, 8–10 mL was injected with a velocity of 4–5 mL/s.

Imaging Technique for MRA

MRA examinations were performed at 3T (Achieva; Philips Healthcare, Best, the Netherlands). Examinations were performed with the following parameters: For 3D-TOF-MRA: TE, 3.45 ms; TR, 18 ms; flip angle, 20°; total acquisition time, 4:59 minutes; number of sections, 140; section thickness, 0.55 mm; FOV, 210 mm; rectangular FOV, 90%; acquisition matrix, 464; reconstruction matrix, 512; reconstructed voxel size, $0.41 \times 0.41 \times 0.55$ mm. For the CE-MRA, the parameters were TE, 1.96 ms; TR, 5.4 ms; flip angle, 30°; total acquisition time, 52 seconds; number of sections, 110; section thickness, 0.5 mm; FOV, 210 mm; rectangular FOV, 85%; acquisition matrix, 480; reconstruction matrix, 512; reconstructed voxel size, $0.41 \times 0.41 \times 0.50$ mm. CE-MRA randomly sampled the central *k*-space during venous injection of a gadolinium-based contrast agent (gadoterate

meglumine, Dotarem; Guerbet, Aulnay-sous-Bois, France). A bolus of 20 mL was used, followed by 30 mL of saline with a scopic-based detection of the bolus (phase-contrast survey).

Data Collection

Clinical and anatomic data regarding the patient (sex, age) and aneurysm (number, localization, size, aneurysm status) were collected. The interval time between aneurysm treatment and anatomic evaluation was also collected. Aneurysm location was classified into 4 groups: anterior cerebral artery/anterior communicating artery, ICA, middle cerebral artery, and posterior circulation/vertebrobasilar artery. We recorded WEB-DL, SL, SLS, and/or EV.

Data Analysis

All examinations (DSA and MRA) were anonymized by different-number random assignment by series. All images were independently evaluated in random order by 2 interventional neuroradiologists (both with > 20 years' experience). Then, in case of disagreement, consensus was found between the 2 radiologists. DSA, 3D-TOF-MRA, and CE-MRA were evaluated separately without knowledge of the MRA or DSA examination results. The pretreatment DSA was withheld, but the location of the aneurysms to be evaluated was provided to the readers. For both 3D-TOF-MRA and CE-MRA, source images and maximum-intensity-projection reconstructions were analyzed. Aneurysm occlusion was evaluated by using a 3-grade scale (total occlusion, neck remnant, and aneurysm remnant).²⁶ A simplified 2-grade scale was used for statistical analysis: adequate occlusion (total occlusion and neck remnant) and aneurysm remnant.

Statistical Analysis

Quantitative variables are reported as extremes, mean \pm SD, and median (interquartile range), while qualitative variables are reported as number and percentage. The κ statistic was used to evaluate interobserver and intermodality agreement for each technique. The interpretation of κ was done according to Landis and Koch.²⁷ Using the consensus evaluation of intra-arterial DSA as a reference test to evaluate the degree of aneurysm occlusion, we calculated the sensitivity, specificity, negative predictive value, and positive predictive value for 3D-TOF-MRA and CE-MRA. All analyses were performed by using MedCalc for Windows, Version 14.12.0 (MedCalc Software, Mariakerke, Belgium).

RESULTS

Study Population

Twenty-six of the 36 patients treated with the WEB were included (age extremes, 34–78 years; mean age, 55 ± 10 years; median age, 57 years; interquartile range, 48–61 years) including 22 women (85%) and 4 men (15%). Ten patients were not included for the following reasons: Six did not have DSA follow-up at the time of data collection, 1 died after treatment, and 3 refused MRA follow-up. The set of imaging data (3D-TOF-MRA, CE-MRA, and DSA) was acquired between 6 and 15 months after the endovascular treatment (mean, 9.2 ± 3.9 months; median, 9 months; interquartile range, 6–13 months). Each patient had 1 aneurysm treated with

the WEB. Detailed characteristics of the aneurysms are shown in Table 1.

Among the aneurysms treated with the WEB, 20 (77%) were treated with the WEB alone; 5 (19%), with coils and the WEB; and 1 (4%), with the WEB and a stent. We used WEBs in the following manner: 14 DLs, 8 SLs (including 5 EVs), and 4 SLSs (including 1 EV).

Interobserver Agreement

When evaluating aneurysm occlusion by using the 3-grade scale, the 2 observers were in agreement in 21 of 26 DSAs (81%), 21 of 26 3D-TOF-MRAs (81%), and 25 of 26 CE-MRAs (96%), resulting in good interobserver agreement for DSA ($\kappa = 0.69$; 95% CI, 0.46–0.93), excellent agreement for CE-MRA ($\kappa = 0.92$; 95% CI, 0.76–1.00), and moderate agreement for 3D-TOF-MRA ($\kappa = 0.59$; 95% CI, 0.30–0.88). When evaluating aneurysm

occlusion by using the simplified 2-grade scale (adequate occlusion versus aneurysm remnant), the 2 observers were in agreement in 24 of 26 DSAs (92%), 24 of 26 3D-TOF-MRAs (92%), and 25 of 26 CE-MRAs (96%), resulting in good interobserver agreement for DSA ($\kappa = 0.71$; 95% CI, 0.32–1.00) and CE-MRA ($\kappa = 0.65$; 95% CI, 0.02–1.00) and moderate interobserver agreement for 3D-TOF-MRA ($\kappa = 0.47$; 95% CI, 0.13–1.00). Despite good raw agreement for all modalities, lower κ values were obtained by 3D-TOF by using the 3-grade occlusion scale and by 3D-TOF and CE-MRA by using the simplified 2-grade scale. This was due to a lower number of aneurysm remnants detected by 3D-TOF-MRA and CE-MRA. Consequently, 1 disagreement for MRA created more imbalance between well-occluded aneurysms versus aneurysm remnants than with DSA, and the corresponding κ dropped more.

Intermodality Agreement

The results of aneurysm occlusion with the Raymond Scale and the simplified 2-grade scale for DSA, 3D-TOF-MRA, and CE-MRA are shown in Table 2. After a consensus reading, by using the simplified 2-grade scale, 3D-TOF-MRA and CE-MRA showed identical results. Both MRAs agreed with DSA in 23 of 26 aneurysms (89%). Disagreement occurred in 3 aneurysm remnants on DSA that were not detected with both MRAs (3 false-negative cases): 2 aneurysm remnants classified as neck remnants from both MRA sequences and 1 aneurysm with complete circulation within the WEB-SL device undetected by both MRAs (Fig 1). 3D-TOF-MRA and CE-MRA showed fair agreement with DSA regarding aneurysm remnant depiction ($\kappa = 0.36$; 95% CI, –0.16;0.88, for both techniques).

Diagnostic Accuracies for Aneurysm Remnant Depiction

With the simplified 2-grade scale for aneurysm-remnant detection, prevalence was low (15%) on the basis of DSA, and both MRA techniques showed low sensitivity (25%), high specificity (100%), very good positive predictive value (100%), and very good negative predictive value (88%).

Analysis by the Type of WEB

Among the 14 patients treated with the WEB-DL, with a simplified 2-grade scale, consensus readings agreed for 13 aneurysms (including 12 adequate occlusions and 1 aneurysm remnant) and disagreed for 1 aneurysm remnant on DSA, classified as adequate

Table 1: Patient and aneurysm characteristics (n = 26)^a

Patients	
Female	22 (84.5%)
Age (yr)	57 (48–61)
Aneurysms	
Aneurysm localization	
Internal carotid artery	6 (23%)
Anterior cerebral artery/anterior communicating artery	9 (35%)
Middle cerebral artery	7 (27%)
Vertebrobasilar artery	4 (15%)
Aneurysm size	
≤5 mm	1 (4%)
5–10 mm	22 (84%)
≥10 mm	3 (12%)
Aneurysm status	
Unruptured	24 (92%)

^a Continuous variables are described as median and interquartile range, and categorical variables, as number and percentage.

Table 2: Aneurysm occlusion evaluation (n = 26)

	DSA (No.) (%)	3D-TOF-MRA (No.) (%)	CE-MRA (No.) (%)
Montreal scale			
Total occlusion	12 (46)	17 (65)	18 (69)
Neck remnant	10 (38.5)	8 (31)	7 (27)
Aneurysm remnant	4 (15.5)	1 (4)	1 (4)
Simplified 2-grade scale			
Adequate occlusion	22 (85)	25 (96)	25 (96)
Aneurysm remnant	4 (15)	1 (4)	1 (4)

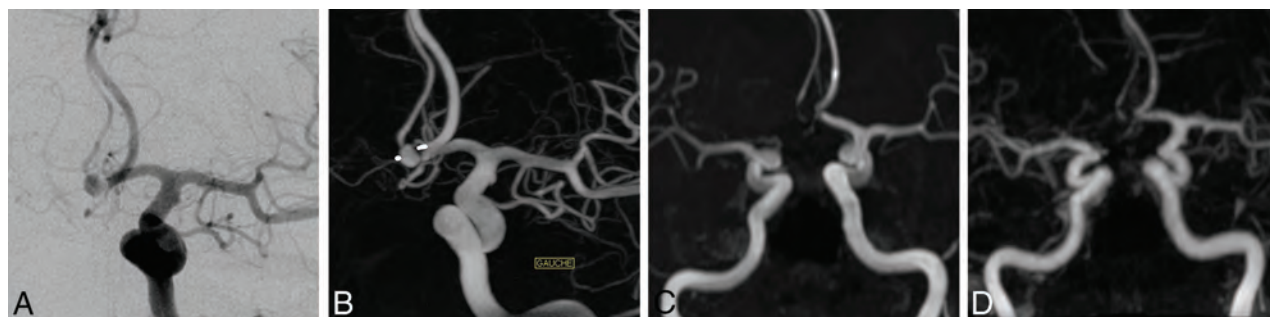


FIG 1. A 78-year-old man with an anterior communicating artery aneurysm treated by the WEB-SL with enhanced visualization. Follow-up images were acquired 7 months after endovascular treatment. 3D-TOF-MRA and CE-MRA were performed 24 hours after DSA. DSA frontal projection (A) and 3D reconstruction in an embolization incidence (B) show aneurysm remnants with complete circulation within the device, while 3D-TOF-MRA and CE-MRA MIP reconstructions (C and D) show total occlusion.

occlusion with both MRA techniques. Among the 12 patients treated with the WEB-SL or SLS (including 6 EVs), with the simplified 2-grade scale, consensus readings agreed for 10 aneurysms (4 EVs and 6 non-EVs) and disagreed for 2 aneurysm remnants (2 EVs) on DSA classified as adequate occlusion with both MRA techniques.

DISCUSSION

In our series of patients with aneurysms treated with the WEB, DSA was superior to CE-MRA and 3D-TOF-MRA for the evaluation of aneurysm remnants, and both MRA techniques had equivalent accuracy ($\kappa = 0.36$); however, the interobserver reproducibility was higher with CE-MRA ($\kappa = 0.65$) than with 3D-TOF-MRA ($\kappa = 0.47$).

WEB treatment of wide-neck bifurcation aneurysms induces intra-aneurysmal thrombosis. Long-term anatomic results after WEB treatment are available,^{28,29} and several follow-up imaging modalities may be used, such as DSA, MRA, or CTA. If it is now accepted that the artifacts produced by coils do not hamper MRA interpretation,¹⁷⁻²¹ it is important to understand the accuracy and reliability of MRA techniques for WEB-treated aneurysms.

The WEB has a different material composition (nickel-titanium-platinum composite wires with radio-opaque platinum markers) compared with coils but is similar to intracranial stents and flow diverters. Despite recent progress in neurovascular device manufacturing, MR imaging of a stent or flow-diverter lumen remains difficult due to a combination of magnetic susceptibility artifacts and the Faraday cage effect. Given the material similarities to neurovascular stents and flow diverters, the above MR imaging effects may be expected with the WEB.

In terms of magnetic susceptibility, the WEB is similar to most commercially available neurovascular stents and flow diverters that are made from nonferromagnetic alloys such as nitinol with either platinum alloy markers or platinum alloy wires for radio-opacity. Of note, a minority of components of these alloys or impurities in the alloy itself are thought to disturb the homogeneity of the magnetic field and cause an alteration of the resonance condition of the protons in the vicinity of the implant, thus leading to intravoxel dephasing with an attendant loss of signal.³⁰ These susceptibility artifacts that prevent visualization of the device lumen may be variable, depending on the materials.³¹ This phenomenon may explain, in part, the loss of signal that prevents the physician from seeing the interior of the WEB on MRA sequences. WEBs are now available with composite nitinol/platinum wires that improve radio-opacity but likely have the same magnetic susceptibility profile as intracranial stents and flow diverters with the same or similar materials.

Given that neurovascular stents and flow diverters are constructed of electrically conductive materials, they likely provide a Faraday cage or Faraday shield effect with MR imaging. The braids prevent the proton spins of water molecules in the stent lumen from being flipped or excited. This phenomenon depends on the wave length of the radiation, the size of the mesh in the cage, the conductivity of the materials, thickness, and other variables.^{32,33} Unlike stainless steel or cobalt alloy stents, nitinol stents are relatively more sensitive to radiofrequency artifacts than to susceptibility artifacts.³⁴ If one drew a parallel between the WEB

and stents/flow diverters of equivalent composition, it seems reasonable that there is also a Faraday shield effect with the WEB and that it contributes to loss of signal from the interior.

The same MRA parameters for stent evaluation were used without optimization for the WEB evaluation. However, it has been shown that optimized sequences can minimize stent-induced artifacts. Using a T1-weighted spin-echo pulse sequence may produce artifacts smaller than those of fast-spoiled gradient-recalled echo pulse sequences, shorter TEs can also decrease stent artifacts, and contrast-enhanced MRA may help to better delineate the stent lumen.³⁰ Also, for nitinol stents, the visualization of the stented segment can be at least partially overcome by using a higher flip angle.³⁵⁻³⁷ Recently, a "silent scan" technique combining ultrashort TEs (to minimize the phase dispersion of the labeled blood flow signal in the voxel) and arterial spin-labeling showed promising improvement of flow visualization in an intracranial stent.³⁸ This technique may theoretically improve visualization within the WEB device and will deserve further dedicated studies.

There are few data in the literature about noninvasive methods for WEB follow-up. MRA was evaluated in a small number of patients at 1.5T, while CTA has not been reported.²⁴ Mine et al²⁴ compared DSA and CE-MRA for the follow-up of intracranial aneurysms treated with the WEB-DL and found a better inter-technique agreement (mean $\kappa = 0.67$) than in the present study ($\kappa = 0.36$). Despite these results, 2/5 (40%) aneurysm remnants were not detected with CE-MRA in their study, while 3/4 (75%) were not detected in ours; these findings underlie the sensitivity limitations of MRA compared with DSA for aneurysm remnant.

There are differences between the 2 studies. Mine et al²⁴ evaluated 16 aneurysms treated with the WEB-DL, by using a 1.5T device, while we used a 3T magnet, which has been reported to be better for the follow-up of coiled intracranial aneurysms²⁰ but may have potentially enhanced artifacts. In addition, the time between CE-MRA and DSA was longer in their study (2 months); this difference could have introduced modifications between the 2 examinations. They chose to evaluate only CE-MRA, while our study also provided data on the value of 3D-TOF-MRA. Finally, they classified the occlusion according to the Raymond classification scale,²⁶ while we decided to use a simplified 2-grade scale closer to our clinical practice. At first sight, one can infer that there will be more disagreement by using a 3-grade scale; nevertheless, the 2-grade scale by gathering completely occluded aneurysms and those with neck remnants can influence strongly the intermodality agreement when several disagreements between neck remnant and aneurysm remnant occur. This difference may sometimes be subjective and related to small differences in measurements. Specific occlusion grading scales have been proposed for aneurysms treated with the WEB such as the WEB occlusion scale. The WEB occlusion scale was approved and validated as the grading scale for the 150 patients in the US WEB-IT Clinical Study and was correlated to histology in an 80-subject preclinical study.^{39,40}

Our study has several limitations. First, a small number of patients were included. Second, the heterogeneity of endovascular implants (different types of WEB and adjunction, in some cases, of stents or coils) might have affected MRA image quality. Despite

disagreement occurring in only 1 of the patients with an adjunctive device (WEB + 2 coils) and the 2 readers not noticing dramatic modifications between different devices, the adjunctive device may have been the source of supplemental artifacts and remains to be evaluated in a larger series of patients. Third, we used standardized MRA stent parameters, and optimization of these parameters for the WEB may reduce artifacts. Future studies of CTA and optimized MRA for WEB follow-up are necessary. Also, the difference between DSA standard views and strict axial and coronal MIP views for MRA images possibly affected the readers' ratings between the neck and aneurysm remnants, underlying the importance of careful reading of axial source images.²³

CONCLUSIONS

In our series, despite acceptable interobserver reproducibility and predictive values, the low sensitivity of CE-MRA and 3D-TOF-MRA for aneurysm remnant detection suggests that MRA is a useful screening procedure for WEB-treated aneurysms, but similar to stents and flow diverters, DSA remains the criterion standard for follow-up. Regarding improving noninvasive follow-up of WEB-treated aneurysms, further studies will have to focus on the analysis of optimized MRA techniques in larger cohorts of patients treated with homogeneous WEB devices.

Disclosures: Laurent Pierot—RELATED: Consulting Fee or Honorarium: Sequent Medical; UNRELATED: Consultancy: Blockade Medical, Medtronic, MicroVention, Neuravi.

REFERENCES

- Molyneux AJ, Kerr RS, Yu LM, et al; International Subarachnoid Aneurysm Trial (ISAT) Collaborative Group. **International Subarachnoid Aneurysm Trial (ISAT) of neurosurgical clipping versus endovascular coiling in 2143 patients with ruptured intracranial aneurysms: a randomised comparison of effects on survival, dependency, seizures, rebleeding, subgroups, and aneurysm occlusion.** *Lancet* 2005;366:809–17 Medline
- Cognard C, Pierot L, Anxionnat R, et al; Clarity Study Group. **Results of embolization used as the first treatment choice in a consecutive nonselected population of ruptured aneurysms: clinical results of the Clarity GDC study.** *Neurosurgery* 2011;69:837–41; discussion 842 CrossRef Medline
- Pierot L, Spelle L, Vitry F; ATENA Investigators. **Immediate clinical outcome of patients harboring unruptured intracranial aneurysms treated by endovascular approach: results of the ATENA study.** *Stroke* 2008;39:2497–504 CrossRef Medline
- Pierot L, Cognard C, Anxionnat R, et al; CLARITY Investigators. **Endovascular treatment of ruptured intracranial aneurysms: factors affecting midterm quality anatomic results—analysis in a prospective, multicenter series of patients (CLARITY).** *AJNR Am J Neuroradiol* 2012;33:1475–80 CrossRef Medline
- Pierot L, Wakhloo A. **Endovascular treatment of intracranial aneurysms: current status.** *Stroke* 2013;44:2046–54 CrossRef Medline
- Pierot L, Liebig T, Sychra V, et al. **Intrasaccular flow-disruption treatment of intracranial aneurysms: preliminary results of a multicenter clinical study.** *AJNR Am J Neuroradiol* 2012;33:1232–38 CrossRef Medline
- Lubicz B, Mine B, Collignon L, et al. **WEB device for endovascular treatment of wide-neck bifurcation aneurysms.** *AJNR Am J Neuroradiol* 2013;34:1209–14 CrossRef Medline
- Pierot L, Klisch J, Cognard C, et al. **Endovascular WEB flow disruption in middle cerebral artery aneurysms: preliminary feasibility, clinical, and anatomical results in a multicenter study.** *Neurosurgery* 2013;73:27–34; discussion 34–35 CrossRef Medline
- Caroff J, Mihalea C, Dargento F, et al. **Woven Endobridge (WEB) Device for endovascular treatment of ruptured intracranial wide-neck aneurysms: a single-center experience.** *Neuroradiology* 2014;56:755–61 CrossRef Medline
- Lubicz B, Klisch J, Gauvrit JY, et al. **WEB-DL endovascular treatment of wide-neck bifurcation aneurysms: short- and midterm results in a European study.** *AJNR Am J Neuroradiol* 2014;35:432–38 CrossRef Medline
- Papagiannaki C, Spelle L, Januel AC, et al. **WEB intrasaccular flow disruptor: prospective, multicenter experience in 83 patients with 85 aneurysms.** *AJNR Am J Neuroradiol* 2014;35:2106–11 CrossRef Medline
- Pierot L, Moret J, Turjman F, et al. **WEB treatment of intracranial aneurysms: feasibility, complications, and 1-month safety results with the WEB DL and WEB SL/SLS in the French Observatory.** *AJNR Am J Neuroradiol* 2015;36:922–27 CrossRef Medline
- Gherasim DN, Gory B, Sivan-Hoffmann R, et al. **Endovascular treatment of wide-neck anterior communicating artery aneurysms using WEB-DL and WEB-SL: short-term results in a multicenter study.** *AJNR Am J Neuroradiol* 2015;36:1150–54 CrossRef Medline
- Pierot L, Costalat V, Moret J, et al. **Safety and efficacy of aneurysm treatment with WEB: results of WEBCAST study.** *J Neurosurg* 2015;18:1–7 CrossRef Medline
- Pierot L, Moret J, Turjman F, et al. **WEB treatment of intracranial aneurysms: clinical and anatomic results in the French Observatory.** *AJNR Am J Neuroradiol* 2016;37:655–59 CrossRef Medline
- Pierot L, Spelle L, Molyneux A, et al; WEBCAST and French Observatory Investigators. **Clinical and anatomical follow-up in patients with aneurysms treated with WEB device: 1-year follow-up report in the cumulated population of 2 prospective, multicenter series (WEBCAST, French Observatory).** *Neurosurgery* 2016;78:133–41 CrossRef Medline
- Boulin A, Pierot L. **Follow-up of intracranial aneurysms treated with detachable coils: comparison of gadolinium-enhanced 3D time-of-flight MR angiography and digital subtraction angiography.** *Radiology* 2001;219:108–13 CrossRef Medline
- van Amerongen MJ, Boogaarts HD, de Vries J, et al. **MRA versus DSA for follow-up of coiled intracranial aneurysms: a meta-analysis.** *AJNR Am J Neuroradiol* 2014;35:1655–61 CrossRef Medline
- Pierot L, Portefaix C, Gauvrit JY. **Follow-up of coiled intracranial aneurysms: comparison of 3D time-of-flight MR angiography at 3T and 1.5T in a large prospective series.** *AJNR Am J Neuroradiol* 2012;33:2162–66 CrossRef Medline
- Pierot L, Portefaix C, Boulin A, et al. **Follow-up of coiled intracranial aneurysms: comparison of 3D-time-of-flight and contrast-enhanced magnetic resonance angiography at 3T in a large, prospective series.** *Eur Radiol* 2012;22:2255–63 CrossRef Medline
- Pierot L, Delcourt C, Bouquigny F, et al. **Follow-up of intracranial aneurysms selectively treated with coils: prospective evaluation of contrast-enhanced MR angiography.** *AJNR Am J Neuroradiol* 2006;27:744–49 Medline
- Agid R, Schaaf M, Farb R. **CE-MRA for follow-up of aneurysms post stent-assisted coiling.** *Interv Neuroradiol* 2012;18:275–83 Medline
- Attali J, Benaissa A, Soize S, et al. **Follow-up of intracranial aneurysms treated by flow diverter: comparison of three-dimensional time-of-flight MR angiography (3D-TOF-MRA) and contrast-enhanced MR angiography (CE-MRA) sequences with digital subtraction angiography as the gold standard.** *J Neurointerv Surg* 2016;8:81–86 CrossRef Medline
- Mine B, Tancredi I, Aljishi A, et al. **Follow-up of intracranial aneurysms treated by a WEB flow disrupter: a comparative study of DSA and contrast-enhanced MR angiography.** *J Neurointerv Surg* 2015 May 21. [Epub ahead of print] CrossRef Medline
- Bossuyt PM, Reitsma JB, Bruns DE, et al; Standards for Reporting of Diagnostic Accuracy. **Towards complete and accurate reporting of**

- studies of diagnostic accuracy: the STARD Initiative. *Radiology* 2003;226:24–28 CrossRef Medline
26. Raymond J, Guilbert F, Weill A, et al. Long-term angiographic recurrences after selective endovascular treatment of aneurysms with detachable coils. *Stroke* 2003;34:1398–403 CrossRef Medline
 27. Landis JR, Koch GG. The measurement of observer agreement for categorical data. *Biometrics* 1977;33:159–74 CrossRef Medline
 28. Pierot L, Klich J, Liebig T, et al. WEB-DL endovascular treatment of wide-neck bifurcation aneurysms: long-term results in a European series. *AJNR Am J Neuroradiol* 2015;36:2314–19 CrossRef Medline
 29. Sivan-Hoffmann R, Gory B, Riva R, et al. One-year angiographic follow-up after WEB-SL endovascular treatment of wide-neck bifurcation intracranial aneurysms. *AJNR Am J Neuroradiol* 2015;36:2320–24 CrossRef Medline
 30. Klemm T, Duda S, Machann J, et al. MR imaging in the presence of vascular stents: a systematic assessment of artifacts for various stent orientations, sequence types, and field strengths. *J Magn Reson Imaging* 2000;12:606–15 Medline
 31. Lenhart M, Völk M, Manke C, et al. Stent appearance at contrast-enhanced MR angiography: in vitro examination with 14 stents. *Radiology* 2000;217:173–78 CrossRef Medline
 32. Acton QA. *Monovalent Cations—Advances in Research and Application*. Atlanta: ScholarlyEditions; 2013:407–08
 33. Camacho CR, Plewes DB, Henkelman RM. Nonsusceptibility artifacts due to metallic objects in MR imaging. *J Magn Reson Imaging* 1995;5:75–88 CrossRef Medline
 34. Hähnel S, Nguyen-Trong TH, Rohde S, et al. 3.0 Tesla contrast-enhanced MR angiography of carotid artery stents: in vitro measurements as compared with 1.5 Tesla. *J Neuroradiol* 2006;33:75–80 CrossRef Medline
 35. Bartels LW, Bakker CJ, Viergever MA. Improved lumen visualization in metallic vascular implants by reducing RF artifacts. *Magn Reson Med* 2002;47:171–80 CrossRef Medline
 36. Choi JW, Roh HG, Moon WJ, et al. Optimization of MR parameters of 3D-TOF-MRA for various intracranial stents at 3.0T MRI. *Neurointervention* 2011;6:71–77 CrossRef Medline
 37. Meyer JM, Buecker A, Spuentrup E, et al. Improved in-stent magnetic resonance angiography with high flip angle excitation. *Invest Radiol* 2001;36:677–81 CrossRef Medline
 38. Irie R, Suzuki M, Yamamoto M, et al. Assessing blood flow in an intracranial stent: a feasibility study of MR angiography using a silent scan after stent-assisted coil embolization for anterior circulation aneurysms. *AJNR Am J Neuroradiol* 2015;36:967–70 CrossRef Medline
 39. Fiorella D, Arthur A, Byrne J, et al. Interobserver variability in the assessment of aneurysm occlusion with the WEB aneurysm embolization system. *J Neurointerv Surg* 2015;7:591–95 CrossRef Medline
 40. Rouchaud A, Brinjikji W, Ding YH, et al. Evaluation of the angiographic grading scale in aneurysms treated with the WEB device in 80 rabbits: correlation with histologic evaluation. *AJNR Am J Neuroradiol* 2016;37:324–29 CrossRef Medline

Incidence and Clinical Significance of Acute Reocclusion after Emergent Angioplasty or Stenting for Underlying Intracranial Stenosis in Patients with Acute Stroke

G.E. Kim, W. Yoon, S.K. Kim, B.C. Kim, T.W. Heo, B.H. Baek, Y.Y. Lee, and N.Y. Yim

ABSTRACT

BACKGROUND AND PURPOSE: A major concern after emergent intracranial angioplasty in cases of acute stroke with underlying intracranial stenosis is the acute reocclusion of the treated arteries. This study reports the incidence and clinical outcomes of acute reocclusion of arteries following emergent intracranial angioplasty with or without stent placement for the management of patients with acute stroke with underlying intracranial atherosclerotic stenosis.

MATERIALS AND METHODS: Forty-six patients with acute stroke received emergent intracranial angioplasty with or without stent placement for intracranial atherosclerotic stenosis and underwent follow-up head CTA. Acute reocclusion was defined as “hypoattenuation” within an arterial segment with discrete discontinuation of the arterial contrast column, both proximal and distal to the hypoattenuated lesion, on CTA performed before discharge. Angioplasty was defined as “suboptimal” if a residual stenosis of $\geq 50\%$ was detected on the postprocedural angiography. Clinical and radiologic data of patients with and without reocclusion were compared.

RESULTS: Of the 46 patients, 29 and 17 underwent angioplasty with and without stent placement, respectively. Acute reocclusion was observed in 6 patients (13%) and was more frequent among those with suboptimal angioplasty than among those without it (71.4% versus 2.6%, $P < .001$). The relative risk of acute reocclusion in patients with suboptimal angioplasty was 27.857 (95% confidence interval, 3.806–203.911). Furthermore, a good outcome was significantly less frequent in patients with acute reocclusion than in those without it (16.7% versus 67.5%, $P = .028$).

CONCLUSIONS: Acute reocclusion of treated arteries was common after emergent intracranial angioplasty with or without stent placement in patients with acute stroke with intracranial atherosclerotic stenosis and was associated with a poor outcome. Suboptimal results of angioplasty appear to be associated with acute reocclusion, irrespective of whether stent placement was performed.

ABBREVIATIONS: ICAS = intracranial atherosclerotic stenosis; IQR = interquartile range

Intracranial atherosclerotic stenosis (ICAS) is rapidly becoming a major concern worldwide in patients with stroke because Asian, Hispanic, and African populations, which are prone to ICAS, constitute an overwhelming majority of the population of the world.¹ Acute stroke caused by an in situ thrombosis at the site of ICAS differs from that caused by cardiogenic embolic occlusion and may not respond to modern mechanical embolectomy procedures such as stent-retriever embolectomy or manual aspiration embolectomy. Few studies have been published hitherto on

the optimal treatment plan for patients with acute stroke with underlying ICAS.^{2–5} Emergent intracranial angioplasty, with or without stent placement, has been recently suggested as an effective treatment option for the management of underlying ICAS following mechanical embolectomy; for example, Yoon et al⁴ reported a successful revascularization rate of 95% and a favorable outcome rate of 65% with this strategy.

Nevertheless, a major concern after emergent intracranial angioplasty in cases of acute stroke is the acute reocclusion of the treated arteries. Acute reocclusion may occur following intracranial angioplasty or stent placement as a result of platelet activation, adherence, and aggregation triggered by the disruption of vulnerable plaque and endothelial damage; unsuccessful or inadequate pretreatment with antiplatelet drugs; dissection; or vasospasm.⁶ Despite the possibility of this complication in patients with acute stroke, data regarding its incidence and clinical consequences have not yet been reported in literature, to our knowledge.

Received November 18, 2015; accepted after revision February 9, 2016.

From the Departments of Radiology (G.E.K., W.Y., S.K.K., T.W.H., B.H.B., Y.Y.L., N.Y.Y.) and Neurology (B.C.K.), Chonnam National University Medical School, Chonnam National University Hospital, Gwangju, Republic of Korea.

Please address correspondence to Woong Yoon, MD, Department of Radiology, Chonnam National University Hospital, 42 Jebong-ro, Dong-gu, Gwangju, 501-757, Republic of Korea; e-mail: radyoon@jnu.ac.kr

<http://dx.doi.org/10.3174/ajnr.A4770>

Thus, this study aimed to investigate the incidence and clinical outcomes of arterial reocclusion in patients with acute stroke undergoing emergent angioplasty with or without stent placement following stent-retriever embolectomy. Additionally, we sought to determine the risk factors associated with acute reocclusion in these patients.

MATERIALS AND METHODS

Patients

Between January 2011 and February 2014, 240 patients with acute ischemic stroke were treated with mechanical embolectomy at our comprehensive regional stroke center. Of these, 50 (20.8%) consecutive patients with underlying ICAS as a cause of acute large-vessel occlusion underwent emergent intracranial angioplasty with or without stent placement subsequent to mechanical embolectomy. Forty-six of these patients underwent follow-up head CTA after endovascular therapy, as per our institutional protocol for acute stroke management. The remaining 4 patients could not undergo CTA during hospitalization due to their poor health status. Thus, 46 patients were finally enrolled in this retrospective study, and their clinical and radiologic data were analyzed. The institutional ethics committee approved this retrospective analysis and waived informed consent due to the retrospective study design.

On admission, a stroke neurologist performed an assessment by using the NIHSS. Before the initiation of endovascular treatment, all patients underwent nonenhanced cranial CT and multimodal MR imaging. The inclusion criteria for endovascular therapy were as follows: presentation within 6 and 8 hours of stroke onset for anterior and posterior circulation stroke, respectively; a baseline NIHSS score of ≥ 4 ; no evidence of intracranial hemorrhage on cranial CT or MR imaging; evidence of major arterial occlusion on MR angiography; a target mismatch pattern on multimodal MR imaging based on visual estimation (time-to-peak map of perfusion imaging showing a lesion volume $\geq 30\%$ larger than that detected with DWI) for an anterior circulation stroke; an infarct volume of less than one-third of the MCA territory for anterior circulation stroke, as determined by DWI or nonenhanced CT; an absence of bilateral diffuse pontine ischemia on DWI for posterior circulation stroke; and a premorbid mRS score of ≤ 3 .

Endovascular Therapy

All endovascular therapy was performed by a single interventional neuroradiologist with 12 years of experience in neurovascular intervention. For each patient, written informed consent for endovascular therapy was obtained from a family member. Both cerebral angiography and endovascular therapy were performed with the patient under conscious sedation. In case of agitation, an intravenous bolus of midazolam was administered and repeated if necessary. When pretreatment diagnostic angiography showed an arterial occlusion, stent-retriever embolectomy with the Solitaire stent (Covidien, Irvine, California) was performed as the first-line endovascular treatment. When stent-retriever embolectomy was unsuccessful, other mechanical approaches were performed, including manual aspiration embolectomy by using a Penumbra aspiration catheter (Penumbra, Alameda, California). The details

of the techniques used for mechanical embolectomy have been described previously.^{7,8}

If severe ($>70\%$) underlying ICAS of the target artery was seen on the initial diagnostic angiography or on follow-up angiography after mechanical embolectomy, intracranial angioplasty with or without stent placement was performed. The severity of arterial stenosis was graded according to the Warfarin-Aspirin Symptomatic Intracranial Disease criteria.⁹ For underlying ICAS seen after the initial mechanical embolectomy, ICAS was determined if the stenotic lesion remained unchanged 3–5 minutes after intra-arterial injection of a vasodilator through the guide catheter. The devices and techniques used for intracranial angioplasty and stent placement have been described in detail elsewhere.⁴

Neither heparin nor glycoprotein IIb/IIIa inhibitor was administered either intravenously or intra-arterially during the endovascular procedure. All patients underwent nonenhanced CT immediately after endovascular therapy. If no intracranial hemorrhage was detected on this scan, aspirin and clopidogrel (Plavix) were administered orally via the nasogastric tube after the procedure. Dual antiplatelet therapy was then continued for at least 3 months after the procedure.

CTA Image Acquisition and Analysis

CTA was performed on a dual-source CT scanner (Somatom Definition Flash; Siemens, Erlangen, Germany) with the following parameters: collimation, 128×0.6 mm; tube voltage, 120 kV; tube current, 250 mA; gantry rotation, 0.28 seconds; pitch factor, 0.6; FOV, 180 mm; and matrix, 512×512 . All patients were administered 100 mL of nonionic contrast agent with 350 mg of iodine per milliliter (iohexol, Omnipaque 350; GE Healthcare, Piscataway, New Jersey), which was injected into the antecubital vein at a rate of 4 mL/s. Scanning was triggered by the bolus-tracking technique with the ROI positioned in the aortic arch and the trigger threshold set at 25 HU. CTA source images were then reconstructed with a section width of 0.75 mm for further evaluation. The source images were transferred to the workstation and processed with the use of a commercial software package (syngo.CT Dynamic Angio; Siemens). Thick, maximum-intensity-projection images (section thickness, 30 mm; increments, 5 mm) were reconstructed in axial, coronal, sagittal, and oblique coronal planes to evaluate the intracranial arteries.

Maximum-intensity-projection and source images of all patients were reviewed by 2 neuroradiologists and were evaluated for the presence or absence of occlusion or stenosis of $\geq 50\%$ at the site of previous angioplasty or stent placement. Decisions were made by consensus between the 2 investigators. Arterial occlusion was defined as a hypoattenuation within the arterial segment with discrete discontinuation of the arterial contrast column between the proximal and distal points of the hypoattenuated lesion.

Outcome Measures

We recorded the clinical and radiologic data from the medical records of the patients. The “start of endovascular therapy” was defined as the moment the needle punctured the common femoral artery. “Symptomatic intracranial hemorrhage” was defined as any intracranial hemorrhage that caused neurologic deteriora-

Table 1: Baseline characteristics of the study population

	All Patients (N = 46)	Patients with Acute Reocclusion (n = 6)	Patients without Acute Reocclusion (n = 40)	P Value
Age (yr) (IQR)	66 (57.75–74.75)	63 (57.5–72.5)	66 (57.5–76.25)	NS
Male sex (No.) (%)	28 (60.9)	3 (50)	25 (62.5)	NS
Risk factors (No.) (%)				
Hypertension	29 (63)	4 (66.7)	25 (62.5)	NS
Diabetes mellitus	20 (43.6)	2 (33.3)	18 (45)	NS
Dyslipidemia	26 (56.5)	4 (66.7)	22 (55)	NS
Smoking	10 (21.7)	2 (33.3)	8 (20)	NS
Atrial fibrillation	4 (8.7)	0 (0)	4 (10)	NS
Previous CAD	1 (2.2)	0 (0)	1 (2.5)	NS
Congestive heart failure	1 (2.2)	0 (0)	1 (2.5)	NS
History of stroke or TIA	8 (17.4)	4 (66.7)	4 (10)	.005
Occlusion site (No.) (%)				
Middle cerebral artery	26 (56.5)	5 (83.3)	21 (52.5)	NS
Internal carotid artery	8 (17.4)	0 (0)	8 (20)	NS
Basilar artery	12 (26.1)	1 (16.7)	11 (27.5)	NS
Baseline NIHSS score (IQR)	12 (8–14)	9.5 (6.5–14.5)	10 (9–14)	NS
Intravenous thrombolysis (No.) (%)	18 (39.1)	4 (66.7)	14 (35)	NS
Intra-arterial thrombolysis (No.) (%)	7 (15.2)	1 (16.7)	6 (15)	NS
Time to procedure (min) (IQR)	270 (207.75–362)	277.5 (233.75–330.00)	252.5 (187.5–360)	NS
Procedural time (min) (IQR)	36 (25–46.75)	33 (22.75–47.25)	37 (25.75–48.75)	NS
Time to revascularization (min) (IQR)	319.5 (231.75–401.5)	305 (264.75–385.75)	301 (217.5–407)	NS
Postprocedural residual stenosis (%) (IQR)	25 (19.5–35.0)	56 (42.3–71.3)	25 (19–33)	0.009
Postprocedural antiplatelet therapy (No.) (%)	41 (89.1)	6 (100)	35 (87.5)	NS

Note:—CAD indicates coronary artery disease; NS, not significant.

tion, which was a ≥ 4 -point increase in the NIHSS score or a 1-point deterioration in the level of consciousness.

Revascularization status was assessed by using the final angiogram according to the modified TICI scale,¹⁰ with “successful revascularization” defined as a modified TICI grade of 2b or 3. “Arterial perforation” was defined by evidence of frank angiographic contrast extravasation on serial angiograms. “Arterial dissection” was defined as an identifiable, intimal flap on the final angiogram. The angiographic findings were characterized as either “optimal” ($< 50\%$ residual stenosis) or “suboptimal” ($\geq 50\%$ residual stenosis) on the final angiogram.^{11,12} Angiographic images were evaluated by 2 neuroradiologists in consensus.

Neurologic evaluation was performed by a stroke neurologist immediately and 24 hours after treatment, before discharge, 3 months after treatment, and when there were any changes in clinical symptoms. Clinical outcome was assessed by a stroke neurologist by using the mRS score during an outpatient visit 3 months after treatment. If patients were unable to attend the outpatient clinic, assessment was made via telephone interviews. A good clinical outcome was defined as an mRS score of ≤ 2 or equal to the premorbid mRS score.

Statistical Analysis

Continuous variables are presented as medians and interquartile ranges (IQRs). Discrete variables are presented as counts and percentages. First, patients were divided into 2 groups for comparison, according to the presence or absence of acute reocclusion on head CTA. The baseline characteristics and clinical outcomes of the 2 groups were compared. Second, the relationship between each clinical and radiologic characteristic and the 3-month outcome was determined. The χ^2 or Fisher exact test was used for comparing categorical and binary data, and the Mann-Whitney *U* test was used for comparing continuous data. Third, a logistic

regression analysis was performed to identify independent predictors of good clinical outcome. The variables tested in the logistic regression models were those with $P < .05$ in the univariate analysis, age, and successful revascularization. All statistical analyses were performed with SPSS software (Version 21.0; IBM, Armonk, New York). A P value $< .05$ was significant.

RESULTS

Data from 46 patients were analyzed. Baseline patient characteristics are shown in Table 1. Of the 46 patients treated with emergent angioplasty with or without stent placement for acute stroke, 26 had ICAS in the MCA; 12, in the basilar artery; and 8, in the intracranial internal carotid artery. Follow-up CTA was performed within 48 hours of endovascular therapy in 45 patients (97.8%). The remaining patient underwent CTA 120 hours after endovascular therapy.

Follow-up CTA showed reocclusion at the site of angioplasty or stent placement in 6 patients (13%), with reocclusion occurring in the MCA in 5 patients and in the basilar artery in 1 patient (Fig 1). A history of previous stroke or TIA was more frequent in patients with reocclusion (66.7% versus 10%, $P = .005$) than in those without it. Postprocedural residual stenosis was significantly greater in patients with acute reocclusion (56% versus 25%, $P = .009$). No significant intergroup differences were noted in terms of patient age, sex, history of other risk factors, occlusion sites, use of intravenous or intra-arterial thrombolysis, time to procedure, duration of the procedure, time to revascularization, and baseline NIHSS score. Severe stenosis ($\geq 50\%$) at the site of angioplasty or stent placement was not observed in the remaining 40 patients.

Thirty-two patients underwent both intracranial angioplasty and stent placement, while 14 patients underwent only angio-

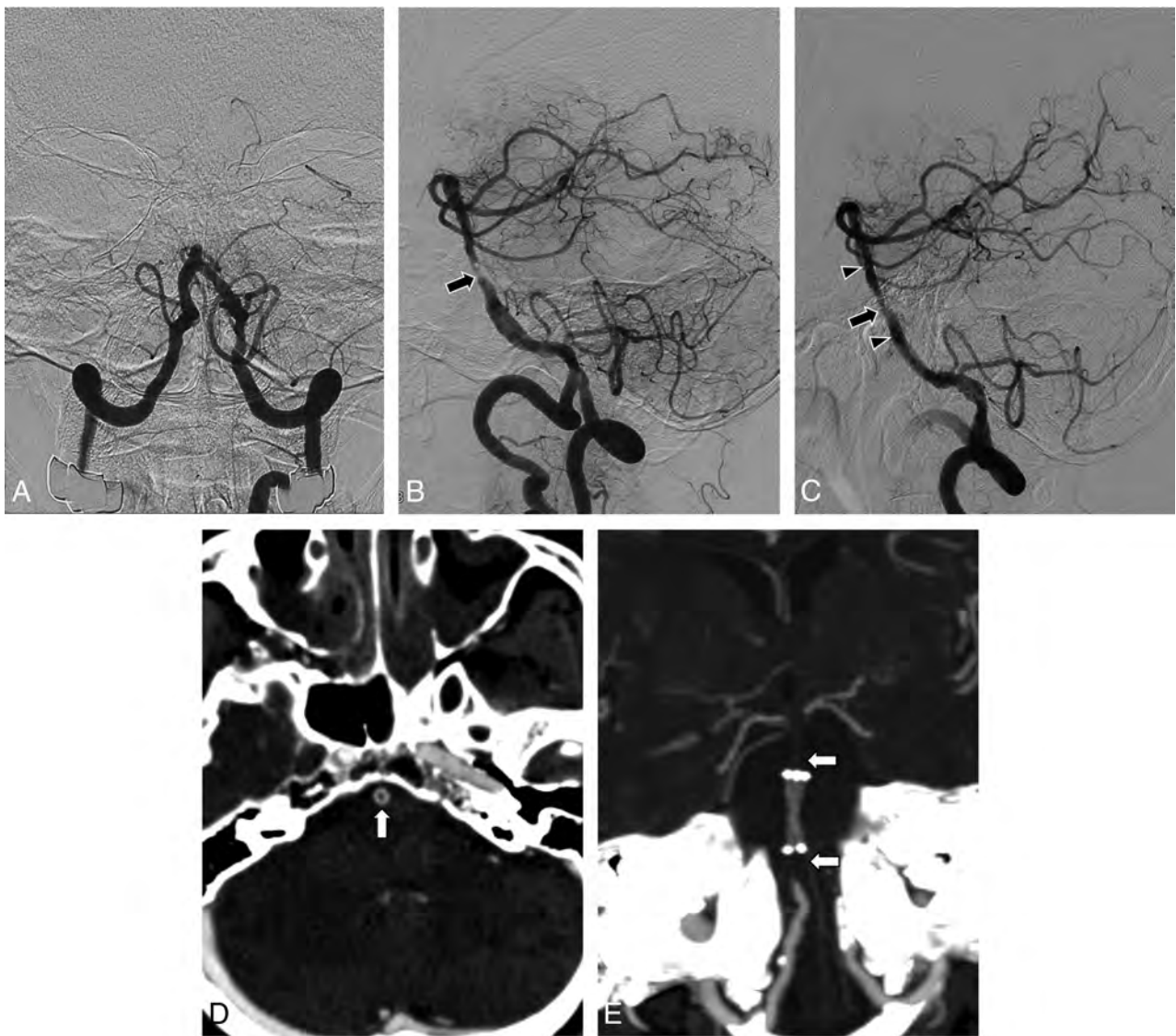


FIG 1. Brain images obtained in a patient with acute stroke. *A*, Anteroposterior view of a vertebral angiogram shows arterial occlusion at the proximal portion of the basilar artery. *B*, Lateral projection of the vertebral angiogram obtained after stent-retriever embolectomy reveals severe underlying stenosis (arrow) at the site of arterial occlusion. There were no retrieved thrombi with the Solitaire stent. *C*, Lateral projection of vertebral angiography performed after intracranial stent placement shows suboptimal angioplasty, with residual stenosis of 60% (arrow). Arrowheads indicate the proximal and distal ends of the stent. *D*, Axial source image of CTA shows hypoattenuation (arrow) within the stented segment of the basilar artery. *E*, Maximum-intensity-projection image of the follow-up CTA 2 days after the procedure shows a discontinuation of the contrast column both proximal and distal to the stent (arrows).

plasty. Acute reocclusion was more frequent among patients treated with intracranial angioplasty alone than among those treated with intracranial stent placement in addition to angioplasty (23.5% versus 6.9%); however, this difference was not statistically significant ($P = .174$). Of the 46 patients, 41 received antiplatelet medication after completion of endovascular therapy; 5 patients did not receive this therapy because they showed evidence of intracranial hemorrhage in the postprocedural CT scan. However, none of these 5 patients exhibited acute reocclusion on follow-up CTA.

Of 6 patients with reocclusion, 4 patients had an ASPECTS of 8, 1 had an ASPECTS of 7, and 1 had a posterior circulation ASPECTS of 5 on pretreatment DWI. The NIHSS score gradually increased by 2–5 points during the first 24 hours after endovascular therapy in all 6 patients with reocclusion. At the time of dis-

charge, the NIHSS score was unchanged in 3 patients, decreased in 2 patients (by 2 and 4 points, respectively), and slightly increased in 1 patient (by 3 points) compared with the score on day 1.

The clinical outcomes of patients with or without acute reocclusion are shown in Table 2. Overall, successful revascularization (modified TICI grade 2b or 3) was achieved in 95.7% (44/46) of patients. There was no significant difference between the 2 groups in terms of the rate of successful revascularization. A suboptimal result ($\geq 50\%$ residual stenosis at the site of angioplasty or stent placement) was observed on the final angiograms in 7 patients (15.2%). Furthermore, acute reocclusion was more frequent among patients with a suboptimal result than among those without (71.4% [5/7] versus 2.6% [1/39], $P < .001$). The relative risk for acute reocclusion in patients with a suboptimal result was

Table 2: Comparison of clinical outcomes between patients with and without acute reocclusion

	All Patients (N = 46)	Patients with Acute Reocclusion (n = 6)	Patients without Acute Reocclusion (n = 40)	P Value
m-TICI grade 2b or 3 (No.) (%)	44 (95.7)	5 (83.3)	39 (97.5)	NS
Suboptimal result (No.) (%)	7 (15.2)	5 (83.3)	2 (5)	<.001
mRS 0–2 (No.) (%)	28 (60.9)	1 (16.7)	27 (67.5)	.028
Symptomatic hemorrhage (No.) (%)	2 (4.3)	0 (0)	2 (5)	NS
Mortality (No.) (%)	3 (6.5)	0 (0)	3 (7.5)	NS

Note:—m-TICI indicates modified TICI; NS, not significant.

27.857 (95% CI, 3.806–203.911). Overall, a good clinical outcome was achieved in 60.9% (28/46) of patients. A good outcome was less frequent in patients with acute reocclusion than in those without it (16.7% versus 67.5%, $P = .028$); the relative risk of a poor outcome in patients with acute reocclusion was 2.564 (95% CI, 1.447–4.544).

Arterial perforation of a thalamoperforating artery by microguidewire occurred in 1 patient. Arterial dissection was not observed in the postprocedural angiograms of any patients. Overall, 2 patients (4.3%) without acute reocclusion had symptomatic hemorrhage, while 3 patients (6.5%) without acute reocclusion died before the 3-month follow-up. However, none of the patients with acute reocclusion showed symptomatic hemorrhage or 3-month mortality. There was no significant difference between the 2 groups in the rate of symptomatic hemorrhage and mortality.

In a univariate analysis, the following variables were identified as predictors of a good outcome at 3 months: acute reocclusion, history of stroke or TIA, and procedural time. A good outcome occurred less frequently among patients with a history of previous stroke or TIA than among those without (12.5% [1/8] versus 71.1% [27/38], $P = .004$). The median procedural time was shorter in patients with a good outcome than in those with a poor outcome (35 minutes [IQR, 25–42 minutes] versus 44 minutes [IQR, 32.75–62 minutes], $P = .019$). When acute reocclusion, history of previous stroke or TIA, procedural time, each year of age, and successful revascularization were selected for the logistic regression analysis, independent predictors of good outcome were a history of previous stroke or TIA (OR, 0.055; 95% CI, 0.004–0.821; $P = .035$) and procedural time (per 1-minute decrease; OR, 1.046; 95% CI, 1.000–1.093; $P = .048$).

DISCUSSION

The main findings of this study are summarized as follows: 1) acute reocclusion of arteries treated with emergent angioplasty with or without stent placement was fairly common in this study population, at a rate of 13%; 2) suboptimal angioplasty with or without stent placement was significantly associated with acute reocclusion; and 3) acute reocclusion was significantly associated with a poor outcome at 3-month follow-up.

Few studies have been published thus far on the incidence of acute reocclusion after intracranial angioplasty in acute stroke. Consistent with our study, Lee et al² reported that early reocclusion occurred within 48 hours in 16.7% (2/12) of patients with acute MCA occlusion after intracranial stent placement for the treatment of underlying ICAS. Additionally, Guo et al¹³ reported that acute reocclusion occurred in 9.1% (1/11) of patients within

1 day of intracranial stent placement. Moreover, Bang et al¹⁴ reported that in-stent thrombosis occurred within 1 week in 18.8% (6/32) of their patients who underwent intracranial stent placement for acute ischemic stroke. However, the latter 2 studies differ from our study and that of Lee et al in that stent placement was attempted to recanalize the embolic occlusions and not to treat the underlying ICAS. Furthermore,

those studies did not provide data on specific stroke etiology or postprocedural antiplatelet medication for the treated patients.

In our study, suboptimal angioplasty ($\geq 50\%$ residual stenosis) seemed to be a main predisposing factor for acute reocclusion. Suboptimal angioplasty was associated with a 28-fold increase in the rate of acute reocclusion in the present study. A suboptimal result may cause insufficient blood flow through the angioplasty-treated or stented arterial segment, thereby accelerating platelet aggregation. Sufficient blood flow at the site of angioplasty, with or without stent placement, prevents acute thrombus formation.¹⁵ Thus, our findings strongly suggest that neurointerventionists should pay particular attention to achieving optimal patency of the target artery during emergent intracranial angioplasty or stent placement for the treatment of underlying ICAS in patients with acute stroke.

A systematic review has shown that the frequency of reocclusion after stent placement is lower than after angioplasty alone in patients undergoing acute coronary interventions.¹⁶ Similarly, intracranial stent placement has been shown to be more effective than angioplasty alone in postoperative residual stenosis or late restenosis in cases of subacute-to-chronic symptomatic ICAS.^{12,17} Stent placement has been associated with a lower incidence of acute reocclusion than angioplasty alone, by eliminating vascular recoil and dissection and allowing increased vessel diameter.¹⁵ In our study, we also noted a trend toward a lower incidence of acute reocclusion among patients treated with stent placement than among those treated with angioplasty alone (6.9% versus 23.5%); however, this difference was not statistically significant, probably due to the small sample size.

Angioplasty with or without stent placement may lead to mechanical disruption of atherosclerotic plaques or endothelial injury that triggers platelet activation, adhesion, and aggregation, which are key features of arterial thrombosis and reocclusion. Therefore, adequate antiplatelet therapy is generally recommended to prevent acute thrombosis and reocclusion in cases of scheduled intracranial angioplasty or stent placement. Although optimal doses of antiplatelet therapy for periprocedural support during endovascular stroke therapy have not yet been established, loading doses of aspirin (300–650 mg) and clopidogrel (600 mg) are generally recommended, followed by daily doses of aspirin (100–300 mg) and clopidogrel (75 mg) for 1–3 months.¹⁸ Most interesting, the administration of periprocedural antiplatelet therapy did not appear to be associated with acute reocclusion in our study. There was no acute reocclusion in the 5 patients who did not receive postprocedural antiplatelet therapy in our study. All patients with acute reocclusion received loading doses of aspirin and clopidogrel after the procedure. Therefore, further studies

are necessary to determine the exact role of periprocedural antiplatelet therapy in patients undergoing emergency angioplasty with or without stent placement for the management of acute ischemic stroke in patients with ICAS.

There have been no studies to date on the clinical consequences of acute reocclusion after emergency angioplasty with or without stent placement in patients with acute stroke due to ICAS. In our study, a good outcome was considerably less frequent among patients with acute reocclusion than among those without it (16.7% versus 67.5%, $P = .028$); in fact, acute reocclusion was associated with a 2.6-fold increase in poor outcome at the 3-month follow-up. Similar results have been reported in a study on the immediate reocclusion of recanalized arteries during intra-arterial thrombolysis for embolic occlusion. Janjua et al¹⁹ showed that a favorable outcome was less frequently achieved in patients with immediate arterial reocclusion after various endovascular treatments than in those without it (6% versus 37%, $P = .01$). The odds ratio of a poor outcome in patients with arterial reocclusion was 3.9 in their analysis.¹⁹

The limitations of our study include its small sample size and retrospective design. While most patients (97.8%) underwent head CTA 2 days after endovascular therapy, 1 patient underwent the procedure 5 days after the operation. In addition, platelet function testing was not routinely performed. Thus, individualizing antiplatelet therapy was not possible; this situation may have influenced the incidence of acute reocclusion in this study. However, the impact of clopidogrel resistance on the effectiveness of endovascular therapy for acute ischemic stroke remains largely unstudied. Furthermore, routine platelet-function testing is not currently recommended in cases of acute coronary intervention.^{18,20}

CONCLUSIONS

Our findings indicate that acute reocclusion of treated vessels with or without stent placement after emergent angioplasty is common in patients with acute stroke due to ICAS and that this complication is associated with a poor outcome. Acute reocclusion in such cases appears to be associated with suboptimal angioplasty or stent placement. In light of these results, neurointerventionists should make every effort to achieve optimal results in restoring the patency of the affected artery during emergent angioplasty in cases of acute stroke due to ICAS.

REFERENCES

- Gorelick PB, Wong KS, Bae HJ, et al. **Large artery intracranial occlusive disease: a large worldwide burden but a relatively neglected frontier.** *Stroke* 2008;39:2396–99 CrossRef Medline
- Lee HK, Kwak HS, Chung GH, et al. **Balloon-expandable stent placement in patients with immediate reocclusion after initial successful thrombolysis of acute middle cerebral arterial obstruction.** *Interv Neuroradiol* 2012;18:80–88 Medline
- Kang DH, Kim YW, Hwang YH, et al. **Instant reocclusion following mechanical thrombectomy of in situ thromboocclusion and the role of low-dose intra-arterial tirofiban.** *Cerebrovasc Dis* 2014;37:350–55 CrossRef Medline
- Yoon W, Kim SK, Park MS, et al. **Endovascular treatment and the outcomes of atherosclerotic intracranial stenosis in patients with hyperacute stroke.** *Neurosurgery* 2015;76:680–86; discussion 686 CrossRef Medline
- Behme D, Weber W, Mpotsaris A. **Acute basilar artery occlusion with underlying high-grade basilar artery stenosis: multimodal endovascular therapy in a series of seven patients.** *Clin Neuroradiol* 2015;25:267–74 CrossRef Medline
- Qureshi AI, Siddiqui AM, Kim SH, et al. **Reocclusion of recanalized arteries during intra-arterial thrombolysis for acute ischemic stroke.** *AJNR Am J Neuroradiol* 2004;25:322–28 Medline
- Yoon W, Jung MY, Jung SH, et al. **Subarachnoid hemorrhage in a multimodal approach heavily weighted toward mechanical thrombectomy with Solitaire stent in acute stroke.** *Stroke* 2013;44:414–19 CrossRef Medline
- Kim SK, Yoon W, Moon SM, et al. **Outcomes of manual aspiration thrombectomy for acute ischemic stroke refractory to stent-based thrombectomy.** *J Neurointerv Surg* 2015;7:473–77 CrossRef Medline
- Samuels OB, Joseph GJ, Lynn MJ, et al. **A standardized method for measuring intracranial arterial stenosis.** *AJNR Am J Neuroradiol* 2000;21:643–46 Medline
- Zaidat OO, Yoo AJ, Khatri P, et al; Cerebral Angiographic Revascularization Grading (CARG) Collaborators, STIR Revascularization working group, STIR Thrombolysis in Cerebral Infarction (TICI) Task Force. **Recommendations on angiographic revascularization grading standards for acute ischemic stroke: a consensus statement.** *Stroke* 2013;44:2650–63 CrossRef Medline
- Yoon W, Seo JJ, Cho KH, et al. **Symptomatic middle cerebral artery stenosis treated with intracranial angioplasty: experience in 32 patients.** *Radiology* 2005;237:620–26 CrossRef Medline
- Siddiq F, Memon MZ, Vazquez G, et al. **Comparison between primary angioplasty and stent placement for symptomatic intracranial atherosclerotic disease: meta-analysis of case series.** *Neurosurgery* 2009;65:1024–33; discussion 1033–34 CrossRef Medline
- Guo XB, Song LJ, Guan S. **Emergent angioplasty and stent placement recanalization without thrombolysis in acute middle cerebral artery occlusions.** *J Stroke Cerebrovasc Dis* 2013;22:694–99 CrossRef Medline
- Bang JS, Oh CW, Jung C, et al. **Intracranial stent placement for recanalization of acute cerebrovascular occlusion in 32 patients.** *AJNR Am J Neuroradiol* 2010;31:1222–25 CrossRef Medline
- Breckenfeld C1, Tinguey P, Schroth G, et al. **Percutaneous transluminal angioplasty and stent placement in acute vessel occlusion: evaluation of new methods for interventional stroke treatment.** *AJNR Am J Neuroradiol* 2009;30:1165–72 CrossRef Medline
- Wilson SH, Bell MR, Rihal CS, et al. **Infarct artery reocclusion after primary angioplasty, stent placement, and thrombolytic therapy for acute myocardial infarction.** *Am Heart J* 2001;141:704–10 CrossRef Medline
- Siddiq F, Vazquez G, Memon MZ, et al. **Comparison of primary angioplasty with stent placement for treating symptomatic intracranial atherosclerotic diseases: a multicenter study.** *Stroke* 2008;39:2505–10 CrossRef Medline
- Nahab F, Kass-Hout T, Shaltoni HM. **Periprocedural antithrombotic strategies in acute ischemic stroke interventional therapy.** *Neurology* 2012;79(13 suppl 1):S174–81 CrossRef Medline
- Janjua N, Alkawi A, Suri MF, et al. **Impact of arterial reocclusion and distal fragmentation during thrombolysis among patients with acute ischemic stroke.** *AJNR Am J Neuroradiol* 2008;29:253–58 CrossRef Medline
- Yousuf O, Bhatt DL. **The evolution of antiplatelet therapy in cardiovascular disease.** *Nat Rev Cardiol* 2011;8:547–59 CrossRef Medline

Suspected Metallic Embolism following Endovascular Treatment of Intracranial Aneurysms

R. Yasuda, M. Maeda, M. Umino, Y. Nakatsuka, Y. Umeda, N. Toma, H. Sakaida, and H. Suzuki

ABSTRACT

SUMMARY: We describe a case series of suspected metallic embolism after coil embolization for intracranial aneurysms. Between January 2012 and December 2014, 110 intracranial aneurysms had been treated by coil embolization in our institution. In 6 cases, the postprocedural MR imaging revealed abnormal spotty lesions not detected on the preprocedural MR imaging. The lesions were also undetectable on the postprocedural CT scan. They were demonstrated as low-intensity spots on T1WI, T2WI, DWI, and T2*-weighted imaging. On DWI, they were accompanied by bright “halo,” and on T2*-weighted imaging, they showed a “blooming” effect. In 3 of the 6 cases, follow-up MR imaging was available and all the lesions remained and demonstrated no signal changes. Although histologic examination had not been performed, these neuroradiologic findings strongly supported the lesions being from metallic fragments. No specific responsible device was detected after reviewing all the devices used for the neuroendovascular treatment in the 6 cases.

Clinically asymptomatic emboli are a common complication of cerebral angiography and neuroendovascular procedures, occurring in approximately 20% of cases.¹ Foreign body emboli after cerebral angiography are a much less known complication, and only a few isolated cases have been reported.^{2–4} Recently, we have noticed abnormal signals suggesting metallic emboli on the postprocedural MR imaging in several cases of coil embolization for cerebral aneurysms. In this report, we describe the particular MR imaging findings of suspected metallic emboli following neuroendovascular procedures and discuss possible sources for these findings.

Case Series

After the retrospective review of our medical data base between January 2012 and December 2014 that contains 110 intracranial aneurysms treated by coil embolization, we encountered 6 cases that showed abnormal spotty lesions on the postprocedural MR imaging. The details of the clinical features of the 6 cases are summarized in Table 1. The devices used for the treatment in the 6 cases are summarized in Table 2. In all 6 cases, the lesions were low

intensity on T1WI, T2WI, DWI, and T2*-weighted images. Additionally, they were accompanied by a hyperintense “halo” on DWI and showed a “blooming” effect on T2*-weighted images. In 5 of the 6 cases (cases 1–5), a postprocedural CT scan was obtained but none of the lesions were detected. Follow-up MR images were available in 3 of the 6 cases (cases 1, 5, and 6), and in all 3 cases, the lesions remained without any signal changes during the follow-up periods (range, 6–34 months). No patients showed any symptoms associated with the lesions.

Illustrative Cases

Case 1. A 68-year-old woman was treated for a left ICA aneurysm (Fig 1A) with coil embolization. On the preprocedural MR imaging, no abnormal findings apart the aneurysm were identified. For the coil embolization procedure, a 5F guiding sheath was placed in the left ICA and a 1.7F microcatheter was inserted into the aneurysm by using a 0.014-inch microguidewire. The aneurysm was embolized with multiple platinum coils (Fig 1B). The MR images were obtained the next day by using a 1.5T MR imaging unit (Achieva Nova Dual; Philips Healthcare, Best, the Netherlands) with a 5-mm section thickness, and DWI revealed low-intensity spots accompanied by a hyperintense halo at the left medial frontal and left parietal regions (Fig 1C, -D). These signals were obviously different from the bright lesion in the left parietal lobe indicating thromboembolism (Fig 1E) that showed no signal changes on T2*-weighted images.

While these lesions were shown as low-intensity spots on T1WI (Fig 1F) and T2WI (Fig 1G), they had a blooming effect on

Received December 27, 2015; accepted after revision March 3, 2016.

From the Departments of Neurosurgery (R.Y., Y.N., Y.U., N.T., H.Sakaida, H.Suzuki) and Radiology (M.U., M.M.), Mie University Graduate School of Medicine, Tsu, Mie, Japan.

Paper previously presented, in part, at: 44th Annual Meeting of the Chubu Society of Neuroendovascular Therapy, August 8, 2015; Fukui, Japan.

Please address correspondence to Ryuta Yasuda, MD, 2-174 Edobashi, Tsu, Mie, Japan 513-8507; e-mail: yasudar1@gmail.com

<http://dx.doi.org/10.3174/ajnr.A4804>

Table 1: Patient characteristics

Case No.	Patient Age (yr)/Sex	Location of Aneurysm	Aneurysm Size (mm)	Procedure	Procedural Time (min)	Postprocedural Symptoms
1	68/F	Left ICA	10.2 × 8.2 × 7.3	Coil embolization	170	None
2	56/M	Right vertebral artery	15.6 × 7.1 × 6.5	Internal trapping	135	None
3	80/F	Right ICA	12.6 × 10.3 × 11.0	Coil embolization	150	None
4	45/F	Right ICA	4.9 × 4.5 × 4.3	Coil embolization	158	None
5	70/M	Anterior communicating artery	9.6 × 7.1 × 9.5	Coil embolization	145	None
6	41/F	Left ICA	5.6 × 4.9 × 3.8	Coil embolization	150	None

Table 2: Devices used for treatment in each case

Devices	1	2	3	4	5	6
0.035-inch Radifocus Standard ^a	○	○	○	○	○	○
0.035-inch Radifocus Stiff ^a			○			
0.035-inch Quick Flex Standard ^b					○	
0.010–0.014-inch Tenrou ^b	○	○	○	○		○
0.014-inch CHIKAI ^c		○	○		○	○
0.010-inch X-Pedion ^d					○	
0.010-inch SilverSpeed ^d				○		
0.014-inch Traxcess ^e						○
Excelsior SL-10 ^f	○	○	○	○	○	
Headway17 ^e				○		○
Prowler Select Plus ^g				○		
Hydrogel coils ^e	○				○	
ED coils ^b	○	○	○		○	
Target coils ^f	○	○				○
Cashmere ^g		○				
VFC ^e		○				
Orbit Galaxy ^g		○		○	○	
Deltapaq ^g		○				
Deltaplus ^g		○				
Matrix coils ^f					○	
Scepter XC ^e			○			○
HyperForm ^d					○	
Enterprise VRD ^g				○		
Amplatz GooseNeck Snare ^d					○	

Note:—○ indicates that the product was used.

^a Terumo, Tokyo, Japan.

^b Kaneka Medix, Osaka, Japan.

^c Asahi Intecc, Aichi, Japan.

^d Covidien, Irvine, California.

^e MicroVention, Tustin, California.

^f Stryker, Kalamazoo, Michigan.

^g Codman & Shurtleff, Raynham, Massachusetts.

T2*-weighted images (Fig 1H). Head CT (Aquilion ONE CT scanner; Toshiba Medical Systems, Tokyo, Japan) obtained on the following day demonstrated no abnormal findings except a coil mass. The patient was discharged from our hospital 1 week after the coil embolization without any symptoms. Follow-up MR imaging was performed at 13 months after the procedure, and both abnormal spots remained without any signal changes (Fig 1I, -L). The patient remained asymptomatic at the last follow-up.

Case 5. A 70-year-old man was referred to our hospital for treatment of his unruptured anterior communicating artery aneurysm (Fig 2A). Preprocedural MR imaging showed no abnormal findings apart from the aneurysm. The coil embolization was performed; a 6F guiding catheter was placed in his left ICA. After a balloon catheter was placed underneath the aneurysmal neck by using a 0.01-inch microguidewire, a 1.7F microcatheter was placed in the aneurysm by using another 0.014-inch microguidewire. During the embolization, the first coil uncoiled, and it was withdrawn by using a retrieval device. Because the hub of the

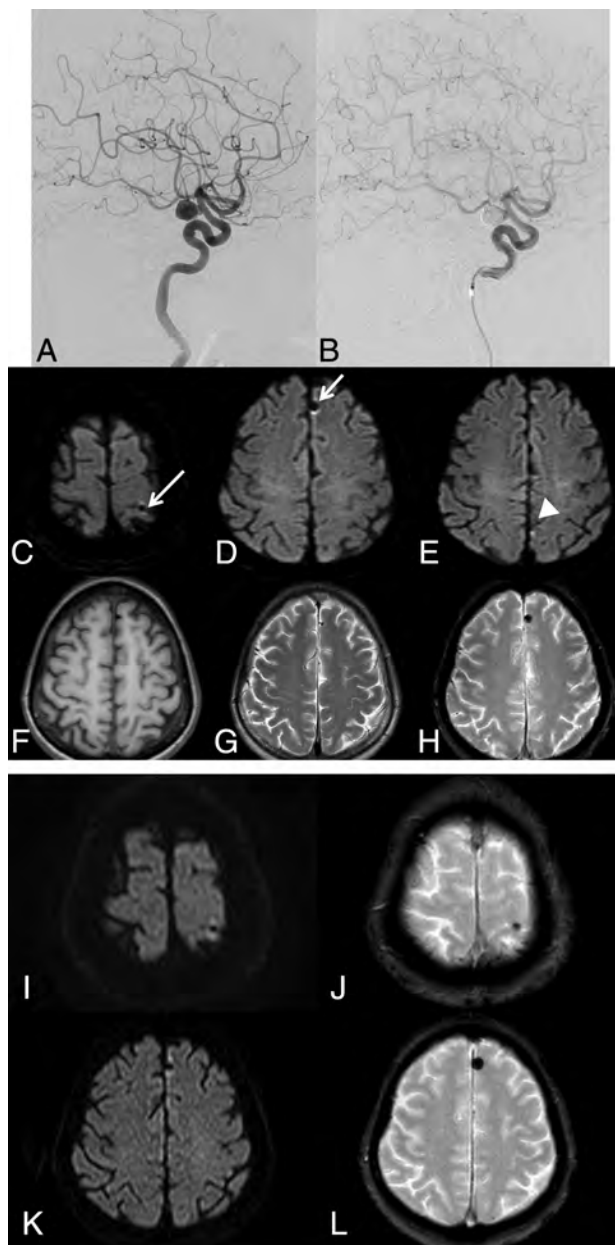


FIG 1. A left ICA aneurysm in case 1 (A) is embolized by using multiple coils (B). Postprocedural DWI shows abnormal low-intensity spots with a hyperintense halo (white arrow) in the left parietal (C) and frontal (D) lobes. These are different from a bright spot in the left parietal lobe (E), indicating thromboembolism. These abnormal spots are low intensity on T1WI (F) and T2WI (G) and show a blooming effect on T2*-weighted images (H). Follow-up MR imaging obtained 13 months after the procedure shows that all the abnormal signal spots remain without any signal changes (I–L).

microcatheter had to be cut to advance the retrieval device, another 1.7F microcatheter was used for the embolization. The aneurysm was finally embolized by using multiple platinum coils (Fig 2B). The MR imaging performed on postoperative day 1 by using a 1.5T machine (Achieva Nova Dual; Philips) with 5-mm section thickness demonstrated a low-intensity spot with a hyperintense halo on DWI in the right frontal lobe (Fig 2C). A head CT scan (Aquilion ONE; Toshiba) with 5-mm section thickness obtained on postoperative day 3 showed no abnormal findings except a coil mass (Fig 2D). The patient's postoperative course was good, and he was discharged from our hospital 1 week after the procedure without any symptoms. Follow-up MR imaging obtained 3 years after the procedure demonstrated that the lesion remained at the right frontal lobe without any signal changes (Fig 2E, -F). The patient remained asymptomatic at the last follow-up.

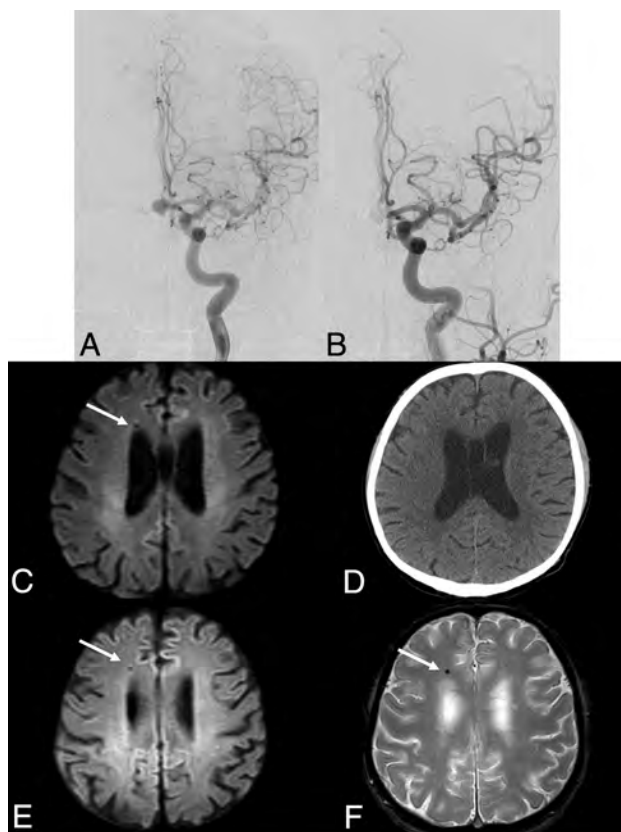


FIG 2. An anterior communicating artery aneurysm in case 5 (A) is embolized by using multiple coils (B). Postprocedural DWI shows an abnormal low-intensity spot with a hyperintense halo (white arrow) in the right frontal lobe (C), which is undetectable on the postprocedural CT (D). Follow-up MR imaging obtained 3 years after the procedure shows that the lesion remains without any signal changes (E and F).

DISCUSSION

Because the new low-signal spotty lesions appeared just after the endovascular procedure and they were restricted to the vascular territory of the catheterized arteries, it is reasonable to believe they represented embolic phenomena.

Potential etiologies of the low-signal spotty lesions include air, thrombus, hemosiderin, calcium deposits, and metal. If they were air or thrombus, resolution of signal changes would be expected with time. Moreover, parenchymal ischemic changes due to an embolism could occur. Hemosiderin is also unlikely because it does not appear at this early stage just after coil embolization. Furthermore, if the lesions were calcium, they might be detected by CT. Metal results in a dark spot on MR imaging because it has no MR imaging signal. Additionally, it can cause substantial MR imaging artifacts,⁵ which could exhibit the hyperintense halo. Because only microscopic metal fragments are required to produce MR imaging artifacts,⁶ it is not surprising that the metal fragments were invisible on CT. Moreover, if microscopic metal fragments were present, it would be reasonable that patients had no embolic complications. Taking these observations into consideration, we believe that the spotty lesions found on the postoperative MR imaging in our cases were from metallic fragments.

Cerebral MR imaging findings suggesting embolic metal fragments are rare, and only 4 cases have been reported (Table 3).⁷⁻¹⁰ In addition to a mechanical prosthetic cardiac valve and robotic surgery, angiographic guidewires used during cardiac catheterization were suspected as an embolic source in 2 cases.^{9, 10} To the best of our knowledge, this cases series is the first in reporting MR imaging metallic signal following neuroendovascular treatment of intracranial aneurysms. Besides the guidewires, various devices (ie, coils, balloons, and stents) composed of metal are used in neuroendovascular procedures, which can provide more frequent opportunities for metallic embolism compared with cardiac catheterization.

Our study has several limitations. First and most important, it was not pathologically confirmed that the lesion represented metallic emboli. Because our patients were completely free from symptoms, it was not reasonable to perform a brain biopsy. Second, we cannot determine which devices and which parts could be a source of metallic emboli in our cases. In neuroendovascular treatment, metallic emboli can be released at any step, including delivery; deployment or withdrawal of the devices; friction between the devices; and detachment of the coils. Coil uncoiling and withdrawal of the uncoiled coil were likely responsible for metallic emboli in case 5. However, in the remainder of cases, coil embolization was completed uneventfully. Although MR imaging susceptibility artifacts vary depending on metals,¹¹ these were not metal-specific and there is no way to differentiate various metals on MR imaging. We have reviewed all the devices used during

Table 3: Past cases of suspected metallic embolism

Author	Patient/Sex	T2WI/Proton	T2*-Weighted Image	CT	Suspected Etiology	Symptom
Wingerchuk et al ⁷	35/F	Low intensity halo	Low intensity blooming	Normal	Prosthetic cardiac valve	None
Naumann et al ⁸	66/M	Low intensity halo	Not available	Not available	Prosthetic cardiac valve	Seizure
Jassal et al ⁹	55/M	Low intensity halo	Not available	Normal	Coronary guidewire	Headache
Roshal et al ¹⁰	55/F	Low intensity	Low intensity blooming, halo	Normal	Coronary guidewire, robotic surgery	Headache

endovascular treatment in these cases (Table 3). No specific devices except one 0.035-inch guidewire (0.035-inch Radifocus Standard; Terumo, Tokyo, Japan) were used in all cases. It is unlikely, however, that the 0.035-inch guidewire is responsible because we have routinely used the guidewire in all endovascular procedures, including diagnostic angiography. Devices for intracranial use seem more likely than the 0.035-inch guidewire. Further investigations should be done in the near future.

Finally, the exact incidence of the abnormal MR imaging signals was unclear. Our retrospective review included 110 coiling procedures for aneurysm treatment. Although periprocedural MR imaging was available in almost all cases, many cases lacked pre- and/or postoperative DWI, T2*-weighted images, or SWI, and only 29 cases had adequate imaging. Prospective registration with a specific perioperative MR imaging protocol is ongoing.

CONCLUSIONS

This is the first report on the brain MR imaging findings suggesting that metallic emboli were found after coil embolization of cerebral aneurysms, to our knowledge. Particular DWI and T2*-weighted imaging findings of low intensity accompanied by a hyperintense halo should be kept in mind for patients undergoing coil embolization.

REFERENCES

1. Bendszus M, Koltzenburg M, Burger R, et al. **Silent embolism in diagnostic cerebral angiography and neurointerventional procedures: a prospective study.** *Lancet* 1999;354:1594–97 CrossRef Medline
2. Mehta RI, Mehta RI, Solis OE, et al. **Hydrophilic polymer emboli: an under-recognized iatrogenic cause of ischemia and infarct.** *Mod Pathol* 2010;23:921–30 CrossRef Medline
3. Cruz JP, Marotta T, O’Kelly C, et al. **Enhancing brain lesions after endovascular treatment of aneurysms.** *AJNR Am J Neuroradiol* 2014;35:1954–58 CrossRef Medline
4. Minks D, Briley D, Schulz U, et al. **Suspected cerebral foreign body granuloma following endovascular treatment of intracranial aneurysm: imaging features.** *Neuroradiology* 2015;57:71–73 CrossRef Medline
5. Hargreaves BA, Worters PW, Pauly KB, et al. **Metal-induced artifacts in MRI.** *AJR Am J Roentgenol* 2011;197:547–55 CrossRef Medline
6. Alanen A, Bondenstam S, Komu M. **Artifacts in MR imaging caused by small quantities of powdered iron.** *Acta Radiol* 1995;36:92–95 Medline
7. Wingerchuk DM, Krecke KN, Fulgham JR. **Multifocal brain MRI artifacts secondary to embolic metal fragments.** *Neurology* 1997;49:1451–53 CrossRef Medline
8. Naumann M, Hofmann E, Toyka KV. **Multifocal brain MRI hypointensities secondary to embolic metal fragments from a mechanical heart valve prosthesis: a possible source of epileptic seizures.** *Neurology* 1998;51:1766–67 CrossRef Medline
9. Jassal DS, Fast MD, McGinn G. **Multifocal brain MRI hypointensities secondary to cardiac catheterization.** *Neurology* 2000;54:2023–24 CrossRef Medline
10. Roshal D, Snapp M, Friedman DP, et al. **Iatrogenic brain and cervical cord magnetic resonance imaging susceptibility artifacts from metallic microemboli.** *Arch Neurol* 2011;68:132–33 CrossRef Medline
11. Matsuura H, Inoue T, Konno H, et al. **Quantification of susceptibility artifacts produced on high-field magnetic resonance images by various biomaterials used for neurosurgical implants: technical note.** *J Neurosurg* 2002;97:1472–75 CrossRef Medline

Endovascular Coiling of Wide-Neck and Wide-Neck Bifurcation Aneurysms: A Systematic Review and Meta-Analysis

 B. Zhao,  R. Yin,  G. Lanzino,  D.F. Kallmes,  H.J. Cloft, and  W. Brinjikji



ABSTRACT

BACKGROUND AND PURPOSE: We present the results of a systematic review and meta-analysis examining outcomes of endovascular coiling of wide-neck and wide-neck bifurcation aneurysms with and without stent assistance. The aim of our study was to assess angiographic and clinical outcomes.

MATERIALS AND METHODS: We performed a comprehensive literature search for all articles on the endovascular coiling of wide-neck and wide-neck bifurcation aneurysms. Studies meeting our inclusion criteria and abstracted data were selected by 2 independent reviewers. Primary outcomes were >6-month complete or near-complete angiographic occlusion, aneurysm recanalization, and aneurysm retreatment. Secondary outcomes included initial complete or near-complete occlusion, long-term good neurologic outcome, procedure-related morbidity, and procedure-related mortality. Data were analyzed by using random-effects meta-analysis.

RESULTS: In total, 38 studies including 2446 patients with 2556 aneurysms were included. For all wide-neck aneurysms, immediate complete or near-complete occlusion rate was 57.4% (95% CI, 48.1%–66.8%). Follow-up near-complete occlusion rate was 74.5% (95% CI, 68.0%–81.0%). Recanalization and retreatment rates were 9.4% (95% CI, 7.1%–11.7%) and 5.8% (95% CI, 4.1%–7.5%), respectively. Long-term good neurologic outcome was 91.4% (95% CI, 88.5%–94.2%). For wide-neck bifurcation aneurysms, initial complete or near-complete occlusion rate was 60.0% (95% CI, 42.7%–77.3%), long-term complete or near-complete occlusion rate was 71.9% (95% CI, 52.6%–91.1%), and the recanalization and retreatment rates were 9.8% (95% CI, 7.1%–12.5%) and 5.2% (95% CI, 1.9%–8.4%), respectively.

CONCLUSIONS: Our study of angiographic and clinical outcomes for patients with wide-neck aneurysms demonstrates that endovascular coiling with or without stent-assisted coiling is safe, with low rates of perioperative morbidity and mortality. Initial and long-term angiographic outcomes were generally satisfactory, but not ideal. These data provide some baseline comparisons against which emergent technologies can be assessed.

With the advent of stent-assisted and balloon-assisted coiling, wide-neck and wide-neck bifurcation intracranial aneurysms are increasingly treated with endovascular techniques to prevent hemorrhage or recurrent bleeding. Both stent-assisted and balloon-assisted coiling have been shown to be safe and effective in the treatment of these aneurysms by allowing for increased packing density and lower rates of parent artery occlusion compared with conventional coiling

alone.^{1–5} Even in the era of endoluminal and intrasaccular flow diverters, many wide-neck and wide-neck bifurcation aneurysms will continue to be treated with conventional coiling, particularly with stent assistance.^{6–8}

We present the results of a systematic review and meta-analysis examining outcomes of endovascular coiling of wide-neck and wide-neck bifurcation aneurysms with and without stent-assisted coiling. The aim of our study was to assess both angiographic and clinical outcomes in order to provide overall data against which current and future emergent techniques can be compared.

MATERIALS AND METHODS


Literature Search

A comprehensive literature search of the PubMed, Ovid MEDLINE, and Ovid EMBASE data bases was designed and conducted by an experienced librarian with input from the authors. The keywords

Received October 22, 2015; accepted after revision March 1, 2016.

From the Departments of Neurosurgery (B.Z., G.L.) and Radiology (D.F.K., H.J.C., W.B.), Mayo Clinic, Rochester, Minnesota; and Department of Neurology (R.Y.), The General Hospital of Lanzhou Military Command, Lanzhou, China.

Please address correspondence to Waleed Brinjikji, MD, Mayo Clinic, Department of Radiology, 200 First St SW, Rochester, MN 55905; e-mail: brinjikji.waleed@mayo.edu; @wbrinjikji

 Indicates article with supplemental on-line table.

<http://dx.doi.org/10.3174/ajnr.A4834>

intracranial aneurysm, cerebral aneurysm, aneurysm, wide-neck, bifurcation, complex, stent, balloon, endovascular, coiling, and coils were used in both “AND” and “OR” combinations. The search was limited to articles published from 1992 to week 18 of 2015 and is summarized in the On-line Table. All studies reporting patients with wide-neck or wide-neck bifurcation aneurysms treated with endovascular coiling with or without stent assistance were included. We used the following inclusion criteria: 1) English language, 2) study reporting a consecutive series of wide-neck and/or wide-neck bifurcation aneurysms treated with coiling, 3) series of at least 10 patients reporting angiographic and/or clinical outcomes, and 4) at least 6 months of angiographic follow-up. Review articles, comments, guidelines, technical notes, and editorials were excluded. The included studies were selected by 2 of the authors (B.Z., R.Y.), both with at least 1 year of experience in meta-analysis. Differences were resolved by a senior author (W.B.) with 5 years of experience in meta-analysis. Patients receiving endovascular treatment with flow diverters and intrasaccular flow diverters such as the Woven EndoBridge (WEB) aneurysm embolization system (Sequent Medical, Aliso Viejo, California) were excluded.

Outcomes and Data Extraction

For each study, we extracted the following baseline information: number of patients, aneurysm rupture status, sex, mean age, number of aneurysms treated, mean aneurysm size, mean aneurysm neck size, definition of wide neck, clinical outcome score used, length of clinical follow-up, and length of angiographic follow-up.

The primary outcomes of this study were >6-month follow-up, complete or near-complete angiographic occlusion, aneurysm recanalization, and aneurysm retreatment. Complete occlusion was defined as 100% occlusion or absence of angiographic filling in aneurysm neck or sac. Near-complete occlusion was defined as either 90%–99% occlusion or small residual neck filling without any filling of the sac.

Secondary outcomes included initial complete or near-complete occlusion, long-term good neurologic outcome, procedure-related morbidity, and procedure-related mortality. Good neurologic outcome was defined as an mRS score of 0–2 or Glasgow Outcome Score of 4–5 (good recovery, moderate disability). In cases where these scores were not available, good neurologic outcome was determined if the study used terms such as “no morbidity,” “good recovery,” or “moderate disability.”

In addition to studying overall outcomes of patients with wide-neck aneurysms receiving endovascular coiling, we performed 3 subgroup analyses including patients treated with non-stent-assisted coiling (ie, with or without balloon remodeling), patients treated with stent-assisted coiling, and patients with wide-neck bifurcation aneurysms. Outcomes of ruptured and unruptured aneurysms could not be separated because most studies did not stratify outcomes by rupture status.

Study Risk of Bias

We modified the New Castle Ottawa Quality Assessment Scale for Case Control Studies to assess the risk of bias of the studies included in this meta-analysis. This tool is designed for use in com-

parative studies; however, because none of the included studies were controlled, we assessed study risk of bias based on selected items from the tool focusing on the following questions: 1) Did the study include all patients or consecutive patients versus a selected sample?; 2) Was the study retrospective or prospective?; 3) Was angiographic and clinical follow-up satisfactory, thus allowing for ascertainment of all outcomes?; 4) Were outcomes clearly reported?; and 5) Were the interventionalists treating the patients the same as those who assessed angiographic and clinical outcomes?

Statistical Analysis

We estimated from each cohort the cumulative incidence (event rate) and 95% CI for each outcome. Event rates for each intervention were pooled in a meta-analysis across studies by using the random-effects model.⁹ Anticipating heterogeneity between studies, we chose this model a priori because it incorporates within-study variance and between-study variance. Heterogeneity of treatment effect across studies was evaluated by using the I^2 statistic, in which $I^2 > 50\%$ suggests substantial heterogeneity.¹⁰ A χ^2 analysis was used to compare outcomes between the stent-assisted and non-stent-assisted coiling groups. Statistical analysis was performed by using the software program OpenMeta[Analyst] (<http://www.ccbm.brown.edu/openmeta/>).

RESULTS

Study Selection and Characteristics

The initial literature search yielded 900 articles. Upon review of the abstracts and titles, 649 articles were excluded. We selected 239 articles for full-text screening. After screening, we excluded 213 articles, most of which were excluded because they did not separate outcomes of wide-neck versus narrow-neck aneurysms or had insufficient data. In total, we included 38 articles including 2446 patients with 2556 aneurysms. Of these, 656 patients had ruptured aneurysms and 1793 patients had unruptured aneurysms; in 107 aneurysms, the rupture status was not known. Among all aneurysms in the study, 496 were wide-neck bifurcation aneurysms. Regarding interventions, 376 were treated with coiling alone and 2090 were treated with stent-assisted coiling.

Of the 38 studies, 4 had a low risk of bias, 11 had a high risk of bias, and 23 had a medium risk of bias. The most commonly used definition for wide-neck aneurysm was a neck size of ≥ 4 mm and/or a dome-to-neck ratio of ≤ 2 (17 studies). In 5 studies, wide-neck aneurysms were defined as those with a neck size of ≥ 4 mm and/or a dome-to-neck ratio of ≤ 1.5 . All included studies had at least 6 months of angiographic follow-up. The smallest study had 10 patients with 10 aneurysms, and the largest study had 468 patients with 500 aneurysms. A summary of included studies is provided in the On-line Table. The flow chart for study selection is provided in Fig 1.

Angiographic Outcomes

Overall, the rate of initial complete or near-complete occlusion was 57.4% (95% CI, 48.1%–66.8%) (Fig 2). Follow-up complete occlusion rates were 74.5% (95% CI, 68.0%–81.0%) overall, 80.1% (95% CI, 70.9%–89.2%) for coiling alone, and 73.0% (95% CI, 65.1%–81.0%) for stent-assisted coiling ($P = .38$).

(Fig 3). Wide-neck bifurcation aneurysms had long-term complete occlusion rates of 71.9% (95% CI, 52.6%–91.1%).

Aneurysm recanalization rates were 9.4% (95% CI, 7.1%–

11.7%) overall, 10.3% (95% CI, 4.3%–16.4%) for coiling alone, 9.2% (95% CI, 6.7%–11.7%) for stent-assisted coiling, and 9.8% (95% CI, 7.1%–12.5%) for wide-neck bifurcation aneurysms ($P = .17$). Aneurysm retreatment rates were 5.8% (95% CI, 4.1%–7.5%) overall, 5.5% (95% CI, 1.7%–9.2%) for coiling alone, 5.7% (95% CI, 3.8%–7.7%) for stent-assisted coiling, and 5.2% (95% CI, 1.9%–8.4%) for wide-neck bifurcation aneurysms ($P = .47$).

Clinical Outcomes

Overall procedure-related permanent morbidity rate for coiling with and without stent-assistance was 2.6% (95% CI, 1.7%–3.4%). Stent-coil procedure-related permanent morbidity rate was 1.9% (95% CI, 0.0%–3.7%), and wide-neck bifurcation procedure-related permanent morbidity rate was 4.4% (95% CI, 1.9%–7.0%). Procedure-related mortality rate was 1.0% (95% CI, 0.6%–1.5%).

The overall rate of good neurologic outcome for coiling with and without stent assistance was 91.4% (95% CI, 88.5%–94.2%). Stent-coil long-term good neurologic outcome rate was 89.0%

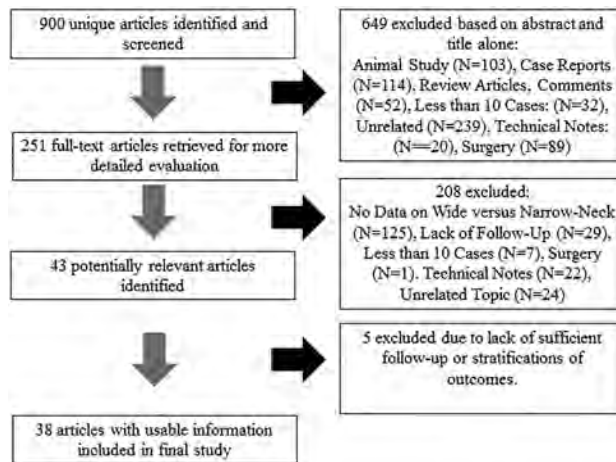


FIG 1. Flow chart of literature search.

Studies	Estimate (95% C.I.)	Ev/Tot
Moret, et al, Interventional Neuroradiology, 1997	0.710 (0.350, 0.869)	22/31
Nakahara, et al, Interventional Neuroradiology, 2000	0.643 (0.392, 0.894)	9/14
Nelson, et al, ANJR, 2001	0.750 (0.560, 0.940)	15/20
Ihn, et al, Acta Neurochirurgica, 2006	0.929 (0.738, 1.000)	6/6
Mu, et al, Chinese Medical Journal, 2008	0.900 (0.807, 0.993)	36/40
Lee, et al, AJNR, 2011	0.912 (0.839, 0.986)	52/57
Ko, et al, Clinical Neurology & Neurosurgery, 2015	0.969 (0.883, 1.000)	15/15
Sani, et al, Neurosurgical Focus, 2005	0.900 (0.714, 1.000)	9/10
Binodi, et al, Neurosurgery, 2007	0.567 (0.389, 0.744)	17/30
Yavuz, et al, JNS, 2007	0.944 (0.839, 1.000)	17/18
De Keukeleire, et al, AJNR, 2008	0.500 (0.154, 0.846)	4/8
Peluso, et al, AJNR, 2008	0.571 (0.312, 0.831)	8/14
Huang, et al, AJNR, 2009	0.917 (0.760, 1.000)	11/12
Gao, et al, Neurological research, 2011	0.855 (0.801, 0.910)	136/159
Maldonado, et al, AJNR, 2011	0.647 (0.533, 0.761)	44/68
Spiotta, et al, 2011, Neurosurgery, 2011	0.632 (0.415, 0.848)	12/19
Lee, et al, Journal of Korean Neurosurgery, 2012	0.958 (0.845, 1.000)	11/11
Liu, et al, Interventional Neuroradiology, 2012	0.556 (0.231, 0.880)	5/9
Mangubat, et al, Neurointervention, 2012	0.667 (0.449, 0.884)	12/18
Wakhloo, et al, AJNR, 2012	0.650 (0.565, 0.735)	78/120
Zhao, et al, AJNR, 2012	0.818 (0.590, 1.000)	9/11
Chalouhi, et al, AJNR, 2013	0.500 (0.327, 0.673)	16/32
Chalouhi, et al, AJNR, 2013 2	0.754 (0.652, 0.855)	52/69
Cho, et al, AJNR, 2013	0.704 (0.531, 0.876)	19/27
Geyik, et al, AJNR, 2013	0.983 (0.971, 0.995)	459/467
Yavuz, et al, AJNR, 2013	0.247 (0.185, 0.309)	46/186
Aguilar-Perez, et al, AJNR, 2014	0.591 (0.385, 0.796)	13/22
Bartolini, et al, AJNR, 2014	0.859 (0.785, 0.933)	73/85
Gory, et al, Neurosurgery, 2014	0.600 (0.471, 0.729)	33/55
Jeon, et al, Acta Neurochirurgica, 2014	0.810 (0.642, 0.977)	17/21
Wu, et al, Journal of Turkish Neurosurgery, 2014	0.742 (0.651, 0.833)	66/89
Wu, et al, Journal of Turkish Neurosurgery, 2014 2	0.755 (0.635, 0.876)	37/49
Zhang, et al, Journal of Clinical Neuroscience, 2014	0.625 (0.388, 0.862)	10/16
Fiorella, et al, J Neurointerv Surg, 2015	0.750 (0.590, 0.910)	21/28
Poncyfus, et al, J Neurointerv Surg, 2015	0.821 (0.735, 0.906)	64/78
Katsaris, et al, Am J Neuroradiol, 2006	0.985 (0.943, 1.000)	32/32
Lee, et al, Interv Neuroradiol, 2007	0.469 (0.296, 0.642)	15/32
Kim, et al, Interv Neuroradiol, 2008	0.740 (0.642, 0.838)	57/77
Lubicz, et al, Neuroradiology, 2009	0.794 (0.658, 0.930)	27/34
Sedat, et al, Neuroradiology, 2009	0.711 (0.566, 0.855)	27/38
Overall (I²=95.48 %, P< 0.001)	0.745 (0.680, 0.810)	1612/2127

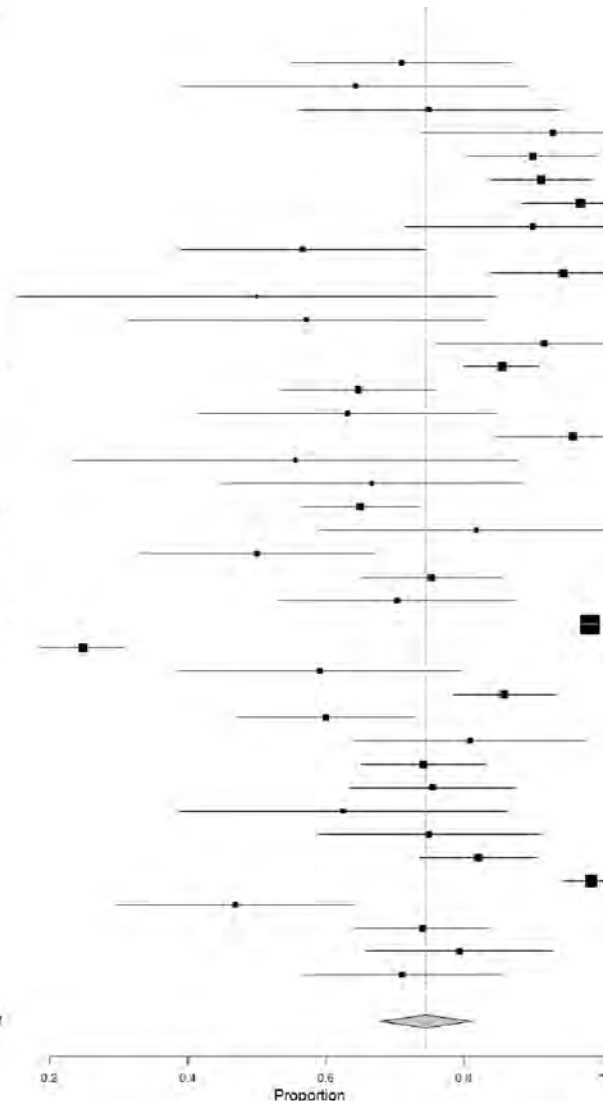


FIG 2. Forest plot for long-term complete or near-complete angiographic occlusion rates.

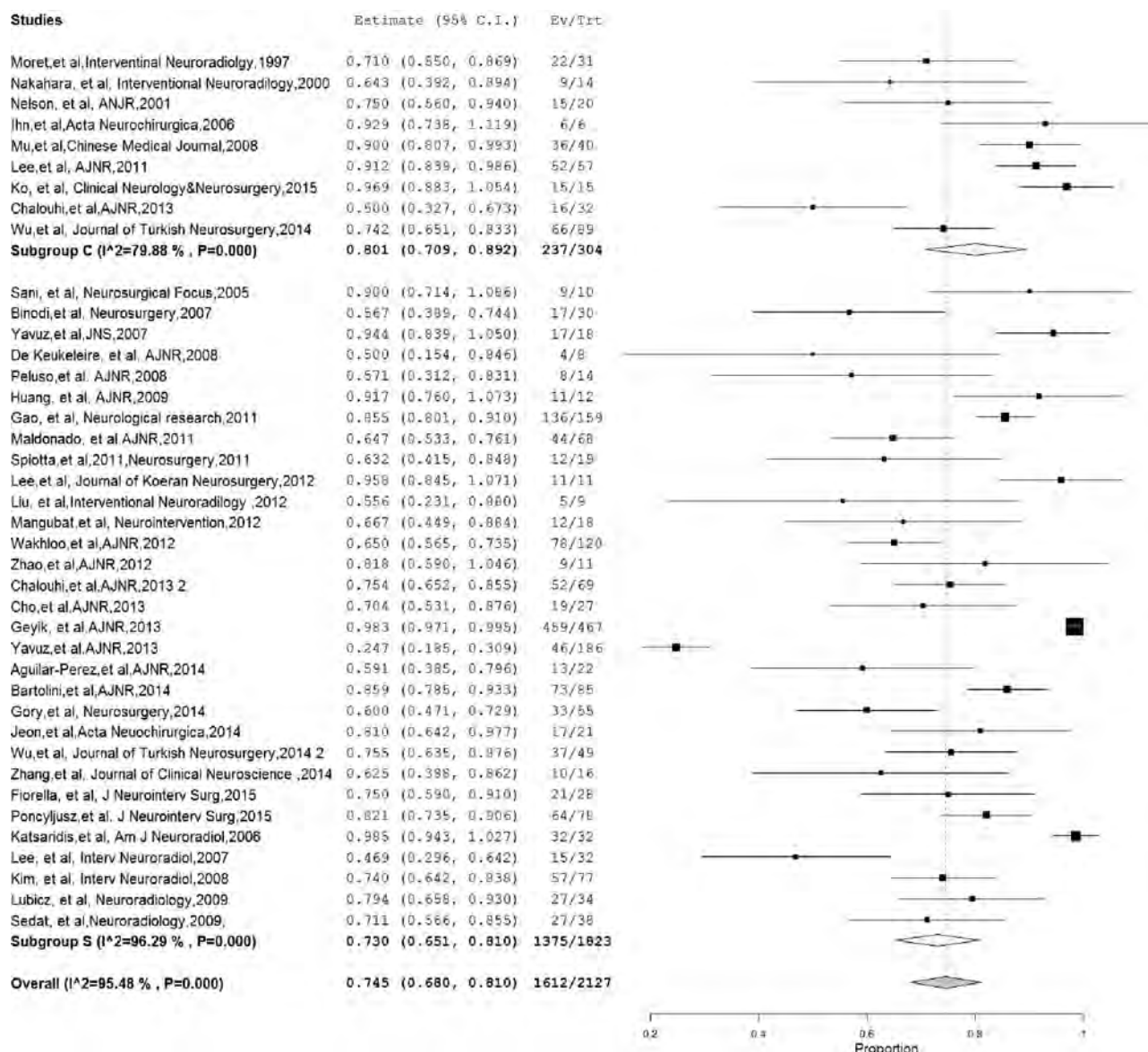


FIG 3. Forest plot for long-term complete or near-complete angiographic occlusion by treatment type.

Results of meta-analysis

	Coil Without				Wide-Neck Bifurcation			
	All	I ² (%)	Stent-Assistance	I ² (%)	Stent-Coil	I ² (%)	P	
Initial complete or near-complete occlusion	57.4 (48.1–66.8)	97	68.0 (54.3–81.6)	90	54.4 (43.0–66.8)	98	.01	60.0 (42.7–77.3)
Long-term complete or near-complete occlusion	74.5 (68.0–81.0)	95	80.1 (70.9–89.2)	80	73.0 (65.1–81.0)	96	.38	71.9 (52.6–91.1)
Aneurysm recanalization	9.4 (7.1–11.7)	67	10.3 (4.3–16.4)	59	9.2 (6.7–11.7)	69	.17	9.8 (7.1–12.5)
Retreatment	5.8 (4.1–7.5)	55	5.5 (1.7–9.2)	40	5.7 (3.8–7.7)	58	.47	5.2 (1.9–8.4)
Long-term good neurologic outcome	91.4 (88.5–94.2)	75	89.0 (82.0–96.1)	57	91.8 (88.6–95.1)	78	.53	86.3 (78.1–93.4)
Procedure-related morbidity	2.6 (1.7–3.4)	26	1.9 (0.0–3.7)	0	2.8 (1.7–3.8)	37	.33	4.4 (1.9–7.0)
Procedure-related mortality	1.0 (0.6–1.5)	0	1.1 (0.0–2.3)	0	1.0 (0.6–1.5)	0	.92	0.9 (0.1–1.8)

(95% CI, 82.0%–96.1%), and the rate of good neurologic outcome for wide-neck bifurcation aneurysms was 86.3% (95% CI, 78.1%–93.4%). These data are summarized in the Table.

Heterogeneity

Heterogeneity of treatment effect across studies was evaluated by using the I^2 statistic, in which $I^2 > 50\%$ suggests substantial

heterogeneity.¹⁰ There was no substantial heterogeneity for procedure-related morbidity and mortality for any of the groups. There was substantial heterogeneity for initial and long-term angiographic outcomes, long-term good neurologic outcome, and aneurysm recanalization rates for all study groups. I^2 values were approximately 50% for retreatment for all groups.

DISCUSSION

Our meta-analysis including 38 studies and over 2000 patients with wide-neck aneurysms treated with coiling and stent-assisted coiling demonstrated that though these techniques are generally safe, initial and long-term complete and near complete occlusion rates are not ideal. Overall, approximately 75% of aneurysms had complete or near-complete occlusion at last angiographic follow-up, and approximately 6% of aneurysms were retreated. Wide-neck aneurysms located at bifurcation points such as the MCA and basilar artery had complete occlusion rates of 72% and retreatment rates of approximately 5%. These findings are important because they suggest that the continued development of newer devices and techniques aimed at treating these complex lesions is needed to improve angiographic outcomes.

In general, treatment of wide-neck and wide-neck bifurcation aneurysms by using endovascular techniques is challenging. Embolization of these aneurysms without the use of adjunctive devices is difficult because of instability of the coil mass leading to the risk of coil protrusion into the parent artery. The risk of coil protrusion often makes attenuated packing of the aneurysm difficult or impossible to achieve, which can lead to lower rates of complete occlusion.¹¹ Neurovascular stents act as a scaffold to prevent coil protrusion into the parent artery. Over the past 2 decades, a number of improvements to flexibility and delivery have been made to neurovascular stents, and as a result, these devices are increasingly used in the treatment of complex intracranial aneurysms.^{11,12} A recently published systematic review of stent-assisted coiling of wide-neck aneurysms including 702 aneurysms treated through 2011 demonstrated initial and long-term complete occlusion rates of 46% and 72%, respectively, and recanalization rates of 13%.¹¹ However, improvements in the design of neurovascular stents and the advent of newer neurovascular stents will likely result in improvements in angiographic outcomes for stent-assisted coiling of wide-neck aneurysms. In fact, a recently published multicenter registry on the use of the LVIS stent (MicroVention, Tustin, California) in treating wide-neck aneurysms found complete and near-complete occlusion rates of 82% and 6%, respectively.¹³

Flow diverters such as the Pipeline Embolization Device (Covidien, Irvine, California) and Silk Device (Balt Extrusion, Montmorency, France) are increasingly being used in the treatment of complex, wide-neck intracranial aneurysms, particularly aneurysms of the ICA. In the Pipeline for Uncoilable or Failed Aneurysms clinical trial including over 100 patients with large and giant wide-neck ICA aneurysms, the rate of complete angiographic occlusion at 12 months was 87%, with only 5.5% of patients having residual aneurysm.¹⁴ There was even improvement in angiographic results with time; more than 95% of patients had complete angiographic occlusion at 5 years.¹⁵ However, it is important to note that flow-diverter treatment of bifurcation aneurysms can be challenging and is associated with higher morbidity rates and lower occlusion rates than those reported for aneurysms of the ICA. In a study of 14 patients with MCA bifurcation aneurysms treated with flow diverters, Caroff et al¹⁶ found complete occlusion rates of 62% and procedure-related morbidity rates of over 20%. Gawlitza et al¹⁷ found occlusion rates of just 33% after treatment of

MCA and anterior communicating artery aneurysms with flow-diverter stents. The challenging factors for treating bifurcation aneurysms with flow diverters include the need to cover branch vessels and perforators with the flow-diverter stent and technical challenges with device delivery.

Over the past several years, intrasaccular flow diverters such as the Woven EndoBridge system have emerged as effective techniques for the treatment of wide-neck bifurcation aneurysms. These devices function by disrupting intra-aneurysmal flow and creating intra-aneurysmal thrombosis.¹⁸ The devices are designed to essentially plug the neck of the aneurysm sac and prevent inward blood flow. One advantage of the Woven EndoBridge device is the lack of a need for dual antiplatelet therapy, which is especially important in the setting of treating ruptured aneurysms. The Woven EndoBridge has been the subject of numerous clinical studies designed to investigate the efficacy of treating intracranial, wide-neck bifurcation aneurysms. Thus far, early small studies suggest that the Woven EndoBridge device is associated with higher angiographic occlusion rates than stent-assisted coiling in the treatment of wide-neck bifurcation aneurysms with similar low rates of procedure-related morbidity and mortality. In a study of 52 patients with 55 aneurysms, Behme et al¹⁹ found favorable angiographic outcomes in 75% of cases, with all patients experiencing good neurologic outcomes on long-term follow-up. In a multicenter study of 45 patients with 45 aneurysms, Lubicz et al²⁰ found complete or near complete occlusion in 90% of cases, with good long-term neurologic outcome rates of 93%. The WEB Clinical Assessment of IntraSaccular Aneurysm Therapy (WEBCAST) study, which examined outcomes for treatment of wide-neck bifurcation aneurysms in 51 patients, found complete and near-complete occlusion rates of 85% and procedure-related morbidity and mortality rates of 2% and 0%, respectively.²¹

Limitations

Although data in this meta-analysis were derived from a strictly defined patient population with at least 6 months of follow-up, our study has limitations. Almost all studies were retrospective case series; thus, our study undoubtedly suffers from selection bias. In our assessment of study risk of bias, most of the studies had a medium to high risk of bias. I^2 values were above 50% for most outcomes, indicating substantial heterogeneity. In addition, most studies did not have neurologic outcomes assessed by an independent physician, and these assessments were not blinded to the aneurysm treatment used. Publication bias is also possible because centers with better outcomes may have been more prone to report their results. We did not have access to individual patient data and, consequently, could not investigate the effect of important factors (including age, aneurysm size and location, medical comorbidities, etc) on angiographic and clinical outcomes. We were unable to stratify outcomes by aneurysm rupture status; however, most aneurysms included in this study were unruptured. Overall, the quality of evidence (confidence in estimates) is low because of imprecision, heterogeneity, and methodologic limitations of the included studies.^{22,23} Nevertheless, this systematic review and meta-analysis provides useful data to share with families when discussing the possible outcomes of stent-assisted coiling of wide-neck and wide-neck bifurcation aneurysms. In

addition, this study could serve as a benchmark for which to compare results of newer stents, flow diverters, and intrasaccular flow diverters.

CONCLUSIONS

Our study of angiographic and clinical outcomes for patients with wide-neck aneurysms demonstrates that endovascular coiling, with or without stent-assisted coiling, is generally safe, with low rates of perioperative morbidity and mortality. Initial and long-term angiographic outcomes were satisfactory, but not ideal, and lower than those reported for treatment of similar aneurysms with newer technologies such as intraluminal and intrasaccular flow diverters. Future comparative clinical trials could be considered to identify the best treatments for wide-neck and wide-neck bifurcation aneurysms.

Disclosures: Giuseppe Lanzino—UNRELATED: Consultancy: Covidien/Medtronic.* David F. Kallmes—UNRELATED: Board Membership: GE Healthcare.* Comments: Cost effectiveness board; Consultancy: Medtronic.* Comments: Planning and implementing clinical trials; Grants/Grants Pending: MicroVention,* Medtronic.* Codman,* Surmodics,* Sequent,* NeuroSigma,* Comments: Preclinical research and clinical trials. *Money paid to the institution.

REFERENCES

- Moret J, Cognard C, Weill A, et al. The “remodelling technique” in the treatment of wide neck intracranial aneurysms: angiographic results and clinical follow-up in 56 cases. *Interv Neuroradiol* 1997;3:21–35 Medline
- Nakahara T, Hidaka T, Kutsuna M, et al. Intraaneurysmal embolization for wide-necked aneurysms: remodeling technique, combined neck-clipping and coiling therapy, scaffolding technique. *Interv Neuroradiol* 2000;6(suppl 1):95–101 Medline
- Biondi A, Janardhan V, Katz JM, et al. Neuroform stent-assisted coil embolization of wide-neck intracranial aneurysms: strategies in stent deployment and midterm follow-up. *Neurosurgery* 2007;61:460–68; discussion 468–69 CrossRef Medline
- Mu SQ, Yang XJ, Li YX, et al. Endovascular treatment of wide-necked intracranial aneurysms using of “remodeling technique” with the HyperForm balloon. *Chin Med J (Engl)* 2008;121:725–29 Medline
- Lee JY, Seo JH, Cho YD, et al. Endovascular treatment of wide-neck intracranial aneurysms using a microcatheter protective technique: results and outcomes in 75 aneurysms. *AJNR Am J Neuroradiol* 2011;32:917–22 CrossRef Medline
- Bartolini B, Blanc R, Pistocchi S, et al. “Y” and “X” stent-assisted coiling of complex and wide-neck intracranial bifurcation aneurysms. *AJNR Am J Neuroradiol* 2014;35:2153–58 CrossRef Medline
- Zhang JZ, Yang PF, Huang QH, et al. Stent-assisted coiling strategies for the treatment of wide-necked basilar artery bifurcation aneurysms. *J Clin Neurosci* 2014;21:962–67 CrossRef Medline
- Ko JK, Han IH, Cho WH, et al. Crossing Y-stent technique with dual open-cell stents for coiling of wide-necked bifurcation aneurysms. *Clin Neurol Neurosurg* 2015;132:54–60 CrossRef Medline
- DerSimonian R, Laird N. Meta-analysis in clinical trials. *Control Clin Trials* 1986;7:177–88 CrossRef Medline
- Higgins JP, Thompson SG, Deeks JJ, et al. Measuring inconsistency in meta-analyses. *BMJ* 2003;327:557–60 CrossRef Medline
- McLaughlin N, McArthur DL, Martin NA. Use of stent-assisted coil embolization for the treatment of wide-necked aneurysms: a systematic review. *Surg Neurol Int* 2013;4:43 CrossRef Medline
- McDonald JS, Norgan AP, McDonald RJ, et al. In-hospital outcomes associated with stent-assisted endovascular treatment of unruptured cerebral aneurysms in the USA. *J Neurointerv Surg* 2013;5:317–20 CrossRef Medline
- Poncylyusz W, Biliński P, Safranow K, et al. The LVIS/LVIS Jr. stents in the treatment of wide-neck intracranial aneurysms: multicentre registry. *J Neurointerv Surg* 2015;7:524–29 CrossRef Medline
- Becske T, Kallmes DF, Saatci I, et al. Pipeline for uncoilable or failed aneurysms: results from a multicenter clinical trial. *Radiology* 2013;267:858–68 CrossRef Medline
- Brinjikji W, Kallmes DF, Bekske T. 5 year follow up results from the Pipeline for Uncoilable or Failed Aneurysms trial. *Stroke* 2015;LB P1
- Caroff J, Neki H, Mihalea C, et al. Flow-diverter stents for the treatment of saccular middle cerebral artery bifurcation aneurysms. *AJNR Am J Neuroradiol* 2016;37:279–84 CrossRef Medline
- Gawlitza M, Januel AC, Tall P, et al. Flow diversion treatment of complex bifurcation aneurysms beyond the circle of Willis: a single-center series with special emphasis on covered cortical branches and perforating arteries. *J Neurointerv Surg* 2016;8:481–87 CrossRef Medline
- Pierot L, Liebig T, Sychra V, et al. Intrasaccular flow-disruption treatment of intracranial aneurysms: preliminary results of a multicenter clinical study. *AJNR Am J Neuroradiol* 2012;33:1232–38 CrossRef Medline
- Behme D, Berlis A, Weber W. Woven EndoBridge intrasaccular flow disrupter for the treatment of ruptured and unruptured wide-neck cerebral aneurysms: report of 55 cases. *AJNR Am J Neuroradiol* 2015;36:1501–06 CrossRef Medline
- Lubicz B, Klisch J, Gauvrit JY, et al. WEB-DL endovascular treatment of wide-neck bifurcation aneurysms: short- and midterm results in a European study. *AJNR Am J Neuroradiol* 2014;35:432–38 CrossRef Medline
- Pierot L, Costalat V, Moret J, et al. Safety and efficacy of aneurysm treatment with WEB: results of the WEBCAST study. *J Neurosurg* 2016;124:1250–56 CrossRef Medline
- Balshem H, Helfand M, Schünemann HJ, et al. GRADE guidelines: 3. Rating the quality of evidence. *J Clin Epidemiol* 2011;64:401–06 CrossRef Medline
- Guyatt GH, Oxman AD, Kunz R, et al. GRADE guidelines 6. Rating the quality of evidence—imprecision. *J Clin Epidemiol* 2011;64:1283–93 CrossRef Medline

Diffusion-Weighted Imaging of Nasopharyngeal Carcinoma: Can Pretreatment DWI Predict Local Failure Based on Long-Term Outcome?

 B.K.H. Law,  A.D. King,  K.S. Bhatia,  A.T. Ahuja,  M.K.M. Kam,  B.B. Ma,  Q.Y. Ai,  F.K.F. Mo,  J. Yuan, and  D.K.W. Yeung

ABSTRACT

BACKGROUND AND PURPOSE: Pretreatment prediction of patients with nasopharyngeal carcinoma who will fail conventional treatment would potentially allow these patients to undergo more intensive treatment or closer posttreatment monitoring. The aim of the study was to determine the ability of pretreatment DWI to predict local failure in patients with nasopharyngeal carcinoma based on long-term clinical outcome.

MATERIALS AND METHODS: One hundred fifty-eight patients with pretreatment DWI underwent analysis of the primary tumor to obtain the ADC mean, ADC skewness, ADC kurtosis, volume, and T-stage. Univariate and multivariate analyses using logistic regression were performed to compare the ADC parameters, volume, T-stage, and patient age in primary tumors with local failure and those with local control, by using a minimum of 5-year follow-up to confirm local control.

RESULTS: Local control was achieved in 131/158 (83%) patients (range, 60.3–117.7 months) and local failure occurred in 27/158 (17%) patients (range, 5.2–79.8 months). Compared with tumors with local control, those with local failure showed a significantly lower ADC skewness (ADC values with the greatest frequencies were shifted away from the lower ADC range) ($P = .006$) and lower ADC kurtosis (curve peak broader) ($P = .024$). The ADC skewness remained significant on multivariate analysis ($P = .044$). There was a trend toward higher tumor volumes in local failure, but the volume, together with T-stage and ADC mean, were not significantly different between the 2 groups.

CONCLUSIONS: Pretreatment DWI of primary tumors found that the skewness of the ADC distribution curve was a predictor of local failure in patients with nasopharyngeal carcinoma, based on long-term clinical outcome.

ABBREVIATIONS: LC = local control; LF = local failure; NPC = nasopharyngeal carcinoma; ROC = receiver operating characteristic

Nasopharyngeal carcinoma (NPC) is a radiosensitive tumor, but despite recent advances in treatment by using intensity-modulated radiation therapy, local tumor recurrence still occurs in 12% of patients.¹ Recurrent primary tumors deep to the naso-

pharyngeal wall may be undetectable by endoscopy, and they are difficult to treat. Moreover, only a small percentage of these recurrent primary tumors present early while the tumor is still amenable to salvage surgery.² It would be beneficial to identify patients with resistant NPC so that more aggressive treatment can be given from the outset, such as an additional radiation therapy boost, chemotherapy, or targeted therapy, or these patients can be selected for posttreatment biopsy or closer posttreatment surveillance imaging.

Hypoxia and high stromal content are 2 of the factors related to a poor treatment outcome in head and neck cancers. Both micronecrosis, believed to be related to hypoxia, and high stromal content³ may decrease the restriction of the diffusion of water molecules in tumors that is reflected by an increase in the ADC on DWI. Indeed, reports of head and neck squamous cell carcinoma suggest a significant association between high pretreatment ADC and poor treatment outcome.^{4–10} However, for NPC, a smaller number of pretreatment predictive DWI studies have been reported. This is probably because local tumor relapse is less com-

Received November 30, 2015; accepted after revision February 27, 2016.

From the Departments of Imaging and Interventional Radiology (B.K.H.L., A.D.K., K.S.B., A.T.A., Q.Y.A.) and Clinical Oncology (M.K.M.K., B.B.M., F.K.F.M., D.K.W.Y.), The Chinese University of Hong Kong, Prince of Wales Hospital, Hong Kong S.A.R., China; and Medical Physics and Research Department (J.Y.), Hong Kong Sanatorium and Hospital, Happy Valley, Hong Kong S.A.R., China.

We report the following author contributions: conception and design: B.K.H.L., A.D.K., D.K.W.Y.; acquisition of data: K.S.B., A.T.A., M.K.M.K., B.B.M., Q.Y.A., D.K.W.Y.; analysis and interpretation of data: B.K.H.L., A.D.K., F.K.F.M., J.Y.; drafting the article or revising it critically for important intellectual content: all authors; final approval of the version to be published: all authors; and agreement to be accountable for all aspects of the work in ensuring that questions related to the accuracy or integrity of any part of the work are appropriately investigated and resolved: all authors.

Please address correspondence to Ann D. King, FRCR, Department of Imaging and Interventional Radiology, Faculty of Medicine, The Chinese University of Hong Kong, Prince of Wales Hospital, 30-32 Ngan Shing St, Shatin, New Territories, Hong Kong S.A.R., China; e-mail: king2015@cuhk.edu.hk

<http://dx.doi.org/10.3174/ajnr.A4792>

mon in NPC than in squamous cell carcinoma and is spread out during a longer posttreatment period. Most relapses in squamous cell carcinoma occur in the first 2 years, whereas for NPC, only around 52% of NPCs relapse in the first 2 years, with a further 39% at 2–5 years and 9% after 5 years.¹¹ Currently, most predictive treatment-response NPC studies are based on a relatively short-term outcome ranging up to 3 months posttreatment,^{12–14} and only 1 study has reported results based on longer term outcome correlating pretreatment DWI with local relapse-free or disease-free survival at 3 years.¹⁵

Therefore, the aim of this study was to determine the diagnostic performance of pretreatment DWI of the primary tumor site for the prediction of local failure (LF) based on long-term follow-up at a minimum of 5 years for patients diagnosed with local control (LC) in NPC.

MATERIALS AND METHODS

Patients

Patients presenting with NPC from an endemic region in southern China underwent MR imaging of the head and neck to obtain conventional anatomic-based images and DWI. Local institutional review board approval was obtained for this retrospective study. Patients were eligible for this study on the basis of the following: 1) biopsy-proved, previously untreated NPC; 2) completion of a full course of treatment with radiation therapy or chemoradiotherapy; and 3) clinical follow-up of at least 5 years from the start of treatment in patients with LC.

MR Imaging Examination and Analysis

All MR imaging examinations were performed on a 1.5T whole-body system (Intera NT; Philips Healthcare, Best, the Netherlands) with a 30 mT m⁻¹ maximum gradient capability. A standard receive-only head and neck coil was used. The diffusion-weighted images were acquired in the axial plane by using a spin-echo single-shot echo-planar imaging sequence (TR, 2000 ms; TE, 75 ms; section thickness, 4 mm without gap; FOV, 23 cm; acquisition matrix, 112 × 112; reconstruction matrix, 256 × 256; number of signal averages, 4) with fat suppression. A pair of rectangular diffusion gradients was applied along all 3 orthogonal axes to obtain isotropic DWI with 6 b-values of 0, 100, 200, 300, 400, and 500 s/mm². Conventional MR imaging, including axial fat-suppressed T2-weighted turbo spin-echo, axial T1-weighted spin-echo, and contrast-enhanced axial T1-weighted spin-echo sequences, was also performed for anatomic correlation. DWI was performed before contrast agent injection.

DWI Analysis

The ADC map was calculated with DWI of all 6 b-values. The primary tumor in the nasopharynx was contoured on the ADC map by using the anatomic images for guidance by using the Extended MR Workspace (Philips Healthcare). Radiologic assessment was performed without knowledge of the clinical outcome. The entire volume of the primary NPC was outlined by a single radiologist (A.D.K.) with >20 years of experience in MR imaging of NPC. A histogram analysis method was used to examine the distribution of ADC values. The distribution of the ADC values

within the primary tumor was assessed by using an in-house-developed Matlab (Version 7.10; MathWorks, Natick, Massachusetts) program.

The ADC parameters obtained from histogram analysis in each tumor were the ADC mean, ADC skewness, and ADC kurtosis. In this study, skewness and kurtosis are defined as $E(x - \mu)^3 / \sigma^3$ and $E(x - \mu)^4 / \sigma^4$, respectively, where E is the expected value, μ is the mean of x , and σ is the SD of x . ADC skewness measures the skew in shape of the ADC distribution curve, with the skewness value being more positive when there is a greater frequency of low ADC values (the curve is “right-skewed” with the peak and short tail of the curve toward the left side and the long tail toward the right side) and more negative when there is a greater frequency of high ADC values (the curve is “left-skewed” with the peak and short tail of the curve toward the right side and the long tail toward the left side). ADC kurtosis measures the shape of the peak of the curve, with the kurtosis value being higher when the peak is more acute and lower when the peak is more flattened/broadened.

Conventional MR Imaging Analysis

The stage of the primary tumor (T-stage according to the seventh edition of the American Joint Committee on Cancer classification) was obtained together with primary tumor volume, calculated manually by tracing the outline of the primary nasopharyngeal tumor on the contrast-enhanced axial T1-weighted image to obtain the cross-sectional area and multiplying by the section thickness.

Clinical End Point Assessment

Regular scheduled clinical follow-up was performed after treatment in all patients. LF was determined by histology (a biopsy positive for NPC at the local site at least 12 weeks after the end of treatment) or increase in tumor size on imaging or endoscopic examination. Most patients with LF present in the first 5 years; therefore, a minimum of 5-year follow-up was required in this study to confirm LC. Patients who had insufficient clinical follow-up before LC could be confirmed (including those who died within 5 years) were excluded from the study.

Statistical Analysis

The ADC parameters (mean, skewness, and kurtosis), primary tumor volume, and patient age were compared in the group of patients with LC and the group of patients with LF by using independent Student t tests. Univariate logistic regression analyses with ADC parameters, primary tumor volume, patient age, and T-stage (T1–T2 versus T3–T4) were performed to determine whether there was a correlation between these parameters and LF. Odds ratios and their corresponding 95% CI were calculated, parameters with P values < .05 were included, and the duration of follow-up was adjusted in a multivariate analysis. Receiver operating characteristic (ROC) analysis with the area under the ROC curve was used to identify the optimal threshold of any significant parameter on multivariate analysis. The optimal threshold was obtained by optimizing the sensitivity and specificity. The sensitivity, specificity, accuracy, positive predictive value, and negative predictive value of the optimal threshold were calculated, and the significance of this threshold was re-evaluated with the χ^2 test to ensure that it remained significant. All statistical tests were

Table 1: ADC parameters, volume, and T-stage of the primary tumor and the patient age for prediction of treatment response

Parameter	Whole Group (N = 158) (Mean)	Local Failure (n = 27) (Mean)	Local Control (n = 131) (Mean)	Student t Test (P Value)	Univariate Logistic Regression	
					P Value	Odds Ratio (95% CI)
ADC mean ($\times 10^{-3}$ mm ² /s)	0.91 \pm 0.11	0.90 \pm 0.12	0.91 \pm 0.11	.879	.878	0.75 (0.02–29.45)
ADC skewness	0.68 \pm 0.47	0.45 \pm 0.40	0.72 \pm 0.47	.006 ^a	.007 ^a	0.22 (0.08–0.67)
ADC kurtosis	4.93 \pm 1.87	4.19 \pm 1.29	5.08 \pm 1.94	.024 ^a	.024 ^a	0.65 (0.44–0.95)
Primary tumor volume (mL)	24.63 \pm 17.99	28.20 \pm 17.90	23.89 \pm 17.99	.256	.298	1.011 (0.99–1.03)
T-stage						
T1, T2	74	12	62	NA	.785	1.123 (0.49–2.58)
T3, T4	84	15	69			
Patient age (yr)	50.19 \pm 10.34	49.74 \pm 11.34	50.28 \pm 10.17	.805	.804	1.00 (0.96–1.04)

Note:—NA indicates not applicable.

^a Statistically significant.

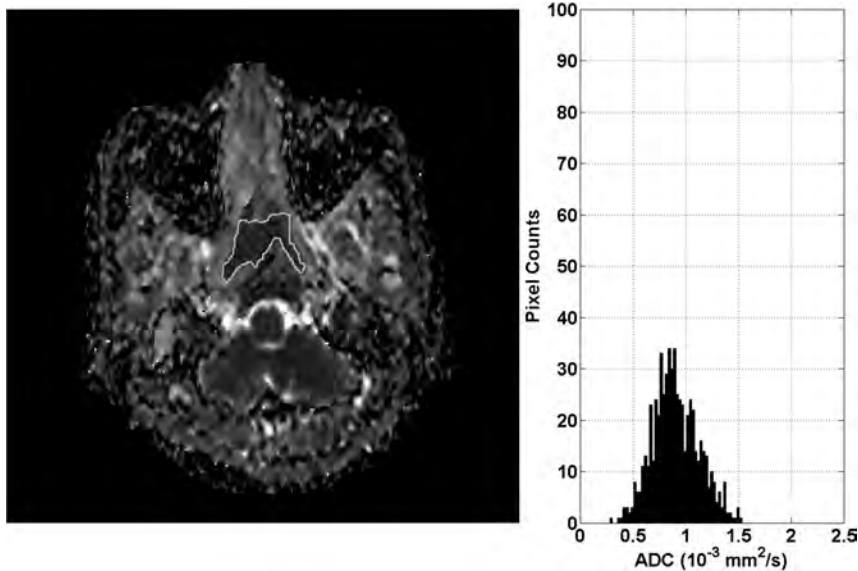


FIG 1. ADC map and histogram of primary NPC before treatment in a 50-year-old woman with local failure. The histogram shows that the greatest frequency of ADC values is shifted toward the central ADC range (ADC skewness = 0.11) and the peak is broadened (ADC kurtosis = 3.89).

2-sided, and *P* values < .05 indicated a statistically significant difference. Statistical analyses were performed by using SPSS software (Version 20.0; IBM, Armonk, New York).

RESULTS

Two hundred sixty-six patients underwent DWI from March 2004 to April 2009, of whom, 108 patients were excluded from analysis for the following reasons: incomplete follow-up data (<5 years of clinical follow-up for patients with LC; *n* = 53) and small lesion size/degradation of DWI for ROI analysis (*n* = 55). The study group comprised 158 patients with NPC (119 men and 39 women; mean age, 50 years; range, 27–81 years) with undifferentiated carcinoma (*n* = 155) or poorly differentiated carcinoma (*n* = 3) who had undergone concurrent chemoradiotherapy (*n* = 100) or radiation therapy alone (*n* = 58). The T-stage was T1 (*n* = 42), T2 (*n* = 32), T3 (*n* = 56), and T4 (*n* = 28). The volume of the primary tumors ranged from 6.1 to 98.7 mL, with a mean of 24.6 mL and a median of 18.4 mL.

Clinical End Point

LC was achieved in 131/158 (83%) patients (undifferentiated carcinoma; *n* = 128; poorly differentiated carcinoma; *n* = 3), with a

median follow-up of 87 months (mean, 88 months; range, 60.3–117.7 months) from the start of treatment. LF occurred in 27/158 (17%) patients (undifferentiated carcinoma; *n* = 27; poorly differentiated carcinoma; *n* = 0) at a median of 25 months (mean, 33 months; range, 5.2–79.8 months) from the start of treatment. LF occurred in the first 2 years in 12/27 (44%) patients; at 2–5 years in 11/27 (41%) patients, of whom, LF occurred in the 2- to 3-year period in 4/27 (15%) patients; and after 5 years in 4/27 (15%) patients.

DWI and Tumor Volume

The pretreatment ADC mean, ADC skewness, ADC kurtosis, primary tumor volume, T-stage, and patient age for the group of patients with LF and the group of patients with LC and the statistical analysis are shown in Table 1. Compar-

ison of these 2 groups showed a statistically significantly lower ADC skewness (ADC values with the greatest frequencies were shifted away from the lower ADC range) and ADC kurtosis (ADC curve peak broader) in the group with LF (Fig 1) compared with the group with LC (Fig 2) (*P* = .006 and .024, respectively). There was a trend toward higher tumor volumes in the group with LF, but the difference was not significant (*P* = .256). The other parameters also showed no significant differences. ADC skewness and kurtosis significantly predicted LF in univariate analysis, but only ADC skewness remained significant (*P* = .044) in multivariate analysis. Side-by-side boxplots of the ADC skewness values of tumors with LF and LC are shown in Fig 3. Moreover, a threshold of ADC skewness of ≤ 0.55 (*P* = .0001) was identified as a predictor of LF in ROC curve analysis (Fig 4); the diagnostic performance of ADC skewness is shown in Table 2.

DISCUSSION

On the basis of long-term clinical follow-up of patients treated for NPC, pretreatment DWI showed that the ADC distribution curves of primary tumors with LF had significantly lower ADC skewness than primary tumors with LC (ie, the ADC distribution

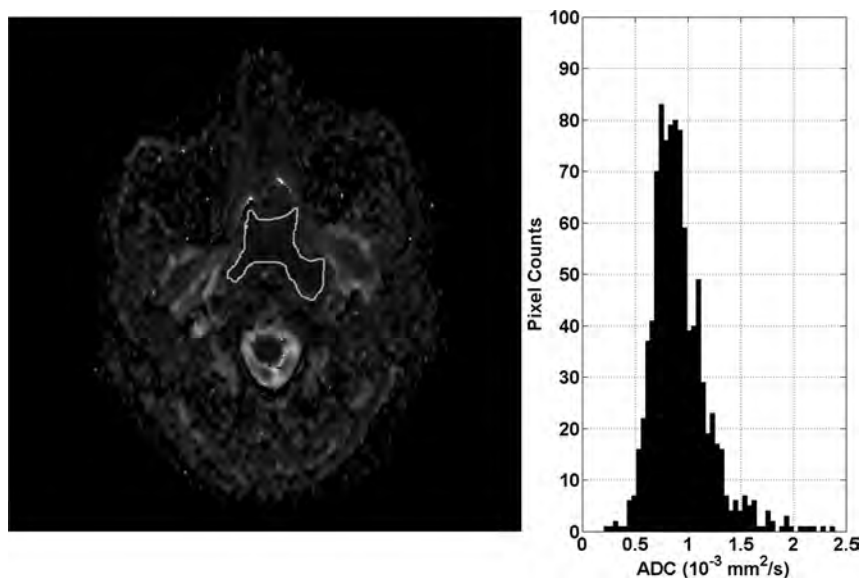


FIG 2. ADC map and histogram of primary NPC before treatment in a 43-year-old man with local control. The histogram shows that the greatest frequency of ADC values is shifted toward the lower ADC range (ADC skewness = 1.42) and the peak is more acute (ADC kurtosis = 8.77).

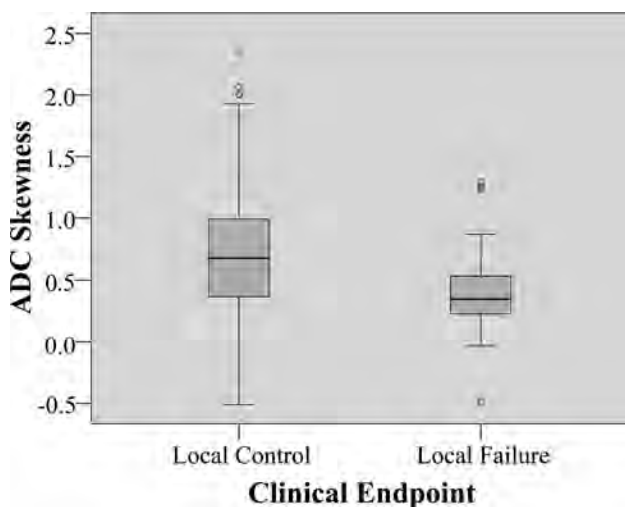


FIG 3. Side-by-side boxplots of ADC skewness comparing local control and local failure.

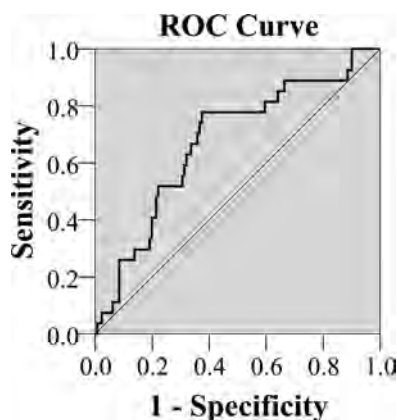


FIG 4. ROC analysis curve for ADC skewness.

curve of tumors with LF showed that the greatest frequencies of ADC values were shifted away from the lower ADC range). Therefore, visually, compared with tumors with LC, those with LF showed a shift of the curve peak away from the left side of the curve (greater frequency of lower ADC values) toward the center (symmetric frequency distribution of low and high ADC values) or right side of the curve (greater frequency of higher ADC values). ADC skewness remained significant on multivariate analysis, and a threshold of ≤ 0.55 produced a relatively high negative predictive value (93%) for LF, though the positive predictive value was low (30%), which could limit the clinical value of using DWI to predict NPC response.

Analysis of the shape of the ADC histogram curve pretreatment also showed that primary tumors with LF had significantly lower ADC kurtosis values than

tumors with LC (ie, their ADC histogram peak was broader and less acute compared with the ADC histogram peak of the tumors with LC). A broader peak suggests that the tumor is more heterogeneous; this finding supports the view that those tumors with greater heterogeneity are more likely to fail treatment.¹⁶ In this study, there was also a trend toward tumors with higher volume having LF, but neither volume difference nor T-stage was significant. These results highlight the potential value of ADC skewness and ADC kurtosis because they stand out as the only parameters that may be able to identify resistant tumors over a range of tumor volumes and T-stages.

Pretreatment tumor ADC values have been shown to be predictors of treatment response in head and neck cancers. Previous head and neck squamous cell carcinoma studies have found significantly higher tumor ADC values in patients with LF,^{5-7,10} nodal failure,⁴ or poor treatment response,⁸⁻⁹ while other studies have shown a similar trend in the ADC values that did not reach statistical significance.¹⁷⁻¹⁹ It has been postulated that poor outcomes of some squamous cell carcinomas are due to tumor factors that are known to increase ADC values, such as micronecrosis, lower cellularity, and, more recently, negative human papillomavirus status and high stromal content.^{3,20-21} Of note, the ratio of stroma to tumor cells is recognized as an important determinant of outcome in head and neck squamous cell carcinoma. In regard to NPC, research now also shows that stroma-rich NPCs are associated with poor prognosis and an increased risk of relapse.²² Therefore, it could be postulated that NPCs with high ADCs are more likely to have a poor outcome compared with those with low ADCs. Currently, there are only a few NPC DWI studies that have correlated diffusion parameters with tumor characteristics at diagnosis, such as T-stage,^{23,24} early intratreatment response,²⁵ and posttreatment response.^{12-15,26} Regarding using pretreatment tumor ADC to predict posttreatment response,¹²⁻¹⁵ 3 of these studies were based on short-term outcome at the end or 3 months after

Table 2: ADC skewness threshold obtained from ROC curve analysis to predict local failure

Parameter	ADC Skewness
Threshold	≤0.55
P value	.0001
Area under the ROC curve	0.68
True-positive	21
False-positive	49
True-negative	82
False-negative	6
Sensitivity	78%
Specificity	63%
Accuracy	65%
Positive predictive value	30%
Negative predictive value	93%

the end of treatment.¹²⁻¹⁴ These 3 studies showed mixed results with both low¹²⁻¹³ and high¹⁴ pretreatment ADCs reported in tumors with poor outcomes, with the results being significant in only 1 of the studies.¹² However, a recent NPC study by Zhang et al¹⁵ with long-term follow-up and a large sample size of 541 patients showed a significant association between a high mean ADC in primary tumors pretreatment and poor survival at 3 years. That study measured the pretreatment mean ADC at the level of the largest primary tumor diameter and used ROC curve analysis to identify an optimal cutoff ADC for LF of $\geq 0.747 \times 10^{-3} \text{ mm}^2/\text{s}$ (area under the ROC curve = 0.68, $P = .004$), which was shown to correlate with both local relapse-free survival and disease-free survival.

Our study broadly supports the findings of Zhang et al,¹⁵ with high primary tumor ADC values being associated with poor local response. However, we were unable to show this correlation by using the ADC mean and could only show such a correlation by using the ADC skewness. This discrepancy between our results and those of Zhang et al¹⁵ may be related to the longer follow-up period in our study, with a subsequently greater incidence of failure at the primary site, 17% (27/158) compared with 4.3% (23/541), of which 44% (13/27) in our study occurred beyond 3 years.

We postulate that more sophisticated ADC measurements such as ADC skewness may be needed to identify primary tumors that will relapse at a longer time after the end of treatment. The assessment of ADC skewness in this study used histogram analysis of the distribution of the ADC values from the entire tumor volume and had an advantage over the ADC mean in that it took tumor heterogeneity into account. Most tumors are heterogeneous, and the proportion of the cancer cell population with high ADC values may influence the final treatment outcome. From the results, we postulate that tumors that are likely to have resistant tumor cells are those in which the proportion of high ADC cells is similar or greater than the proportion of low ADC cells. However, other reasons for the discrepancy in the significance of the ADC mean between the 2 studies could include the smaller sample size in our study and the difference in the outcome measures used to denote response. Specifically, we did not use survival data such as local relapse-free survival to assess primary site response; instead, we took a simple approach and directly compared the ADC values of the primary tumors with LC against the ADC values of primary tumors with LF.

Previous NPC studies have shown that larger tumor volumes are associated with more unfavorable outcomes at the primary

site.²⁷⁻³⁵ This finding was also a trend in this study but did not reach significance, possibly because the mean volume of our primary tumors (24.6 mL) was in the lower range of previously reported cutoff thresholds, which have ranged from 13 to 60 mL.²⁷⁻³⁵ In addition, the T-stage was not significant. This finding is possibly explained by the better treatment outcomes as a result of intensity-modulated radiation therapy³⁶ and also the wide use of MR imaging for staging, which can lead to upstaging to T3 disease as a result of greater sensitivity to bone invasion compared with CT.³⁷ Histologic NPC subtype also has a major influence on treatment outcome, whereby the undifferentiated form of NPC has a better prognosis than the other subtypes.³⁸ In our fairly large study of 158 patients, we think that the histologic subtype did not influence the results because most (98%) were of the same undifferentiated carcinoma subtype, with only 2% (3 tumors) being poorly differentiated, none of which showed LF.

Use of ADC measures of tumor heterogeneity such as ADC skewness and kurtosis is fairly new to the DWI research, but a few cancer studies in head and neck squamous cell carcinoma and tumors of the ovary/peritoneum and brain have shown that pretreatment^{39,40} or intratreatment^{19,39,40} ADC skewness and kurtosis may predict treatment outcome.

NPC may relapse many years after treatment; therefore, one of the main strengths of this study was the long-term clinical follow-up of the primary site (mean, ~7.5 years and maximum, ~10 years) with a minimum of 5 years for patients with LC. However, because of the long clinical follow-up required for this study, one of the main limitations was that the DWI protocol was set up some time ago when, to reduce susceptibility artifacts at the skull base, the fitted 6 b-values used were up to a maximum of 500 s/mm². It has been shown subsequently that more advanced non-Gaussian models for ADC analysis influence the ADC in NPC.⁴¹ In head and neck squamous cell carcinoma, the choice of b-values may also influence the accuracy of ADC for the prediction of treatment response, and some authors have proposed using ADCs calculated from the mid/high b-range (300/500-1000 s/mm²)^{9,10} to predict locoregional response.

CONCLUSIONS

This study correlated the ADC values of the pretreatment primary NPC with treatment outcome at the primary site on the basis of long-term clinical follow-up. Compared with primary tumors with LC, those with LF had lower ADC skewness and kurtosis. The ADC skewness remained significant on multivariate analysis. The simple ADC measurement using the mean value was not a predictor of outcome in this study, suggesting that more sophisticated measurements, such as skewness, may be needed to reflect the predictive value of high ADC cancer cell populations in heterogeneous tumors. The primary tumor volume and T-stage of NPC were not significant parameters in this study for predicting treatment response at the primary site, suggesting that ADC skewness and kurtosis may have the potential to predict tumor response, even in smaller volume or earlier stage tumors.

ACKNOWLEDGMENTS

We acknowledge the assistance of H.L.E. Chan, S.T. Chan, C.H. Chen, Z. He, F.Y. Lam, and L.L. Leung.

REFERENCES

- Lee AW, Sze WM, Au JS, et al. Treatment results for nasopharyngeal carcinoma in the modern era: the Hong Kong experience. *Int J Radiat Oncol Biol Phys* 2005;61:1107–16 CrossRef Medline
- Yu KH, Leung SF, Tung SY, et al; Hong Kong Nasopharyngeal Carcinoma Study Group. Survival outcome of patients with nasopharyngeal carcinoma with first local failure: a study by the Hong Kong Nasopharyngeal Carcinoma Study Group. *Head Neck* 2005;27:397–405 CrossRef Medline
- Driessen JP, Caldas-Magalhaes J, Janssen LM, et al. Diffusion-weighted MR imaging in laryngeal and hypopharyngeal carcinoma: association between apparent diffusion coefficient and histologic findings. *Radiology* 2014;272:456–63 CrossRef Medline
- Kim S, Loevner L, Quon H, et al. Diffusion-weighted magnetic resonance imaging for predicting and detecting early response to chemoradiation therapy of squamous cell carcinomas of the head and neck. *Clin Cancer Res* 2009;15:986–94 CrossRef Medline
- Hatakenaka M, Nakamura K, Yabuuchi H, et al. Pretreatment apparent diffusion coefficient of the primary lesion correlates with local failure in head-and-neck cancer treated with chemoradiotherapy or radiotherapy. *Int J Radiat Oncol Biol Phys* 2011;81:339–45 CrossRef Medline
- Hatakenaka M, Shioyama Y, Nakamura K, et al. Apparent diffusion coefficient calculated with relatively high b-values correlates with local failure of head and neck squamous cell carcinoma treated with radiotherapy. *AJNR Am J Neuroradiol* 2011;32:1904–10 CrossRef Medline
- Ohnishi K, Shioyama Y, Hatakenaka M, et al. Prediction of local failures with a combination of pretreatment tumor volume and apparent diffusion coefficient in patients treated with definitive radiotherapy for hypopharyngeal or oropharyngeal squamous cell carcinoma. *J Radiat Res* 2011;52:522–30 CrossRef Medline
- Srinivasan A, Chenevert TL, Dwamena BA, et al. Utility of pretreatment mean apparent diffusion coefficient and apparent diffusion coefficient histograms in prediction of outcome to chemoradiation in head and neck squamous cell carcinoma. *J Comput Assist Tomogr* 2012;36:131–37 CrossRef Medline
- Lambrecht M, Van Calster B, Vandecaveye V, et al. Integrating pretreatment diffusion weighted MRI into a multivariable prognostic model for head and neck squamous cell carcinoma. *Radiother Oncol* 2014;110:429–34 CrossRef Medline
- Hatakenaka M, Nakamura K, Yabuuchi H, et al. Apparent diffusion coefficient is a prognostic factor of head and neck squamous cell carcinoma treated with radiotherapy. *Jpn J Radiol* 2014;32:80–89 CrossRef Medline
- Lee AW, Foo W, Law SC, et al. Recurrent nasopharyngeal carcinoma: the puzzles of long latency. *Int J Radiat Oncol Biol Phys* 1999;44:149–56 CrossRef Medline
- Zheng D, Chen Y, Chen Y, et al. Early assessment of induction chemotherapy response of nasopharyngeal carcinoma by pretreatment diffusion-weighted magnetic resonance imaging. *J Comput Assist Tomogr* 2013;37:673–80 CrossRef Medline
- Chen Y, Liu X, Zheng D, et al. Diffusion-weighted magnetic resonance imaging for early response assessment of chemoradiotherapy in patients with nasopharyngeal carcinoma. *Magn Reson Imaging* 2014;32:630–37 CrossRef Medline
- Hong J, Yao Y, Zhang Y, et al. Value of magnetic resonance diffusion-weighted imaging for the prediction of radiosensitivity in nasopharyngeal carcinoma. *Otolaryngol Head Neck Surg* 2013;149:707–13 CrossRef Medline
- Zhang Y, Liu X, Zhang Y, et al. Prognostic value of the primary lesion apparent diffusion coefficient (ADC) in nasopharyngeal carcinoma: a retrospective study of 541 cases. *Sci Rep* 2015;5:12242 CrossRef Medline
- Mroz EA, Tward AD, Pickering CR, et al. High intratumor genetic heterogeneity is related to worse outcome in patients with head and neck squamous cell carcinoma. *Cancer* 2013;119:3034–42 CrossRef Medline
- Matoba M, Tuji H, Shimode Y, et al. Fractional change in apparent diffusion coefficient as an imaging biomarker for predicting treatment response in head and neck cancer treated with chemoradiotherapy. *AJNR Am J Neuroradiol* 2014;35:379–85 CrossRef Medline
- Chawla S, Kim S, Dougherty L, et al. Pretreatment diffusion-weighted and dynamic contrast-enhanced MRI for prediction of local treatment response in squamous cell carcinomas of the head and neck. *AJR Am J Roentgenol* 2013;200:35–43 CrossRef Medline
- King AD, Chow KK, Yu KH, et al. Head and neck squamous cell carcinoma: diagnostic performance of diffusion-weighted MR imaging for the prediction of treatment response. *Radiology* 2013;266:531–38 CrossRef Medline
- Driessen JP, van Bommel AJ, van Kempen PM, et al. Correlation of human papillomavirus status with apparent diffusion coefficient of diffusion-weighted MRI in head and neck squamous cell carcinomas. *Head Neck* 2015 Mar 17. [Epub ahead of print] CrossRef Medline
- Nakahira M, Saito N, Yamaguchi H, et al. Use of quantitative diffusion-weighted magnetic resonance imaging to predict human papilloma virus status in patients with oropharyngeal squamous cell carcinoma. *Eur Arch Otorhinolaryngol* 2014;271:1219–25 CrossRef Medline
- Zhang XL, Jiang C, Zhang ZX, et al. The tumor-stroma ratio is an independent predictor for survival in nasopharyngeal cancer. *Oncol Res Treat* 2014;37:480–84 CrossRef Medline
- Abdel Razek AA, Kamal E. Nasopharyngeal carcinoma: correlation of apparent diffusion coefficient value with prognostic parameters. *Radiol Med* 2013;118:534–39 CrossRef Medline
- Lai V, Li X, Lee VH, et al. Nasopharyngeal carcinoma: comparison of diffusion and perfusion characteristics between different tumour stages using intravoxel incoherent motion MR imaging. *Eur Radiol* 2014;24:176–83 CrossRef Medline
- Chen Y, Ren W, Zheng D, et al. Diffusion kurtosis imaging predicts neoadjuvant chemotherapy responses within 4 days in advanced nasopharyngeal carcinoma patients. *J Magn Reson Imaging* 2015;42:1354–61 CrossRef Medline
- Xu JF, Wu XW, Wang WQ, et al. Value of diffusion-weighted magnetic resonance imaging on the follow-up of nasopharyngeal carcinoma after radiotherapy. *J Xray Sci Technol* 2014;22:605–12 CrossRef Medline
- Wu Z, Su Y, Zeng RF, et al. Prognostic value of tumor volume for patients with nasopharyngeal carcinoma treated with concurrent chemotherapy and intensity-modulated radiotherapy. *J Cancer Res Clin Oncol* 2014;140:69–76 CrossRef Medline
- Feng M, Wang W, Fan Z, et al. Tumor volume is an independent prognostic indicator of local control in nasopharyngeal carcinoma patients treated with intensity-modulated radiotherapy. *Radiat Oncol* 2013;8:208 CrossRef Medline
- Guo R, Sun Y, Yu XL, et al. Is primary tumor volume still a prognostic factor in intensity modulated radiation therapy for nasopharyngeal carcinoma? *Radiother Oncol* 2012;104:294–99 CrossRef Medline
- Lee CC, Huang TT, Lee MS, et al. Clinical application of tumor volume in advanced nasopharyngeal carcinoma to predict outcome. *Radiat Oncol* 2010;5:20 CrossRef Medline
- Shen C, Lu JJ, Gu Y, et al. Prognostic impact of primary tumor volume in patients with nasopharyngeal carcinoma treated by definitive radiation therapy. *Laryngoscope* 2008;118:1206–10 CrossRef Medline
- Kim JH, Lee JK. Prognostic value of tumor volume in nasopharyngeal carcinoma. *Yonsei Med J* 2005;46:221–27 CrossRef Medline
- Sze WM, Lee AW, Yau TK, et al. Primary tumor volume of nasopharyngeal carcinoma: prognostic significance for local control. *Int J Radiat Oncol Biol Phys* 2004;59:21–27 CrossRef Medline
- Chua DT, Sham JS, Leung LH, et al. Tumor volume is not an independent prognostic factor in early-stage nasopharyngeal carcinoma treated by radiotherapy alone. *Int J Radiat Oncol Biol Phys* 2004;58:1437–44 CrossRef Medline
- Chua DT, Sham JS, Kwong DL, et al. Volumetric analysis of tumor

- extent in nasopharyngeal carcinoma and correlation with treatment outcome. *Int J Radiat Oncol Biol Phys* 1997;39:711–19 CrossRef Medline
36. Lai SZ, Li WF, Chen L, et al. How does intensity-modulated radiotherapy versus conventional two-dimensional radiotherapy influence the treatment results in nasopharyngeal carcinoma patients? *Int J Radiat Oncol Biol Phys* 2011;80:661–68 CrossRef Medline
 37. Liao XB, Mao YP, Liu LZ, et al. How does magnetic resonance imaging influence staging according to AJCC staging system for nasopharyngeal carcinoma compared with computed tomography? *Int J Radiat Oncol Biol Phys* 2008;72:1368–77 CrossRef Medline
 38. Cheng SH, Tsai SY, Horng CF, et al. A prognostic scoring system for locoregional control in nasopharyngeal carcinoma following conventional radiotherapy. *Int J Radiat Oncol Biol Phys* 2006;66:992–1003 CrossRef Medline
 39. Kyriazi S, Collins DJ, Messiou C, et al. Metastatic ovarian and primary peritoneal cancer: assessing chemotherapy response with diffusion-weighted MR imaging—value of histogram analysis of apparent diffusion coefficients. *Radiology* 2011;261:182–92 CrossRef Medline
 40. Nowosielski M, Recheis W, Goebel G, et al. ADC histograms predict response to anti-angiogenic therapy in patients with recurrent high-grade glioma. *Neuroradiology* 2011;53:291–302 CrossRef Medline
 41. Yuan J, Yeung DK, Mok GS, et al. Non-Gaussian analysis of diffusion weighted imaging in head and neck at 3T: a pilot study in patients with nasopharyngeal carcinoma. *PLoS One* 2014;9:e87024 CrossRef Medline

Childhood Cerebral Adrenoleukodystrophy: MR Perfusion Measurements and Their Use in Predicting Clinical Outcome after Hematopoietic Stem Cell Transplantation

A.M. McKinney, J. Benson, D.R. Nascene, J. Eisengart, M.B. Salmela, D.J. Loes, L. Zhang, K. Patel, G.V. Raymond, and W.P. Miller



ABSTRACT

BACKGROUND AND PURPOSE: MR perfusion has shown abnormalities of affected WM in cerebral X-linked adrenoleukodystrophy, but serial data is needed to explore the import of such findings after hematopoietic stem cell transplantation. Our aim was to prospectively measure MR perfusion parameters in patients with cerebral adrenoleukodystrophy pre- and post-hematopoietic stem cell transplantation, and to correlate those measurements with clinical outcome.

MATERIALS AND METHODS: Ten patients with cerebral adrenoleukodystrophy prospectively underwent DSC-MR perfusion imaging at <45 days pre- (baseline), 30–60 days post-, and 1 year post-hematopoietic stem cell transplantation. MR perfusion measurements in the 10 patients and 8 controls were obtained from the parieto-occipital WM, splenium of the corpus callosum, leading enhancing edge, and normal-appearing frontal white matter. MR imaging severity scores and clinical neurologic function and neurocognitive scores were also obtained. MR perfusion values were analyzed in the patients with cerebral adrenoleukodystrophy at each time point and compared with those in controls. Correlations were calculated between the pre-hematopoietic stem cell transplantation MR perfusion values and 1-year clinical scores, with *P* value adjustment for multiple comparisons.

RESULTS: At baseline in patients with cerebral adrenoleukodystrophy, both relative CBV and relative CBF within the splenium of the corpus callosum and parieto-occipital WM significantly differed from those in controls ($P = .005-.031$) and remained so 1 year post-hematopoietic stem cell transplantation ($P = .003-.005$). Meanwhile, no MR perfusion parameter within the leading enhancing edge differed significantly from that in controls at baseline or at 1 year ($P = .074-.999$) or significantly changed by 1 year post-hematopoietic stem cell transplantation ($P = .142-.887$). Baseline Loes scores correlated with 1-year clinical neurologic function ($r = 0.813, P < .0001$), while splenium of the corpus callosum relative CBV also significantly correlated with 1-year neurologic function scale and the neurocognitive full-scale intelligence quotient and performance intelligence quotient scores ($r = -0.730-.815, P = .007-.038$).

CONCLUSIONS: Leading enhancing edge measurements likely remain normal post-hematopoietic stem cell transplantation in cerebral adrenoleukodystrophy, suggesting local disease stabilization. Meanwhile, parieto-occipital WM and splenium of the corpus callosum relative CBV and relative CBF values worsened; this change signified irreversible injury. Baseline splenium of the corpus callosum relative CBV may predict clinical outcomes following hematopoietic stem cell transplantation.

ABBREVIATIONS: ALD = adrenoleukodystrophy; cALD = cerebral X-linked adrenoleukodystrophy; HSCT = hematopoietic stem cell transplantation; K2 = the coefficient obtained by leakage correction of the dynamic bolus; LEE = leading edge of enhancement; MRP = MR perfusion; NAFWM = normal-appearing frontal white matter; PH = peak height; POWM = parietal-occipital white matter; *r* = relative; SCC = splenium of the corpus callosum

Adrenoleukodystrophy (ALD) is a rare, inherited peroxisomal disorder (1 in 20,000 live births); about 35% of males with ALD develop childhood-onset cerebral X-linked adrenoleu-

kodystrophy (cALD).¹⁻⁵ Hematopoietic stem cell transplantation (HSCT) can halt further demyelination and improve survival and neurologic function in cALD.⁶⁻¹⁰ While not fully elucidated, the therapeutic effect of HSCT may relate to relief of the inflamma-

Received December 6, 2015; accepted after revision February 8, 2016.

From the Departments of Radiology (A.M.M., J.B., D.R.N., M.B.S.) and Pediatrics (J.E., G.R.), Division of Clinical Behavioral Neuroscience, University of Minnesota Masonic Children's Hospital, Minneapolis, Minnesota; Suburban Radiologic Consultants (D.J.L.), Minneapolis, Minnesota; Clinical and Translational Science Institute (L.Z.), University of Minnesota, Minneapolis, Minnesota; Radiology Associates of the Fox Valley (K.P.), Neenah, Wisconsin; and Department of Pediatrics (W.P.M.), Pediatric Blood and Marrow Transplantation Division, University of Minnesota Amplatz Children's Hospital, Minneapolis, Minnesota.

This publication was supported by Grant Number 1UL1RR033183 from the National Center for Research Resources (NCRR) of the National Institutes of Health (NIH) to

the University of Minnesota Clinical and Translational Science Institute (CTSI). Its contents are solely the responsibility of the authors and do not necessarily represent the official views of CTSI or the NIH. University of Minnesota CTSI is part of a national Clinical and Translational Science Award consortium created to accelerate laboratory discoveries into treatments for patients.

Please address correspondence to Alexander M. McKinney, MD, Department of Radiology, Mayo Building, University of Minnesota, 420 Delaware St SE, Minneapolis, MN 55418; e-mail: mckinrad@umn.edu

Indicates open access to non-subscribers at www.ajnr.org

<http://dx.doi.org/10.3174/ajnr.A4773>

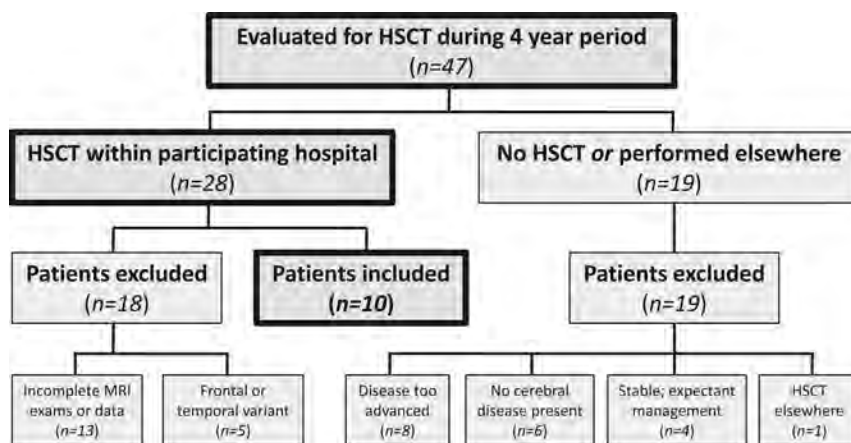


FIG 1. Organizational chart delineating how the 10 patients with cerebral ALD were included for MRP review from the initial 47 patients with ALD.

tion, which is the prominent histologic finding in untreated cALD.⁵ Most important, those with less cerebral disease are more likely to benefit from HSCT; thus, timely HSCT is critical.⁶⁻¹⁰

MR imaging of cALD is vital in predicting disease course and outcomes. The Loes MR imaging severity score, which quantifies the burden of WM disease, correlates with survival and neurologic outcomes after HSCT.⁶⁻¹⁰ The extent of enhancement on postcontrast T1WI, particularly the leading edge of enhancement (LEE), predicts disease progression in untreated cALD, suggesting that blood-brain barrier dysfunction plays a role in cALD.^{3,11,12} Thus, monitoring the LEE and noting that it is halted may be important in defining treatment response.

DSC-MR perfusion parameters such as relative CBV (rCBV), relative CBF (rCBF), relative TTP (rTTP), relative peak height (rPH), and dynamic leakage correction coefficient (K2) can reflect the pathophysiology of various disorders.¹²⁻¹⁷ Elevated CBV reflects high capillary permeability, while low CBV suggests irreversibly injured tissue.¹²⁻¹⁷ CBF reflects tissue perfusion, being increased in high-grade tumors or inflammation, while TTP elevation indicates a delay in perfusion.¹²⁻¹⁷ Peak height is the signal-intensity change from the baseline of a dynamic enhancement curve, while K2 is the coefficient obtained by leakage correction of the dynamic bolus, reflecting permeability at sites of blood-brain barrier injury.^{14,17}

Scant literature exists regarding MRP parameters in cALD at baseline or how they change following HSCT; 1 sole study of 8 patients noted low rCBV within the core of nonenhancing parietal-occipital white matter (POWM) at baseline, while within the LEE rCBV was preserved.¹² However, other MRP parameters should be explored, and the prognostic impact of baseline (pre-HSCT) regional DSC-MRP parameters on outcome is of primary importance. Thus, according to these limited prior data, the hypothesis of this study was that MRP parameters, in particular rCBV, would be abnormal in the POWM and perhaps the splenium of the corpus callosum, compared with these parameters in controls, while perfusion within the LEE would be preserved following successful HSCT. Hence, the aims of this study were the following: 1) to determine whether MRP parameters at baseline in various regions of the cALD-affected brain differ from those of controls, 2) to describe several MRP parameters on the pre- and

post-HSCT cALD MR imaging, and 3) to determine whether any of the measured baseline (pre-HSCT) MRP parameters in various locations correlate with the neurologic outcomes.

MATERIALS AND METHODS

Patient Selection

Institutional review board approval was obtained for this study; all patients were enrolled after informed consent. MR imaging examinations were performed at 3 time points relative to transplantation: baseline pre-HSCT (<45 days before transplantation), 30–60 days post-HSCT, and 1 year post-HSCT. There was retrospective measurement of the DSC-MRP values. Patients with cALD

were included if they met all of the following criteria: 1) biochemical confirmation of ALD, 2) posterior-type cALD variant (the most common type), 3) clinical and neurocognitive evaluations both at baseline and at 1 year, 4) HSCT being performed between January 2010 and January 2014, 5) younger than 18 years of age and, 6) each MR imaging study adequate for the MRP evaluation (Fig 1). Eight male controls were assessed for DSC-MRP values. Controls lacked any cerebral abnormality on MR imaging (which was typically performed to evaluate the skull base or upper neck), had no previous radiation or chemotherapy, and were matched to the ages of patients with cALD at pre-HSCT (baseline) MR imaging.

MR Imaging Acquisition Technique

The 3T MR imaging protocol included FLAIR, precontrast 3D T1WI, and postcontrast 3D T1WI. Noncontrast 3D T1WI, necessary for coregistration, used an MPRAGE sequence: TR/TE/NEX/FOV/parallel factor, 1810/3.5 ms/1/230 mm/2; 0.9 × 0.9 × 0.9 mm isotropic voxel; and 6-minute acquisition.¹⁸ For postcontrast 3D T1WI, an intravenous 0.1-mmol/kg of body weight–based dose of gadopentetate dimeglumine (Magnevist; Bayer HealthCare Pharmaceuticals, Wayne, New Jersey) was administered at 4 mL/s for a 10-mL maximum dose (Figs 2–4). The echo-planar DSC-MRP parameters were the following: TR/TE/NEX/FOV/parallel factor, 1500/43 ms/1/230 mm/0; 1.8 × 1.8 × 5 mm voxel size; and approximately 1-minute acquisition. The postcontrast 3D T1WI sequence was identical to that of the noncontrast 3D T1WI, being initiated at approximately 10 minutes after the contrast injection.

MRP Postprocessing and Review

The postprocessing of 38 total DSC-MRP examinations (10 patients with cALD with 3 time points each; 8 controls with 1 study each) was retrospectively processed on a DynaSuite Neuro MR Workstation (Invivo, Gainesville, Florida) by a staff neuroradiologist (A.M.M., with >10 years' experience in pediatric neuroimaging) who was blinded to the clinical data. The noncontrast 3D T1WI and FLAIR images were automatically coregistered with the DSC-MRP maps by the postprocessing software and were confirmed visually, with both a neuroradiology fellow and radiology

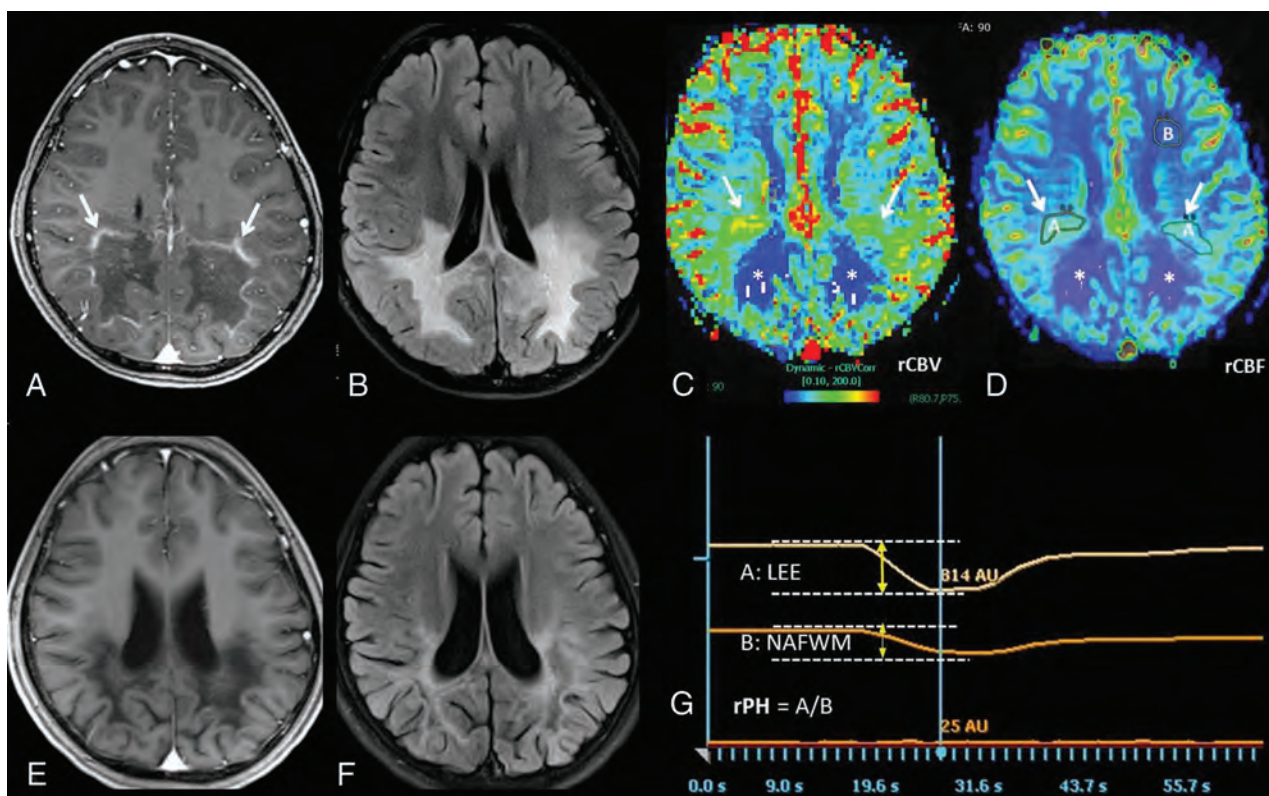


FIG 2. Example of DSC-MRP measurements in a 10-year-old boy with cALD. Baseline (pre-HSCT) MR images show the LEE (arrows) on postcontrast TIWI (A), with typical findings of posterior-type cALD on FLAIR at that time (B). On DSC-MRP at that time, both rCBV (C) and rCBF (D) are mildly elevated at the LEE (arrows) but appear low centrally within the POWM (asterisks). G, The method of relative peak height measurement within the LEE and NAFWM ROIs on the baseline (pre-HSCT) MR imaging examination, via measurement of the dynamic contrast curve. Follow-up MR imaging at 1 year shows that the LEE has resolved on postcontrast TIWI (E) and that the WM abnormalities did not progress on FLAIR (F), though moderate overlying parieto-occipital-predominant atrophy has ensued, with interval sulcal enlargement.

resident present to aid in confirming the adequacy of the coregistration, the presence/absence of contrast enhancement, and the ROI site. Freehand ROIs of ≥ 5 -mm diameter were measured centrally within the normal-appearing frontal white matter (NAFWM) and within 3 affected sites: the POWM, centrally within the splenium of the corpus callosum (SCC), and the visibly enhancing LEE (such enhancing regions occurred within areas of FLAIR abnormality in either the POWM or SCC) as demonstrated in Figs 2–4.^{3,11,12} At least 3 ROIs were measured at each site, and the mean was recorded; if lesions were bilateral, the mean of 6 ROIs (3 ROIs on each side) was used. In controls, normal POWM was substituted for the LEE measurement because no enhancement was present. Notably, LEE lesions being either bilateral, unilateral, or midline prevented a side-to-side comparison of MRP values and thus necessitated the incorporation of measurements for both sides for a conglomerate mean of at least 3 MRP parameter values.

After ROI placement, leakage-corrected CBV, CBF, TTP, and K2 maps were automatically generated in patients and controls, while PH was calculated by manual analysis of the dynamic contrast curve (Fig 2).^{13–18} Regarding the LEE, because enhancement typically resolves following HSCT for cALD, the post-HSCT MR images were automatically coregistered to the pre-HSCT MR images, with visual confirmation to ensure that the same anatomic site of the LEE was measured across time. Relative values of each parameter were calculated from the POWM, SCC, or LEE by di-

viding by the value of that parameter with the measurement obtained from NAFWM; the exception was that only raw K2 was recorded because relative K2 cannot be calculated given its zero value within the NAFWM.

MR Imaging Severity Scoring (Loes Score)

Two neuroradiologists with >5 years' experience with cALD (D.J.L., D.R.N.) reviewed the FLAIR images by consensus to generate MR imaging severity (Loes) scores. This review was performed according to the method of prior studies.^{8,19} Both neuroradiologists were blinded to the clinical data.

Measurement of Clinical Outcome

The gross neurologic function at baseline (pre-HSCT) and 1 year post-HSCT was determined by using a previously described 25-point cALD severity neurologic function scale; notably, increasing scores on the scale denotes worsening function.^{9,10} For the cALD cohort, the neurologic function scale was retrospectively constructed from detailed clinical assessments in the medical record by a pediatric HSCT specialist (W.P.M.).^{9,10,19} Neurocognitive scores from the Wechsler Intelligence Scale Series, including full-scale intelligence quotient, performance intelligence quotient, and verbal intelligence quotient, were prospectively obtained by dedicated examination from 1 of several neuropsychologists both pre-HSCT and at 1 year, as described previously.^{19–21} Both the pediatric transplantation specialist

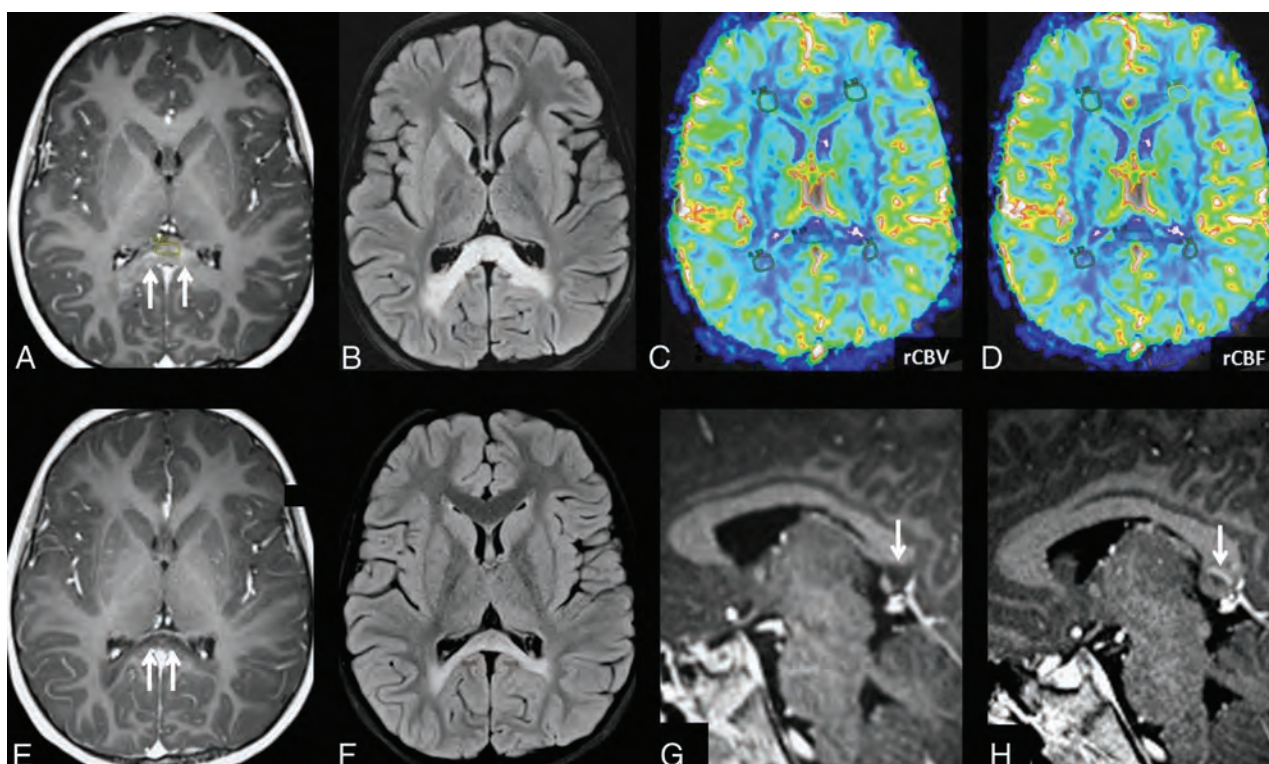


FIG 3. A 6-year-old boy with cALD. Pre-HSCT, a LEE (arrows) is present along the anterior SCC on postcontrast TIWI (A), with edema on FLAIR within the SCC and, to a lesser degree, within the POWM (B). Also at baseline, the CBV (C) and CBF (D) maps demonstrate ROIs obtained from the NAFWM, POWM, and SCC. After HSCT, on 1-year follow-up postcontrast TIWI (E), the LEE has disappeared, with decreased swelling and no worsening of the extent on FLAIR (F). Note that the sagittal postcontrast TIWI at 1 year (G) demonstrates the disappearance of the enhancing LEE (arrow) within the SCC, compared with the initial postcontrast image at baseline (H).

and the neuropsychologists were blinded to the MR imaging data.

Statistical Analysis

Mann-Whitney tests were used to assess differences between patients with cALD and controls regarding the regional DSC-MRP values at each MR imaging time point (notably, the MRP values at a single time point in controls were compared for each of the 3 cALD cohort time points). Inpatient pre- and post-HSCT MRP values were compared via the linear mixed model, with *P* value adjustment for multiple comparisons applied by using the Tukey method. Both the pre-HSCT (baseline) MRP values and the Loes scores were correlated with the 1-year clinical outcome functional and neurocognitive scores (neurologic function scale, full-scale intelligence quotient, performance intelligence quotient, and verbal intelligence quotient) by the Spearman method. Statistical analyses were performed by using SAS software (Version 9.3; SAS Institute, Cary, North Carolina). The significance threshold was set to $P < .05$.

RESULTS

Ten boys with cALD were ultimately included for analysis from the initial population of 47 males with ALD who were evaluated in the clinic during the same period. Reasons for exclusion are provided in Fig 1. Neither the baseline ages nor the Loes scores differed between the included and excluded patients (both $P > .05$). The mean age at baseline MR imaging for the 10 patients was 8.2 ± 2.7 years (range, 5–14 years), and for controls, it was $7.8 \pm$

3.2 years (range, 4–12 years); these ages were not significantly different ($P = .748$). During the study period, none of the 10 patients with cALD incurred other cerebral pathology that confounded the DSC-MRP evaluation. The mean MRP measurements for the cALD cohort at all 3 time points are provided, with *P* values when comparing with controls, in Table 1.

Regarding the SCC, both rCBV and rCBF were significantly less in patients than in controls at both baseline and 1-year post-HSCT (Table 1). At the 30- to 60-day post-HSCT time point, only rPH significantly differed between patients and controls. As for inpatient rCBV and rCBF, both parameters decreased from pre- to 1-year post-HSCT by 5.6% and 10.0%, respectively; however, such changes were not statistically significant between the 2 time points for either parameter ($P = .057-.076$).

As for the POWM, there were significant differences between the patients with cALD and controls; rCBV, rCBF, and rTTP differed significantly between patients and controls at all 3 time points (Table 1). Within the cALD cohort, both inpatient rCBV and rCBF decreased from the pre- (baseline) to 1-year post-HSCT time points by 30.7% and 33.0%, respectively; however, these were not found to be significantly different between the 2 time points for either parameter ($P = .101-.118$).

All patients had an enhancing LEE before HSCT, and each had resolution of that visibly enhancing edge by 1 year post-HSCT (Figs 2–4). Within the LEE, the day 30–60 rPH was the only MRP parameter that differed significantly between the 10 patients with cALD and controls, while the pre- (baseline) and 1-year post-

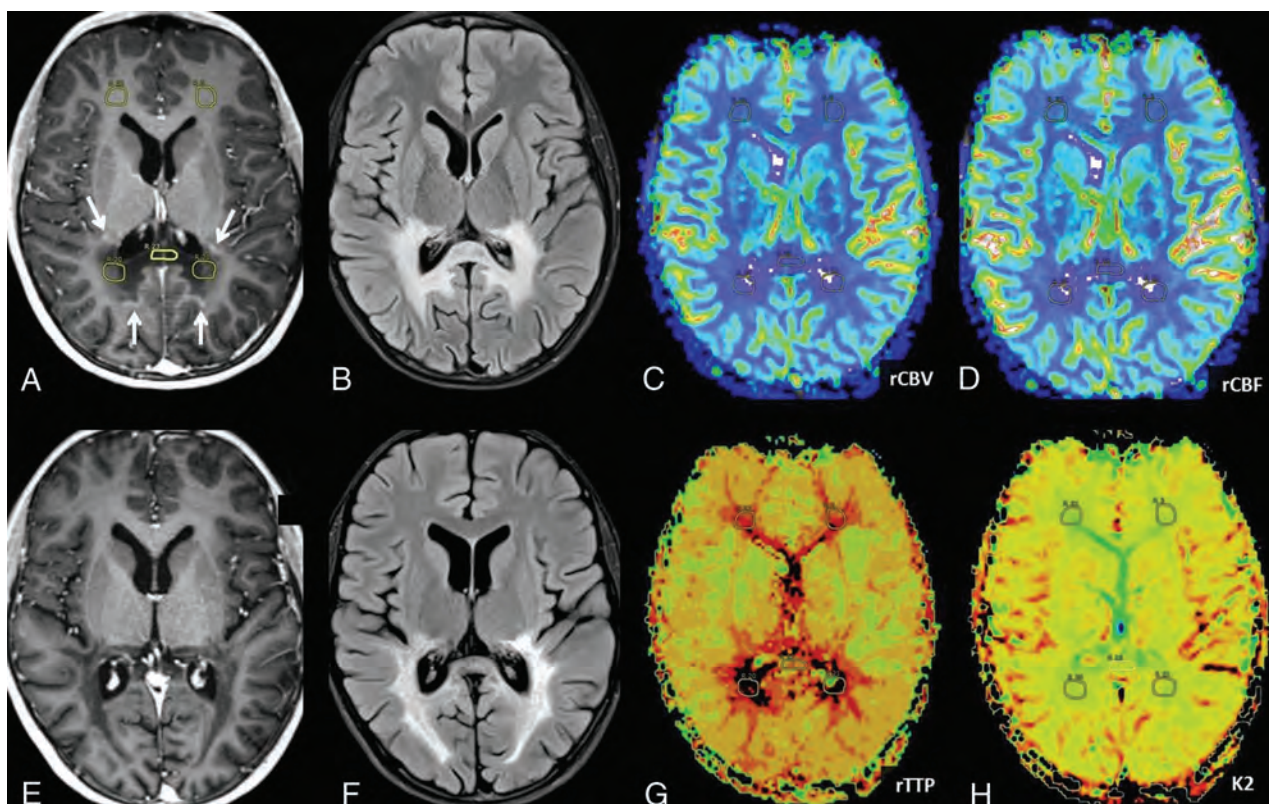


FIG 4. A 15-year-old adolescent boy with ALD. Pre-HSCT postcontrast TIWI (A) demonstrates a LEE (arrows) in the POWM and optic radiations, with edema on noncontrast FLAIR (B). Baseline pre-HSCT ROIs from the NAFWM, POWM, and SCC are depicted on postcontrast TIWI (A) and on the MRP CBV (C), CBF (D), TTP (G), and K2 (H) maps. After HSCT, the 1-year follow-up MR imaging demonstrates resolution of the LEE on postcontrast TIWI (E), with no overt change in the extent of abnormality on FLAIR (F), though mild-moderate cerebral atrophy has ensued, being more prominent within the SCC.

Table 1: Mean of DSC-MRP parameters with *P* values comparing patients with ALD with controls at each time^a

DSC-MRP Parameter	Pre-HSCT		Post-HSCT (30–60 Days)		Post-HSCT (1 year)	
	Mean	<i>P</i> Value versus Controls	Mean	<i>P</i> Value versus Controls	Mean	<i>P</i> Value versus Controls
SCC: rCBV	0.71 ± 0.32	.005 ^b	1.02 ± 0.47	.404	0.67 ± 0.25	.005 ^b
SCC: rCBF	0.70 ± 0.34	.005 ^b	1.00 ± 0.47	.553	0.63 ± 0.24	.003 ^b
SCC: rTTP	0.26 ± 1.83	.813	0.13 ± 1.51	.887	0.35 ± 2.94	.377
SCC: rPH	0.96 ± 0.38	.093	0.85 ± 0.30	.025 ^b	0.82 ± 0.36	.019 ^b
SCC: K2	0.004 ± 0.001	.177	0.00 ± 0.00	.824	0.00 ± 0.00	.999
POWM: rCBV	0.72 ± 0.30	.031 ^b	0.63 ± 0.31	.004 ^b	0.50 ± 0.40	.004 ^b
POWM: rCBF	0.70 ± 0.27	.023 ^b	0.61 ± 0.30	.004 ^b	0.47 ± 0.34	.004 ^b
POWM: rTTP	1.92 ± 1.46	.007 ^b	1.95 ± 0.95	<.001 ^b	0.42 ± 5.22	.043 ^b
POWM: rPH	1.19 ± 0.26	.092	0.92 ± 0.34	.552	0.87 ± 0.38	.238
POWM: K2	0.002 ± 0.003	.662	0.00 ± 0.00	.999	0.00 ± 0.00	.999
LEE: rCBV	1.38 ± 0.63	.168	1.43 ± 0.62	.301	1.25 ± 0.48	.618
LEE: rCBF	1.39 ± 0.64	.153	1.43 ± 0.66	.651	1.28 ± 0.46	.554
LEE: rTTP	0.24 ± 1.34	.982	−0.11 ± 0.88	.432	−1.29 ± 3.76	.601
LEE: rPH	1.62 ± 0.67	.074	1.43 ± 0.43	.020 ^b	1.12 ± 0.46	.459
LEE: K2	0.004 ± 0.005	.177	0.00 ± 0.00	.662	0.003 ± 0.004	.999

^a The relative MRP ratios in patients with ALD compared with NAFWM.

^b *P* values <.05.

HSCT values did not (Table 1). Regarding the LEE within the cALD cohort, the inpatient rCBV and rCBF both decreased by 9.4% and 7.9%, respectively, though neither these nor any other measured MRP parameter changed significantly between the baseline and 1-year time points (*P* = .142–.887).

Regarding the Loes MR imaging severity scores, the mean Loes scores at each time point for the cALD cohort (based on FLAIR) were 6.35 ± 5.5 at baseline (pre-HSCT), 6.40 ± 5.5 at 30–60 days

post-HSCT, and 7.90 ± 5.6 on the 1-year follow-up MR imaging examinations. As would be expected on the basis of prior literature, the pre-HSCT Loes score strongly correlated with the 1-year clinical neurologic function scale score (*r* = 0.813, *P* < .0001).^{9,10,19} Regarding the neurocognitive measures, moderate correlations existed between the baseline Loes score and the 1-year neurocognitive full-scale intelligence quotient, performance intelligence quotient, and verbal intelligence quotient

Table 2: Correlations between both the pre-HSCT MRI severity and MRP parameters with the 1-year follow-up clinical outcome scores^a

Parameter	NFS	FSIQ	PIQ	VIQ
SCC: rCBV	−0.730, .016 ^b	0.735, .038 ^b	0.815, .007 ^b	0.500, .171
SCC: rCBF	−0.451, .191	0.590, .123	0.678, .045 ^b	0.233, .546
SCC: rTTP	−0.291, .414	0.205, .627	0.033, .932	0.400, .286
SCC: rPH	0.118, .745	−0.012, .977	0.059, .881	−0.017, .966
POWM: rCBV	−0.555, .096	0.325, .432	0.301, .431	0.367, .332
POWM: rCBF	−0.557, .095	0.325, .432	0.301, .431	0.360, .342
POWM: rTTP	0.569, .086	−0.663, .073	−0.619, .075	−0.550, .125
POWM: rPH	−0.326, .358	−0.036, .932	−0.126, .748	0.250, .517
LEE: rCBV	0.045, .901	−0.217, .606	−0.126, .748	−0.326, .391
LEE: rCBF	−0.090, .804	0.024, .955	0.042, .915	−0.017, .967
LEE: rTTP	0.083, .819	−0.217, .606	−0.226, .559	−0.150, .700
LEE: rPH	0.111, .760	−0.506, .201	−0.452, .222	−0.250, .517
Loes score	0.813, <.0001 ^b	−0.646, .084	−0.633, .068	−0.596, .090

Note:—NFS indicates neurologic function scale; FSIQ, full-scale intelligence quotient; PIQ, performance intelligence quotient; VIQ, verbal intelligence quotient.

^a Numbers are rounded to the one-thousandth place. In addition, the correlations for K2 are not shown because most measurements were 0.00.

^b *P* values < .05.

scores, but these did not reach clinical significance ($r = -0.596$ to -0.646 , $P = .068-.090$) after correction for multiple comparisons (Table 2).

Regarding correlating the baseline DSC-MRP parameters with the functional and neurocognitive scores at 1 year post-HSCT, the only parameters that correlated with the clinical and neurocognitive outcomes were rCBV and rCBF within the SCC (Table 2). In particular, baseline SCC rCBV had an inverse, significant correlation with the clinical neurologic function scale score at 1 year ($r = -0.730$, $P = .016$) and a positive correlation with the neurocognitive scores full-scale intelligence quotient ($r = 0.735$, $P = .038$) and performance intelligence quotient ($r = 0.815$, $P = .007$); there was a positive, significant correlation also found between baseline SCC rCBF and performance intelligence quotient ($r = 0.678$, $P = .045$). Notably, no significant correlation was found between any regional MRP parameter and the 1-year neurocognitive verbal intelligence quotient scores, after correction for multiple comparisons. Additionally, no MRP measure within the POWM or LEE significantly correlated with the 1-year neurologic function scale or neurocognitive outcome scores (each $P > .05$).

DISCUSSION

Because childhood cALD is typically a progressive and severe disorder in the absence of HSCT, the primary goals of this study were the following: 1) to determine whether MRP parameters differ from those in controls in various regions of the cALD-affected brain, 2) to describe a variety of DSC-MRP parameters both pre- and post-HSCT, and 3) to determine whether any baseline (pre-HSCT) MRP markers portend the clinical outcome following HSCT.⁶⁻¹⁰ Regarding the former goal, both this study and that of Musolino et al¹² seem to be in accord, because this study confirms that in untreated cALD, rCBV within the “core” of nonenhancing POWM but not the LEE is significantly lower than that in controls. In our transplanted cohort, this difference in rCBV from controls persisted at 1 year following HSCT. Such findings indicate that the core of abnormal POWM (termed “Zone A” in the prior study by Musolino et al¹²) likely comprises severely injured and perhaps nonviable tissue. Accordingly, slowly progressing parieto-occipital regional atrophy typically develops in this region,

which was also observed in the current study.¹² Meanwhile, the arrest of enhancement at the LEE, along with the preserved rCBV and rCBF at 1 year post-HSCT, would imply viable tissue therein. Notably, in our cohort, the POWM rCBV was, on average, about 50% of that of the NAFWM, whereas the rCBV was about 20% of that of the NAFWM in the prior study.¹² This difference in rCBV could relate to the higher mean Loes score (13.4 versus 6.4 in this study) in the prior study, perhaps reflecting more severe tissue injury overall.¹²

The mechanism of how HSCT attenuates the neuroinflammation in cALD is unknown; however, the normal rCBV within the LEE that persists after HSCT

suggests a correction of the blood-brain barrier abnormality, along with preservation of regional parenchyma.^{3,5,10-12} Similarly, the study by Musolino et al¹² found that rCBV was preserved in the LEE (termed “Zone B”) but was lower in adjacent, centrifugally located areas (Zone C); hence, the current study corroborates the Zone B findings of that study. Such an arrest in demyelination may have a histopathologic precedent, in which murine studies have shown that certain microglial cells are absent initially at the demyelinating edge, but there is a subsequent slow return of microglial guard cells by about 1 year post-HSCT as progression of the disease halts.²²⁻²⁶ Thus, 1 theory, which remains speculative, is that blood-brain barrier dysfunction is actually helpful or is required for the marrow-derived precursor cells to return into the cerebrum and differentiate into microglia because a LEE is nearly always present before HSCT in those patients who have undergone a successful HSCT and ultimately have stabilized cerebral disease.²²⁻²⁶ Thus, this theory suggests that microglia reflect an overall return of hematopoietic precursor stem cells to the cerebrum, resulting in the observed disease arrest, along with the subsequent repair.²²⁻²⁶ Zonal measurements within and adjacent to the LEE were not the focus of the current study but could be considered in future ones.

Regarding the SCC, this aforementioned theory may, at least in part, explain the lack of a significant difference in the large majority of the various MRP measures at 30–60 days post-HSCT, even though there were significant differences at baseline and at 1 year post-HSCT (especially in rCBV and rCBF).²²⁻²⁶ Thus, we surmise that there could be both components of irreversible injury and healing of the blood-brain barrier occurring macroscopically in the SCC, which may be an “inflection point” in the disease process. For example, according to the above-mentioned theory, HSCT can correct the underlying microglial dysfunction by way of bone marrow resident and progenitor cells entering the cerebrum through a patent and abnormal blood-brain barrier via capillary recruitment and resultant increased microperfusion; we opine that this might be represented by a transient relatively decreased rTTP and relatively increased rCBV and CBF.²²⁻²⁶ In the current study, such transient changes (ie, increased rCBF and rCBV) were indeed noted in the SCC, where the rTTP transiently

decreased at 30–60 days post-HSCT and then rose again to above baseline at 1 year post-HSCT. However, by 1 year post-HSCT, both SCC rCBF and rCBV decreased to below baseline, suggesting that such increased perfusion at 30–60 days post-HSCT was indeed only a temporary phenomenon.

Hence, the measurements at 30–60 days post-HSCT might reflect an attempt for the cerebrum to undergo healing by temporarily increasing perfusion to the SCC by a vascular response, though there is also likely a component of underlying irreversible injury, as evidenced by the lower 1-year rCBV and rCBF values. If so, then this combination of findings might explain the SCC being the 1 site where the baseline DSC-MRP measurements predict the neurocognitive outcomes (hence, the term “inflection point”) because it is a region that has both viable tissue that can potentially be saved, along with nonviable tissue. In contrast, the POWM appears to be a region where the tissue injury is largely irreversible, as evidenced by the lack of such transient findings at 30–60 days post-HSCT. Accordingly, within the POWM, rTTP remained higher and rCBV and rCBF both progressively decreased after HSCT. Thus, the POWM seems mostly unaffected by successful transplantation.

This study also found that the baseline SCC rCBV and rCBF values strongly correlated with various measures of neurologic function at 1 year after successful HSCT, perhaps due to the reasons described above. While the Loes MR imaging score is known to correlate with the gross neurologic outcome after HSCT, the findings in the current study suggest that regional DSC-MRP values could augment the Loes score in predicting outcomes better.^{7–11} However, this study was limited, in that most boys within the cohort had generally favorable baseline Loes scores. Hence, these findings may not be applicable to those patients with more severe initial disease. Thus, the utility of MRP in predicting outcomes in patients with cALD with more severe disease needs to be further studied.

There has been an ongoing search for the best baseline (pre-HSCT) imaging marker of clinical outcome following transplantation (HSCT). Regarding such biomarkers, to our knowledge, the Loes score is the most reproducible and strongest predictor of outcome, being proved across multiple centers.^{6–10} While the Loes score is a “continuous” marker of radiographic severity between 0.5 (minimum nonzero score) and 34 (maximum score), its predictive value mostly rests on a binary correlation with quite broad outcomes. Specifically, boys with a score of <10 generally do well after HSCT, while those with a Loes ≥ 10 generally do poorly after transplantation. Thus, there is a need for imaging biomarkers within both subgroups of less affected (ie, Loes of <10) and more severely affected (ie, Loes of ≥ 10) patients at baseline. Thus, to our knowledge, there has been no baseline imaging biomarker within the less affected subgroup shown to correlate with eventual posttransplantation neurocognition; the current data suggest that DSC-MRP could be of some utility in this subgroup. Meanwhile, within a subgroup of patients with higher Loes scores (≥ 10), a recent study found that the intensity of visible enhancement on postcontrast T1WI may lend predictive value to clinical outcome, and this was found to be relatively simple to measure, as well as reproducible between observers.²⁷

Limitations of this study include the relatively small size of the patient cohort with cALD. Thus, the expense of travel, care, and MR imaging for multiple trips is a known factor contributing to

this limitation.¹⁹ Similarly, it is difficult to obtain a large number of age-matched controls for MRP because most pediatric indications for MR imaging do not necessitate contrast. A third potential limitation was the use of relative rather than absolute perfusion measurements; however, relative measurements of CBV or CBF are typically more reproducible than absolute ones.^{15,16} Additionally, a limitation could be the lack of interobserver reliability calculations between readers regarding the 3+ ROI placements (6+ if the measurement was bilateral) and subsequent MRP values obtained. However, it was not feasible to have 2 readers, given the expertise needed in interpretation of cALD along with familiarity with the postprocessing software for coregistration and MRP calculation; such postprocessing steps including the MRP measurements and calculations were too exhaustive and time-consuming for multiple readers. Particularly, the numerous steps in this process could inherently cause variability among observers.

Finally, a limitation may be that the patient cohort of this study demonstrated relatively low pretransplantation Loes scores (eg, compared with a study by Musolino et al¹²), while there was no significant difference in scores between the excluded ($n = 37$) and included cohort ($n = 10$); this could raise the question of an underlying selection bias in our patient pool.^{6–12} Thus, factors that decreased the mean Loes score in the excluded group were that 6 patients had no cerebral disease (Loes score of 0), while 4 were stable (having very low Loes scores near zero); however, this apparent lowering in mean Loes score at baseline may, to some degree, be counterbalanced because some of the excluded patients had disease too severe to be transplanted ($n = 8$) or they did not travel back after transplantation for each MR imaging due to severe dysfunction ($n = 13$) (Fig 1).

Meanwhile, among the 10 included patients, the mean Loes score was relatively low because those with very high scores are very unlikely to undergo transplantation, for example, compared with the prior study by Musolino et al,¹² which focused on patients with higher mean Loes scores. Hence, there may be an inherent selection bias in this study because those with much higher Loes scores are not likely to undergo HSCT and thus would be excluded, while those patients who did undergo HSCT but were too sick or dysfunctional to travel and return for an adequate follow-up MR imaging were also likely to be excluded. Therefore, as mentioned previously, the findings of this study regarding the clinical response to HSCT cannot be generalized to the subset of patients with cALD who present with much higher Loes MR imaging severity scores on initial evaluation for HSCT. The prediction of outcomes, based on MRI, may be better addressed by gadolinium-intensity measurements, which has been a focus of a recent study by Miller et al.²⁷

CONCLUSIONS

This study found that certain DSC-MRP values in patients with cALD, as measured within the POWM and SCC pre-HSCT, are significantly different from those in controls, while the LEE values are not. With time, rCBV within the LEE remained normal in the patients with cALD relative to controls. This outcome suggests stabilization of a dysfunctional blood-brain barrier at the LEE; conversely, the finding that rCBV worsens within the POWM following HSCT suggests irreversible injury. This study also found that the rCBV is the only baseline MRP measurement that

seems to be a reliable predictor of clinical outcome. Thus, MRP could be a useful adjunct to the Loes MR imaging severity score in predicting the functional and neurocognitive outcomes of boys with cALD with lower Loes scores who are to undergo HSCT.

Disclosures: Alexander M. McKinney—UNRELATED: Board Membership: Vital Images, a division of Toshiba Medical, Minneapolis, Minnesota, Comments: less than \$5000 reimbursement for travel and consultation per year; Expert Testimony: legal consultation, less than \$10,000 total this year. Daniel J. Loes—UNRELATED: Consultancy: Bluebird Bio, Comments: consultant for Bluebird Bio research Phase 2 and Phase 3 trials involving viral vector gene therapy for adrenoleukodystrophy; Gerald Raymond—UNRELATED: Consultancy: Minoryx (Barcelona, Spain), Comments: consultant for a company developing products to treat adult adrenoleukodystrophy; Expert Testimony: Department of Health and Human Services, Comments: served as expert in the Division of Vaccine Injury; Grants/Grants Pending: Bluebird Bio (Cambridge, Massachusetts). * Comments: participating in industry-funded research in ALD gene therapy. *Money paid to the institution.

REFERENCES

- Moser HW, Smith KD, Watkins PA, et al. **X-linked adrenoleukodystrophy**. In: Scriver CR, Beaudet AL, Sly WS, et al, eds. *The Metabolic and Molecular Bases of Inherited Disease*. 8th ed. New York: McGraw-Hill; 2001:3257–301
- Bezman L, Moser HW. **Incidence of X-linked adrenoleukodystrophy and the relative frequency of its phenotypes**. *Am J Med Genet* 1998;76:415–19 Medline
- Melhem ER, Loes DJ, Georgiades CS, et al. **X-linked adrenoleukodystrophy: the role of contrast-enhanced MR imaging in predicting disease progression**. *AJNR Am J Neuroradiol* 2000;21:839–44 Medline
- Schaumburg HH, Powers JM, Raine CS, et al. **Adrenoleukodystrophy: a clinical and pathological study of 17 cases**. *Arch Neurol* 1975;33:577–91 Medline
- Powers JM, Pei Z, Heinzer AK, et al. **Adreno-leukodystrophy: oxidative stress of mice and men**. *J Neuropathol Exp Neurol* 2005;64:1067–79 CrossRef Medline
- Shapiro E, Krivit W, Lockman L, et al. **Long-term effect of bone-marrow transplantation for childhood onset cerebral X-linked adrenoleukodystrophy**. *Lancet* 2000;356:713–18 CrossRef Medline
- Peters C, Charnas LR, Tan Y, et al. **Cerebral X-linked adrenoleukodystrophy: the international hematopoietic cell transplantation experience from 1982 to 1999**. *Blood* 2004;104:881–88 CrossRef Medline
- Loes DJ, Hite S, Moser H, et al. **Adrenoleukodystrophy: a scoring method for brain MR observations**. *AJNR Am J Neuroradiol* 1994;15:1761–66 Medline
- Miller WP, Rothman SM, Nascene D, et al. **Outcomes following allogeneic hematopoietic cell transplantation for childhood cerebral adrenoleukodystrophy: the largest single-institution cohort report**. *Blood* 2011;118:1971–78 CrossRef Medline
- Moser H, Raymond G, Koehler W, et al. **Evaluation of the preventive effect of glyceryl trioleate-trierycate (“Lorenzo’s oil”) therapy in X-linked adrenoleukodystrophy: results of two concurrent trials**. *Adv Exp Med Biol* 2003;544:369–87 CrossRef Medline
- Loes DJ, Fatemi A, Melhem ER, et al. **Analysis of MRI patterns aids prediction of progression in X-linked adrenoleukodystrophy**. *Neurology* 2003;61:369–74 CrossRef Medline
- Musolino PL, Rapalino O, Caruso P, et al. **Hypoperfusion predicts lesion progression in cerebral X-linked adrenoleukodystrophy**. *Brain* 2012;135:2676–83 CrossRef Medline
- Grandin CB, Duprez TP, Smith AM, et al. **Which MR-derived perfusion parameters are the best predictors of infarct growth in hyperacute stroke? Comparative study between relative and quantitative measurements**. *Radiology* 2002;223:361–70 CrossRef Medline
- Cha S, Lupo JM, Chen MH, et al. **Differentiation of glioblastoma multiforme and single brain metastasis by peak height and percentage of signal intensity recovery derived from dynamic susceptibility-weighted contrast-enhanced perfusion MR imaging**. *AJNR Am J Neuroradiol* 2007;28:1078–84 CrossRef Medline
- Knopp EA, Cha S, Johnson G, et al. **Glial neoplasms: dynamic contrast-enhanced T2*-weighted MR imaging**. *Radiology* 1999;211:791–98 CrossRef Medline
- Wetzel SG, Cha S, Johnson G, et al. **Relative cerebral blood volume measurements in intracranial mass lesions: interobserver and intraobserver reproducibility study**. *Radiology* 2002;224:797–803 CrossRef Medline
- Brubaker LM, Smith JK, Lee YZ, et al. **Hemodynamic and permeability changes in posterior reversible encephalopathy syndrome measured by dynamic susceptibility perfusion-weighted MR imaging**. *AJNR Am J Neuroradiol* 2005;26:825–30 Medline
- Boxerman JL, Schmainda KM, Weisskoff RM. **Relative cerebral blood volume maps corrected for contrast agent extravasation significantly correlate with glioma tumor grade, whereas uncorrected maps do not**. *AJNR Am J Neuroradiol* 2006;27:859–67 Medline
- McKinney AM, Nascene D, Miller WP, et al. **Childhood cerebral X-linked adrenoleukodystrophy: diffusion tensor imaging measurements for prediction of clinical outcome after hematopoietic stem cell transplantation**. *AJNR Am J Neuroradiol* 2013;34:641–49 CrossRef Medline
- Wechsler D. *Wechsler Intelligence Scale for Children-Fourth Edition (WISC-IV)*. San Antonio: Psychological Corporation; 2003
- Riva D, Bova SM, Bruzzone MG. **Neuropsychological testing may predict early progression of asymptomatic adrenoleukodystrophy**. *Neurology* 2000;54:1651–55 CrossRef Medline
- Cartier N, Aubourg P. **Hematopoietic stem cell transplantation and hematopoietic stem cell gene therapy in X-linked adrenoleukodystrophy**. *Brain Pathol* 2010;20:857–62 CrossRef Medline
- Eichler FS, Ren JQ, Cossoy M, et al. **Is microglial apoptosis an early pathogenic change in cerebral X-linked adrenoleukodystrophy?** *Ann Neurol* 2008;63:729–42 CrossRef Medline
- Cartier N, Hacein-Bey-Abina S, Bartholomae CC, et al. **Hematopoietic stem cell gene therapy with a lentiviral vector in X-linked adrenoleukodystrophy**. *Science* 2009;326:818–23 CrossRef Medline
- Kennedy DW, Abkowitz JL. **Kinetics of central nervous system microglial and macrophage engraftment: analysis using a transgenic bone marrow transplantation model**. *Blood* 1997;9:986–93 Medline
- Mildner A, Mack M, Schmidt H, et al. **CCR2 + Ly-6Chi monocytes are crucial for the effector phase of autoimmunity in the central nervous system**. *Brain* 2009;132:2487–500 CrossRef Medline
- Miller WP, Mantovani LF, Muzic J, et al. **Intensity of MRI gadolinium enhancement in cerebral adrenoleukodystrophy: a biomarker for inflammation and predictor of outcome following transplantation in higher risk patients**. *AJNR Am J Neuroradiol* 2016;37:367–72 CrossRef Medline

Widespread Focal Cortical Alterations in Autism Spectrum Disorder with Intellectual Disability Detected by Threshold-Free Cluster Enhancement

V.E. Contarino, S. Bulgheroni, S. Annunziata, A. Erbetta, and D. Riva

ABSTRACT

BACKGROUND AND PURPOSE: In the past decades, a large body of work aimed at investigating brain structural anomalies accrued in autism spectrum disorder. Autism spectrum disorder is associated with intellectual disability in up to 50% of cases. However, only a few neuroimaging studies were conducted in autism spectrum disorder with intellectual disability, and none of them benefited from a nonsyndromic intellectual disability control group.

MATERIALS AND METHODS: We performed a voxelwise investigation of the structural alterations in 25 children with autism spectrum disorder with intellectual disability by comparing them with 25 typically developing children and 25 nonsyndromic children with an intellectual disability. Besides a classic voxel-based morphometry statistical approach, the threshold-free cluster enhancement statistical approach was adopted.

RESULTS: Classic voxel-based morphometry results did not survive family-wise error correction. The threshold-free cluster enhancement–based analysis corrected for family-wise error highlighted the following: 1) widespread focal cortical anomalies and corpus callosum alteration detected in autism spectrum disorder with intellectual disability; 2) basal ganglia and basal forebrain alteration detected both in autism spectrum disorder with intellectual disability and in nonsyndromic intellectual disability; and 3) differences in the frontocingulate-parietal cortex between autism spectrum disorder with intellectual disability and nonsyndromic intellectual disability.

CONCLUSIONS: The present study suggests that the frontocingulate-parietal cortex may be the eligible key region for further investigations aiming at detecting imaging biomarkers in autism spectrum disorder with intellectual disability. The detection of structural alterations in neurodevelopmental disorders may be dramatically improved by using a threshold-free cluster enhancement statistical approach.

ABBREVIATIONS: ASD = autism spectrum disorder; CC = corpus callosum; ID = intellectual disability; IQ = intelligence quotient; TD = typically developing; TFCE = threshold-free cluster enhancement; VBM = voxel-based morphometry

The autism spectrum disorder (ASD) is a life-long neurodevelopmental disorder, the underlying biologic causes of which remain to be established. The ASD includes diverse endophenotypes sharing 2 clusters of core symptoms, such as persistent deficits in social communication and social interaction across multiple contexts and restricted, repetitive patterns of behaviors, interests, and activities.¹

In past decades, a large body of work has accrued investigating anomalies in ASD by using neuroimaging techniques. Most of the

studies were performed in normally gifted (not affected by mental retardation) patients with ASD or Asperger syndrome. However, a large proportion of patients with ASD are intellectually impaired. The patients with ASD with an intelligence quotient (IQ) lower than 70 are usually referred to as having low-functioning ASD or ASD with intellectual disability (ID). Epidemiologic surveys of ASD reported up to a 50% prevalence of ASD with ID, with a degree of variation due to differences in diagnostic criteria and difficulty in assessing IQ in patients with ASD as well as genetic and environmental variables.^{2,3} Despite the high prevalence of ASD with ID, these patients were rarely examined, probably because of the difficulties in cooperation for neuroradiologic investigations.

Only a few studies performed voxelwise investigation of structural anomalies in ASD with ID,⁴⁻⁷ and none of them benefited from a nonsyndromic ID control group.

In past years, advanced nonparametric statistical approaches were developed in neuroimaging. Among these, threshold-free

Received November 5, 2015; accepted after revision February 14, 2016.

From the Neuroradiology Department (V.E.C., A.E.) and Developmental Neurology Division (S.B., S.A., D.R.), Fondazione Istituto di Ricovero e Cura a Carattere Scientifico (IRCCS) Istituto Neurologico C. Besta, Milano, Italy.

Please address correspondence to Valeria Elisa Contarino, MEng, Fondazione IRCCS Istituto Neurologico C. Besta, via Celoria 11, 20133, Milano, Italy; e-mail: contarino.v@istituto-besta.it

<http://dx.doi.org/10.3174/ajnr.A4779>

cluster enhancement (TFCE) aims to address some well-known voxel-based morphometry (VBM) criticalities, such as smoothing kernel extent, threshold dependence, and localization of the results. TFCE was shown to improve the detection of structural anomalies in neurodegenerative disease and psychiatric disorder studies.^{8–10} However, the nature of structural anomalies in neurodevelopmental disorders may differ from those in neurodegenerative diseases and psychiatric disorders, and detection improvements in such disorders have not yet been evaluated.

According to our hypotheses, ASD with ID may show structural differences from both typically developing (TD) children and nonsyndromic ID that can be better detected by TFCE-VBM. The present study had the following aims: 1) to detect structural anomalies in the under-researched condition of ASD with ID, also directly comparing those patients with subjects with nonsyndromic ID; and 2) to verify the improvement in detecting structural anomalies in neurodevelopmental disorders by using TFCE in comparison with the classic VBM approach.

MATERIALS AND METHODS

Participants

Twenty-five subjects with idiopathic ASD with ID (22 males, 3 females; age range, 2.4–12.7 years; mean, 6.11 ± 3.10 years) and 25 age-matched children with nonsyndromic ID (16 males, 9 females; age range, 2.1–12.4 years; mean, 7 ± 3.1 years) were recruited from patients attending the Developmental Neurology Unit from January 2008 to January 2012. All patients were evaluated by a pediatric neurologist, a clinical geneticist, and a child neuropsychologist. The patients with ASD were diagnosed in accordance with the *Diagnostic and Statistical Manual of Mental Disorders-DSM-5* criteria and confirmed by the Autism Diagnostic Observation Schedule-Generic¹¹ and the Autism Diagnostic Interview-Revised.¹²

Twenty-five age-matched TD children (12 males, 13 females; age range, 2.1–12.3 years; mean, 6.11 ± 2.6 years) were also enrolled. The TD children were recruited among the children of the staff involved in the study and among inpatients with suspected spinal cord abnormalities whose brain and spine examination findings were normal.

Cognitive functioning was assessed by using the Wechsler Intelligence Scales,^{13,14} according to their age, and the Griffiths Mental Developmental Scale^{15,16} for children with a chronologic or mental age younger than 4 years, considering the correlation between the Wechsler Preschool Scale Full IQ and the General Quotient obtained by the Griffiths Scales.¹⁷

The parents of ID and TD children were asked to fill out the lifetime version of the Social Communication Questionnaire,¹⁸ a self-report questionnaire that provides valuable information on a child's body movements, use of language or gestures, and style of interacting, through 40 questions based on the Autism Diagnostic Interview-Revised items. It is not meant to provide a detailed diagnosis of ASD but to indicate whether a child needs a more careful and in-depth evaluation. The cutoff score is 15.

The exclusion criteria were as follows: 1) preterm birth or known pregnancy complications or perinatal injury history; 2) associated seizures or neurologic diseases, known infectious, metabolic, or genetic diseases (high-resolution karyotype, DNA anal-

ysis of fragile-X syndrome); 3) the presence of major cerebral malformations (details in Erbetta et al¹⁹); 4) anomalies of the visceral organs and/or facial dysmorphisms; 5) Social Communication Questionnaire score higher than the cutoff of 15 for children with ID and TD; 6) the presence of severe ID because the clinical differential diagnosis between ASD and severe ID is arguable and the administration of autism diagnostic tools is not recommended in such patients.

All patients and TD children younger than 6 years of age were examined under propofol sedation (1 mg/Kg).

All the examinations were performed with written informed consent of the subject's parents. The study was approved by the Ethics Committee of Fondazione Istituto di Ricovero e Cura a Carattere Scientifico (IRCCS) Istituto Neurologico C. Besta.

Data Acquisition

Volumetric T1-weighted images were acquired on a 1.5T MR imaging system (Magnetom Avanto; Siemens, Erlangen, Germany) by using a magnetization-prepared rapid acquisition of gradient echo sequence (TR = 1640 ms, TE = 2.48 ms, TI = 552 ms, FOV = 256×256 mm, matrix = 256×256 , 160 sagittal sections, voxel size = $1 \times 1 \times 1$ mm). Structural imaging included axial proton-density/T2-weighted images (TR = 3500 ms, TE = 17/84 ms, FOV = 208×256 mm, matrix = 208×256 , section thickness = 5 mm) and coronal turbo spin-echo T2-weighted images (TR = 4100 ms, TE = 143 ms, FOV = 324×384 mm, matrix = 324×384 , section thickness = 5 mm). Structural imaging was visually assessed by a senior neuroradiologist for the presence or absence of supratentorial and infratentorial abnormalities and signal-intensity changes in patients and TD subjects.

Image Processing

A VBM study was conducted to investigate the local differences in GM and WM volume among ASD with ID, TD, and ID groups. The T1-weighted volumetric images were analyzed with the Statistical Parametric Mapping 8 (SPM8) package (<http://www.fil.ion.ucl.ac.uk/spm/software/spm12/>) and VBM8 toolbox (<http://dbm.neuro.uni-jena.de/vbm8/>). We used the Diffeomorphic Anatomical Registration by using the Exponentiated Lie algebra (DARTEL) algorithm,²⁰ implemented in VBM8 to generate a study-specific template and to perform the registration of the subjects to that template.²¹

The VBM preprocessing steps are as follows: 1) checking for scanner artifacts and gross anatomic abnormalities in each subject; 2) image origin setting to the anterior commissure; 3) VBM8 segmentation of brain tissues with default settings based on the DARTEL template in Montreal Neurological Institute space derived from the IXI data base (<http://www.brain-development.org>); 4) creation of a study-specific template from all the segmented images by using the VBM8 toolbox; 5) a second VBM8 segmentation of brain tissues, with alignment of the subjects to the study-specific template and “nonlinear only” modulation to account for different individual brain sizes; 6) check for suboptimal overlapping by visual inspection of the normalized images and dishomogeneities by using a covariance matrix; and 7) spatial smoothing of the preprocessed GM and WM images, applying

Total volumes in ASD with ID, ID, and TD groups and 2-way unrelated ANOVA output

	ASD with ID (Mean) (SD)		ID (Mean) (SD)		TD (Mean) (SD)		2-Way ANOVA (Mean)	
	Male	Female	Male	Female	Male	Female		
TIV (mL)	1396.1 (116.2)	1222.2 (61.7)	1293.5 (136.2)	1177.7 (105.7)	1326.7 (100.1)	1235.5 (74.7)	Group	1.910 ± .156
							Sex	16.793 ± .000
							Group × sex	.523 ± .595
Total GM (mL)	724.0 (92.4)	569.6 (55.1)	662.6 (71.5)	628.2 (83.4)	654.3 (40.8)	602.5 (73.4)	Group	.377 ± .687
							Sex	2.373 ± .000
							Group × sex	14.003 ± .101
Total WM (mL)	411.8 (54.4)	353.7 (31.8)	378.4 (53.1)	330.7 (47.3)	387.5 (40.9)	361.3 (31.7)	Group	1.668 ± .196
							Sex	10.874 ± .002
							Group × sex	.532 ± .590
CSF (mL)	260.2 (53.6)	298.9 (56.7)	252.5 (55.7)	218.8 (51.3)	284.8 (55.9)	271.7 (51.4)	Group	4.449 ± .015
							Sex	.032 ± .858
							Group × sex	1.639 ± .202

Note:—TIV indicates total intracranial volume.

different isotropic Gaussian kernels such as 2-, 4-, 8-mm full width at half maximum kernels.

The GM, WM, and CSF volumes were calculated by the relevant VBM8 function, and the total intracranial volume, as the sum.

Statistical Analysis

Differences in age, total intracranial volume, total GM, total WM, and CSF volumes among the 3 groups were assessed by 2-way ANOVA by using group (ASD with ID, ID, and TD) and sex as independent variables. One-way ANOVA was performed to assess IQ differences.

Classic Parametric Analysis

A parametric statistical analysis based on the random field theory was performed. Two 1-way ANOVAs were designed by using the general linear model to investigate local GM and local WM volume differences among the 3 groups. We used age, sex, IQ, and total GM/WM volume as covariates in the local GM/WM volume analysis to correct for any differences due to nuisance variables. *T* tests were performed to investigate group differences in local GM/WM volume between the following: 1) ASD with ID and TD, 2) ASD with ID and ID, 3) ID and TD.

The above-described classic analysis was performed on normalized and modulated GM/WM images with the standard smoothing level (8-mm full width at half maximum) and, in addition, with lower smoothing levels (4-mm, 2-mm full-width half-maximum) to allow comparison with the following nonparametric approach.

Threshold-Free Cluster Enhancement Analysis

A TFCE nonparametric permutative statistical analysis was performed. The TFCE method is extensively described in the related article¹⁰ and implemented in the freely available toolbox (<http://dbm.neuro.uni-jena.de/tfce/>). Briefly, the TFCE algorithm takes an input raw statistical image and produces an output image in which the voxelwise values represent the amount of clusterlike local spatial support. Then, for each contrast, the group labels are randomly permuted to obtain an empirically derived null distribution against which one can compare the observed effects.

In the same way as in the classic parametric analysis, two 1-way ANOVAs with 4 nuisance regressors (age, sex, IQ, and total GM/WM volume) were designed by using the general linear model to investi-

gate local GM and WM volume differences. Then, TFCE nonparametric tests were performed to investigate group differences in local GM/WM volume between the following: 1) ASD with ID and TD, 2) ASD with ID and ID, and 3) ID and TD. The group labels were randomly permuted 5000 times (default setting) for each test. A Bonferroni correction was applied to each pair-wise test in order to correct for multiple comparisons across groups.

TFCE does not explicitly require image smoothing and allows small smoothing kernels.¹⁰ Thus, the above-described TFCE analysis was performed on normalized and modulated GM/WM images with no smoothing and, in addition, with 2- and 4-mm full width at half maximum isotropic Gaussian kernels.

RESULTS

The 3 groups were matched for age ($F = 0.16$, $P = .985$), and the 2 clinical groups were comparable for IQ. The mean IQ was 56 ± 7 (range, 41–66) and 53 ± 10 (range, 37–66) for ASD with ID and ID respectively ($t = -1.127$, $P = .266$). The mean IQ in TD was 103 ± 9 (range, 91–126), which is significantly higher than that in the 2 clinical groups ($F = 251.41$, $P = .000$).

Increased Total Volumes in ASD with ID

The 2-way unrelated ANOVA showed that a significant effect was obtained on total GM volume, total WM volume, and total intracranial volume for sex but not for group and their interactions. Males had total volume measures higher than females in all 3 groups. The main effect of group on CSF volume is significant, with significantly less volume in those with ID compared with TD ($P = .016$). Total volumes in the ASD with ID, ID, and TD groups and 2-way unrelated ANOVA output are shown in the Table.

Classic Parametric VBM Analysis

No differences in local GM volumes and local WM volumes among the 3 groups survived the multiple comparison correction ($P < .05$ family-wise error–corrected), regardless of the smoothing kernel applied during preprocessing.

TFCE-Based VBM Analysis

The TFCE-based analysis was sensitive to local GM and WM volume differences ($P < .05$ family-wise error–corrected), and Bonferroni-corrected *P* values were lower than the significant threshold (.05), regardless of the smoothing kernel applied during

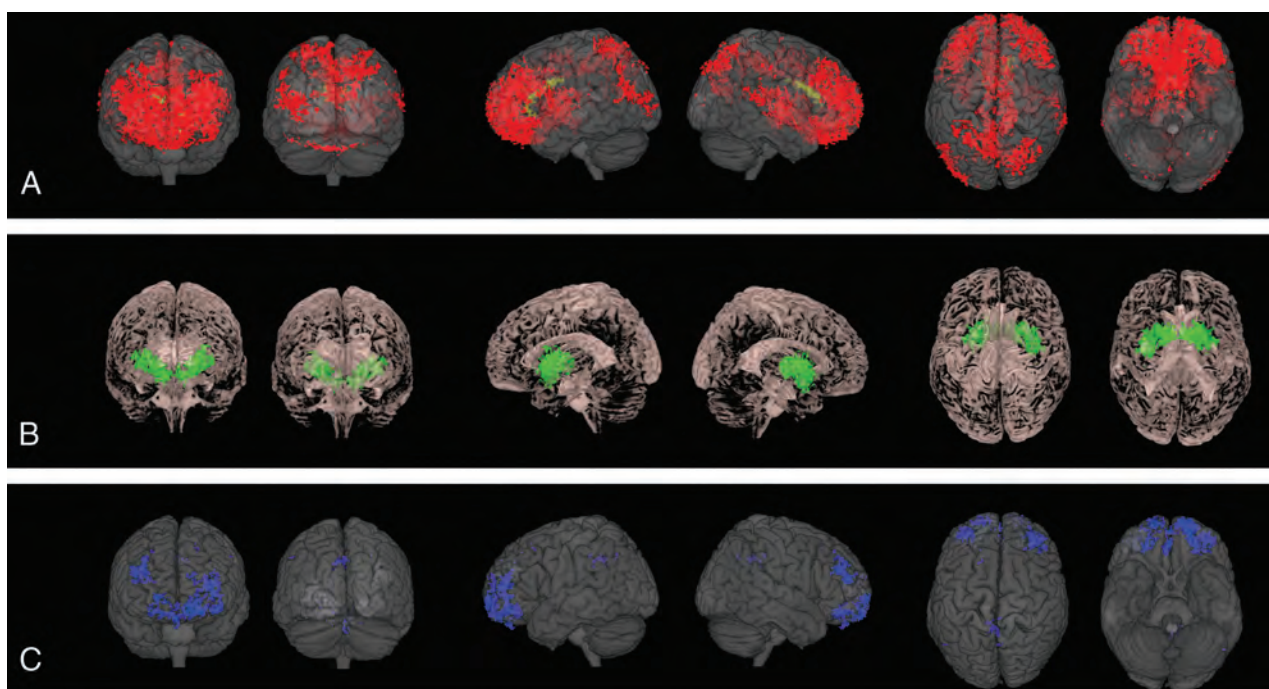


FIG 1. TFCE nonparametric analysis ($P < .05$ family-wise error–corrected) based on unsmoothed images. **A**, ASD with ID shows cortical and subcortical GM decrease (red) and WM decrease (yellow) in comparison with TD. **B**, ID shows subcortical GM decrease (green) in comparison with TD. **C**, ASD with ID shows cortical GM decrease (blue) in comparison with ID.

preprocessing. The effect of the smoothing was an enlargement of the blobs. TFCE nonparametric analysis results based on unsmoothed images are shown in Figure.

Widespread Cortical and Subcortical Anomalies in ASD with ID

ASD with ID showed widespread cortical and subcortical GM decreases, compared with TD (Fig 1A, red). Frontobasal regions together with the anterior cingulate cortex and dorsolateral prefrontal cortex compounded the largest and most statistically significant cluster. More spotty differences were detected in the middle and posterior cingulate; parietal (precuneus and superior parietal lobule bilaterally, left inferior parietal lobule), occipital (cuneus bilaterally, left lateral occipital cortex, and right superior occipital gyrus), and temporal (right superior temporal gyrus and left middle temporal gyrus) cortices; insula; and thalamus.

Analysis focused on WM revealed decreased WM in the body, genu, and forceps minor of the corpus callosum (CC) (Fig 1A, yellow). Increased WM was detected in a small area in the midbrain.

Subcortical Anomalies in ID

GM decrease in ID compared with TD was detected in the basal ganglia and basal forebrain (Fig 1B, green). Two small areas of increased WM were found in the midbrain and the medulla oblongata.

Frontocingulate-Parietal Differences between ASD with ID and ID

GM decrease in ASD with ID compared with ID was detected in the fronto-orbital cortex, middle and posterior cingulate cortices, and precuneus (Fig 1C, blue).

DISCUSSION

Classic VBM voxel-based inference and cluster-based inference are known to carry some criticisms such as smoothing kernel extent and statistical threshold.^{22,23} In theory, the definition should be based on the expected study-specific effect (that is actually unknown), while in common practice, the extent of the smoothing kernel and the statistical significance threshold are defined arbitrarily. TFCE was proposed to address the criticisms of smoothing kernel extent, threshold dependence, and localization of the results and to optimize the detection of both diffuse, low-amplitude signals and sharp, focal signals, while keeping strong control over family-wise error.¹⁰ Moreover, while cluster-based inference requires an adjustment to ensure homogeneity of the local smoothness, TFCE inference is robust to nonstationarity.²⁴ Several recent studies transversely adopted TFCE in several neuroimaging modalities, and it was demonstrated that it improves the sensitivity of VBM statistical analysis in neurodegenerative and psychiatric diseases.^{8–10}

Our goal was to detect structural anomalies in the under-researched condition of ASD with ID, also directly comparing it with nonsyndromic ID, and to verify the improvement of structural anomaly detection in neurodevelopmental disorders by using TFCE. In this study, no significant voxelwise differences among the groups survived correction for multiple comparisons by using a classic parametric VBM approach, and significant voxelwise differences among the groups survived correction for multiple comparisons by using a TFCE nonparametric statistical approach. The cortical and subcortical alterations in ASD with ID are discussed in the following paragraphs.

Widespread Focal Cortical Alterations in ASD with ID

Local GM volume decrease was distributed throughout the lobes in ASD with ID. The larger the smoothing kernel applied during image preprocessing, the larger were the blobs. When no smoothing was applied, anomalies were characterized by a focal appearance, the attenuation of which seemed not constant across the cortical lobes. Indeed, such attenuation seemed to follow a negative gradient from the ventromedial prefrontal cortex to the occipital and temporal regions, through the cingulate and medial parietal cortex. Image smoothing did impact on anomaly focality and made it difficult to observe the variation of focal abnormality attenuation across the lobes. Thus, we showed the results based on unsmoothed images. However, we used the analysis based on smoothed images to exclude results based on the unsmoothed images being due to noise and to make classic and TFCE-based VBM analyses comparable (ie, the same preprocessing pipeline). The TFCE method allows the use of unsmoothed images that in turn, allows investigating focal cortical anomalies.

Among the cortical regions altered in ASD with ID, significant differences in the frontocingulate-parietal cortex were also detected between ASD with ID and ID, while ID had no significant anomalies in cortical regions. The frontocingulate-parietal network involves cortical areas that some authors have assumed to underlie general intelligence,²⁵ while others are associated with specific higher cognitive abilities, such as working memory or executive functions.²⁶ The present study suggests that the frontocingulate-parietal cortex may be the eligible key region for further investigations aiming at detecting imaging biomarkers in ASD with ID.

The widespread focal cortical anomalies in ASD with ID shown in the present study might be related to patches of disorganization in the neocortex²⁷; subtle focal cortical dysplasias are most abundant within the prefrontal lobes and are explicitly associated with focal and distributed thinning of the cortex in postmortem investigations.²⁸

Corpus Callosum Alterations in ASD with ID

The genu and body of the CC showed decreased local WM volume in ASD with ID. The CC is one of the most consistently altered regions in ASD, according to conventional MR imaging²⁹ and DTI.³⁰ The anterior sector of the CC seems to be more involved than the posterior sectors.³¹ WM decrease in the genu and body of the CC supports the hypothesis of impaired interhemispheric communication, particularly involving the frontal and parietal regions.

No significant differences were detected in the CC by comparing ASD with ID and ID as well as ID and TD. Diffusion MR imaging studies are needed to subcharacterize the WM in ASD with ID.

Basal Ganglia Alterations Shared between ASD with ID and ID

Alterations of the basal ganglia were repeatedly described in patients with ASD, and they were often found to correlate with impaired motor performance or repetitive and stereotyped behavior.^{32,33} Alterations in the basal forebrain were also previously described in patients with ASD with ID.⁶ The basal forebrain

comprises a group of structures located in the medial and ventral surface of the frontal lobe, implicated in a number of cognitive functions and social behavior patterns.³⁴

In the present study, local volumetric anomalies in the basal ganglia and basal forebrain were detected in both ASD with ID and ID. Further multimodal research in the complex basal ganglia system is needed to deepen the role of basal ganglia alteration in neurodevelopmental disorders.

Present Limitations and Future Prospects

One limitation of the present study may be the restricted number of participants (75 children in total). Twenty-five participants in each group were the largest sample available, taking into account image artifacts, exclusion criteria, IQ matching between the 2 clinical groups, and age matching among the 3 groups. Larger samples would also allow studying the dynamics of the structural anomalies across ages. Although our experimental model controlled for sex differences and related total volume differences, the study would have benefited from sex matching and a balanced sex ratio.

In addition, the comparison with a group with ASD and normal intelligence would deepen the comprehension of the structural anomalies in ASD with ID.

The administration of propofol to only TD children younger than 6 years of age might impact the results. To exclude this outcome, we performed quantitative image quality control by the relevant tool available in VBM8, besides a qualitative visual check of original and preprocessed images. The images of the unsedated TD subjects did not differ from those of subjects who were administered propofol.

Future neuroimaging research ought to focus on studying the different features that characterize the cortical surfaces (ie, intensity, cortical thickness, surface area, sulcal depth, gyrification) in ASD with ID, taking into account the focal nature of the expected anomalies. In light of the recent postmortem studies on the laminar architecture in ASD,^{27,28} the investigation into each of the 6 cortical layers would be crucial. However, in vivo detection of a particular cortical layer is still a challenge for MR brain imaging and future developments might allow ultra-high-resolution acquisitions in clinical settings.

CONCLUSIONS

The present voxelwise structural MR imaging investigation shows widespread focal cortical anomalies and subcortical alterations in ASD with ID. The comparison with nonsyndromic ID suggests the frontocingulate-parietal cortex as the key region eligible for further investigations to detect imaging biomarkers in ASD with ID. The detection of structural alterations in neurodevelopmental disorders may be dramatically improved by the TFCE statistical approach.

REFERENCES

1. American Psychiatric Association; DSM-5 Task Force. *Diagnostic and Statistical Manual of Mental Disorders: DSM-5*. Arlington, Virginia: American Psychiatric Association; 2013
2. Autism and Developmental Disabilities Monitoring Network Surveillance Year 2010 Principal Investigators. Prevalence of autism spectrum disorder among children aged 8 years—autism and developmen-

- tal disabilities monitoring network, 11 sites, United States, 2010. Surveillance Summaries. March 28, 2014. <http://www.cdc.gov/mmwr/preview/mmwrhtml/ss6302a1>. Accessed October 14, 2015
3. Lai MC, Lombardo MV, Baron-Cohen S. **Autism**. *Lancet* 2014;383:896–910 CrossRef Medline
4. Boddaert N, Chabane N, Gervais H, et al. **Superior temporal sulcus: anatomical abnormalities in childhood autism: a voxel based morphometry MRI study**. *Neuroimage* 2004;23:364–69 Medline
5. Bonilha L, Cendes F, Rorden C, et al. **Gray and white matter imbalance: typical structural abnormality underlying classic autism?** *Brain Dev* 2008;30:396–401 CrossRef Medline
6. Riva D, Bulgheroni S, Aquino D, et al. **Basal forebrain involvement in low-functioning autistic children: a voxel-based morphometry study**. *AJNR Am J Neuroradiol* 2011;32:1430–35 CrossRef Medline
7. Riva D, Annunziata S, Contarino V, et al. **Gray matter reduction in the vermis and CRUS-II is associated with social and interaction deficits in low-functioning children with autistic spectrum disorders: a VBM-DARTEL study**. *Cerebellum* 2013;12:676–85 CrossRef Medline
8. Rajagopalan V, Yue GH, Pioro EP. **Do preprocessing algorithms and statistical models influence voxel-based morphometry (VBM) results in amyotrophic lateral sclerosis patients? A systematic comparison of popular VBM analytical methods**. *J Magn Reson Imaging* 2014;40:662–67 CrossRef Medline
9. Radua J, Canales-Rodríguez EJ, Pomarol-Clotet E, et al. **Validity of modulation and optimal settings for advanced voxel-based morphometry**. *Neuroimage* 2014;86:81–90 CrossRef Medline
10. Smith SM, Nichols TE. **Threshold-free cluster enhancement: addressing problems of smoothing, threshold dependence and localization in cluster inference**. *Neuroimage* 2009;44:83–98 CrossRef Medline
11. Lord C, Risi S, Lambrecht L, et al. **The Autism Diagnostic Observation Schedule-Generic: a standard measure of social and communication deficits associated with the spectrum of autism**. *J Autism Dev Disord* 2000;30:205–23 Medline
12. Lord C, Rutter M, Le Couteur A. **Autism Diagnostic Interview-Revised: a revised version of a diagnostic interview for caregivers of individuals with possible pervasive developmental disorders**. *J Autism Dev Disord* 1994;24:659–85 Medline
13. Wechsler D. *WISC-III: Wechsler Intelligence Scale for Children. Italian Adaptation by Orsini and Picone*. Firenze: Organizzazioni Speciali; 2006
14. Wechsler D. *Wechsler Preschool and Primary Scale of Intelligence-III: Italian Adaptation by Sannio Fancello G. and Cianchetti C*. Firenze: Organizzazioni Speciali; 2008
15. Griffiths R. *GMDS-ER Griffiths Mental Development Scales-Extended Revised*. Firenze: Giunti Organizzazioni Speciali; 2006
16. Griffiths R. *The Griffiths Mental Development Scales 1996 Revision*. Henley: Association for Research in Infant and Child Development; 1996
17. Sutcliffe AG, Soo A, Barnes J. **Predictive value of developmental testing in the second year for cognitive development at five years of age**. *Pediatr Rep* 2010;2:e15 CrossRef Medline
18. Rutter M, Bailey A, Lord C. *The Social Communication Questionnaire*. Los Angeles: Western Psychological Services; 2003
19. Erbetta A, Bulgheroni S, Contarino V, et al. **Neuroimaging findings in 41 low-functioning children with autism spectrum disorder: a single-center experience**. *J Child Neurol* 2014;29:1626–31 CrossRef Medline
20. Ashburner J. **A fast diffeomorphic image registration algorithm**. *Neuroimage* 2007;38:95–113 Medline
21. Yassa MA, Stark CE. **A quantitative evaluation of cross-participant registration techniques for MRI studies of the medial temporal lobe**. *Neuroimage* 2009;44:319–27 CrossRef Medline
22. Henley SM, Ridgway GR, Scahill RI, et al; EHDN Imaging Working Group. **Pitfalls in the use of voxel-based morphometry as a biomarker: examples from Huntington disease**. *AJNR Am J Neuroradiol* 2010;31:711–19 CrossRef Medline
23. Shen S, Sterr A. **Is DARTEL-based voxel-based morphometry affected by width of smoothing kernel and group size? A study using simulated atrophy**. *J Magn Reson Imaging* 2013;37:1468–75 CrossRef Medline
24. Salimi-Khorshidi G, Smith SM, Nichols TE. **Adjusting the effect of nonstationarity in cluster-based and TFCE inference**. *Neuroimage* 2011;54:2006–19 CrossRef Medline
25. Jung RE, Haier RJ. **The Parieto-Frontal Integration Theory (P-FIT) of intelligence: converging neuroimaging evidence**. *Behav Brain Sci* 2007;30:135–54; discussion 154–87 Medline
26. Blair C. **How similar are fluid cognition and general intelligence? A developmental neuroscience perspective on fluid cognition as an aspect of human cognitive ability**. *Behav Brain Sci* 2006;29:109–25; discussion 125–60 Medline
27. Stoner R, Chow ML, Boyle MP, et al. **Patches of disorganization in the neocortex of children with autism**. *N Engl J Med* 2014;370:1209–19 CrossRef Medline
28. Casanova MF, El-Baz AS, Kamat SS, et al. **Focal cortical dysplasias in autism spectrum disorders**. *Acta Neuropathol Commun* 2013;1:67 CrossRef Medline
29. Stanfield AC, McIntosh AM, Spencer MD, et al. **Towards a neuroanatomy of autism: a systematic review and meta-analysis of structural magnetic resonance imaging studies**. *Eur Psychiatry* 2008;23:289–99 Medline
30. Travers BG, Adluru N, Ennis C, et al. **Diffusion tensor imaging in autism spectrum disorder: a review**. *Autism Res* 2012;5:289–313 CrossRef Medline
31. Bellani M, Calderoni S, Muratori F, et al. **Brain anatomy of autism spectrum disorders, I: focus on corpus callosum**. *Epidemiol Psychiatr Sci* 2013;22:217–21 CrossRef Medline
32. Estes A, Shaw DW, Sparks BF, et al. **Basal ganglia morphometry and repetitive behavior in young children with autism spectrum disorder**. *Autism Res* 2011;4:212–20 CrossRef Medline
33. Hardan AY, Kilpatrick M, Keshavan MS, et al. **Motor performance and anatomic magnetic resonance imaging (MRI) of the basal ganglia in autism**. *J Child Neurol* 2003;18:317–24 Medline
34. Baxter MG, Chiba AA. **Cognitive functions of the basal forebrain**. *Curr Opin Neurobiol* 1999;9:178–83 Medline

In Vivo T1 of Blood Measurements in Children with Sickle Cell Disease Improve Cerebral Blood Flow Quantification from Arterial Spin-Labeling MRI

 L. Václavů,  V. van der Land,  D.F.R. Heijtel,  M.J.P. van Osch,  M.H. Cnossen,  C.B.L.M. Majoie,  A. Bush,  J.C. Wood,  K.J. Fijnvandraat,  H.J.M.M. Mutsaerts, and  A.J. Nederveen



ABSTRACT

BACKGROUND AND PURPOSE: Children with sickle cell disease have low hematocrit and elevated CBF, the latter of which can be assessed with arterial spin-labeling MR imaging. Quantitative CBF values are obtained by using an estimation of the longitudinal relaxation time of blood ($T_{1\text{blood}}$). Because $T_{1\text{blood}}$ depends on hematocrit in healthy individuals, we investigated the importance of measuring $T_{1\text{blood}}$ in vivo with MR imaging versus calculating it from hematocrit or assuming an adult fixed value recommended by the literature, hypothesizing that measured $T_{1\text{blood}}$ would be the most suited for CBF quantification in children with sickle cell disease.

MATERIALS AND METHODS: Four approaches for $T_{1\text{blood}}$ estimation were investigated in 39 patients with sickle cell disease and subsequently used in the CBF quantification from arterial spin-labeling MR imaging. First, we used 1650 ms as recommended by the literature ($T_{1\text{blood}}$ -fixed); second, $T_{1\text{blood}}$ calculated from hematocrit measured in patients ($T_{1\text{blood}}$ -hematocrit); third, $T_{1\text{blood}}$ measured in vivo with a Look-Locker MR imaging sequence ($T_{1\text{blood}}$ -measured); and finally, a mean value from $T_{1\text{blood}}$ measured in this study in children with sickle cell disease ($T_{1\text{blood}}$ -sickle cell disease). Quantitative flow measurements acquired with phase-contrast MR imaging served as reference values for CBF.

RESULTS: $T_{1\text{blood}}$ -measured (1818 ± 107 ms) was higher than the literature recommended value of 1650 ms, was significantly lower than $T_{1\text{blood}}$ -hematocrit (2058 ± 123 ms, $P < .001$), and, most interesting, did not correlate with hematocrit measurements. Use of either $T_{1\text{blood}}$ -measured or $T_{1\text{blood}}$ -sickle cell disease provided the best agreement on CBF between arterial-spin labeling and phase-contrast MR imaging reference values.

CONCLUSIONS: This work advocates the use of patient-specific measured $T_{1\text{blood}}$ or a standardized value (1818 ms) in the quantification of CBF from arterial spin-labeling in children with SCD.

ABBREVIATIONS: ASL = arterial spin-labeling; Hct = hematocrit; pCASL = pseudocontinuous ASL; PC-MRI = phase-contrast MR imaging; SCD = sickle cell disease; $T_{1\text{blood}}$ = longitudinal relaxation time of blood

Sickle cell disease (SCD) is associated with a considerable risk of stroke,¹ which is reduced by blood transfusion therapy² and identified by screening blood flow velocities in intracranial arteries with transcranial Doppler.³ Additionally, microvascular tissue perfusion, or CBF, is also increased in patients with SCD^{4,5}; which is related to low hematocrit (Hct).^{6,7} CBF measurements are in-

strumental in understanding the pathophysiology of impaired perfusion in the occurrence of silent cerebral infarcts in SCD.^{4,8,9} Noninvasive CBF measurements can be performed with arterial spin-labeling (ASL) and a quantification model to calculate physiological CBF values. The wide range of CBF values reported in the literature in SCD^{1,4,9} emphasizes the need for either more accurate estimates or direct measurements of the often-assumed parameters required for CBF quantification models.

The longitudinal relaxation time of the blood ($T_{1\text{blood}}$) parameter accounts for the decay of the ASL signal with time, and


Received December 15, 2015; accepted after revision February 24, 2016.

From the Department of Radiology (L.V., D.F.R.H., C.B.L.M.M., H.J.M.M.M., A.J.N.), Academic Medical Center, Amsterdam, the Netherlands; Department of Pediatric Hematology (V.v.d.L., K.J.F.), Emma Children's Hospital, Academic Medical Center, Amsterdam, the Netherlands; C.J. Gorter Center for High Field MRI (M.J.P.v.O.), Department of Radiology, Leiden University Medical Center, Leiden, the Netherlands; Department of Pediatric Hematology (M.H.C.), Erasmus University Medical Center—Sophia Children's Hospital, Rotterdam, the Netherlands; Department of Biomedical Engineering (A.B.), Viterbi School of Engineering, University of Southern California, Los Angeles, California; Department of Pediatrics (J.C.W.), Children's Hospital Los Angeles, Los Angeles, California; and Sunnybrook Research Institute (H.J.M.M.M.), Toronto, Ontario, Canada.

Patients were recruited and scanned by V.v.d.L., H.J.M.M.M., and D.F.R.H.; the study was designed by K.J.F. and A.J.N. The data were analyzed by L.V. and H.J.M.M.M., and the final manuscript was drafted, reviewed, and edited by all authors.

This work was funded by the Dutch NutsOhra Foundation, Amsterdam, the Netherlands (grant 1303-055).

Paper previously presented, in part, at: Annual Meeting of the International Society for Magnetic Resonance in Medicine Benelux, January 16, 2015; Ghent, Belgium. Please address correspondence to Lena Václavů, MSc, Department of Radiology, Z0-178, Academic Medical Center, Meibergdreef 9, 1105 AZ, Amsterdam, the Netherlands; e-mail: l.vaclavu@amc.uva.nl

 Indicates article with supplemental on-line photo.

<http://dx.doi.org/10.3174/ajnr.A4793>

inaccurate estimates of $T1_{\text{blood}}$ could result in over- or underestimation of CBF.^{10–12} For healthy adults, with a stable Hct, a fixed $T1_{\text{blood}}$ value of 1650 ms is recommended for CBF quantification from pseudocontinuous ASL (pCASL) at 3T.^{13,14} $T1_{\text{blood}}$ is inversely correlated with Hct,^{10,13,15–19} and a linear relationship has been proposed in the literature permitting the calculation of $T1_{\text{blood}}$ from measured Hct values.^{12,13,16} While Hct ranges from 38% to 45% in healthy children,²⁰ it is as low as 18%–30% in children with SCD.²¹ Hence, if measured Hct values are available, $T1_{\text{blood}}$ can be derived accordingly. However, recent studies suggest that $T1_{\text{blood}}$ may additionally differ in children with SCD.^{12,22,23}

Owing to recent developments in MR imaging, direct measurements of the inversion recovery of $T1_{\text{blood}}$ are now possible by combining a global inversion pulse and a subsequent section-selective Look-Locker readout in the sagittal sinus.^{16,17} Patient-specific, in vivo $T1_{\text{blood}}$ measurements are noninvasive, robust, and fast, making them preferable to calculating $T1_{\text{blood}}$ from blood samples. Our first hypothesis was that in vivo–measured $T1_{\text{blood}}$ would be higher in children with SCD than the adult reference value of 1650 ms due to anemia. We also considered that conformational changes inherent to sickle red blood cells may produce additional unforeseen changes in $T1_{\text{blood}}$.¹² We investigated the importance of measuring patient-specific differences in $T1_{\text{blood}}$ for the accuracy of ASL quantification in patients with SCD. We hypothesized that patient-specific $T1_{\text{blood}}$ values acquired in vivo would improve CBF quantification in SCD compared with CBF quantification with $T1_{\text{blood}}$ calculated from Hct or $T1_{\text{blood}}$ -fixed at 1650 ms.

The aim of this study was to determine which of the following 4 $T1_{\text{blood}}$ derivatives would provide the best CBF quantification compared with quantitative reference CBF values measured with 2D phase-contrast MR imaging (PC-MRI): 1) literature-recommended adult $T1_{\text{blood}}$ of 1650 ms,¹⁴ 2) $T1_{\text{blood}}$ calculated from Hct, 3) in vivo–measured $T1_{\text{blood}}$, or 4) a fixed average SCD value from the mean $T1_{\text{blood}}$ measured in vivo in this study.

MATERIALS AND METHODS

Experiments were performed according to principles of the Declaration of Helsinki, and the study was approved by the local institutional review board at the Academic Medical Center, Amsterdam, the Netherlands.

Patients

Eligible children were approached prospectively from 2 outpatient clinics as described previously.²⁴ Informed consent was obtained from parents or guardians and children older than 12 years of age. Inclusion criteria were HbSS or HbS β^0 genotypes and 8–17 years of age. Exclusion criteria were a history of stroke, stenosis of the intracranial arteries and velocity of >155 cm/s on transcranial Doppler imaging, current chronic blood transfusion therapy, bone marrow transplant, MR imaging contraindications, and major concomitant health problems. Patients were in a steady-state of SCD, without evidence of infection or sickle cell crisis up to 1 month before participation.

Hematocrit

Venous blood samples were drawn from an antecubital vein on the day of the MR imaging assessment and processed according to

Table 1: Demographic and clinical characteristics

Demographic or Clinical Parameter	Mean and SD
Total No.	39
Females (No. and % of total)	16 (41%)
Males (No. and % of total)	23 (59%)
Age (yr)	12 \pm 2
Hematocrit (%)	23 \pm 3
Hemoglobin (g/d/L) ^a	8.4 \pm 1.1
Hemoglobin F (%) ^b	10 \pm 6
Hemoglobin A2 (%) ^c	4.8 \pm 1
Hemoglobin S (%)	84 \pm 5
Mean corpuscular volume (mL) ^d	82 \pm 10
Mean corpuscular hemoglobin concentration (mmol/L) ^e	21 \pm 0.6

^a Normal range reference values: Hb = 10–16.

^b HbF < 1%.

^c HbA2 = 2–3.

^d MCV = 75–95.

^e MCHC = 19.0–22.5.

standard procedures in the hospital laboratory. Hct values were used to calculate $T1_{\text{blood}}$ -Hct values.

MR Imaging Acquisition

Thirty-two children underwent 3T imaging on an Intera scanner (Philips Healthcare, Best, the Netherlands) with an 8-channel head coil, and due to a scanner upgrade, the remaining 8 children were scanned at 3T on an Ingenia (Philips Healthcare) with a 15-channel head coil. The protocol included 3D-TOF MRA, 2D T2-weighted, $T1_{\text{blood}}$, 2D pseudocontinuous ASL, and 2D phase-contrast sequences.

The $T1_{\text{blood}}$ acquisition section was planned perpendicular to the posterior sagittal sinus¹⁶ and comprised a multi time-point inversion recovery experiment. This technique uses a global inversion pulse followed by a series of 95° section-selective readout pulses, which are intended to saturate the tissue surrounding the sinus. Assuming complete replenishment of inverted blood between 2 consecutive pulses, a high contrast is achieved between tissue and blood, allowing the detection of the inversion recovery of blood. A nonselective adiabatic 180° inversion pulse (hyperbolic secant pulse, B1 value/duration of the pulse = 13.5 mT/13 ms) preceded a single section Look-Locker EPI readout (flip angle, 95°; voxel size, 1.5 \times 1.5 mm; matrix, 240 \times 240 mm; section thickness, 2 mm; TE/TR, 15/10,000 ms; $T1_1$, 200 ms; $\Delta T1$, 150 ms; 60 readouts; 6 signal averages; scan duration, 1 minute 20 seconds).

A gradient-echo single-shot EPI pCASL sequence was used to acquire perfusion-weighted images (75 subtracted label-control pairs; resolution, 3 \times 3 \times 7 mm; FOV, 240 \times 240 mm; 17 continuous axial sections; TE/TR, 17/4000 ms; flip angle, 90°; labeling duration, 1650 ms; postlabeling delay, 1525 ms; background suppression, 1680 and 2830 ms after a prelabeling saturation pulse; scan duration, 10 minutes 7 seconds).

Quantitative flow measurements were obtained with a non-triggered 2D single-section PC-MRI acquisition in the internal carotid and vertebral arteries. Imaging parameters were the following: FOV, 230 \times 230 mm; voxel size, 0.45 \times 0.45 mm; TR/TE, 15/5 ms; flip angle, 15°; maximum velocity-encoding, 140 cm/s; section thickness, 4 mm; scan duration, 1 minute.

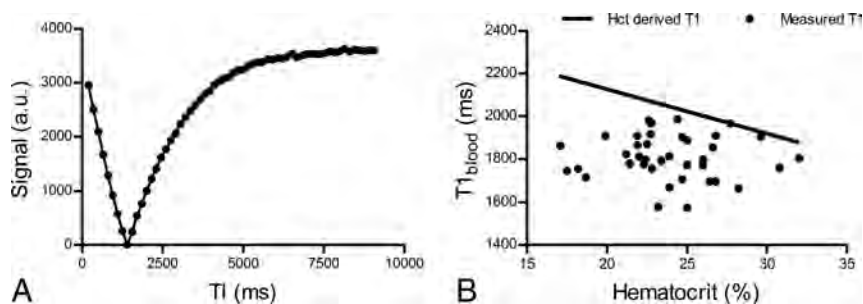


FIG 1. A, Representative inversion recovery of the venous T_{1_{blood}} signal acquired in the sagittal sinus in a child with sickle cell disease. B, In vivo-measured T_{1_{blood}} values are significantly lower than Hct-derived T_{1_{blood}} values. T_{1_{blood}}-measured does not correlate with patient hematocrit (mean Hct, 23% ± 3%) (Pearson $r = 0.02$, $P = .89$; $n = 39$).

Table 2: T_{1_{blood}} values and corresponding CBF values quantified from ASL^a

T _{1_{blood}}	Method (Value)	ASL-CBF (mL/100 g/min)	P Value
T _{1_{blood}} -fixed	Literature (1650 ms)	114 ± 13	<.05
T _{1_{blood}} -Hct	Calculated from patient's hematocrit (variable)	95 ± 10	<.05
T _{1_{blood}} -measured	Measured with MR in vivo in patients with SCD (variable)	106 ± 14	NS
T _{1_{blood}} -SCD	Mean of T _{1_{blood}} -measured (1818 ms)	105 ± 12	NS

Note:—NS indicates not significant.

^a Repeated-measures ANOVA was performed to test the significance (P in the final column) of differences between CBF from ASL and reference CBF obtained from phase-contrast MRI flow measurements.

Data Postprocessing

T_{1_{blood}}. Blood-filled voxels within the sagittal sinus were selected on the basis of the highest signal intensity. Voxel values were subsequently averaged, and the data were fitted to a 3-parameter model (Nelder-Mead method; MathWorks, Natick, Massachusetts), with the parameters M_0 , Offset, and T_{1_{blood}},¹⁷ and solved for T_{1_{blood}}:

$$1) \quad M(nTI) = \text{abs} \left(M_0 \times \left[1 - 2 \times \exp \left(- \frac{\text{Offset} + TI_1 + (nTI - 1) \times \Delta TI}{T_{1\text{blood}}} \right) \right] \right),$$

where M models the T1 recovery from the data, nTI is the readout number, abs denotes the absolute values, M_0 is the net magnetization, "Offset" accounts for imperfect inversion, TI_1 is 200 ms, and ΔTI is the sampling interval (150 ms). The sum of squared errors of the final (optimal) iteration after solving the Nelder-Mead function indicated how well the data fitted the model and served as a quality check.

Cerebral Blood Flow. Raw pCASL data were processed as described previously²⁵ by using a processing pipeline for the registration and quantification of the data. A 2-compartment quantification model was used, as published in detail previously^{9,26} (except that the equilibrium magnetization of arterial blood was derived from the M_0 of CSF multiplied by the blood-water partition coefficient,²⁷ and labeling efficiency was 0.7). The T_{1_{blood}} parameter was adjusted for each CBF quantification as follows: first, adult fixed T_{1_{blood}} of 1650 ms taken from literature¹³; second, patient-specific Hct-calculated T_{1_{blood}} values¹⁶; third, patient-specific in vivo-measured T_{1_{blood}}

values; and finally an average T_{1_{blood}} value obtained from the mean of in vivo T_{1_{blood}} measurements in our patients with SCD. T_{1_{blood}}-Hct was calculated per patient according to the relationship proposed by Varela et al¹⁶ derived from venous blood in neonates:

$$2) \quad T_{1\text{blood}} = \frac{1}{0.5 \times \text{Hct} + 0.37}.$$

PC-MRI. The internal carotid and vertebral arteries were segmented manually from phase difference images by using ITK-SNAP (<http://www.itksnap.org>) to

obtain total flow (milliliters per minute). Total flow was then divided by brain mass (gram), which was calculated from the product of the volume (estimated from segmented anatomic images in SPM8; <http://www.fil.ion.ucl.ac.uk/spm/software/spm12>) and an assumed brain density of 1.05 g/L,²⁸ to obtain PC-MRI CBF in milliliters/100 g/min,²⁹ which served as the reference value for CBF.^{22,29}

Statistical Analysis

A Pearson correlation was performed between T_{1_{blood}}-measured and Hct. Repeated-measures ANOVA was used to test the statistical significance of the differences among the 5 CBF quantification methods: 1) CBF (T_{1_{blood}}-fixed at 1650 ms), 2) CBF (T_{1_{blood}}-Hct), 3) CBF (T_{1_{blood}}-measured in vivo), 4) CBF (T_{1_{blood}}-SCD fixed at the average measured value), and 5) PC-MRI reference CBF. Paired t tests were used to test the statistical significance of individual group differences post hoc. Agreement between PC-MRI and the 4 ASL methods was investigated with linear regression and Bland-Altman analyses in Matlab (MathWorks, Natick, Massachusetts). Linear regression analysis was performed to show agreement between PC-MRI and the 4 CBF quantification methods from ASL. Bland-Altman analysis was performed to indicate the bias corresponding to over- or underestimation of the ASL CBF method compared with the PC-MRI method. The limits of agreement (dotted lines) indicate the 95% confidence intervals.

RESULTS

Demographic and clinical characteristics are summarized in Table 1. One patient's T_{1_{blood}} scan was discarded due to poor image quality, so the mean CBF values from pCASL are based on 39 datasets. For PC-MRI, only 33 datasets were of sufficient quality to quantify reference CBF.

Measured T_{1_{blood}}

The mean Hct was 23% ± 3% for 39 children. The mean T_{1_{blood}}-measured value was 1818 ± 107 ms, which was significantly lower than mean T_{1_{blood}}-Hct values (2045 ± 69 ms; paired t test, $P < .001$) but higher compared to the fixed adult value of 1650 ms. T_{1_{blood}}-measured was not significantly different between scanners (t test, $P = .94$). Figure 1A shows a representative inversion recovery curve from 1 patient as a function of the sum of least-squares fit. The sum of squared errors from fitting the T_{1_{blood}}-measured values to the model is shown in On-line Fig 1. T_{1_{blood}}-measured values did not correlate

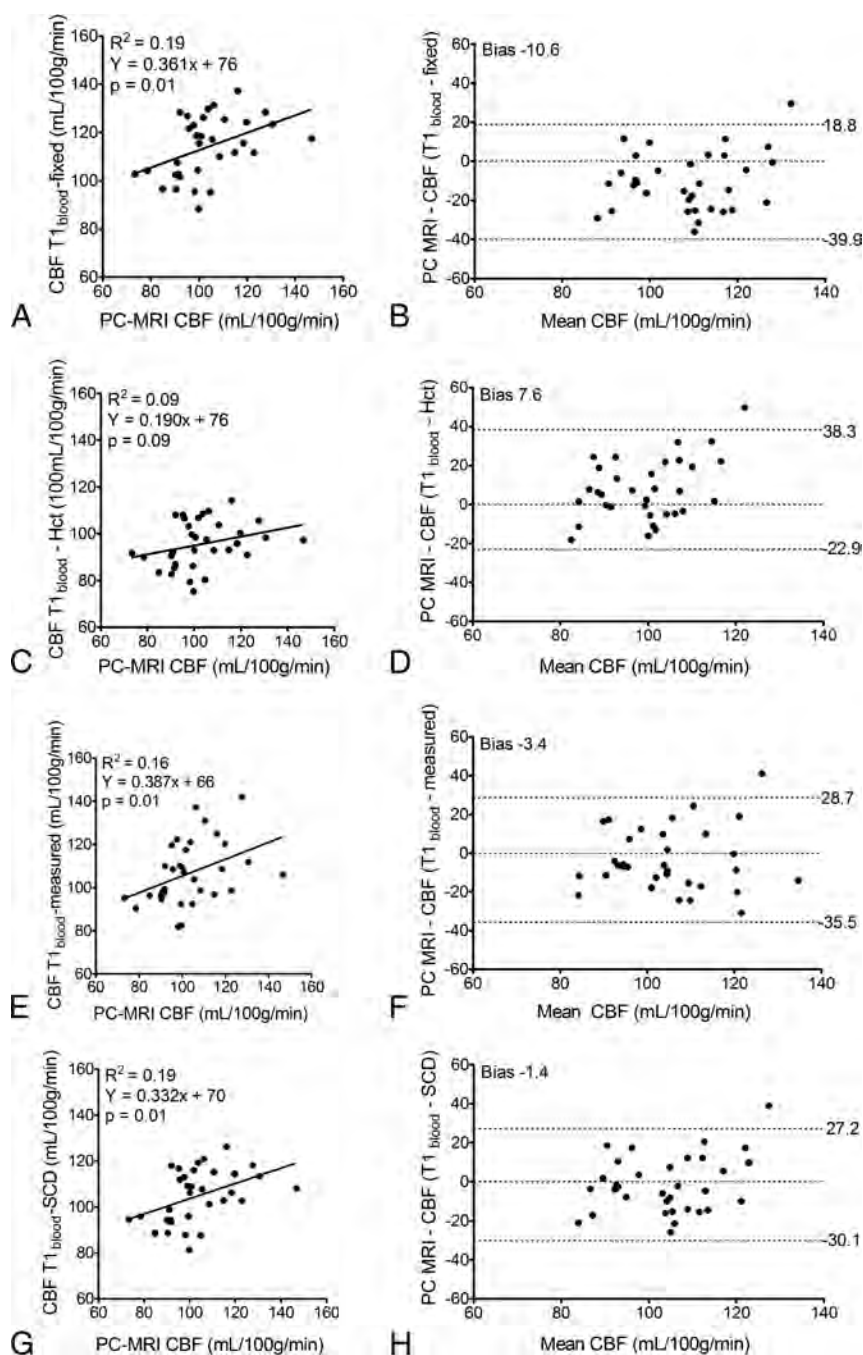


FIG 2. Linear regression and Bland-Altman plots between CBF values measured with PC-MRI and ASL, which was quantified by using 4 different $T_{1\text{blood}}$ values: a fixed literature value of 1650 ms (CBF $T_{1\text{blood}}$ -fixed) (A and B); $T_{1\text{blood}}$ calculated from hematocrit (CBF $T_{1\text{blood}}$ -Hct), $T_1 = 0.5 \cdot \text{Hct} + 0.37$ (C and D)⁶; in vivo-measured $T_{1\text{blood}}$ (CBF $T_{1\text{blood}}$ -measured) (E and F); and a fixed SCD value obtained from the mean of the in vivo-measured $T_{1\text{blood}}$ (CBF $T_{1\text{blood}}$ -SCD) (G and H). The left panel shows linear regressions (solid line), and the right panel shows the mean on the x-axis versus the difference on the y-axis between pCASL and PC-MRI CBF with limits of agreement (dotted lines above and below) ($n = 33$).

with Hct values measured from blood samples ($r = 0.02$, $P = .89$; Fig 1B) or with age ($r = 0.03$, $P = .85$) and did not differ significantly between males and females (t test, $P = .37$).

Cerebral Blood Flow

Four CBF quantification methods were compared with PC-MRI CBF, the results of which are summarized in Table 2. Linear regression analyses between PC-MRI and pCASL CBF

are shown in the left panel of Fig 2 and reveal slopes significantly different from zero for all CBF quantifications except for the $T_{1\text{blood}}$ -Hct CBF quantification. The Bland-Altman plots in the right panel of Fig 2 show the bias and limits of agreement between the measurements. $T_{1\text{blood}}$ -fixed overestimated CBF and $T_{1\text{blood}}$ -Hct underestimated CBF, while the individual in vivo $T_{1\text{blood}}$ -measured values and mean $T_{1\text{blood}}$ -SCD value provided the best agreement with PC-MRI values, both on an absolute level, revealed by no significant difference between PC-MRI and CBF in the repeated-measures ANOVA analysis (Table 2), but also on a one-to-one basis, as demonstrated in the linear regression plots (Fig 2). A representative example of CBF maps quantified with $T_{1\text{blood}}$ -measured from 2 patients is shown in Fig 3.

DISCUSSION

We demonstrate that in vivo-measured venous $T_{1\text{blood}}$ values in children with SCD were higher than the literature-recommended 1650 ms, were not significantly correlated with measured Hct, and were lower than the Hct-derived values for $T_{1\text{blood}}$. CBF quantified with in vivo-measured $T_{1\text{blood}}$ provided better agreement with PC-MRI reference measurements than CBF quantified with fixed adult $T_{1\text{blood}}$ and Hct-derived $T_{1\text{blood}}$.

$T_{1\text{blood}}$ and Hematocrit

Previous literature suggests that healthy children 6–18 years of age (assuming a stable Hct of 40%–45%) have $T_{1\text{blood}}$ values between 1680 and 1880 ms.¹⁸ In this study, in patients with a much lower Hct than healthy children, we measured $T_{1\text{blood}}$ values closer to the upper range of the literature-reported $T_{1\text{blood}}$ values.¹⁸ Yet, our $T_{1\text{blood}}$ values were lower than expected, considering the low Hct

values obtained from our patients' blood samples. It is unlikely that we underestimated $T_{1\text{blood}}$ due to sequence-related limitations because the Look-Locker T_1 technique has previously provided robust results in the same ROI.^{16,17,27}

Reports of $T_{1\text{blood}}$ values ranging from 1500 to 2100 ms follow a linear relationship with Hct between 23% and 50%.^{13,16,18} It is possible that we did not have sufficient precision to detect this inverse relationship in our dataset or that the range of Hct values

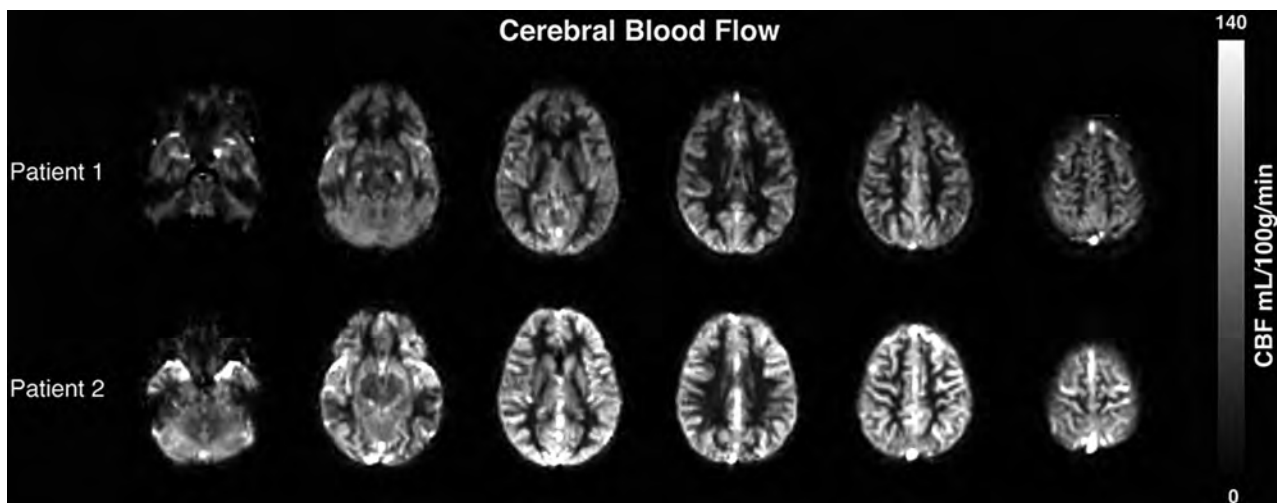


FIG 3. Axial brain sections showing CBF from 2 representative examples of 2 fourteen-year-old boys with SCD. The upper row shows a patient with low CBF and the lower row shows a patient with high CBF.

was too narrow in our patients (17%–32%). Abnormalities in SCD blood, other than low Hct, may account for the incongruity between $T_{1\text{blood}}$ and Hct measured here. While we did not measure blood rheology, abnormalities such as decreased red blood cell deformability, increased aggregation, and increased viscosity have been demonstrated consistently.^{21,30–34} Furthermore, red blood cells in SCD exhibit different membrane properties and viscosity, which may have reduced $T_{1\text{blood}}$ due to shrinkage of cells and therefore lower water content.³⁵

CBF Quantification

Our CBF results fall within the large range of reported values in children with SCD (~70–150 mL/100 g/min).^{1,4,9,36,37} The necessary reliance on a quantification model for obtaining physiologically meaningful CBF values means that the method is sensitive to the assumptions of the model used, which could differ between healthy adults and children with SCD. The fact that measured $T_{1\text{blood}}$ ameliorates the CBF quantification but Hct-calculated $T_{1\text{blood}}$ does not opposes the use of Hct-corrected CBF quantification in SCD and, instead, advocates the use of measured $T_{1\text{blood}}$. $T_{1\text{blood}}$ measurements are advantageous over Hct-calculated $T_{1\text{blood}}$ because they are faster (1 minute 20 seconds) and less invasive. In the absence of $T_{1\text{blood}}$ measurements, we propose using a mean value of 1818 ms, as measured in this study in children with SCD, which would suffice in improving the absolute agreement with PC-MRI for CBF quantification from ASL.

Limitations

This study should be considered in light of the technical limitations of the $T_{1\text{blood}}$ measurement and the potentially inaccurate reference flow measurements from PCMR.

Whereas $T_{1\text{blood}}$ measurements were acquired in venous blood, the quantification model requires arterial estimates. However, because we compared venous $T_{1\text{blood}}$ measurements with $T_{1\text{blood}}$ values derived from venous Hct, the potential mismatch would have been similar for both methods. Moreover, we demonstrate that the measured venous $T_{1\text{blood}}$, used to quantify CBF, improved the agreement with independently acquired flow measurements in arterial

vessels with PC-MRI, which shows that although the arterial measurement may be better, the venous measurement is sufficient.

PC-MRI as a surrogate for CBF could be critiqued for CBF overestimation due to partial volume effects³⁸ and inaccurate brain density estimates or underestimated flow due to noncardiac-triggered acquisition. Still, recent literature suggests that errors in flow values associated with nontriggered 2D PC-MRI are <3% compared with triggered acquisitions.^{29,39} Despite these limitations, a recent study has shown high agreement (intraclass correlation coefficient, 0.73) between PC-MRI and pCASL,⁴⁰ emphasizing that PC-MRI is currently the best noninvasive reference for pCASL CBF.

CONCLUSIONS

Inaccurate $T_{1\text{blood}}$ estimates can be a major confounder for quantitative perfusion assessment from ASL. Patient-specific, in vivo-measured $T_{1\text{blood}}$ measurements provided more accurate CBF values than $T_{1\text{blood}}$ derived from Hct values. To avoid overestimation of CBF in SCD, we recommend the use of a fixed value of 1818 ms ($T_{1\text{blood-SCD}}$) for CBF quantification from ASL in SCD if measured $T_{1\text{blood}}$ values are not available.

ACKNOWLEDGMENTS

The authors thank the participants and the medical and technical staff who helped with recruitment, scanning, and blood measurements.

Disclosures: Lena Václavů—*RELATED:* Grant: Fonds NutsOhra (grant from Dutch Sickle Cell Research Foundation). * Dennis F.R. Heijtel—*UNRELATED:* Employment: Philips Healthcare (currently employed). Matthias J.P. van Osch—*UNRELATED:* Employment: Philips Healthcare; *Patents (planned, pending or issued):* joint patent with Philips Healthcare* and a joint patent with the Florey Institute of Neuroscience and Mental Health (Melbourne, Australia) and Lund University (Sweden). * both pending; *Other:* research support by Philips Healthcare. * Charles B.L.M. Majoie—*UNRELATED:* Payment for Lectures (including service on Speakers Bureaus): Stryker. * John C. Wood—*UNRELATED:* Consultancy: BioMed Informatics, ApoPharma, Isis Pharmaceuticals, Pfizer, Celgene, WorldCare Clinical; *Grants/Grants Pending:* National Institutes of Health (1U01HL117718–01 from the National Heart, Lung, and Blood Institute). * National Institutes of Health National Institute of Diabetes and Digestive and Kidney Diseases (1R01DK097115–01A1). * Payment for Development of Educational Presentations: American Society of Hematology; *Other:* Philips Healthcare. * Comments: Work-in-Kind—Philips provided technical expertise, pulse sequences, and engineering staff and we have tested new MRI techniques, product feedback, and academic productivity (abstracts and papers). * Money paid to the institution.

REFERENCES

- Helton KJ, Adams RJ, Kesler KL, et al. SWiTCHe Investigators. **Magnetic resonance imaging/angiography and transcranial Doppler velocities in sickle cell anemia: results from the SWiTCHe trial.** *Blood* 2014;124:891–98 CrossRef Medline
- Adams RJ, McKie VC, Hsu L, et al. **Prevention of a first stroke by transfusions in children with sickle cell anemia and abnormal results on transcranial Doppler ultrasonography.** *N Engl J Med* 1998;339:5–11 CrossRef Medline
- Arkuszewski M, Krejza J, Chen R, et al. **Sickle cell disease: reference values and interhemispheric differences of nonimaging transcranial Doppler blood flow parameters.** *AJNR Am J Neuroradiol* 2011;32:1444–50 CrossRef Medline
- Oguz K, Golay X, Pizzini FB, et al. **Sickle cell disease: continuous arterial spin-labeling perfusion MR imaging in children.** *Radiology* 2003;227:567–74 CrossRef Medline
- Arkuszewski M, Krejza J, Chen R, et al. **Sickle cell anemia: reference values of cerebral blood flow determined by continuous arterial spin labeling MRI.** *Neuroradiol J* 2013;26:191–200 CrossRef Medline
- Prohovnik I, Hurler-Jensen A, Adams R, et al. **Hemodynamic etiology of elevated flow velocity and stroke in sickle-cell disease.** *J Cereb Blood Flow Metab* 2009;29:803–10 CrossRef Medline
- Doepp F, Kebelmann-Betzing C, Kivi A, et al. **Stenosis or hyperperfusion in sickle cell disease: ultrasound assessment of cerebral blood flow volume.** *Ultrasound Med Biol* 2012;38:1333–38 CrossRef Medline
- Helton KJ, Glass JO, Reddick WE, et al. **Comparing segmented ASL perfusion of vascular territories using manual versus semiautomated techniques in children with sickle cell anemia.** *J Magn Reson Imaging* 2015;41:439–46 CrossRef Medline
- Gevers S, Nederveen AJ, Fijnvandraat K, et al. **Arterial spin labeling measurement of cerebral perfusion in children with sickle cell disease.** *J Magn Reson Imaging* 2012;35:779–87 CrossRef Medline
- Varela M, Petersen ET, Golay X, et al. **Cerebral blood flow measurements in infants using look-locker arterial spin labeling.** *J Magn Reson Imaging* 2015;41:1591–600 CrossRef Medline
- Wu WC, St Lawrence KS, Licht DJ, et al. **Quantification issues in arterial spin labeling perfusion magnetic resonance imaging.** *Top Magn Reson Imaging* 2010;21:65–73 CrossRef Medline
- Hales PW, Kirkham FJ, Clark CA. **A general model to calculate the spin-lattice (T1) relaxation time of blood, accounting for haematocrit, oxygen saturation and magnetic field strength.** *J Cereb Blood Flow Metab* 2016;36:370–74 CrossRef Medline
- Lu H, Clingman C, Golay X, et al. **Determining the longitudinal relaxation time (T1) of blood at 3.0 Tesla.** *Magn Reson Med* 2004;52:679–82 CrossRef Medline
- Alsop DC, Detre JA, Golay X, et al. **Recommended implementation of arterial spin-labeled perfusion MRI for clinical applications: a consensus of the ISMRM perfusion study group and the European consortium for ASL in dementia.** *Magn Reson Med* 2015;73:102–16 CrossRef Medline
- De Vis JB, Hendrikse J, Groenendaal F, et al. **Impact of neonate haematocrit variability on the longitudinal relaxation time of blood: implications for arterial spin labelling MRI.** *Neuroimage Clin* 2014;4:517–25 CrossRef Medline
- Varela M, Hajnal JV, Petersen ET, et al. **A method for rapid in vivo measurement of blood T1.** *NMR Biomed* 2011;24:80–88 CrossRef Medline
- Zhang X, Petersen ET, Ghariq E, et al. **In vivo blood T(1) measurements at 1.5 T, 3 T, and 7 T.** *Magn Reson Med* 2013;70:1082–86 CrossRef Medline
- Wu WC, Jain V, Li C, et al. **In vivo venous blood T1 measurement using inversion recovery true-FISP in children and adults.** *Magn Reson Med* 2010;64:1140–47 CrossRef Medline
- Shimada K, Nagasaka T, Shidahara M, et al. **In vivo measurement of longitudinal relaxation time of human blood by inversion-recovery fast gradient-echo MR imaging at 3T.** *Magn Reson Imaging Sci* 2012;11:265–71 CrossRef Medline
- Hollowell J, van Assendelft O, Gunter E, et al. **Hematological and iron-related analytes: reference data for persons aged 1 year and over: United States, 1988–94.** *Vital Health Stat 11* 2005;247:1–156 Medline
- Trippette J, Alexy T, Hardy-Dessources M, et al. **Red blood cell aggregation, aggregate strength and oxygen transport potential of blood are abnormal in both homozygous sickle cell anemia and sickle-hemoglobin C disease.** *Haematologica* 2009;94:1060–65 CrossRef Medline
- Jain V, Duda J, Avants B, et al. **Longitudinal reproducibility and accuracy of pseudo-continuous arterial spin-labeled perfusion MR imaging in typically developing children.** *Radiology* 2012;263:527–36 CrossRef Medline
- Hales PW, Kawadler JM, Aylett SE, et al. **Arterial spin labeling characterization of cerebral perfusion during normal maturation from late childhood into adulthood: normal “reference range” values and their use in clinical studies.** *J Cereb Blood Flow Metab* 2014;34:776–84 CrossRef Medline
- van der Land V, Hijmans CT, de Ruiter M, et al. **Volume of white matter hyperintensities is an independent predictor of intelligence quotient and processing speed in children with sickle cell disease.** *Br J Haematol* 2015;168:553–56 CrossRef Medline
- Mutsaerts HJ, van Osch MJ, Zelaya FO, et al. **Multi-vendor reliability of arterial spin labeling perfusion MRI using a near-identical sequence: implications for multi-center studies.** *Neuroimage* 2015;113:143–52 CrossRef Medline
- Gevers S, Heijtel D, Ferns SP, et al. **Cerebral perfusion long term after therapeutic occlusion of the internal carotid artery in patients who tolerated angiographic balloon test occlusion.** *AJNR Am J Neuroradiol* 2012;33:329–35 CrossRef Medline
- Heijtel DF, Mutsaerts HJ, Bakker E, et al. **Accuracy and precision of pseudo-continuous arterial spin labeling perfusion during baseline and hypercapnia: a head-to-head comparison with ¹⁵O H₂O positron emission tomography.** *Neuroimage* 2014;92:182–92 CrossRef Medline
- Herscovitch P, Raichle ME. **What is the correct value for the brain-blood partition coefficient for water?** *J Cereb Blood Flow Metab* 1985;5:65–69 CrossRef Medline
- Aslan S, Xu F, Wang PL, et al. **Estimation of labeling efficiency in pseudocontinuous arterial spin labeling.** *Magn Reson Med* 2010;63:765–71 CrossRef Medline
- Vent-Schmidt J, Waltz X, Romana M, et al. **Blood thixotropy in patients with sickle cell anaemia: role of haematocrit and red blood cell rheological properties.** *PLoS One* 2014;9:e114412 CrossRef Medline
- Connes P, Coates TD. **Autonomic nervous system dysfunction: implication in sickle cell disease.** *CR Biol* 2013;336:142–47 CrossRef Medline
- Brandão MM, Fontes A, Barjas-Castro ML, et al. **Optical tweezers for measuring red blood cell elasticity: application to the study of drug response in sickle cell disease.** *Eur J Haematol* 2003;70:207–11 CrossRef Medline
- Heibel RP, Yamada O, Moldow CF, et al. **Abnormal adherence of sickle erythrocytes to cultured vascular endothelium: possible mechanism for microvascular occlusion in sickle cell disease.** *J Clin Invest* 1980;65:154–60 CrossRef Medline
- Prengrer M, Pavlakis SG, Prohovnik I, et al. **Sickle cell disease: the neurological complications.** *Ann Neurol* 2002;51:543–52 CrossRef Medline
- Kiihne S, Bryant RG. **Protein-bound water molecule counting by resolution of (1)H spin-lattice relaxation mechanisms.** *Biophys J* 2000;78:2163–69 CrossRef Medline
- Strouse JJ, Cox CS, Melhem ER, et al. **Inverse correlation between cerebral blood flow measured by continuous arterial spin-labeling (CASL) MRI and neurocognitive function in children with sickle cell anemia (SCA).** *Blood* 2006;108:379–81 CrossRef Medline
- van den Tweel XW, Nederveen AJ, Majoie CB, et al. **Cerebral blood flow measurement in children with sickle cell disease using continuous arterial spin labeling at 3.0-Tesla MRI.** *Stroke* 2009;40:795–800 CrossRef Medline
- Lotz J, Meier C, Leppert A, et al. **Measurement with imaging: basic facts and implementation.** *Radiographics* 2002;22:651–71 CrossRef Medline
- Spilt A, Box FM, van der Geest RJ, et al. **Reproducibility of total cerebral blood flow measurements using phase contrast magnetic resonance imaging.** *J Magn Reson Imaging* 2002;16:1–5 CrossRef Medline
- Ambarki K, Wahlin A, Zarrinkoob L, et al. **Accuracy of parenchymal cerebral blood flow measurements using pseudocontinuous arterial spin-labeling in healthy volunteers.** *AJNR Am J Neuroradiol* 2015;36:1816–21 CrossRef Medline

Normal Developmental Globe Morphology on Fetal MR Imaging

M.T. Whitehead and G. Vezina

ABSTRACT

BACKGROUND AND PURPOSE: Age-dependent structural changes of the globes occur during gestation. The posterolateral globe margins bulge outward, and the eyes are conical in early gestation. Later, the globes are ellipsoid. The purpose of this study was to establish normal developmental fetal globe morphology.

MATERIALS AND METHODS: The fetal MR imaging data base at an academic children's hospital was queried for all brain MRIs performed during 8 years. Motion artifacts, brain/craniofacial/globe malformations, and chromosomal defects were exclusion criteria. Two board-certified neuroradiologists evaluated each examination for globe shape (elliptic/nonelliptic) and hyaloid visibility. Logistic regression was used to evaluate correlations among variables. Age-specific cut-points for globe shape and hyaloid visibility were chosen to optimize specificity.

RESULTS: We identified 1243 examinations from 1177 patients. Six hundred eighty-two examinations met the inclusion criteria (17–39 weeks). Receiver operating characteristic analysis showed that age was highly predictive of globe shape (area under the curve = 0.99) and fetal vasculature visibility (area under the curve = 0.94). Nonelliptic globes were universal up to 22 weeks. Thereafter, globes gradually assumed an elliptic shape, present in nearly all patients 29 weeks and older (sensitivity, 81%; 95% CI, 76%–85%; specificity, 99%; 95% CI, 98%–100%). The hyaloid vasculature was visible in most patients up to 19 weeks and occasionally in those at 20–24 weeks, but never in those 25 weeks and older (sensitivity, 69%; 95% CI, 65%–72%; specificity, 100%; 95% CI, 95%–100%).

CONCLUSIONS: Physiologic nonspheric globe shapes are normal up to 29 weeks' gestation and should not be misinterpreted as pathologic. Thereafter, globes are generally elliptic. The timing of this process coincides with the resolution of the primary vitreous and may be related.

The eyes are complex organs of sight. Primordial ocular tissue originates at the end of the first gestational month, just before neural tube closure, as paired projections from the basal forebrain. Ectoderm, mesoderm, and neural crest cells all contribute to the formation of the mature globe and related orbital components.¹ During gestation, the globes undergo progressive enlargement, corresponding best to a quadratic curve.^{2–4} The composition of the largest segment of the eye, the vitreous chamber, changes during gestation as well. The primary vitreous transmits primitive vasculature called the “hyaloid artery,” which supports the developing vitreous and lens. Then, the primary vitreous is replaced with secondary (mature) vitreous in normal situations.

Meanwhile, the hyaloid vasculature regresses contemporaneously for weeks, sometime during the second and third trimesters.^{5–9}

As the ocular globes grow and develop, their shapes evolve from asymmetric elongated/conical toward a nearly spheric, elliptical morphology. Ellipsoid globe shape is not typically achieved until late in gestation. On fetal MR imaging, the developing globes display a focal convexity along their posterolateral margins in the axial plane and a conical, keel shape in the sagittal plane. Knowledge of age-specific fetal globe anatomy is necessary to distinguish normal development from structural pathology as can be seen in diseases such as microphthalmia, coloboma, and persistent fetal vasculature, all of which may be occasionally associated with various syndromes and chromosomal defects.^{2,10} The purpose of this study was to establish the normal morphologic appearance of the developing globes at different gestational ages.

MATERIALS AND METHODS

This Health Insurance Portability and Accountability Act–compliant retrospective study was performed after institutional review board approval. The fetal MR imaging data base at a single

Received November 3, 2015; accepted after revision February 8, 2016.

From the Department of Radiology, Children's National Medical Center, Washington, DC.

Please address correspondence to Matthew T. Whitehead, MD, Department of Radiology, Children's National Medical Center, 111 Michigan Ave NW, Washington, DC 20010; e-mail: MWhitehe@childrensnational.org

<http://dx.doi.org/10.3174/ajnr.A4785>

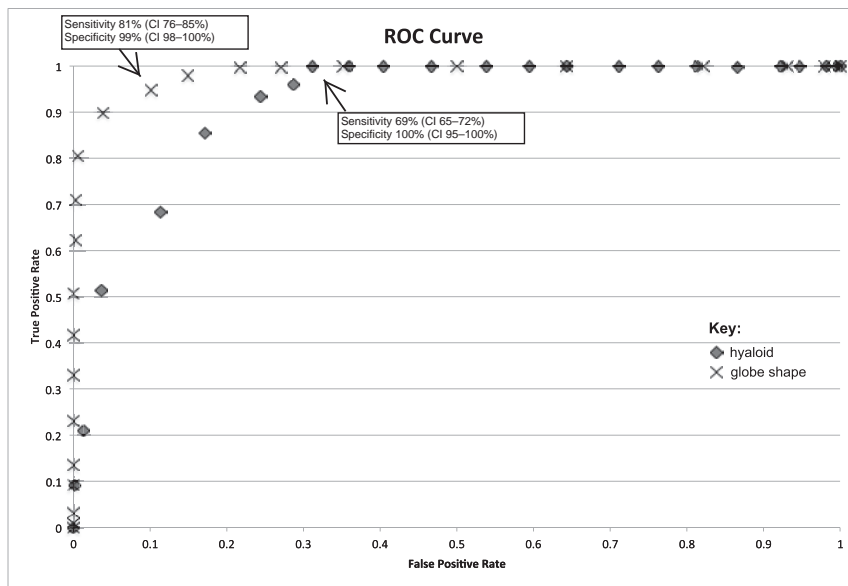


FIG 1. Receiver operating characteristic curves demonstrate sensitivity (true-positive) versus 1-specificity (false-positive) of MR imaging of the fetal brain for elliptic globe shape (X) and hyaloid vasculature visibility (diamond) as a function of age.

Frequency of hyaloid visibility and elliptic, transitional, nonelliptic, and combined transitional and nonelliptic globe morphology at various gestational ages (16–39 weeks)

GA	F	H (F)	H (%)	E (F)	E (%)	T (F)	T (%)	NE (F)	NE (%)	T + NE (F)	T + NE (%)
17	7	6	86	0	0	0	0	7	100	7	100
18	16	9	89	0	0	0	0	16	100	16	100
19	37	23	62	0	0	0	0	37	100	37	100
20	60	13	22	0	0	0	0	60	100	60	100
21	48	13	27	0	0	0	0	48	100	48	100
22	50	6	12	0	0	3	6	47	94	50	100
23	28	2	7	0	0	3	11	25	89	28	100
24	18	3	17	0	0	5	27	13	73	18	100
25	29	0	0	6	21	18	62	5	17	23	79
26	27	0	0	11	46	16	59	0	0	16	59
27	38	0	0	17	45	21	75	0	0	21	75
28	43	0	0	32	74	11	6	0	0	11	6
29	34	0	0	33	97	1	3	0	0	0	0
30	30	0	0	30	100	0	0	0	0	0	0
31	41	0	0	40	98	1	2	0	0	1	2
32	31	0	0	31	100	0	0	0	0	0	0
33	30	0	0	30	100	0	0	0	0	0	0
34	34	0	0	34	100	0	0	0	0	0	0
35	33	0	0	33	100	0	0	0	0	0	0
36	15	0	0	15	100	0	0	0	0	0	0
37	21	0	0	21	100	0	0	0	0	0	0
38	8	0	0	8	100	0	0	0	0	0	0
39	3	0	0	3	100	0	0	0	0	0	0

Note:—GA indicates gestational age in weeks; F, frequency; H, hyaloid vasculature; E, elliptic; T, transitional globe morphology/mild nonellipsoid shape; NE, nonelliptic.

academic children's hospital was queried for all fetal brain MR imaging examinations performed during an 8-year period (February 2007 to February 2015). Examinations with excessive motion artifacts, structural brain and craniofacial malformations, brain growth retardation, and overt globe malformations were excluded. Gestational age at the time of imaging was extracted from each patient's medical record. Gestational age was established by the clinicians caring for the patient on the basis of the last menstrual period and sonographic data.

Studies were performed on a 1.5T MR imaging scanner (GE Healthcare, Milwaukee, Wisconsin; or Siemens, Erlangen, Germany). Sequences included multiplanar single-shot fast spin-echo T2-weighted images (flip angle, 90°; TR/TE, 910–1090/60–160 ms; 2- to 5-mm section spacing with no gap; NEX, 0.53; echo-train length, 1); multiplanar heavily T2WI ("hydrography" or "fetography") (flip angle, 90°; TR/TE, 5000/163 ms; 2- to 5-mm section spacing with no gap; NEX, 0.54; echo-train length, 1) (GE Healthcare); or multiplanar half-Fourier acquisition single-shot turbo spin-echo images (flip angle, 150°; TR/TE, 1270/80 ms; 3- to 5-mm section spacing with no gap; NEX, 1; echo-train length, 250) (Siemens).

A qualitative structural analysis of bilateral fetal globes was undertaken by 2 fellowship-trained neuroradiologists with American Board of Radiology subspecialty certificates in neuroradiology. Gestational ages were not provided to the reviewers before interpretation. Both readers had >4 years of clinical experience after subspecialty board certification. Although the entire imaging dataset included visibility of the brain and globes, reviewers were careful to focus on the appearance of the globes and ignored the brain to the extent possible. Each reader reviewed 200 cases independently with excellent interreader reliability (Cohen κ coefficient = 0.98). The few initial discrepancies between readers were resolved in consensus. A consensus reading was also reached in all other cases.

Ocular globes were assessed in axial, sagittal, and coronal planes. Ocular globe shape was recorded either as "elliptic," "nonelliptic," or "transitional." All intermediate, ambiguous, and mild cases of nonellipsoid globe morphology in ≥ 1 imaging plane were considered "transitional." For statistical simplicity,

transitional and definitively nonelliptic cases were grouped together and considered "nonelliptic." Hyaloid vasculature was noted to be either present or absent on the basis of whether tubular/linear hypointense signal was seen extending from the posterior globe margin to the lens.

Data Collection and Statistics

Data were stored and analyzed by using an Excel 2011 spreadsheet (Microsoft, Redmond, Washington). Logistic regression analyses

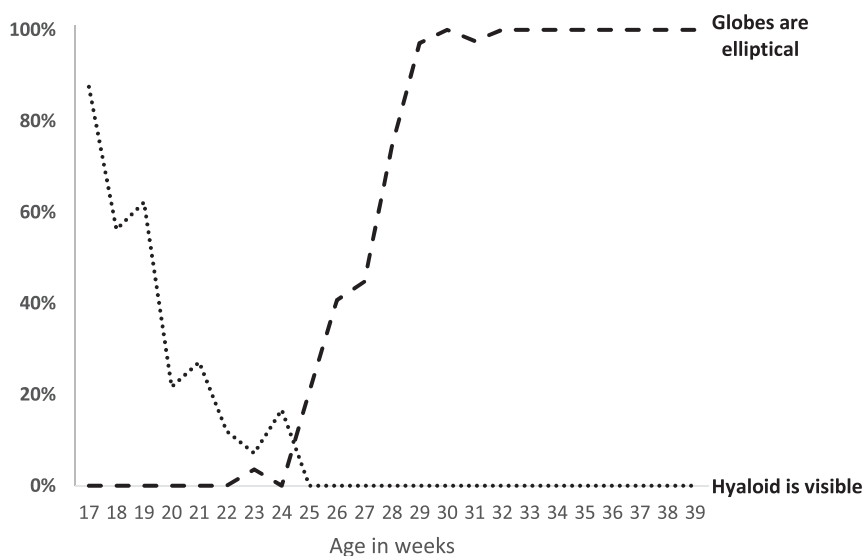


FIG 2. Age-related changes in globe morphology and hyaloid vasculature visibility from 17 to 39 weeks' gestation.

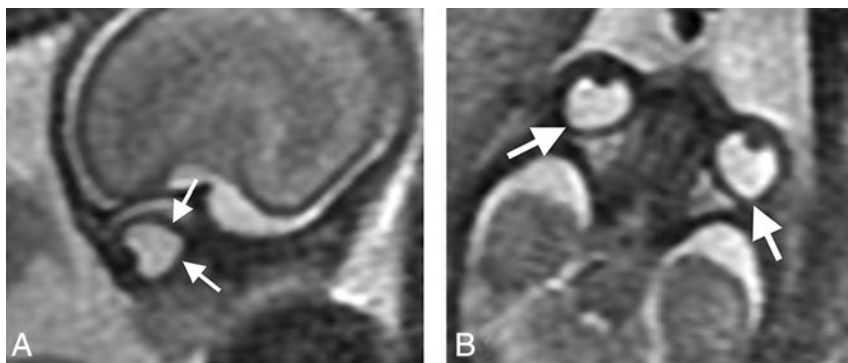


FIG 3. Sagittal (A) and axial (B) "fetography" T2WI (TR/TE, 5000/163 ms) of a normal fetal brain at 20 weeks' gestational age. The globe morphology is conical, with angulation of its posterior (arrows, A) and posterolateral (arrows, B) margins.

were used to evaluate the relationship between age and globe shape as well as age and visibility of hyaloid vasculature. Receiver operating curve characteristics were subsequently calculated. Sensitivity and specificity at each gestational week data-point were calculated to determine the optimal cut-points for visibility of fetal vasculature and ellipsoid globe morphology. Cut-points were chosen to optimize specificity at the expense of sensitivity. *P* values < .05 were considered significant.

RESULTS

We reviewed 1243 examinations from 1177 patients; 561 examinations were excluded. Six hundred eighty-two examinations from patients of 17–39 weeks' gestational age met the inclusion criteria (mean, 27 ± 0.4 weeks' gestation). Receiver operating characteristic analysis showed that age was highly predictive of globe shape (area under the curve = 0.99) and visibility of the fetal vasculature (area under the curve = 0.94) (Fig 1). Gestational age cut-points were determined to be 29 weeks (sensitivity, 81%; 95% CI, 76%–85%; specificity, 99%; 95% CI, 98%–100%) and 25 weeks (sensitivity, 69%; 95% CI, 65%–72%; specificity, 100%; 95% CI, 95%–100%) for the presence of elliptic globes and the absence of fetal vasculature,

respectively (Fig 1). Globe morphology and internal signal corresponding to the presence or absence of hyaloid vasculature changed during gestation (Table and Fig 2).

All globes were generally symmetric to one another in shape bilaterally. Nonelliptic globe morphology (focal convexity of the posterolateral margins) was universal until 22 weeks' gestation in both the axial and sagittal planes (Figs 3 and 4A, -B). Thereafter, globe morphology gradually changed. At 22–24 weeks, most patients had nonelliptic globes (sagittal and axial planes), and a few were transitional, approaching an elliptic shape (abnormal only on axial images). At 25–28 weeks, noticeably milder changes occurred, with minor nonelliptic globe morphology generally only visible in the axial plane in most patients. At 29 weeks and beyond, almost all patients demonstrated elliptic globe morphology with no more than minimal contour deformity noted (Fig 4 and Table). All patients with follow-up fetal MR imaging examinations ($n = 25$) had progression of globe morphology toward an elliptic shape in accordance with this timeline.

The hyaloid vasculature was visible in most patients up to 19 weeks, then occasionally up to 24 weeks (Fig 5). After that, the hyaloid vasculature system was no longer detectable.

DISCUSSION

The embryologic origin of the ocular globe and its components is varied and complex. Multiple cell types contribute

to ocular formation, including neuroectoderm, surface ectoderm, mesoderm, and neural crest cells. Thus, globe malformations can be seen in conjunction with craniofacial and brain malformations and as part of a number of syndromes. On imaging, eye abnormalities may take the form of alterations in size and/or shape of the ocular globes, either symmetric or asymmetric, underscoring the importance of in utero globe structure assessment. Size and shape asymmetries can be found in both acquired diseases (eg, infectious, inflammatory, or ischemic injury) and congenital processes (eg, microphthalmia, colobomas, persistent fetal vasculature, chromosomal abnormalities, and dystroglycanopathies).^{2,10} Furthermore, abnormalities of globe structure may impart valuable information regarding the integrity of the brain and surrounding craniofacial structures.

The primary vitreous appears in the first gestational month, begins to regress at the end of the first trimester, and is nearly completely replaced by the secondary vitreous by 30 weeks.^{1,6,9–11} The hyaloid vasculature is a marker for the primary vitreous; it involutes in conjunction with the primary vitreous but may persist until the 34th gestational week.¹² The hyaloid artery and canal are small struc-

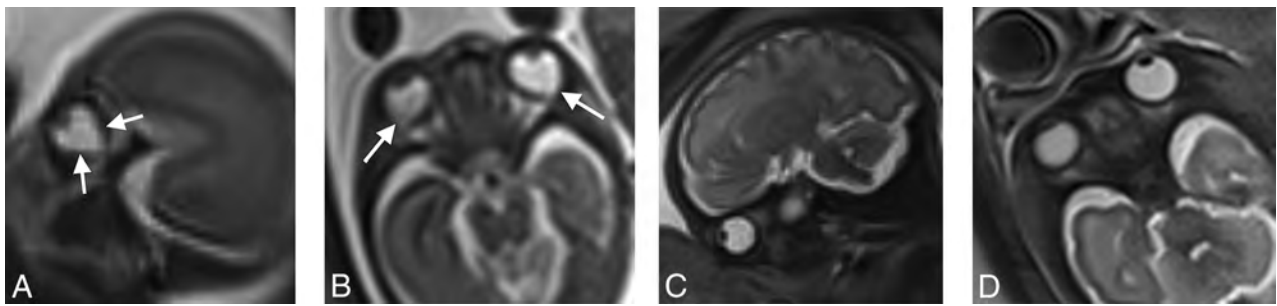


FIG 4. Sagittal (A) and axial (B) T2 HASTE (TR/TE, 1270/80 ms) of a normal fetal brain at 18 weeks' gestational age. The globe morphology is conical with angulation of its posterior (arrows, A) and posterolateral (arrows, B) margins. Follow-up sagittal (C) and axial (D) T2 HASTE (TR/TE, 1270/81 ms) of a normal fetal brain from imaging performed on the same patient at 30 weeks' gestational age. Ocular globe morphology is round/elliptic in the axial and sagittal planes. Fetal vasculature is not visible.

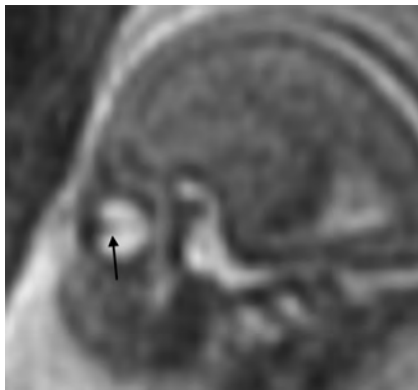


FIG 5. Sagittal single-shot fast spin-echo T2WI (TR/TE, 1087/56 ms) of a normal fetal brain at 19 weeks' gestation. Linear hypointense signal extending from the posterior margin of the lens through the vitreous toward the apex represents the hyaloid vasculature (arrow).

tures that challenge the resolution of imaging. On sonography, the hyaloid artery is normally seen up to the beginning of the third trimester and can be seen up to 28–30 gestational weeks.^{6,8,9} Sonographic visibility of the hyaloid vascular system after 30 weeks is abnormal and indicates residual primary vitreous or persistent fetal vasculature. Persistent fetal vasculature is generally unilateral. Bilateral persistent fetal vasculature should raise a differential diagnosis of Walker-Warburg syndrome, Norrie disease, and chromosomal trisomies.^{6,10,13}

Sparse literature exists regarding the regression of the hyaloid system on fetal MR imaging; however, hyaloid vasculature is not generally visible after 20 weeks.¹⁰ Our findings are in general agreement in that most examinations performed after 20 weeks had homogeneous vitreous signal; however, we did identify anteroposteriorly oriented linear hypointense signal traversing the vitreous in several patients of 17–24 weeks' gestational age, more commonly in younger patients, consistent with components of the hyaloid vascular system. The hyaloid vasculature is not normally visible in patients 25 weeks or older on MR imaging, assuming an identical imaging technique. Hyaloid visibility beyond this time should raise suspicion of persistent fetal vasculature.

Mature fetal globe shapes are generally described as round or spheric. However, Li et al³ reported that the normal fetal globe shape is better classified as elliptic because globes are consistently larger in the transverse than the anteroposterior dimension

throughout gestation. Our study demonstrates that elliptic ocular globe morphology is not fully achieved until the third trimester. Convexity of the posterolateral globe margins in the axial plane and conical, keel-shaped globes in the sagittal plane are transient and normal in the early developing eyes. This morphology may persist until around 29 weeks. Thereafter, the globes assume a nearly round or elliptic shape. Nonelliptic globes in patients older than 29 weeks' gestational age should raise suspicion of possible structural pathology. Most important, our study also shows that ocular globe morphology is symmetric on fetal MR imaging in the second and third trimesters (17–39 weeks) under normal circumstances. All apparent asymmetries between the ocular globes should be closely inspected; definitive asymmetries should be considered pathologic unless proved otherwise.

Limitations of this study include its retrospective design and the inability to ensure that each patient's ocular globes were entirely normal. However, globe morphology differences were consistent among patients during gestation. Motion artifacts could have caused apparent shape alterations and ghosting artifacts that simulated the hyaloid vascular system. Some degree of patient motion artifacts was an inevitable limitation; however, examinations with excessive motion artifacts were excluded. Although gestational ages were not provided to the readers during assessment and the brain was ignored to the extent possible when assessing the globes, images of the brain were visible to the reader in each study, potentially introducing an interpretation bias. However, between 23 and 28 weeks of gestation, when globe shapes transition from nonelliptic to elliptic, the extent of brain sulcation and gyration changes only modestly, whereas anterior frontal lobe sulcation near the orbits does not. Therefore, it was relatively easy for the readers to remain uninformed as to the gestational age during these critical weeks.

CONCLUSIONS

Physiologic nonelliptic globe shapes are normal up to 29 weeks' gestation and should not be misinterpreted as pathologic. Thereafter, the ocular globes assume an elliptic morphology. Transient symmetric, nonelliptic globes with convexity of the posterolateral margins are a normal developmental phenomenon. The timing of this process coincides with the resolution of the primary vitreous and hyaloid vasculature and may be related. Any major morphologic asymmetry between the ocular globes should be considered pathologic.

REFERENCES

1. Mafee MF. **Eye and orbit.** In: Mafee MF, Valvasorri GE, Becker M, eds. *Imaging of the Head and Neck*. 2nd ed. New York: Thieme; 2005:137–39
2. Paquette LB, Jackson HA, Tavaré CJ, et al. **In utero eye development documented by fetal MR imaging.** *AJNR Am J Neuroradiol* 2009;30:1787–91 CrossRef Medline
3. Li XB, Kasprian G, Hodge JC, et al. **Fetal ocular measurements by MRI.** *Prenat Diagn* 2010;30:1064–71 CrossRef Medline
4. Bojikian KD, de Moura CR, Tavares IM, et al. **Fetal ocular measurements by three-dimensional ultrasound.** *J AAPOS* 2013;17:276–81 CrossRef Medline
5. Anand-Apte B, Hollyfield JG. **Developmental anatomy of the retinal and choroidal vasculature.** In: Dana R, Dartt DA, Besharse, eds. *Encyclopedia of the Eye*. Amsterdam: Elsevier; 2010:9–15
6. Achiron R, Kreiser D, Achiron A. **Axial growth of the fetal eye and evaluation of the hyaloid artery: in utero ultrasonographic study.** *Prenat Diagn* 2000;20:894–99 Medline
7. Achiron R, Gottlieb Z, Yaron Y, et al. **The development of the fetal eye: in utero ultrasonographic measurements of the vitreous and lens.** *Prenat Diagn* 1995;15:155–60 CrossRef Medline
8. Birnholz JC. **Ultrasonic fetal ophthalmology.** *Early Hum Dev* 1985;12:199–209 CrossRef Medline
9. Birnholz JC, Farrell EE. **Fetal hyaloid artery: timing of regression with US.** *Radiology* 1988;166:781–83 CrossRef Medline
10. Robinson AJ, Blaser S, Toi A, et al. **MRI of the fetal eyes: morphologic and biometric assessment for abnormal development with ultrasonographic and clinicopathologic correlation.** *Pediatr Radiol* 2008;38:971–81 CrossRef Medline
11. Saint-Geniez M, D'Amore PA. **Development and pathology of the hyaloid, choroidal and retinal vasculature.** *Int J Dev Biol* 2004;48:1045–58 CrossRef Medline
12. Tortori-Donati P, Rossi A, Biancheri R. **The orbit.** In: Tortori-Donati P, Rossi A, Biancheri R, eds. *Pediatric Neuroradiology: Brain, Head, Neck and Spine*. Berlin: Springer-Verlag; 2009:1320
13. Haddad R, Front RL, Reeser F. **Persistent hyperplastic primary vitreous: a clinicopathologic study of 62 cases and review of the literature.** *Surv Ophthalmol* 1978;23:123–34 CrossRef Medline

Gray Matter Growth Is Accompanied by Increasing Blood Flow and Decreasing Apparent Diffusion Coefficient during Childhood

N.D. Forkert, M.D. Li, R.M. Lober, and K.W. Yeom



ABSTRACT

BACKGROUND AND PURPOSE: Normal values of gray matter volume, cerebral blood flow, and water diffusion have not been established for healthy children. We sought to determine reference values for age-dependent changes of these parameters in healthy children.

MATERIALS AND METHODS: We retrospectively reviewed MR imaging data from 100 healthy children. Using an atlas-based approach, age-related normal values for regional CBF, apparent diffusion coefficient, and volume were determined for the cerebral cortex, hippocampus, thalamus, caudate, putamen, globus pallidus, amygdala, and nucleus accumbens.

RESULTS: All gray matter structures grew rapidly before the age of 10 years and then plateaued or slightly declined thereafter. The ADC of all structures decreased with age, with the most rapid changes occurring prior to the age of 5 years. With the exception of the globus pallidus, CBF increased rather linearly with age.

CONCLUSIONS: Normal brain gray matter is characterized by rapid early volume growth and increasing CBF with concomitantly decreasing ADC. The extracted reference data that combine CBF and ADC parameters during brain growth may provide a useful resource when assessing pathologic changes in children.

ABBREVIATION: ASL = arterial spin-labeling

At birth, brain volume is approximately one-third that of a healthy adult brain and undergoes rapid growth during the first 3 months.¹ By the age of 1 year, brain volume has already doubled in size.² Initially, most hemispheric growth relates to an increase in gray matter volume,³ thought to reflect synapse formation occurring earliest in the primary motor and sensory cortices and later in the prefrontal cortex,⁴ directing a posterior-to-anterior pattern of hemispheric white matter maturation.⁵ After the first few years, white matter volume increases at a higher rate during the rest of the childhood,⁶ while synaptic pruning occurs concurrently in the gray matter.⁴

Compared with macrostructural analysis using image-based volume extraction, diffusion-weighted MR imaging can be used to probe microstructural changes, including myelination patterns^{7,8} and white matter connectivity,⁹ and has also shown utility for brain tumor characterization¹⁰ and metabolic diseases.¹¹ Various studies have examined apparent diffusion coefficient changes of white matter in children.¹²⁻¹⁴ However, at present, the ADC of the gray matter, notably at the cortical level, is not well-documented.

While volumetric and diffusion analysis can be used to probe macro- and microstructural changes, respectively, arterial spin-labeling (ASL) cerebral blood flow is increasingly used clinically to obtain advanced physiologic information.¹⁵⁻¹⁸ ASL may be particularly useful in the pediatric population because it does not require intravenous contrast or ionizing radiation. However, only a few studies have examined ASL CBF changes in children.^{19,20}

These few studies have included ASL CBF of unsedated healthy term and preterm neonates²¹ or infants 3–5 months of age.²² Apart from these 2 studies, normal values have also been assessed as part of studies investigating CBF changes across the whole life span with only limited data from children²⁰ or for feasibility analysis of ASL imaging, also using only a limited number of healthy children.¹⁹

Received December 10, 2015; accepted after revision February 8, 2016.

From the Department of Radiology and Hotchkiss Brain Institute (N.D.F.), University of Calgary, Calgary, Alberta, Canada; Department of Radiology (M.D.L., K.W.Y.), Lucile Packard Children's Hospital, Stanford University, Palo Alto, California; and Department of Neurosurgery (R.M.L.), Dayton Children's Hospital, Boonshoft School of Medicine, Dayton, Ohio.

This work was supported by a Brain and Behavior Center Award in Pediatric Neurosciences at Stanford Lucile Packard Children's Hospital.

Please address correspondence to Nils Daniel Forkert, PhD, Department of Radiology and Hotchkiss Brain Institute, University of Calgary, HSC Building, Rm 2913, 3330 Hospital Drive NW, Calgary, Alberta T2N 4N1, Canada; e-mail: nils.forkert@ucalgary.ca



Indicates article with supplemental on-line photo.

<http://dx.doi.org/10.3174/ajnr.A4772>

At present, no study has examined the CBF of a healthy pediatric cohort across the age spectrum. Therefore, the goal of this study was to extract and establish age-related CBF values in gray matter along with corresponding volume and diffusion metrics.

MATERIALS AND METHODS

Study Cohort

All children presenting for evaluation by a 3T MR imaging system at our children's hospital from May 2010 to October 2013 were retrospectively reviewed after approval by the Stanford University institutional review board (protocol 28674). The study cohort included patients 4 months to 18 years of age with no known neurologic, neurocognitive, or developmental deficits, who had a normal appearing brain MRI protocol that included ASL and DWI datasets. All MR imaging brain studies with normal findings were additionally reviewed and confirmed by at least 1 pediatric neuroradiologist with a Certificate of Added Qualification (K.W.Y. or P. Barnes both with >7 years of dedicated experience). Patients who had brain MR imaging with any focal intensity on FLAIR or other sequences, cysts, wide Sylvian fissures, or other nonspecific structural appearances were excluded. Patients with dental braces/metal artifacts and motion-degraded or non-diagnostic-quality imaging were also excluded.

A thorough chart review was performed (M.D.L.) to identify any disease history. Examples of clinical reasons for obtaining MR imaging included syncope, nausea, family history of aneurysm or cancers, scalp nevus, isolated facial lesions (eg, orbital or glabellar dermoid) without associated syndromes or intracranial extension, orbital strabismus, cholesteatoma of the ear, isolated headaches, sinus disease or inflammatory nasal obstruction, and short stature that was considered familial without intracranial or endocrine abnormality.

Patients with any systemic or non-central nervous system diseases (eg, diseases of the renal, gastrointestinal, cardiac systems), cancers, history of prematurity, phacomatoses, genetic or syndromic conditions, epilepsy, migraines, hearing loss, hemorrhage, vascular lesions (aneurysm, AVM, fistula, or steno-occlusive disease of the CNS or elsewhere), acute or recent infection and fever of unknown origin, prior radiation or chronic medical therapy, or endocrine symptoms/laboratory abnormalities were excluded. Patients were also screened for all psychiatric and abnormal behavioral conditions (attention deficit/hyperactivity disorder, autism, psychosis) and were excluded if present.

Finally, subjects with insufficient data or registration results (see below) were also excluded from the final analysis.

Imaging Methods

All subjects had brain MR imaging obtained at 3T (Discovery 750; GE Healthcare, Milwaukee, Wisconsin) using an 8-channel head coil. Pseudocontinuous ASL MR imaging was performed using the technique described by Dai et al.²³ Briefly, this vendor-supplied ASL was performed using a pseudocontinuous labeling period of 1500 ms, followed by a 1500-ms postlabel delay. Whole-brain images were acquired with a 3D background-suppressed fast spin-echo stack-of-spirals method. Multiarm spiral imaging was used, with 8 arms and 512 points acquired on each arm (bandwidth = 62.5 kHz), yielding a 3-mm² in-plane spatial reso-

lution and a 4-mm section thickness. A high level of background suppression was achieved using 4 separate inversion pulses spaced around the pseudocontinuous labeling pulse. The acquisition time for this sequence is approximately 5 minutes, which also includes proton-density images required for CBF quantification. For a graphic setup of the ASL, the sagittal image following the 3-plane localizer was used for alignment. Postprocessing was performed using an automated reconstruction procedure using the microsphere methodology described by Buxton et al.²⁴ Other pseudocontinuous ASL MR imaging parameters were TR = 4632 ms, TE = 10.5 ms, FOV = 24 cm, and NEX = 3.

Additionally, echo-planar DWI was performed using TR = 1500 ms, TE = 37 ms, flip angle = 90°, acceleration factor = 2, in-plane resolution = 0.94 mm², acquisition matrix = 128 × 128 interpolated to a 256 × 256 matrix, 44 sections with 4-mm section thickness, no skip, FOV = 24 cm, 2 diffusion-weightings of $b=0$ s/mm² and $b=1000$ s/mm², with diffusion gradients acquired in 3 directions averaged for the latter.

Image Processing

The image-processing pipeline used for extraction of quantitative values of regional brain volume, ADC, and CBF is illustrated in Fig 1. The complete image-processing pipeline used was custom-developed and implemented in C++ using the Insight Segmentation and Registration Toolkit (ITK, <http://www.itk.org/>). In the first step of this pipeline, the ASL CBF and $b=1000$ s/mm² DWI dataset were registered to the corresponding T2-weighted DWI dataset ($b=0$ s/mm²) using rigid transformations, linear interpolation, and maximization of the mutual information.²⁵ The registered DWI datasets were then used to calculate the corresponding ADC map for each subject using the Stejskal-Tanner equation.²⁶

Finally, the Montreal Neurological Institute-152 brain atlas²⁷ was registered to each $b=0$ s/mm² DWI dataset using a concatenated affine and nonlinear spline transformation. The affine transformation was determined using a linear interpolation and maximization of the mutual information metric. The calculated affine transformation was used to prealign the atlas to the patient anatomy in terms of initialization of a b-spline transformation, which was used for the fine nonlinear alignment of the Montreal Neurological Institute atlas to the $b=0$ s/mm² DWI dataset. This b-spline transformation was optimized using linear interpolation and maximization of the mutual information metric.

All registrations were performed within a multiresolution registration framework with 3 levels, while the calculation of the mutual information similarity metric was restricted in all cases to the brain mask of the $b=0$ s/mm² DWI dataset, which was generated using the method described by Forkert et al.²⁸ Two experienced observers (N.D.F., K.W.Y.) checked all registration results to ensure suitable data and registration quality.

For quantitative assessment of volume, ADC, and CBF of the different gray matter brain regions, the resulting nonlinear spatial deformation field for alignment of the Montreal Neurological Institute atlas to each subject was used to warp the Harvard-Oxford subcortical brain regions, as defined in the Montreal Neurological Institute atlas space, to each $b=0$ s/mm² DWI dataset by applying nearest neighbor interpolation.

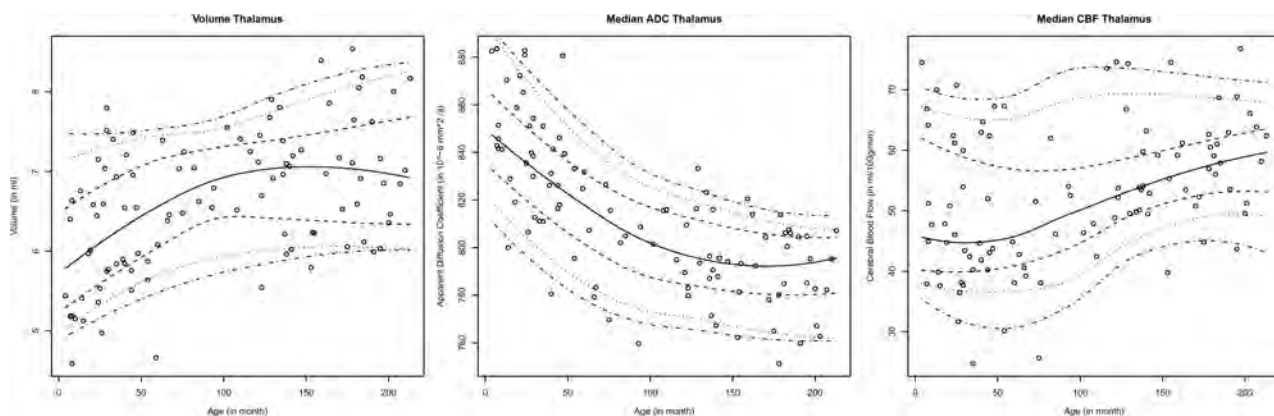


FIG 2. Graphic representation of the age-dependent volumetric, ADC, and CBF normal values for the thalamus illustrated using the 5%, 10%, 25%, 50%, 75%, 90%, and 95% centile curves.

CBF of the Gray Matter

Cerebral blood flow was more variable than volume and ADC, particularly in the first 5 years of childhood. Unlike the rapid volume and ADC changes in the first 5 years of life, CBF increased rather linearly with age, with decreased variability at older ages. CBF in all gray matter structures increased with age, except for the globus pallidus, which was stable throughout childhood. The degree of CBF increase did not differ considerably among the caudate, thalamus, putamen, nucleus accumbens, and amygdala, but a smaller degree of CBF increase was found for the hippocampus, and a larger CBF increase, for the cerebral cortex with age.

Sedated versus Nonsedated Children

The comparison of sedated ($n = 7$; mean age, 7.6 years) and nonsedated children ($n = 4$; mean age, 7.9 years) revealed no significant CBF differences in any brain region studied (Welch 2-tailed t test, $P > .01$; Bonferroni-adjusted significance level = .005).

DISCUSSION

Gray matter CBF increased with age, except in the globus pallidus. Notably, the cerebral cortex, amygdala, and nucleus accumbens showed the highest CBF increase. These CBF changes were accompanied by a progressive ADC decrease and volumetric increase for all gray matter structures, with ADC stabilizing at about 10–12 years and peak volume occurring at around 8–12 years, with a slight decrease thereafter. To our knowledge, this is the first study to investigate age-related changes of gray matter CBF accompanied by corresponding volume and ADC values in a single cohort of neurologically healthy children throughout childhood and adolescence.

Our volumetric results are consistent with prior studies of healthy subjects that showed an overall increase in cortical gray matter volume in the preadolescent years and a decline in the postadolescent period.³⁰ Volumetric analysis for infancy and early childhood remains sparse, but our results are also consistent with the growth pattern described in a study of 28 children 1 month to 10 years of age, in whom a rapid growth pattern was followed by a more gradual increase.³¹ A more recent study that focused on infants (3–13 months of age) also observed an increasing volume of all gray matter regions with some regionally different growth patterns.³²

While volume increased, the ADC of the gray matter declined rapidly, with a fast exponential component in the first few years, which then stabilized in early adolescence. These findings likely reflect the combined effects of neuronal development, myelination, and decrease in water content³³ and associated MR imaging signal changes^{34,35} that rapidly occur in the early years of development. Potential contributions of iron-deposition that decrease T2 relaxation time may also be considered, particularly in the deep gray nuclei, which has been observed in children older than 4 years of age and in adolescents.³⁶

Although various studies have reported ADC changes of cerebral white matter in children,^{12–14} gray matter structures have remained relatively unexplored. We observed a steep decline with an exponential component in early childhood with a decreasing trend continuing into later childhood, consistent with results of prior ROI-based studies in selected deep gray regions (caudate, putamen, globus pallidus).^{37,38}

Compared with volume and ADC changes, a wider variation in CBF values was seen across age. In addition, median CBF values and the magnitude of increase varied among the gray matter regions. Previous studies have described a close relationship between CBF and the cerebral metabolic rate^{39–41}; and in a study of cerebral metabolism in 29 children (5 days to 15 years of age) using ¹⁸F-FDG positron-emission tomography, a similar pattern of highest proportional increase in metabolic activity was seen in the cerebral cortex compared with the other brain regions.⁴²

We observed a gradual increase in CBF in all gray matter regions, except for the globus pallidus, throughout childhood and adolescence, which differs from a previous ASL CBF study that described a relatively stable-to-decreased CBF between 4 and 12 years of age, followed by a sharp decline in adolescence²⁰ in 23 children aged 4–19 years. One possible explanation might be differences in postlabel delay periods. Because the ASL tracer lifetime is dependent on the longitudinal relaxation time of blood, which is similar to the transport time from the labeling position to the tissue (arterial transit time), a shorter postlabel delay period of 1000 ms used in the study by Biagi et al²⁰ may be insufficient for complete delivery of labeled blood to the tissue, a potential limitation when assessing adolescents with slower arterial transit time compared with younger children.^{43,44} The present data in our study were obtained from a pseudocontinuous ASL technique,

which has been shown to have a superior labeling efficiency,²³ signal-to-noise ratio, and reproducibility,⁴⁵ and is thus preferred over other ASL methods. We also used a postlabel delay of 1500 ms recommended by the current guidelines of the International Society for Magnetic Resonance in Medicine for clinical imaging of the pediatric brain.⁴⁶

Biagi et al²⁰ also observed increased gray matter CBF in pediatric patients receiving halogenated anesthesia relative to awake patients, which was rather similar to those receiving only intravenous propofol. A review of adult functional imaging studies noted that propofol was associated with decreased CBF, determined by PET, in all brain regions in multiple studies.⁴⁷ Thus, a disproportionate number of younger children requiring halogenated anesthesia could have affected their results. For example, an ASL study in 4 patients with Moyamoya disease found that halogenated anesthesia (sevoflurane) was associated with consistently higher global gray matter CBF.⁴⁸ In our study, intravenous propofol sedation, with or without mask induction using a halogenated anesthetic, was performed for all children 3 months to 6 years of age. Between 6 and 9 years of age, there were variable rates of sedation. The statistical analysis of children with and without sedation in this age range showed no significant differences. This could possibly be explained by a balancing effect of increased CBF with halogenated anesthesia and decreased CBF with propofol.²⁰ Thus, no correction was necessary in this study.

Brain development has been shown to be associated with regional changes in the glucose cerebral metabolic rate⁴² and CBF.⁴⁹ Thus, continued increases in ASL CBF during childhood and adolescence may reflect a more protracted period of functional development and maturation. While global cerebral volume has been shown to peak at 14.5 years for boys and 11.5 years for girls, changes in cortical gray matter volume are more complex and have shown regional heterochronicity.⁵⁰ For example, in a study of 145 subjects 4–21 years of age, the frontal and parietal lobes showed an earlier peak at 11–12 years of age, while maximal temporal gray matter volumes occurred at 16–17 years of age, and the occipital lobes had a linear increase through 20 years of age without signs of decline.³⁰ Previous studies have also reported periods of postnatal rapid brain growth up to 20 years of age based on electroencephalography energy metrics in the α frequencies.^{51,52} A spike in CBF was observed preceding these stages of brain growth, suggesting a higher energy requirement during these periods,⁵³ a pattern also seen in the rat cerebral cortex that has shown increased vascular sprouting shortly before rapid growth stages.⁵⁴

Individual differences in brain growth spurts may also explain variations of CBF observed in the present study to some degree. While the definitive reasons for relatively stable CBF in the globus pallidus and a slower rate of CBF increase in the hippocampus compared with the other brain regions analyzed remain unknown, it is possible that these regions demonstrate different rates of growth or metabolism. For example, a morphometric analysis of infants 3–13 months of age showed a slower growth rate in certain brain regions, such as the globus pallidus and hippocampus, relative to the whole brain, despite an overall increase in volume in absolute values.³²

We recognize certain limitations of this study. For example,

for our analysis, the adult Montreal Neurological Institute atlas was registered to the pediatric brain. While registration of a pediatric atlas might be more accurate for this purpose, different brain atlases generated by using different age ranges and subjects (eg, described by Fonov et al⁵⁵) would be necessary, potentially making the results not directly comparable. Therefore, we decided to use the well-established Montreal Neurological Institute adult brain atlas with the available Harvard-Oxford atlas brain regions for this purpose so that the same reference was used for each subject to analyze CBF, ADC, and volume data metrics. To minimize any effects of suboptimal registration results, we performed further quality control, including visual inspection by our team members with knowledge of brain imaging and anatomy. Within this context, 22 subjects not part of the 100 subjects described in this study were excluded from the final analysis due to insufficient registration of the Montreal Neurological Institute brain atlas.

In addition, the $b=0$ s/mm² DWI datasets were used as a reference for atlas registration. These datasets do not offer the same high spatial resolution compared with T1-weighted datasets usually used for this purpose, which limits the precision of the extracted regional brain volumes, especially for small structures such as the amygdala.

However, although our goal was to demonstrate CBF changes against volume and ADC across various age groups for various brain regions rather than to define precise metrics for volume, the growth patterns found are well in line with previous findings, suggesting reasonable registration results.

Finally, the regional brain volumes were averaged between corresponding left and right hemispheric structures, while median ADC and CBF values were calculated for each combined corresponding left and right hemisphere brain structure. This procedure was selected to decrease the influence of noise in the data, especially for the small structures such as the amygdala and nucleus accumbens. When analyzed separately, no significant difference between the age-related trends of corresponding left and right brain structures was found for the regional brain volume, ADC, and CBF metrics.

CONCLUSIONS

Normal gray matter is characterized by rapid early volume growth and increasing CBF, with concomitantly decreasing ADC. The extracted reference data that combine CBF and ADC parameters during brain growth may provide a useful resource when assessing pathologic changes in children.

ACKNOWLEDGMENTS

The authors would like to thank Patrick Barnes, Department of Pediatric Neuroradiology, Stanford University, for his support in reviewing the MR imaging brain studies used in this work.

REFERENCES

1. Holland D, Chang L, Ernst TM, et al. **Structural growth trajectories and rates of change in the first 3 months of infant brain development.** *JAMA Neurol* 2014;71:1266–74 CrossRef Medline
2. Gilmore JH, Lin W, Prastawa MW, et al. **Regional gray matter growth, sexual dimorphism, and cerebral asymmetry in the neonatal brain.** *J Neurosci* 2007;27:1255–60 CrossRef Medline
3. Knickmeyer RC, Gouttard S, Kang C, et al. **A structural MRI study of**

- human brain development from birth to 2 years. *J Neurosci* 2008;28:12176–82 CrossRef Medline
4. Huttenlocher PR, Dabholkar AS. **Regional differences in synaptogenesis in human cerebral cortex.** *J Comp Neurol* 1997;387:167–78 Medline
5. Sampaio CS, Truwit CL. **Myelination in the developing brain.** In: Nelson CA, Luciana M, eds. *Handbook of Developmental Cognitive Neuroscience*. Cambridge, Massachusetts: MIT Press; 2001:35–44
6. Dubois J, Dehaene-Lambertz G, Kulikova S, et al. **The early development of brain white matter: a review of imaging studies in fetuses, newborns and infants.** *Neuroscience* 2014;276:48–71 CrossRef Medline
7. Loh KB, Ramli N, Tan LK, et al. **Quantification of diffusion tensor imaging in normal white matter maturation of early childhood using an automated processing pipeline.** *Eur Radiol* 2012;22:1413–26 CrossRef Medline
8. Uda S, Matsui M, Tanaka C, et al. **Normal development of human brain white matter from infancy to early adulthood: a diffusion tensor imaging study.** *Dev Neurosci* 2015;37:182–94 CrossRef Medline
9. Alcauter S, Lin W, Smith JK, et al. **Development of thalamocortical connectivity during infancy and its cognitive correlations.** *J Neurosci* 2014;34:9067–75 CrossRef Medline
10. Löbel U, Sedlacik J, Reddick WE, et al. **Quantitative diffusion-weighted and dynamic susceptibility-weighted contrast-enhanced perfusion MR imaging analysis of T2 hypointense lesion components in pediatric diffuse intrinsic pontine glioma.** *AJNR Am J Neuroradiol* 2011;32:315–22 CrossRef Medline
11. Dyke JP, Voss HU, Sondhi D, et al. **Assessing disease severity in late infantile neuronal ceroid lipofuscinosis using quantitative MR diffusion-weighted imaging.** *AJNR Am J Neuroradiol* 2007;28:1232–36 CrossRef Medline
12. Löbel U, Sedlacik J, Güllmar D, et al. **Diffusion tensor imaging: the normal evolution of ADC, RA, FA, and eigenvalues studied in multiple anatomical regions of the brain.** *Neuroradiology* 2009;51:253–63 CrossRef Medline
13. Engelbrecht V, Scherer A, Rassek M, et al. **Diffusion-weighted MR imaging in the brain in children: findings in the normal brain and in the brain with white matter diseases.** *Radiology* 2002;222:410–18 CrossRef Medline
14. Rollins NK, Glasier P, Seo Y, et al. **Age-related variations in white matter anisotropy in school-age children.** *Pediatr Radiol* 2010;40:1918–30 CrossRef Medline
15. Chen J, Licht DJ, Smith SE, et al. **Arterial spin labeling perfusion MRI in pediatric arterial ischemic stroke: initial experiences.** *J Magn Reson Imaging* 2009;29:282–90 CrossRef Medline
16. Yeom KW, Lober RM, Alexander A, et al. **Hydrocephalus decreases arterial spin-labeled cerebral perfusion.** *AJNR Am J Neuroradiol* 2014;35:1433–39 CrossRef Medline
17. Yeom KW, Lober RM, Barnes PD, et al. **Reduced cerebral arterial spin-labeled perfusion in children with neurofibromatosis type 1.** *AJNR Am J Neuroradiol* 2013;34:1823–28 CrossRef Medline
18. Yeom KW, Mitchell LA, Lober RM, et al. **Arterial spin-labeled perfusion of pediatric brain tumors.** *AJNR Am J Neuroradiol* 2014;35:395–401 CrossRef Medline
19. Wang J, Licht DJ, Jahng GH, et al. **Pediatric perfusion imaging using pulsed arterial spin labeling.** *J Magn Reson Imaging* 2003;18:404–13 CrossRef Medline
20. Biagi L, Abbruzzese A, Bianchi MC, et al. **Age dependence of cerebral perfusion assessed by magnetic resonance continuous arterial spin labeling.** *J Magn Reson Imaging* 2007;25:696–702 CrossRef Medline
21. Miranda MJ, Olofsson K, Sidas K. **Noninvasive measurements of regional cerebral perfusion in preterm and term neonates by magnetic resonance arterial spin labeling.** *Pediatr Res* 2006;60:359–63 CrossRef Medline
22. Duncan AF, Caprihan A, Montague EQ, et al. **Regional cerebral blood flow in children from 3 to 5 months of age.** *AJNR Am J Neuroradiol* 2014;35:593–98 CrossRef Medline
23. Dai W, Garcia D, de Bazelaire C, et al. **Continuous flow-driven inversion for arterial spin labeling using pulsed radio frequency and gradient fields.** *Magn Reson Med* 2008;60:1488–97 CrossRef Medline
24. Buxton RB, Frank LR, Wong EC, et al. **A general kinetic model for quantitative perfusion imaging with arterial spin labeling.** *Magn Reson Med* 1998;40:383–96 CrossRef Medline
25. Wells WM 3rd, Viola P, Atsumi H, et al. **Multi-modal volume registration by maximization of mutual information.** *Med Image Anal* 1996;1:35–51 CrossRef Medline
26. Stejskal EO, Tanner JE. **Spin diffusion measurements: spin echoes in the presence of a time-dependent field gradient.** *J Chem Phys* 1965;42:288–92 CrossRef
27. Mazziotta JC, Toga AW, Evans A, et al. **A probabilistic atlas of the human brain: theory and rationale for its development—the International Consortium for Brain Mapping (ICBM).** *Neuroimage* 1995;2:89–101 CrossRef Medline
28. Forkert ND, Cheng B, Kemmling A, et al. **ANTONIA perfusion and stroke: a software tool for the multi-purpose analysis of MR perfusion-weighted datasets and quantitative ischemic stroke assessment.** *Methods Inf Med* 2014;53:469–81 CrossRef Medline
29. Sakov A, Golani I, Lipkind D, et al. **High-throughput data analysis in behavior genetics.** *Ann Appl Stat* 2010;4:743–63 CrossRef
30. Giedd JN, Blumenthal J, Jeffries NO, et al. **Brain development during childhood and adolescence: a longitudinal MRI study.** *Nat Neurosci* 1999;2:861–63 CrossRef Medline
31. Matsuzawa J, Matsui M, Konishi T, et al. **Age-related volumetric changes of brain gray and white matter in healthy infants and children.** *Cereb Cortex* 2001;11:335–42 CrossRef Medline
32. Choe MS, Ortiz-Mantilla S, Makris N, et al. **Regional infant brain development: an MRI-based morphometric analysis in 3 to 13 month olds.** *Cereb Cortex* 2013;23:2100–17 CrossRef Medline
33. Dobbing J, Sands J. **Quantitative growth and development of human brain.** *Arch Dis Child* 1973;48:757–67 CrossRef Medline
34. Barkovich AJ, Kjos BO, Jackson DE J, et al. **Normal maturation of the neonatal and infant brain: MR imaging at 1.5 T.** *Radiology* 1988;166:173–80 CrossRef Medline
35. Autti T, Raininko R, Vanhanen SL, et al. **MRI of the normal brain from early childhood to middle age, II: age dependence of signal intensity changes on T2-weighted images.** *Neuroradiology* 1994;36:649–51 CrossRef Medline
36. Thomas LO, Boyko OB, Anthony DC, et al. **MR detection of brain iron.** *AJNR Am J Neuroradiol* 1993;14:1043–48 Medline
37. Mukherjee P, Miller JH, Shimony JS, et al. **Normal brain maturation during childhood: developmental trends characterized with diffusion-tensor MR imaging.** *Radiology* 2001;221:349–58 CrossRef Medline
38. Pal D, Trivedi R, Saksena S, et al. **Quantification of age- and gender-related changes in diffusion tensor imaging indices in deep grey matter of the normal human brain.** *J Clin Neurosci* 2011;18:193–96 CrossRef Medline
39. Raichle ME. **Behind the scenes of functional brain imaging: a historical and physiological perspective.** *Proc Natl Acad Sci U S A* 1998;95:765–72 CrossRef Medline
40. Jueptner M, Weiller C. **Review: does measurement of regional cerebral blood flow reflect synaptic activity? Implications for PET and fMRI.** *Neuroimage* 1995;2:148–56 CrossRef Medline
41. Sokoloff L. **Localization of functional activity in the central nervous system by measurement of glucose utilization with radioactive deoxyglucose.** *J Cereb Blood Flow Metab* 1981;1:7–36 CrossRef Medline
42. Chugani HT, Phelps ME, Mazziotta JC. **Positron emission tomography study of human brain functional development.** *Ann Neurol* 1987;22:487–97 CrossRef Medline
43. Petersen ET, Mouridsen K, Golay X. **The QUASAR reproducibility study, part II: results from a multi-center arterial spin labeling test-retest study.** *Neuroimage* 2010;49:104–13 CrossRef Medline
44. Bokkers RP, van der Worp HB, Mali WP, et al. **Noninvasive MR imaging of cerebral perfusion in patients with a carotid artery stenosis.** *Neurology* 2009;73:869–75 CrossRef Medline

45. Chen Y, Wang DJ, Detre JA. **Test-retest reliability of arterial spin labeling with common labeling strategies.** *J Magn Reson Imaging* 2011;33:940–49 CrossRef Medline
46. Alsop DC, Detre JA, Golay X, et al. **Recommended implementation of arterial spin-labeled perfusion MRI for clinical applications: a consensus of the ISMRM perfusion study group and the European consortium for ASL in dementia.** *Magn Reson Med* 2015;73:102–16 CrossRef Medline
47. Song XX, Yu BW. **Anesthetic effects of propofol in the healthy human brain: functional imaging evidence.** *J Anesth* 2015;29:279–88 CrossRef Medline
48. Venkatraghavan L, Poubanc J, Bharadwaj S, et al. **Noninvasive measurement of cerebral blood flow under anesthesia using arterial spin labeling MRI: a pilot study.** *J Neurosurg Anesthesiol* 2015 Sep 20. [Epub ahead of print] Medline
49. Chiron C, Raynaud C, Mazière B, et al. **Changes in regional cerebral blood flow during brain maturation in children and adolescents.** *J Nucl Med* 1992;33:696–703 Medline
50. Lenroot RK, Gogtay N, Greenstein DK, et al. **Sexual dimorphism of brain developmental trajectories during childhood and adolescence.** *Neuroimage* 2007;36:1065–73 CrossRef Medline
51. Epstein HT. **EEG developmental stages.** *Dev Psychobiol* 1980;13:629–31 CrossRef Medline
52. Hudspeth WJ, Pribram KH. **Stages of brain and cognitive maturation.** *J Educ Psychol* 1990;82:881–84 CrossRef
53. Epstein HT. **Stages of increased cerebral blood flow accompany stages of rapid brain growth.** *Brain Dev* 1999;21:535–39 CrossRef Medline
54. Rowan RA, Maxwell DS. **Patterns of vascular sprouting in the post-natal development of the cerebral cortex of the rat.** *Am J Anat* 1981;160:247–55 CrossRef Medline
55. Fonov V, Evans AC, Botteron K, et al; Brain Development Cooperative Group. **Unbiased average age-appropriate atlases for pediatric studies.** *Neuroimage* 2011;54:313–27 CrossRef Medline

Correlation of MRI Brain Injury Findings with Neonatal Clinical Factors in Infants with Congenital Diaphragmatic Hernia

 R. Radhakrishnan,  S. Merhar,  J. Meinen-Derr,  B. Haberman,  F.Y. Lim,  P. Burns,  E. Zorn, and  B. Kline-Fath



ABSTRACT

BACKGROUND AND PURPOSE: Infants with congenital diaphragmatic hernia are reported to have evidence of brain MR imaging abnormalities. Our study aimed to identify perinatal clinical factors in infants with congenital diaphragmatic hernia that are associated with evidence of brain injury on MR imaging performed before hospital discharge.

MATERIALS AND METHODS: MRIs performed before hospital discharge in infants with congenital diaphragmatic hernia were scored for brain injury by 2 pediatric neuroradiologists. Perinatal variables and clinical variables from the neonatal intensive care unit stay were analyzed for potential associations with brain MR imaging findings.

RESULTS: Fifty-three infants with congenital diaphragmatic hernia (31 boys) were included. At least 1 abnormality was seen on MR imaging in 32 infants (60%). The most common MR imaging findings were enlarged extra-axial spaces (36%), intraventricular hemorrhage (23%), ventriculomegaly (19%), white matter injury (17%), and cerebellar hemorrhage (17%). The MR imaging brain injury score was associated with extracorporeal membrane oxygenation ($P = .0001$), lack of oral feeding at discharge ($P = .012$), use of inotropes ($P = .027$), and gastrostomy tube placement before hospital discharge ($P = .024$). The MR imaging brain injury score was also associated with a large diaphragmatic defect size ($P = .011$).

CONCLUSIONS: Most infants with congenital diaphragmatic hernia have at least 1 abnormality identified on MR imaging of the brain performed before discharge. The main predictors of brain injury in this population are a requirement for extracorporeal membrane oxygenation, large diaphragmatic defect size, and lack of oral feeding at discharge.

ABBREVIATIONS: CDH = congenital diaphragmatic hernia; ECMO = extracorporeal membrane oxygenation

Congenital diaphragmatic hernia (CDH), with an incidence of 1 case per 2000 live births, is an anomaly associated with substantial morbidity and mortality.¹ Survivors of CDH are at risk for long-term respiratory, gastrointestinal, nutritional, hearing, and neurologic sequelae, requiring multidisciplinary support, especially during early childhood.¹ Prenatal predictive factors for increased morbidity and mortality include prenatal imaging findings of liver herniation into the chest, lung to head ratio on prenatal sonography, or lung volumes on fetal MR imaging.²⁻⁴ The size of the diaphragmatic defect is another factor that likely plays a major role in morbidity and mortality in infants with

congenital diaphragmatic hernia.⁵ However, the association of the defect size with evidence of injury on brain imaging has not been studied, to our knowledge.

Long-term neurodevelopmental and neurobehavioral disabilities are reported in up to 70% of infants with congenital diaphragmatic hernia.⁶⁻⁹ Both brain maturational delays and evidence of brain injury have been reported on imaging.^{8,9} There continues to be some controversy about the correlation of neuroimaging abnormalities in CDH with neurologic outcome. In a small cohort of patients with CDH with prenatal and postnatal imaging, Tracy et al⁹ identified an association between brain injury seen on postnatal CT/MR imaging in 4 infants and neurodevelopmental outcome at 1 year. There was no correlation between prenatal factors and neurodevelopmental outcome in this study.⁹ In another study by Danzer et al,¹⁰ postnatal brain MR imaging abnormalities were associated with lower cognitive scores, motor dysfunction, and language deficits.

The impact of extracorporeal membrane oxygenation (ECMO) on neonates with CDH requiring ECMO is of clinical relevance. Studies suggest that neonates with CDH who require

Received November 18, 2015; accepted after revision February 24, 2016.

From the Departments of Radiology (R.R., B.K.-F.), Biostatistics and Epidemiology (J.M.-D.), and Pediatrics (E.Z.); Perinatal Institute (S.M., B.H.), Division of Neonatology; and Fetal Care Center (F.Y.L., P.B.), Cincinnati Children's Hospital Medical Center, Cincinnati, Ohio.

Please address correspondence to Rupa Radhakrishnan, MD, Cincinnati Children's Hospital Medical Center, 3333 Burnet Ave, Cincinnati, OH 45229; e-mail: rupa.radhakrishnan@cchmc.org; @radrupa

<http://dx.doi.org/10.3174/ajnr.A4787>

ECMO have a greater incidence of adverse neurodevelopmental sequelae, though it unclear whether the severity of the illness leading up to ECMO (hypercapnia, hypotension, and so forth) or the ECMO itself should be implicated.^{6,11}

Which clinical factors in the neonatal intensive care unit play a role in brain injury in infants with CDH is yet to be determined.

In this study, we have developed a brain injury score to determine whether brain injury seen on predischARGE MRI in infants with CDH is associated with diaphragmatic defect size and postnatal clinical factors in the NICU.

MATERIALS AND METHODS

After institutional review board approval, we retrospectively identified infants with CDH born between February 2009 and March 2014. We included infants with CDH with MR imaging of the brain before discharge as described in the flow chart (Fig 1).

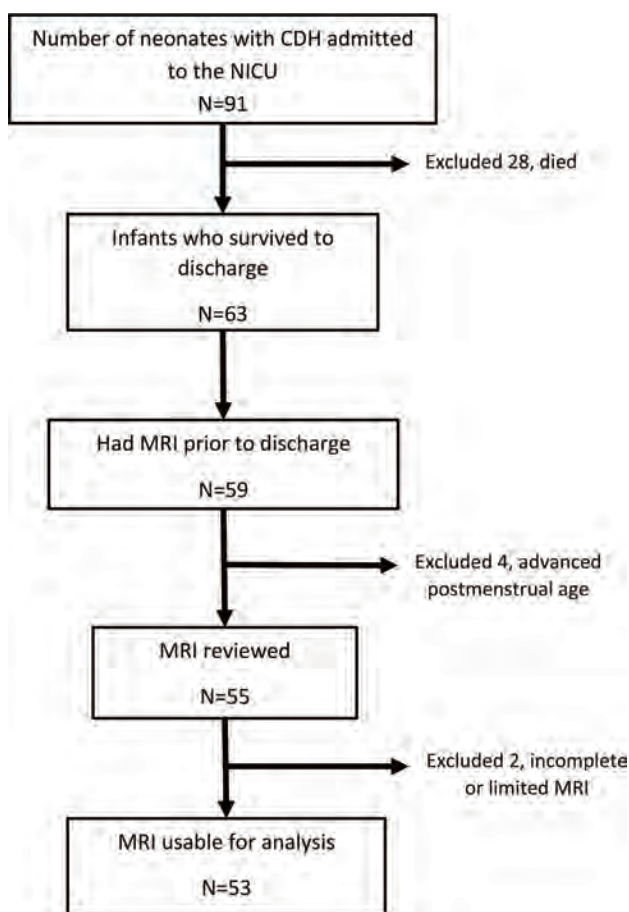


FIG 1. Flowchart of subject inclusion.

Table 1: Brain injury scoring system

MRI Findings vs Score	0	1	2	3	4
Ventriculomegaly	<10 mm	10–15 mm	>15 mm	Obstructive	
Extra-axial spaces	<5 mm	5–10 mm	>10 mm		
Intraventricular hemorrhage	None	Grade 1	Grade 2	Grade 3	Grade 4
Parenchymal hemorrhage (not grade 4 intraventricular hemorrhage)	Absent	Present			
Cerebellar hemorrhage	None	<3 foci, <5-mm size	>3 foci or >5-mm size		
White matter injury	None	<3 foci, unilateral	>3 foci or bilateral	Multiregional	
Cortical injury	None	Single	Multiple	Extensive	
Basal ganglia injury	None	Single	Multiple	Extensive	

MR imaging was performed on these infants on 1.5T and 3T, and with a small-bore extremity 1.5T MR imaging scanner that was adapted for neonatal imaging in the neonatal intensive care unit.¹² MR imaging was performed without sedation after feeding and swaddling, except when excessive motion required light sedation. All studies included standard T1, T2, and susceptibility- and diffusion-weighted sequences.

The MR images were independently reviewed by 2 pediatric neuroradiologists who were blinded to the clinical variables except for postmenstrual age at the time of MR imaging. Conflicts were resolved by consensus. The brain was evaluated for evidence of injury and then was scored on the basis of a system modified from previous work by Danzer et al^{8,10} and Tracy et al.⁹ Table 1 lists the brain injury scoring guide. The total brain injury score was calculated in each infant. Examples of our scoring system are provided in Fig 2.

The medical charts were reviewed to identify perinatal clinical factors and courses in the neonatal intensive care unit. The clinical variables extracted from the electronic medical record included type of diaphragmatic defect, gestational age, birth weight, Apgar scores at 1 and 5 minutes, the presence of congenital heart disease, the need for ECMO, days on a ventilator, the presence of blood stream infection, the need for and type of inotropic support, the need for oxygen at 28 days of life, any oral feeding at discharge, and gastrostomy tube placement before hospital discharge. The size of the diaphragmatic defect identified at surgery was classified according to the Congenital Diaphragmatic Hernia Study Group classification from A to D, A being a small defect and D indicating diaphragmatic agenesis.⁵

Data were entered into REDCap (<http://www.project-redcap.org/software.php>), a secure on-line Web application. Statistical analysis was performed by using SAS software (Version 9.3; SAS Institute, Cary, North Carolina). Nonparametric tests and multivariable linear regression were performed by using clinical variables as potential predictors with the brain injury score as the continuous outcome.

RESULTS

There were 91 neonates with CDH admitted to the neonatal intensive care unit during the study; 28 died and 53 remained suitable for the study (Fig 1). Demographic details are provided in Table 2. Nine of the 53 neonates required ECMO during their treatment. In the 9 neonates who had ECMO, 2 had a type D defect and 7 had a type C defect.

MR imaging was performed at a mean corrected gestational age of 43.6 weeks (range, 37.0–64.6 weeks). Fifty of the 53 infants were imaged at <48 weeks' corrected gestational age. MR imaging

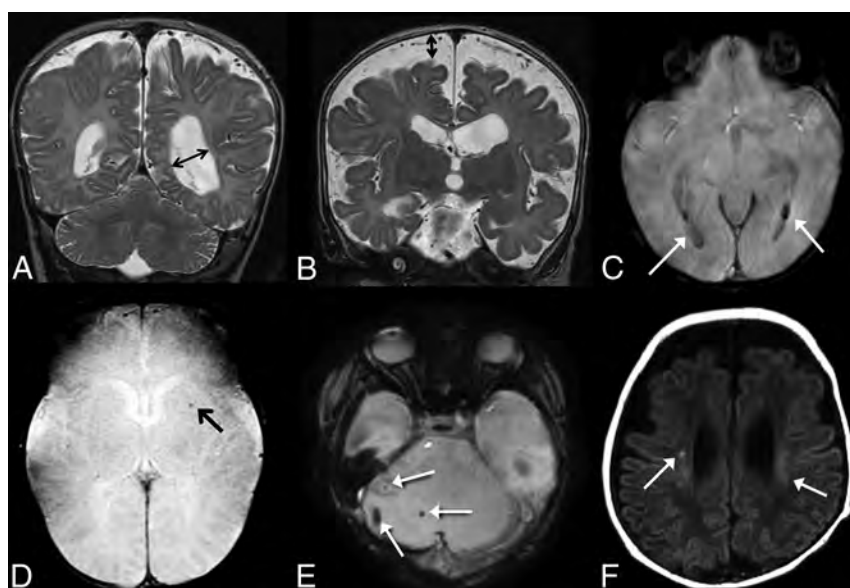


FIG 2. A, Coronal T2-weighted image demonstrates ventriculomegaly, scored as grade 2 on our scale; B, Coronal T2-weighted image demonstrates enlarged extra-axial spaces, scored as grade 2 on our scale. C, SWI shows evidence of grade 2 intraventricular hemorrhage (arrows). D, SWI shows evidence of parenchymal hemorrhage, grade 1 on our scale (arrow). E, SWI shows foci of cerebellar hemorrhage, grade 2 on our scale (arrows). F, Axial T1 weighted images demonstrate foci of bilateral white matter injury, grade 2 on our scale (arrows).

Table 2: Demographic table

	Total Infants in the Study (N = 53)
Male (%)	31 (58%)
Gestational age at birth (wk) ^a	38 (32.9–40.6)
Birth weight (g) ^a	2960 (1430–4175)
Diaphragmatic defect	
A	8 (15%)
B	16 (30%)
C	22 (42%)
D	7 (13%)
Days on ventilator ^a	27 (8–88)
Length of stay (day) ^a	60 (15–210)
Age at repair (wk) ^a	9 (1–54)
Required inotropic support (%)	35 (66%)
Required ECMO (%)	9 (17%)
Required O ₂ at 28 days of life (%)	37 (70%)
Any oral feeding at discharge (%)	40 (75%)

^a Data are expressed as median (range).

findings were considered abnormal (injury score of >0) in 32/53 (60%) infants. Enlarged extra-axial spaces were the most common abnormal finding on MR imaging, seen in 36% of infants. Other abnormal findings on MR imaging included intraventricular hemorrhage in 23%, ventriculomegaly in 19%, white matter injury in 17%, cerebellar hemorrhage in 17%, parenchymal hemorrhage in 8%, cortical injury in 4%, and basal ganglia injury in 2% of infants. The distribution of brain injury scores in infants with CDH treated with ECMO and those without it is provided in Fig 3. Ventriculomegaly, enlarged extra-axial spaces, parenchymal hemorrhage, and white matter injury were seen significantly more often in neonates who required ECMO compared with those without it (Table 3).

With the Spearman correlation for continuous predictor variables, there was a weak but significant correlation of the brain

injury score with the number of ventilator days (correlation coefficient, 0.34; $P = .0014$) and diaphragmatic defect severity (correlation coefficient, 0.30; $P = .027$). There was no correlation between total injury score and gestational age in weeks, birth weight, Apgar scores, or bloodstream infection.

Univariate analysis of median differences in the brain injury scores and clinical variables in the neonatal intensive care unit showed that the use of ECMO ($P = .0001$), use of inotropes ($P = .027$), gastronomy tube placement before discharge ($P = .012$), and not taking any oral feeding at discharge ($P = .024$) were significantly associated with higher MR imaging brain injury scores. When we grouped the diaphragmatic defects into small (A and B) and large (C and D) defects, analysis with the Wilcoxon rank sum test showed that infants with type C or D diaphragmatic defects had significantly higher brain injury scores compared with infants with type A or B defects ($P = .011$).

Table 4 lists the clinical predictors of brain injury. There was a significant association among the use of ECMO, the presence of C or D diaphragmatic defect, and evidence of brain injury. Infants who were taking any feeding by mouth (as opposed to being entirely tube-fed) at the time of discharge had a greater chance of having normal brain MR imaging findings.

To better understand the etiology of ventriculomegaly and enlarged extra-axial spaces, we plotted the head circumference measurements of infants imaged before 50 weeks' corrected gestational age on a standard Fenton head circumference chart (Fig 4).¹³ Head circumference was measured within 5 days of the brain MR imaging in all cases. Infants with moderate or severe enlargement of the extra-axial spaces had normal or enlarged head size.

DISCUSSION
Management of CDH is complex, with various strategies used to improve outcomes. In general, our clinical management strategy for infants with CDH includes gentle ventilation, aggressive management of pulmonary hypertension with pulmonary vasodilators such as nitric oxide and epoprostenol, and surgical repair when pulmonary hypertension is subsystemic or has stabilized. ECMO is reserved for extremely sick infants who do not respond to standard medical management. Despite improved therapies, the early course in infants with CDH continues to be an extremely vulnerable period with great morbidity. In this article, we report the associations between clinical variables in the critical neonatal intensive care unit period and MR imaging evidence of brain injury in infants with CDH.

DISCUSSION

Management of CDH is complex, with various strategies used to improve outcomes. In general, our clinical management strategy for infants with CDH includes gentle ventilation, aggressive management of pulmonary hypertension with pulmonary vasodilators such as nitric oxide and epoprostenol, and surgical repair when pulmonary hypertension is subsystemic or has stabilized. ECMO is reserved for extremely sick infants who do not respond to standard medical management. Despite improved therapies, the early course in infants with CDH continues to be an extremely vulnerable period with great morbidity. In this article, we report the associations between clinical variables in the critical neonatal intensive care unit period and MR imaging evidence of brain injury in infants with CDH.

MR imaging has been used as a tool to identify evidence of perinatal brain injury in vulnerable populations and to predict

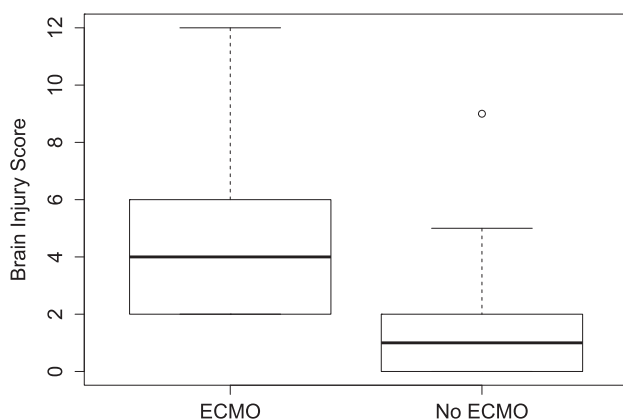


FIG 3. Boxplots of the distribution of the brain injury score in infants with CDH with ECMO and those without it. The *central thick line* in each box is the median score. The limits of the box indicate upper and lower quartiles. The *whisker* limits indicate the highest or lowest score, not considering outliers. There is 1 outlier with a higher brain injury score in the non-ECMO group with a score of >1.5 interquartile range above the upper quartile. This infant had a CDH defect D.

Table 3: Differences in the presence of brain injury between infants with and without ECMO

	ECMO (n = 9)	No ECMO (n = 44)	P Value ^a
Ventriculomegaly	5 (56%)	8 (18%)	.03
Extra-axial spaces	8 (89%)	11 (25%)	<.0001
Intraventricular hemorrhage	4 (44%)	8 (18%)	.18
Parenchymal hemorrhage	3 (33%)	1 (2%)	.013
Cerebellar hemorrhage	3 (33%)	6 (14%)	.17
White matter injury	4 (44%)	5 (11%)	.035
Cortical injury	1 (11%)	1 (2%)	.31
Basal ganglia injury	1 (11%)	0	.17

^a Calculated using the Fisher exact test.

Table 4: Predictors of any brain injury on MRI

	Any Injury (n = 32)	No Injury (n = 21)	P Value
Any oral feeding at discharge	21 (65.6%)	19 (90.5%)	.04
Requirement for NG feeding at discharge	9 (28.1%)	10 (47.6%)	.15
G-tube placement before discharge	13 (40.6%)	4 (19.1%)	.10
No inotropes	9 (28.1%)	9 (42.9%)	.27
Blood stream infection ^a	3 (9.4%)	0	.27 ^b
Lung infection	7 (22.6%)	2 (9.5%)	.28 ^b
Required ECMO ^a	9 (28.1%)	0	.008 ^b
Diaphragmatic defect			.01
A or B	10 (31.3%)	14 (66.7%)	
C or D	22 (68.8%)	7 (33.3%)	

Note:—NG indicates nasogastric tube; G-tube, gastrostomy tube.

^a All infants had injury.

^b Fisher exact P value.

neurodevelopmental outcome.^{8,9,11,14-16} Consistent with previous small cohort studies, our results indicate that most infants with CDH have evidence of brain injury on MR imaging performed before discharge. Hunt et al¹⁷ identified white matter and deep gray matter injury in 8 of 10 patients with CDH. Tracy et al⁹ identified evidence of brain injury before discharge on 14 of 42 head ultrasounds, 7 of 8 brain MRIs, and 11 of 14 head CTs in infants with CDH.

In our CDH population, enlarged extra-axial space was the

most common abnormality, seen in 36% of the cases. This finding is similar to that in the cohort of Danzer et al,¹⁰ in which enlarged extra-axial spaces were present in 40% of the patients with CDH. The enlarged extra-axial spaces were associated with lower cognitive scores in their study, and the presence of intracranial hemorrhage was associated with motor dysfunction. However, the effect of isolated enlarged extra-axial spaces on neurodevelopmental outcome, especially in neonates who have had ECMO, is somewhat controversial.¹⁸ Enlargement of the extra-axial spaces is a common finding in neonates with ECMO, particularly in venovenous ECMO.¹⁸⁻²⁰ The obstruction of the internal jugular vein and/or the superior vena cava causes an elevation in intracranial venous pressure and poor resorption of CSF by the arachnoid villi.²¹ In neonates with CDH, intrathoracic mass effect can cause relative obstruction of the central veins without ECMO. The large head circumferences in 2 of the 3 infants with ECMO with moderate-to-severe enlarged extra-axial spaces in our cohort support this hypothesis.

While our prevalence of parenchymal hemorrhage is similar to that in the study of Danzer et al,¹⁰ our cohort had a much higher incidence of intraventricular hemorrhage (23% compared with 2%). This may be due to use of susceptibility-weighted imaging in our population, which increases the sensitivity for the detection of blood products. In our study, infants on ECMO had a higher proportion of intraventricular and intraparenchymal hemorrhage compared with those without it. In 3 of these infants, minor intracranial hemorrhage was identified on screening head sonography during the course of ECMO, but this did not necessitate withdrawal of ECMO in these infants. We did not include small amounts of subdural or extra-axial hemorrhage in infants younger than 4 weeks of age as abnormal, given that this can be seen in healthy neonates following both vaginal and cesarean delivery.²² Although previous reports describe subdural hemorrhage in infants with CDH, we did not see any abnormal subdural hemorrhage in our cohort.

Cerebellar hemorrhage was seen in 17% of our population and has not been previously described in infants with CDH. Again, the use of SWI in our cohort may have increased the detection of this abnormality. The proposed etiology of cerebellar hemorrhage is impaired brain autoregulation, elevated venous pressure, and fetal distress.²³ We did not find a significant difference in cerebellar hemorrhage between infants with and without ECMO.

Multiple intrauterine, perinatal, and surgical factors are described as associated with neonatal neurodevelopmental outcome, including the need for ECMO, the use of patch repair (a surrogate for large defect size), the presence of liver in the chest, the need for oxygen at 4 weeks of life, and hypotonicity.^{24,25} These factors would presumably also be associated with brain injury on imaging. Among the clinical variables assessed in our study, both large defect size and ECMO were predictors of the severity of brain injury identified on MR imaging. In our study, all the infants who needed ECMO had a large diaphragmatic defect; however, there was a substantial percentage (38%) of infants with large defects who did not require ECMO. The need for supplemental oxygen at 4 weeks of life was not associated with brain injury on imaging in our study. As expected, all our patients who required ECMO had evidence of intracranial abnormality, com-

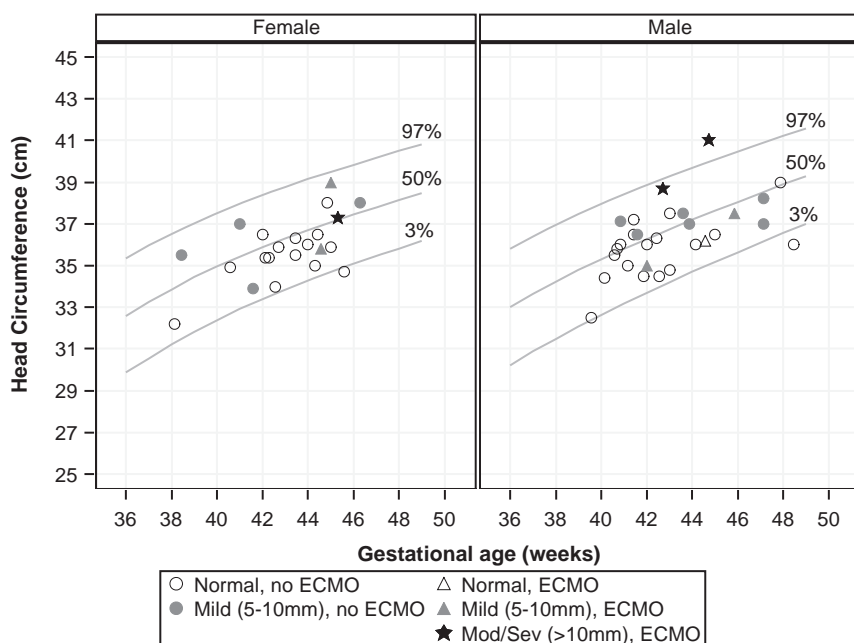


FIG 4. Enlarged extra-axial spaces versus head circumference, plotted on Fenton head circumference charts.¹³

pared with 52% of the group without ECMO. In a previous study from 1999, Ahmad et al¹¹ showed that only 35% of patients with CDH and ECMO had evidence of CNS abnormality. This study used head sonography and CT to identify brain injury, and our numbers are likely higher due to the greater sensitivity of MR imaging in identifying subtle brain injury. In a study of infants with CDH from 1997, McGahren et al⁶ showed a greater incidence of intracranial findings on head sonography and poor neurologic outcome in infants with CDH requiring ECMO. Rollins et al²⁶ performed a retrospective review of 50 neonates (24 with CDH) who underwent brain MR imaging after neonatal ECMO. MR imaging findings were abnormal in 62% of the infants, and MR imaging was more sensitive than head sonography at detecting brain abnormalities. Similar to findings in our study, abnormal carotid flow, ventriculomegaly, and increased extra-axial spaces were common. They found that neuroimaging was, in fact, not correlated with neurodevelopmental outcomes in the 20 patients who had 12-month follow-up. However, they only classified neuroimaging findings as “normal” or “abnormal” and did not attempt to categorize the severity of imaging abnormalities, which could have potentially impacted their results.

Venoarterial ECMO, which is used at our center for infants with CDH, requires cannulation of the right internal carotid artery. In addition to this vascular injury, systemic anticoagulation is required, greatly increasing the risk of cerebral hemorrhage. The initiation of ECMO launches a systemic inflammatory response, which also appears to affect the brain.²⁷ Use of ECMO has been found to have an effect on neurodevelopmental outcome. Gross motor skills are delayed in many children who received ECMO as neonates compared with healthy controls, though severe disability is uncommon.²⁸ Survivors of CDH who received ECMO appear to be more affected than those who required ECMO for other reasons,²⁹ and the cause of poor outcome in this cohort is unclear. Cognitive development in ECMO survivors also

appears to be overall within the normal range, but lower than that in healthy controls.²⁸ Decreased performance is seen on neuropsychological tasks such as verbal reasoning and spatial abilities,³⁰ and children treated with ECMO are at risk for school difficulties despite normal overall intelligence.^{31,32} The increased brain injury seen in infants with CDH requiring ECMO in our study could provide a mechanism for some of these findings seen later in childhood.

Our study has several limitations. Because this is a retrospective study, we could not control for imaging timing, which might affect the identification of brain injury. PredischARGE MR imaging examinations assessed in this study were performed when the infants were clinically stable after surgical correction and ECMO if used. The exact cause of brain injury in this CDH population, especially in those requiring ECMO, is difficult

to postulate. Neonates who require ECMO are usually sicker than those who do not require ECMO, and they may have had a period of clinical instability with hypotension, hypercarbia, and impaired cerebral autoregulation before the initiation of ECMO. It is therefore difficult to determine whether ECMO itself or the illness requiring ECMO contributes more to brain injury. Even if they do not require ECMO, infants with CDH are often initially very sick, with episodes of hypoxia, hypercarbia, hypotension, and acidosis. Use of inotropes can be associated with altered cerebral perfusion leading to brain injury.^{33,34} Major surgery with anesthesia would also contribute to brain injury in these neonates.^{35,36}

Only 53 of the 91 infants admitted to our neonatal intensive care unit during the study were included, mainly due to high mortality. Of the 28 infants who died, 21 had been on ECMO. Of the 63 survivors, 14 infants had ECMO and 9 were included in the study. The ECMO survivors that were included in our cohort may have represented the relatively less sick infants on ECMO who were clinically stable enough to be imaged. Because all our infants with ECMO had evidence of brain injury and the brain injury score was higher in infants with ECMO compared with those without it, it may be reasonably assumed that we imaged only the milder end of the spectrum and that infants with CDH needing ECMO would have a greater association with brain injury.

Imaging was performed on both 1.5T and 3T clinical scanners, which might affect the sensitivity of detection of brain abnormalities. We did not include sonography and CT reviews, because we believed that MR imaging was more sensitive in identifying brain injury. Neurodevelopmental tests on our group of infants with CDH are ongoing, and results are not included in this study. The clinical significance of the brain imaging abnormalities is therefore currently unknown. However, on the basis of available evi-

dence of brain injury in infants with CDH, all infants with CDH now undergo brain MR imaging before discharge.

CONCLUSIONS

In this study, we demonstrated an association between perinatal clinical factors and brain imaging abnormalities in infants with congenital diaphragmatic hernia. The strongest association with brain abnormality is the use of ECMO, with the most common abnormality being enlarged extra-axial spaces. The presence of a large diaphragmatic defect was an intrinsic factor associated with abnormal brain imaging findings. Infants who were fed orally at the time of discharge were more likely to have normal neuroimaging findings.

ACKNOWLEDGMENTS

We thank Meredith Tabangin, PhD, from the Division of Biostatistics and Epidemiology, Cincinnati Children's Hospital Medical Center, for her help in plotting the extra-axial space score against infant head circumference (Fig 4).

Disclosures: Jareen Meinzen-Derr—UNRELATED: Grants/Grants Pending: March of Dimes.* *Money paid to the institution.

REFERENCES

- Robinson PD, Fitzgerald DA. Congenital diaphragmatic hernia. *Paediatr Respir Rev* 2007;8:323–34; quiz 334–35 CrossRef Medline
- Hedrick HL, Danzer E, Merchant A, et al. Liver position and lung-to-head ratio for prediction of extracorporeal membrane oxygenation and survival in isolated left congenital diaphragmatic hernia. *Am J Obstet Gynecol* 2007;197:422.e1–4 CrossRef Medline
- Tsukimori K, Masumoto K, Morokuma S, et al. The lung-to-thorax transverse area ratio at term and near term correlates with survival in isolated congenital diaphragmatic hernia. *J Ultrasound Med* 2008;27:707–13 Medline
- Laudy JA, Van Gucht M, Van Dooren MF, et al. Congenital diaphragmatic hernia: an evaluation of the prognostic value of the lung-to-head ratio and other prenatal parameters. *Prenat Diagn* 2003;23:634–39 CrossRef Medline
- Tsao K, Lally KP. The Congenital Diaphragmatic Hernia Study Group: a voluntary international registry. *Semin Pediatr Surg* 2008;17:90–97 CrossRef Medline
- McGahren ED, Mallik K, Rodgers BM. Neurological outcome is diminished in survivors of congenital diaphragmatic hernia requiring extracorporeal membrane oxygenation. *J Pediatr Surg* 1997;32:1216–20 CrossRef Medline
- Peetsold MG, Huisman J, Hofman VE, et al. Psychological outcome and quality of life in children born with congenital diaphragmatic hernia. *Arch Dis Child* 2009;94:834–40 CrossRef Medline
- Danzer E, Gerdes M, D'Agostino JA, et al. Longitudinal neurodevelopmental and neuromotor outcome in congenital diaphragmatic hernia patients in the first 3 years of life. *J Perinatol* 2013;33:893–98 CrossRef Medline
- Tracy S, Estroff J, Valim C, et al. Abnormal neuroimaging and neurodevelopmental findings in a cohort of antenatally diagnosed congenital diaphragmatic hernia survivors. *J Pediatr Surg* 2010;45:958–65 CrossRef Medline
- Danzer E, Zarnow D, Gerdes M, et al. Abnormal brain development and maturation on magnetic resonance imaging in survivors of severe congenital diaphragmatic hernia. *J Pediatr Surg* 2012;47:453–61 CrossRef Medline
- Ahmad A, Gangitano E, Odell RM, et al. Survival, intracranial lesions, and neurodevelopmental outcome in infants with congenital diaphragmatic hernia treated with extracorporeal membrane oxygenation. *J Perinatol* 1999;19(6 pt 1):436–40 CrossRef Medline
- Tkach JA, Merhar SL, Kline-Fath BM, et al. MRI in the neonatal ICU: initial experience using a small-footprint 1.5-T system. *AJR Am J Roentgenol* 2014;202:W95–W105 CrossRef Medline
- Fenton TR, Kim JH. A systematic review and meta-analysis to revise the Fenton growth chart for preterm infants. *BMC Pediatr* 2013;13:59 CrossRef Medline
- Barkovich AJ, Hajnal BL, Vigneron D, et al. Prediction of neuromotor outcome in perinatal asphyxia: evaluation of MR scoring systems. *AJNR Am J Neuroradiol* 1998;19:143–49 Medline
- Martinez-Biarge M, Bregant T, Wusthoff CJ, et al. White matter and cortical injury in hypoxic-ischemic encephalopathy: antecedent factors and 2-year outcome. *J Pediatr* 2012;161:799–807 CrossRef Medline
- Inder TE, Warfield SK, Wang H, et al. Abnormal cerebral structure is present at term in premature infants. *Pediatrics* 2005;115:286–94 CrossRef Medline
- Hunt RW, Kean MJ, Stewart MJ, et al. Patterns of cerebral injury in a series of infants with congenital diaphragmatic hernia utilizing magnetic resonance imaging. *J Pediatr Surg* 2004;39:31–36 CrossRef Medline
- van Heijst AF, de Mol AC, Ijsselstijn H. ECMO in neonates: neuroimaging findings and outcome. *Semin Perinatol* 2014;38:104–13 CrossRef Medline
- Bulas DI, Taylor GA, O'Donnell RM, et al. Intracranial abnormalities in infants treated with extracorporeal membrane oxygenation: update on sonographic and CT findings. *AJNR Am J Neuroradiol* 1996;17:287–94 Medline
- Brunberg JA, Kewitz G, Schumacher RE. Venovenous extracorporeal membrane oxygenation: early CT alterations following use in management of severe respiratory failure in neonates. *AJNR Am J Neuroradiol* 1993;14:595–603 Medline
- Stolar CJ, Reyes C. Extracorporeal membrane oxygenation causes significant changes in intracranial pressure and carotid artery blood flow in newborn lambs. *J Pediatr Surg* 1988;23:1163–68 CrossRef Medline
- Rooks VJ, Eaton JP, Ruess L, et al. Prevalence and evolution of intracranial hemorrhage in asymptomatic term infants. *AJNR Am J Neuroradiol* 2008;29:1082–89 CrossRef Medline
- Limperopoulos C, Benson CB, Bassan H, et al. Cerebellar hemorrhage in the preterm infant: ultrasonographic findings and risk factors. *Pediatrics* 2005;116:717–24 CrossRef Medline
- Danzer E, Gerdes M, Bernbaum J, et al. Neurodevelopmental outcome of infants with congenital diaphragmatic hernia prospectively enrolled in an interdisciplinary follow-up program. *J Pediatr Surg* 2010;45:1759–66 CrossRef Medline
- Danzer E, Hedrick HL. Neurodevelopmental and neurofunctional outcomes in children with congenital diaphragmatic hernia. *Early Hum Dev* 2011;87:625–32 CrossRef Medline
- Rollins MD, Yoder BA, Moore KR, et al. Utility of neuroradiographic imaging in predicting outcomes after neonatal extracorporeal membrane oxygenation. *J Pediatr Surg* 2012;47:76–80 CrossRef Medline
- Chen Q, Yu W, Shi J, et al. The effect of extracorporeal membrane oxygenation therapy on systemic oxidative stress injury in a porcine model. *Artif Organs* 2014;38:426–31 CrossRef Medline
- Glass P, Wagner AE, Papero PH, et al. Neurodevelopmental status at age five years of neonates treated with extracorporeal membrane oxygenation. *J Pediatr* 1995;127:447–57 CrossRef Medline
- Bernbaum J, Schwartz IP, Gerdes M, et al. Survivors of extracorporeal membrane oxygenation at 1 year of age: the relationship of primary diagnosis with health and neurodevelopmental sequelae. *Pediatrics* 1995;96(5 pt 1):907–13 Medline
- Bennett CC, Johnson A, Field DJ, et al. UK Collaborative ECMO Trial Group. UK collaborative randomised trial of neonatal extracorporeal membrane oxygenation: follow-up to age 4 years. *Lancet* 2001;357:1094–96 CrossRef Medline
- Madderom MJ, Reuser JJ, Utens EM, et al. Neurodevelopmental, educational and behavioral outcome at 8 years after neonatal

- ECMO: a nationwide multicenter study.** *Intensive Care Med* 2013;39:1584–93 CrossRef Medline
32. Rais-Bahrami K, Wagner AE, Coffman C, et al. **Neurodevelopmental outcome in ECMO vs near-miss ECMO patients at 5 years of age.** *Clin Pediatr (Phila)* 2000;39:145–52 CrossRef Medline
 33. Kidokoro H, Anderson PJ, Doyle LW, et al. **Brain injury and altered brain growth in preterm infants: predictors and prognosis.** *Pediatrics* 2014;134:e444–53 CrossRef Medline
 34. Hahn GH, Hyttel-Sorensen S, Petersen SM, et al. **Cerebral effects of commonly used vasopressor-inotropes: a study in newborn piglets.** *PLoS One* 2013;8:e63069 CrossRef Medline
 35. Filan PM, Hunt RW, Anderson PJ, et al. **Neurologic outcomes in very preterm infants undergoing surgery.** *J Pediatr* 2012;160:409–14 CrossRef
 36. Walker K, Badawi N, Halliday R, et al. **Early developmental outcomes following major noncardiac and cardiac surgery in term infants: a population-based study.** *J Pediatr* 2012;161:748–752.e1 CrossRef Medline

Limitations of T2*-Gradient Recalled-Echo and Susceptibility-Weighted Imaging in Characterizing Chronic Subdural Hemorrhage in Infant Survivors of Abusive Head Trauma

J.A. Cramer, U.A. Rassner, and G.L. Hedlund

ABSTRACT

SUMMARY: A possible misconception among radiologists is that chronic subdural hemorrhage should show some degree of blooming on T2*-gradient recalled-echo or susceptibility-weighted sequences such as SWI and susceptibility-weighted angiography, which is not necessarily true. We present 5 cases of chronic subdural hemorrhages in infants, demonstrating intensity near or greater than that of CSF with variable amounts of hemosiderin staining along the neomembranes. We review the physiology and MR imaging physics behind the appearance of a chronic subdural hemorrhage, highlighting that the absence of a BBB can allow hemosiderin to be completely removed from the subdural compartment. Finally, we stress the importance of reviewing all multiplanar sequences for the presence of neomembranes, which can be quite subtle in the absence of hemosiderin staining and are critical for making the diagnosis of chronic subdural hemorrhage.

ABBREVIATIONS: GRE = gradient recalled-echo; cSDH = chronic subdural hemorrhage; SDH = subdural hemorrhage; SDHy = subdural hygroma; SWAN = susceptibility-weighted angiography

Much of the literature characterizing the MR imaging appearance of subdural hemorrhage (SDH) refers to T1 and T2 signal, with no explicit discussion of the appearance on T2*-gradient recalled-echo (GRE) or susceptibility-weighted sequences such as SWI or susceptibility-weighted angiography (SWAN). Moreover, one may reason that a chronic subdural hemorrhage (cSDH) should show blooming or hypointensity on T2*-GRE or SWI, but this is not necessarily true.¹⁻³ We present 5 infant survivors of abusive head trauma with subdural collections demonstrating intensity near that of CSF on T2*-GRE or hyperintensity on SWAN with variable amounts of hemosiderin staining. These cases either exhibited other imaging features compatible with cSDH or were called cSDH on surgical drainage. We provide a review of the physics and physiology relevant to the appearance of chronic SDHs on MR imaging and offer an explanation for the subdural fluid signal and variable hemosiderin staining on T2*-GRE and SWI.

CASE SERIES

Illustrative cases were obtained by reviewing neurosurgical patients in whom drainage of a subdural collection was performed at Primary Children's Hospital between 2009 and 2014. We selected infants (younger than 12 months of age) with an operative report indicating chronic subdural hematoma and MR imaging <1 week before surgical drainage. Those with acute or chronic subdural hematomas were excluded. One hundred fifty-six total subdural drainage procedures were performed during our study period, and 5 patients were selected. A large majority of cases were not used due to acute hemorrhage, subdural hygromas, or lack of MR imaging within 1 week of drainage. In all 5 selected patients, a diagnosis of abusive head trauma was confirmed by the institutional child protective services team. Operative description and pathology were recorded when available. Results are summarized in the Table.

Case 1

A 4-month-old boy presented with increasing head circumference and no outward signs of trauma. Bilateral subdural hematomas were demonstrated on NCCT. Findings of 2 osseous surveys were negative, but subsequent investigation led to the diagnosis of inflicted trauma/abusive head trauma. NCCT and MR imaging (Fig 1) were performed 4 and 3 days before surgical drainage, respectively. NCCT demonstrated bilateral subdural collections that were hyperattenuating to CSF. On MR imaging, the subdural fluid was hyperintense to CSF on FLAIR and slightly hyperintense

Received November 16, 2015; accepted after revision February 8, 2016.

From the Department of Radiology (J.A.C., U.A.R.), University of Utah Hospital, Salt Lake City, Utah; and Department of Radiology (G.L.H.), Primary Children's Hospital, Salt Lake City, Utah.

Paper previously presented at: Annual Meeting of the American Society of Neuroradiology and the Foundation of the ASNR Symposium, April 25–30, 2015; Chicago, Illinois.

Please address correspondence to Justin A. Cramer, MD, University of Utah - Radiology, 30 N 1900 E #1A71, Salt Lake City, UT 84132; e-mail: jrcramer10@gmail.com; @justincramer

<http://dx.doi.org/10.3174/ajnr.A4769>

Case series of infants with CSF-like subdural collections on T2*-GRE/SWI

Case	Age (mo)	Sex	MRI Diagnosis	Operative Description	Pathology (If Available)
1	4	M	cSDH (↑ T1/T2/FLAIR/SWAN, hemosiderin along neomembranes)	"Subdural hematoma"	Culture, no growth; no cell count
2	5	M	cSDH (↑ T1/FLAIR/SWAN/GRE, iso T2, hemosiderin along neomembranes)	"Reddish-brown CSF"	Culture, no growth; no cell count
3	6	M	SDHy (iso to CSF, no neomembranes)	"Chronic subdural hematoma"	Not sent
4	4	M	cSDH (↑ T1/FLAIR, ↓ GRE/T2, 1 neomembrane with no hemosiderin)	"Blood-tinged hematoma fluid"	Culture, no growth; WBC 945/ μ L (H); RBC 149,188/ μ L (H)
5	4	M	cSDH (↑ T1/FLAIR/GRE, iso T2, hemosiderin along neomembranes)	"Blood-tinged CSF"	Culture, no growth; no cell count

Note:—↑ indicates increased signal; ↓, decreased signal; iso, isointense; WBC, white blood cell count; RBC, red blood cell count; H, high.

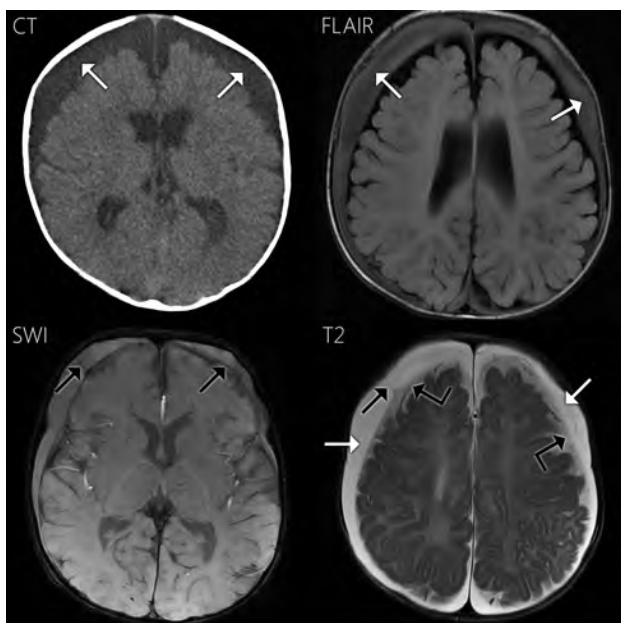


FIG 1. Case 1. Axial NCCT demonstrates bilateral subdural collections, slightly hyperattenuating to CSF (*white arrows*). The collections are hyperintense to CSF on FLAIR and more subtly hyperintense on T1WI (not shown). On SWAN, the fluid is hyperintense to CSF. Neomembranes with hemosiderin staining are present bilaterally within the subdural compartment on SWAN and T2WI (*black arrows*). Hemosiderin staining along the right-sided neomembrane shown is quite subtle. On T2WI, the subdural fluid is hyperintense to the adjacent subarachnoid CSF (*angled black arrows*) and isointense to ventricular CSF (not shown).

on T1WI. On SWAN, subdural compartment neomembranes with hemosiderin staining were seen bilaterally, compatible with cSDH. The subdural fluid was hyperintense to CSF on SWAN. T2WI also demonstrates subdural compartment neomembranes. On T2WI, the subdural collections (*white arrows* in Fig 1) were hyperintense to the adjacent subarachnoid fluid (*angled black arrows*) and isointense to ventricular CSF (not shown). The neomembranes did not enhance. The operative report described the fluid as "subdural hematoma."

Case 2

A 5-month-old boy was brought in for vomiting and was found to be somnolent. NCCT showed subdural compartment collections prompting an inflicted trauma evaluation, which revealed a healing left humerus fracture. NCCT was performed 1 day before surgery, and MR imaging was performed the day of surgical drainage (Fig 2). NCCT demonstrated slightly hyperattenuating

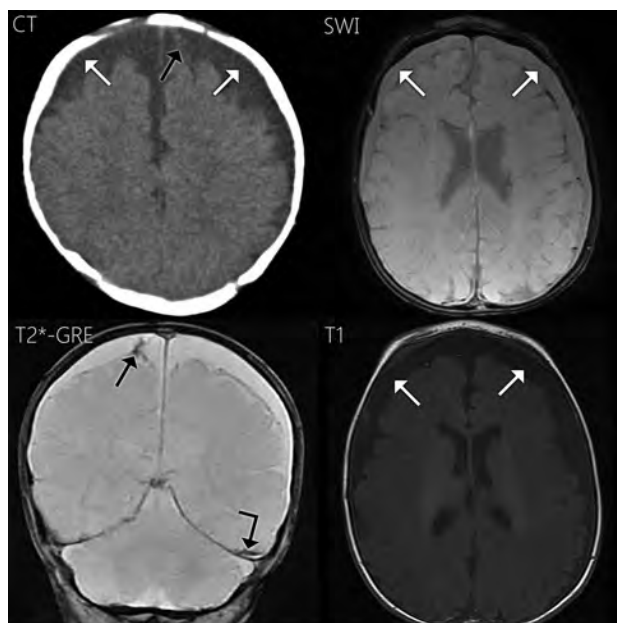


FIG 2. Case 2. Axial NCCT shows bilateral subdural collections slightly hyperattenuating to CSF (*white arrows*) and hyperattenuation along a neomembrane within the medial left frontal subdural collection (*black arrow*). The subdural fluid is slightly hyperintense to CSF on FLAIR (not shown) and T1WI (*white arrows*). On T2*-GRE, the subdural fluid is slightly hyperintense to CSF with blooming along a subdural compartment neomembrane (*black arrow*) and the left tentorium (*angled black arrow*). On SWAN, the subdural fluid is hyperattenuating to CSF (*white arrows*). Hemosiderin staining was less conspicuous in the axial plane on SWAN.

bilateral subdural collections and a left frontal subdural compartment neomembrane. On MR imaging, the subdural fluid was slightly hyperintense to CSF on FLAIR and T1WI. The subdural fluid was slightly hyperintense to CSF on T2*-GRE. Blooming was noted along a subdural compartment neomembrane and along the left tentorium. Contrast was administered with no enhancement along the membranes observed. The subdural fluid was hyperintense to CSF on SWAN, and neomembranes were less conspicuous on SWAN in the axial plane. On T2WI, the subdural fluid was isointense to CSF and the neomembranes were also seen. The neomembranes were compatible with cSDHs. The operative report described the fluid as "reddish-brown CSF."

Case 3

This 6-month-old boy was a survivor of witnessed inflicted injury. Skeletal survey revealed numerous healing fractures. NCCT

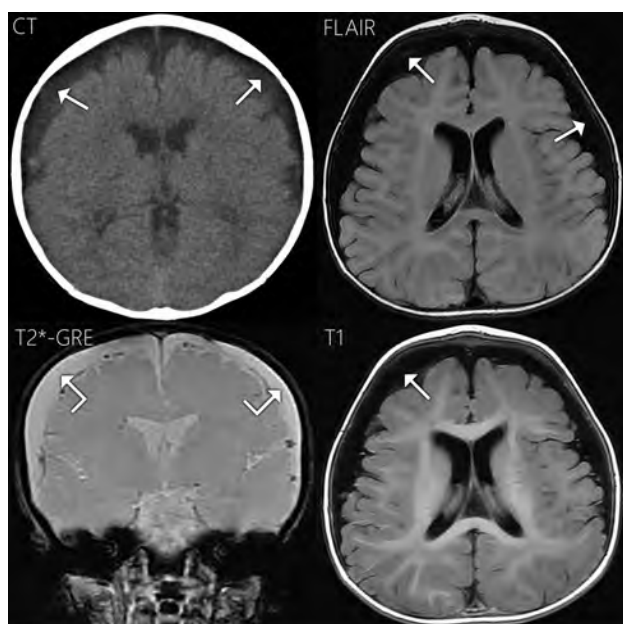


FIG 3. Case 3. Axial NCCT demonstrates bilateral subdural collections slightly hyperattenuating to CSF (white arrows). On FLAIR and T1WI, the subdural fluid is nearly isointense to CSF with subtle areas of hyperintensity reflecting CSF flow artifacts (white arrows). On T2*-GRE, the subdural fluid is isointense to CSF (angled white arrows) with no blooming or susceptibility effects along the dural surface. The multiple tubular hypointense structures on T2*-GRE are cortical veins.

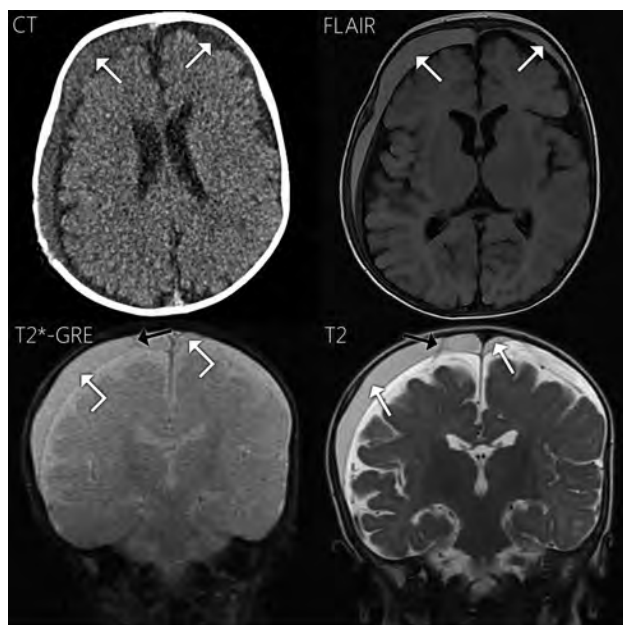


FIG 4. Case 4. Axial NCCT shows right-larger-than-left subdural hematomas hyperattenuating to CSF (white arrows). On MR imaging, the collections are hyperintense to CSF on T1WI and FLAIR (white arrows). The collections approximate the signal of CSF on T2*-GRE (angled white arrows) and are notably hypointense on T2WI (white arrows). Note the right frontal subdural compartment neomembrane on T2*-GRE (black arrow), with very subtle hemosiderin staining, slightly more conspicuous on T2WI (black arrow).

(Fig 3) showed bilateral subdural collections that were isoattenuating to CSF. The fluid was predominantly isointense to CSF on FLAIR and T1WI, with subtle areas of hyperintensity. The fluid

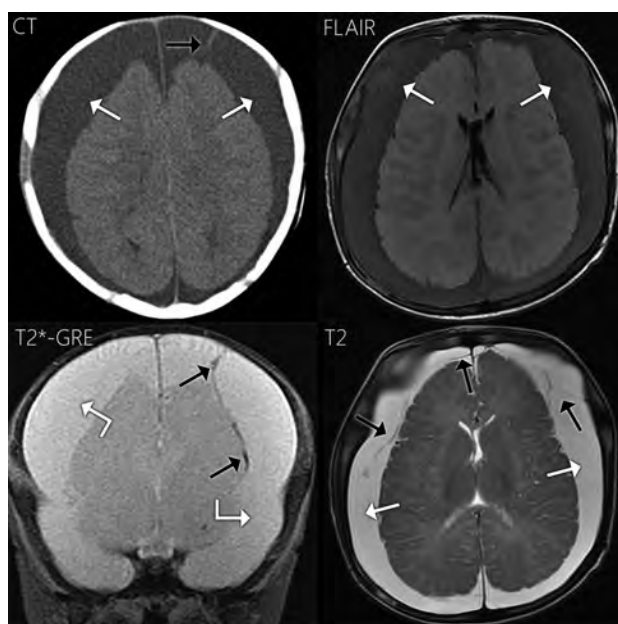


FIG 5. Case 5. Axial NCCT demonstrates large bilateral subdural collections hyperattenuating to CSF (white arrows) and a hyperattenuating subdural compartment neomembrane (black arrow). On T1WI (not shown) and FLAIR, the subdural fluid is hyperintense to CSF (white arrows). On T2*-GRE, the subdural fluid is slightly hyperintense to CSF (angled white arrows), with hemosiderin staining along a left-sided neomembrane (black arrows). On T2WI, the subdural fluid is isointense to CSF (white arrows) and nicely demonstrates multiple neomembranes (black arrows).

was isointense to CSF on T2*-GRE and T2WI with no apparent neomembranes or hemosiderin staining (Fig 3). Contrast was not administered. The collections were interpreted as hygromas on the basis of the imaging appearance. The operative report 3 days later described the fluid as “chronic subdural hematoma.”

Case 4

This 4-month-old boy was evaluated for increasing head circumference and was subsequently found to have bilateral subdural hematomas on NCCT (Fig 4). Child protective services evaluation raised concern for inflicted injury. On MR imaging (Fig 4), the subdural collections were hyperintense to CSF on FLAIR and T1WI and slightly hypointense to CSF on T2*-GRE. Hypointensity of the collections was more pronounced on T2WI. A single subdural compartment neomembrane was also observed on T2*-GRE with no hemosiderin staining. This membrane was slightly more conspicuous on T2WI. Contrast was not administered. The collections were called cSDHs based on the MR imaging appearance. Surgical drainage the next day resulted in a description of the subdural fluid as “blood-tinged hematoma fluid.”

Case 5

This 4-month-old boy presented with increasing head circumference and vomiting. NCCT (Fig 5) revealed bilateral subdural hematomas with internal neomembranes. In addition, there were bilateral parietal bone fractures. On MR imaging (Fig 5), the subdural fluid was hyperintense to CSF on FLAIR and T1WI. On T2*-GRE, the fluid was slightly hyperintense to CSF and demonstrated internal neomembranes with hemosiderin staining along

the neomembranes. The membranes were also quite conspicuous on T2WI. Contrast was not administered. Surgical drainage 2 days later revealed “blood-tinged CSF.”

DISCUSSION

We present 5 infants with chronic posttraumatic subdural hemorrhage in which the signal of the subdural fluid was near that of CSF on T2*-GRE or hyperintense on SWAN. Four cases demonstrated subdural compartment neomembranes, with very subtle or absent hemosiderin staining along the neomembranes in 2 cases. These observations of subdural fluid signal near or greater than that of CSF and subtle or absent hemosiderin staining may be somewhat counterintuitive because one may reason that chronic subdural hemorrhage should exhibit hypointensity due to susceptibility effects. However, this supposition is not necessarily true and raises several important points.

Wittschieber et al⁴ posited that most acute SDH resolves completely and only rarely goes on to form cSDH. More commonly, a subdural hygroma (SDHy) serves as an intermediary step between acute SDH and cSDH. Essential to the formation of a cSDH is the development of vascularized subdural compartment neomembranes. These neomembranes are prone to effusing CSF and microhemorrhages.⁴ Therefore, a cSDH is a mixture of blood-breakdown products, CSF, and neomembranes.

How do these components of a cSDH contribute to MR imaging signal? First, consider the evolution of subdural blood. It goes through the same hyperacute, acute, early subacute, and late subacute stages as parenchymal blood, just more slowly. This slower progression has been attributed to greater oxygen tension in the subdural compartment.^{2,5} However, the chronic stage of subdural hemorrhage differs from that in parenchymal hemorrhage. A cSDH is characterized by repeat episodes of rebleeding along vascularized neomembranes, thus containing varying amounts of albumin, hemoglobin, and hemoglobin breakdown products, including hemosiderin and globin proteins.^{6,7} The various proteins increase T1 and FLAIR signal, and paramagnetic/ferromagnetic hemosiderin causes blooming on T2*-GRE/SWI. Hemosiderin tends to layer along the dural surface and along neomembranes. However, hemosiderin may be completely absent from the subdural compartment¹⁻³ because absence of a BBB allows hemosiderin-laden macrophages to scavenge blood products and exit the subdural compartment.² Contrast this scenario with chronic parenchymal hemorrhage, which typically shows hemosiderin staining. This explains the range of cSDH signal in our 5 cases: variable T1/FLAIR hyperintensity to CSF due to proteins and variable hemosiderin staining on T2*-GRE/SWI. Several of our cases demonstrated absent or very subtle hemosiderin staining along the neomembranes. Finally, the fluid in chronic subdural hemorrhage does not need to be hypointense on T2*-GRE/SWI.³ In our cases using SWAN, the fluid was hyperintense to CSF. On T2*-GRE, 2 of our cases demonstrated slight hyperintensity relative to CSF: One demonstrated slight hypointensity, and another demonstrated isointensity. The hyperintensity relates to the same proteinaceous content that elevates the T1 and FLAIR signal, and the slight hypointensity reflects the susceptibility effects of blood products.

Neomembranes are important to note because they are diag-

nostic of cSDH and, along with non-CSF-like subdural fluid signal, represent the key observations allowing differentiation from SDHy. However, they are of varying conspicuity, with one of our cases demonstrating no definite neomembranes. T2*-GRE/SWI can make neomembranes more conspicuous, particularly in the presence of hemosiderin staining. Additionally, neomembranes can enhance, and contrasted imaging may improve membrane conspicuity in some authors' experience.^{5,8} Of note, intravenous contrast provided no additional information in our 3 contrast-enhanced cases. Finally, membranes may be much more conspicuous in a particular plane, which highlights the importance of multiplanar imaging. If no membranes are identified and there is no hemosiderin staining, differentiating among hyperacute SDH, SDHy, and cSDH can be difficult. In such challenging cases, complementary nonenhanced CT and serial imaging are useful because these collections will evolve differently.⁹

Variable detail in the operative reports limits our correlation of imaging appearance with surgical drainage findings. cSDH fluid has often been described as having the gross appearance of “crank case oil”—that is, thick and dark red/brown.^{4,6,10} Most interesting, cases 4 and 5 had operative descriptions more typical of SDHy, yet they still had membranes compatible with cSDH. This further highlights the complex and varying nature of cSDH fluid. Case 3 had the imaging appearance of an SDHy, yet it was called “chronic subdural hematoma” in the operative report. Given the retrospective nature of this report, it is unclear how to reconcile this discrepancy, but it is possible that this collection was indeed an SDHy. Case 1 similarly just described “subdural hematoma.” Only case 2 described “reddish-brown CSF,” a description close to that of classic cSDH.

In summary, we present 5 cases of cSDH in infant survivors of abusive head trauma, which illustrate important caveats regarding the T2*-GRE and SWI signal characteristics of chronic subdural hemorrhage. First, the fluid in cSDH is often isointense or hyperintense to CSF on T2*-GRE or SWI. Second, hemosiderin staining along the dural surfaces or neomembranes is commonly yet not universally present. When there is a paucity of hemosiderin, neomembranes can be very subtle. Because neomembranes are a key observation in diagnosing cSDH, careful examination of all MR imaging sequences in multiple planes is necessary. These observations serve to further refine the described appearance of cSDH on T2*-GRE/SWI in infants with abusive head trauma and dispel any notion that chronic subdural hemorrhage must demonstrate hypointense fluid or hemosiderin. This refinement is particularly important in the setting of child abuse, given the critical medicolegal and forensic implications of accurate subdural collection description and dating.

Disclosures: Ulrich A. Rassner—UNRELATED: Consultancy: Elsevier (author); Payment for Lectures (including service on Speakers Bureaus): Siemens, Comments: speaker at Siemens 3T courses.

REFERENCES

1. Bradley WG Jr. MR appearance of hemorrhage in the brain. *Radiology* 1993;189:15–26 CrossRef Medline
2. Fobben ES, Grossman RI, Atlas SW, et al. MR characteristics of subdural hematomas and hygromas at 1.5 T. *AJR Am J Roentgenol* 1989;153:589–95 CrossRef Medline

3. Kleinman PK. *Diagnostic Imaging of Child Abuse*. Cambridge: University Press; 2015
4. Wittschieber D, Karger B, Niederstadt T, et al. **Subdural hygromas in abusive head trauma: pathogenesis, diagnosis, and forensic implications.** *AJNR Am J Neuroradiol* 2015;36:432–39 CrossRef Medline
5. Vezina G. **Assessment of the nature and age of subdural collections in nonaccidental head injury with CT and MRI.** *Pediatr Radiol* 2009;39:586–90 CrossRef Medline
6. Hymel KP, Jenny C, Block RW. **Intracranial hemorrhage and rebleeding in suspected victims of abusive head trauma: addressing the forensic controversies.** *Child Maltreat* 2002;7:329–48 Medline
7. Weir B. **The osmolality of subdural hematoma fluid.** *J Neurosurg* 1971;34:528–33 CrossRef Medline
8. Hedlund GL. **Subdural hemorrhage in abusive head trauma: imaging challenges and controversies.** *Am Osteopath Coll Radiol* 2012;1:23–30
9. Bradford R, Choudhary AK, Dias MS. **Serial neuroimaging in infants with abusive head trauma: timing abusive injuries.** *J Neurosurg Pediatr* 2013;12:110–19 CrossRef Medline
10. Lee KS, Bae WK, Park YT, et al. **The pathogenesis and fate of traumatic subdural hygroma.** *Br J Neurosurg* 1994;8:551–58 Medline

Demonstration of Normal and Abnormal Fetal Brains Using 3D Printing from In Utero MR Imaging Data

 D. Jarvis,  P.D. Griffiths, and  C. Majewski

ABSTRACT

SUMMARY: 3D printing is a new manufacturing technology that produces high-fidelity models of complex structures from 3D computer-aided design data. Radiology has been particularly quick to embrace the new technology because of the wide access to 3D datasets. Models have been used extensively to assist orthopedic, neurosurgical, and maxillofacial surgical planning. In this report, we describe methods used for 3D printing of the fetal brain by using data from in utero MR imaging.

The data used to produce the 3D printed fetal brain models were acquired by using a 3D in utero MR imaging volume acquisition. This was achieved by imaging the fetal brain by using an ultrafast, fully balanced steady-state sequence on a 1.5T whole-body MR imaging scanner as detailed in the Table.

3D volume imaging has an inherently higher signal-to-noise ratio compared with 2D imaging because the whole-brain volume is excited at each repetition rather than section. In addition, the homogeneous excitation across the imaging volume results in more uniform section profiles compared with 2D imaging because partial saturation of signal between sections does not occur. These characteristics enable a smaller partition thickness and FOV to improve anatomic resolution, and the contiguous thin partitions permit postprocessing reconstruction for visualization of the anatomy in different planes. The contrast mechanism of steady-state imaging and flip angle determines the signal intensity from fluids, providing good tissue contrast between the fluid and brain interfaces, which assists in the creation of surface projections. We currently use a flip angle of 60°–70° because higher flip angles are associated with greater aliasing artifacts.¹ Scan time is kept short by optimizing the bandwidth (to permit shorter TRs and TEs) and by partial Fourier techniques. These features allow acquisition during maternal suspended respiration leading to reduced movement artifacts.

Postacquisition Image Processing

The images from the 3D dataset are transferred onto a desktop PC and loaded into a free open-source software package, 3D Slicer (<http://www.slicer.org>), for segmentation.² Once loaded into 3D Slicer, the brightness and contrast are user-selected to optimize visualization of the CSF/brain interfaces (both external and ventricular). Each brain is manually segmented on a section-by-section basis in the plane used for acquisition (usually axial), with other anatomic planes and fetal brain atlases used for cross-reference to improve accuracy.^{3,4} Manual outlining of the fetal brain anatomy takes approximately 50–60 minutes for second-trimester brains and 90–120 minutes for more mature fetuses; the longer time is due to the increased complexity of sulcation/gyration.

3D Slicer identifies anatomic areas by using labels, each represented by an index value and associated color. Once all the ROIs have been annotated, the software reconstructs electronic 3D surface models of the fetal brain by using the resultant labels. The surface model data are then saved in the correct file format (STereoLithography or .stl) required for 3D printing. The STereoLithography file cannot be edited, and the resultant 3D printed model is an exact representation of the generated 3D surface model; therefore, the latter should be examined for any extraneous parts to ensure that the contours are in keeping with anatomic detail. Laplacian smoothing can be applied at the model-building stage to smooth contours if necessary.

3D Printing Technique

“3D printing” is the collective term for a number of technologies that create parts in a layer-by-layer manner directly from 3D computer-aided design data without the need for tooling. The major benefits of 3D printing stem from the ability to produce complex

Received December 15, 2015; accepted after revision February 15, 2016.

From the Academic Unit of Radiology (D.J., P.D.G.) and Centre for Advanced Additive Manufacturing (C.M.), University of Sheffield, Sheffield, England.

Please address correspondence to Deborah Jarvis, MD, Academic Unit of Radiology, Floor C, Royal Hallamshire Hospital, Glossop Rd, Sheffield S10 2JF, England; e-mail: deborah.jarvis@sheffield.ac.uk

<http://dx.doi.org/10.3174/ajnr.A4783>

geometries efficiently and effectively. Most 3D printing systems use data in the STereoLithography format, whereby the 3D object is reproduced as a triangulated surface.

The laser sintering process was chosen for models of the fetal brain described in this article. This is a powder bed fusion process, whereby a layer of powder is deposited and selectively scanned by a CO₂ laser. Areas scanned by the laser melt and, on re-solidification, form the layers of the part. Laser sintering can produce parts from a range of materials, including metals and ceramics. In our examples, polymer material Nylon-12 (<http://www.eos.info/>

Imaging sequence parameters for the 3D FIESTA acquisition	
3D FIESTA Steady-State Balanced Gradient-Echo	
TR (ms)	4.2
TE (ms)	2.1
Flip angle	60°
Bandwidth (Hz)	125
NEX	0.75
Section thickness/gap (mm)	2.2/0
No. of partitions	26
FOV (mm)	340 × 270
Matrix size	320/256
Interpolation phase/secondary phase	ZIP 512/ ZIP 2
Scan time (sec)	21

Note:—ZIP indicates interpolation values.

material-p) was used to construct the models of the fetal brain. Specifically, the models were produced by using PA 2200 material on a Formiga P100 laser sintering system (EOS, Munich, Germany).

While high strength is not a key requirement for production of most models, they must be strong enough to endure handling by potentially large numbers of users. Parts produced via laser sintering generally have relatively high mechanical strength compared with other 3D printing processes, again making this a suitable process. While it is possible to build the model in 2 separate materials, most 3D printing processes only allow the production of parts in a single color. However, a number of processes allow the production of multiple colors and/or materials within a single part as demonstrated later.

Additionally, the lack of a requirement for tooling allows the production of small volumes (including production of single units) at no cost penalty. This can provide major advantages in personalization for medical use, whereby every individual may have different geometric or functional needs from a similar part. The ability to produce one-off models economically makes 3D printing highly suitable for the production of training models and demonstrators as discussed in this article. More comprehensive

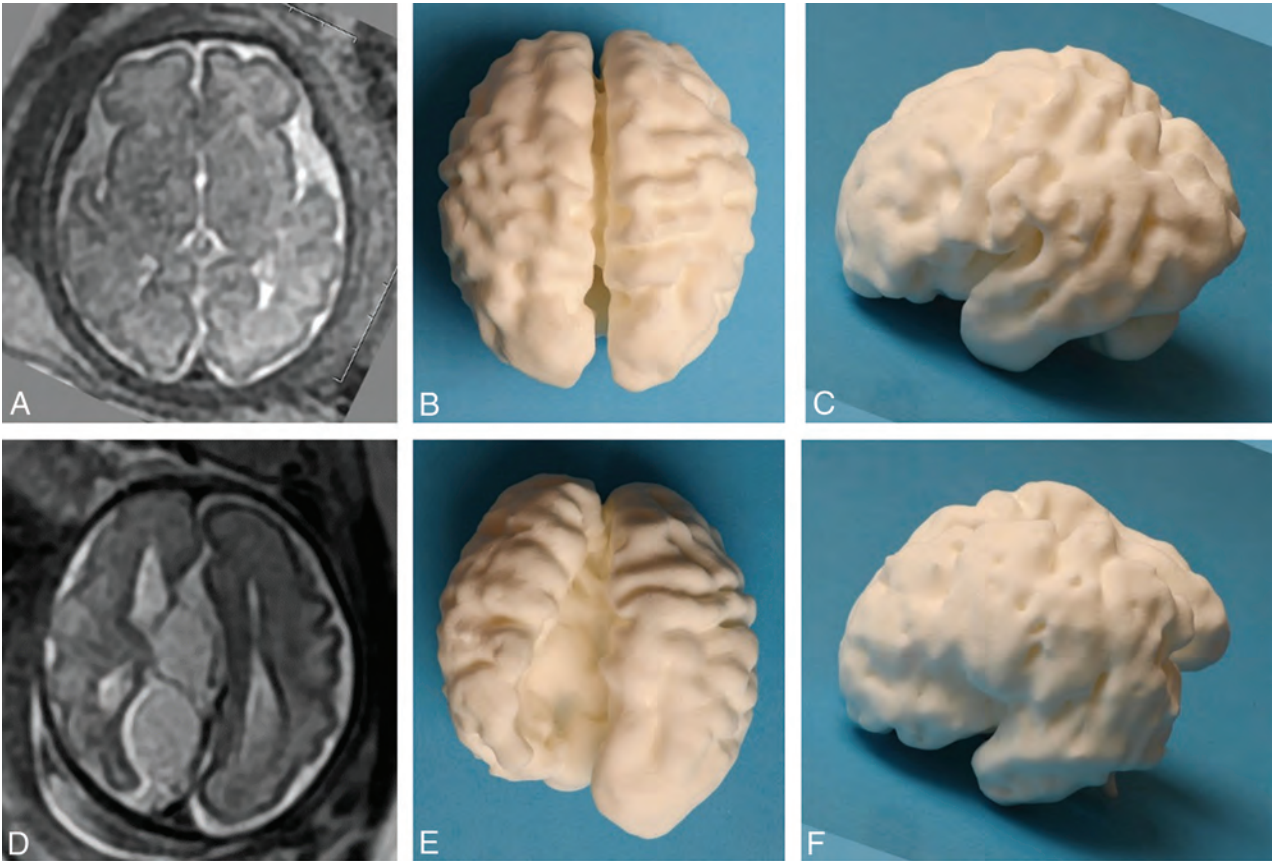


FIG 1. Images of the 3D printed model produced via laser sintering from an in utero MR imaging study performed at 30 weeks' gestational age in a fetus with ventriculomegaly and an interhemispheric cyst recognized on ultrasonography, compared with an age-matched fetus with no brain abnormality. A 2D single-shot fast spin-echo image in the axial plane of the normal brain is shown (A), along with superior (B) and left lateral (C) views of the 3D printed model. D–F, The matching images from the fetus with agenesis of the corpus callosum and extra-axial cysts, which do not communicate with the ventricular system (type II cysts of Barkovich et al),⁷ are shown. Note that the orientation of the 2D image has been altered to match the 3D model for ease of interpretation. The left hemisphere contains widespread heterotopia, a feature that was confirmed at postmortem examination.

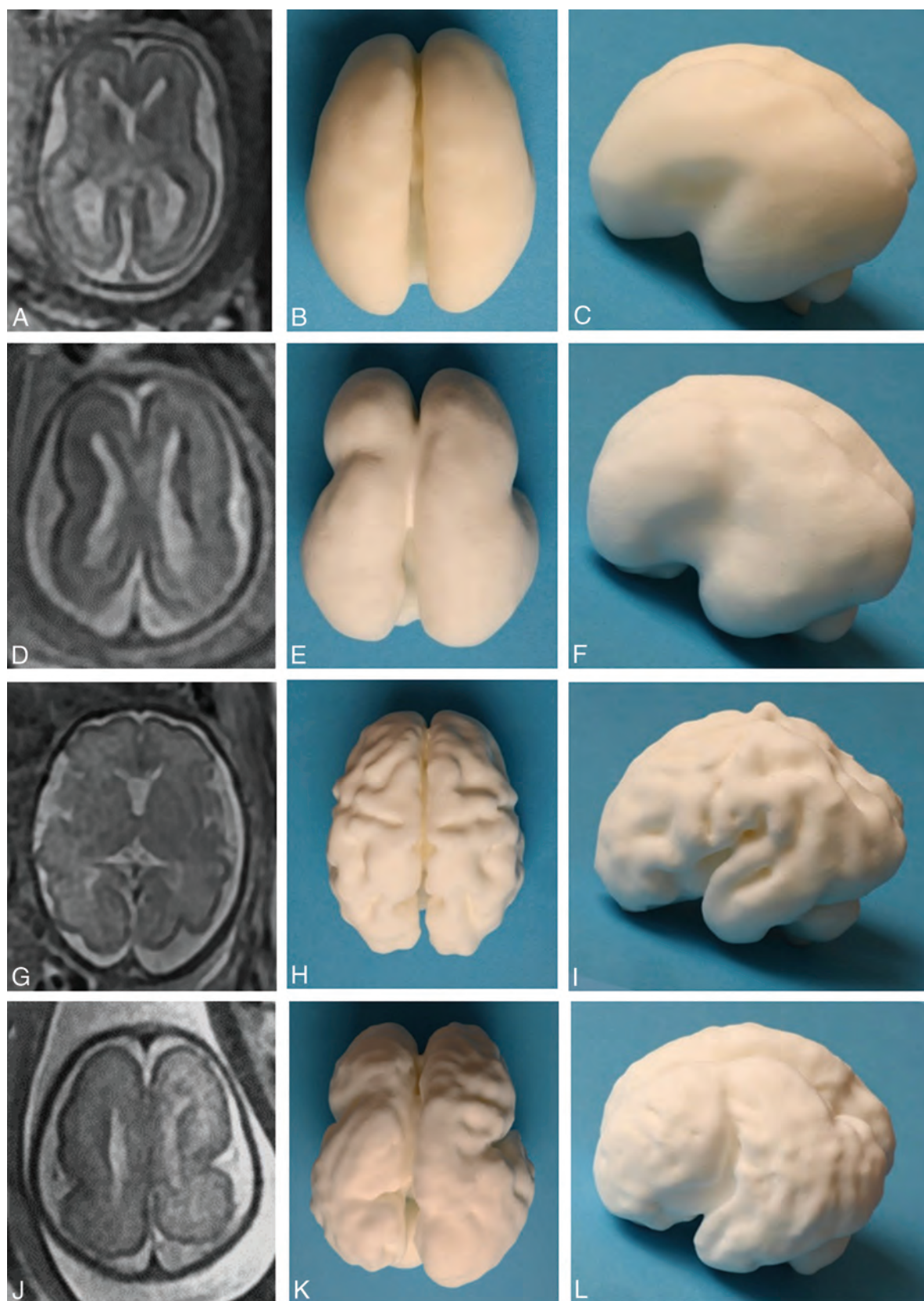


FIG 2. Images of the 3D printed models produced via laser sintering from 2 in utero MR imaging studies performed at 2 gestational ages in a fetus with lissencephaly compared with an age-matched fetus with no brain abnormality. A 2D single-shot fast spin-echo image in the axial plane of the normal brain at 22 weeks' gestation is shown (A), along with superior (B) and left lateral (C) views of the 3D printed model. The same format is shown for a healthy 30-week fetus (D–F) and the fetus with lissencephaly (G–L).

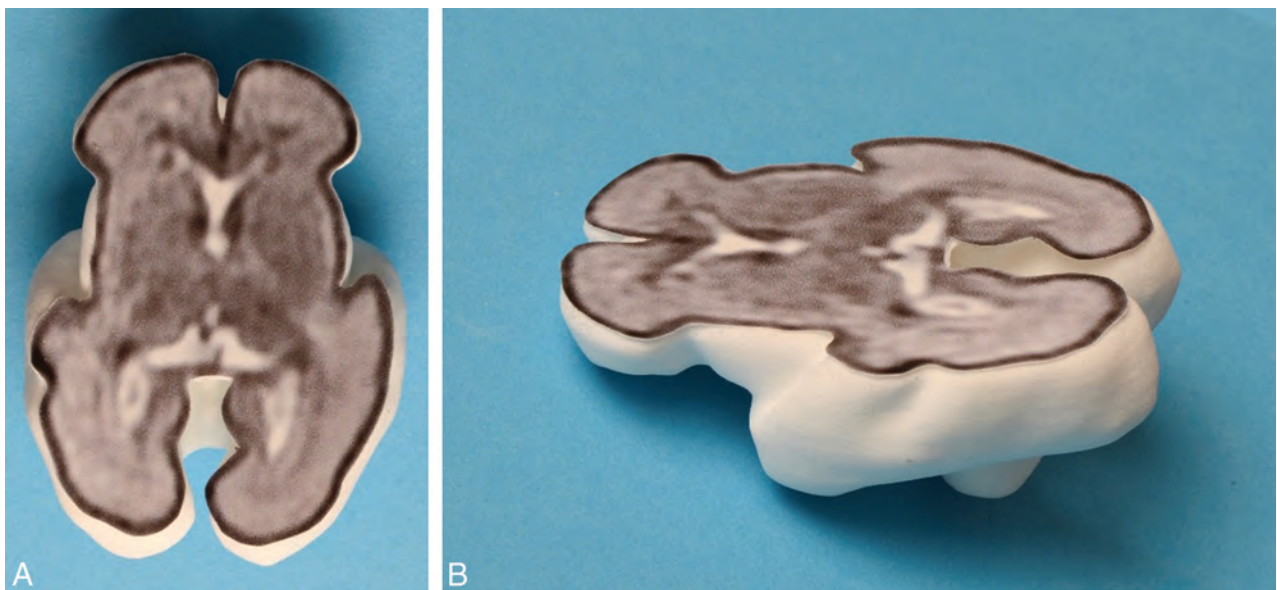


FIG 3. A 3D printed model produced via laser sintering with the internal anatomy of the brain shown from an attached 2D single-shot fast spin-echo image to produce a section of the fetal brain—superior (A) and oblique (B) projections.

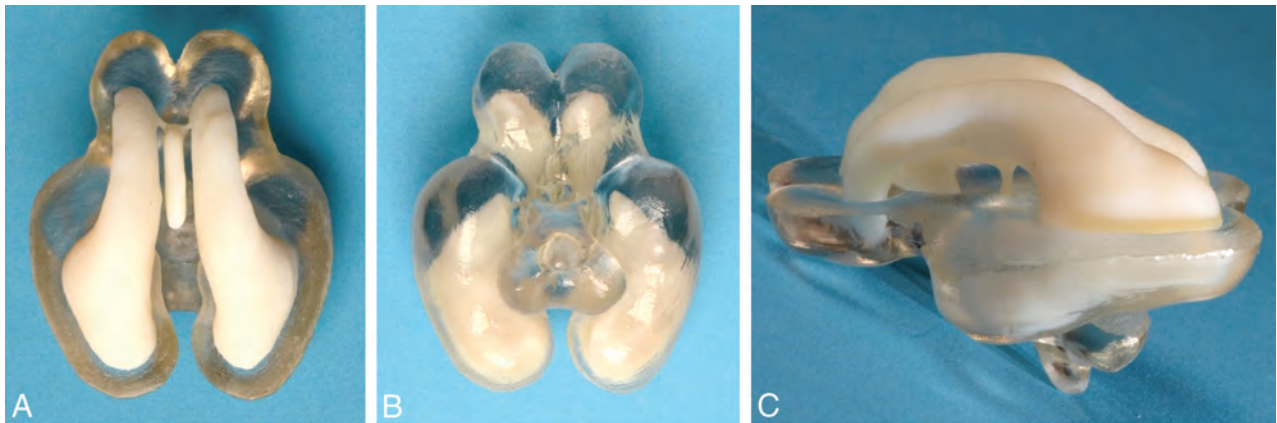


FIG 4. Dual-material 3D printed brain produced on an Objet Connex 500 jetting system (manufactured courtesy of Professor Richard Bibb, Loughborough Design School, Loughborough, UK). Separate STereoLithography files were exported from 3D Slicer, one consisting of the segmented entire ventricular system and the other of part of the brain parenchyma. The ventricular system is printed in the same white material as the other brains, while the parenchyma is printed in a clear material. The superior (A), inferior (B), and left lateral (C) views show the relationship between the ventricles and brain to advantage.

discussions of methods for and applications of 3D printing within the medical sector can be found elsewhere.^{5,6}

Application of 3D Models of the Fetal Brain

One of the major applications we envisage for this technology is trying to improve anatomic understanding and training of radiologists to develop their skills in fetal neuroimaging. We have created a fetal brain teaching file available for review, which consists of a number of cases with sample reports and background of the condition, with images from both the 2D studies and 3D printed models produced via laser sintering. The abnormal brain models consist of several of the more common brain malformations at various gestational ages along with age-matched controls (Figs 1 and 2). It is also possible to transpose 2D images from in utero MR imaging studies onto 3D models to enhance the understanding of fetal anatomy further. The 3D volume images can be manipulated into the same plane as the 2D images, and those

images are copied onto clear plastic with adhesive on 1 side to produce “transfers.” The STereoLithography file of the matched sections from the 3D printed model can be exported to produce a limited print of the model to produce discrete 3D printed sections of the fetal brain as shown in Fig 3. A further possibility is the production of models from multiple materials. For example in the case of the fetal brain models, it can be useful for showing clear differentiation of the ventricular system compared with the remainder of the brain parenchyma as shown in Fig 4. This is a 2-color part produced on an Objet Connex 500 Multi-Material 3D Printing system (<https://www.mcad.com/3d-printing/objet-connex-printers/connex-500/>).

In summary, we have outlined a method that can be used to produce 3D printed models and have described our approach to constructing 3D models of the fetal brain. The field is developing rapidly and presents a wide range of therapeutic and teaching opportunities for medicine and radiology in particular.

Disclosures: Paul D. Griffiths—*UNRELATED: Grants/Grants Pending:* research agreements with GE Healthcare* and Philips MS.* *Money paid to the institution.

REFERENCES

1. Wu ML, Ko CW, Chen TY, et al. **MR ventriculocisternography by using 3D balanced steady-state free precession imaging: technical note.** *AJNR Am J Neuroradiol* 2005;26:1170–73 Medline
2. Fedorov A, Beichel R, Kalpathy-Cramer J, et al. **3D Slicer as an image computing platform for the Quantitative Imaging Network.** *Magn Reson Imaging* 2012;30:1323–41 CrossRef Medline
3. Griffiths PD, Morris J, Larroche JC, et al. *Atlas of Fetal and Postnatal Brain MR*. Philadelphia: Mosby/Elsevier; 2010
4. Bayer SA, Altman J. *The Human Brain during the Third Trimester*. Boca Raton, Florida: CRC Press; 2004
5. Eggbeer D, Bibb R, Paterson AM. *Medical Modelling: The Application of Advanced Design and Rapid Prototyping Techniques in Medicine: Second Edition*. Cambridge: Elsevier Imprint: Woodhead Publishing Series in Biomaterials; 2015
6. Matsumoto JS, Morris JM, Foley TA, et al. **Three-dimensional physical modeling: applications and experience at Mayo Clinic.** *Radio-graphics* 2015;35:1989–2006 CrossRef Medline
7. Barkovich AJ, Simon EM, Walsh CA. **Callosal agenesis with cyst: a better understanding and new classification.** *Neurology* 2001;56:220–27 CrossRef Medline

Celebrating 35 Years of the AJNR

September 1981 edition

Central Nervous System Leukemia and Lymphoma: Computed Tomographic Manifestations

John J. Pagan¹
Herman I. Libshitz²
Sidney Wallace¹
L. Anne Hayman²

Computed tomographic (CT) abnormalities in the brain of patients with leukemia or lymphoma. Abnormalities included hemorrhage (nine), abscess (two), other brain tumor (one), and leucoencephalopathy (one). CT was normal in 374 patients. Diseases diagnosed by cerebrospinal fluid cytologic examination. Malignant masses were isodense or of greater density than normal brain. Increase in size or number of the masses indicated progression of disease. Chemotherapy was manifested by development of an enhancing rim. CT findings correlated with clinical course. The differential diagnosis of the various abnormalities is discussed.

Central nervous system involvement in leukemia and lymphoma is usually manifested as leptomeningeal dissemination of malignant disease into the brain parenchyma. Computed tomographic (CT) recognition of leptomeningeal dissemination of malignant disease is quite difficult. The CT description of brain involvement in leukemia and lymphoma is reviewed. Evidence of response to chemotherapy as differential diagnostic considerations are presented.

Materials and Methods

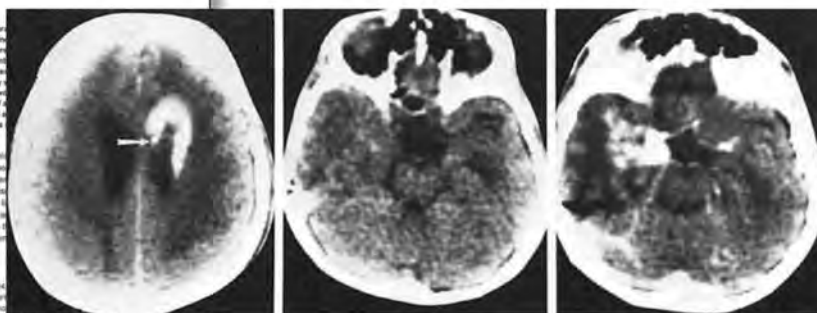
Over a 4 year period, 405 patients with leukemia (24 non-Hodgkin; 12 Hodgkin) underwent cerebral CT. The lesions following contrast administration. The CT scans correlated with the underlying malignancy, cerebrospinal fluid cytology, and treatment. All CT studies were performed with an EM 1010 scanner using a 60 sec scan time, 180° x 160 matrix, and 13 mm collimation. All scans were obtained either immediately after administration of 40 g of intravenous iodine or 1 hr following high dose (80 g) iodine contrast infusion [10]. Most patients also had noncontrast scans.

Results

Abnormalities in 24 of the 245 patients with leukemia, hemorrhages, abscesses, other tumors. These are limited by type of leukemia in table 1. Abnormalities in the lymphoma group and were patients (table 2).

Leukemia

Of the 245 leukemia patients, 59 underwent a



Received December 15, 1980; accepted after revision April 20, 1981.

¹Department of Diagnostic Radiology, University of Texas System Cancer Center, M. D. Anderson Hospital and Tumor Institute, 1515 Holcombe, Houston, TX 77030. Address reprint requests to J.J.P.

²Department of Radiology, University of Texas Health Science Center, Houston, TX 77030. This article appears in September/October 1981 AJNR and December 1981 AJR.

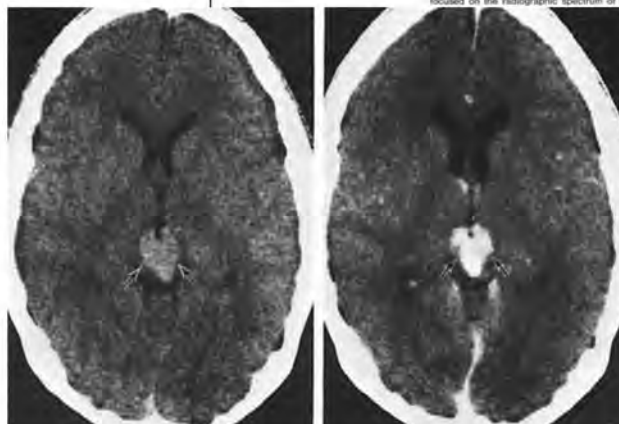
AJNR 2:387-403, September/October 1981
0195-9581/81/0005-0387\$01.00
© American Radiological Society

Pineal Region Tumors: Computed Tomographic-Pathologic Spectrum

Nancy N. Futrell¹
Anne G. Osborn¹
Bruce D. Cheson²

While several computed tomographic (CT) studies of pineal region tumors, few reports have concentrated on these uncommon lesions. Some authors have asserted that the CT appearance of many pineal tumors is virtually pathognomonic. A series of nine biopsy-proven pineal gland and eight other presumed pineal tumors is presented that illustrates their remarkable heterogeneity in both histopathologic and CT appearance. These tumors included germinomas, teratomas, astrocytomas, and other varieties. They had variable margins, attenuation, calcification, and supratentorial extension. Germinomas have the best response to radiation therapy. Biopsy of pineal region tumors is now feasible and is recommended for treatment planning.

Tumors of the pineal region account for less than 2% of all intracranial neoplasms [1]. While several reports of computed tomography (CT) of third ventricular neoplasms have included an occasional pineal tumor [2, 3], few have focused on the radiographic spectrum of these uncommon lesions [4]. Some of many pineal tumors is virtually pathognomonic. A series of nine biopsy-proven pineal gland and eight other presumed pineal tumors is presented that illustrates their remarkable heterogeneity in both histopathologic and CT appearance.



Over 15,000 consecutive CT scans. Four for the females was 27 years; for the males, ranging from 1 to 64 years. The histologic, roentgen, and roentgen, to histologic and hypophyseal (table 1). Pineal and other presumed pineal tumors is presented that illustrates their remarkable heterogeneity in both histopathologic and CT appearance.

Germinomas were either nodular or (1A) and showed marked, uniform enhancement (fig. 1B). Several were well

The Clinical Outcome of Posterior Reversible Encephalopathy Syndrome



We read with great interest the article by Karia et al¹ on posterior reversible encephalopathy syndrome (PRES) evaluating the association between the presence of enhancement in PRES and various clinical factors in a large series of 176 patients with PRES. They found that the presence or pattern of enhancement in posterior reversible encephalopathy syndrome was not associated with any of the tested variables. However, they found a statistical association between MR imaging severity and outcomes, confirming that the grading of MR imaging severity may aid in determining the prognosis of patients with PRES. While we agree with the conclusions of the study, prediction of clinical outcomes in patients with PRES remains a challenging and controversial subject. The purpose of this correspondence is to discuss the current ideas regarding prognosis of PRES, which is still uncertain and open to discussion.

Although PRES is increasingly being recognized and successfully treated, the most important factors affecting its outcomes, such as permanent neurologic deficits, discharge status, and mortality, have not yet been well characterized.² In our study including 70 patients with PRES, we found that there was no significant correlation between imaging patterns and clinical risk factors. Cytotoxic edema, intracranial hemorrhage, and abnormal enhancement did not show correlation with blood pressure, but correlated with higher edema scores. Furthermore, our recent study demonstrated that cytotoxic edema in PRES is frequently found in association with a larger area of vasogenic edema, which is probably related to regional decreased perfusion and vasculopathy. Presence of atypical neuroimaging appearances, such as cytotoxic edema, intracranial hemorrhage, and abnormal enhancement, are useful for prognosis in PRES because these findings may reflect intrinsic endothelial injury or BBB disruption.³ Based on the results of these studies, severity of brain edema in patients with PRES should be considered as one of the most significant risk factors in the clinical prognosis of this disorder. The specific etiology of PRES and biochemical parameters may represent the other important factors for its prognosis.⁴ Physicians should be aware of the various etiologies of PRES to allow for rapid diagno-

sis and treatment and to reduce morbidity of PRES. Prospective exploration is warranted to establish the imaging biomarker associated with unfavorable clinical outcomes in PRES.

The most widely used outcome measure of the degree of disability or dependence in patients with stroke is mRS score. Some investigators have used mRS score as a prognostic index during clinical follow-up of patients with acute illness at 1- and 3-month intervals after discharge. Clinical outcome was assessed as degree of disability or death by using mRS score. In this original research, the authors adopted a similar 5-category clinical outcome evaluation based on one of their prior studies of PRES and acute toxic leukoencephalopathy: grade 0, return to baseline clinical condition; grade 1, minimal residual cognitive deficit; grade 2, mild persistent neurologic deficit; grade 3, moderate persistent neurologic deficit; and grade 4, severe outcome, including no improvement, seizures, coma, or death. Glasgow Outcome Scale score on day 90 (67 days after onset of severe PRES) was also adopted as the primary evaluation criterion by some investigators, which may better reflect both mortality and morbidity, especially in critically ill patients or fatal cases.⁵

The diagnosis of PRES relies mainly on clinical symptoms and radiologic findings. We do agree with Fugate and Rabinstein's⁶ statement that "the diagnosis of PRES is not mainly radiological; the clinical context and the judgment of the clinician are crucial to making the correct diagnosis." Clinical symptoms are the prerequisite in the diagnosis of PRES, and imaging findings are the essential condition. Neuroimaging is critical for prompt recognition of this entity and differentiation from other diseases. Though conventional MR imaging protocol is considered to be the criterion standard for the diagnosis or evaluation of PRES, DWI combined with ADC maps is sensitive for differentiating cytotoxic edema from vasogenic edema. Therefore, it is preferable to include DWI and ADC maps in work-up. In practice, ADC mapping is also helpful in some cases in which clinical diagnosis is unclear or difficult to determine.

In conclusion, the roles of imaging findings, clinical symptoms, and biochemical parameters in predicting prognosis of PRES warrant further investigation. A unified diagnostic algorithm should be sought to standardize the diagnosis of PRES and description of clinical outcomes, which will facilitate future research in exploring the role of neuroimaging for this disorder.

Indicates open access to non-subscribers at www.ajnr.org

<http://dx.doi.org/10.3174/ajnr.A4853>

Disclosures: We declare no competing interests. Bo Gao reports a research grant from National Natural Science Foundation of China (No. 81471645). Meng Law reports grant support from Toshiba American Medical,* a consulting fee/honorarium from Bracco Diagnostics, and travel support from Guerbet. *Money paid to the institution.

REFERENCES

1. Karia SJ, Rykken JB, McKinney ZJ, et al. **Utility and significance of gadolinium-based contrast enhancement in posterior reversible encephalopathy syndrome.** *AJNR Am J Neuroradiol* 2016;37:415–22 CrossRef Medline
2. Lv C, Gao B. **Can clinical and MRI findings predict the prognosis of variant and classical type of posterior reversible encephalopathy syndrome (PRES)? Still a challenge.** *Acta Radiol* 2015;56:NP3–4 CrossRef Medline
3. Junewar V, Verma R, Sankhwar PL, et al. **Neuroimaging features and predictors of outcome in eclamptic encephalopathy: a prospective observational study.** *AJNR Am J Neuroradiol* 2014;35:1728–34 CrossRef Medline
4. Alhilali LM, Reynolds AR, Fakhra S. **A multi-disciplinary model of risk factors for fatal outcome in posterior reversible encephalopathy syndrome.** *J Neurol Sci* 2014;347:59–65 CrossRef Medline
5. Legriel S, Schraub O, Azoulay E, et al. **Determinants of recovery from severe posterior reversible encephalopathy syndrome.** *PLoS One* 2012;7:e44534 CrossRef Medline
6. Fugate JE, Rabinstein AA. **Posterior reversible encephalopathy syndrome: clinical and radiological manifestations, pathophysiology, and outstanding questions.** *Lancet Neurol* 2015;14:914–25 CrossRef Medline

 **B. Gao**

Department of Radiology
Yantai Yuhuangding Hospital
Qingdao University
Yantai, Shandong, China
Department of Radiology
Keck School of Medicine
University of Southern California
Los Angeles, California

 **A. Lerner**

 **M. Law**

Department of Radiology
Keck School of Medicine
University of Southern California
Los Angeles, California

REPLY:

We appreciate the interest in our article and comments made by Dr Gao et al. We agree that prediction of clinical outcomes in patients with posterior reversible encephalopathy syndrome (PRES) is a challenging subject. Dr Gao et al raised interesting points in their letter regarding both measures of MR imaging severity and clinical outcomes.

First, while clinical outcomes were addressed in the study, the study in question focused primarily on the presence of enhancement in PRES and whether it was associated with any of the measured clinical factors. Because no such associations were found, we suggested that gadolinium-based contrast may not be necessary in diagnosing or assessing the degree of severity of PRES.¹ As noted, however, our results did show a significant association between clinical outcomes and the extent of the T2 signal abnormalities used to grade the radiologic severity.

Dr Gao et al suggested that regions of cytotoxic edema in PRES (visible on DWI) are frequently associated with larger areas of vasogenic edema. This observation may be in agreement with a hypothesis regarding the pathophysiology of restricted diffusion in PRES, in which endothelial dysfunction and vasogenic edema and ensuing potential compression of local microcirculation or vasospasm lead to resultant ischemia or infarction.²⁻⁴ Previous studies have shown that this phenomenon occurs in a minority of patients with PRES and that such areas of reduced diffusion (ie, cytotoxic edema, low ADC values) typically occur within larger areas of elevated diffusion (ie, vasogenic edema, high ADC values) and may assume a punctate or gyriform pattern.^{2,5} Better evidence is needed to determine whether the presence of cytotoxic edema correlates with clinical outcome. We also opine that the presence of hemorrhage, ranging from frank parenchymal (in up to 20%) to microhemorrhage (in >50%), needs to be further assessed with regard to its effect on outcome.^{2,6}

In regard to the different scales used to predict outcome, we believe that our outcome score scale is not entirely dissimilar to the modified Rankin Scale, reflecting the degree of residual neurologic disability in patients with stroke, or from the Glasgow Outcome Score (GOS), useful for global assessment following brain injury. The GOS has been used by Legriel et al⁷ to determine

outcomes of severe PRES 90 days after the presentation. Future studies could evaluate whether any of these clinical scales best reflect eventual outcome and ultimately whether MR imaging severity or any of the MR imaging findings at initial presentation correlate with outcome.

REFERENCES

1. Karia SJ, Rykken JB, McKinney ZJ, et al. **Utility and significance of gadolinium-based contrast enhancement in posterior reversible encephalopathy syndrome.** *AJNR Am J Neuroradiol* 2016;37:415–22 CrossRef Medline
2. McKinney AM, Short J, Truwit CL, et al. **Posterior reversible encephalopathy syndrome: incidence of atypical regions of involvement and imaging findings.** *AJR Am J Roentgenol* 2007;189:904–12 CrossRef Medline
3. Covarrubias DJ, Luetmer PH, Campeau NG. **Posterior reversible encephalopathy syndrome: prognostic utility of quantitative diffusion-weighted MR images.** *AJNR Am J Neuroradiol* 2002;23:1038–48 Medline
4. Ay H, Buonanno FS, Schaefer PW, et al. **Posterior leukoencephalopathy without severe hypertension: utility of diffusion-weighted MRI.** *Neurology* 1998;51:1369–76 CrossRef Medline
5. Gao B, Yu BX, Li RS, et al. **Cytotoxic edema in posterior reversible encephalopathy syndrome: correlation of MRI features with serum albumin levels.** *AJNR Am J Neuroradiol* 2015;36:1884–89 CrossRef Medline
6. McKinney AM, Sarikaya B, Gustafson C, et al. **Detection of microhemorrhage in posterior reversible encephalopathy syndrome using susceptibility-weighted imaging.** *AJNR Am J Neuroradiol* 2012;33:896–903 CrossRef Medline
7. Legriel S, Schraub O, Azoulay E, et al. **Determinants of recovery from severe posterior reversible encephalopathy syndrome.** *PLoS One* 2012;7:e44534 CrossRef Medline

S. Khanipour Roshan

A.M. McKinney

Department of Radiology

University of Minnesota

Minneapolis, Minnesota

S.J. Karia

Department of Neuroradiology

John Radcliffe Hospital

Oxford University Hospitals

Oxford, UK

H. Tore

J.B. Rykken

Department of Radiology

University of Minnesota

Minneapolis, Minnesota

<http://dx.doi.org/10.3174/ajnr.A4876>

Utility and Significance of Gadolinium-Based Contrast Enhancement in Posterior Reversible Encephalopathy Syndrome

We read with considerable interest the article concerning the significance of gadolinium-based contrast enhancement in patients with posterior reversible encephalopathy syndrome (PRES).¹ The authors have performed a retrospective study on a large patient population and have demonstrated that gadolinium administration is not warranted in these patients because PRES is a clinical-radiologic diagnosis made in appropriate settings and the presence or lack of contrast enhancement does not add to the existing diagnosis algorithm or help in the prognosis of the patients.

A few points merit consideration after reading this article. First, they included 135 patients with a mean age of 40 ± 20 years with range from 7 to 82 years. However, they have not separately mentioned the pediatric patients, who have been shown to follow a different clinical-radiologic spectrum.¹ In our review of pediatric patients with PRES, we have found that contrast enhancement is variably seen in pediatric populations, ranging from 2% to 53%. This variability is likely due to the multiple etiologies leading to PRES, with imaging in patients having hemato-oncologic malignancies and undergoing chemotherapy predominantly showing enhancement. In our own pediatric PRES cohort, renal disease was seen in 62.5% of patients and contrast could not be given. Only 2 patients undergoing chemotherapy showed leptomeningeal enhancement. In addition, pediatric patients commonly show atypical MR imaging findings.² These findings indicate that endothelial dysfunction may be the primary mechanism in addition to loss of autoregulation.

We also did not find any correlation among contrast enhancement, MR imaging severity of disease, and patient outcome in our

pediatric PRES cohort. A description from the authors of their pediatric cohort, with underlying diseases and pattern of enhancement, may further add to our existing knowledge.

Second, they compared the clinical outcome with the MR imaging severity index as described previously. However, as per our review, the pediatric population frequently shows atypical findings such as frontal lobe, basal ganglia, and brain stem involvement²; thus, the conventional MR imaging severity index, based on location, may not be applicable when assessing the prognostic significance in children.

We find the published article useful because it reinforces our own experience of not using contrast unless some alternative pathology is being considered. A pediatric population in which the predominant etiologic cohort is underlying renal disease may not be given contrast, and other patients with PRES may not benefit much from contrast administration as far as diagnosis and clinical outcome are concerned.

REFERENCES

1. Karia SJ, Rykken JB, McKinney JK, et al. **Utility and significance of gadolinium-based contrast enhancement in posterior reversible encephalopathy syndrome.** *AJNR Am J Neuroradiol* 2016;37:415–22 CrossRef Medline
2. Gupta V, Bhatia V, Khandelwal N, et al. **Imaging findings in pediatric posterior reversible encephalopathy syndrome (PRES): 5 years of experience from a tertiary care center in India.** *J Child Neurol* 2016 Apr 12. [Epub ahead of print] CrossRef Medline

© V. Bhatia

© V. Gupta

© N. Khandelwal

Department of Radio-Diagnosis
Postgraduate Institute of Medical Education and Research
Chandigarh, India

<http://dx.doi.org/10.3174/ajnr.A4847>

REPLY:

We would like to thank Dr Bhatia and colleagues for their interest in our article and their comments. Indeed, we did not separately analyze the pediatric population in our cohort, and we acknowledge it would be interesting to further evaluate this group and compare our findings with theirs.

Therefore, we further investigated our subpopulation of posterior reversible encephalopathy syndrome cases and updated our data base to include additional pediatric patients to evaluate the importance of contrast enhancement. In total, we identified 30 contrast-enhanced MR imaging cases of pediatric patients with posterior reversible encephalopathy syndrome. Of these, 26 (87%) patients were immunosuppressed. Our cohort's characteristics substantially differ from the authors' own cohort (62.5% with renal disease); hence, there is a limitation in comparing findings between both studies.¹

Within this group, 60% ($n = 18$) of patients demonstrated evidence of contrast enhancement, a rate higher than our earlier findings of 43.7% in the general population.² Similarly, we found no correlation between presence/pattern of contrast enhancement and any of the outcome scores of tested variables. However, and interestingly, we no longer found an association between MR imaging severity and outcome scores in the new pediatric cohort ($P < .05$). This contrasts with our earlier findings in the general population, but this new cohort suffers considerably from its much smaller size and diminished statistical power.

We find the authors' observations regarding the frequency of atypical MR imaging features and how that could limit our proposed MR severity index scale interesting. However, we believe that in both our current study and a previous study from 1 of the authors (A.M.M), these atypical findings would be appropriately covered in this scale.³ In particular, Casey et al⁴ and Covarrubias et al⁵ previously suggested high severity in posterior reversible

encephalopathy syndrome when basal ganglia or brain stem involvement was found, which was taken into account when grading MR imaging severity. Atypical features in posterior reversible encephalopathy syndrome previously were shown to be relatively frequent, with frontal involvement seen in up to 78.9% of patients, thalamic involvement in up to 30.3%, and cerebellar involvement in up to 34.2%.³

REFERENCES

1. Gupta V, Bhatia V, Khandelwal N, et al. **Imaging findings in pediatric posterior reversible encephalopathy syndrome (PRES): 5 years of experience from a tertiary care center in India.** *J Child Neurol* 2016 Apr 12. [Epub ahead of print] Medline
2. Karia SJ, Rykken JB, McKinney ZJ, et al. **Utility and significance of gadolinium-based contrast enhancement in posterior reversible encephalopathy syndrome.** *AJNR Am J Neuroradiol* 2016;37:415–22 CrossRef Medline
3. McKinney AM, Short J, Truwit CL, et al. **Posterior reversible encephalopathy syndrome: incidence of atypical regions of involvement and imaging findings.** *AJR Am J Roentgenol* 2007;189:904–12 CrossRef Medline
4. Casey SO, Sampaio RC, Michel E, et al. **Posterior reversible encephalopathy syndrome: utility of fluid-attenuated inversion recovery MR imaging in the detection of cortical and subcortical lesions.** *AJNR Am J Neuroradiol* 2000;21:1199–206 Medline
5. Covarrubias DJ, Luetmer PH, Campeau NG. **Posterior reversible encephalopathy syndrome: prognostic utility of quantitative diffusion-weighted MR images.** *AJNR Am J Neuroradiol* 2002;23:1038–48 Medline

S.J. Karia

Department of Neuroradiology
John Radcliffe Hospital
Oxford University Hospitals
Oxford, United Kingdom

A.M. McKinney

J.B. Rykken

S. Khanipour Roshan

H. Tore

Department of Radiology
University of Minnesota
Minneapolis, Minnesota

<http://dx.doi.org/10.3174/ajnr.A4872>

Measures of Neuroradiologic Activities in the “*Air du Temps*”

We read with great interest the article by Wintermark et al, “Non-Relative Value Unit–Generating Activities Represent One-Fifth of Academic Neuroradiologist Productivity,”¹ published on-line in March. It is in the “*air du temps*” (ie, spirit of the time or timely), when everything is quantified by being more economically productive.

In many hospitals in Switzerland and probably in most European countries, the clinical, scientific, and management times are not clearly defined and separated. This shortcoming is a real problem. Additionally, we do not have just specialized tumors boards as mentioned in the article but also other multidisciplinary meetings to discuss daily “routine” cases. These cases have been read and interpreted with formal reports written by different neuroradiologists. The additional question raised in our environment is whether these boards bring any additional value and whether, in this situation, the neuroradiologist’s time task is measured correctly. Indeed, we are confronted with not just presenting the case once but very often rediscussing it and repreparing it, sometimes with additional postprocessing and follow-up discussions.

Therefore, in our opinion, this type of application could be a double-edged sword because as Wintermark et al have reported,

recording time accurately is a difficult task. Indeed, by appearing to be very exact, it can fully underestimate the time devoted to different tasks. However, if correctly adapted and used, this type of application will be generalized in neuroradiology departments, first, to obtain enough resources; second, to determine the standards for the recommended number of cases that each working neuroradiologist should report²; third, to detect unnecessary or redundant tasks; and finally, to plan the necessary future workforce.

REFERENCES

1. Wintermark M, Zeineh M, Zaharchuk G, et al. **Non-relative value unit–generating activities represent one-fifth of academic neuroradiologist productivity.** *AJNR Am J Neuroradiol* 2016 Mar 3. [Epub ahead of print] CrossRef Medline
2. Board of the Faculty of Clinical Radiology. The Royal College of Radiologists. Clinical radiology workload: guidance on radiologists’ reporting figures. January 2012. https://www.rcr.ac.uk/sites/default/files/publication/BFCR%2812%2912_workload_0.pdf. Accessed April 29, 2016

© M.I. Vargas

© K. Lövblad

Division of Neuroradiology
Geneva University Hospitals
Geneva, Switzerland

<http://dx.doi.org/10.3174/ajnr.A4854>

Is There a Need for Contrast and Local Anesthetic in Cervical Epidural Steroid Injections?

We read with great interest the recent article by Lagemann et al¹ regarding the extraforaminal needle tip position for CT-fluoroscopic cervical transforaminal epidural steroid injections to reduce the risk of intravascular injection.

The technique for injection is outlined in the “Materials and Methods” section. The authors administered a trial dose of 0.3 mL of iohexol contrast (Omnipaque 300; GE Healthcare, Piscataway, New Jersey) to determine whether the needle was intravascular, followed by a cocktail of 1.2 mL of 2.5–5 mg/mL of bupivacaine analgesic, 8 mg of dexamethasone, and 0.3 mL of iohexol.

First, we question the use of bupivacaine in transforaminal epidural steroid injections. The inadvertent intravascular injection of bupivacaine has been associated with vasospasms of arterioles and increases the risk of CNS infarction.² There is also no lasting analgesic benefit from the extraforaminal injection of local anesthetic; thus, we propose the use of local anesthetic to the skin at the time of induction of the needle and none further in the procedure.

As highlighted in our Letter previously published in this journal, we question the use of contrast in cervical injections.³ The inclusion of contrast gives the radiologist a false sense of security (as seen in the article by Lagemann et al with over half [55%] of the intravascular injections of dexamethasone having no evidence of the intravascular positioning on the trial contrast dose). Real-time imaging, such as digital subtraction angiography, would be needed to accurately detect the intravascular injection. Evidence shows that dexamethasone is likely safe when inadvertently in-

jected intravascularly.^{4,5} By including contrast in this cocktail, you also introduce the risk of contrast reaction. Given the lack of adverse events with intravascular injection of dexamethasone and the poor sensitivity for identifying intravascular positioning, we propose the omission of contrast from this procedure.

In our center during the past 8 years of transforaminal extraforaminal injections with this technique, there have been no adverse events. We propose the use of a small volume of 1% lidocaine to the skin and 2–8 mg of dexamethasone injected extraforaminally under CT guidance.

REFERENCES

1. Lagemann GM, Yannes MP, Ghodadra A, et al. **CT-fluoroscopic cervical transforaminal epidural steroid injections: extraforaminal needle tip position decreases risk of intravascular injection.** *AJNR Am J Neuroradiol* 2016;37:766–72 CrossRef Medline
2. MacMahon PJ, Eustace SJ, Kavanagh EC. **Injectable corticosteroid and local anesthetic preparations: a review for radiologists.** *Radiology* 2009;252:647–61 CrossRef Medline
3. Ryan TM, Kavanagh EC, MacMahon PJ. **Is there a need for contrast administration prior to CT-guided cervical nerve root block?** *AJNR Am J Neuroradiol* 2013;34:E45 CrossRef Medline
4. Scanlon GC, Moeller-Bertram T, Romanowsky SM, et al. **Cervical transforaminal epidural steroid injections: more dangerous than we think?** *Spine* 2007;32:1249–56 CrossRef Medline
5. Okubadejo GO, Talcott MR, Schmidt RE, et al. **Perils of intravascular methylprednisolone injection into the vertebral artery: an animal study.** *J Bone Joint Surg Am* 2008;90:1932–38 CrossRef Medline

✉ M.P. Bolger

✉ P.J. MacMahon

✉ E.C. Kavanagh

Department of Radiology
Mater Misericordiae University Hospital
Dublin, Ireland

<http://dx.doi.org/10.3174/ajnr.A4881>

REPLY:

We thank Bolger et al for their commentary regarding our recent article. CT guidance is still a relatively new technique for cervical transforaminal epidural steroid injections (TFESIs), with the optimal methodology for many details of the procedure yet to be elucidated by empiric investigation. We hope that academic discussion will improve procedural methodology for all practitioners.

In response to the first issue raised by our colleagues, we argue that bupivacaine is an important component of cervical TFESIs because it provides an almost immediate local analgesic effect, which allows us to assess pain relief before the patient leaves our procedure facility. This diagnostic information is invaluable to our referring surgeons, who often use our cervical TFESIs as a presurgical planning tool to determine the exact level of radiculopathy before spine surgery. In these cases, determining the patient's almost immediate response to bupivacaine is the clinician's principal goal, not long-term pain relief from steroid. The clear benefit of bupivacaine in these cases must be balanced against what appears to be a largely theoretical risk of complications from intravascular injection of bupivacaine at the small doses we use: During more than 2 decades of performing thousands of cervical injections, we have never had a known minor or major complication attributable to bupivacaine.

We also argue that the trial contrast dose is a valuable step in cervical TFESI. Our use of the trial contrast dose, nevertheless, was followed, in many cases, by intravascular injection of steroid. Concluding, however, that contrast should not be used falls into

the nirvana fallacy (that is, reasoning that because a solution is imperfect, it should be rejected). In our article, the trial contrast dose was successfully used to identify intravascular needle-tip position, with subsequent needle repositioning and no intravascular injection of steroid, in 10/13 (77%) large-volume intravascular injections. If one used the technique described by Bolger et al, these intravascular needle positions would be missed, and all steroids for these cases would be injected intravascularly. This result would effectively remove the local delivery of anti-inflammatory steroid from the region of the targeted nerve root, which is, for Bolger et al, the intent of the procedure. In regard to the small risk of contrast reaction, we follow the American College of Radiology recommendations for premedication.¹ If the patient has a mild allergy (hives), then we premedicate with oral prednisone and diphenhydramine; if the allergy is more severe, then we do not use iodinated contrast and may not perform the procedure at all, at the discretion of the proceduralist. During more than 2 decades of performing cervical injections, we have never had a known complication attributable to contrast reaction.

REFERENCE

1. Manual on Contrast Media. Version 10.1, 2015. American College of Radiology Committee on Drugs and Contrast Media. <http://www.acr.org/Quality-Safety/Resources/Contrast-Manual>. Accessed May 29, 2016

G.M. Lagemann

M.P. Yannes

A. Ghodadra

W.E. Rothfus

V. Agarwal

Department of Radiology
University of Pittsburgh Medical Center
Pittsburgh, Pennsylvania

<http://dx.doi.org/10.3174/ajnr.A4880>